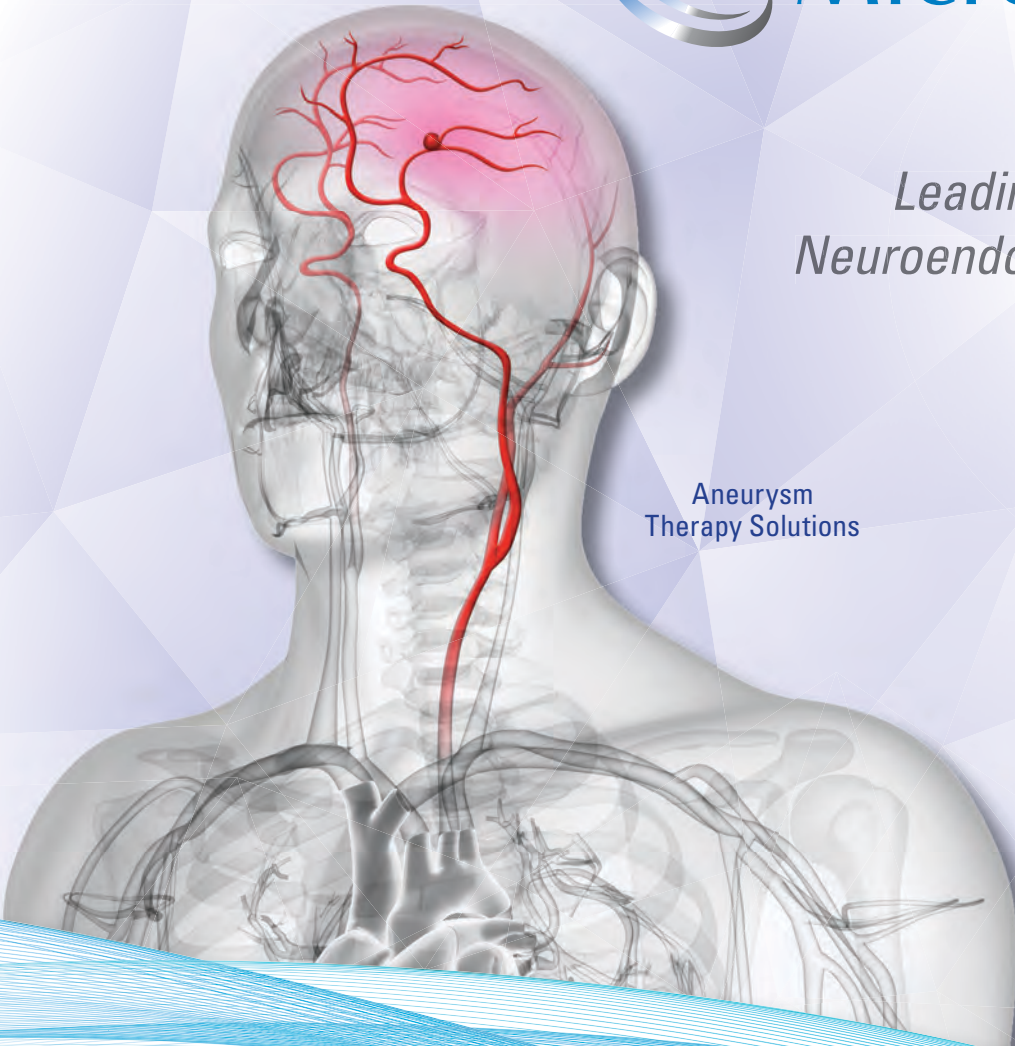




*Leading the Way in  
Neuroendovascular Therapy*

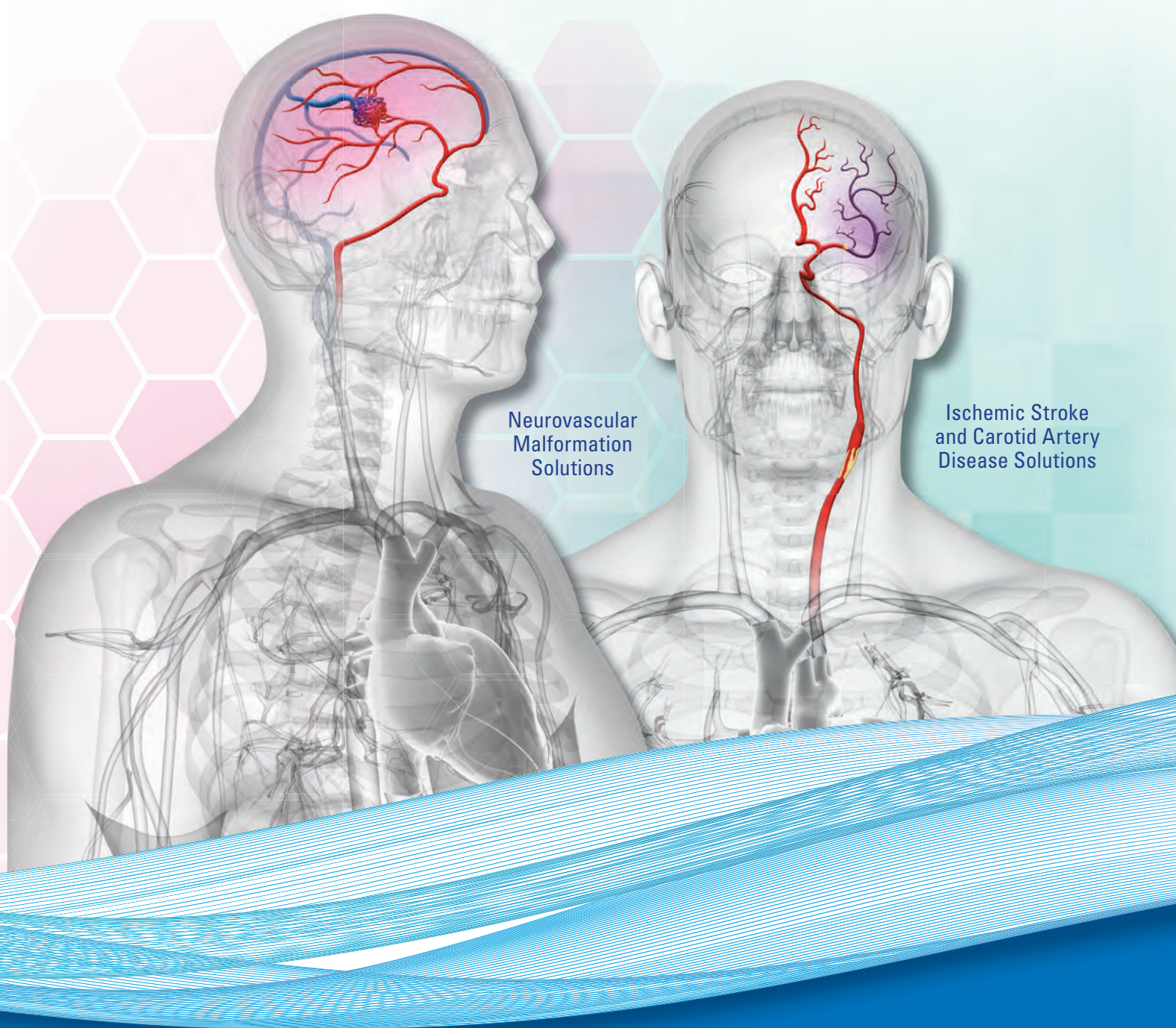
Aneurysm  
Therapy Solutions



**A 360-Degree Approach to  
Performance Based Solutions**

**[microvention.com](http://microvention.com)**

MICROVENTION is a registered trademark of MicroVention, Inc. Refer to Instructions for Use for additional information. © 2016 MicroVention, Inc. 11/16



Neurovascular  
Malformation  
Solutions

Ischemic Stroke  
and Carotid Artery  
Disease Solutions

For more information or a product demonstration,  
contact your local MicroVention representative:



**MicroVention, Inc.**  
**Worldwide Headquarters**  
1311 Valencia Avenue  
Tustin, CA 92780 USA  
MicroVention UK Limited  
MicroVention Europe, S.A.R.L.  
MicroVention Deutschland GmbH

PH +1.714.247.8000

PH +44 (0) 191 258 6777

PH +33 (1) 39 21 77 46

PH +49 211 210 798-0

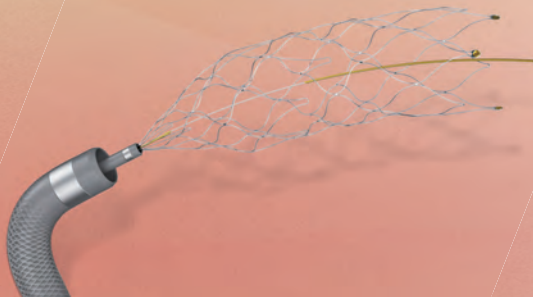
**INNOVATIVE SOLUTIONS** for the treatment of neurovascular diseases



**DERIVO<sup>®</sup> Embolisation Device and ACCLINO<sup>®</sup> flex Stent**  
for the treatment of intracranial aneurysms



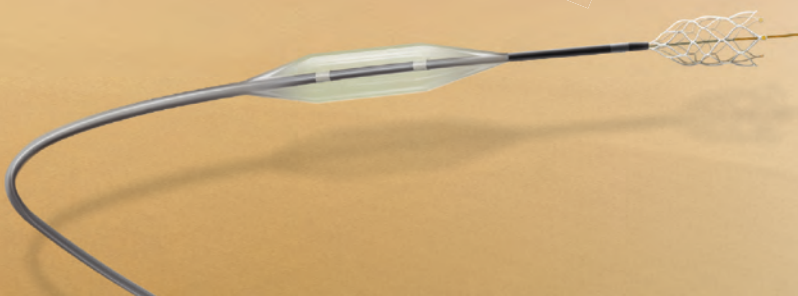
NeuroSlider<sup>®</sup> Microcatheter



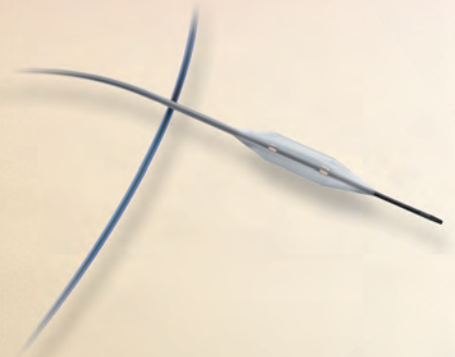
**APERIO<sup>®</sup> Thrombectomy Device, NeuroSlider<sup>®</sup> and NeuroBridge<sup>®</sup>** for acute stroke care



NeuroBridge<sup>®</sup> Intermediate Catheter



**CREDO<sup>®</sup> Stent with NeuroSpeed<sup>®</sup> PTA Balloon Catheter**  
for the treatment of intracranial stenosis



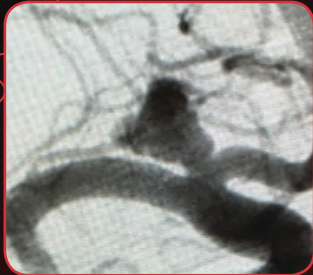
NeuroSpeed<sup>®</sup> PTA Balloon Catheter

CREDO<sup>®</sup> Stent only available within ASSISTENT – Acandis Stenting of Intracranial STENosis-regisTry

# BARRICADE™ COIL SYSTEM

## COILS THAT PERFORM

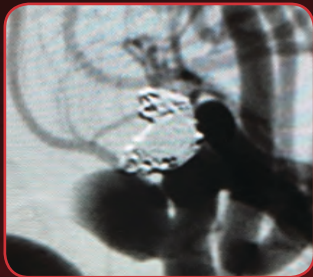
Treatment and 10 Month Follow-up of Right ICA Terminus Aneurysm and Left Pcom Aneurysm



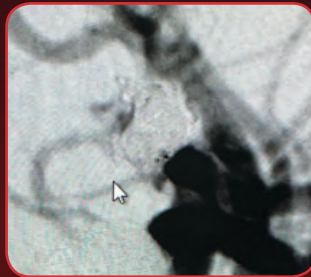
PRE-TREATMENT RIGHT ICA



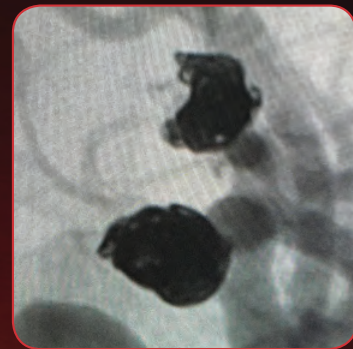
POST-TREATMENT RIGHT ICA



PRE-TREATMENT LEFT PCOM



POST-TREATMENT LEFT PCOM



10 MONTH FOLLOW-UP

“The Barricade Coil System provided great versatility in treating these two aneurysms with diverse morphologies. I am impressed with the stable and complete occlusion of both aneurysms at follow-up.”

-Timothy Malisch, M.D.

## COILS THAT SAVE \$

BARRICADE  
COILS  
SAVED  
\$6,710\*

Images courtesy of Timothy Malisch, M.D.

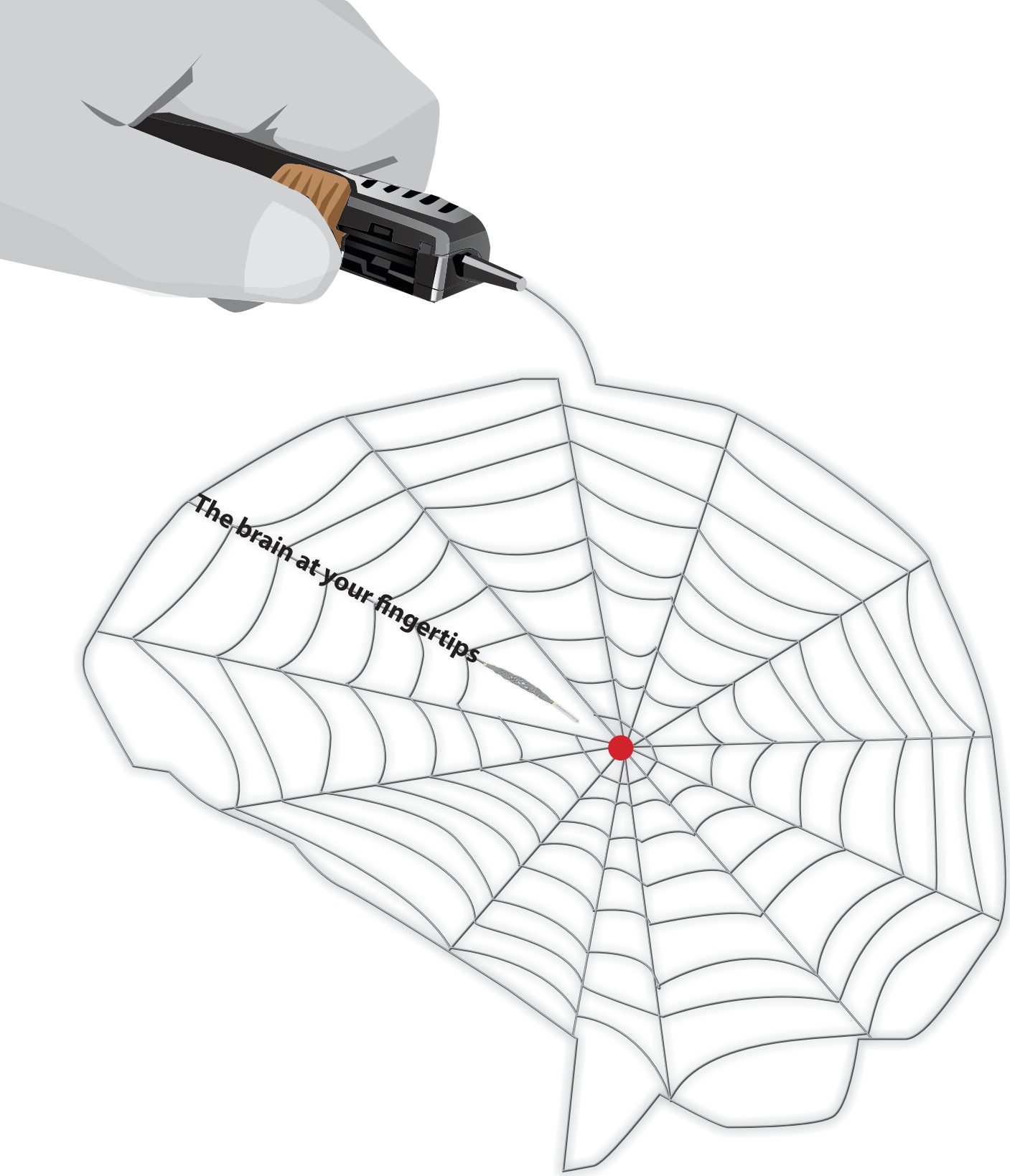
\* Estimated savings in this case, data on file.

The Barricade Coil System is intended for the endovascular embolization of intracranial aneurysms and other neurovascular abnormalities such as arteriovenous malformations and arteriovenous fistulae. The System is also intended for vascular occlusion of blood vessels within the neurovascular system to permanently obstruct blood flow to an aneurysm or other vascular malformation and for arterial and venous embolizations in the peripheral vasculature. Refer to the instructions for use for complete product information.

18 TECHNOLOGY DRIVE #169, IRVINE CA 92618 | p: 949.788.1443 | f: 949.788.1444  
[WWW.BLOCKADEMEDICAL.COM](http://WWW.BLOCKADEMEDICAL.COM)

MKTG-060 Rev. A





The brain at your fingertips

 **Rapid Medical**

[www.rapid-medical.com](http://www.rapid-medical.com) > tigertriever

## Smooth and stable.

Target Detachable Coils deliver consistently smooth deployment and exceptional microcatheter stability. Designed to work seamlessly together for framing, filling and finishing. Target Coils deliver the high performance you demand.

For more information, please visit [www.strykerneurovascular.com/Target](http://www.strykerneurovascular.com/Target) or contact your local Stryker Neurovascular sales representative.



**Target**<sup>®</sup>  
DETACHABLE COILS

# The Foundation of the ASNR Symposium 2017: *Discovery and Didactics* April 22-23, 2017

## ASNR 55<sup>th</sup> Annual Meeting: *Diagnosis and Delivery* April 24-27, 2017



Long Beach Convention & Entertainment Center  
© Long Beach Convention & Visitors Bureau

**Jacqueline A. Bello, MD, FACR**  
**ASNR 2017 Program Chair/President-Elect**  
*Programming developed in cooperation with and appreciation of the...*

**American Society of Functional Neuroradiology (ASFNR)**  
Kirk M. Welker, MD

**American Society of Head and Neck Radiology (ASHNR)**  
Rebecca S. Cornelius, MD, FACR

**American Society of Pediatric Neuroradiology (ASPNR)**  
Susan Palasis, MD

**American Society of Spine Radiology (ASSR)**  
Joshua A. Hirsch, MD, FACR, FSIR

**Society of NeuroInterventional Surgery (SNIS)**  
Blaise W. Baxter, MD

**American Society of Neuroradiology (ASNR)  
Health Policy Committee**  
Robert M. Barr, MD, FACR

**Computer Sciences & Informatics (CSI) Committee**  
John L. Go, MD, FACR

**Research Scientist Committee**  
Dikoma C. Shungu, PhD and Timothy, P.L. Roberts, PhD

**The International Hydrocephalus Imaging Working Group (IHIWG)/CSF Flow Group**  
William G. Bradley, Jr., MD, PhD, Harold L. Rekate, MD  
and Bryn A. Martin, PhD

**Meeting Registration Opening SOON!**  
Visit [2017.asnr.org](http://2017.asnr.org) for more information.



**ASNR 55<sup>th</sup> Annual Meeting**  
c/o American Society of Neuroradiology  
800 Enterprise Drive, Suite 205 • Oak Brook, Illinois 60523-4216  
Phone: 630-574-0220 • Fax: 630 574-0661 • [2017.asnr.org](http://2017.asnr.org)



ASFNR ASHNR ASPNR ASSR SNIS

THE FOUNDATION OF THE ASNR 

**Come to the beach!** Please join us in Long Beach, California, April 22-27, 2017, for the 55<sup>th</sup> Annual Meeting of the ASNR. Known for its 5.5 miles of Pacific Ocean waterfront, this southern California beach resort boasts a blend of city sophistication and seaside serenity. ASNR is delighted to provide a “4D” focus for this meeting, as depicted by our meeting logo: **Discovery and Didactics** for The Foundation of the ASNR Symposium 2017: **Diagnosis and Delivery** for the ensuing Annual Meeting Program.

Centered on Discovery and Didactics, the symposium will feature sessions on “What’s New?” in the role neuroimaging plays defining CNS disease mechanisms and how to best prepare for “What’s Next?” for our subspecialty in terms of training, teaching, and leading the process of lifelong learning. The annual meeting programming will address best practices in Diagnosis and Delivery, as we strive to provide value, promote quality in better health and care and consider cost. Our discussions will consider how to navigate the changing landscape of healthcare reform and reimbursement as subspecialists in a field that is changing at an equally “fast forward” pace!



Hyatt Regency Long Beach  
© Hyatt Regency Long Beach



Westin Long Beach  
© The Westin Long Beach

# CALL FOR AJNR EDITORIAL FELLOWSHIP CANDIDATES

ASNR and AJNR are pleased once again to join efforts with other imaging-related journals that have training programs on editorial aspects of publishing for trainees or junior staff (3–5 years after training), including Radiology (Olmsted fellowship), AJR (Figley and Rogers fellowships), JACR (Bruce J. Hillman fellowship), and Radiologia.

## 2017 Candidate Information and Requirements

### GOALS

- Increase interest in “editorial” and publication-related activities in younger individuals.
- Increase understanding and participation in the AJNR review process.
- Incorporate into AJNR’s Editorial Board younger individuals who have previous experience in the review and publication process.
- Fill a specific need in neuroradiology not offered by other similar fellowships.
- Increase the relationship between “new” generation of neuroradiologists and more established individuals.
- Increase visibility of AJNR among younger neuroradiologists.

### ACTIVITIES OF THE FELLOWSHIP

- Serve as Editorial Fellow for one year. This individual will be listed on the masthead as such.
- Review at least one manuscript per month for 12 months. Evaluate all review articles submitted to AJNR.
- Learn how electronic manuscript review systems work.
- Be involved in the final decision of selected manuscripts together with the Editor-in-Chief.
- Participate in all monthly Senior Editor telephone conference calls.
- Participate in all meetings of the Editors and Publications Committee during the annual meetings of ASNR and RSNA as per candidate’s availability. The Foundation of the ASNR will provide \$2000 funding for this activity.
- Evaluate progress and adjust program to specific needs in annual meeting or telephone conference with the Editor-in-Chief.
- Embark on an editorial scientific or bibliometric project that will lead to the submission of an article to AJNR or another appropriate journal as determined by the Editor-in-Chief. This project will be presented by the Editorial Fellow at the ASNR annual meeting.
- Serve as liaison between AJNR and ASNR’s Young Professionals Network and the 3 YPs appointed to AJNR as special consultants. Participate in meetings and telephone calls with this group. Design one electronic survey/year, polling the group regarding readership attitudes and wishes.
- Recruit trainees as reviewers as determined by the Editor-in-Chief.
- Participate in Web improvement projects.
- Serve as Guest Editor for an issue of AJNR’s News Digest with a timely topic.

### QUALIFICATIONS

- Be a fellow in neuroradiology from North America, including Canada (this may be extended to include other countries).
- Be a junior faculty neuroradiology member (< 3 years) in either an academic or private environment.
- Be an “in-training” or member of ASNR in any other category.

### APPLICATION

- Include a short letter of intent with statement of goals and desired research project. CV must be included.
- Include a letter of recommendation from the Division Chief or fellowship program director. A statement of protected time to perform the functions outlined is desirable.
- Applications will be evaluated by AJNR’s Senior Editors and the Chair of the Publications Committee prior to the ASNR meeting. The name of the selected individual will be announced at the meeting.
- Applications should be received by March 1, 2017 and sent to Ms. Karen Halm, AJNR Managing Editor, electronically at [khalm@asnr.org](mailto:khalm@asnr.org).

# INTRODUCING FULLY AUTOMATED STROKE APPLICATIONS



## ZERO CLICK

Calculation of infarct  
penumbra & mismatch

## AUTOMATED STROKE REPORT

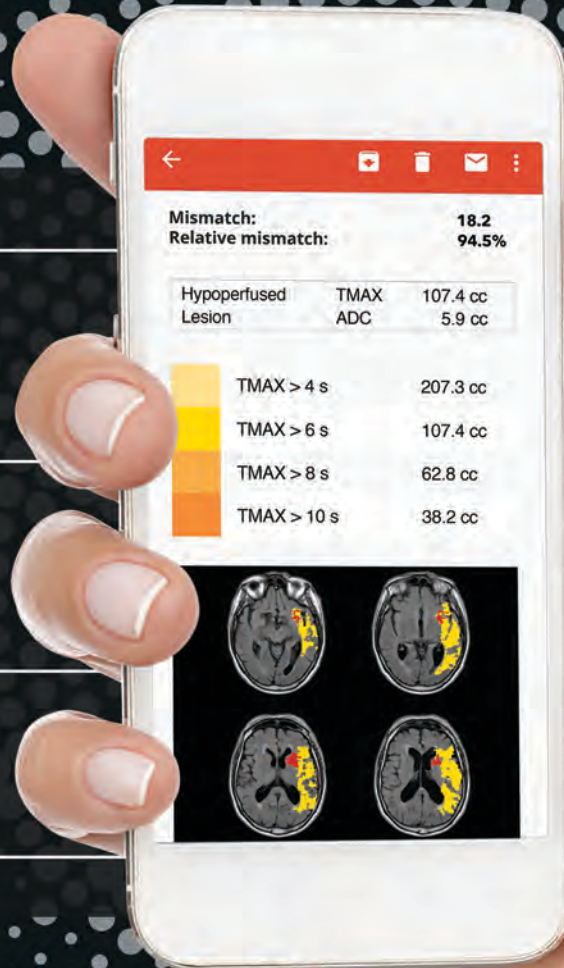
(MRI & CT) by email

## VENDOR-NEUTRAL

& easy integration  
into IT systems

Ask for a free trial

[www.olea-medical.com](http://www.olea-medical.com)



“ Innovation is in our DNA. ”

\* FDA cleared



Improved diagnosis for life™



# Simplify the MOC Process



# Manage your CME Credits Online

## CMEgateway.org

### Available to Members of Participating Societies

American Board of Radiology (ABR)  
American College of Radiology (ACR)  
American Roentgen Ray Society (ARRS)  
American Society of Neuroradiology (ASNR)  
Commission on Accreditation of Medical  
Physics Educational Programs, Inc. (CAMPEP)  
Radiological Society of North America (RSNA)  
Society of Interventional Radiology (SIR)  
SNM  
The Society for Pediatric Radiology (SPR)

### It's Easy and Free!

Log on to CME Gateway to:

- View or print reports of your CME credits from multiple societies from a single access point.
- Print an aggregated report or certificate from each participating organization.
- Link to SAMs and other tools to help with maintenance of certification.

### American Board of Radiology (ABR) participation!

By activating ABR in your organizational profile, your MOC-fulfilling CME and SAM credits can be transferred to your own personalized database on the ABR Web site.

### Sign Up Today!

go to [CMEgateway.org](http://CMEgateway.org)



## Strengthen ASNR's representation at the national level.

Your membership in the American Medical Association strengthens ASNR's representation in the AMA House of Delegates—the policymaking body of the AMA that brings forth the views and interests of all physicians to establish national policy on health, medical, professional and governance matters.

Please activate your 2017 AMA membership, visit [ama-assn.org](http://ama-assn.org) or call AMA Member Relations at (800) 262-3211. If you are currently a member, thank you.

### AMA member benefits and resources include:

- Unlimited access to **The JAMA Network**<sup>®</sup> which brings together *JAMA* and all 11 specialty journals with CME.  
[jamanetwork.com](http://jamanetwork.com)
- **STEPS Forward**<sup>™</sup>, the AMA's new practice transformation series designed to help physicians achieve the Quadruple Aim: better patient experience, better population health and lower overall costs with improved professional satisfaction.  
[stepsforward.org](http://stepsforward.org)
- Free 18-month trial of **DynaMed Plus**<sup>®</sup>, an evidence-based, clinical support tool that features thousands of images and provides immediate answers to clinical questions.  
[offers.jamanetwork.com](http://offers.jamanetwork.com)

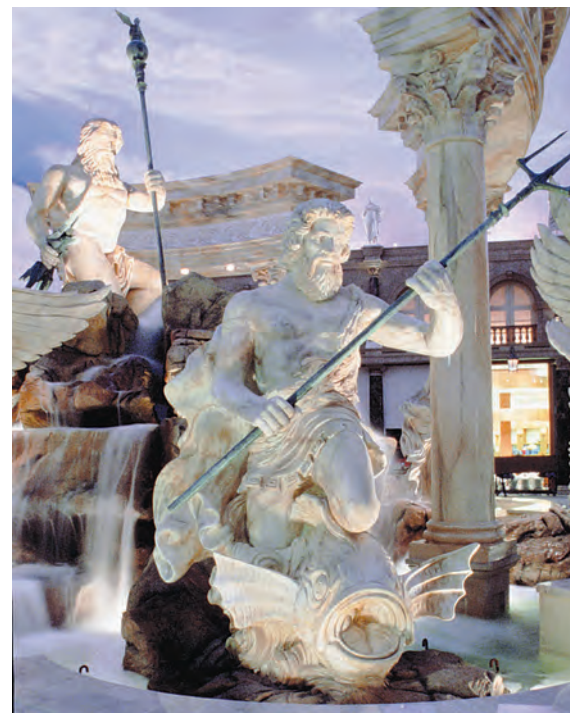




*51<sup>st</sup> Annual Meeting*

American Society of  
**Head & Neck  
Radiology**

Head and Neck Imaging in the City of Lights



**Caesars Palace • Las Vegas, NV**

September 16 – 20, 2017  
(Saturday - Wednesday)

---

Please contact Educational Symposia at 813-806-1000 or [ASHNR@edusymp.com](mailto:ASHNR@edusymp.com) or visit [www.ASHNR.org](http://www.ASHNR.org) for additional information.

# Go Green!

*AJNR* urges American Society of Neuroradiology members to reduce their environmental footprint by voluntarily suspending their print subscription.

The savings in paper, printing, transportation, and postage not only help members cut down on clutter, but go to fund new electronic enhancements and expanded content.

The digital edition of *AJNR* presents the print version in its entirety, along with extra features including:

- Publication Preview
- Case of the Week
- Podcasts
- Special Collections
- The *AJNR* Blog
- Weekly Poll

It also **reaches subscribers much faster than print**. An **electronic table of contents** will be sent directly to your mailbox to notify you as soon as it publishes.

Readers can **search, reference, and bookmark** current and archived content 24 hours a day on [www.ajnr.org](http://www.ajnr.org), rather than thumb through stacks of accumulated paper issues for articles and images they need.



<http://www.ajnr.org/cgi/feedback>

ASNR members who wish to opt out of print can do so by using the Feedback form on the *AJNR* Website (<http://www.ajnr.org/cgi/feedback>). Just type "Go Green" in the subject line to stop print and spare our ecosystem.

## Trevo® XP ProVue Retrievers

See package insert for complete indications, complications, warnings, and instructions for use.

### INDICATIONS FOR USE

1. The Trevo Retriever is indicated for use to restore blood flow in the neurovasculature by removing thrombus for the treatment of acute ischemic stroke to reduce disability in patients with a persistent, proximal anterior circulation, large vessel occlusion, and smaller core infarcts who have first received intravenous tissue plasminogen activator (IV t-PA). Endovascular therapy with the device should start within 6 hours of symptom onset.
2. The Trevo Retriever is indicated to restore blood flow in the neurovasculature by removing thrombus in patients experiencing ischemic stroke within 8 hours of symptom onset. Patients who are ineligible for intravenous tissue plasminogen activator (IV t-PA) or who fail IV t-PA therapy are candidates for treatment.

### COMPLICATIONS

Procedures requiring percutaneous catheter introduction should not be attempted by physicians unfamiliar with possible complications which may occur during or after the procedure. Possible complications include, but are not limited to, the following: air embolism; hematoma or hemorrhage at puncture site; infection; distal embolization; pain/headache; vessel spasm, thrombosis, dissection, or perforation; emboli; acute occlusion; ischemia; intracranial hemorrhage; false aneurysm formation; neurological deficits including stroke; and death.

### COMPATIBILITY

3x20mm retrievers are compatible with Trevo® Pro 14 Microcatheters (REF 90231) and Trevo® Pro 18 Microcatheters (REF 90238). 4x20mm retrievers are compatible with Trevo® Pro 18 Microcatheters (REF 90238). 4x30mm retrievers are compatible with Excelsior® XT-27® Microcatheters (150cm x 6cm straight REF 275081) and Trevo® Pro 18 Microcatheters (REF 90238). 6x25mm Retrievers are compatible with Excelsior® XT-27® Microcatheters (150cm x 6cm straight REF 275081). Compatibility of the Retriever with other microcatheters has not been established. Performance of the Retriever device may be impacted if a different microcatheter is used.

Balloon Guide Catheters (such as Merci® Balloon Guide Catheter and FlowGate® Balloon Guide Catheter) are recommended for use during thrombus removal procedures.

Retrievers are compatible with the Abbott Vascular DOC® Guide Wire Extension (REF 22260).

Retrievers are compatible with Boston Scientific RHV (Ref 421242).

### SPECIFIC WARNINGS FOR INDICATION 1

- The safety and effectiveness of the Trevo Retrievers in reducing disability has not been established in patients with large core infarcts (i.e., ASPECTS ≤ 7). There may be increased risks, such as intracerebral hemorrhage, in these patients.
- The safety and effectiveness of the Trevo Retrievers in reducing disability has not been established or evaluated in patients with occlusions in the posterior circulation (e.g., basilar or vertebral arteries) or for more distal occlusions in the anterior circulation.

### WARNINGS APPLIED TO BOTH INDICATIONS

- Administration of IV t-PA should be within the FDA-approved window (within 3 hours of stroke symptom onset).
- Contents supplied STERILE, using an ethylene oxide (EO) process. Nonpyrogenic.
- To reduce risk of vessel damage, adhere to the following recommendations:
  - Take care to appropriately size Retriever to vessel diameter at intended site of deployment.
  - Do not perform more than six (6) retrieval attempts in same vessel using Retriever devices.
  - Maintain Retriever position in vessel when removing or exchanging Microcatheter.
- To reduce risk of kinking/fracture, adhere to the following recommendations:
  - Immediately after unsheathing Retriever, position Microcatheter tip marker just proximal to shaped section. Maintain Microcatheter tip marker just proximal to shaped section of Retriever during manipulation and withdrawal.
  - Do not rotate or torque Retriever.
  - Use caution when passing Retriever through stented arteries.
- Do not resterilize and reuse. Structural integrity and/or function may be impaired by reuse or cleaning.
- The Retriever is a delicate instrument and should be handled carefully. Before use and when possible during procedure, inspect device carefully for damage. Do not use a device that shows signs of damage. Damage may prevent device from functioning and may cause complications.

- Do not advance or withdraw Retriever against resistance or significant vasospasm. Moving or torquing device against resistance or significant vasospasm may result in damage to vessel or device. Assess cause of resistance using fluoroscopy and if needed resheat the device to withdraw.
- If Retriever is difficult to withdraw from the vessel, do not torque Retriever. Advance Microcatheter distally, gently pull Retriever back into Microcatheter, and remove Retriever and Microcatheter as a unit. If undue resistance is met when withdrawing the Retriever into the Microcatheter, consider extending the Retriever using the Abbott Vascular DOC guidewire extension (REF 22260) so that the Microcatheter can be exchanged for a larger diameter catheter such as a DAC® catheter. Gently withdraw the Retriever into the larger diameter catheter.
- Administer anti-coagulation and anti-platelet medications per standard institutional guidelines.

### PRECAUTIONS

- Prescription only – device restricted to use by or on order of a physician.
- Store in cool, dry, dark place.
- Do not use open or damaged packages.
- Use by “Use By” date.
- Exposure to temperatures above 54°C (130°F) may damage device and accessories. Do not autoclave.
- Do not expose Retriever to solvents.
- Use Retriever in conjunction with fluoroscopic visualization and proper anti-coagulation agents.
- To prevent thrombus formation and contrast media crystal formation, maintain a constant infusion of appropriate flush solution between guide catheter and Microcatheter and between Microcatheter and Retriever or guidewire.
- Do not attach a torque device to the shaped proximal end of DOC® Compatible Retriever. Damage may occur, preventing ability to attach DOC® Guide Wire Extension.



**Concentric Medical**  
301 East Evelyn Avenue  
Mountain View, CA 94041

**Stryker Neurovascular**  
47900 Bayside Parkway  
Fremont, CA 94538

[strykerneurovascular.com](http://strykerneurovascular.com)

Date of Release: SEP/2016

EX\_EN\_US

Copyright © 2016 Stryker  
NV00018973.AB

## Target® Detachable Coil

See package insert for complete indications, contraindications, warnings and instructions for use.

### INTENDED USE / INDICATIONS FOR USE

Target Detachable Coils are intended to endovascularly obstruct or occlude blood flow in vascular abnormalities of the neurovascular and peripheral vessels.

Target Detachable Coils are indicated for endovascular embolization of:

- Intracranial aneurysms
- Other neurovascular abnormalities such as arteriovenous malformations and arteriovenous fistulae
- Arterial and venous embolizations in the peripheral vasculature

### CONTRAINDICATIONS

None known.

### POTENTIAL ADVERSE EVENTS

Potential complications include, but are not limited to: allergic reaction, aneurysm perforation and rupture, arrhythmia, death, edema, embolus, headache, hemorrhage, infection, ischemia, neurological/intracranial sequelae, post-embolization syndrome (fever, increased white blood cell count, discomfort), TIA/stroke, vasospasm, vessel occlusion or closure, vessel perforation, dissection, trauma or damage, vessel rupture, vessel thrombosis. Other procedural complications including but not limited to: anesthetic and contrast media risks, hypotension, hypertension, access site complications.

### WARNINGS

- Contents supplied STERILE using an ethylene oxide (EO) process. Do not use if sterile barrier is damaged. If damage is found, call your Stryker Neurovascular representative.
- For single use only. Do not reuse, reprocess or resterilize. Reuse, reprocessing or resterilization may compromise the structural integrity of the device and/or lead to device failure which, in turn, may result in patient injury, illness or death. Reuse, reprocessing or resterilization may also create a risk of contamination of the device and/or cause patient infection or cross-infection, including, but not limited to, the transmission of infectious disease(s) from one patient to another. Contamination of the device may lead to injury, illness or death of the patient.

- After use, dispose of product and packaging in accordance with hospital, administrative and/or local government policy.

- **This device should only be used by physicians who have received appropriate training in interventional neuroradiology or interventional radiology and preclinical training on the use of this device as established by Stryker Neurovascular.**

- Patients with hypersensitivity to 316LVM stainless steel may suffer an allergic reaction to this implant.
- MR temperature testing was not conducted in peripheral vasculature, arteriovenous malformations or fistulae models.
- The safety and performance characteristics of the Target Detachable Coil System (Target Detachable Coils, InZone Detachment Systems, delivery systems and accessories) have not been demonstrated with other manufacturer's devices (whether coils, coil delivery devices, coil detachment systems, catheters, guidewires, and/or other accessories). Due to the potential incompatibility of non Stryker Neurovascular devices with the Target Detachable Coil System, the use of other manufacturer's device(s) with the Target Detachable Coil System is not recommended.
- To reduce risk of coil migration, the diameter of the first and second coil should never be less than the width of the ostium.
- In order to achieve optimal performance of the Target Detachable Coil System and to reduce the risk of thromboembolic complications, it is critical that a continuous infusion of appropriate flush solution be maintained between a) the femoral sheath and guiding catheter, b) the 2-tip microcatheter and guiding catheters, and c) the 2-tip microcatheter and Stryker Neurovascular guidewire and delivery wire. Continuous flush also reduces the potential for thrombus formation on, and crystallization of infusate around, the detachment zone of the Target Detachable Coil.
- Do not use the product after the “Use By” date specified on the package.
- Reuse of the flush port/dispenser coil or use with any coil other than the original coil may result in contamination of, or damage to, the coil.
- Utilization of damaged coils may affect coil delivery to, and stability inside, the vessel or aneurysm, possibly resulting in coil migration and/or stretching.
- The fluoro-saver marker is designed for use with a Rotating Hemostatic Valve (RHV). If used without an RHV, the distal end of the coil may be beyond the alignment marker when the fluoro-saver marker reaches the microcatheter hub.

- If the fluoro-saver marker is not visible, do not advance the coil without fluoroscopy.
- Do not rotate delivery wire during or after delivery of the coil. Rotating the Target Detachable Coil delivery wire may result in a stretched coil or premature detachment of the coil from the delivery wire, which could result in coil migration.
- Verify there is no coil loop protrusion into the parent vessel after coil placement and prior to coil detachment. Coil loop protrusion after coil placement may result in thromboembolic events if the coil is detached.
- Verify there is no movement of the coil after coil placement and prior to coil detachment. Movement of the coil after coil placement may indicate that the coil could migrate once it is detached.
- Failure to properly close the RHV compression fitting over the delivery wire before attaching the InZone® Detachment System could result in coil movement, aneurysm rupture or vessel perforation.
- Verify repeatedly that the distal shaft of the catheter is not under stress before detaching the Target Detachable Coil. Axial compression or tension forces could be stored in the 2-tip microcatheter causing the tip to move during coil delivery. Microcatheter tip movement could cause the aneurysm or vessel to rupture.
- Advancing the delivery wire beyond the microcatheter tip once the coil has been detached involves risk of aneurysm or vessel perforation.
- The long term effect of this product on extravascular tissues has not been established so care should be taken to retain this device in the intravascular space.

Damaged delivery wires may cause detachment failures, vessel injury or unpredictable distal tip response during coil deployment. If a delivery wire is damaged at any point during the procedure, do not attempt to straighten or otherwise repair it. Do not proceed with deployment or detachment. Remove the entire coil and replace with undamaged product.

- After use, dispose of product and packaging in accordance with hospital, administrative and/or local government policy.

### CAUTIONS / PRECAUTIONS

- Federal Law (USA) restricts this device to sale by or on the order of a physician.
- Besides the number of InZone Detachment System units needed to complete the case, there must be an extra InZone Detachment System unit as back up.

- Removing the delivery wire without grasping the introducer sheath and delivery wire together may result in the detachable coil sliding out of the introducer sheath.
- Failure to remove the introducer sheath after inserting the delivery wire into the RHV of the microcatheter will interrupt normal infusion of flush solution and allow back flow of blood into the microcatheter.
- Some low level overhead light near or adjacent to the patient is required to visualize the fluoro-saver marker; monitor light alone will not allow sufficient visualization of the fluoro-saver marker.
- Advance and retract the Target Detachable Coil carefully and smoothly without excessive force. If unusual friction is noticed, slowly withdraw the Target Detachable Coil and examine for damage. If damage is present, remove and use a new Target Detachable Coil. If friction or resistance is still noted, carefully remove the Target Detachable Coil and microcatheter and examine the microcatheter for damage.
- If it is necessary to reposition the Target Detachable Coil, verify under fluoroscopy that the coil moves with a one-to-one motion. If the coil does not move with a one-to-one motion or movement is difficult, the coil may have stretched and could possibly migrate or break. Gently remove both the coil and microcatheter and replace with new devices.
- Increased detachment times may occur when:
  - Other embolic agents are present.
  - Delivery wire and microcatheter markers are not properly aligned.
  - Thrombus is present on the coil detachment zone.
- Do not use detachment systems other than the InZone Detachment System.
- Increased detachment times may occur when delivery wire and microcatheter markers are not properly aligned.
- Do not use detachment systems other than the InZone Detachment System.



**Stryker Neurovascular**  
47900 Bayside Parkway  
Fremont, CA 94538

[strykerneurovascular.com](http://strykerneurovascular.com)

Date of Release: MAR/2016

EX\_EN\_US

Copyright © 2016 Stryker  
NV00018669.AB

**NEW**

# Indication for Trevo<sup>®</sup> Retrievers

A New Standard of Care in Stroke



**FIRST**

mechanical thrombectomy device  
indicated to reduce disability in stroke.\*

**FIRST**

new treatment indication for  
stroke in 20 years.

## Trevo XP

PROVUE RETRIEVER

Success accelerated.

\*The Trevo Retriever is indicated for use to restore blood flow in the neurovasculature by removing thrombus for the treatment of acute ischemic stroke to reduce disability in patients with a persistent, proximal anterior circulation, large vessel occlusion, and smaller core infarcts who have first received intravenous tissue plasminogen activator (IV t-PA). Endovascular therapy with the device should start within 6 hours of symptom onset.

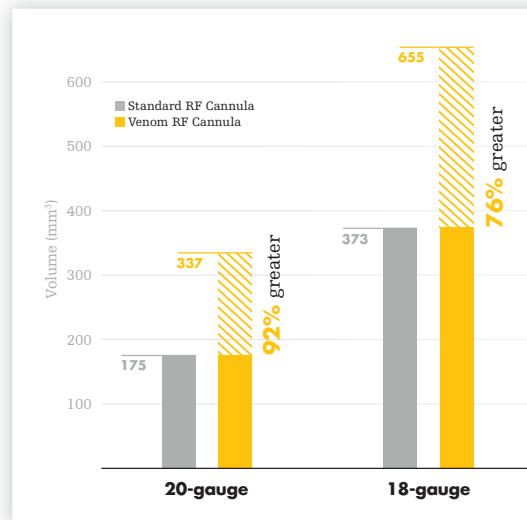
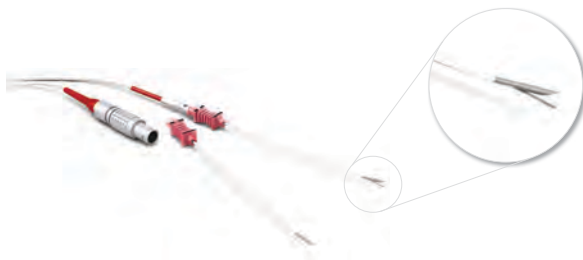


With the acquisition of the CareFusion vertebral compression fracture (VCF) portfolio from BD (Becton, Dickinson and Company), **Stryker has the most comprehensive and least invasive portfolio** of VCF treatment options



## Celebrating two years of **excellence**

An elegant, cost effective approach to large lesions. The **Venom Cannula and Electrode combination** celebrates **two years of excellence** in helping you achieve larger RF lesions<sup>1</sup> to treat your patients suffering from chronic pain.



Stryker Corporation or its divisions or other corporate affiliated entities own, use or have applied for the following trademark: Venom. All other trademarks are trademarks of their respective owners or holders.

The information presented in this overview is intended to demonstrate the breadth of Stryker product offerings. Always refer to the package insert, product label and/or user instructions before using any Stryker product. Products may not be available in all markets. Product availability is subject to the regulatory or medical practices that govern individual markets. Please contact your Stryker representative if you have questions about the availability of Stryker products in your area.

<sup>1</sup> Effect of the Stryker Venom Cannula and Venom Electrode combination on Lesion Size and Anesthesia Delivery During Radiofrequency Ablation Stryker Instruments, 4100 East Milham Avenue, Kalamazoo, Michigan 49001.

**strykerIVS.com**

1000-025-340 Rev C

# AJNR

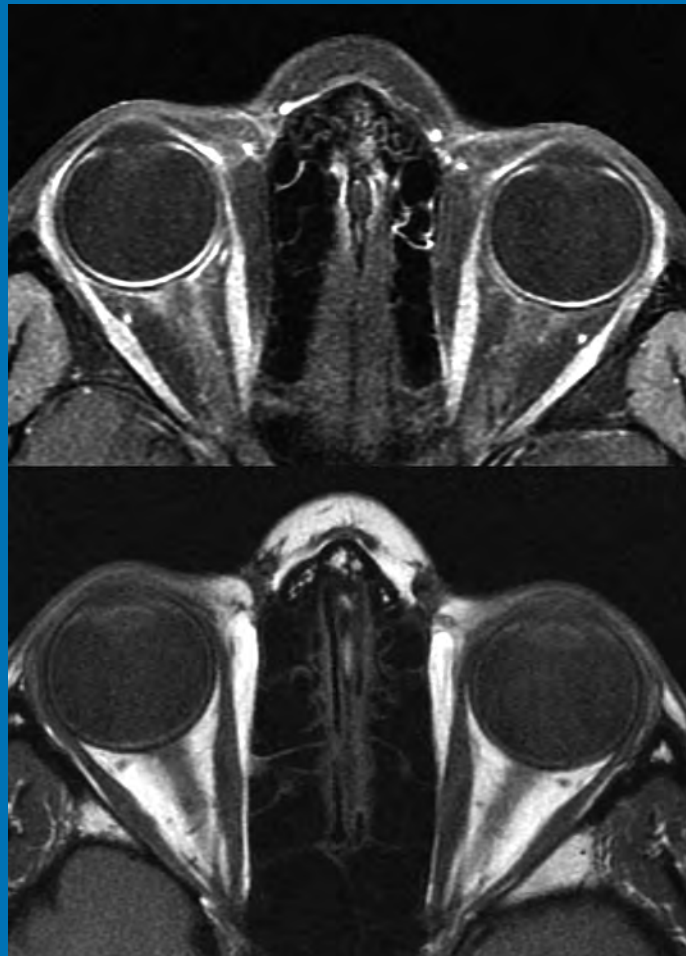
## AMERICAN JOURNAL OF NEURORADIOLOGY

DECEMBER 2016  
VOLUME 37  
NUMBER 12  
WWW.AJNR.ORG

THE JOURNAL OF DIAGNOSTIC AND  
INTERVENTIONAL NEURORADIOLOGY

Dose reduction in 4D cerebral CT angiography  
Computer-extracted texture features distinguishing radionecrosis  
Imaging in the diagnosis of scleritis

Official Journal ASNR • ASFNR • ASHNR • ASPNR • ASSR



# AJNR

## AMERICAN JOURNAL OF NEURORADIOLOGY

DECEMBER 2016  
VOLUME 37  
NUMBER 12  
WWW.AJNR.ORG

Publication Preview at [www.ajnr.org](http://www.ajnr.org) features articles released in advance of print. Visit [www.ajnrblog.org](http://www.ajnrblog.org) to comment on AJNR content and chat with colleagues and AJNR's News Digest at <http://ajnrndigest.org> to read the stories behind the latest research in neuroimaging.

2179 **PERSPECTIVES** *E.C. Kavanagh*

### EDITORIALS

2180 **Point: Don't Call Me a DOC!** *D.M. Yousem*

2181 **Counterpoint: Appropriately Ambiguous—The Disc Osteophyte Complex** *J.S. Ross*

### REVIEW ARTICLE

 2182 **Neuroimaging Wisely** *J. Bueth, et al.*

**PATIENT SAFETY**

### PATIENT SAFETY

2189 **Radiation Dose Reduction in 4D Cerebral CT Angiography by Individualized Estimation of Cerebral Circulation Time** *M.R. Radon, et al.*

### HEALTH CARE REFORM VIGNETTE

 2195 **PQRS and the MACRA: Value-Based Payments Have Moved from Concept to Reality** *J.A. Hirsch, et al.*

### GENERAL CONTENTS

  2201 **Progressing Bevacizumab-Induced Diffusion Restriction Is Associated with Coagulative Necrosis Surrounded by Viable Tumor and Decreased Overall Survival in Patients with Recurrent Glioblastoma** *H.S. Nguyen, et al.*

**ADULT BRAIN**

  2209 **Improving the Grading Accuracy of Astrocytic Neoplasms Noninvasively by Combining Timing Information with Cerebral Blood Flow: A Multi-TI Arterial Spin-Labeling MR Imaging Study** *S. Yang, et al.*

**ADULT BRAIN**

2217 **Correlation of Tumor Immunohistochemistry with Dynamic Contrast-Enhanced and DSC-MRI Parameters in Patients with Gliomas** *T.B. Nguyen, et al.*

**ADULT BRAIN**

 2224 **Preradiotherapy MR Imaging: A Prospective Pilot Study of the Usefulness of Performing an MR Examination Shortly before Radiation Therapy in Patients with Glioblastoma** *C. Majós, et al.*

**ADULT BRAIN**

   2231 **Computer-Extracted Texture Features to Distinguish Cerebral Radionecrosis from Recurrent Brain Tumors on Multiparametric MRI: A Feasibility Study** *P. Tiwari, et al.*

**ADULT BRAIN**

AJNR (Am J Neuroradiol ISSN 0195–6108) is a journal published monthly, owned and published by the American Society of Neuroradiology (ASNR), 800 Enterprise Drive, Suite 205, Oak Brook, IL 60523. Annual dues for the ASNR include \$170.00 for journal subscription. The journal is printed by Cadmus Journal Services, 5457 Twin Knolls Road, Suite 200, Columbia, MD 21045; Periodicals postage paid at Oak Brook, IL and additional mailing offices. Printed in the U.S.A. POSTMASTER: Please send address changes to American Journal of Neuroradiology, P.O. Box 3000, Denville, NJ 07834, U.S.A. Subscription rates: nonmember \$390 (\$460 foreign) print and online, \$310 online only; institutions \$450 (\$520 foreign) print and basic online, \$895 (\$960 foreign) print and extended online, \$370 online only (basic), extended online \$805; single copies are \$35 each (\$40 foreign). Indexed by PubMed/Medline, BIOSIS Previews, Current Contents (Clinical Medicine and Life Sciences), EMBASE, Google Scholar, HighWire Press, Q-Sensei, RefSeek, Science Citation Index, and SCI Expanded. Copyright © American Society of Neuroradiology.

	2237	<b>Commentary</b> “Am I about to Lose my Job?!”: A Comment on “Computer-Extracted Texture Features to Distinguish Cerebral Radiation Necrosis from Recurrent Brain Tumors on Multiparametric MRI: A Feasibility Study” <i>A.I. Holodny</i>	
	2239	<b>CT Perfusion in Acute Lacunar Stroke: Detection Capabilities Based on Infarct Location</b> <i>J.C. Benson, et al.</i>	ADULT BRAIN
  	2245	<b>Comparison of High-Resolution MR Imaging and Digital Subtraction Angiography for the Characterization and Diagnosis of Intracranial Artery Disease</b> <i>N.J. Lee, et al.</i>	ADULT BRAIN
	2251	<b>A Simplified Model for Intravoxel Incoherent Motion Perfusion Imaging of the Brain</b> <i>J. Conklin, et al.</i>	ADULT BRAIN
	2258	<b>Vascular Dysfunction in Leukoaraiosis</b> <i>K. Sam, et al.</i>	ADULT BRAIN
 	2265	<b>Comparison of Quantitative Cerebral Blood Flow Measurements Performed by Bookend Dynamic Susceptibility Contrast and Arterial Spin-Labeling MRI in Relapsing-Remitting Multiple Sclerosis</b> <i>R.M. D’Ortenzio, et al.</i>	ADULT BRAIN
 	2273	<b>Metabolic Abnormalities in the Hippocampus of Patients with Schizophrenia: A 3D Multivoxel MR Spectroscopic Imaging Study at 3T</b> <i>E.J. Meyer, et al.</i>	ADULT BRAIN
	2280	<b>Are Anatomic Results Influenced by WEB Shape Modification? Analysis in a Prospective, Single-Center Series of 39 Patients with Aneurysms Treated with the WEB</b> <i>D. Herbreteau, et al.</i>	INTERVENTIONAL
	2287	<b>Efficacy and Safety of the Woven EndoBridge (WEB) Device for the Treatment of Intracranial Aneurysms: A Systematic Review and Meta-Analysis</b> <i>S. Asnafi, et al.</i>	INTERVENTIONAL
	2293	<b>Does Arterial Flow Rate Affect the Assessment of Flow-Diverter Stent Performance?</b> <i>H.G. Morales, et al.</i>	INTERVENTIONAL
	2299	<b>Yield of Repeat 3D Angiography in Patients with Aneurysmal-Type Subarachnoid Hemorrhage</b> <i>R.S. Bechan, et al.</i>	INTERVENTIONAL
	2304	<b>Porcine In Vivo Validation of a Virtual Contrast Model: The Influence of Contrast Agent Properties and Vessel Flow Rates</b> <i>T.W. Peach, et al.</i>	INTERVENTIONAL
	2310	<b>Cognitive Impairment and Basal Ganglia Functional Connectivity in Vascular Parkinsonism</b> <i>V. Dunet, et al.</i>	FUNCTIONAL
	2317	<b>Prognostic Value of Labyrinthine 3D-FLAIR Abnormalities in Idiopathic Sudden Sensorineural Hearing Loss</b> <i>J.I. Lee, et al.</i>	HEAD & NECK
	2323	<b>Prospective Validation of Two 4D-CT–Based Scoring Systems for Prediction of Multigland Disease in Primary Hyperparathyroidism</b> <i>S. Sho, et al.</i>	HEAD & NECK
	2328	<b>Intravoxel Incoherent Motion in Normal Pituitary Gland: Initial Study with Turbo Spin-Echo Diffusion-Weighted Imaging</b> <i>K. Kamimura, et al.</i>	HEAD & NECK
	2334	<b>CT and MR Imaging in the Diagnosis of Scleritis</b> <i>M.C. Diogo, et al.</i>	HEAD & NECK
	2340	<b>Pediatric Patients Demonstrate Progressive T1-Weighted Hyperintensity in the Dentate Nucleus following Multiple Doses of Gadolinium-Based Contrast Agent</b> <i>D.R. Roberts, et al.</i>	PEDIATRICS PATIENT SAFETY
  	2348	<b>Automated MRI Volumetric Analysis in Patients with Rasmussen Syndrome</b> <i>Z.I. Wang, et al.</i>	PEDIATRICS
	2356	<b>Quantitative Evaluation of Medial Temporal Lobe Morphology in Children with Febrile Status Epilepticus: Results of the FEBSTAT Study</b> <i>A.C. McClelland, et al.</i>	PEDIATRICS
	2363	<b>Early Antiretroviral Therapy in HIV-Infected Children Is Associated with Diffuse White Matter Structural Abnormality and Corpus Callosum Sparing</b> <i>C. Ackermann, et al.</i>	PEDIATRICS



### Official Journal:

American Society of Neuroradiology  
American Society of Functional Neuroradiology  
American Society of Head and Neck Radiology  
American Society of Pediatric Neuroradiology  
American Society of Spine Radiology

### EDITOR-IN-CHIEF

#### Jeffrey S. Ross, MD

Professor of Radiology, Department of Radiology,  
Mayo Clinic College of Medicine, Phoenix, AZ

### SENIOR EDITORS

#### Harry J. Cloft, MD, PhD

Professor of Radiology and Neurosurgery,  
Department of Radiology, Mayo Clinic College of  
Medicine, Rochester, MN

#### Thierry A.G.M. Huisman, MD

Professor of Radiology, Pediatrics, Neurology, and  
Neurosurgery, Chairman, Department of Imaging  
and Imaging Science, Johns Hopkins Bayview,  
Director, Pediatric Radiology and Pediatric  
Neuroradiology, Johns Hopkins Hospital,  
Baltimore, MD

#### C.D. Phillips, MD, FACR

Professor of Radiology, Weill Cornell Medical  
College, Director of Head and Neck Imaging,  
New York-Presbyterian Hospital, New York, NY

#### Pamela W. Schaefer, MD

Clinical Director of MRI and Associate Director of  
Neuroradiology, Massachusetts General Hospital,  
Boston, Massachusetts, Associate Professor,  
Radiology, Harvard Medical School, Cambridge, MA

#### Charles M. Strother, MD

Professor of Radiology, Emeritus, University of  
Wisconsin, Madison, WI

#### Jody Tanabe, MD

Professor of Radiology and Psychiatry,  
Chief of Neuroradiology,  
University of Colorado, Denver, CO

### STATISTICAL SENIOR EDITOR

#### Bryan A. Comstock, MS

Senior Biostatistician,  
Department of Biostatistics,  
University of Washington, Seattle, WA

### EDITORIAL BOARD

Ashley H. Aiken, *Atlanta, GA*  
Lea M. Alhilali, *Phoenix, AZ*  
John D. Barr, *Dallas, TX*  
Ari Blitz, *Baltimore, MD*  
Barton F. Branstetter IV, *Pittsburgh, PA*  
Jonathan L. Brisman, *Lake Success, NY*  
Julie Bykowski, *San Diego, CA*  
Keith Cauley, *Danville, PA*  
Asim F. Choudhri, *Memphis, TN*  
Alessandro Cianfoni, *Lugano, Switzerland*  
J. Matthew Debnam, *Houston, TX*  
Seena Dehkharghani, *New York, NY*  
Colin Derdeyn, *Iowa City, IA*  
Rahul S. Desikan, *San Francisco, CA*  
Yonghong Ding, *Rochester, MN*  
Clifford J. Eskey, *Hanover, NH*  
Saeed Fakhraan, *Phoenix, AZ*  
Massimo Filippi, *Milan, Italy*  
Allan J. Fox, *Toronto, Ontario, Canada*  
Wende N. Gibbs, *Los Angeles, CA*  
Christine M. Glastonbury, *San Francisco, CA*  
John L. Go, *Los Angeles, CA*  
Allison Grayev, *Madison, WI*  
Brent Griffith, *Detroit, MI*  
Wan-Yuo Guo, *Taipei, Taiwan*  
Ajay Gupta, *New York, NY*  
Rakesh K. Gupta, *Lucknow, India*  
Lotfi Hacein-Bey, *Sacramento, CA*  
Christopher P. Hess, *San Francisco, CA*  
Andrei Holodny, *New York, NY*  
Benjamin Huang, *Chapel Hill, NC*  
George J. Hunter, *Boston, MA*  
Mahesh V. Jayaraman, *Providence, RI*  
Valerie Jewells, *Chapel Hill, NC*  
Christof Karmonik, *Houston, TX*  
Timothy J. Kaufmann, *Rochester, MN*  
Hillary R. Kelly, *Boston, MA*  
Toshibumi Kinoshita, *Akita, Japan*  
Kenneth F. Layton, *Dallas, TX*  
Michael M. Lell, *Nürnberg, Germany*  
Michael Lev, *Boston, MA*  
Karl-Olof Lovblad, *Geneva, Switzerland*  
Franklin A. Marden, *Chicago, IL*  
M. Gisele Matheus, *Charleston, SC*  
Joseph C. McGowan, *Merion Station, PA*  
Stephan Meckel, *Freiburg, Germany*  
Christopher J. Moran, *St. Louis, MO*  
Takahisa Mori, *Kamakura City, Japan*  
Suresh Mukherji, *Ann Arbor, MI*  
Amanda Murphy, *Toronto, Ontario, Canada*  
Alexander J. Nemeth, *Chicago, IL*  
Sasan Partovi, *Cleveland, OH*  
Laurent Pierot, *Reims, France*  
Jay J. Pillai, *Baltimore, MD*  
Whitney B. Pope, *Los Angeles, CA*

Andrea Poretti, *Baltimore, MD*  
M. Judith Donovan Post, *Miami, FL*  
Tina Young Poussaint, *Boston, MA*  
Joana Ramalho, *Lisbon, Portugal*  
Otto Rapalino, *Boston, MA*  
Álex Rovira-Cañellas, *Barcelona, Spain*  
Paul M. Ruggieri, *Cleveland, OH*  
Zoran Rumboldt, *Rovinj-Rovigno, Croatia*  
Amit M. Saindane, *Atlanta, GA*  
Erin Simon Schwartz, *Philadelphia, PA*  
Lubdha M. Shah, *Salt Lake City, UT*  
Aseem Sharma, *St. Louis, MO*  
J. Keith Smith, *Chapel Hill, NC*  
Maria Vittoria Spampinato, *Charleston, SC*  
Gordon K. Sze, *New Haven, CT*  
Krishnamoorthy Thamburaj, *Hershey, PA*  
Cheng Hong Toh, *Taipei, Taiwan*  
Thomas A. Tomsick, *Cincinnati, OH*  
Aquila S. Turk, *Charleston, SC*  
Willem Jan van Rooij, *Tilburg, Netherlands*  
Arastoo Vossough, *Philadelphia, PA*  
Elysa Widjaja, *Toronto, Ontario, Canada*  
Max Wintermark, *Stanford, CA*  
Ronald L. Wolf, *Philadelphia, PA*  
Kei Yamada, *Kyoto, Japan*  
Carlos Zamora, *Chapel Hill, NC*

### EDITORIAL FELLOW

Daniel S. Chow, *San Francisco, CA*

### SPECIAL CONSULTANTS TO THE EDITOR

#### AJNR Blog Editor

Neil Lall, *Denver, CO*

#### Case of the Month Editor

Nicholas Stence, *Aurora, CO*

#### Case of the Week Editors

Juan Pablo Cruz, *Santiago, Chile*

Sapna Rawal, *Toronto, Ontario, Canada*

#### Classic Case Editor

Sandy Cheng-Yu Chen, *Taipei, Taiwan*

#### Facebook Editor

Peter Yi Shen, *Sacramento, CA*

#### Health Care and Socioeconomics Editor

Pina C. Sanelli, *New York, NY*

#### Physics Editor

Greg Zaharchuk, *Stanford, CA*

#### Podcast Editor

Yvonne Lui, *New York, NY*

#### Twitter Editor

Ryan Fitzgerald, *Little Rock, AR*

### YOUNG PROFESSIONALS

#### ADVISORY COMMITTEE

Asim K. Bag, *Birmingham, AL*

Anna E. Nidecker, *Sacramento, CA*

Peter Yi Shen, *Sacramento, CA*

Founding Editor

Juan M. Taveras

Editors Emeriti

Mauricio Castillo, Robert I. Grossman,  
Michael S. Huckman, Robert M. Quencer

Managing Editor

Karen Halm

Assistant Managing Editor

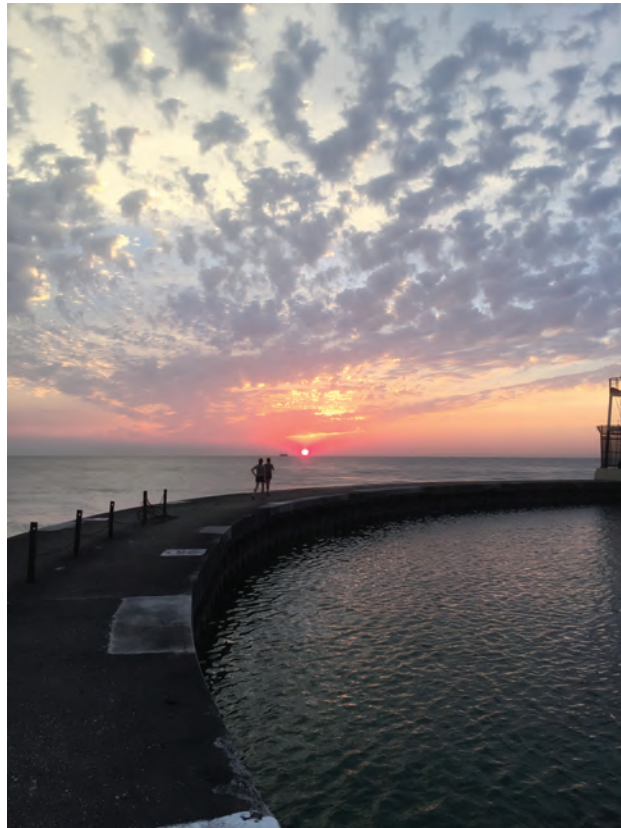
Laura Wilhelm

Executive Director, ASNR

Mary Beth Hepp

Director of Communications, ASNR

Angelo Artemakis



Title: Sunrise over Lake Michigan. This photo was taken while attending the Society for Magnetic Resonance Angiography meeting in September 2016. Being jet-lagged, I was running along North Avenue Beach in Chicago in the early morning. This photo of the sunrise over Lake Michigan was taken on an iPhone 6.

*Eoin C. Kavanagh, Clinical Professor, University College Dublin; Consultant Radiologist, Mater Misericordiae University Hospital, Cappagh National Orthopaedic Hospital, Dublin, Ireland*

## Point: Don't Call Me a DOC!

 D.M. Yousem

The words we use matter. That is why we build lexicons. I want to petition for the removal of the phrase “disc osteophyte complex” (DOC) from the neuroradiology lexicon. I am seeing this phrase used very frequently in descriptions of every level of the cervical spine by residents coming to neuroradiology—and it galls me. To prepare for this editorial, I consulted the 3 most active orthopedic and neurosurgery spine surgeons at Johns Hopkins, and they endorsed my call to eliminate the use of disc osteophyte complex.

We can readily distinguish discs from osteophytes on the basis of our gradient-echo (GRE) low flip-angle thin-section cervical spine axial scans (Figure). On these sequences, the disc is bright and the osteophyte is dark. By contrast, on fast spin-echo T2-weighted images both may be dark, so the inclusion of this gradient-echo scan is critical to accurate interpretation. Rarely, we may see a severely desiccated disc that defies this GRE classification, but for most cases, we can tell a disc (bright) from an osteophyte (dark), and they do not necessarily coexist. Why should we care? Because the spine surgeons do! They told me!

<http://dx.doi.org/10.3174/ajnr.A4927>

If the disease is exclusively a disc, the surgeons may attempt a discectomy alone, or they may do watchful waiting for the disc to regress. Jay Khanna, orthopedic surgeon, said, “The larger, more hydrated discs tend to resorb. So if the patient is neuro-intact, we can try to treat them nonoperatively.” Osteophytes do not regress. If the disease is predominantly an osteophyte, it requires more drilling from an anterior approach, and according to Jean-Paul Wolinsky, neurosurgeon, it is a much more difficult procedure. He will warn the patient as such. Foraminotomies are more commonly required when osteophytes and uncovertebral joint spurs are present—the distraction of the intervertebral graft alone may not relieve the stenosis. From a posterior approach, Wolinsky says, a herniation is removed, whereas an “osteophyte is left alone, and instead the nerve is decompressed widely.” If there is coexistent ossification of the posterior longitudinal ligament, the approach is exclusively posterior, with indirect decompression. Neurosurgeons Ali Bydon and Dan Sciubba state, “lumping DOC generically doesn't help us determine the best approach” and “differentiating the two can change the management.”

Therefore, I implore you, my colleagues, to say that either there is a disc, there is an osteophyte, or there is a disc and osteophyte. Calling every level a disc osteophyte complex is a cop-out.

I used to say to my young children, “Use your words” (ie, do not hit). To my adult colleagues, I say, “Use your words wisely.”

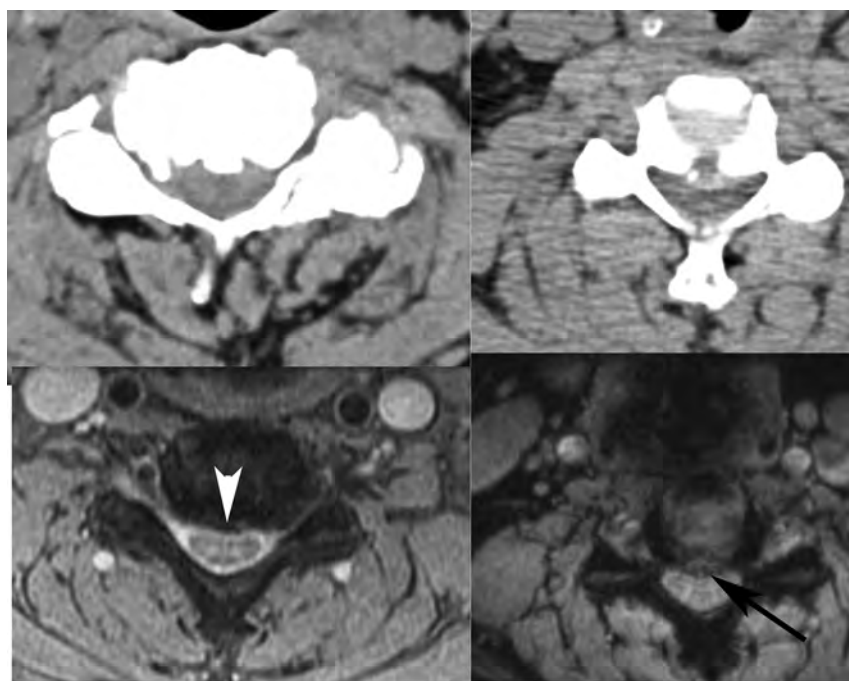


**FIGURE.** Disc bright, osteophyte dark. Note the high-intensity disc herniation (*black arrow*) to be distinguished from the low-intensity osteophyte (*white arrowhead*), with confirmatory corresponding CT scans above.

## Counterpoint: Appropriately Ambiguous—The Disc Osteophyte Complex

J.S. Ross, *AJNR Editor-in-Chief*

The nomenclature for lumbar spine degenerative disc disease has been painstakingly conceived, revised, and condoned by numerous societies.<sup>1</sup> Not so for the cervical spine. I would like to promote the term “disc osteophyte complex” (DOC) for standard usage in the cervical spine lexicon, with certain caveats.

### Why DOC?

Cervical spondylosis is unique to the cervical spine because of the anatomy and presence of the uncovertebral joints and spinal cord. This is often manifest over several segments with mass effect on the ventral thecal sac and cord from ventral disease (DOC) and posterior ligamentous hypertrophy. On MR imaging, we are often faced with a low-signal, posterior extension of the disc margin, which compresses or effaces the dura and neural structures. This low-signal-intensity lesion may be composed of various aspects of disc degeneration, including a bulging annulus, disc herniation, osteophyte, cartilage, and calcification, which are not easily separated by routine MR imaging. Differences in image quality due to section thickness, magnet strength, and patient cooperation make more specific parsing of the images impossible. It is reasonable and prudent to use a term that is morphologically accurate, but also purposefully nonspecific for the large number of cases in which we just cannot tell the precise underlying (and microscopic) pathology.

### Surgeons

Ideally, we would craft our reports about cervical spondylosis on the basis of an intimate knowledge of the practice patterns and training of the surgeons with whom we work. The reality is that we often dictate with limited clinical information and little knowledge of the physicians the individual patient might end up consulting, be it family practice, pain management, or neuro- and

orthopedic surgery. Opinions among surgeons vary widely regarding whether surgery should be performed for specific clinical indications, and if it should be performed, which approach (anterior or posterior) should be used (Figure).<sup>2</sup> Given the vagaries involved, it seems reasonable to use nomenclature that is simple, easy, and widely understandable while also focusing on the important descriptors such as alignment, the degree of cord compression, and cord signal intensity. In the end, if the referring physicians are concerned about the presence of calcifications or osteophytes before surgery, they can always get a CT and correlate that data with the MR imaging study.

### Caveats

1) Disc osteophyte complex should not be used in the lumbar spine. The pathophysiology is different, so stick to using the standard nomenclature of bulge, osteophyte, and disc herniation.

2) DOC should not be used to the exclusion of the terms “osteophyte” and “disc herniation” (protrusion, extrusion) when they are obvious in the cervical spine. Some patients will have a plump herniation showing high signal on gradient-echo, and these should be called “herniations.” Some patients will have obvious osteophytes with fatty marrow signal, so go ahead and call them “osteophytes.” Many, many patients, however, will end up having DOC!

3) DOC should be part of the analysis for central canal stenosis and separate from the analysis of uncovertebral joint and foraminal narrowing.

4) DOC is an abbreviation for this editorial only. If you use this term in your reports, please expand and use “disc osteophyte complex.”

It is time to embrace the ambiguity of the DOC and use it guilt-free as standard nomenclature in cervical spondylosis.

### REFERENCES

1. Fardon DF, Williams AL, Dohring EJ, et al. **Lumbar disc nomenclature: version 2.0—recommendations of the combined task forces of the North American Spine Society, the American Society of Spine Radiology, and the American Society of Neuroradiology.** *Spine (Phila Pa 1976)* 2014;39:E1448–65 CrossRef Medline
2. Lee JY, Hohl JB, Fedorka CJ, et al. **Surgeons agree to disagree on surgical options for degenerative conditions of the cervical and lumbar spine.** *Spine (Phila Pa 1976)* 2011;36:E203–12 CrossRef Medline

<http://dx.doi.org/10.3174/ajnr.A4928>

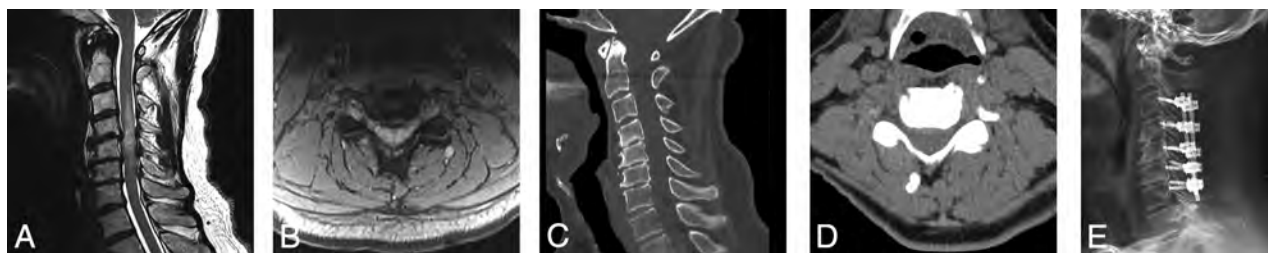


**FIGURE.** A 65-year-old patient with upper extremity numbness and paresthesias. An MR imaging study performed first (A and B) shows a low-signal DOC effacing the cord, with a long segment of cord myelomalacia. Nonenhanced CT study (C and D) obtained preoperatively shows that the bulk of the anterior disease is not ossified. Nevertheless, the patient went on to undergo posterior decompression (E).

# Neuroimaging Wisely

J. Buethe, J. Nazarian, K. Kalisz, and M. Wintermark



## ABSTRACT

**SUMMARY:** Diagnostic imaging is the most rapidly growing physician service in the Medicare and privately insured population. The growing share of medical costs devoted to imaging procedures has led to increasing concerns among the key federal agencies and private payers. In an attempt to educate health care providers, patients, and families on the importance of making optimal clinical decisions, the American Board of Internal Medicine Foundation organized the Choosing Wisely initiative with strong collaboration from specialty societies representing nearly all medical disciplines. Among 45 tests and treatments listed on the Choosing Wisely Web site, 24 are directly related to imaging. Eleven of the 24 are associated with neuroimaging. The listing of imaging tests in the Choosing Wisely program by multiple medical societies other than the radiology societies acknowledges that appropriate use of medical imaging is a shared responsibility between radiologists and referring physicians. In this article, we highlight why radiologists are uniquely positioned to support the appropriate use of imaging. We review some of the strategies that radiologists can use to help their referring physicians with appropriate ordering of neuroimaging in real-world practice and address some of the challenges and pitfalls in implementing patient-centered imaging decision-making and shifting to a value-based focus in radiology.

**ABBREVIATIONS:** AAFP = American Academy of Family Physicians; AAO-HNS = Academy of Otolaryngology–Head and Neck Surgery; ACR = American College of Radiology; R-SCAN = Radiology Support, Communication, and Alignment Network

Starting in the late 1990s, rates of use of diagnostic imaging studies within all modalities have seen a dramatic rise, with average growth rates in the use of CT, MR imaging, and nuclear medicine studies of >10% each year in ambulatory settings between 1995 and 2001.<sup>1</sup> Additionally, from 2000 to 2007, the use of imaging studies grew faster than any other physician service among Medicare patients,<sup>2</sup> raising concerns about overuse of imaging.<sup>3</sup> Diagnostic imaging undoubtedly plays an essential role in the diagnosis and treatment planning of many patients. The increasing use of advanced imaging techniques, however, has substantial financial implications, with approximately \$100 billion spent on outpatient imaging alone in 2006, and is a major driving

force for increasing governmental health care expenditures and rising insurance premiums faced by employers and individuals.<sup>4</sup>

The purpose of this article was to highlight the unique role radiologists play in ensuring the appropriate use of imaging studies, particularly neuroimaging. We will review how clinical guidelines can help frame decisions about the appropriate use of neuroimaging studies. We will then review ways in which radiologists can collaborate with clinicians in ensuring appropriate ordering and discuss potential challenges in making the transition to a value-centered practice approach.

## Appropriate Neuroimaging Guidelines

**Choosing Wisely Campaign.** To heighten awareness of overused diagnostic tests and treatments, the American Board of Internal Medicine launched the Choosing Wisely initiative<sup>5</sup> in 2012. As a part of this campaign, 9 leading medical organizations, including the American College of Radiology (ACR) and leadership bodies from various medicine subspecialties, were asked to choose 5 common tests or treatments whose use should be re-evaluated by the ordering physicians. Among 45 tests and procedures listed, half were directly related to imaging.<sup>6</sup> Since 2012, other medical societies have joined the original 9 and offered their own lists of overused tests or procedures. According to a recent compilation from Rao and Levin,<sup>7</sup> nearly half of this expanded list of overused

From the Department of Radiology (J.B.), Johns Hopkins Hospital, Baltimore, Maryland; Department of Radiology (K.K.), University Hospitals Case Medical Center Case Western Reserve University, Cleveland, Ohio; Department of Neuroradiology (J.N.), Mallinckrodt Institute of Radiology, St. Louis, Missouri; and Department of Radiology (M.W.), Neuroradiology Section, Stanford University School of Medicine, Stanford, California.

Please address correspondence to Max Wintermark, MD, MAS, MBA, Department of Radiology, Stanford University School of Medicine, 300 Pasteur Dr, S047, Stanford, CA 94305; e-mail: max.wintermark@gmail.com

Indicates open access to non-subscribers at [www.ajnr.org](http://www.ajnr.org)

Indicates article with supplemental on-line tables.

<http://dx.doi.org/10.3174/ajnr.A4821>

tests and treatments relates to either diagnostic radiology or cardiac imaging. Furthermore, in an expanded survey of 26 major medical societies, 38 of the 130 (29%) listed overused services targeted imaging, more than any other category.<sup>8</sup> Nearly a quarter of the most overused imaging tests related to neuroimaging, which placed second among all subspecialties behind cardiac testing. This finding reflects neurologic symptoms and disorders, both acute and chronic, having such a high prevalence and accounting for a significant proportion of chief symptoms in both emergency and outpatient settings.<sup>9,10</sup> Although the Choosing Wisely campaign was inspired primarily from the overuse of diagnostic testing and therapies, it should not be viewed exclusively as an initiative to ration or restrict care to patients. Rather, the primary goal of the campaign is to encourage a more patient-centered care model and “to promote physician and patient conversations about making choices about treatments.”<sup>5</sup>

**Imaging 3.0.** In response to pressure placed on the field as a result of the Choosing Wisely initiative, several radiology societies, including the American Board of Radiology, ACR, and Radiological Society of North America, have made the concept of value and quality-based care, rather than volume-driven care, a pillar of their Imaging 3.0 initiative.<sup>11</sup> One of the key components of the value-based Imaging 3.0 campaign is development and refinement of clear, evidenced-based guidelines regarding the appropriateness of different imaging modalities in wide varieties of clinical settings and scenarios among all subspecialties. These encompass a number of tools, including appropriateness criteria, practice guidelines or parameters, and different software solutions to support clinical decision-making and the selection of the most appropriate imaging test in any particular clinical setting.

### **Imaging Appropriateness: Illustration of Selected Adult and Pediatric Neurologic Conditions**

Practice parameters describe recommended conduct of specific imaging tests or image-guided interventions. They are derived from the current literature and the consensus opinion of experts. Practice parameters are not intended to be legal standards of care or conduct and may be modified as determined by individual circumstances and available resources. The ACR, in collaboration with the American Society of Neuroradiology, the Society of NeuroInterventional Surgery, and the Society of Pediatric Radiology, has developed 20 practice parameters and technology standards that pertain to neuroimaging and neurointervention (<http://www.acr.org/Quality-Safety/Standards-Guidelines/Practice-Guidelines-by-Technique/Neuroradiology>).

Appropriateness criteria are guidelines to assist the referring physicians and other providers in making the most appropriate imaging or treatment decisions for specific clinical conditions. Examples of appropriateness criteria include the ACR Appropriateness Criteria and the Canadian Association of Radiology guidelines. The ACR Appropriateness Criteria include more than 20 separate topics discussing the appropriateness of imaging in adult and pediatric neurologic conditions (<http://www.acr.org/Quality-Safety/Standards-Guidelines/Practice-Guidelines-by-Modality/Neuroradiology>).

Reviewing all the neuroimaging-related practice parameters and appropriateness criteria and the underlying evidence goes

beyond the scope of this article and has been addressed elsewhere.<sup>12</sup> Following are examples illustrating selected adult and pediatric neurologic conditions in which the selection of appropriate imaging is often challenging for referring physicians, and in which different rules, guidelines, and practice parameters have been developed by different professional societies and entities to help the referring physician’s decision process.

**Traumatic Brain Injury.** Traumatic brain injury is a common reason for presentation in emergency settings, with most injuries classified as “mild.”<sup>13</sup> Mild traumatic brain injury is typically defined according to clinical criteria such as the Glasgow Coma Scale and other clinical signs and symptoms at the time of presentation.<sup>14,15</sup> Several sets of basic clinical criteria, such as the New Orleans Criteria and the Canadian Head CT Rule and clinical guidelines from the American College of Emergency Physicians/Centers for Disease Control and Prevention<sup>16</sup> and the ACR Appropriateness Criteria<sup>17</sup> detail “high-risk” criteria that warrant evaluation of patients with mild traumatic brain injury with CT of the head, which is the preferred method of evaluation of head trauma (On-line Table 1). Further details on neuroimaging guidelines for patients with traumatic brain injury are provided in a white paper written jointly by the ACR, American Society of Neuroradiology, and American Society of Functional Neuroradiology.<sup>18,19</sup>

**Headache.** Headache is among the most common medical symptoms, both in emergency and outpatient settings.<sup>20</sup> Most primary headaches can be evaluated via history and physical examination alone. Neuroimaging is warranted to distinguish primary headaches from secondary causes (On-line Table 1). While guidelines such as the Headache Consortium guidelines in migraine work-up,<sup>21</sup> multispecialty consensus on diagnosis and treatment of headache,<sup>22</sup> and the ACR Appropriateness Criteria<sup>23</sup> offer precise, evidence-based guidelines for headache types such as migraines, vascular origin, and post traumatic, recommendations for some headache types such as tension are still not well-defined. Indications for neuroimaging are strongly based on clinical history and a detailed physical examination. MR imaging is generally the preferred technique for a change in headache character or chronic headache with new neurologic examination findings (On-line Table 1). Conversely, stable headaches or headaches with stable examination findings or classic migraine patterns should not be evaluated via neuroimaging.

**Low Back Pain.** Low back pain is one of the most common reasons for seeking outpatient medical care.<sup>24</sup> Given the chronicity of most back pain relative to other presenting neurologic symptoms, duration of symptoms and response to conservative treatment play an important role in imaging strategies, as detailed in a meta-analysis<sup>25</sup> and in multiple published guidelines (On-line Table 1).<sup>26-28</sup> Specifically, in the absence of “red flag” features, imaging should be reserved for pain lasting >4–6 weeks and not responding to an appropriate trial of conservative therapy. Imaging work-up should be pursued with MR imaging with little-to-no role for plain radiographs in the absence of acute trauma (On-line Table 1).

**Syncope.** Although syncope and syncope mimics are common reasons for emergency department visits, the etiology of a synco-

pal episode can usually be determined from a detailed history and physical examination.<sup>29</sup> Imaging is not recommended unless underlying neurologic etiology is suspected in the initial work-up as advocated by the San Francisco Syncope Rule,<sup>30</sup> European Society of Cardiology Guidelines,<sup>29</sup> and the American Academy of Family Physicians (AAFP) guidelines (On-line Table 1).<sup>31</sup>

**Hearing and Vision Loss.** Hearing and vision loss are common neurologic symptoms, especially in an aging population.<sup>32,33</sup> While most of these conditions require further work-up with a proper clinical history and examination, there are settings in which diagnostic imaging may help identify life-threatening or reversible causes from more benign, age-related etiologies. With vision loss, imaging should only be considered for acute vision loss or new concerning vision examination findings as described by the guidelines from the American Academy of Ophthalmology,<sup>34</sup> AAFP,<sup>35</sup> and ACR (On-line Table 1).<sup>36</sup> In the absence of trauma, evaluation is generally performed with MR imaging. According to the American Academy of Otolaryngology–Head and Neck Surgery (AAO-HNS),<sup>37</sup> there is a role for imaging in conductive hearing loss, generally evaluated with CT of the temporal bones, and sensorineural hearing loss, generally evaluated with MR imaging. Cases of explained progressive, symmetric conductive or sensorineural hearing loss, which account for most hearing loss referrals, do not warrant imaging evaluation (On-line Table 1).

**Other Head and Neck Disorders.** Uncomplicated acute rhinosinusitis and hoarseness are encountered routinely in the ambulatory setting.<sup>38</sup> While most of these cases are benign and self-limited, more extensive evaluation with focused diagnostic imaging may be necessary in selected cases. The proper imaging evaluation algorithm for rhinosinusitis follows published guidelines from the Infectious Diseases Society of America,<sup>39</sup> AAO-HNS,<sup>40</sup> AAFP,<sup>41</sup> and ACR (On-line Table 1).<sup>42</sup> For cases meeting the clinical criteria of acute or subacute uncomplicated rhinosinusitis, imaging is not to be pursued. CT is recommended only in cases of complicated sinusitis, immunocompromised hosts, or recurrence. In contrast, there is generally a lesser role of imaging in the initial evaluation of hoarseness. In fact, according to guidelines from the AAO-HNS,<sup>43</sup> imaging should only be considered after a clinical examination with direct laryngoscopy.

**Pediatric Neurologic Conditions.** Although there is some overlap between the frequently encountered neurologic conditions of children and adults, several neurologic symptoms are unique to children. Additionally, work-up and imaging of the common symptoms may differ between children and adults. Because children are also likely to present in the emergency setting, it is imperative that emergency department physicians, in addition to pediatricians, be aware of the appropriateness of imaging pediatric patients. Furthermore, because children are more sensitive to ionizing radiation effects, these patients should be imaged judiciously.

As with adults, mild traumatic brain injury is a common emergency department presentation with potentially devastating sequelae.<sup>44</sup> Several sets of criteria such as the Pediatric Emergency Care Applied Research Network rule,<sup>45</sup> the Children's Head Injury Algorithm for the Prediction of Important Clinical Events

rule,<sup>46</sup> the Canadian Assessment of Tomography for Childhood Head Injury rule,<sup>47</sup> and the ACR Appropriateness Criteria<sup>48</sup> outline high-risk criteria specific to the pediatric population that warrant evaluation with CT (On-line Table 2). Alternatively, pediatric patients with mild traumatic brain injury in the emergency department may have CT substituted if no neurologic symptoms are observed.

Acute rhinosinusitis is another head and neck pathology common to both adults and pediatric patients.<sup>49</sup> Indications for imaging pediatric patients have been specifically evaluated in guidelines by the Infectious Diseases Society of America,<sup>39</sup> the American Academy of Pediatrics,<sup>50</sup> and the ACR<sup>51</sup> and are similar to recommendations for adult patients. These indications include any high-risk signs and symptoms as detailed in On-line Table 2.

Last, febrile seizure is a unique entity to pediatric patients.<sup>52</sup> According to the guidelines from American Academy of Pediatrics<sup>53</sup> and the ACR,<sup>54</sup> patients meeting the criteria for simple febrile seizure (lasting <15 minutes and not recurring within 24 hours) should not undergo imaging (On-line Table 2). Complex febrile seizures (prolonged, recurring more than once in 24 hours, or focal) are rarely associated with underlying pathology such as meningitis, encephalitis, or child abuse. Imaging, preferably with MR imaging or CT, may be performed in selected patients with complex febrile seizures when meningitis/encephalitis or underlying trauma is suspected.<sup>54-56</sup>

### **Barriers to Implementation**

Application of the imaging appropriateness principles discussed above can prove challenging. The most important factors contributing to the referring physicians' inappropriate use of imaging include time constraints and demanding patients.<sup>57,58</sup> Many physicians face greater pressure because the fee-for-service payment model, which still dominates US health care, rewards physicians who see patients in bulk. The propensity for shorter patient visits is now ubiquitous in medicine because the primary care physician generates revenue per visit.<sup>57</sup> This results in a shorter time for the referring physicians to research appropriate tests, consult a radiologist, or convince a patient that an imaging test is not necessary. Furthermore, there is increased scrutiny of the medical decision-making and displacement of financial risk to the practitioner. Defensive medicine, a term describing alterations in clinical behavior due to the threat of malpractice liability,<sup>59</sup> has a disputed impact on ordering practices in the emergency setting.<sup>60</sup> Last, a potential barrier to the implementation of clinical decision-support tools, discussed in greater detail in the following section, is the potential for circumventing their use with out-of-network referrals, though this was shown not to be the case in a recent study by Prabhakar et al.<sup>61</sup>

One of the important obstacles to promoting adoption of resource-conscious neuroimaging ordering habits relates to the difficulty of disseminating the relevant guidelines among the referring physicians. Despite the inclusion of "systems-based practice" as one of the 6 core competencies of the Accreditation Council for Graduate Medical Education, awareness of imaging appropriateness is not being emphasized in residency training. As an illustration, Taragin et al<sup>62</sup> administered a survey in which internal medicine residents were asked to choose the appropriate examination for specific clinical situations. Less than 50% of the respondents

answered more than half of the 12 questions correctly. A similar study conducted with emergency medicine residents demonstrated no significant improvement in the ability to choose appropriate studies over the course of a 4-year residency.<sup>63</sup> Given the lack of emphasis placed on this topic in residency training, physicians are more likely to turn to Google searches than the appropriateness criteria when determining the most appropriate imaging technique for patients.<sup>63,64</sup> Although ahead of their peers in other specialties, radiology residents' knowledge of appropriateness guidelines is still incomplete, with residents answering a median of 15 of 20 appropriateness questions correctly in study by Chiunda and Mohammed.<sup>65</sup> In a survey by Powell et al,<sup>66</sup> while most radiology trainees were familiar with the ACR Appropriateness Criteria, only 14% of residents reported regular inclusion of the Criteria in formal faculty didactics.

### **Importance of Ordering Wisely and Clinical Decision Support**

Beginning in January 2017, the Centers for Medicare and Medicaid Services will require all referring physicians to use some form of Clinical Decision Support technology before ordering advanced imaging examinations for Medicare patients ([https://www.cms.gov/Medicare/Demonstration-Projects/DemoProjects/EvalRpts/downloads/RAND\\_EMID\\_Report\\_to\\_Congress.pdf](https://www.cms.gov/Medicare/Demonstration-Projects/DemoProjects/EvalRpts/downloads/RAND_EMID_Report_to_Congress.pdf)). This law specifies that the Clinical Decision Support system must use appropriate-use criteria "developed or endorsed by national professional medical specialty societies or other provider-led entities." Additionally, the criteria used must be scientifically valid and evidence-based.<sup>64</sup> Physicians ordering advanced imaging services will be reimbursed only if claims for reimbursement confirm that the appropriate-use criteria were consulted, whether the examination ordered adhered or did not adhere to an acceptable clinical decision-support rating.

Several decision-support tools have been developed to meet this need; examples include Medicalis (<https://consult.medicalis.com/>) and ACR Select (<http://www.acr.org/Quality-Safety/Appropriateness-Criteria/ACR-Select>) in the United States. ACR Select is a commercially available tool developed by National Decision Support Company (<https://www.linkedin.com/company/national-decision-support-company/>), which licensed the ACR Appropriateness Criteria and incorporated them into a digitally consumable version that can be integrated into electronic medical records and computerized order systems. Other international radiology organizations such as the Royal College of Radiologists in the United Kingdom (referral guidelines) and the Canadian Association of Radiologists (Diagnostic Imaging Referral Guidelines) have created similar tools and documents to facilitate the appropriate use of imaging. Insurers contract radiology benefit managers to provide authorization for advanced imaging services. These radiology benefit managers are private companies that use their own proprietary algorithms to determine appropriateness. These software solutions can be incorporated into the electronic medical records. Since its adoption, various implemented decision-support tools have led to improvement in appropriateness adherence in numerous settings. For example, Ip et al<sup>67</sup> showed a 12% sustained reduction in cross-sectional imaging for the outpatient, while Dunne et al<sup>68</sup> showed a 12% sustained reduction in

CT pulmonary angiography use in the emergency department after implementation of clinical decision-support systems. Although early data on imaging use with support tools are promising, their effect on clinical outcomes has yet to be fully evaluated.

In what may be the most critical element of the implementation of this mandate, the Centers for Medicare and Medicaid Services released its determination of what constitutes acceptable appropriate-use criteria at the end of 2015.<sup>69,70</sup> The Centers for Medicare and Medicaid Services selection of these criteria will have to meet the following measures: 1) Criteria must be developed or endorsed by national professional medical specialty societies or provider-led entities, 2) Criteria must be scientifically valid and evidence-based, and 3) Criteria must be based on published studies that are reviewable by stakeholders.

### **What Can Radiologists Practically Do to Address the Situation?**

This change in culture provides an opportunity for radiologists to guide and support our clinician colleagues during the transition to value-based care. Effectively guiding referring providers toward appropriate imaging use will rely on improving clinicians' knowledge and effective communication among all members involved in the care of patients, which includes radiologists. These goals can be achieved on a clinician-to-radiologist level or as a part of larger clinician-support projects and initiatives.

To effectively influence clinicians' ordering behavior, improving knowledge about imaging appropriateness must be made a top priority. Furthermore, optimal communication between radiologists and referrers is critical because the effective exchange of information can both prevent unnecessary or inappropriate testing and help ensure that patients experience fewer delays in care.<sup>71,72</sup> Continued strong bonds between radiologists and clinicians will also allow development of educational and quality-improvement programs in imaging appropriateness. A recent article reported the initiatives undertaken by a progressive group of radiologists, which included Continuing Medical Education programs for referring physicians and midlevel practitioners.<sup>30</sup> This group developed a mobile ordering guidelines app for the referrers to use as a reference when ordering imaging examinations. They even provide a communication center that allows the ordering physicians to connect directly with radiologists at any time of day. Interventions like these will be invaluable in changing the ordering patterns that have become ingrained in clinical practice and residency training programs. In some cases, referring clinicians have initiated educational programs within their own departments in an effort to optimize their imaging examination-ordering behavior.<sup>73</sup> Similarly, the Kaiser Permanente Colorado branch has tried to use the recommendations of the Choosing Wisely campaign for affordable health care at the management level.<sup>74</sup>

Any radiologist can engage in a similar effort by participating in the Radiology Support, Communication, and Alignment Network (R-SCAN) project, for which the ACR received one of the 39 health care collaborative network grants of the CMS Transforming Clinical Practice Initiative to support new levels of care coordination and integration as health care payment systems transition from volume-driven to value-based ([www.acr.org/rscan](http://www.acr.org/rscan)).

R-SCAN is a Practice Quality Improvement project that focuses on improving imaging use for 11 topics defined in the Choosing Wisely campaign, including the neuroimaging topics discussed individually in the first part of this article. In R-SCAN, radiologists collaborate with their referring clinicians, assess the baseline use of a certain imaging test, implement a series of interventions to improve the use of such test, and finally measure the effect of the interventions on the use rate of this test. R-SCAN program participants are guided by a step-by-step “recipe” and can earn Continuing Medical Education credits and American Board of Radiology approved Maintenance of Certification Part 4 credit and position themselves for success under new payment structures of the Medicare Access and CHIP Reauthorization Act of 2015, which will govern how radiologists are paid in the near future (<https://www.congress.gov/bill/114th-congress/house-bill/2>).

In addition to improving referring clinicians’ knowledge of imaging recommendations, continuing knowledge of imaging appropriateness among radiologists should not be overlooked. To ensure that the next generation of radiologists is ready to guide referring clinicians, this skill should be mastered in residency. Thus, the ACR Appropriateness Criteria have been an increasingly incorporated feature in radiology resident curricula.<sup>75</sup> Emerging evidence suggests that the clinicians are changing how they practice in response to the Choosing Wisely campaign. Alterations in radiation therapy practices in patients with breast cancer in response to the Choosing Wisely campaign have been reported recently. Clinical decision-support systems have thus far shown substantial promise in reining in unnecessary imaging examination orders. A 2013 study demonstrated a reduction of >75% in the number of inappropriately ordered imaging studies for evaluation of coronary artery disease when a point-of-order decision support tool was used, with a simultaneous significant increase in the percentage of appropriate studies ordered.<sup>76</sup> Siström et al<sup>77</sup> demonstrated significant reductions in the outpatient volume of CT, sonography, and MR imaging examinations after implementation of a computerized electronic medical record order-entry system with integrated Clinical Decision Support. Finally, a study showed that targeted use of an imaging decision-support system could reduce inappropriate neuroimaging orders, with resultant substantial decreases in use rates of lumbar MR imaging for low back pain, head MR imaging for headache, and sinus CT for sinusitis.<sup>78</sup>

## CONCLUSIONS

There is a shift toward more appropriate use of health care resources in medicine, particularly imaging. Despite imaging being a crucial tool for better diagnosis and effective patient management, we have not optimized its use. One of the important reasons for inappropriate imaging referral is increasing financial pressure of the fee-for-service payment model, resulting in insufficient, short patient visits, leaving the referring physicians insufficient time to evaluate patients, research the appropriate imaging study, consult a radiologist, or talk to the patient about the appropriateness of imaging. Additional barriers include demanding patients and fear of poor physician evaluations and medical malpractice. Deficiency of knowledge on when and how to use imaging may also cause inappropriate imaging referrals.

Current campaigns such as Choosing Wisely and Imaging 3.0 raise awareness and encourage a culture of appropriate use of imaging. This coupled with greater physician knowledge and use of the criteria for appropriate imaging can help ensure that each patient gets exactly the imaging he or she needs, to the benefit of both our patients and our health care system. Implementing a practical medical imaging decision-making process is a complex undertaking requiring resource organization at every level of process-referral, scheduling, point-of-care, and follow-up.

Collaborative partnership among radiologists, referring physicians, and payers is critical for this transition, and radiologists can play a very important role. The R-SCAN project provides an opportunity for radiologists to positively influence the appropriate use of imaging and to emphasize their value as integral members of the health care team.

Disclosures: Max Wintermark—UNRELATED: Board Membership: GE National Football League Advisory Board.

## REFERENCES

1. Bhargavan M, Sunshine JH. **Utilization of radiology services in the United States: levels and trends in modalities, regions, and populations.** *Radiology* 2005;234:824–32 CrossRef Medline
2. Iglehart JK. **Health insurers and medical-imaging policy: a work in progress.** *N Engl J Med* 2009;360:1030–37 CrossRef Medline
3. American Health Insurance Plans. **Ensuring Quality through Appropriate Use of Diagnostic Imaging.** July 2008. <http://ahipcoverage.com/wp-content/uploads/2011/01/QualityAppropriateImaging.pdf>. Accessed August 10, 2015
4. Mitchell JM, Lagalia RR. **Controlling the escalating use of advanced imaging: the role of radiology benefit management programs.** *Med Care Res* 2009;66:339–51 CrossRef Medline
5. Cassel CK, Guest JA. **Choosing wisely: helping physicians and patients make smart decisions about their care.** *JAMA* 2012;307:1801–02 CrossRef Medline
6. Rao VM, Levin DC. **The overuse of diagnostic imaging and the Choosing Wisely initiative.** *Ann Intern Med* 2012;157:574–76 CrossRef Medline
7. Rao VM, Levin DC. **The Choosing Wisely initiative of the American Board of Internal Medicine Foundation: what will its impact be on radiology practice?** *AJR Am J Roentgenol* 2014;202:358–61 CrossRef Medline
8. Morden NE, Colla CH, Sequist TD, et al. **Choosing wisely—the politics and economics of labeling low-value services.** *N Engl J Med* 2014;370:589–92 CrossRef Medline
9. Weiss AJ, Wier LM, Stocks C, et al. **Overview of emergency department visits in the United States, 2011.** HCUP Statistical Brief #174 [Internet]. Rockville, Maryland: Agency for Healthcare Research and Quality; June 2014. <http://www.hcup-us.ahrq.gov/reports/statbriefs/sb174-Emergency-Department-Visits-Overview.pdf> Medline
10. St Sauver JL, Warner DO, Yawn BP, et al. **Why patients visit their doctors: assessing the most prevalent conditions in a defined American population.** *Mayo Clin Proc* 2013;88:56–67 CrossRef Medline
11. Ellenbogen PH. **Imaging 3.0: what is it?** *J Am Coll Radiol* 2013;10:229 CrossRef Medline
12. Medina LS, Sanelli PC, Jarvik JG. *Evidence-Based Neuroimaging Diagnosis and Treatment: Improving the Quality of Neuroimaging in Patient Care.* New York: Springer-Verlag; 2013
13. Rutland-Brown W, Langlois JA, Thomas KE, et al. **Incidence of traumatic brain injury in the United States, 2003.** *J Head Trauma Rehabil* 2006;21:544–48 CrossRef Medline
14. Kay T. **Neuropsychological treatment of mild traumatic brain injury.** *J Head Trauma Rehabil* 1993;8:74–85
15. Report to Congress on Mild Traumatic Brain Injury in the United

- States: Steps to Prevent a Serious Public Health Problem. 2003. <http://www.cdc.gov/traumaticbraininjury/pdf/mtbireport-a.pdf>. Accessed August 10, 2015
16. Jagoda AS, Bazarian JJ, Bruns JJ, et al; American College of Emergency Physicians, Centers for Disease Control and Prevention. **Clinical policy: neuroimaging and decisionmaking in adult mild traumatic brain injury in the acute setting.** *Ann Emerg Med* 2008;52:714–48 CrossRef Medline
  17. Davis PC, Drayer BP, Anderson RE, et al. **Head trauma: American College of Radiology—ACR Appropriateness Criteria.** *Radiology* 2000;215(suppl):507–24 Medline
  18. Wintermark M, Sanelli PC, Anzai Y, et al; American College of Radiology Head Injury Institute. **Imaging evidence and recommendations for traumatic brain injury: advanced neuro- and neurovascular imaging techniques.** *AJNR Am J Neuroradiol* 2015;36:E1–11 CrossRef Medline
  19. Wintermark M, Sanelli PC, Anzai Y, et al. **Imaging evidence and recommendations for traumatic brain injury: conventional neuroimaging techniques.** *J Am Coll Radiol* 2015;12:e1–14 CrossRef Medline
  20. Gaini SM, Fiori L, Cesana C, et al. **The headache in the emergency department.** *Neurol Sci* 2004;25(suppl 3):S196–201 CrossRef Medline
  21. Morey SS. **Headache Consortium releases guidelines for use of CT or MRI in migraine work-up.** *Am Fam Physician* 2000;62:1699–701 Medline
  22. Silberstein SD. **Practice parameter: evidence-based guidelines for migraine headache (an evidence-based review): report of the Quality Standards Subcommittee of the American Academy of Neurology.** *Neurology* 2000;55:754–62 CrossRef Medline
  23. Douglas AC, Wippold FJ 2nd, Broderick DF, et al. **ACR Appropriateness Criteria Headache.** *J Am Coll Radiol* 2014;11:657–67 CrossRef Medline
  24. Deyo RA, Phillips WR. **Low back pain: a primary care challenge.** *Spine* 1996;21:2826–32 CrossRef Medline
  25. Chou R, Fu R, Carrino JA, et al. **Imaging strategies for low-back pain: systematic review and meta-analysis.** *Lancet* 2009;373:463–72 CrossRef Medline
  26. Chou R, Qaseem A, Owens DK, et al; Clinical Guidelines Committee of the American College of Physicians. **Diagnostic imaging for low back pain: advice for high-value health care from the American College of Physicians.** *Ann Intern Med* 2011;154:181–89 CrossRef Medline
  27. Kochen MM, Blozik E, Scherer M, et al. **Imaging for low-back pain.** *Lancet* 2009;373:436–37 CrossRef Medline
  28. Davis PC, Wippold FJ 2nd, Brunberg JA, et al. **ACR Appropriateness Criteria on low back pain.** *J Am Coll Radiol* 2009;6:401–07 CrossRef Medline
  29. Moya A, Sutton R, Ammirati F, et al; Task Force for the Diagnosis and Management of Syncope; European Society of Cardiology (ESC); European Heart Rhythm Association (EHRA); Heart Failure Association (HFA); Heart Rhythm Society (HRS). **Guidelines for the diagnosis and management of syncope (version 2009).** *Eur Heart J* 2009;30:2631–71 CrossRef Medline
  30. Neeman N, Quinn K, Soni K, et al. **Reducing radiology use on an inpatient medical service: choosing wisely.** *Arch Intern Med* 2012;172:1606–08 CrossRef Medline
  31. Gauer RL. **Evaluation of syncope.** *Am Fam Physician* 2011;84:640–50 Medline
  32. Cruickshanks KJ, Wiley TL, Tweed TS, et al. **Prevalence of hearing loss in older adults in Beaver Dam, Wisconsin: the Epidemiology of Hearing Loss Study.** *Am J Epidemiol* 1998;148:879–86 CrossRef Medline
  33. Congdon N, O’Colmain B, Klaver CC, et al; Eye Diseases Prevalence Research Group. **Causes and prevalence of visual impairment among adults in the United States.** *Arch Ophthalmol* 1960 2004;122:477–85 Medline
  34. Feder RS, Olsen TW, Prum BE Jr, et al. **Comprehensive Adult Med- ical Eye Evaluation Preferred Practice Pattern(®) Guidelines.** *Ophthalmology* 2016;123:P209–36 CrossRef Medline
  35. Pelletier AL, Thomas J, Shaw FR. **Vision loss in older persons.** *Am Fam Physician* 2009;79:963–70 Medline
  36. Hasso AN, Drayer BP, Anderson RE, et al. **Orbits, vision, and visual loss.** *American College of Radiology. ACR Appropriateness Criteria.* *Radiology* 2000;215(suppl):579–87 Medline
  37. Stachler RJ1, Chandrasekhar SS, Archer SM, et al; American Academy of Otolaryngology-Head and Neck Surgery. **Clinical practice guideline: sudden hearing loss.** *Otolaryngol Head Neck Surg* 2012;146(3 suppl):S1–35 CrossRef Medline
  38. Schappert SM, Burt CW. **Ambulatory care visits to physician offices, hospital outpatient departments, and emergency departments: United States, 2001–02.** *Vital Health Stat 13* 2006;1–66 Medline
  39. Chow AW, Benninger MS, Brook I, et al; Infectious Diseases Society of America. **IDSA clinical practice guideline for acute bacterial rhinosinusitis in children and adults.** *Clin Infect Dis* 2012;54:e72–112 CrossRef Medline
  40. Rosenfeld RM, Piccirillo JF, Chandrasekhar SS, et al. **Clinical practice guideline (update): adult sinusitis.** *Otolaryngol Head Neck Surg* 2015;152:S1–39 CrossRef Medline
  41. Huntzinger A. **Guidelines for the diagnosis and management of rhinosinusitis in adults.** *Am Fam Physician* 2007;76:1718–24
  42. Cornelius RS, Martin J, Wippold FJ, et al; American College of Radiology. **ACR appropriateness criteria sinonasal disease.** *J Am Coll Radiol* 2013;10:241–46 CrossRef Medline
  43. Schwartz SR, Cohen SM, Dailey SH, et al. **Clinical practice guideline: hoarseness (dysphonia).** *Otolaryngol Head Neck Surg* 2009;141: S1–31 CrossRef Medline
  44. Schneier AJ, Shields BJ, Hostetler SG, et al. **Incidence of pediatric traumatic brain injury and associated hospital resource utilization in the United States.** *Pediatrics* 2006;118:483–92 CrossRef Medline
  45. Kuppermann N, Holmes JF, Dayan PS, et al; Pediatric Emergency Care Applied Research Network (PECARN). **Identification of children at very low risk of clinically-important brain injuries after head trauma: a prospective cohort study.** *Lancet* 2009;374:1160–70 CrossRef Medline
  46. Dunning J, Daly JP, Lomas JP, et al; Children’s head injury algorithm for the prediction of important clinical events study group. **Derivation of the children’s head injury algorithm for the prediction of important clinical events decision rule for head injury in children.** *Arch Dis Child* 2006;91:885–91 CrossRef Medline
  47. Osmond MH, Klassen TP, Wells GA, et al; Pediatric Emergency Research Canada (PERC) Head Injury Study Group. **CATCH: a clinical decision rule for the use of computed tomography in children with minor head injury.** *CMAJ* 2010;182:341–48 CrossRef Medline
  48. Ryan ME, Palasis S, Saigal G, et al. **ACR Appropriateness Criteria head trauma—child.** *J Am Coll Radiol* 2014;11:939–47 CrossRef Medline
  49. Sharp HJ, Denman D, Puumala S, et al. **Treatment of acute and chronic rhinosinusitis in the United States, 1999–2002.** *Arch Otolaryngol Head Neck Surg* 2007;133:260–65 CrossRef Medline
  50. Wald ER, Applegate KE, Bordley C, et al; American Academy of Pediatrics. **Clinical practice guideline for the diagnosis and management of acute bacterial sinusitis in children aged 1 to 18 years.** *Pediatrics* 2013;132:e262–80 CrossRef Medline
  51. McAlister WH, Parker BR, Kushner DC, et al. **Sinusitis in the pediatric population.** *American College of Radiology. ACR Appropriateness Criteria.* *Radiology* 2000;215(suppl):811–18 Medline
  52. Waruiru C, Appleton R. **Febrile seizures: an update.** *Arch Dis Child* 2004;89:751–56 CrossRef Medline
  53. Subcommittee on Febrile Seizures, American Academy of Pediatrics. **Neurodiagnostic evaluation of the child with a simple febrile seizure.** *Pediatrics* 2011;127:389–94 CrossRef Medline
  54. Strain JD, Kushner DC, Babcock DS, et al. **Imaging of the pediatric patient with seizures.** *American College of Radiology. ACR Appropriateness Criteria.* *Radiology* 2000;215(suppl):787–800 Medline
  55. Hesdorffer DC, Chan S, Tian H, et al. **Are MRI-detected brain ab-**

- normalities associated with febrile seizure type? *Epilepsia* 2008;49:765–71 CrossRef Medline
56. DiMario FJ. **Children presenting with complex febrile seizures do not routinely need computed tomography scanning in the emergency department.** *Pediatrics* 2006;117:528–30 CrossRef Medline
  57. Freidson E. **Prepaid group practice and the new “demanding patient.”** *Milbank Mem Fund Q Health Soc* 1973;51:473–88 CrossRef Medline
  58. Landon BE, Wilson IB, Cleary PD. **A conceptual model of the effects of health care organizations on the quality of medical care.** *JAMA* 1998;279:1377–82 CrossRef Medline
  59. Studdert DM, Mello MM, Sage WM, et al. **Defensive medicine among high-risk specialist physicians in a volatile malpractice environment.** *JAMA* 2005;293:2609–17 CrossRef Medline
  60. Waxman DA, Ridgely MS, Heaton P. **The effect of malpractice reform on emergency department care.** *N Engl J Med* 2015;372:192 CrossRef Medline
  61. Prabhakar AM, Harvey HB, Misono AS, et al. **Imaging decision support does not drive out-of-network leakage of referred imaging.** *J Am Coll Radiol* Feb 19. [Epub ahead of print] CrossRef Medline
  62. Taragin BH, Feng L, Ruzal-Shapiro C. **Online radiology appropriateness survey: results and conclusions from an academic internal medicine residency.** *Acad Radiol* 2003;10:781–85 CrossRef Medline
  63. Dym RJ, Burns J, Taragin BH. **Appropriateness of imaging studies ordered by emergency medicine residents: results of an online survey.** *AJR Am J Roentgenol* 2013;201:W619–25 CrossRef Medline
  64. Bautista AB, Burgos A, Nickel BJ, et al; American College of Radiology Appropriateness. **Do clinicians use the American College of Radiology Appropriateness criteria in the management of their patients?** *AJR Am J Roentgenol* 2009;192:1581–85 CrossRef Medline
  65. Chiunda AB, Mohammed TL. **Knowledge of ACR thoracic imaging Appropriateness Criteria® among trainees: one institution’s experience.** *Acad Radiol* 2012;19:635–39 CrossRef Medline
  66. Powell DK, Silberzweig JE. **The use of ACR Appropriateness Criteria: a survey of radiology residents and program directors.** *Clin Imaging* 2015;39:334–38 CrossRef Medline
  67. Ip IK, Schneider L, Seltzer S, et al. **Impact of provider-led, technology-enabled radiology management program on imaging.** *Am J Med* 2013;126:687–92 CrossRef Medline
  68. Dunne RM, Ip IK, Abbett S, et al. **Effect of evidence-based clinical decision support on the use and yield of CT pulmonary angiographic imaging in hospitalized patients.** *Radiology* 2015;276:167–74 CrossRef Medline
  69. Protecting Access to Medicare Act of 2014. Pub L No. 113–93, §218, 128 Stat 1040
  70. Timbie JW, Hussey PS, Burgette LF, et al. **Medicare Imaging Demonstration Final Evaluation.** 2014. [http://www.rand.org/pubs/research\\_reports/RR706.html](http://www.rand.org/pubs/research_reports/RR706.html). Accessed August 10, 2015
  71. Gunn AJ, Alabre CI, Bennett SE, et al. **Structured feedback from referring physicians: a novel approach to quality improvement in radiology reporting.** *AJR Am J Roentgenol* 2013;201:853–57 CrossRef Medline
  72. Teske K. **Three ways radiology groups can be more proactive about utilization management.** The Advisory Board Company. September 24, 2014. <https://www.advisory.com/research/imaging-performance-partnership/the-reading-room/2014/09/three-ways-radiology-groups-can-be-more-proactive-about-utilization-management>. Accessed August 10, 2015
  73. **Choosing Wisely.** An initiative of the ABIM Foundation. **Choosing Wisely Prompts Kaiser Permanente Branch to Action.** February 6, 2014. <http://www.choosingwisely.org/resources/updates-from-the-field/choosing-wisely-prompts-kaiser-permanente-branch-to-action/>. Accessed March 7, 2016
  74. Curry HA, Palladino ML, Jaggi R. **Utilization of hypofractionated regimens for treatment of breast cancer in an insured population before and after initiation of ASTRO’s “Choosing Wisely” campaign.** *Int J Radiat Oncol Biol Phys* 2014;90:S62 CrossRef
  75. Mainiero MB. **Incorporating ACR Practice Guidelines, technical standards, and appropriateness criteria into resident education.** *J Am Coll Radiol* 2004;1:277–79 CrossRef Medline
  76. Lin FY, Dunning AM, Narula J, et al. **Impact of an automated multimodality point-of-order decision support tool on rates of appropriate testing and clinical decision making for individuals with suspected coronary artery disease: a prospective multicenter study.** *J Am Coll Cardiol* 2013;62:308–16 CrossRef Medline
  77. Siström CL, Dang PA, Weilburg JB, et al. **Effect of computerized order entry with integrated decision support on the growth of outpatient procedure volumes: seven-year time series analysis.** *Radiology* 2009;251:147–55 CrossRef Medline
  78. Blackmore CC, Medina LS. **Evidence-based radiology and the ACR Appropriateness Criteria.** *J Am Coll Radiol* 2006;3:505–09 CrossRef Medline
  79. Smits M, Dippel DWJ, de Haan GG, et al. **External validation of the Canadian CT Head Rule and the New Orleans Criteria for CT scanning in patients with minor head injury.** *JAMA* 2005;294:1519–25 CrossRef Medline
  80. Quinn JV, Stiell IG, McDermott DA, et al. **Derivation of the San Francisco Syncope Rule to predict patients with short-term serious outcomes.** *Ann Emerg Med* 2004;43:224–32 CrossRef Medline

# Radiation Dose Reduction in 4D Cerebral CT Angiography by Individualized Estimation of Cerebral Circulation Time

M.R. Radon, A. Chandran, M. Bhojak, and K.V. Das

## ABSTRACT

**BACKGROUND AND PURPOSE:** The novel technique of 4D CTA for dynamic assessment of the intracranial vessels has a greater radiation burden than conventional CTA. Previous descriptions of the technique used a fixed-duration exposure protocol. This study examines the potential for dose reduction by individualizing exposure time to patient physiology by the use of time-enhancement curve techniques as previously applied in CT angiography and venography.

**MATERIALS AND METHODS:** 4D-CTA examinations performed at our institution were retrospectively reviewed. Scan protocols used a test-bolus scan with either a subjective estimate of the main acquisition timing (estimated-duration method) or a quantitative measure (measured-duration method). The estimated-duration method used peak arterial enhancement to determine the start of exposure, with the duration chosen at the radiologist's discretion. The measured-duration method used arterial and venous time-enhancement curves to determine exposure start and duration. Exposure duration, study adequacy, quality score, and maximum venous enhancement were compared among groups.

**RESULTS:** One hundred fifty-one examinations used the estimated-duration method, and 53 used measured-duration. The measured-duration method used a shorter exposure time (10 versus 15.8 seconds;  $P < .001$ ). There was no statistically significant difference in the study adequacy rate, subjective quality score, or maximum venous enhancement. The radiation dose was reduced by 51% in the measured-duration method (3021 mGy  $\times$  cm, 6.9 mSv, versus 1473 mGy  $\times$  cm, 3.4 mSv). Both methods showed good agreement with DSA ( $\kappa = 0.88$  for estimated-duration,  $\kappa = 1.0$  for measured duration).

**CONCLUSIONS:** Exposure time in 4D-CTA can be reduced with dual time-enhancement curves to match exposure to physiology without degrading study adequacy or quality.

**ABBREVIATIONS:**  $t_{OA}$  = time to onset of arterial enhancement;  $t_{PA}$  = time delay to peak arterial enhancement;  $t_{PV}$  = time to peak venous enhancement

The recent development of time-resolved 4D-CTA provides a new technique for the assessment of intracranial flow dynamics, which can serve as a less invasive alternative to intra-arterial DSA. Potential uses for this technique include assessment of dural arteriovenous fistulas<sup>1-4</sup> and arteriovenous malformations<sup>5</sup> and classification of vessel clot burden and collateral flow in occlusive stroke.<sup>6,7</sup>

Due to the multiphasic nature of 4D-CTA, the radiation burden is higher than in a single-phase study. Concern over the total dose has previously been raised for CT perfusion,<sup>8,9</sup> and due to the

similarity of the techniques, it carries over to 4D-CTA. The effective dose for 4D-CTA reported in the literature ranges between 5.1 and 5.62 mSv.<sup>2,3,5,10</sup> These previously described techniques use a dynamic acquisition with a predetermined exposure time (between 15 and 22 seconds), with or without a preceding test-bolus acquisition. In addition to variance in exposure time, there is also variability in the rotation period and, therefore, temporal resolution. Earlier literature reports used a 1000-ms rotation period, but more recent studies have cited shorter rotation periods of 500 and 350 ms, though using a higher tube current.<sup>3,10,11</sup>

Test-bolus techniques yielding a time-attenuation curve have previously been shown beneficial in both 3D-CTA<sup>12</sup> and CT venography,<sup>13</sup> by allowing the time of acquisition to be matched to the time of peak contrast enhancement within the vessels of interest. A similar approach has been applied in previous descriptions of 4D-CTA to trigger the start of the acquisition. The benefit of accurate timing in 4D-CTA is not on peak enhancement, but

Received March 10, 2016; accepted after revision July 5.

From the Department of Neuroradiology, The Walton Centre, Liverpool, United Kingdom.

Please address correspondence to Mark Radon, MD, Department of Neuroradiology, The Walton Centre, Liverpool, L9 7UJ, UK; e-mail: Mark.radon@thewaltoncentre.nhs.uk

<http://dx.doi.org/10.3174/ajnr.A4911>

instead, it assists in achieving adequate temporal coverage. While an arterial time-enhancement curve provides information about contrast arrival, the venous time-enhancement curve provides information about contrast washout. We hypothesized that knowledge of these parameters can be used to tune the acquisition duration and provide an opportunity for dose reduction, while simultaneously avoiding inadequate studies in patients with a slow cerebral circulation time.

The primary end point of this study was to demonstrate diagnostic equivalence and reduced exposure time by using the measured-duration method in comparison with the estimated-duration method.

## MATERIALS AND METHODS

### Study Design

4D-CTA has been in use locally in selected patients since November 2013. Following a routine audit of radiation doses, which showed doses higher than published reports from other institutions, the CT protocol was modified in January 2015. The exposure factors were shown to be higher than those in prior literature reports, and previously published parameters were adopted as part of the review.<sup>1</sup>

At the same time, reducing exposure durations was attempted. The scan protocol was changed from using a subjective assessment of a test-bolus acquisition (estimated-duration method) to a replacement protocol using quantitative, objective measurements from the test bolus (measured-duration method). Patients were identified by searching the radiology information system for 4D-CTA examinations performed from November 2013 to July 2015. Retrospective analysis of these studies was performed to determine the adequacy of the method.

Because this study represents a retrospective review of these methods, the institutional research and development department waived the requirement for regional ethics committee approval or informed consent.

### CT Scanner and Scan Parameters

All studies were performed by using a 320-section CT scanner with maximum 160-mm volume coverage capability. A 3-phase protocol was used, consisting of a test-bolus, unenhanced subtraction mask, and dynamic acquisition. The test bolus used 15 mL of iodinated contrast (iopamidol, Niopam 370; Bracco UK, High Wycombe, UK) given intravenously at 6 mL/s, followed by 30 mL of saline at 6 mL/s. Repeat single 2-mm sections (80 kV, 100 mAs) through the circle of Willis at 2-second intervals were performed from which time-enhancement curves were derived. The mask acquisition used a single volumetric acquisition of the whole head (80 kV, 300 mAs).

Scan parameters for the estimated-duration protocol were those determined during the initial protocol development (80 kV, 150 mA, 750 ms) and were determined on the basis of local preference and empiric assessment of adequacy. Parameters for the measured-exposure protocol were based on a prior literature report (80 kV, 100 mA, 1000 ms).<sup>1</sup> In both protocols, the temporal reconstruction interval was 500 ms. The z-axis coverage was the whole head from the vertex to C1 and was usually the maximum,

160 mm. A total of 35 mL of contrast was given at 6 mL/s for the main acquisition, followed by 30 mL of saline at 6 mL/s.

### Acquisition Timing

An ROI was placed on a major artery (basilar or ICA) on the test-bolus images. The time delay between the start of contrast injection and the peak of arterial enhancement ( $t_{PA}$ ) was measured.

**Estimated-Duration Protocol.** The volume acquisition was triggered at a  $t_{PA}$  of 4 seconds. The exposure duration was at the discretion of the supervising radiologist, from a starting point of 16 seconds. This could be adjusted depending on clinical features and review of the arterial enhancement curve.

**Measured-Duration Exposure Protocol.** In addition to a major artery ROI, a second venous sinus ROI was used. The time delay to peak venous enhancement ( $t_{PV}$ ) was measured, and the arterial ROI was used to determine the time to onset of arterial enhancement ( $t_{OA}$ ), defined as an increase of attenuation of 100 HU over baseline. Acquisition was triggered at the  $t_{OA}$ , and duration was set at  $t_{PV}$  to  $t_{OA}$ . This process is illustrated schematically, together with typical subtracted image appearances, in Fig 1.

### Image Analysis

**Study Adequacy.** The dynamic acquisitions were examined for the visible inflow of contrast into the terminal ICA. Volumes at the start of the dynamic acquisitions that showed <40 HU of enhancement of the ICA were regarded as noncontributory. Volumes at the end of the acquisition that showed venous enhancement less than peak were also regarded as noncontributory. When the final volume showed rising venous enhancement, an adequate venous enhancement was defined arbitrarily as enhancement of >200 HU. A study was also judged as having inadequate time coverage if no prepeak arterial volumes were acquired. A subjective diagnostic quality score was also recorded by 2 experienced neuroradiologists in consensus. A score of 1 indicated a nondiagnostic study (for any reason), and 5 indicated excellent quality.

**Dose Reporting.** Dose-length products for the mask, test bolus, and dynamic components of the study were recorded. Effective doses were computed by using the conversion factor of 2.3  $\mu\text{Sv}/\text{mGy}/\text{cm}$ .<sup>14</sup>

**Concordance with DSA.** When patients subsequently underwent DSA, this was used as the criterion standard for comparison. To minimize bias, we used the initial blinded radiology report for the 4D-CTA as the basis of concordance. When there was discordance, the studies were reviewed to determine the cause. In view of the variety of pathology and indications for scanning, sensitivity and specificity were not calculated. Studies were considered concordant when both the DSA and 4D-CTA had the same category of diagnosis (eg, no vascular abnormality, AVF, AVM, aneurysm, vascular occlusion/stenosis).

### Statistical Analysis

The estimated-duration and measured-duration methods were compared on parameters of exposure duration, peak venous enhancement, study adequacy rate, and subjective quality score.

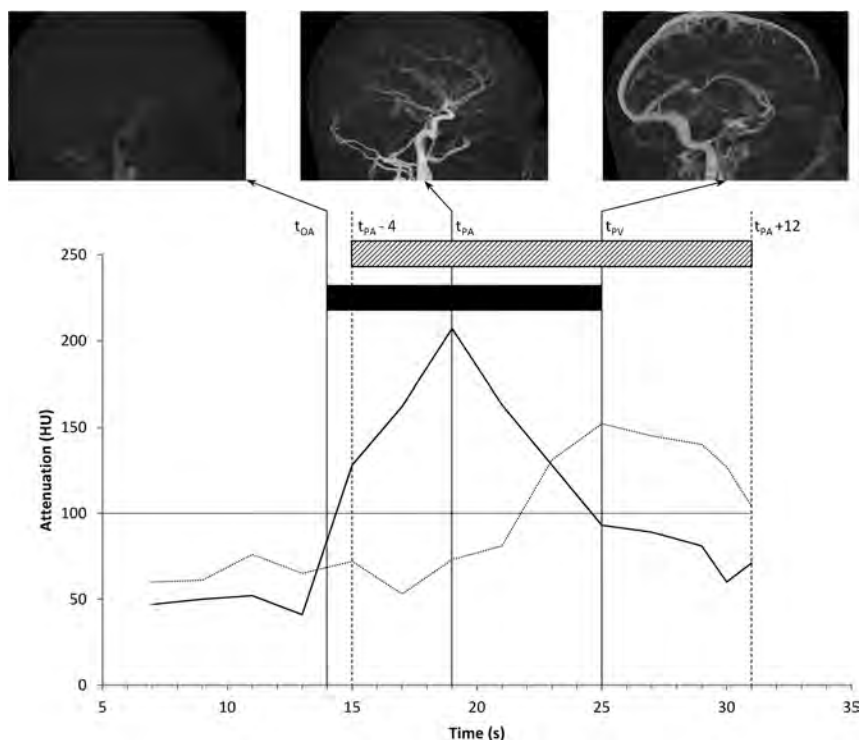


**FIG 1.** Schematic representation showing typical time-attenuation curves for arterial (*solid line*) and venous (*dotted line*) profiles. The  $t_{OA}$  was set to the nearest integer second in which the arterial attenuation crossed 100 HU (14 seconds in this figure, but note that measurements were only made on odd-numbered seconds). The  $t_{PA}$  and  $t_{PV}$  represent times of peak arterial and venous attenuation, respectively. The *gray bar* indicates the exposure time for the estimated duration protocol (16 seconds), and the *black bar* indicates the exposure time for the measured-duration protocol. Subtracted MIP images illustrate typical appearances of the acquisition at key phases.

**Table 1: Demographics and breakdown of indications for imaging**

	Estimated Duration (n = 151)	Measured Duration (n = 53)
<b>Demographics</b>		
Age (yr)	53.4 (19–87)	51.8 (21–79)
Sex (M/F)	67:84	25:28
<b>Indications (No.) (%)</b>		
Intraparenchymal hemorrhage	47 (31%)	20 (38%)
Suspected vascular lesion	37 (25%)	11 (21%)
Tinnitus	21 (14%)	5 (9%)
Tumor vascular assessment	11 (7%)	5 (9%)
Subdural hemorrhage	5 (3%)	0 (0%)
Subarachnoid hemorrhage	4 (3%)	0 (0%)
Untreated AVM/F assessment	7 (5%)	5 (9%)
Treated AVM/F assessment	6 (4%)	3 (6%)
Venous stenosis/thrombosis (including assessment of idiopathic intracranial hypertension)	8 (5%)	3 (6%)
Other	5 (3%)	1 (2%)

**Note:**—AVM/F indicates arteriovenous malformation or fistula.

Peak venous enhancement was compared by using the independent-samples  $t$  test after confirming normality with the Shapiro-Wilk test. The Mann-Whitney  $U$  test was used for non-normally distributed variables (exposure duration and study quality score), and the  $\chi^2$  test, for study adequacy rates. The Bonferroni correction for multiple comparisons was applied to the above 4 tests, by multiplying  $P$  values by the number of tests, subject to a maximum of 1.0. Statistical significance was defined as 5% after cor-

rection. The unweighted Cohen  $\kappa$  statistic was used to calculate concordance between DSA and 4D-CTA. Calculations were performed by using R statistical and computing software (<http://www.r-project.org/>). Because the radiation doses and number of acquired volumes were directly proportional to the exposure duration and radiation doses were additionally confounded by the change in exposure factors, no hypothesis testing was performed on these parameters.

Post hoc testing of the number of noncontributory volumes was performed. Testing was with the Mann-Whitney  $U$  test, with Bonferroni correction applied by multiplying  $P$  values by the number of tests ( $n = 2$ ).

## RESULTS

Two hundred four patients underwent whole-head 4D-CTA during the study period. Four studies were excluded due to deviations from the protocol (changes in anatomic coverage in 3 cases and intentional exclusion of the early arterial phase in 1). One hundred fifty-one patients were scanned with the estimated-duration method, and 53, with the measured-duration method. Demographics

and indications for 4D-CTA are summarized in Table 1.

With the subjective method, 145 scans were performed by using 160-mm coverage, 5 were performed with 140-mm coverage, and 1, with 150-mm coverage. All scans performed with the objective method had 160-mm coverage.

The measured-duration method used a shorter exposure time (10 versus 15.8 seconds,  $P < .001$ ), acquired fewer volumes, and achieved lower radiation doses (3021 mGy  $\times$  cm, 6.9 mSv, versus 1473 mGy  $\times$  cm, 3.4 mSv). These findings are summarized in Table 2. There was no statistically significant difference after correction for multiple comparisons in maximum venous enhancement, subjective study quality, or adequate time coverage rate. The distribution of maximum venous enhancement is illustrated in Fig 2. Both methods showed good intermodality concordance between 4D-CTA and DSA ( $\kappa = 0.88$  for estimated duration,  $\kappa = 1.0$  for measured duration).

For examinations using the full 160-mm anatomic coverage, the contributions to the radiation dose of the individual components of the examinations were the following: test bolus (dose-length product = 84 mGy  $\times$  cm, effective dose = 0.19 mSv), mask acquisition (339 mGy  $\times$  cm, 25.2 mGy, 0.78 mSv, CT dose index = 25.2 mGy), collimated estimated-duration volume acquisition (162 mGy  $\times$  cm/s, 0.37 mSv/s, 10.1 mGy/s), and measured-duration volume acquisition (108 mGy  $\times$  cm/s, 0.25 mSv/s, 6.8 mGy/s). For studies with less coverage, doses for mask and main acquisitions were proportionally lower.

**Table 2: Diagnostic performance of original and measured-duration protocols<sup>a</sup>**

	Estimated Duration (n = 151)	Measured Duration (n = 53)	P Value	Adjusted P Value
<b>Exposure and dose</b>				
Exposure time (sec)	15.75 (8.25–25.5)	10.0 (8–12)	<.001	<.001 <sup>b</sup>
No. of volumes	31 (26–36)	19 (19–19)		
Dose-length product (mGy × cm)	3021 (2536–3502)	1473 (1459–1526)		
Volume CT dose index (mGy)	185 (162–223)	88.9 (88.9–88.9)		
Effective dose (mSv)	6.9 (5.8–8.0)	3.4 (3.4–3.5)		
<b>Study quality</b>				
Maximum venous enhancement (HU)	372 (352–392)	324 (294–353)	.019	.076
Adequate time coverage (No.)	134 (88.7%)	49 (92.5%)	.444	1.00
Quality score	5 (5–5)	5 (5–5)	.837	1.00
No. of prearterial volumes	6 (4–10)	0 (0–1)	<.001 <sup>c</sup>	<.001 <sup>b,c</sup>
No. of postpeak venous volumes	2 (0–6)	0 (0–2)	<.001 <sup>c</sup>	<.001 <sup>b,c</sup>
<b>Diagnostic performance</b>				
Positive findings (No.)	58 (38.4%)	21 (39.6%)		
No. having DSA	56 (37.1%)	22 (41.5%)		
Intermodality concordance between 4D-CTA and DSA (No.)	51 (91.0%)	22 (100.0%)		
Cohen $\kappa$ statistic	$\kappa = 0.88$	$\kappa = 1.0$		

<sup>a</sup> Noncount values are shown as median (interquartile range), except for exposure time shown as median (range) and enhancement shown as mean (95% CI). Values for dose-length product include the entire examination, including test-bolus acquisition. CT dose index values include only whole-head acquisitions.

<sup>b</sup> Significant at the 5% level after Bonferroni correction.

<sup>c</sup> Post hoc test.

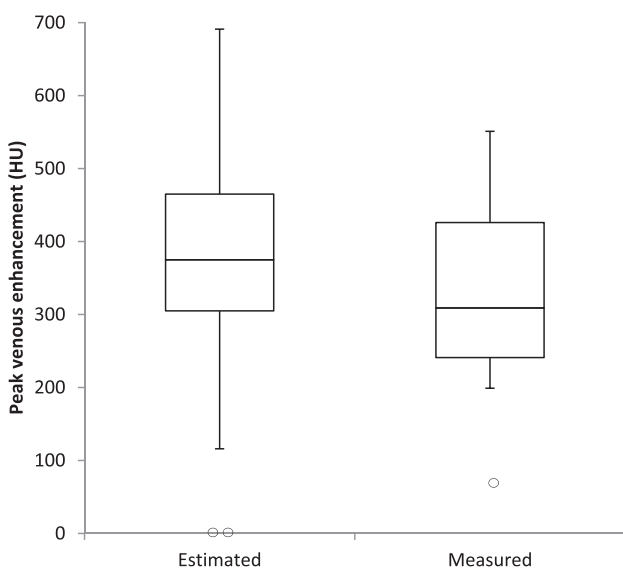


**FIG 2.** Boxplot illustrating distribution of peak venous enhancement between the estimated- and measured-duration scan protocols. Two outliers are shown in the estimated-duration group, in which no venous enhancement was present due to inadequate time coverage, and 1 outlier with very poor venous enhancement is shown in the measured-duration group.

## DISCUSSION

The main aim of this study was to demonstrate a technique for reducing the radiation dose by reducing total exposure time, with the intention of discarding only data of minimal diagnostic value. Other approaches to controlling dose in CTA and CTP have been previously reported. These include the use of iterative reconstruction algorithms, which can reduce the dose while retaining image quality,<sup>15</sup> and the use of a reduced tube potential (80 kV) to improve contrast with better matching to the iodine K-edge.<sup>16</sup> All prior reports of 4D-CTA make use of both techniques.

The use of the measured-duration method presented here has shown a reduced exposure time both in comparison with our historical control data and prior literature (Table 3). In addition, our measured-duration method both reduced the tube current and increased the rotation time (and therefore reduced the temporal resolution) over and above the estimated-duration method. The overall effect on per-image exposure was small (112 versus 100 mAs) with no subjectively perceptible change in noise. Subjective assessment of study quality included the adequacy of temporal resolution for the detection of abnormalities. This was not thought to be different among techniques, possibly due to the retention of the same reconstruction interval of 500 ms. A further small contribution to dose-saving was setting the rotation time to a multiple of the temporal reconstruction interval; when the total exposure time is not a multiple

of the reconstruction interval, part of the final rotation may not be reconstructable. In the estimated-duration group, the contribution of this effect was <1% of the total dose.

The recent description of higher temporal resolution techniques<sup>3,11,10</sup> may enable better characterization of flow dynamics. However, these techniques are associated with increased noise, which can be offset by the use of a higher tube current. These higher dose techniques for 4D-CTA may particularly benefit from strict control of exposure duration.

In this series, the measured-exposure group showed a trend toward a lower mean maximum venous enhancement value. This can be attributed to acquisition terminating before peak venous enhancement. One potential limitation of defining the end of the acquisition as the  $t_{pV}$  on the test bolus is that the duration of the main injection (5 seconds) is longer than that of the test injection (2.5 seconds); therefore, peak venous enhancement may be later. Thus, the timing derived in the measured-duration method is only an estimate because timing is inferred from the test-bolus scan. This is illustrated in Fig 3, which shows that the distribution of the number of postvenous volumes is heavily skewed toward zero in both groups, indicating a tendency toward early termination. We propose that to further reduce the rate of inadequate studies, the end of the acquisition should be set at  $t_{pV} + 1$  or  $t_{pV} + 2$  seconds. Even with this additional exposure time, the exposure duration would still be expected to be lower than that in the fixed-duration methods previously reported (the mean effective dose reported in this study would be 3.65 mSv if  $t_{pV} + 1$  had been used as the end of acquisition time). This additional late venous phase exposure could potentially be performed by using intermittent rather than continuous scanning.<sup>3</sup>

Figure 3A shows the distribution of exposure duration within the 2 groups. The measured-duration group shows relatively tight clustering of duration around 10 seconds. The outlying study

used 15 seconds, but this was due to incorrect measurement of the  $t_{PV}$ . If this had been measured correctly, the duration would have been 12 seconds. The estimated-duration group did demonstrate 7 studies that used exposures of  $>20$  seconds. In 6 of these cases, there were substantial intracranial hematomas; hence, a prolonged exposure was prescribed. However, in these cases, there were at least 10 postpeak venous volumes acquired, which indicated that the exposure could have been terminated up to 5 seconds earlier. In the final case, the patient had a history of cardiac failure and a severely prolonged circulation time so that venous enhancement was still rising at 25 seconds. There were no patients with similar features in the measured-duration group, which is a potential confounding factor.

In the measured-duration group, 4 studies showed inadequate time coverage. Three were due to inadequate venous-phase images, and 1 was due to the start of the acquisition in the late arterial phase. In 3 of these cases, incorrect determination of the  $t_{OA}$  and  $t_{PV}$  from ROIs placed to include bone,

allowed small-scale patient motion to cause severe degradation of the time-enhancement curves. Given the relatively high radiation dose associated with this procedure, it is essential to verify that the shapes of the time-enhancement curves are appropriate before measurement. In the final case, the ROIs were correctly placed, but the  $t_{PV}$  was measured from a broad plateau, in which peak enhancement was early within this plateau.

No discordant results were found in the measured-duration group; this finding may be a reflection of increased experience with the interpretation of 4D-CTA.<sup>17</sup> In addition, the sample size for this group was smaller. This article reports 2 false-positives within the estimated-exposure group. In both cases, the 4D-CTA did not demonstrate early venous enhancement, but suspicion had been raised on the basis of the “prominence” of the veins adjacent to a hematoma. These false-positives could potentially be regarded as interpretation errors, rather than a limitation of the image acquisition.

Methodologic limitations included the definition of adequate venous enhancement by an arbitrary threshold. Enhancement was also measured on postprocessed, subtracted whole-brain maximum-intensity-projection images computed by subtracting the mask acquisition from each postcontrast volume. Because maximum enhancement was reported, there is a potential source of bias because the maximum-intensity-projection images can capture the peak values of noise voxels within the projection, causing sensitivity to the through-plane length of the vessel and therefore to the location of ROIs and anatomic configuration.

**Table 3: Comparison of the currently reported techniques with 4D-CTA techniques (excluding combined 4D-CTA/CTP techniques) reported by other groups**

Report	Exposure Duration (sec)	Rotation Time (ms)	Exposure Parameters	Effective Dose (mSv)
Brouwer et al (2010) <sup>2</sup>	22	NS	80 kV, 120 mA	5.1
Hoogenboom et al (2012) <sup>11</sup>	15	500	80 kV, 240 mA	NS
Fujiwara et al (2013) <sup>3</sup>	12 <sup>a</sup>	500	80 kV, 200 mA	5.2
Willems et al (2011) <sup>1</sup> and (2012) <sup>5</sup>	22	1000	80 kV, 100 mA	5.2
D’Orazio et al (2014) <sup>10</sup>	15	350	80 kV, 120 mA	5.62
This study				
Estimated duration	15.6 (16 with option to adjust)	750	80 kV, 150 mA	6.9
Measured exposure	10.1 (mean)	1000	80 kV, 100 mA	3.4

**Note:**—NS indicates not stated.

<sup>a</sup>Ten-second continuous exposure followed by 4 intermittent exposures.

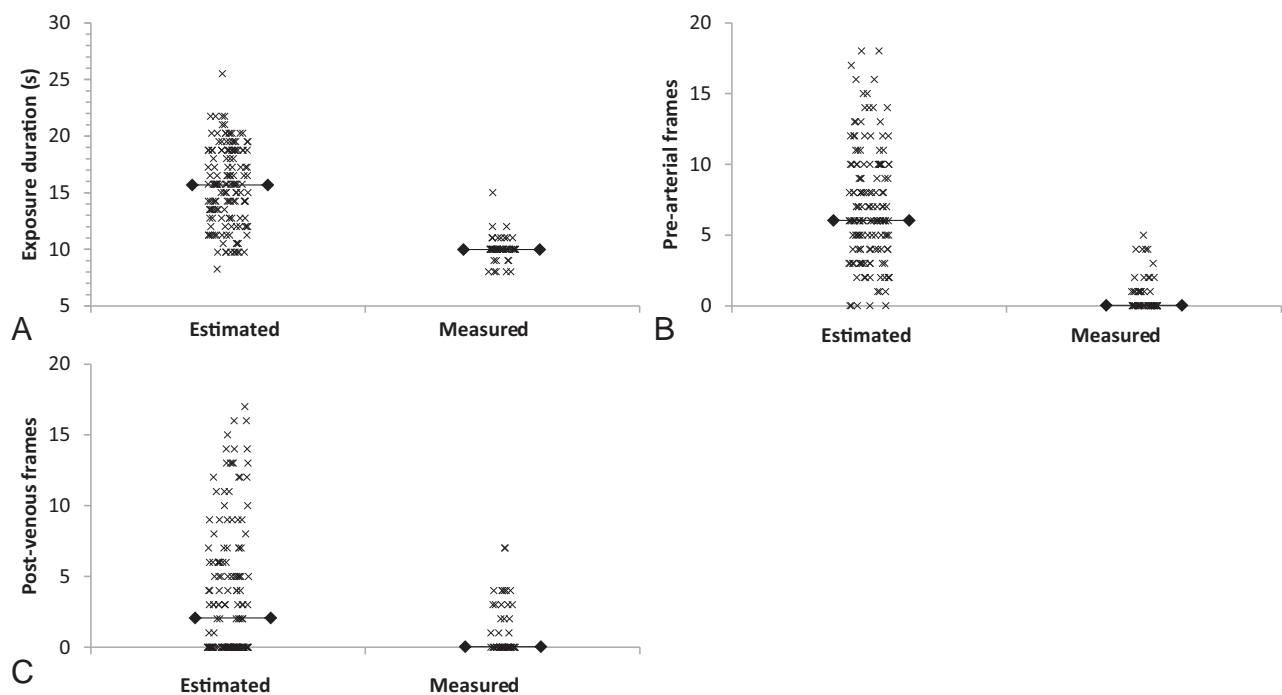


**FIG 3.** Scatterplots indicating exposure duration (A) and the number of nondiagnostic volumes due to the start of the acquisition before contrast arrival (B) and the end of the acquisition following contrast washout (C). Horizontal lines indicate the median.

## CONCLUSIONS

We have demonstrated that there is potential for reducing the radiation dose of 4D-CTA by more precisely matching the exposure duration to cerebral circulation time as determined by arterial and venous time-enhancement curves. This finding may be of particular value when combined with higher temporal resolution techniques.

## ACKNOWLEDGMENTS

The authors thank Debasree Purkayastha for advice on statistics and data presentation and for helpful comments about the manuscript.

## REFERENCES

1. Willems PW, Brouwer PA, Barfett JJ, et al. **Detection and classification of cranial dural arteriovenous fistulas using 4D-CT angiography: initial experience.** *AJNR Am J Neuroradiol* 2011;32:49–53 CrossRef Medline
2. Brouwer PA, Bosman T, van Walderveen MA, et al. **Dynamic 320-section CT angiography in cranial arteriovenous shunting lesions.** *AJNR Am J Neuroradiol* 2010;31:767–70 CrossRef Medline
3. Fujiwara H, Momoshima S, Akiyama T, et al. **Whole-brain CT digital subtraction angiography of cerebral dural arteriovenous fistula using 320-detector row CT.** *Neuroradiology* 2013;55:837–43 CrossRef Medline
4. Beijer TR, van Dijk EJ, de Vries J, et al. **4D-CT angiography differentiating arteriovenous fistula subtypes.** *Clin Neurol Neurosurg* 2013;115:1313–16 CrossRef Medline
5. Willems PW, Taeshineetanakul P, Schenk B, et al. **The use of 4D-CTA in the diagnostic work-up of brain arteriovenous malformations.** *Neuroradiology* 2012;54:123–31 CrossRef Medline
6. Frölich AM, Wolff SL, Psychogios MN, et al. **Time-resolved assessment of collateral flow using 4D CT angiography in large-vessel occlusion stroke.** *Eur Radiol* 2014;24:390–96 CrossRef Medline
7. Frölich AM, Schrader D, Klotz E, et al. **4D CT angiography more closely defines intracranial thrombus burden than single-phase CT angiography.** *AJNR Am J Neuroradiol* 2013;34:1908–13 CrossRef Medline
8. Ringelstein A, Lechel U, Fahrendorf DM, et al. **Radiation exposure in perfusion CT of the brain.** *J Comput Assist Tomogr* 2014;38:25–28 CrossRef Medline
9. Imanishi Y, Fukui A, Niimi H, et al. **Radiation-induced temporary hair loss as a radiation damage only occurring in patients who had the combination of MDCT and DSA.** *Eur Radiol* 2005;15:41–46 CrossRef Medline
10. D’Orazio F, Splendiani A, Gallucci M. **320-Row detector dynamic 4D-CTA for the assessment of brain and spinal cord vascular shunting malformations: a technical note.** *Neuroradiol J* 2014;27:710–17 CrossRef Medline
11. Hoogenboom TC, van Beurden RM, van Teylingen B, et al. **Optimization of the reconstruction interval in neurovascular 4D-CTA imaging: a technical note.** *Interv Neuroradiol* 2012;18:377–79 Medline
12. Das K, Biswas S, Roughley S, et al. **3D CT cerebral angiography technique using a 320-detector machine with a time density curve and low contrast medium volume: comparison with fixed time delay technique.** *Clinical Radiol* 2014;69:e129–35 CrossRef Medline
13. Biswas S, Chandran A, Roughley S, et al. **Cerebral CT venography using a 320-MDCT scanner with a time-density curve technique and low volume of contrast agent: comparison with fixed time-delay technique.** *AJR Am J Roentgenol* 2015;205:1269–75 CrossRef Medline
14. European Commission. *European Guidelines for Quality Criteria for Computed Tomography.* Luxembourg: European Commission; 2000. Report EUR 16262 EN.
15. Lin CJ, Wu TH, Lin CH, et al. **Can iterative reconstruction improve imaging quality for lower radiation CT perfusion? Initial experience.** *AJNR Am J Neuroradiol* 2013;34:1516–21 CrossRef Medline
16. Bahner ML, Bengel A, Brix G, et al. **Improved vascular opacification in cerebral computed tomography angiography with 80 kVp.** *Invest Radiol* 2005;40:229–34 Medline
17. Biswas S, Chandran A, Radon M, et al. **Accuracy of four-dimensional CT angiography in detection and characterisation of arteriovenous malformations and dural arteriovenous fistulas.** *Neuroradiol J* 2015;28:376–84 CrossRef Medline

# PQRS and the MACRA: Value-Based Payments Have Moved from Concept to Reality

 J.A. Hirsch,  T.M. Leslie-Mazwi,  G.N. Nicola,  M. Bhargavan-Chatfield,  D.J. Seidenwurm,  E. Silva, and  L. Manchikanti



From its beginnings in 1965, Medicare costs quickly exceeded initial projections, prompting policy makers to enact a number of remedies during the history of the program. The most recent example is the Medicare Access and Children's Health Insurance Program (CHIP) Reauthorization Act of 2015 (MACRA).<sup>1</sup> Embedded within the MACRA is the concept of quality metrics being used to assess performance. This concept is not new in American health care delivery. This article will explore the evolution of Medicare physician payments and the concurrent development of this quality-reporting element. Table 1 provides a glossary of terms that are commonly used in the discussion of delivery of care quality.

## SELECTED HISTORY

Medicare was established as part of President Johnson's great society in 1965. A mere 10 years later, costs had grown alarmingly; this growth prompted the enactment of several measures to both control and regulate expenses. In 1975, growth in physician payments was statutorily limited on the basis of the Medicare Economic Index (MEI), which was devised as means of measuring and controlling practice growth.<sup>2</sup> In 1984, Congress attempted further spending control by an annual adjustment in professional fees.<sup>2</sup> The following year researchers at Harvard began a multiyear effort published in 1988 proposing a resource-based relative value system that established a national relativity scale for all physician services.<sup>3</sup> This was incorporated into the Medicare Physician Payment System in 1989.<sup>4</sup> Then in 1997, the Balanced Budget Act created the Sustainable Growth Rate Formula (SGR) under which Medicare physician payments were directly linked to the United States economy, the covered population, health care innovation, and overall inflation.<sup>2,5,6</sup>

Despite these incremental efforts to control spending, with time costs exceeded the SGR targets, prompting annual reductions in physician payment. These reductions arose due to a number of factors captured collectively by the economic phenomenon known as Baumol Disease—that is, the declining relative productivity of the personal services sector of the economy, in which productivity is largely determined by the amount of time that one person spends with another. Medicine is one of the sectors most affected. The amount of time whereby medical visits can be shortened is self-limited before the quality of the interaction is adversely affected. This limit results in an ever greater share of the gross domestic product being diverted to personal services compared with sectors such as manufacturing, telecommunications, and data processing in which, in relative terms, productivity has continued to increase per hour worked. As such, physician costs rise faster than gross domestic product. The magnitude of the discrepancy is further accentuated by a combination of factors, including fee-for-service payment methodologies, third party payment, first dollar coverage with supplemental insurance, and the behavioral offset among providers.<sup>7</sup>

Reversing the annual mandated reductions in physicians' payments became an important focus of medical professional societies (including the American Society of Neuroradiology and multiple additional radiology societies), an effort that has stretched for multiple consecutive years.<sup>8,9</sup> Concurrently, an increasing focus was being applied to the need to improve quality within the health care system. The Institute of Medicine (IOM) published the landmark report *Crossing the Quality Chasm: A New Health System for the 21st Century* in 2001.<sup>10</sup> This highlighted challenges in delivering consistent quality of care across the United States and proposed methods to improve care quality. A key approach was "pay for performance," using financial incentives to help develop better quality and value.<sup>11</sup> The IOM report provided momentum to legislatively mandate "pay for performance," prompting the emergence of new programs.<sup>12</sup> One of these, the Physician Quality Reporting System (PQRS), was established as the Physician Quality Reporting Initiative under the 2006 Tax Relief and Health Care Act (TRHCA), based on the notion that health care providers should be able to provide quality and outcome information not otherwise readily available from existing

From the Departments of Neuroendovascular Imaging (J.A.H., T.M.L.-M.), Radiology (J.A.H.), and Neurology (T.M.L.-M.), Massachusetts General Hospital, Boston, Massachusetts; Hackensack Radiology Group (G.N.N.), River Edge, New Jersey; American College of Radiology (M.B.-C.), Reston, Virginia; Department of Radiology (D.J.S.), Sutter Medical Group, Sacramento, California; South Texas Radiology Group (E.S.), San Antonio, Texas; and Pain Management Center (L.M.), Paducah, Kentucky.

Please address correspondence to T.M. Leslie-Mazwi, MD, Department of Neuroendovascular Imaging, Massachusetts General Hospital, GRB 2-241, 55 Fruit St, Boston, MA 02114; e-mail: tleslie-mazwi@mgh.harvard.edu; @JoshuaAHirsch

 Indicates article with supplemental on-line table.

<http://dx.doi.org/10.3174/ajnr.A4936>

**Table 1: Glossary of terms commonly used in literature regarding care delivery and quality metrics**

---

ABR: American Board of Radiology
ACA: Patient Protection and Affordable Care Act
ACO: Accountable Care Organization
ACR: American College of Radiology
AMA: American Medical Association
API: Application program interfaces
APM: Alternative Payments Model
ASNR: American Society of Neuroradiology
CEHRT: Certified EHR Technology
CHIP: Children's Health Insurance Program
CMS: Centers for Medicare & Medicaid Services
CPIA: Clinical Practice Improvement Activities
EHR: Electronic Health Record
EP: Eligible Professionals
HCPLAN: Health Care Payment Learning Action Network
IOM: Institute of Medicine
MACRA: Medicare Access and CHIP Reauthorization Act
MAP: Measures Application Partnership
MEI: Medicare Economic Index
MIPS: Merit-Based Incentive Payment System
MPFS: Medicare Physician Fee Schedule
NQF: National Quality Forum
NQS: National Quality Strategy
NRDR: National Radiology Data Registry
OBRA: Omnibus Budget Reconciliation Act
PQI: Practice Quality Improvement
PQRS: Physician Quality Reporting System
QCDRs: Qualified Clinical Data Registries
QRUR: Quality and Resource Use Reports
SCHIP: State Children's Health Insurance Program
SGR: Sustainable Growth Rate Formula
TRHCA: Tax Relief and Health Care Act

---

Medicare claims.<sup>13</sup> Early data suggested limited eligible provider participation.<sup>14</sup>

### THE CURRENT FIELD OF PLAY

The Patient Protection and Affordable Care Act of 2010 (ACA) brought in the next chapter of physician quality reporting.<sup>15</sup> The ACA included specific language that mandated the Centers for Medicare & Medicaid Services (CMS) incorporate Quality alongside Cost and Resource Use as an element in considering payment.<sup>16</sup> The Secretary of the Department of Health and Human Services, Sylvia Burwell, published the Obama administration's payment policy goals in early 2015,<sup>17</sup> describing the transition to payments based on quality and value through alternative payment model participation. The goals were impressive in both their scale and speed of implementation: 85% of all Medicare fee-for-service payments were to be tied to quality or value by 2016, and 90%, by 2018.<sup>18</sup> This statement occurred in the context of several CMS initiatives founded on value-based approaches to providing health care.<sup>19-21</sup>

Congress took advantage of a budgetary opportunity produced by decreased health care inflation (due to the economic downturn and slow economic growth) and replaced the SGR with the MACRA in early 2015.<sup>1</sup> This bipartisan legislation left little doubt about the value-oriented future of health care in the United States during 2015–2021 and beyond.<sup>22,23</sup>

The MACRA attempts to align various preexisting performance programs, consolidating aspects of the PQRS, Value-Based

Payment Modifier Program, and the Meaningful Use initiative with which many readers will be familiar. The MACRA defines 2 methods for payment to enable the transition toward the goal of paying for better care value. The first is Alternate Payment Models (APMs); the second is the Merit-Based Incentive Payment System (MIPS). Essentially APMs offer novel alternatives to pay health care providers for the care they give Medicare beneficiaries and encompasses Accountable Care Organizations (ACOs), Patient-Centered Medical Homes, and bundled payment models. MIPS, detailed further below, is particularly important to understand because MIPS applies to physicians still billing under fee-for-service, initially likely most radiologists.

### MERIT-BASED INCENTIVE PAYMENT SYSTEM

Under MIPS, eligible professionals (EP) will receive a composite performance score based on 4 performance categories: Quality, Resource Use, Meaningful Use (since renamed “Advancing Care Information”), and Clinical Practice Improvement Activities (CPIA). The EP designation encompasses physicians (including podiatrists and chiropractors), nurse practitioners, physician assistants, therapists, clinical nurse specialists, dietitians, clinical social workers, and others involved in direct patient care. Quality in this context refers directly to PQRS (ie, PQRS should be viewed as 1 of the 4 components of the MACRA). The MACRA, largely through MIPS, attempts to align these disparate performance programs. One important method of accomplishing this alignment is the development and use of Qualified Clinical Data Registries (QCDRs). QCDRs collect medical data for data tracking to affect performance improvement in patient care and are important in that participation in QCDRs may satisfy portions of all 4 performance categories of the MIPS (if the reporting registries are appropriately designed). Compliance with QCDRs stands to completely satisfy the “Quality” component of MIPS and can be used from 2015 to 2018 to satisfy reporting requirements in the years preceding MACRA. The current proposed weighting for 2019, which can be modified by the CMS going forward, is 50% for Quality measures, 10% for Resource Use, 25% for Advancing Care Information, and 15% for CPIA.<sup>24</sup>

At first glance, MIPS appears to be the preexisting CMS quality programs reconfigured; however, a recent alternate position presents MIPS as one of the progressive classifications leading to the end goal of population-based payments as the dominant payment paradigm of the US health care system.<sup>25,26</sup> In this context, MIPS may allow fee-for-service participants to collect relevant data that may be useful, while the provider restructures services with a focus on quality, value, and practice improvement, all metrics considered important in providing accountable care.

The categories under MIPS also include what most stakeholders in APMs care about—quality, prudent resource use, interoperability, and a culture of quality improvement. Therefore, any practice using MIPS for some of its patients can use the same activities to negotiate contracts within APM plans, such as ACOs, or with other payers on the basis of their performance and the value of the care they deliver.

## DIRECT FINANCIAL IMPLICATIONS

Demonstration of effort directed toward quality and value has long been tied to financial consequences for physicians, radiologists included. It is important to keep this in mind in the context of the current expectations. The 2006, TRHCA allowed a 1.5% bonus payment for EPs who satisfactorily reported quality measures for services that were relevant to Medicare. This was simply a reporting standard; no data were submitted or required, and payments were capped. In 2007, the Medicare, Medicaid, and State Children's Health Insurance Program (SCHIP) Extension Act authorized continuation of this incentive for 2008 and 2009.<sup>1</sup> The 2008 Medicare Improvements for Patients and Providers Act increased the potential incentive payment to 2% and made PQRS permanent.<sup>27</sup>

The pendulum swung back the other way in 2010. The ACA, while championing value approaches, mandated a decrease with time in the PQRS incentive payment from the 2% peak established in 2008.<sup>28</sup> The year 2011 saw the potential bonus payment decreased to a maximum of 1% of the total allowed charges for professional services. From 2012 to 2014, the maximum benefit was capped at 0.5%. Per the ACA, in 2015, negative payment adjustments (or, in other words, penalties) began if the quality measure reporting requirements were not met, rising to potentially 2% of Part B-covered professional services. Medicare penalties and bonuses for any given year are determined by reporting in a prior performance period.<sup>29</sup>

The MACRA further complicates the mathematics of bonuses or penalties around quality metrics. The legislation mandates positive 0.5% conversion factor updates affecting all Medicare Physician Fee Schedule (MPFS) payments until 2019 and then no increase or decrease until 2026. Payments will also be adjusted on the basis of a physician's composite performance score. The 4 components of Quality, Resource Use, Advancing Care Information, and CPIA are scored on a 100-point basis with aggregates compared with other eligible providers. As of 2019, if a provider is on par with the mean (or median) base performance measure, referred to as the threshold score, there is no bonus or penalty. If a physician rises above or falls below the threshold score, there will be positive or negative adjustments, respectively. The magnitude of these adjustments increases (or decreases) from 4% in 2019 to 9% in 2022 and thereafter. An additional \$500 million is potentially available from calendar years 2019 to 2024 for individual providers or groups that perform exceptionally well.<sup>22</sup> For providers, therefore, there is great financial incentive to both deliver and document quality care. It is important to initiate efforts to meet these requirements in a timely and thoughtful manner, to maximize the chance of practice success.

## RULES OF ENGAGEMENT

To satisfy a specific PQRS measure, one must successfully report a minimum percentage of the total patient encounters to which the measure applies. That minimum percentage stands at 50% currently. The numerator equals the number of services satisfied under the PQRS measure being studied. The denominator represents the total number of eligible cases/patient population associated with the quality measure.<sup>30</sup>

On what measures should you as an EP choose to be judged? Much depends on measures available and information currently gathered in your practice. Measure development is an important aspect of the PQRS program. The Affordable Care Act mandated the establishment of a national strategy for quality improvement in health care, which is dubbed the National Quality Strategy (NQS). The NQS informs measure development based on improved and affordable care, focusing on 6 different domains, including patient safety, person- and caregiver-centered experience and outcomes, care coordination, effective clinical care, population health, and cost reduction.

Remembering the reporting need for a minimum percentage of the total patient encounters to which the measure applies, EPs then select the measures for which they would prefer to be held accountable, ideally choosing those most applicable to them, focused on the various domains. In 2016, there are almost 300 possible measures, including some that are uniquely suited to radiology.

## MEASURES FROM WHICH TO SELECT

Quality measures are a moving target. For an EP, staying abreast with current developments and understanding their historical context is of great import. Traditionally, creation of a metric was an arduous task requiring ample clinical evidence of effectiveness before approval by the governing body of such metrics, the National Quality Forum (NQF). With the advent of QCDRs, CMS has shown the willingness to explore broader criteria for the creation of metrics and offers opportunity for use of clinical data registry measures in the PQRS. This feature has provided the radiology community a real avenue for experimentation in territories that were off limits using the older NQF approach, and therefore a certain flexibility. The On-line Table provides examples of current PQRS measures that could be selected, with their definitions.

Other options exist besides selecting measures from established PQRS metrics, specifically if a comfortable fit is not found in that list of options. The American College of Radiology (ACR) National Radiology Data Registry (NRDR) ([acr.org/nrdr](http://acr.org/nrdr)) is a clinical data registry serving as the umbrella for a collection of data bases covering a range of radiology-specific measures.<sup>31</sup> Clinical data registries such as these self-nominate to CMS to become QCDRs for enabling PQRS participation. QCDRs self-nominate annually, and CMS reviews the measures for acceptability and allows the "non-PQRS measures" of the QCDRs defined in the registry to be reported for PQRS credit. CMS reviewing non-PQRS measures for PQRS credit presents an alternate route for a measure to be selected, implemented, and met. A QCDR may also offer PQRS measures to be reported as well. From across the NRDR, a selection of measures can be chosen for use in the QCDRs. The QCDRs provide a pathway for trying and testing measures while eligible professionals receive credit for monitoring and reporting them. Table 2 provides examples of categories of QCDRs that provide a focus for recording quality-improvement effort.

In addition, CMS evaluates measures that are not NQF-endorsed and accepts them for use in PQRS with recommendations from the Measures Application Partnership (MAP). The MAP is a

**Table 2: Select examples from the Qualified Clinical Data Registry<sup>a</sup>**

Non-PQRS Measure	Measure Title	Description of Measure	NQS Domain	NRDR Data Base
ACRad 3	Screening Mammography Cancer Detection Rate	Fraction of screening mammograms interpreted as abnormal with tissue diagnosis of cancer confirmed within 12 mo	Effective Clinical Care	National Mammography Database
ACRad 9	Median Dose-Length Product for CT Head/Brain Without Contrast	Median dose-length product for CT head/brain without contrast, measured at a facility/group level for all physicians who interpret CT scans	Patient Safety	Dose Index Registry
ACRad 14	Participation in a National Dose Index Registry	No. of CT examinations performed at the facility and submitted to the Dose Index Registry	Patient Safety	Dose Index Registry
ACRad 17	Report Turnaround Time: MRI	Mean MRI report turnaround time	Communication and Care	General Radiology Improvement Database
ACRad 20	CT IV Contrast Extravasation Rate	Percentage of CT examinations with contrast performed that resulted in extravasation, measured at a facility/group level for all physicians who interpret CT scans	Patient Safety	General Radiology Improvement Database
ACRad 23	Lung Cancer Screening Abnormal Interpretation Rate	The percentage of screenings for lung cancer interpreted as positive	Efficiency and Cost	Lung Cancer Screening Registry

**Note:**—ACRad indicates American College of Radiology.

<sup>a</sup> These represent non-PQRS measures. QCDRs collect medical and/or clinical data for the purpose of patient and disease tracking. Data from the National Radiology Data Registry.<sup>31</sup>

public-private partnership coordinated by the NQF to provide input from stakeholders on proposed measures and to build consensus around them. The MAP therefore represents a potential target for advocacy and lobbying from the radiology community. While the goal for CMS is to be able to work toward NQF endorsement for all these measures, having them in use provides radiology with the data necessary to seek endorsement in the future. One series of examples of such explorations are the new 2016 CMS-approved PQRS measures of incidental findings in the liver, kidneys, adrenal glands, and thyroid. These incidental findings have the potential to cause meaningful downstream costs with no change in patient morbidity or mortality, and hence poor resource use. The CMS with the MAP developed metrics created around these incidental radiographic findings to allow measurement of adherence to expert opinion and to serve as a potential benchmark for those who wish to improve their clinical practice, goals identical to the MIPS performance categories of “Resource Use” and “Clinical Practice Improvement”!<sup>32</sup>

### CONSIDERATIONS WITH THE EVOLUTION OF MEASURES

Traditionally, PQRS measures for radiology have been process measures; clinical actions or data supporting successful reporting on specific measures are generally not submitted to CMS but must be documented in the medical record. For example, measure 145 (On-line Table) requires the reporting of fluoroscopy dose indices or the time and number of images, but the actual data are not directly submitted to CMS. There has been an increasing emphasis on reporting outcome measures. Outcomes are defined broadly to include intermediate outcomes and the patient experience of care, for example, recall rates or cancer-detection rates

for mammography and average report turnaround times. It is challenging to measure such outcomes within the constraints of claims reporting, and QCDRs offer many more options for monitoring and reporting measures like these because they are based on broader clinical data. This consideration may be important in selecting measures. Outcome-focused measures may have greater longevity ultimately, though they may have greater implementation needs for initially establishing them.

Most efficiently, EPs would meet multiple regulatory requirements through the same effort. As an example, all of the ACR NRDR data bases have American Board of Radiology (ABR)-approved Practice Quality Improvement (PQI) projects associated with them. Registry participation by itself has recently been approved by the ABR as a PQI activity eligible for credit toward Maintenance of Certification Part 4, and PQI activities closely match the MIPS description of clinical practice improvement activities. Several of the NRDR data bases accept data by electronic upload or transmission or through Web service application program interfaces (APIs). Furthermore, if these data are extracted from a certified electronic health record (EHR) technology (CEHRT), the submission meets a Public Health Reporting objective, under Advancing Care Information. Because QCDRs support multiple components of MIPS for the same activity, they feature prominently in MACRA.<sup>22</sup>

The transparency of this quality effort will also evolve. Since the 2013 performance period, CMS has been providing EPs and groups with confidential feedback reports: Quality and Resource Use Reports (QRUR) that allow PQRS participants to compare themselves with other groups of providers on the basis of specific episodes of care. The QRUR give group practices an opportunity to “preview” their outcomes in the Value Modifier program. The

**Table 3: Strategic approach to assist with preparation for the impact of quality measures in health care reimbursement**

What Should I Do?	Where Should I Find It?
Learn about quality measures and the impact on your practice, including effort made by the practice to date	Read articles and Web sites (including material referenced in this article), engage practice administration, share insights with other providers
Select measures for which to be accountable (PQRS and QCDR)	www.acr.org/nrd, www.cms.gov
Ensure method presently exists to record the metrics required for the selected measures and if not then establish one	Discuss with practice administration
Assess whether current EHR meets criteria for a CEHRT; if so, configure to enable direct database reporting to www.acr.org/nrd	EHR vendor, hospital, or practice information technology service
Access QRUR to evaluate performance compared with other groups, including public reporting from CMS	https://www.cms.gov/medicare/quality-initiatives-patient-assessment-instruments/physician-compare-initiative/
Adjust accordingly (either data collection or metric chosen)	Practice administration
Adjust budgeting on the basis of impact quality performance will have on practice finances	Practice administration

**Note:**—PQRS indicates Physician Quality Reporting System; QCDR, Qualified Clinical Data Registry; EHR, Electronic Health Record; CEHRT, Certified EHR Technology; QRUR, Quality and Resource Use Reports.

reports are mandated to be more frequent and timely under MACRA. CMS is additionally stepping into publicly reporting more measures for a broader group of providers each year via Physician Compare.<sup>33</sup>

Satisfactory PQRS reporting in 2015 and 2016 will avoid the 2017 and 2018 negative payment adjustments, respectively. Starting in 2019, payment will be adjusted on the basis of performance within the MIPS.<sup>32</sup> As indicated above, there will no longer be any incentive or penalty for just reporting quality measures; incentives and penalties will be assessed on aggregate performance across the 4 specified MIPS categories, similar to how quality and cost performance are currently evaluated in the Value Modifier program. Physicians or groups with performance significantly better than average will have positive adjustments. Physicians or groups who do not perform as well as average will have downward adjustments. Table 3 provides an approach to preparing for this change in health care reimbursement.

### SUMMARY

Medicare is in a period of transition. Approximately 10 years ago, the 2006 Tax Relief and Health Care Act established the Physician Quality Reporting System and eligible providers were given an opportunity to earn incentives by successfully reporting quality metrics. The Affordable Care Act brought important refinements to PQRS, including the introduction of negative adjustments for nonparticipation. The MACRA recognized that one of the challenges facing practitioners was the disparate nature of the various CMS programs designed to facilitate quality of care and measure resource use. Going forward, these metrics will be aggregated into a single numeric score, which may be attractive to providers. Understanding this evolution is important for radiologists, given the potential modification of provider payments over a range of 18% ± 9% based on successful participation in these programs.

### ACKNOWLEDGMENTS

We wish to acknowledge Judy Burleson for her invaluable assistance with the content of Table 2 and the On-line Table, and suggestions for the manuscript.

Disclosures: Joshua A. Hirsch—UNRELATED: Consultancy: Medtronic (interventional spine), Codman Neurovascular (Data and Safety Monitoring Board), CareFusion (single event <36 months ago, teaching a non-Continuing Medical Education course). Mythreyi Bhargavan-Chatfield—UNRELATED: Employment: American College of Ra-

diology. David J. Seidenwurm—UNRELATED: Consultancy: medical legal (personal injury, medical liability); Board Membership: Radiological Associates of Sacramento; Employment: Sutter Health; Grants/Grants Pending: Stanford Institutes of Medicine Summer Research Program \* (imaging appropriateness); Payment for Lectures (including service on Speakers Bureaus): State University of New York, Stanford; Stock/Stock Options: RASMG; Travel/Accommodations/Meeting Expenses Unrelated to Activities Listed: American College of Radiology, National Quality Forum, The Alliance; Other: Sutter Medical Group, Sutter Medical Foundation. Laxmaiah Manchikanti—UNRELATED: Consultancy: Semnur Pharmaceuticals (limited amount of \$1400); Employment: Pain Management Center of Paducah. \*Money paid to the institution.

### REFERENCES

1. The Medicare Access and CHIP Reauthorization Act of 2015. <https://www.congress.gov/bill/114th-congress/house-bill/2>. Accessed June 2, 2015
2. Manchikanti L, Singh V, Caraway DL, et al. Medicare physician payment systems: impact of 2011 schedule on interventional pain management. *Pain Physician* 2011;14:E5–33 Medline
3. Hsiao WC, Braun P, Kelly NL, et al. Results, potential effects, and implementation issues of the Resource-Based Relative Value Scale. *JAMA* 1988;260:2429–38 CrossRef Medline
4. Hirsch JA, Silva E 3rd, Nicola GN, et al. The RUC: a primer for neurointerventionalists. *J Neurointerv Surg* 2014;6:61–64 CrossRef Medline
5. Seidenwurm DJ, Burleson JH. The Medicare conversion factor. *AJNR Am J Neuroradiol* 2014;35:242–43 CrossRef Medline
6. Balanced Budget Act of 1997. <https://www.gpo.gov/fdsys/pkg/PLAW-105publ33/content-detail.html>. Accessed July 1, 2015
7. Baumol WJ. *The Cost Disease: Why Computers Get Cheaper and Health Care Doesn't*. New Haven: Yale University Press; 2012:16–32
8. Hirsch JA, Rosman DA, Liu RW, et al. Sustainable growth rate 2013: time for definitive intervention. *J Neurointerv Surg* 2013;5:382–86 CrossRef Medline
9. Hirsch JA, Manchikanti L. The sustainable growth rate: a 2014 update. *J Neurointerv Surg* 2014;6:411–12 CrossRef Medline
10. Committee on Quality of Health Care in America, Institute of Medicine. *Crossing the Quality Chasm: A New Health System for the 21st Century*. Washington DC: National Academies Press; 2001
11. Committee on Redesigning Health Insurance Performance Measures, Payment, and Performance Improvement Programs and Board on Health Care Services. *Rewarding Provider Performance: Aligning Incentives in Medicare (Pathways to Quality Health Care Series)*. Washington DC: National Academies Press; 2007
12. Tompkins CP, Higgins AR, Ritter GA. Measuring outcomes and efficiency in Medicare value-based purchasing. *Health Aff (Millwood)* 2009;28:w251–61 CrossRef Medline
13. Tax Relief and Health Care Act of 2006. <https://www.gpo.gov/fdsys/pkg/PLAW-109publ432/html/PLAW-109publ432.htm>. Accessed April 15, 2016

14. Centers for Medicare & Medicaid Services, Department of Health and Human Services. Physician Quality Reporting Initiative: 2007 Reporting Experience. December 3, 2008; <https://www.cms.gov/Medicare/Quality-Initiatives-Patient-Assessment-Instruments/PQRS/downloads/PQRI2007ReportFinal12032008CSG.pdf>. Accessed April 14, 2016
15. Patient Protection and Affordable Care Act. 2010. <https://www.hhs.gov/healthcare/about-the-law/read-the-law/index.html>. Accessed April 14, 2016
16. Manchikanti L, Hirsch JA. **Patient Protection and Affordable Care Act of 2010: a primer for neurointerventionalists.** *J Neurointerv Surg* 2012;4:141–46 CrossRef Medline
17. Burwell SM. **Setting value-based payment goals: HHS efforts to improve U.S. health care.** *N Engl J Med* 2015;372:897–99 CrossRef Medline
18. Hirsch JA, Leslie-Mazwi TM, Barr RM, et al. **The Burwell roadmap.** *J Neurointerv Surg* 2016;8:544–46 CrossRef Medline
19. Hirsch JA, Leslie-Mazwi TM, Barr RM, et al. **The Bundled Payments for Care Improvement Initiative.** *J Neurointerv* 2016;8:547–48 CrossRef Medline
20. Hirsch JA, Leslie-Mazwi TM, Meyers PM, et al. **Accountable care.** *J Neurointerv* 2015 Jun 17. [Epub ahead of print] Medline
21. Meehan TM, Harvey HB, Duszak R Jr, et al. **Accountable Care Organizations: what they mean for the country and for neurointerventionalists.** *J Neurointerv Surg* 2016;8:654–57 CrossRef Medline
22. Hirsch JA, Leslie-Mazwi TM, Patel AB, et al. **MACRA: background, opportunities and challenges for the neurointerventional specialist.** *J Neurointerv Surg* 2016;8:868–74 CrossRef Medline
23. Hirsch JA, Harvey HB, Barr RM, et al. **Sustainable growth rate repealed, MACRA revealed: historical context and analysis of recent changes in Medicare physician payment methodologies.** *AJNR Am J Neuroradiol* 2016;37:210–14 CrossRef Medline
24. Department of Health and Human Services, Centers for Medicare & Medicaid Services. Medicare Program: Merit-Based Incentive Payment System (MIPS) and Alternative Payment Model (APM) Incentive under the Physician Fee Schedule, and Criteria for Physician-Focused Payment Models. 2016; <https://s3.amazonaws.com/public-inspection.federalregister.gov/2016-10032.pdf>. Accessed May 17, 2016
25. Centers for Medicare & Medicaid Services. Health Care Payment Learning and Action Network. <https://innovation.cms.gov/initiatives/Health-Care-Payment-Learning-and-Action-Network/>. Accessed April 14, 2016
26. Alternative Payment Model Framework and Progress Tracking (APM FPT) Work Group. Alternative Payment Model (APM) Framework: Final White Paper. <https://hcp-lan.org/workproducts/apm-white-paper.pdf>. Accessed April 14, 2016
27. Anumula N, Sanelli PC. **Physician Quality Reporting System.** *AJNR Am J Neuroradiol* 2011;32:2000–01 CrossRef Medline
28. Manchikanti L, Hirsch JA. **Obama health care for all Americans: practical implications.** *Pain Physician* 2009;12:289–304 Medline
29. United States Government. Federal Register. <https://www.gpo.gov/fdsys/pkg/FR-2015-11-16/pdf/2015-28005.pdf>. Accessed April 12, 2016
30. Manchikanti L, Hammer M, Benyamin RM, et al. **Physician Quality Reporting System (PQRS) for interventional pain management practices: challenges and opportunities.** *Pain Physician* 2016;19:E15–32 Medline
31. National Radiology Data Registry. <http://www.acr.org/~media/ACR/Documents/PDF/QualitySafety/NRDR/2014%20NonPQRS%20QCDR%20Measures.pdf>. Accessed April 9, 2016
32. Centers for Medicare & Medicaid Services. The Merit-Based Incentive Payment System (MIPS) & Alternative Payment Models (APMs): Delivery System Reform, Medicare Payment Reform, & the MACRA. <https://www.cms.gov/Medicare/Quality-Initiatives-Patient-Assessment-Instruments/Value-Based-Programs/MACRA-MIPS-and-APMs/MACRA-MIPS-and-APMs.html>. Accessed April 10, 2016
33. Centers for Medicare & Medicaid Services. Physician Compare Initiative. <https://www.cms.gov/medicare/quality-initiatives-patient-assessment-instruments/physician-compare-initiative/>. Accessed April 10, 2016
34. Centers for Medicare & Medicaid Services, Physician Quality Reporting System. <https://www.cms.gov/Medicare/Quality-Initiatives-Patient-Assessment-Instruments/PQRS/MeasuresCodes.html>. Accessed April 10, 2016

# Progressing Bevacizumab-Induced Diffusion Restriction Is Associated with Coagulative Necrosis Surrounded by Viable Tumor and Decreased Overall Survival in Patients with Recurrent Glioblastoma

H.S. Nguyen, N. Milbach, S.L. Hurrell, E. Cochran, J. Connelly, J.A. Bovi, C.J. Schultz, W.M. Mueller, S.D. Rand, K.M. Schmainda, and P.S. LaViolette



## ABSTRACT

**BACKGROUND AND PURPOSE:** Patients with recurrent glioblastoma often exhibit regions of diffusion restriction following the initiation of bevacizumab therapy. Studies suggest that these regions represent either diffusion-restricted necrosis or hypercellular tumor. This study explored postmortem brain specimens and a population analysis of overall survival to determine the identity and implications of such lesions.

**MATERIALS AND METHODS:** Postmortem examinations were performed on 6 patients with recurrent glioblastoma on bevacizumab with progressively growing regions of diffusion restriction. ADC values were extracted from regions of both hypercellular tumor and necrosis. A receiver operating characteristic analysis was performed to define optimal ADC thresholds for differentiating tissue types. A retrospective population study was also performed comparing the overall survival of 64 patients with recurrent glioblastoma treated with bevacizumab. Patients were separated into 3 groups: no diffusion restriction, diffusion restriction that appeared and progressed within 5 months of bevacizumab initiation, and delayed or stable diffusion restriction. An additional analysis was performed assessing tumor *O*<sup>6</sup>-methylguanine-DNA-methyltransferase methylation.

**RESULTS:** The optimal ADC threshold for differentiation of hypercellularity and necrosis was  $0.736 \times 10^{-3} \text{ mm}^2/\text{s}$ . Progressively expanding diffusion restriction was pathologically confirmed to be coagulative necrosis surrounded by viable tumor. Progressive lesions were associated with the worst overall survival, while stable lesions showed the greatest overall survival ( $P < .05$ ). Of the 40% of patients with *O*<sup>6</sup>-methylguanine-DNA-methyltransferase methylated tumors, none developed diffusion-restricted lesions.

**CONCLUSIONS:** Progressive diffusion-restricted lesions were pathologically confirmed to be coagulative necrosis surrounded by viable tumor and associated with decreased overall survival. Stable lesions were, however, associated with increased overall survival. All lesions were associated with *O*<sup>6</sup>-methylguanine-DNA-methyltransferase unmethylated tumors.

**ABBREVIATIONS:** GBM = glioblastoma; MGMT = *O*<sup>6</sup>-methylguanine-DNA-methyltransferase; OS = overall survival

Glioblastoma (GBM) is the most common primary brain tumor in adults, and the standard treatment of surgery, radiation, and chemotherapy is associated with a median survival of 15 months.<sup>1</sup> At recurrence, patients typically survive only another 30

weeks.<sup>2-4</sup> Bevacizumab is a monoclonal antibody that selectively binds to human vascular endothelial growth factor. It is FDA-approved for recurrent GBM<sup>5</sup> and has been shown to improve progression-free survival<sup>6</sup> but not overall survival (OS). When given in initial treatment regimens, it has shown no benefit in OS.<sup>7,8</sup> The permeability of the blood-brain barrier is reduced by bevacizumab; this reduction complicates the use of gadolinium contrast enhancement for the evaluation of tumor response because tumor enhancement can recede without a true antitumor response.<sup>9</sup> As a result, the Response Assessment for Neuro-Oncology group published new suggestions that include antiangiogenic therapy.<sup>10</sup>

Other multiparametric MR imaging sequences are beginning to gain momentum in detecting infiltrative tumor and determining treatment response. Perfusion imaging methods such as DSC have been shown to be effective at measuring the response to bevacizumab.<sup>11-13</sup> Diffusion-weighted imaging and apparent dif-

Received March 29, 2016; accepted after revision June 23.

From the Departments of Neurosurgery (H.S.N., W.M.M.), Radiology (N.M., S.L.H., S.D.R., K.M.S., P.S.L.), Pathology (E.C.), Neurology (J.C.), Radiation Oncology (J.A.B., C.J.S.), and Biophysics (K.M.S., P.S.L.), Medical College of Wisconsin, Milwaukee, Wisconsin.

This work was supported by Advancing a Healthier Wisconsin, Medical College of Wisconsin Research Affairs Committee, National Cancer Institute U01-CA176110, National Institutes of Health/National Cancer Institute R01 CA082500, American Brain Tumor Association Discovery Grant DGI600004, NIH UL1TR001436, and partial funding allotted by the Medical College of Wisconsin, Department of Neurology.

Please address correspondence to Peter S. LaViolette, PhD, Department of Radiology, Medical College of Wisconsin, 8701 Watertown Plank Rd, Milwaukee, WI 53226; e-mail: plaviole@mcw.edu

Indicates open access to non-subscribers at www.ajnr.org

<http://dx.doi.org/10.3174/ajnr.A4898>

**Table 1: Patient clinical summaries for the 6 patients included in the autopsy study**

Patient No.	Last MRI to Death (day)	Age at Death (yr)	Tumor Type	Surgery	XRT	TMZ	Location of Focal Region of Diffusion Restriction	Bevacizumab (day)		
								Before Death	Before Focal Region Appears	Between Focal Region and Death
1	10	40	Grade III mixed glioma	+	+	+	Corpus callosum	44	34	10
2	3	68	GBM	+	+	+	Corona radiata	435	306	129
3	23	53	GBM	+	+	+	Corona radiata	85	34	51
4	37	65	GBM	+	+	+	Centrum semiovale	343	264	79
5	29	58	GBM	+	+	+	Corpus callosum	827	728	99
6	62	42	GBM	+	+	+	Centrum semiovale	700	534	166

**Note:**—XRT indicates radiation therapy; TMZ, temozolomide; +, yes.

## Shape Preserving Patient Specific Brain Fixation Mold

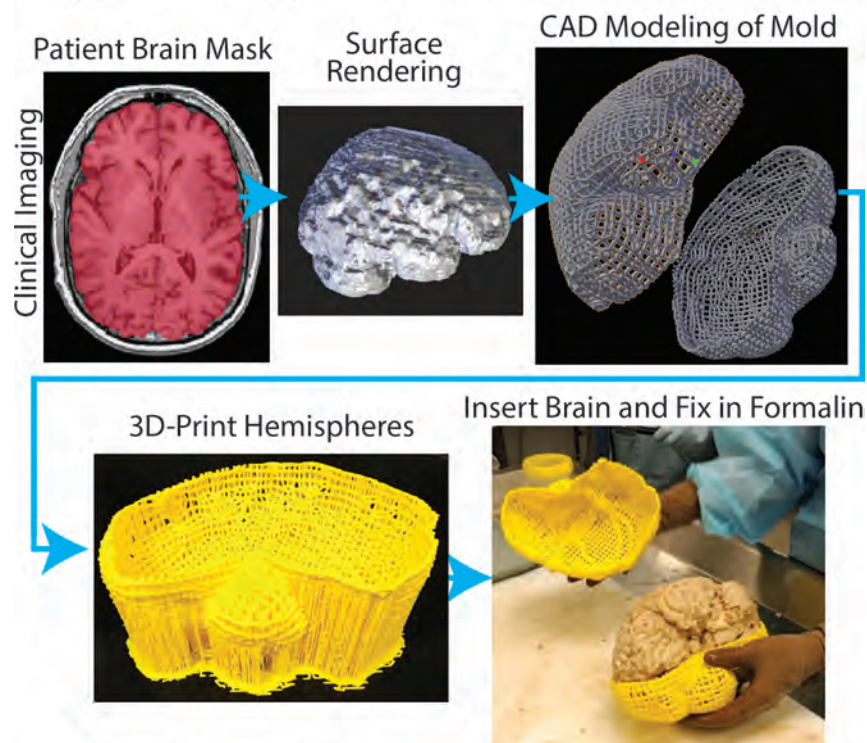


**FIG 1.** Demonstration of the creation of a patient-specific brain mold for minimizing tissue distortion during fixation. The patient’s MR imaging is used to generate a brain mask, which is then used as a guide for generating the mold in 3D modeling software. Molds are then 3D-printed in plastic.

fusion coefficient temozolomide maps measure the free diffusion of water in tissue. ADC has been shown to inversely correlate with tumor cellularity in glioma,<sup>14,15</sup> and ADC difference maps or functional diffusion maps are predictive of response to chemotherapy,<sup>16,17</sup> radiation therapy,<sup>18</sup> and bevacizumab.<sup>19,20</sup>

Some patients, when given bevacizumab, develop focal regions of diffusion restriction. These lesions, when stable, have been shown to be associated with increased survival.<sup>21</sup> Conflicting studies have shown these regions to be either diffusion-restricted necrosis or hypercellular tumor.<sup>21–28</sup> One recent article reported regions of both within ADC-FLAIR mismatch (ie, diffusion restriction within fluid-attenuated inversion recovery hyperintensity) and found that diffusion-restricted necrosis had significantly lower ADC values compared with hypercellular tumor.<sup>29,30</sup>

Glioblastomas are typically associated with liquefactive necrosis, characterized by its purulent appearance and liquid texture.

This generally results in high diffusion and consequent hyperintensity on ADC images. Coagulative necrosis, however, is grossly firm with microscopic “ghostly” cells, in which only the outline and cytoplasm remain but all organelles are absent.<sup>31</sup>

This study explored regions of diffusion restriction following bevacizumab therapy in 2 ways: First, we analyzed tissue samples from patients at postmortem to pathologically confirm tumor cellularity or coagulative necrosis. Next, we assessed a patient population to determine the effect that these lesions have on OS. We then performed a subanalysis on tumor *O*<sup>6</sup>-methylguanine-DNA-methyltransferase (*MGMT*) methylation, a predictor of overall survival.<sup>23,32</sup>

## MATERIALS AND METHODS

### Patient Population

The brains from 6 patients with recurrent GBM and regions of focal diffusion restriction (while on bevacizumab therapy) were assessed at postmortem as part of an internal review board–compliant study (PRO17446). Table 1 provides a brief clinical history of each patient. The cohort consisted of 1 woman and 5 men, with a mean age of 54 years (range, 39.9–67.8 years). All patients had surgical resection, concurrent radiation, and temozolomide therapy and bevacizumab at tumor recurrence. The mean period between the initiation of bevacizumab therapy and the appearance of focal regions of diffusion restriction was 316.6 days (range, 34–728 days); the mean period between initiation of bevacizumab therapy and death was 405.6 days (range, 44–827 days); and the mean period between the appearance of a focal diffusion-restricted region and death was 89 days (range, 10–166 days).

### Imaging

The patients were clinically imaged on either a 1.5T Symphony or Espree (Siemens, Erlangen, Germany) or a 1.5T Optima or 3T Discovery (GE Healthcare, Milwaukee, Wisconsin) scanner by

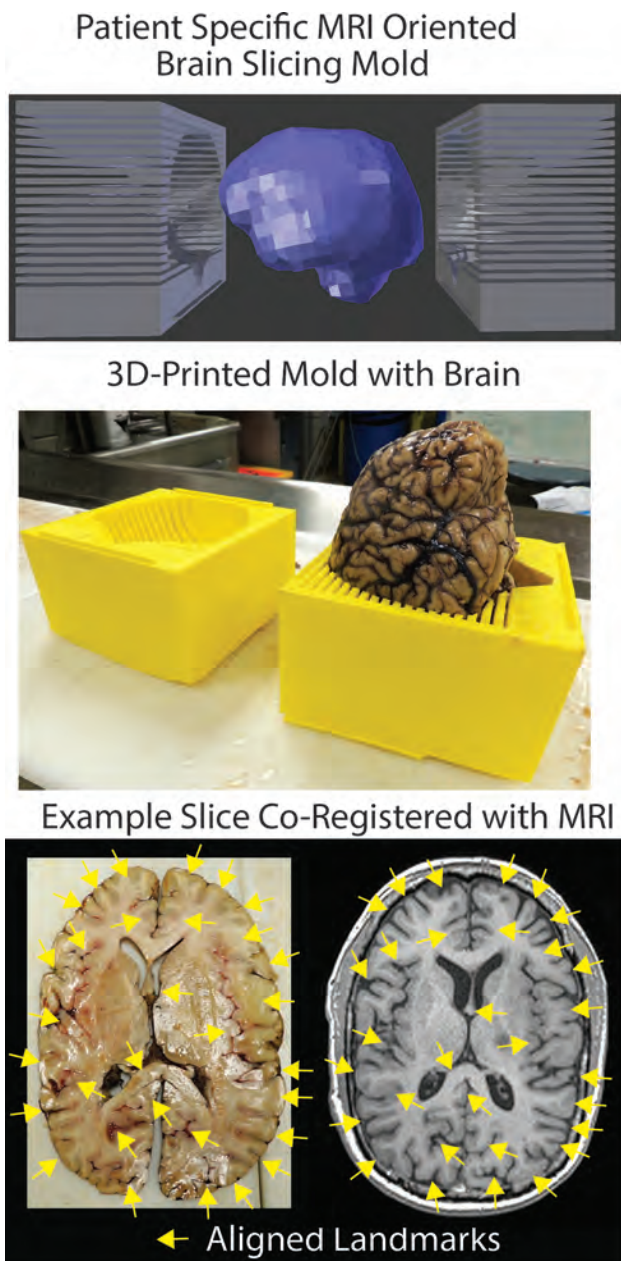


**FIG 2.** Demonstration of the use of a custom 3D-printed slicing jig for sectioning the brain in the same axial orientation as the imaging. Shown on the lower right are examples of gyri and sulci that align well with the imaging (yellow arrows).

using DWI ( $b=0$  and 1000), T1 pre- and postgadolinium, and T2 FLAIR. ADC maps were calculated from DWI by using Analysis of Functional Neuro Images software (AFNI; <http://afni.nimh.nih.gov/afni>) and the equation  $ADC = (1/1000) \times \ln(B0/B1000)$ . Imaging, including the ADC maps, was coregistered to the T1-weighted image by using the FMRIB Linear Image Registration Tool (FLIRT; <http://www.fmrib.ox.ac.uk/>).

#### **Histology Processing and ADC Correlation**

The tissue was processed as previously published,<sup>29</sup> with some modifications. To prevent tissue distortion during brain fixation, for 4 of the 6 postmortem cases, at the time of removal, we placed brains in patient-specific, MR imaging–derived, 3D-printed

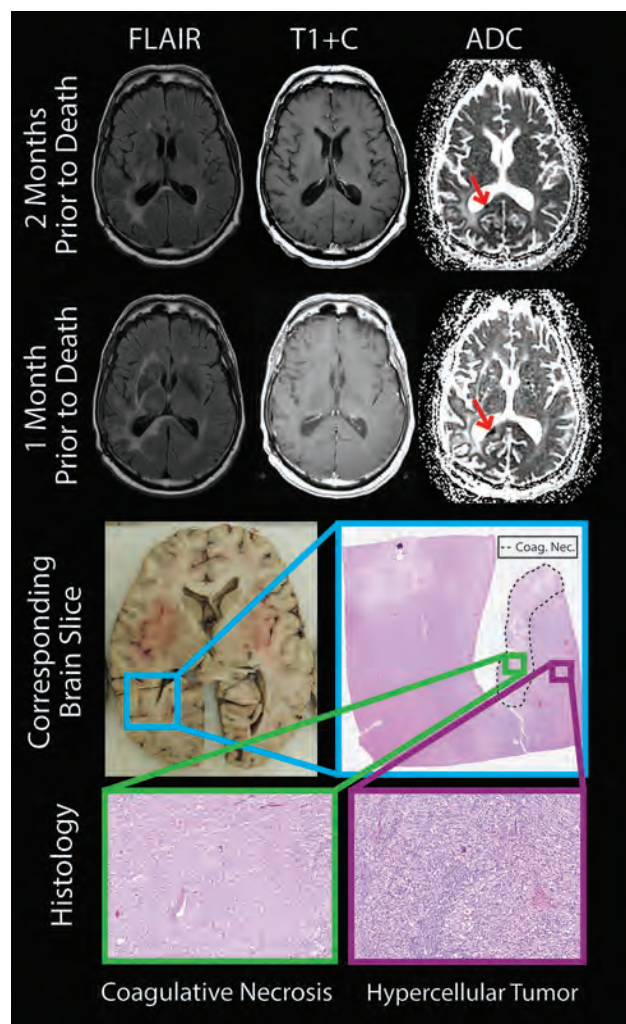


**FIG 3.** The brain section and corresponding imaging from a representative patient. The diffusion-restricted lesion (red arrows) was growing between the 2 imaging sessions, shown 2 months and 1 month before death. Histology revealed coagulative necrosis surrounded by viable hypercellular tumor (lower section). T1+C indicates T1 + gadolinium contrast.

molds (Fig 1).<sup>33</sup> Molds were generated by using open-source software, including the FSL Brain Extraction Tool (<http://fsl.fmrib.ox.ac.uk/fsl/fslwiki/BET>) for generating a brain mask, 3D Slicer ([www.slicer.org](http://www.slicer.org)) for wrapping a surface model around the mask, and Blender ([www.blender.org](http://www.blender.org)) for creating the final mold design. Each was then printed by using a MakerBot Replicator 3D-printer (fifth-generation) ([www.makerbot.com](http://www.makerbot.com)). Postmortem slicing of the brains was done by using a universal slicing jig for 2 patients and a customized 3D-printed slicing jig for 4 patients (Fig 2). Each jig was similarly designed in Blender by using the patient's imaging as described above and printed by using the same 3D printer. Tissue specimens were taken from regions of diffusion restriction as defined by radiologic criteria. Samples were paraffin-embedded, hematoxylin-eosin–stained, and digitized for interpretation and quantification. Each sample was graded to differentiate necrotic regions from viable tumor, and ROIs were manually drawn on each sample to differentiate the 2 tissue types. The digitized histology was then segmented to highlight individual cells<sup>29</sup> and coregistered to the imaging by using custom software and

**Table 2: Demographics for the retrospective bevacizumab study**

	NDR ( <i>n</i> = 45) <sup>a</sup> (Meth [ <i>n</i> = 8]/Unmeth [ <i>n</i> = 10])	StDR ( <i>n</i> = 10) <sup>b</sup> (Unmeth [ <i>n</i> = 7])	PrDR ( <i>n</i> = 9) <sup>c</sup> (Unmeth [ <i>n</i> = 4])
Age at death (yr) (mean) (SD)	55 (13) (58/63)	55 (11) (55)	52 (8) (58)
Sex			
Male	23 (4/4)	6 (4)	8 (4)
Female	22 (4/6)	4 (3)	1 (0)
Days between bevacizumab initiation and death (median) (lower/upper CI)	256 (213–298) (524–352)	516 (197–835) (484)	183 (125–241) (252)
Recurrences/progression (median) (range)	2 (1–5) (2.5/2.2)	2 (1–5) (2.57)	2 (1–3) (1.5)
Initial pathology			
Grade II	5 (1/1)	1 (1)	0 (0)
Grade III	2 (0/1)	2 (2)	1 (0)
GBM	38 (7/8)	7 (4)	8 (4)
Therapeutic regimen			
Surgery + XRT/TMZ + adjuvant TMZ	45 (8/10)	10 (7)	9 (4)
Reoperation	22 (2/5)	6 (4)	2 (0)
Bevacizumab	45 (8/10)	10 (7)	9 (4)
Stopped? <sup>a</sup>	10 (1/3)	3 (1)	1 (0)
Irinotecan	6 (0)	2 (0)	3 (0)
Isotretinoin	15 (2/3)	2 (2)	1 (0)
CCNU/BCNU	8 (3/1)	2 (2)	3 (2)
Interferon	2 (0)	0 (0)	0 (0)
Optune <sup>d</sup> TTF	0 (0)	1 (1)	0 (0)
PLDR	12 (5/4)	5 (4)	3 (2)

**Note:**—PLDR indicates pulsed low-dose rate radiation; NDR, no diffusion restriction; StDR, stable diffusion restriction; PrDR, progressive diffusion restriction; TTF, tumor treating fields; Meth, methylation; Unmeth, no methylation; CCNU/BCNU, carmustine/lomustine; XRT, radiation therapy; TMZ, temozolomide.

<sup>a</sup> Bevacizumab was stopped for further surgery (for resection, *n* = 5; for infection, *n* = 1; for shunting, *n* = 1; for hemorrhage, *n* = 1; buttock abscess, *n* = 1; and hip fracture, *n* = 1).

<sup>b</sup> Bevacizumab was stopped for neutropenia/thrombocytopenia (*n* = 1), fatigue (*n* = 1), and hemorrhage (*n* = 1).

<sup>c</sup> Bevacizumab was stopped for further surgery (resection, *n* = 1).

<sup>d</sup> Novocure, Portsmouth, New Hampshire.

previously published methods.<sup>29</sup> Figure 3 shows a representative patient in whom the target region of diffusion restriction as defined by imaging is compared with the matching brain section and sample location. The ROIs defining necrotic areas were down-sampled to the MR imaging resolution, and ADC values were then extracted from regions of diffusion-restricted necrosis and areas classified as hypercellular. We performed a receiver operating characteristic analysis, iteratively adjusting ADC cutoff values until a maximal area under the curve was obtained for differentiating diffusion-restricted necrosis from hypercellularity for each patient.

Sixty-four patients who underwent bevacizumab treatment for recurrent GBM were retrospectively assessed by using our clinical PACS system to determine whether diffusion-restricted lesions developed following treatment onset (Table 2). Two reviewers (H.S.N. and P.S.L.) determined by consensus which patients developed diffusion-restricted lesions, which were then verified by a board-certified neuroradiologist (S.D.R.). It is the standard practice in our neuro-oncology clinic for patients to undergo MR imaging each month following the onset of bevacizumab therapy for the first 6 months. Follow-up imaging intervals are then extended at the discretion of our neuro-oncologist.

Patients were separated into 3 groups: 1) no diffusion restriction (*n* = 45), 2) new diffusion restriction that appeared and progressively grew within 5 months of bevacizumab initiation (*n* = 9), and 3) delayed onset (the lesion appeared >5 months after bevacizumab initiation) or new diffusion restriction (<3 months postbevacizumab) that remained stable for >3 months (onset and progression totaling >5 months) (*n* = 10). Diffusion-restricted lesion progression or growth was assessed qualitatively

and verified by our neuroradiologist (S.D.R.). Progression was defined by any increase in lesion size beyond the initial lesion appearance (see Fig 4 for examples). Conditions of patients with multiple lesions were classified as progressive if any lesion was progressing, and conditions in patients with lesions decreasing in size were classified as stable. The OS after initiation of bevacizumab therapy within each group was then compared with Kaplan-Meier curves and a log-rank test via SPSS 22 (IBM, Armonk, New York). An additional survival analysis was performed separating patients on the basis of *MGMT* methylation status of initial tumor samples.

## RESULTS

Regions of diffusion-restricted necrosis had significantly lower ADC values than nearby hypercellularity (Table 3). The ADC threshold that best differentiated these tissue types was  $0.736 \times 10^{-3} \text{mm}^2/\text{s}$ , corresponding to an average area under the curve of 0.816 (Table 3). The average ADC value within diffusion-restricted necrosis was  $0.663 \times 10^{-3} \text{mm}^2/\text{s}$ , while the average ADC

within regions of hypercellularity was  $0.925 \times 10^{-3} \text{mm}^2/\text{s}$ . In 5 of the 6 patients, the diffusion-restricted necrosis was progressively growing at the time of the patient's final scan. For these 6 patients, the necrotic regions were surrounded by viable hypercellular non-enhancing tumor. The patient without progressively growing diffusion restriction had recurrent tumor elsewhere, not directly adjacent to the diffusion-restricted lesion.

Figure 5 shows the survival curves comparing no diffusion restriction, progressive diffusion restriction, and stable diffusion restriction, in which patients with stable diffusion restriction had a significantly greater OS than the group with no diffusion restriction (*P* < .05), while the progressive diffusion restriction group had significantly lower OS than the stable diffusion restriction group (*P* < .05) (Fig 5, upper section). Although initially stable, at the time of death all diffusion-restricted lesions were progressing in the group with stable diffusion restriction.

Of the 64 retrospective patients, 37 were tested for *MGMT* methylation. Tumor samples from 8 of 18 patients in the no-diffusion-restriction group were found to be *MGMT* methylated (40%). None of the patients with methylation developed diffusion-restricted lesions. The patients without methylation, when separated by diffusion-restriction status, showed the same survival trend as that in the overall population analysis (Fig 5, middle section). There was no survival difference between patients with unmethylated stable diffusion restriction compared with the patients with methylation and no diffusion restriction (Fig 5, lower section).

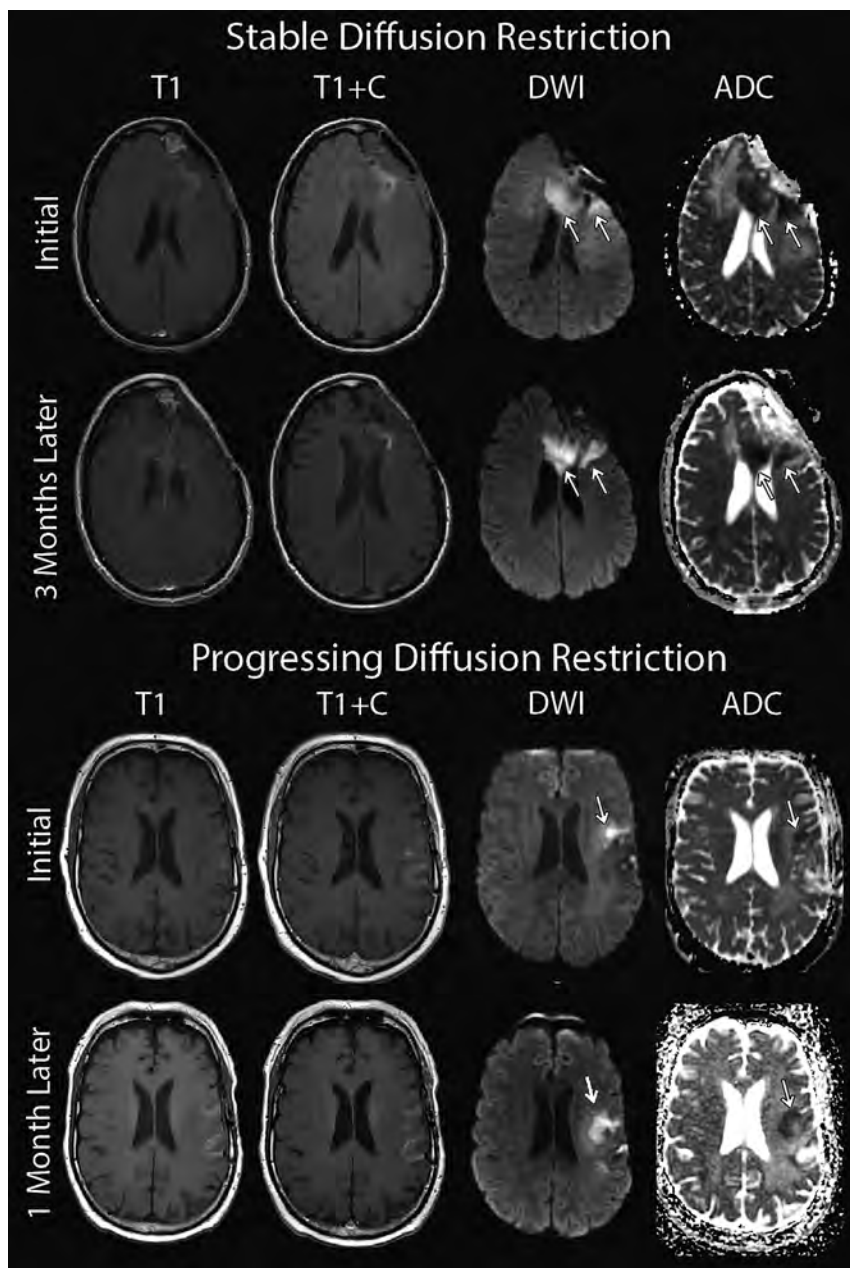


**FIG 4.** Examples of stable and progressive diffusion-restricted lesions occurring following the onset of bevacizumab treatment.

**Table 3: Summary of the ADC values within regions of DRN and hypercellularity**

Patient No.	ADC DRN	DRN Nvox	ADC HypCel	HypCel Nvox	Scanner	Field Strength
1	0.578	142	0.694	256	Optima <sup>a</sup>	1.5T
2	0.552	122	1.000	143	Symphony <sup>b</sup>	1.5T
3	0.622	88	1.076	72	Optima <sup>a</sup>	1.5T
4	0.786	237	1.170	950	Discovery <sup>a</sup>	3T
5	0.699	96	0.775	584	Symphony <sup>b</sup>	1.5T
6	0.743	121	0.838	129	Espre <sup>b</sup>	1.5T
Average	0.663	134	0.926	356		

**Note:**—DRN indicates diffusion restricted necrosis; Nvox, number of voxels; HypCel, hypercellular.

<sup>a</sup> GE Healthcare, Milwaukee, Wisconsin.

<sup>b</sup> Siemens, Erlangen, Germany.

## DISCUSSION

This study explored focal regions of diffusion restriction following bevacizumab treatment. At postmortem, we found that pro-

gressively growing lesions were predominantly coagulative necrotic tissue surrounded by viable nonenhancing hypercellular tumor. Analysis of ADC values showed that a cutoff of  $0.736 \times 10^{-3} \text{mm}^2/\text{s}$  best separated diffusion-restricted necrosis and viable hypercellular tumor. We also found that patients with stable diffusion-restricted lesions had significantly greater OS, while those with progressing diffusion restriction had shorter OS than those who never developed lesions. We also found that all the patients who developed diffusion-restricted lesions had unmethylated *MGMT* and that the patients with stable diffusion restriction showed a survival benefit similar to that of those with *MGMT* methylation with no diffusion restriction.

Several recent studies have explored these diffusion-restricted lesions. Gupta et al<sup>24</sup> noted that diffusion restriction preceded the development of enhancing tumor in a subset of patients with glioblastoma, independent of bevacizumab therapy; this finding suggested that such restriction represented hypercellular tumor. A case report from Gerstner et al<sup>25</sup> showed pathologically confirmed, non-enhancing tumor colocalized with diffusion restriction. Pope et al<sup>34</sup> investigated low ADC values through histogram analysis and agreed with the conclusion that low values indicated areas of hypercellularity. Other studies, however, have hypothesized that these regions could not correspond to tumor because not all conditions of patients progressed.<sup>35,36</sup> They instead hypothesized that these regions would most likely be chronic hypoxia and necrosis.<sup>36</sup>

Population studies examining these lesions have likewise found contradictory results. Studies by Mong et al<sup>21</sup> and Bähr et al<sup>37</sup> found that patients who demonstrated stable diffusion restriction following bevacizumab treatment had increased overall survival, again suggesting that the lesions were not viable tumor. The study of Mong et al<sup>21</sup> confirmed gelatinous necrosis in 1 patient through biopsy. In addition, 5 patients from the literature with sampled biopsies and 2 brain donations demonstrated necrosis within these focal regions.<sup>21,26,28,37,38</sup> Zhang et al,<sup>23</sup> however, found that survival was dependent on the size of the focal lesion.

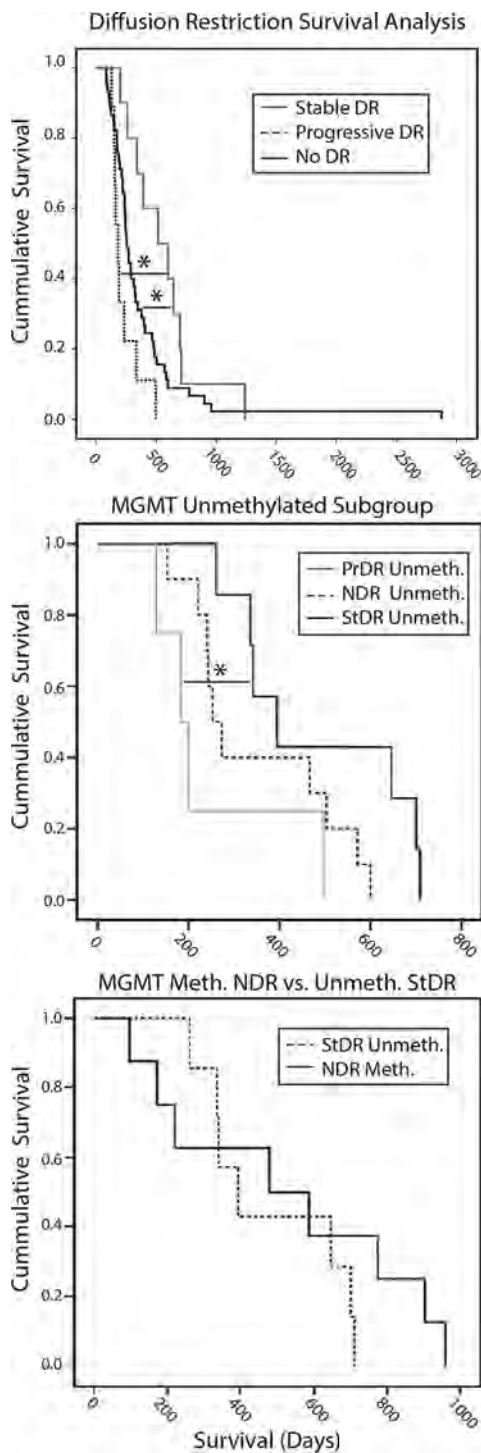


**FIG 5.** Survival analyses comparing groups. *Upper Section*, Overall survival is significantly greater in patients with stable diffusion restriction compared with those with no diffusion restriction ( $P < .05$ ). OS is significantly lower in patients with progressive diffusion restriction compared with those with stable diffusion restriction ( $P < .05$ ). *Middle Section*, Unmethylated tumors show survival trends similar to those in the overall population, in which patients with stable diffusion restriction survived longer than those with no diffusion restriction and progressive diffusion restriction ( $P < .05$ ). *Lower Section*, Patients with unmethylated stable diffusion restriction show survival similar to those with no diffusion-restriction methylation. DR indicates diffusion restriction; PrDR, progressive diffusion restriction; NDR, no diffusion restriction; StDR, stable diffusion restriction; Meth, methylation; Unmeth, no methylation.

Our postmortem findings suggest that regions of diffusion restriction themselves are diffusion-restricted coagulative necrosis. Most important, in 5 of 6 patients, the lesions were progressing at the time of death and were surrounded by viable nonenhancing hypercellular tumor. These tumorous regions are deceptively invisible on contrast-enhanced T1-weighted imaging. This finding may clarify previous reports; if viable tumor was found it would have been reported preferentially to necrosis and given the nature of biopsies, samples could be associated with the incorrect location just adjacent to the actual dark spot.

Diffusion restriction has gained traction as an alternative marker to assess treatment response and tumor progression. Prior glioma studies have found an inverse correlation between ADC and cellularity, tumor grade, and Ki-67 proliferation indices.<sup>24,34</sup> Increasing ADC values have been associated with a reduction in cellularity attributed to effective treatment, edema, and/or radiation necrosis.<sup>15,34</sup> Our study finds, however, that coagulative necrosis, which is rare in the brain, is associated with extremely low diffusion values. Two other studies found similar ADC values within diffusion-restricted necrosis of  $0.71^{29}$  and  $0.63 \times 10^{-3} \text{ mm}^2/\text{s}$ .<sup>35</sup> One study examined the change in ADC values with the onset of bevacizumab treatment for predictive power in survival rates.<sup>19</sup> The authors found that smaller negative changes were more indicative of OS than larger negative changes. We suggest that this finding is because a small drop in ADC value indicates hypercellularity, whereas a large change indicates diffusion-restricted necrosis.

Our results showed that diffusion-restricted lesions could indicate either decreased or increased OS, depending on lesion progression. In our population study, we determined that patients with stable diffusion restriction had a significantly greater OS than those with no diffusion restriction, while patients with progressive diffusion restriction had significantly lower OS than those with both stable diffusion restriction and no diffusion restriction. Patients with stable diffusion restriction may predominantly exhibit necrosis in diffusion-restricted regions, leading to greater OS, while patients with progressive diffusion restriction may exhibit less necrosis surrounded by greater expanding tumor, leading to shortened survival.

Diffusion restriction is typically seen along the ventricles and corpus callosum in qualitative analyses of patients with GBM.<sup>21,31</sup> This finding was true in most of our patients, with diffusion restriction occurring along the lateral ventricles or corpus callosum.

Methylation has been shown to be a strong indicator of survival in patients with GBM.<sup>39</sup> We found that patients with unmethylated stable diffusion restriction on bevacizumab had similar survival compared with those with *MGMT* methylation with no diffusion restriction. Further investigation is needed to understand the inverse correlation between diffusion restriction and *MGMT* methylation.

The mechanism behind diffusion-restricted necrosis has been postulated in prior literature. In a case report, Jeyaretna et al<sup>38</sup> hypothesized that bevacizumab exacerbated radiation necrosis, which may lead to the development of focal regions of coagulative necrosis. Others hypothesized that such regions result from bevacizumab-induced chronic hypoxia.<sup>26</sup> These regions were detectable as early as 4 weeks after the initiation of bevacizumab and were maintained for up to 80 weeks.<sup>26</sup> In addition, they have been predominantly observed along white matter tracts, particularly the corpus callosum and corona radiata.<sup>24</sup> Similarly, our cohort of

patients also exhibited a wide time range between the initiation of bevacizumab therapy and the appearance of a focal region of diffusion restriction. Moreover, all regions, except 1, were within white matter.

There are several sources of potential error in this study. First, our patients were not scanned in the same machine, which could produce differences in our ADC threshold calculation. Although ADC is quantitative, magnet strength and other factors contribute to heterogeneity in ADC values. Coregistration of the histology and imaging is also a source of potential error. We minimized tissue distortion and sectioned the brains according to imaging; however, small errors could have occurred during the slicing. Further research is necessary to determine the accuracy of our brain-slicing technology. In addition, because the CSF drains following brain removal, this phenomenon causes the ventricles to shrink, with irreversible distortion compared with in vivo imaging.

Future studies should look at using our calculated ADC threshold for mapping necrotic-versus-hypercellular tumor. This would then allow quantitative monitoring of tumor growth on a voxelwise basis. Future studies should also look at including additional multiparametric MR images that may potentially help differentiate tumor, such as blood-volume maps.

## CONCLUSIONS

We pathologically confirmed that progressively expanding diffusion restriction in patients undergoing bevacizumab treatment indicates coagulative necrosis surrounded by viable hypercellular tumor. We also determined an optimal ADC cutoff for differentiating diffusion-restricted necrosis from hypercellular tumor. In the population analysis, patients with progressively growing regions of diffusion restriction have decreased overall survival, suggesting that the lesions themselves, when expanding, are necrosis surrounded by viable tumor. Patients with stable lesions, however, showed increased OS over the group with no diffusion restriction. Further research is necessary to establish the biologic basis for bevacizumab causing these lesions.

## ACKNOWLEDGMENTS

We thank the patients and their families who graciously chose to participate in this study.

Disclosures: Jennifer Connelly—UNRELATED: Board Membership: Novocure.\* Comments: Advisory Board. Christopher Schultz—UNRELATED: Board Membership: Prism Imaging (Scientific Advisory Board, unpaid); Grants/Grants Pending: Elekta AB.\* Comments: MR Linac Consortium research support; Travel/Accommodations/Meeting Expenses Unrelated to Activities Listed: Elekta AB.\* Kathleen M. Schmainda—RELATED: Grant: National Institutes of Health\*; UNRELATED: Grants/Grants Pending: National Institutes of Health\*; Other: Imaging Biometrics. Comments: ownership interest in a company that develops MRI postprocessing software. \*Money paid to the institution.

## REFERENCES

1. Stupp R, Mason WP, van den Bent MJ, et al; European Organisation for Research and Treatment of Cancer Brain Tumor and Radiotherapy Groups, National Cancer Institute of Canada Clinical Trials Group. **Radiotherapy plus concomitant and adjuvant temozolomide for glioblastoma.** *N Engl J Med* 2005;352:987–96 CrossRef Medline
2. Iwamoto FM, Abrey LE, Beal K, et al. **Patterns of relapse and prognosis after bevacizumab failure in recurrent glioblastoma.** *Neurology* 2009;73:1200–06 CrossRef Medline
3. Wong ET, Hess KR, Gleason MJ, et al. **Outcomes and prognostic factors in recurrent glioma patients enrolled onto phase II clinical trials.** *J Clin Oncol* 1999;17:2572–78 Medline
4. Lamborn KR, Yung WK, Chang SM, et al; North American Brain Tumor Consortium. **Progression-free survival: an important end point in evaluating therapy for recurrent high-grade gliomas.** *Neuro Oncol* 2008;10:162–70 CrossRef Medline
5. Cohen MH, Shen YL, Keegan P, et al. **FDA drug approval summary: bevacizumab (Avastin) as treatment of recurrent glioblastoma multiforme.** *Oncologist* 2009;14:1131–38 CrossRef Medline
6. Friedman HS, Prados MD, Wen PY, et al. **Bevacizumab alone and in combination with irinotecan in recurrent glioblastoma.** *J Clin Oncol* 2009;27:4733–40 CrossRef Medline
7. Chinot OL, Wick W, Mason W, et al. **Bevacizumab plus radiotherapy-temozolomide for newly diagnosed glioblastoma.** *N Engl J Med* 2014;370:709–22 CrossRef Medline
8. Gilbert MR, Dignam JJ, Armstrong TS, et al. **A randomized trial of bevacizumab for newly diagnosed glioblastoma.** *N Engl J Med* 2014;370:699–708 CrossRef Medline
9. de Groot JF, Fuller G, Kumar AJ, et al. **Tumor invasion after treatment of glioblastoma with bevacizumab: radiographic and pathologic correlation in humans and mice.** *Neuro Oncol* 2010;12:233–42 CrossRef Medline
10. Wen PY, Macdonald DR, Reardon DA, et al. **Updated response assessment criteria for high-grade gliomas: Response Assessment in Neuro-Oncology Working Group.** *J Clin Oncol* 2010;28:1963–72 CrossRef Medline
11. LaViolette PS, Cohen AD, Prah MA, et al. **Vascular change measured with independent component analysis of dynamic susceptibility contrast MRI predicts bevacizumab response in high-grade glioma.** *Neuro Oncol* 2013;15:442–50 CrossRef Medline
12. Schmainda KM, Prah M, Connelly J, et al. **Dynamic-susceptibility contrast agent MRI measures of relative cerebral blood volume predict response to bevacizumab in recurrent high-grade glioma.** *Neuro Oncol* 2014;16:880–88 CrossRef Medline
13. Sawlani RN, Raizer J, Horowitz SW, et al. **Glioblastoma: a method for predicting response to antiangiogenic chemotherapy by using MR perfusion imaging—pilot study.** *Radiology* 2010;255:622–28 CrossRef Medline
14. Sugahara T, Korogi Y, Kochi M, et al. **Usefulness of diffusion-weighted MRI with echo-planar technique in the evaluation of cellularity in gliomas.** *J Magn Reson Imaging* 1999;9:53–60 Medline
15. Ellingson BM, Malkin MG, Rand SD, et al. **Validation of functional diffusion maps (fDMs) as a biomarker for human glioma cellularity.** *J Magn Reson Imaging* 2010;31:538–48 CrossRef Medline
16. Moffat BA, Chenevert TL, Lawrence TS, et al. **Functional diffusion map: a noninvasive MRI biomarker for early stratification of clinical brain tumor response.** *Proc Natl Acad Sci U S A* 2005;102:5524–29 CrossRef Medline
17. Hamstra DA, Galbán CJ, Meyer CR, et al. **Functional diffusion map as an early imaging biomarker for high-grade glioma: correlation with conventional radiologic response and overall survival.** *J Clin Oncol* 2008;26:3387–94 CrossRef Medline
18. Ellingson BM, Cloughesy TF, Zaw T, et al. **Functional diffusion maps (fDMs) evaluated before and after radiochemotherapy predict progression-free and overall survival in newly diagnosed glioblastoma.** *Neuro Oncol* 2012;14:333–43 CrossRef Medline
19. Ellingson BM, Cloughesy TF, Lai A, et al. **Graded functional diffusion map-defined characteristics of apparent diffusion coefficients predict overall survival in recurrent glioblastoma treated with bevacizumab.** *Neuro Oncol* 2011;13:1151–61 CrossRef Medline
20. Ellingson BM, Kim E, Woodworth DC, et al. **Diffusion MRI quality control and functional diffusion map results in ACRIN 6677/RTOG 0625: a multicenter, randomized, phase II trial of bevacizumab and chemotherapy in recurrent glioblastoma.** *Int J Oncol* 2015;46:1883–92 CrossRef Medline
21. Mong S, Ellingson BM, Nghiemphu PL, et al. **Persistent diffusion-restricted lesions in bevacizumab-treated malignant gliomas are**

- associated with improved survival compared with matched controls. *AJNR Am J Neuroradiol* 2012;33:1763–70 CrossRef Medline
22. Hwang EJ, Cha Y, Lee AL, et al. **Early response evaluation for recurrent high grade gliomas treated with bevacizumab: a volumetric analysis using diffusion-weighted imaging.** *J Neurooncol* 2013;112:427–35 CrossRef Medline
  23. Zhang M, Gulotta B, Thomas A, et al. **Large-volume low apparent diffusion coefficient lesions predict poor survival in bevacizumab-treated glioblastoma patients.** *Neuro Oncol* 2016;18:735–43 CrossRef Medline
  24. Gupta A, Young RJ, Karimi S, et al. **Isolated diffusion restriction precedes the development of enhancing tumor in a subset of patients with glioblastoma.** *AJNR Am J Neuroradiol* 2011;32:1301–06 CrossRef Medline
  25. Gerstner ER, Frosch MP, Batchelor TT. **Diffusion magnetic resonance imaging detects pathologically confirmed, nonenhancing tumor progression in a patient with recurrent glioblastoma receiving bevacizumab.** *J Clin Oncol* 2010;28:e91–93 CrossRef Medline
  26. Rieger J, Bähr O, Müller K, et al. **Bevacizumab-induced diffusion-restricted lesions in malignant glioma patients.** *J Neurooncol* 2010;99:49–56 CrossRef Medline
  27. Rieger J, Bähr O, Ronellenfitsch MW, et al. **Bevacizumab-induced diffusion restriction in patients with glioma: tumor progression or surrogate marker of hypoxia?** *J Clin Oncol* 2010;28:e477; author reply e478 CrossRef Medline
  28. Farid N, Almeida-Freitas DB, White NS, et al. **Restriction-spectrum imaging of bevacizumab-related necrosis in a patient with GBM.** *Front Oncol* 2013;3:258 CrossRef Medline
  29. LaViolette PS, Mickevicius NJ, Cochran EJ, et al. **Precise ex vivo histological validation of heightened cellularity and diffusion-restricted necrosis in regions of dark apparent diffusion coefficient in 7 cases of high-grade glioma.** *Neuro Oncol* 2014;16:1599–606 CrossRef Medline
  30. Farid N, Almeida-Freitas DB, White NS, et al. **Combining diffusion and perfusion differentiates tumor from bevacizumab-related imaging abnormality (bria).** *J Neurooncol* 2014;120:539–46 CrossRef Medline
  31. Robbins SL, Cotran RS, Kumar V. *Robbins and Cotran Pathologic Basis of Disease*. Philadelphia: Saunders/Elsevier; 2010
  32. Hegi ME, Diserens AC, Gorlia T, et al. **MGMT gene silencing and benefit from temozolomide in glioblastoma.** *N Engl J Med* 2005;352:997–1003 CrossRef Medline
  33. Pellatt B, Mickevicius NJ, Cochran EJ, et al. **3D-printed MRI-based custom brain molds for minimizing tissue distortion and precisely slicing tissue for co-registration with clinically acquired MRI in glioma patients.** *Neuro-Oncology* 2014;16(suppl 5):v152 CrossRef
  34. Pope WB, Kim HJ, Huo J, et al. **Recurrent glioblastoma multiforme: ADC histogram analysis predicts response to bevacizumab treatment.** *Radiology* 2009;252:182–89 CrossRef Medline
  35. Reiger J, Bähr O, Müller K, et al. **Bevacizumab-induced diffusion-restricted lesions in malignant glioma patients.** *J Neurooncol* 2010;99:49–56 CrossRef Medline
  36. Rahman R, Hamdan A, Zweifler R, et al. **Histogram analysis of apparent diffusion coefficient within enhancing and nonenhancing tumor volumes in recurrent glioblastoma patients treated with bevacizumab.** *J Neurooncol* 2014;119:149–58 CrossRef Medline
  37. Bähr O, Harter P, Weise L, et al. **Sustained focal antitumor activity of bevacizumab in recurrent glioblastoma.** *Neurology* 2014;83:227–34 CrossRef Medline
  38. Jeyaretna DS, Curry WT Jr, Batchelor TT, et al. **Exacerbation of cerebral radiation necrosis by bevacizumab.** *J Clin Oncol* 2011;29:e159–62 CrossRef Medline
  39. Rivera AL, Pelloski CE, Gilbert MR, et al. **MGMT promoter methylation is predictive of response to radiotherapy and prognostic in the absence of adjuvant alkylating chemotherapy for glioblastoma.** *Neuro Oncol* 2010;12:116–21 CrossRef Medline

# Improving the Grading Accuracy of Astrocytic Neoplasms Noninvasively by Combining Timing Information with Cerebral Blood Flow: A Multi-TI Arterial Spin-Labeling MR Imaging Study

S. Yang, B. Zhao, G. Wang, J. Xiang, S. Xu, Y. Liu, P. Zhao, J. Pfeuffer, and T. Qian



## ABSTRACT

**BACKGROUND AND PURPOSE:** Systematic and accurate glioma grading has clinical significance. We present the utility of multi-TI arterial spin-labeling imaging and provide the bolus arrival time maps for grading astrocytomas.

**MATERIALS AND METHODS:** Forty-three patients with astrocytomas (21 men; mean age, 51 years) were recruited. The classification abilities of conventional MR imaging features, normalized CBF value derived from multi-TI arterial spin-labeling imaging, normalized bolus arrival time, and normalized CBF derived from single-TI arterial spin-labeling were compared in patients with World Health Organization (WHO) grade II, III, and IV astrocytomas.

**RESULTS:** The normalized CBF value derived from multi-TI arterial spin-labeling imaging was higher in patients with higher grade astrocytoma malignancies compared with patients with lower grade astrocytomas, while the normalized bolus arrival time showed the opposite tendency. The normalized CBF value derived from the multi-TI arterial spin-labeling imaging showed excellent performance with areas under the receiver operating characteristic curve of 0.813 (WHO II versus III), 0.964 (WHO II versus IV), 0.872 (WHO III versus IV), and 0.883 (low-grade-versus-high-grade gliomas). The normalized CBF value derived from single-TI arterial spin-labeling imaging could statistically differentiate the WHO II and IV groups (area under the receiver operating characteristic curve = 0.826). The normalized bolus arrival time effectively identified the WHO grades II and III with an area under the receiver operating characteristic curve of 0.836. Combining the normalized CBF value derived from multi-TI arterial spin-labeling imaging and normalized bolus arrival time improved the diagnostic accuracy from 65.10% to 72.10% compared with the normalized CBF value derived from multi-TI arterial spin-labeling imaging being applied independently. The combination of multi-TI arterial spin-labeling imaging and conventional MR imaging had the best performance, with a diagnostic accuracy of 81.40%.

**CONCLUSIONS:** Multi-TI arterial spin-labeling imaging can evaluate perfusion dynamics by combining normalized bolus arrival time and normalized CBF values derived from multiple TIs. It is superior to single-TI arterial spin-labeling imaging and conventional MR imaging features when applied independently and can improve the diagnostic accuracy when combined with conventional MR imaging for grading astrocytomas.

**ABBREVIATIONS:** ASL = arterial spin-labeling; AUC = area under the receiver operating characteristic curve; BAT = bolus arrival time; HGG = high-grade glioma; LGG = low-grade glioma; mTI-ASL = multi-TI arterial spin-labeling imaging; nBAT = normalized bolus arrival time; nCBF-mTI = normalized CBF value derived from mTI-ASL; nCBF-sTI = normalized CBF value derived from single-TI ASL; sTI-ASL = single-TI arterial spin-labeling imaging; WHO = World Health Organization

**G**liomas are the most common primary brain tumor in adults. More than 75% of gliomas have astrocytic features.<sup>1</sup> MR imaging is important in tumor diagnosis, surgical guidance, and therapeutic monitoring of brain tumors. Conventional MR imaging, especially gadolinium-based contrast-enhanced MR imaging, is commonly used to evaluate tumor morphology and distinguish

the degree of malignancy in astrocytic neoplasms. Generally, obvious enhancements suggest high malignancy. However, these contrast enhancements are limited by low specificity because the enhancement after contrast agent injection may not be a true assessment of tumor vascularity but may instead reflect BBB disruption effects. In addition to conventional MR imaging, some

Received January 24, 2016; accepted after revision July 1.

From the Department of MR Imaging (S.Y., B.Z., G.W., J.X.), Shandong Medical Imaging Research Institute, Shandong University, Jinan, P.R. China; Department of Neurosurgery (S.X., Y.L., P.Z.), Shandong Provincial Hospital affiliated to Shandong University, Jinan, Shandong, China; Application Development (J.P.), Siemens, Erlangen, Germany; and MR Collaborations NE Asia (T.Q.), Siemens Healthcare, Beijing, China.

Please address correspondence to Bin Zhao, MD, Department of MR Imaging, Shandong Medical Imaging Research Institute, Shandong University, 324# Jingwu Road, Jinan, 250021, P.R. China; e-mail: zhaobin6025@163.com

Indicates article with supplemental on-line appendix and tables.

Indicates article with supplemental on-line photos.

<http://dx.doi.org/10.3174/ajnr.A4907>

**Table 1: Patient characteristics**

	Histologic Diagnosis		
	Diffuse Astrocytoma (WHO II)	Anaplastic Astrocytoma (WHO III)	Glioblastoma (WHO IV)
No. of patients	15	15	13
Male/female ratio	7:8	6:9	8:5
Median age (yr) (range)	54 (17–70)	52 (15–73)	57 (28–67)

other MR imaging modalities such as PWI, DWI, MR spectroscopy, and PET/MR imaging, have also found their place in brain tumor evaluation.<sup>2–4</sup>

Various PWI methods have shown clinical usefulness in adult gliomas, including the use of relative maximal CBV and relative CBF from DSC-MR imaging to predict tumor grade and behavior.<sup>5,6</sup> Moreover, recent studies have shown that arterial spin-labeling (ASL) may be a reliable alternative to DSC-MR imaging for evaluating tumor perfusion.<sup>7,8</sup>

However, standard 3D ASL MR imaging with a single TI (typically ~2000 ms) does not allow the temporal characteristics of blood inflow and tissue perfusion to be evaluated.<sup>7</sup> Other previous studies have used multiple (4–8) TIs to calculate the timing information; however, despite the longer acquisition times, the temporal resolution is not sensitive enough to observe the small bolus arrival time (BAT) changes that are characteristic of glioma cases.<sup>9,10</sup>

Recently, the multiparametric multi-TI ASL (mTI-ASL) technique has been proposed, which fits the data collected from several different TIs to a kinetic model.<sup>11</sup> This technique can provide quantified CBF information and accurate BAT estimations that allow the perfusion changes to be characterized within a clinically feasible 5-minute protocol.<sup>10,12</sup> Here, we tested the performance abilities of different perfusion parameters obtained from mTI-ASL and other conventional MR imaging modalities in grading astrocytic neoplasms and investigated the potential advantages of the mTI-ASL method.

## MATERIALS AND METHODS

### Subjects

This prospective study was approved by the Shandong University institutional review board, and all patients provided written informed consent. Forty-three patients (21 men; mean age, 51 ± 15.34 years; range, 15–73 years) with new-onset astrocytomas were consecutively included (Table 1). Patients were histologically divided into 3 groups: glioblastomas (*n* = 13, World Health Organization [WHO] IV), anaplastic astrocytomas (*n* = 15, WHO III), and diffuse astrocytomas (*n* = 15, WHO II); all lesions were located in the supratentorial region. No multicentric or multifocal tumors were included in this study. Patients with histologically verified abscesses, granulomas, and recurrent tumors were excluded, as were those with oligodendroglial elements, because oligodendrogliomas have different perfusion patterns.<sup>13</sup> Tissue samples were graded according to the 2007 World Health Organization brain tumor classification, by 2 experienced neuropathologists (both of whom have >5 years of experience).<sup>14</sup>

### MR Imaging

Data were collected on a Magnetom Skyra 3T scanner (Siemens, Erlangen, Germany) with a 32-channel head coil. Before the scans, padding was arranged around the subject's head to minimize head movement. MR imaging was performed by using the following sequences and parameters: an axial T2-weighted TSE sequence (TR/TE = 3000/80 ms, FOV = 230 × 230 mm<sup>2</sup>, matrix = 512 × 408, section thickness = 4 mm, gap = 50%, 20 sections) and a T1-weighted TSE sequence (TR/TE = 400/10 ms, FOV = 230 × 230 mm<sup>2</sup>, matrix = 512 × 408, section thickness = 4 mm, gap 50%, 20 sections); contrast-enhanced T1-weighted images were obtained after the intravenous administration of 0.1 mmol/kg of gadodiamide (Omniscan; GE Healthcare, Piscataway, New Jersey). For all patients, the acquisition of ASL data was performed before the application of contrast media because of the known T1-shortening effect of gadolinium-based contrast agents, which results in a reduction of the SNR ratio.<sup>15</sup>

We used a pulsed ASL sequence with flow-sensitive alternating inversion recovery labeling and a quantitative imaging of perfusion with a single subtraction with a thin-section TI<sub>1</sub> periodic saturation scheme combined with a 3D gradient and spin-echo readout at multiple TIs.<sup>16</sup> The sequence was extended to include an M0 scan and automated in-line processing of the multiple TI data. The model of Buxton et al<sup>11</sup> was fitted with a nonlinear fitting algorithm to obtain quantitative CBF and BAT maps. The model function used the following parameters: λ = 0.9, T1 of arterial blood = 1650 ms, T1 of brain tissue = 1330 ms, and bolus length = 700 ms. The mTI-ASL parameters were the following: TR/TE = 4600/22 ms, FOV = 220 × 220 mm<sup>2</sup>, iPAT mode = generalized autocalibrating partially parallel acquisition phase encoding (PE) 2, section thickness = 4 mm, voxel size = 1.7 × 1.7 × 4.0 mm<sup>3</sup>, 20 sections, turbo factor = 12, echo-planar imaging factor = 31, number of segments = 2, bandwidth = 2242 Hz/pixel, 16 TIs of 480–4080 ms with increments of 240 ms, 1 measurement for each TI, and total acquisition time = 5 minutes 9 seconds. The common and default ASL MR imaging sequences with a single TI (sTI-ASL) generally use a TI of 2000 ms (usually the flow-sensitive alternating inversion recovery model).<sup>17</sup> In addition, the CBF values for both sTI-ASL and mTI-ASL were normalized, and the variables in the quantification equation for sTI-ASL were all invariant constants under a fixed protocol. Therefore, instead of executing a conventional sTI-ASL sequence, we only selected the perfusion-weighted images from a single TI (TI = 1920 ms) to measure the normalized CBF of sTI-ASL (nCBF-sTI).

### Data Analysis

The conventional MR images were evaluated by 2 neuroradiologists with >10 years of experience. A score ranging from 1 to 3 was assigned to the 5 MR imaging features of edema, mass effect, contrast enhancement, heterogeneity, and necrosis/cyst, while scores of 1–2 were assigned for the borders, hemorrhage, and flow void. The scoring criteria are listed in Table 2.<sup>18,19</sup> The mean of the summed scores from the 2 observers for the MR imaging features of each patient was used for the analyses.

To measure the values for the parameters obtained by ASL, we used the MRIcron software (Chris Rorden, <http://people.cas>).

**Table 2: MR imaging scoring criteria<sup>a</sup>**

Tumor Feature	Scores
Edema	None or mild (1); smaller than tumor volume (2); larger than tumor volume (3)
Mass effect	Subarachnoid space effacement (1); ventricular system compression (2); midline shift (3)
Contrast enhancement	None (1); mild or nodular (2); marked and heterogeneous (3)
Borders	Well-defined (1); poorly defined (2)
Heterogeneity	Homogeneous (1); heterogeneous on T2WI (2); heterogeneous on T1WI and T2WI (3)
Necrosis/cyst	None (1); involving less than half the volume of the tumoral mass (2); involving more than half the volume of the tumoral mass (3)
Hemorrhage	None (1); present (2)
Flow void	None (1); present (2)

<sup>a</sup> The numbers in parentheses are the scores assigned for the grades of tumor features.

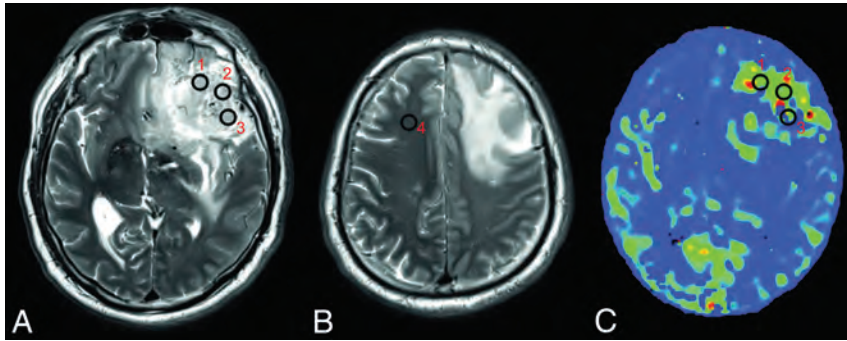


**FIG 1.** VOI positioning. Three VOIs are placed on the solid part of the tumor (VOI 1, 2, and 3) (A), and 1 is placed on the contralateral normal-appearing white matter of the frontal lobe (VOI 4) (B) on T2-weighted images by each of the 2 neuroradiologists. The VOIs are projected onto the maps derived from ASL (eg, the CBF-mTI map) (C).

sc.edu/rorden/mricron/index.html) to draw VOIs and to calculate the average value within each VOI.<sup>20</sup> Two neuroradiologists each drew 3 VOIs (8–10 voxels) on the solid tumor area and 1 similarly sized VOI in the contralateral normal-appearing white matter of the frontal lobe on each subject's T2-weighted images (Fig 1). The neuroradiologists were blinded to the histologic diagnosis, clinical data, age, and sex of the subjects and were unaware of the relationship between the CBF and BAT values. When drawing VOIs, we avoided areas involving vessels, calcification, necrosis, hemorrhages, and CSF spaces. When tumors crossed the midline, the reference VOI was drawn on the nondominant side. All VOIs were then projected onto the maps derived from ASL by using MRICron. On the basis of previous reports,<sup>21</sup> the normalized values were obtained by dividing the mean value of the 3 tumor VOIs by that of the contralateral normal-appearing white matter VOI for each patient, and they were marked as the normalized CBF value derived from mTI-ASL (nCBF-mTI), normalized BAT (nBAT), and nCBF-sTI. The normalized values measured by each neuroradiologist were then averaged for further analysis.

### Statistical Analysis

Statistical analysis was performed by using SPSS 19.0 (IBM, Armonk, New York). Receiver operating characteristic curves and areas under the receiver operating characteristic curve (AUCs) were calculated by using MedCalc version 11.4.2.0 for Windows (MedCalc Software, Mariakerke, Belgium). WHO grade II tumors were defined as low-grade gliomas (LGGs), while those with WHO grades III and IV were defined as high-grade gliomas (HGGs).<sup>22</sup> The interrater reliability was evaluated by using the intraclass correlation coefficient. Intergroup differences (among the WHO II, III, and IV grades) were calculated by applying

Kruskal-Wallis tests. We used Mann-Whitney *U* tests to detect the differences between the LGG and HGG groups.

Wilcoxon signed rank tests were performed to detect the differences between the nCBF-mTI and nCBF-sTI values. Spearman correlation coefficients were calculated between the nCBF-mTI and nBAT values and between the nCBF-sTI and nBAT values.

The diagnostic accuracy percentage of each parameter and the combined parameters was calculated by using the Fisher linear classification algorithm in Matlab (Version 7.14.0. 739, R2012a; MathWorks, Natick, Massachusetts).

All data are presented as median and range. Multiplication of the *P* values acquired by performing the multiple comparisons among the WHO II, III, and IV grades was performed for the Bonferroni correction. A *P* value of < .05 was considered statistically significant. Note that CBF and BAT refer to the parameter maps, while normalized CBF and nBAT refer to the single tumor-to-contralateral normal-appearing white matter ratio values.

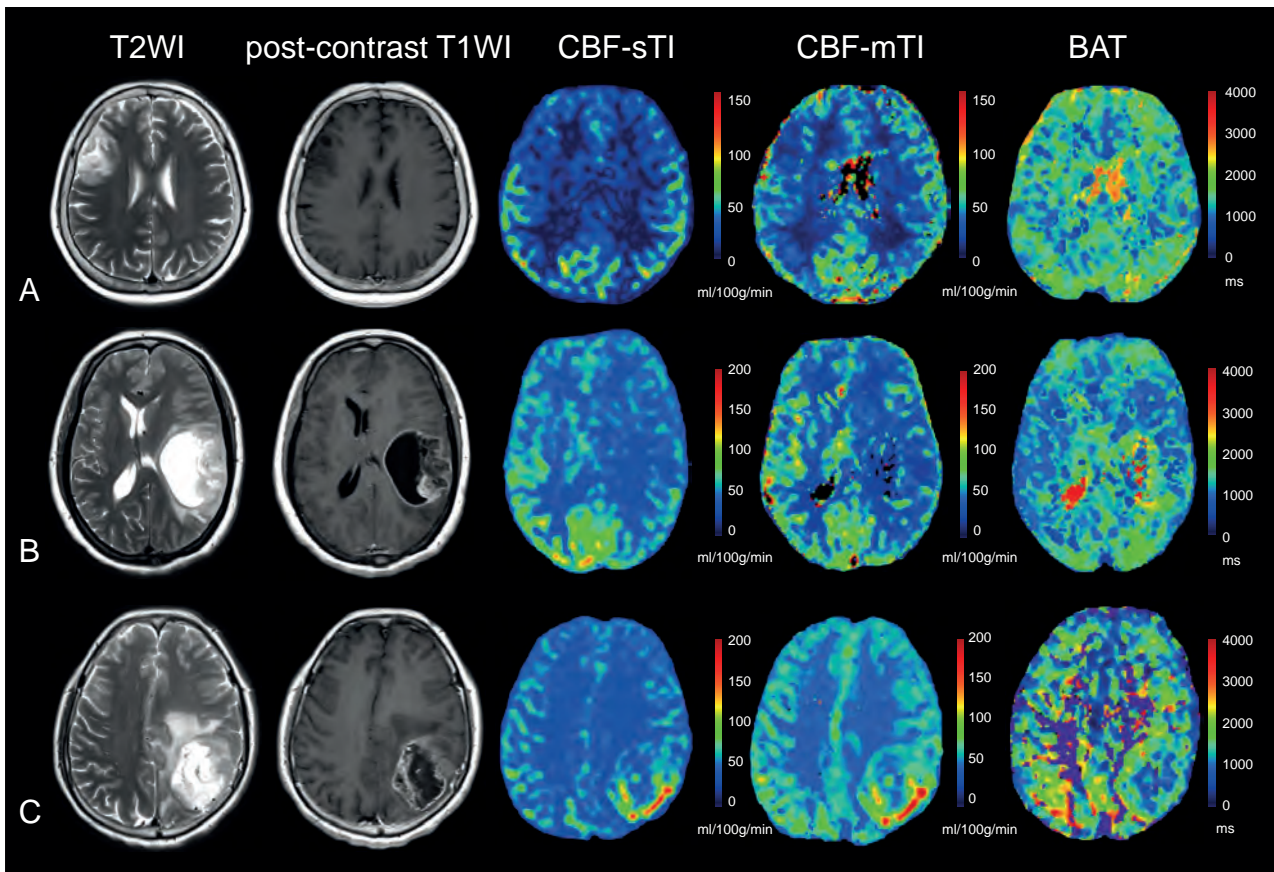
### RESULTS

Table 1 summarizes the patient characteristics and tumor types. No significant differences in age or sex (Kruskal-Wallis tests; *P* = .737, .521, respectively) were observed among the WHO II, III, and IV groups.

Examples of CBF-sTI, CBF-mTI, BAT maps, the corresponding T2-weighted images, and postcontrast T1-weighted images for a diffuse astrocytoma, an anaplastic astrocytoma, and a glioblastoma are shown in Fig 2.

An intraclass correlation coefficient above 0.75 was considered good interrater reliability in our study. The 2 observers demonstrated good consistency because the intraclass correlation coefficient values for the 8 MR imaging feature scores and nCBF-mTI, nCBF-sTI, and nBAT values were all  $\geq 0.80$  in our study. All intraclass correlation coefficients are shown in On-line Table 1.

As shown in Tables 3 and 4, the sum of scores (*P* = .006), nCBF-sTI (*P* = .003), nCBF-mTI (*P* < .001), and nBAT (*P* = .002) all could independently differentiate LGGs from HGGs (Fig 3A). When we compared 2 grades, a significant difference was detected by the sum of scores (*P* = .015) only between WHO grades II and IV. Significant differences in the nCBF-mTI values were observed between the WHO II and III groups (*P* = .021),



**FIG 2.** Examples of the 3 different astrocytomas. *A*, A 60-year-old female patient with a diffuse astrocytoma (WHO II) in the right frontal-parietal region. The lesion demonstrates high signal on the T2-weighted image, a relatively low CBF value on both the CBF-sTI and CBF-mTI maps, and moderate signal intensity on the BAT map. No obvious enhancement is visible on the postcontrast T1-weighted image. *B*, Images from a 50-year-old woman with an anaplastic astrocytoma (WHO III) in the left temporal lobe demonstrate high signal intensity in the T2-weighted image and moderate enhancement in the postcontrast T1-weighted image for the solid part of the tumor. Both the CBF-sTI and CBF-mTI maps demonstrate low signal intensity, but the BAT value for the tumor areas is longer than that for the corresponding contralateral normal cerebral region. *C*, A 56-year-old female patient with a glioblastoma (WHO IV) in the left parietal lobe. The solid part of the tumor appears as an area of high signal intensity in the T2-weighted image and as obvious enhancement in the postcontrast T1-weighted image. Hyperperfusion is visible in both the CBF-sTI and CBF-mTI maps, and the BAT value is shortened.

**Table 3: Comparison of the sum of scores for the MR imaging features and ASL parameters (average values obtained by the 2 readers) among the 3 pathologic grades<sup>a</sup>**

WHO Grade	Sum of Scores (Median) (Range)	nCBF-sTI (Median) (Range)	nCBF-mTI (Median) (Range)	nBAT (Median) (Range)
II (LGGs)	13 (8.5–19)	1.28 (0.36–8.7)	1.62 (0.68–8.56)	1.21 (0.68–4.52)
III	15 (12–19)	3.33 (0.72–10.78)	4.93 (1.78–14.85)	0.77 (0.53–1.70)
IV	16.5 (11.5–19.5)	4.07 (1.07–15.23)	13.40 (5.18–22.36)	0.90 (0.53–1.55)
III and IV (HGGs)	16.5 (11.5–19.5)	3.7 (0.72–14.51)	6.7 (1.78–22.36)	0.86 (0.53–1.70)

<sup>a</sup> Values are presented as median and range.

WHO II and IV groups ( $P < .001$ ), and WHO III and IV groups ( $P = .023$ ). The nBAT values for the WHO II and III groups were significantly different ( $P = .005$ ), but the values for the other group pairs were not significantly different. For the nCBF-sTI values, a significant difference was detected only between the WHO II and IV groups ( $P = .006$ ) (Fig 3B).

Figure 3 also shows that the nCBF-mTI value is higher than the nCBF-sTI value. A Wilcoxon signed rank test was performed to examine this difference, with all patients being treated as 1 group, and a statistically significant difference was observed ( $P = .012$ ). In patients with HGG, a significant difference was also detected between the nCBF-mTI and nCBF-sTI values ( $P = .023$ ), but a

difference was not identified between these values in patients with LGG. The nCBF-mTI value was nonsignificantly higher than the nCBF-sTI value for the separate WHO grade II, III, and IV groups. Additionally, we found that the nCBF-mTI and nCBF-sTI values increased as the tumor malignancy grade increased, while the nBAT values demonstrated the opposite trend. The nBAT

value was negatively correlated with the nCBF-mTI ( $r = -0.467$ ,  $P = .002$ ) and nCBF-sTI ( $r = -0.302$ ,  $P = .049$ ) values.

Figure 4 shows the receiver operating characteristic curves for the sum of scores, nCBF-mTI, nCBF-sTI, and nBAT concerning their ability to differentiate the grade groups. The sum of scores was able to separate different grades with AUCs of 0.716 (WHO II versus III), 0.805 (WHO II versus IV), 0.603 (WHO III versus IV), and 0.757 (LGGs versus HGGs). The nCBF-mTI value showed excellent performance with AUCs of 0.813 (WHO II versus III), 0.964 (WHO II versus IV), 0.872 (WHO III versus IV), and 0.883 (LGGs versus HGGs). The nBAT could discriminate the WHO II and III grades with an AUC of 0.836. The nCBF-sTI could only

statistically differentiate the WHO II and IV groups (AUC = 0.826). We used the method of DeLong et al<sup>23</sup> for the calculation of the difference between 2 AUCs. The AUC of nCBF-mTI was non-significantly higher than that of the sum of scores in all intergroup comparisons (all  $P > .05$ ). There was no significant difference between any other 2 AUCs of the parameters.

As mentioned above, the nCBF-mTI and nCBF-sTI values were positively correlated with the tumor grade, while the nBAT value was negatively correlated with the tumor grade. Therefore, a tumor value that was equal to or higher than the best cutoff value suggested a higher grade when using the nCBF-mTI and nCBF-sTI values. In contrast, an nBAT value that was higher than the best cutoff value indicated a lower grade. The best cutoff values for discriminating among the WHO II, III, and IV grades were 13.00 and 16.00 for the summed scores of the conventional MR imaging features, 1.88 and 6.64 for nCBF-sTI, 2.43 and 8.55 for nCBF-mTI, and 0.97 and 0.77 for the nBAT.

The diagnostic accuracies of parameters for simultaneously discriminating among the WHO II, III, and IV grades are shown in Fig 5. The histogram shows that the nCBF-mTI value had the

best performance, with an accuracy of 65.10%, compared with the sum of scores of conventional MR imaging features (55.80%), nCBF-sTI value (51.20%), and nBAT value (37.20%). Combining the nCBF-mTI and nBAT values effectively improved the diagnostic accuracy to 72.10%, which represented the overall efficiency of mTI-ASL, compared with the accuracy obtained by using only the nCBF-mTI value (65.10%). The diagnostic accuracy of combining nCBF-sTI and the sum of scores was 55.50%. Although it was slightly higher than that obtained with only the nCBF-sTI, there was no great improvement compared with applying the sum of scores independently. When we combined nCBF-mTI, nBAT, and the sum of scores, the diagnostic accuracy increased to 81.40%.

On-line Fig 1 shows the hyperplane obtained by the Fisher linear classification algorithm with the maximum class separation distance criterion for discriminating LGGs and HGGs (On-line Fig 1A) and the 3 tumor grades (On-line Fig 1B) by using 2 parameter dimensions, nBAT and nCBF-mTI, respectively.

## DISCUSSION

Clinically, conventional MR imaging sequences are commonly used to define the malignancy degree of astrocytomas, but these definitions are usually subjective and depend on the observer's experience. For independent application of the parameters, the summed scores of conventional MR imaging features performed better than the nCBF-sTI and nBAT values, with a diagnostic accuracy of 55.80%. Nevertheless, the nCBF-mTI value demonstrated better diagnostic accuracy (65.10%) in the simultaneous discrimination of WHO grades II, III, and IV. When the nBAT

**Table 4: P values of comparisons for the sum of scores for the MR imaging features and ASL parameters among the 3 pathologic grades**

WHO Grade	Sum of Scores	nCBF-sTI	nCBF-mTI	nBAT
II vs III	.139	.098	.021 <sup>a</sup>	.005 <sup>a</sup>
II vs IV	.015 <sup>a</sup>	.006 <sup>a</sup>	<.001 <sup>a</sup>	.078
III vs IV	1	.905	.023 <sup>a</sup>	1
LGGs vs HGGs	.006 <sup>a</sup>	.003 <sup>a</sup>	<.001 <sup>a</sup>	.002 <sup>a</sup>

<sup>a</sup> Significant at 95% (for intergroup comparisons among the WHO II, III, and IV grades. P values have been multiplied by 3 for Bonferroni correction).

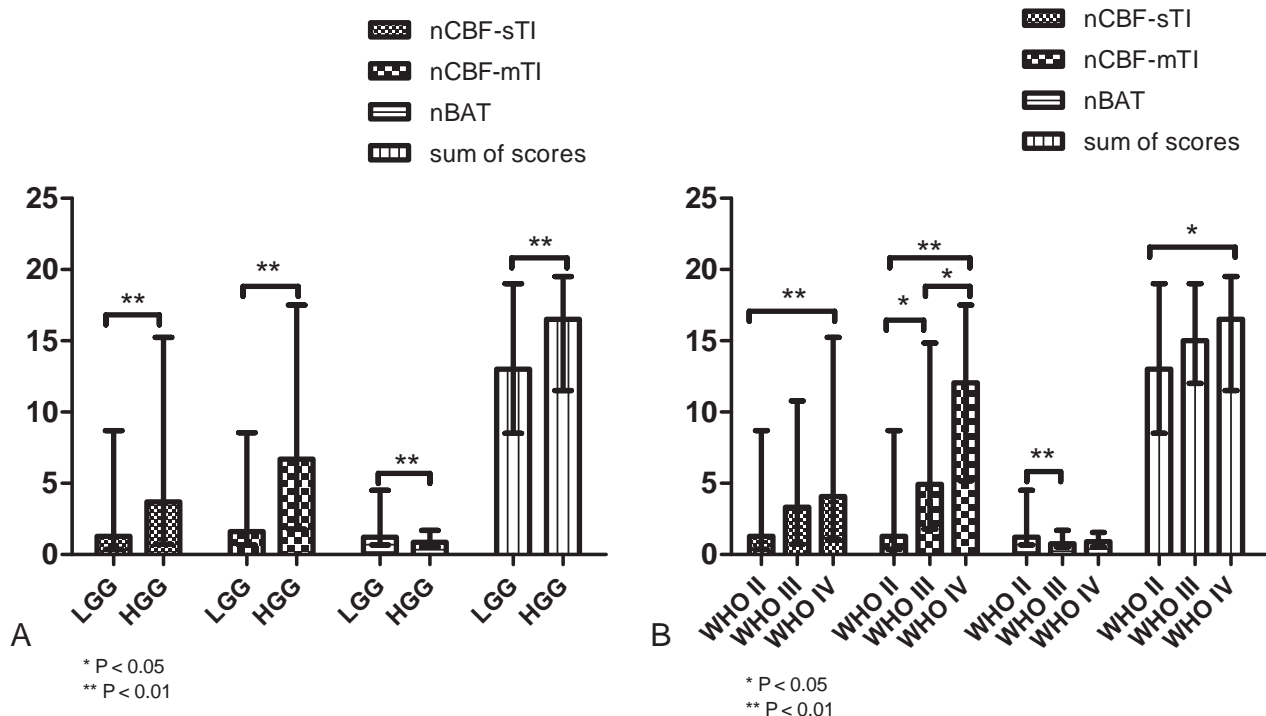


**FIG 3.** The values of the different parameters are plotted as bar graphs by median and range. Significant differences between groups are indicated by asterisks. Error bars indicate the range. A, The bar graph shows the 4 indices of nCBF-mTI, nBAT, and nCBF-sTI and the sum of scores for the LGG and HGG groups. All indices indicate a significant difference between the LGG and HGG groups. B, The values in the bar graph show the parameters of each tumor grade. The nCBF-mTI shows significant differences between each pair of grades. The nBAT shows a significant difference between the WHO II and III groups. The nCBF-sTI and sum of scores show significant differences between only the WHO II and IV groups.

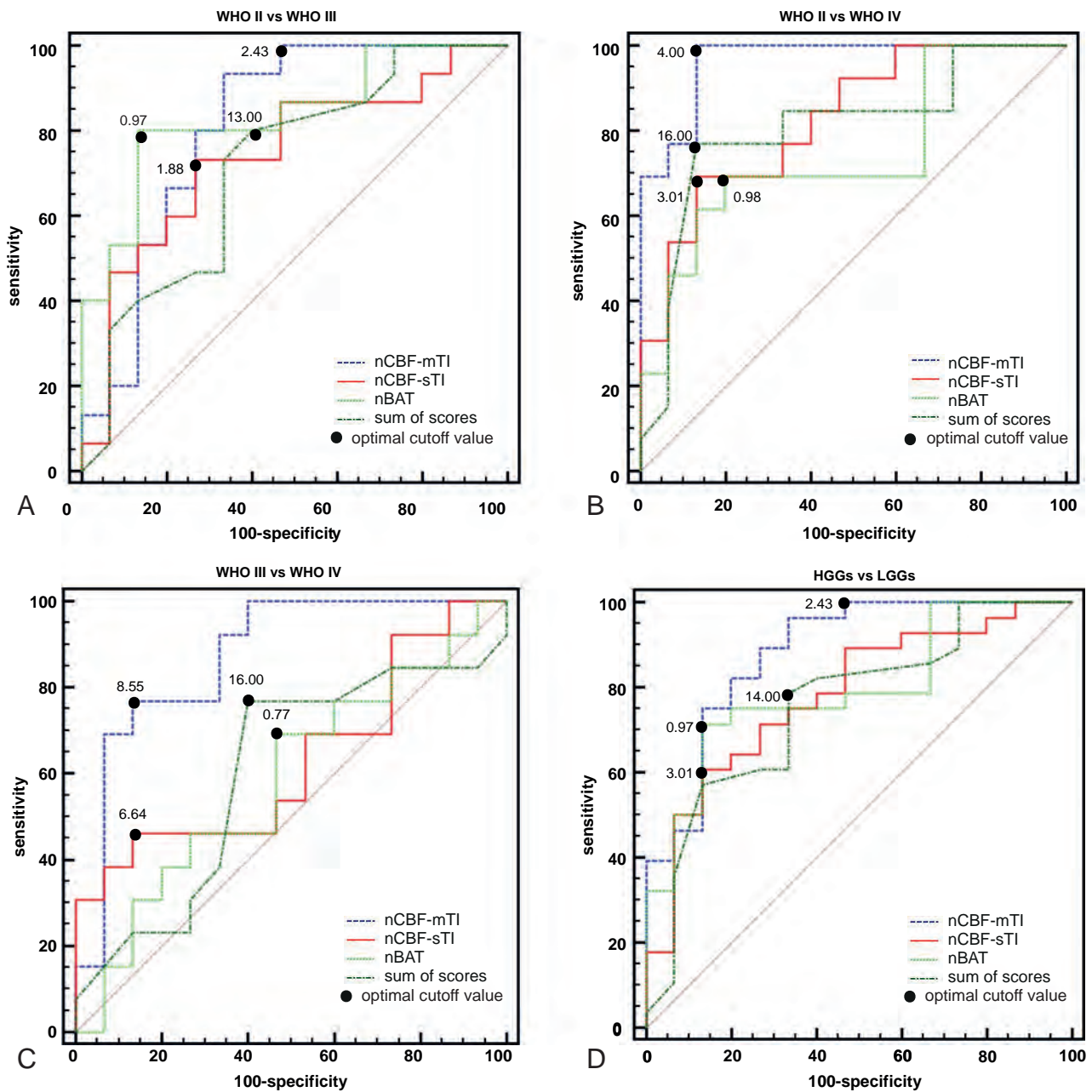


**FIG 4.** Results of the receiver operating characteristic curve analyses. A, The receiver operating characteristic (ROC) curve for the nCBF-mTI, nCBF-sTI, nBAT, and sum of scores for MR imaging features in differentiating the WHO II and III groups. The nBAT has the best performance with an AUC of 0.836, followed by the nCBF-mTI with an AUC of 0.813, the nCBF-sTI with an AUC of 0.742, and the sum of scores with an AUC of 0.716. B, The ROC curves for the nCBF-mTI, nCBF-sTI, nBAT, and the sum of scores in differentiating the WHO II and IV groups. The nCBF-mTI has the best performance with an AUC of 0.964, followed by the nCBF-sTI, sum of scores, and nBAT, with AUCs of 0.826, 0.805, and 0.744, respectively. C, The ROC curves for the nCBF-mTI, nCBF-sTI, nBAT, and the sum of scores in differentiating the WHO III and IV groups. The nCBF-mTI has the best performance with an AUC of 0.872, followed by the nCBF-sTI, sum of scores, and nBAT, with AUCs of 0.631, 0.603, and 0.585, respectively. D, The ROC curves for the nCBF-mTI, nCBF-sTI, nBAT, and the sum of scores in differentiating the LGG and HGG groups. The nCBF-mTI has the best performance with an AUC of 0.883, followed by the nBAT, nCBF-sTI, and the sum of scores with AUCs of 0.793, 0.781, and 0.757, respectively.

and nCBF-mTI values were combined, the diagnostic accuracy increased to 72.10%. The combination of mTI-ASL and conventional MR imaging had the best performance, with a diagnostic accuracy of 81.40%. These findings indicate that mTI-ASL is more efficient than sTI-ASL and conventional MR imaging when applied independently, and the findings also demonstrate the usefulness of the nBAT value for grading astrocytomas. Furthermore, combining the mTI-ASL with conventional MR imaging can efficiently improve diagnostic accuracy.

In previous reports, the CBF obtained by sTI-ASL could only differentiate LGGs and HGGs.<sup>24</sup> Here, we obtained similar results by using the nCBF-sTI value. Regarding mTI-ASL, recently, Cebeci et al<sup>10</sup> demonstrated the value of CBF derived from ASL with 8 TIs in discriminating LGGs and HGGs and made a comparison with DSC-MR imaging. In our study, the mTI-ASL with 16 TIs provided a more accurate CBF value, and the nCBF-mTI was confirmed to be efficient in further comparative analyses among the WHO II, III, and IV grades.

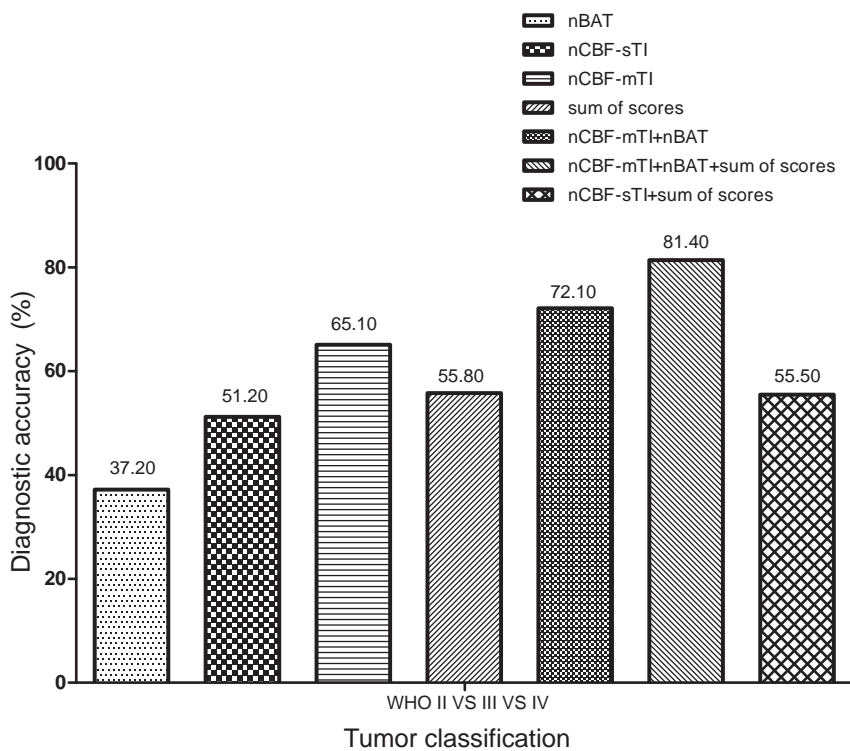


**FIG 5.** The independent and combined diagnostic accuracies (as percentages) of nCBF-mTI, nBAT, nCBF-sTI, and the sum of scores for discriminating among the WHO II, III, and IV astrocytoma grades, as calculated. All of the diagnostic accuracy values are indicated at the top of the columns.

In this study, the nCBF-mTI values were significantly higher than the nCBF-sTI values. If we assume that the absolute BAT and CBF underestimation was much less for normal white matter than it was for tumor tissue owing to the TI and that it is optimized for white matter, then in these lesion areas, the sTI-ASL CBF value might have been underestimated. This possibility may suggest that mTI-ASL has a better contrast-to-noise ratio for detecting lesions than conventional sTI-ASL. Because the estimation of CBF is highly dependent on the BAT, any acquisition with a TI/postlabeling delay that is shorter than the BAT (ie, before the labeled bolus has reached the capillary bed) will lead to an underestimation of CBF. On the other hand, acquisitions with a very long TI/postlabeling delay will also result in signal loss because of the magnetization attenuation of the labeled blood owing to T1 relaxation.<sup>25</sup> Therefore, although sTI-ASL imaging provides rapid and robust measures of CBF, abnormally long/short BATs in the lesion areas theoretically have higher risks of underestimation than in mTI-ASL. In this study, we used only one of the TIs from the mTI-ASL data for the sTI-ASL analysis; thus, the sTI-ASL analysis used only a fraction (1/16) of the data compared with the mTI-ASL analysis. This data acquisition imbalance may also explain the lower SNR and contrast-to-noise ratio for sTI-ASL in terms of lesion detection.

In this study, the ASL data were acquired with multiple TIs, and the temporal behavior of the inflowing bolus can be monitored (On-line Appendix). Buxton et al<sup>11</sup> first introduced the kinetic model for estimating the BAT of single voxels. Despite abundant literature on ASL, limited reports exist on the utility of the BAT for evaluating the temporal dynamics in astrocytomas. Re-

cently, Hales et al<sup>26</sup> applied a kind of mTI-ASL technique by using a modified “two-stage” version of the Buxton general kinetic model in 8 pediatric patients with brain tumors. However, they did not perform statistical comparisons between different tumor subtypes/grades for the CBF or BAT. Here, the nBAT effectively evaluated the temporal dynamics of astrocytomas and improved the diagnostic accuracy of mTI-ASL when combined with the normalized CBF value. The nBAT was significantly different between the WHO II and III grades. Histologically differentiating WHO III and IV astrocytomas is still a challenge, owing to their similar and mixed cytologic and histologic features. This feature may explain why the nBAT was not significantly different between the WHO grade III and IV groups. The nBAT value for the WHO grade IV group (median, 0.90) was nonsignificantly ( $P > .05$ ) higher than that for WHO grade III group (median, 0.77). This slightly higher nBAT for the WHO grade IV may have been caused by variations and random errors and accounts for the inefficient discrimination of

nBAT between WHO grades II and IV.

For the normalized CBF, we found that as the value increased, the histologic grade increased; this finding was consistent with that in previous studies.<sup>7,24</sup> However, the nBAT demonstrated the opposite tendency. The normalized CBF characteristics of tumors may be partly explained by the microcirculation and angiogenesis of neoplasms. Researchers believe that a well-recognized prominence of vasculature exists in HGGs.<sup>7,27</sup> Such characteristics may lead to high CBF in high-grade astrocytomas. The BAT represents the time it takes for the blood water to move from the tagging plane to the imaging voxel. The relationship between the BAT and tumor pathophysiology remains unclear because few reports refer to it. An ASL study of pediatric brain tumors observed high-grade tumors with hyperperfusion and a shortened BAT and low-grade tumors with hypoperfusion and a relatively prolonged BAT<sup>28</sup>; these findings were similar to our results for the nBAT. The shortening of the BAT may be due to vessel shunts, which generally appear in malignancy.

Of course, there are some drawbacks to mTI-ASL: It is more complex, requires more measurements and processing, and has a longer acquisition time. Therefore, as recently proposed by Alsop et al,<sup>29</sup> it is not recommended as the default ASL method at the present time; however, for those interested in the estimation of BAT or the most precise quantitation of CBF, Alsop et al encouraged the use of multi-TI methods.

Our study has several limitations. First, it may have been better for us to perform an independent sTI-ASL scan with 16 repetitions to obtain a more balanced dataset, similar to that obtained

for mTI-ASL. Second, the VOIs were mostly selected in solid parts of the tumors that were visible on T2-weighted images and did not include the entire tumor; this process may have introduced a selection bias owing to tumor heterogeneity. It would be more accurate to examine the tumor tissue histologically exactly in accordance with the VOIs drawn with stereotactic technology. Third, the patient population was relatively small. Finally, future studies should use more repetitions for the different TIs to allow better data fitting.

## CONCLUSIONS

The nCBF-mTI was superior to conventional MR imaging features, nCBF-sTI, and nBAT for grading WHO II, III, and IV astrocytomas independently. The nBAT reflects the temporal dynamic behavior of astrocytomas and can improve the diagnostic accuracy when combined with the nCBF-mTI. Combining the mTI-ASL with conventional MR imaging can efficiently improve the diagnostic accuracy for grading astrocytomas.

## REFERENCES

1. Surawicz TS, McCarthy BJ, Kupelian V, et al. **Descriptive epidemiology of primary brain and CNS tumors: results from the Central Brain Tumor Registry of the United States, 1990–1994.** *Neuro Oncol* 1999;1:14–25 CrossRef Medline
2. Suchorska B, Tonn JC, Jansen NL. **PET imaging for brain tumor diagnostics.** *Curr Opin Neurol* 2014;27:683–88 CrossRef Medline
3. Fudaba H, Shimomura T, Abe T, et al. **Comparison of multiple parameters obtained on 3T pulsed arterial spin-labeling, diffusion tensor imaging, and MRS and the Ki-67 labeling index in evaluating glioma grading.** *AJNR Am J Neuroradiol* 2014;35:2091–98 CrossRef Medline
4. Puttick S, Bell C, Dowson N, et al. **PET, MRI, and simultaneous PET/MRI in the development of diagnostic and therapeutic strategies for glioma.** *Drug Discov Today* 2015;20:306–17 CrossRef Medline
5. Shin JH, Lee HK, Kwun BD, et al. **Using relative cerebral blood flow and volume to evaluate the histopathologic grade of cerebral gliomas: preliminary results.** *AJR Am J Roentgenol* 2002;179:783–89 CrossRef Medline
6. Järnum H, Steffensen EG, Knutsson L, et al. **Perfusion MRI of brain tumours: a comparative study of pseudo-continuous arterial spin labeling and dynamic susceptibility contrast imaging.** *Neuroradiology* 2010;52:307–17 CrossRef Medline
7. Warmuth C, Gunther M, Zimmer C. **Quantification of blood flow in brain tumors: comparison of arterial spin labeling and dynamic susceptibility weighted contrast-enhanced MR imaging.** *Radiology* 2003;228:523–32 CrossRef Medline
8. Chen Y, Wang DJ, Detre JA. **Test-retest reliability of arterial spin labeling with common labeling strategies.** *J Magn Reson Imaging* 2011;33:940–49 CrossRef Medline
9. Wang DJ, Alger JR, Qiao JX, et al. **Multi-delay multi-parametric arterial spin-labeled perfusion MRI in acute ischemic stroke: comparison with dynamic susceptibility contrast enhanced perfusion imaging.** *Neuroimage Clin* 2013;3:1–7 CrossRef Medline
10. Cebeci H, Aydin O, Ozturk-Isik E, et al. **Assessment of perfusion in glial tumors with arterial spin labeling: comparison with dynamic susceptibility contrast method.** *Eur J Radiol* 2014;83:1914–19 CrossRef Medline
11. Buxton RB, Frank LR, Wong EC, et al. **A general kinetic model for quantitative perfusion imaging with arterial spin labeling.** *Magn Reson Med* 1998;40:383–96 CrossRef Medline
12. Martin SZ, Madai VI, von Samson-Himmelstjerna FC, et al. **3D GRASE pulsed arterial spin labeling at multiple inflow times in patients with long arterial transit times: comparison with dynamic susceptibility-weighted contrast-enhanced MRI at 3 Tesla.** *J Cereb Blood Flow Metab* 2015;35:392–401 CrossRef Medline
13. Lev MH, Ozsunar Y, Henson JW, et al. **Glial tumor grading and outcome prediction using dynamic spin-echo MR susceptibility mapping compared with conventional contrast-enhanced MR: confounding effect of elevated rCBV of oligodendrogliomas [corrected].** *AJNR Am J Neuroradiol* 2004;25:214–21 Medline
14. Louis DN, Ohgaki H, Wiestler OD, et al. **The 2007 WHO classification of tumours of the central nervous system.** *Acta Neuropathol* 2007;114:97–109 CrossRef Medline
15. Deibler AR, Pollock JM, Kraft RA, et al. **Arterial spin-labeling in routine clinical practice, part 1: technique and artifacts.** *AJNR Am J Neuroradiol* 2008;29:1228–34 CrossRef Medline
16. Günther M, Oshio K, Feinberg DA. **Single-shot 3D imaging techniques improve arterial spin labeling perfusion measurements.** *Magn Reson Med* 2005;54:491–98 CrossRef Medline
17. Kim SG. **Quantification of relative cerebral blood flow change by flow-sensitive alternating inversion recovery (FAIR) technique: application to functional mapping.** *Magn Reson Med* 1995;34:293–301 CrossRef Medline
18. Pierallini, M. Bonamini, A. Bozzao, et al. **Supratentorial diffuse astrocytic tumors: proposal of an MRI classification.** *Eur Radiol* 1997;7:395–99 CrossRef Medline
19. Riemann B, Papke K, Hoess N, et al. **Noninvasive grading of untreated gliomas: a comparative study of MR imaging and 3-(iodine 123)-L-alpha-methyltyrosine SPECT.** *Radiology* 2002;225:567–74 CrossRef Medline
20. Sahin N, Melhem ER, Wang S, et al. **Advanced MR imaging techniques in the evaluation of nonenhancing gliomas: perfusion-weighted imaging compared with proton magnetic resonance spectroscopy and tumor grade.** *Neuroradiol J* 2013;26:531–41 CrossRef Medline
21. Hirai T, Kitajima M, Nakamura H, et al. **Quantitative blood flow measurements in gliomas using arterial spin-labeling at 3T: inter-modality agreement and inter- and intraobserver reproducibility study.** *AJNR Am J Neuroradiol* 2011;32:2073–79 CrossRef Medline
22. Furtner J, Schöpf V, Schewzow K, et al. **Arterial spin-labeling assessment of normalized vascular intratumoral signal intensity as a predictor of histologic grade of astrocytic neoplasms.** *AJNR Am J Neuroradiol* 2014;35:482–89 CrossRef Medline
23. DeLong ER, DeLong DM, Clarke-Pearson DL. **Comparing the areas under two or more correlated receiver operating characteristic curves: a nonparametric approach.** *Biometrics* 1988;44:837–45 CrossRef Medline
24. Wolf RL, Wang J, Wang S, et al. **Grading of CNS neoplasms using continuous arterial spin labeled perfusion MR imaging at 3 Tesla.** *J Magn Reson Imaging* 2005;22:475–82 CrossRef Medline
25. Noguchi T, Yoshiura T, Hiwatashi A, et al. **Arterial spin-labeling magnetic resonance imaging: the timing of regional maximal perfusion-related signal intensity revealed by a multiphase technique.** *Jpn J Radiol* 2012;30:137–45 CrossRef Medline
26. Hales PW, Phipps KP, Kaur R, et al. **A two-stage model for in vivo assessment of brain tumor perfusion and abnormal vascular structure using arterial spin labeling.** *PLoS One* 2013;8:e75717 CrossRef Medline
27. Folkert RD. **Descriptive analysis and quantification of angiogenesis in human brain tumors.** *J Neurooncol* 2000;50:165–72 CrossRef Medline
28. Vidyasagar R, Abernethy L, Pizer B, et al. **Quantitative measurement of blood flow in paediatric brain tumours: a comparative study of dynamic susceptibility contrast and multi time-point arterial spin labelled MRI.** *Br J Radiol* 2016;89:20150624 CrossRef Medline
29. Alsop DC, Detre JA, Golay X, et al. **Recommended implementation of arterial spin-labeled perfusion MRI for clinical applications: a consensus of the ISMRM perfusion study group and the European consortium for ASL in dementia.** *Magn Reson Med* 2015;73:102–16 CrossRef Medline

# Correlation of Tumor Immunohistochemistry with Dynamic Contrast-Enhanced and DSC-MRI Parameters in Patients with Gliomas

T.B. Nguyen, G.O. Cron, K. Bezzina, K. Perdrizet, C.H. Torres, S. Chakraborty, J. Woulfe, G.H. Jansen, R.E. Thornhill, B. Zanette, and I.G. Cameron

## ABSTRACT

**BACKGROUND AND PURPOSE:** Tumor CBV is a prognostic and predictive marker for patients with gliomas. Tumor CBV can be measured noninvasively with different MR imaging techniques; however, it is not clear which of these techniques most closely reflects histologically-measured tumor CBV. Our aim was to investigate the correlations between dynamic contrast-enhanced and DSC-MR imaging parameters and immunohistochemistry in patients with gliomas.

**MATERIALS AND METHODS:** Forty-three patients with a new diagnosis of glioma underwent a preoperative MR imaging examination with dynamic contrast-enhanced and DSC sequences. Unnormalized and normalized cerebral blood volume was obtained from DSC MR imaging. Two sets of plasma volume and volume transfer constant maps were obtained from dynamic contrast-enhanced MR imaging. Plasma volume obtained from the phase-derived vascular input function and bookend T1 mapping ( $V_p\_Φ$ ) and volume transfer constant obtained from phase-derived vascular input function and bookend T1 mapping ( $K^{trans}\_Φ$ ) were determined. Plasma volume obtained from magnitude-derived vascular input function ( $V_p\_SI$ ) and volume transfer constant obtained from magnitude-derived vascular input function ( $K^{trans}\_SI$ ) were acquired, without T1 mapping. Using CD34 staining, we measured microvessel density and microvessel area within 3 representative areas of the resected tumor specimen. The Mann-Whitney *U* test was used to test for differences according to grade and degree of enhancement. The Spearman correlation was performed to determine the relationship between dynamic contrast-enhanced and DSC parameters and histopathologic measurements.

**RESULTS:** Microvessel area, microvessel density, dynamic contrast-enhanced, and DSC-MR imaging parameters varied according to the grade and degree of enhancement ( $P < .05$ ). A strong correlation was found between microvessel area and  $V_p\_Φ$  and between microvessel area and unnormalized blood volume ( $r_s \geq 0.61$ ). A moderate correlation was found between microvessel area and normalized blood volume, microvessel area and  $V_p\_SI$ , microvessel area and  $K^{trans}\_Φ$ , microvessel area and  $K^{trans}\_SI$ , microvessel density and  $V_p\_Φ$ , microvessel density and unnormalized blood volume, and microvessel density and normalized blood volume ( $0.44 \leq r_s \leq 0.57$ ). A weaker correlation was found between microvessel density and  $K^{trans}\_Φ$  and between microvessel density and  $K^{trans}\_SI$  ( $r_s \leq 0.41$ ).

**CONCLUSIONS:** With dynamic contrast-enhanced MR imaging, use of a phase-derived vascular input function and bookend T1 mapping improves the correlation between immunohistochemistry and plasma volume, but not between immunohistochemistry and the volume transfer constant. With DSC-MR imaging, normalization of tumor CBV could decrease the correlation with microvessel area.

**ABBREVIATIONS:** DCE = dynamic contrast-enhanced;  $K^{trans}$  = volume transfer constant; MVA = microvessel area; MVD = microvessel density;  $Φ$  = phase-derived vascular input function and bookend T1 mapping; rCBV = ratio of tumor blood volume and normal-appearing contralateral white matter blood volume (also known as relative blood volume or normalized blood volume);  $r_s$  = Spearman rank correlation coefficient; SI = magnitude-derived signal intensity; uCBV = unnormalized tumor blood volume (ie, the CBV not divided by the value in contralateral white matter); VIF = vascular input function;  $V_p$  = plasma volume

Tumor CBV has been found to be a prognostic and predictive marker for patients with gliomas.<sup>1-5</sup> Measurements of

blood volume can be obtained by using dynamic contrast-enhanced (DCE) MR imaging or dynamic susceptibility contrast MR imaging. Both techniques have their own advantages and disadvantages.

Received February 20, 2016; accepted after revision July 1.

From the Departments of Radiology (T.B.N., G.O.C., C.H.T., R.E.T., I.G.C., S.C.), Medical Physics (I.G.C.), Pathology (G.H.J., J.W.), Internal Medicine (K.P.), and Psychiatry (K.B.), The Ottawa Hospital, University of Ottawa, The Ottawa Hospital Research Institute, Ottawa, Ontario, Canada; and Department of Medical Biophysics (B.Z.), University of Toronto, Toronto, Ontario, Canada.

This work was supported by an investigator-initiated research grant from Bayer Healthcare.

Abstract previously presented at: Annual Meeting of the American Society of Neuroradiology and the Foundation of the ASNR Symposium, April 25–30, 2015; Chicago, Illinois.

Please address correspondence to Thanh Binh Nguyen, MD, Department of Radiology, The Ottawa Hospital, 1053 Carling Ave, Ottawa, ON, K1Y 4E9, Canada; e-mail: thnguyen@toh.on.ca

<http://dx.doi.org/10.3174/ajnr.A4908>

DSC-MR imaging can provide a semiquantitative measurement of cerebral blood volume, but measurement reliability depends on image acquisition and postprocessing approaches such as normalization techniques.<sup>6</sup> DCE-MR imaging requires an accurate measurement of the vascular input function (VIF) and T1 mapping for absolute quantification of the plasma volume ( $V_p$ ) and volume transfer constant ( $K^{trans}$ ).<sup>7</sup> Recently, phase-based VIFs have been used in DCE-MR imaging to circumvent the limitations of magnitude-based VIFs, such as signal saturation and inflow artifacts.<sup>8-11</sup> MR imaging signal data are complex numbers, composed of magnitude and phase. The magnitude is the strength of the signal and is affected by T1, T2, proton density, inflow, and magnetic field inhomogeneity. The phase is an angle that is proportional to the nuclear MR frequency of the signal. In routine clinical MR imaging, images are composed of just the magnitude, with the phase discarded. Contrast agents change the nuclear MR frequency (and therefore the phase) of nearby tissue via a physical, spatial effect, which depends only on the contrast agent concentration and the geometry of the nearby tissue. In blood vessels running parallel with the main magnetic field, the relationship between phase and concentration is linear and can be calculated from first principles. The magnitude part of the signal, on the other hand, saturates at a high concentration and can be severely affected by inflow. The phase, therefore, has the potential to provide more reliable measures of the arterial input function than the magnitude.

To our knowledge, correlation between DCE-MR imaging-derived parameters by using phase-derived VIFs with microvessel density (MVD) and microvessel area (MVA) from immunohistochemistry has not been investigated in patients with gliomas. The purpose of this study was to investigate the correlations among MR imaging contrast enhancement, DSC parameters, DCE parameters, and immunohistochemistry, by using both phase-derived VIFs (with T1 mapping) and magnitude-derived VIFs (without T1 mapping).

## MATERIALS AND METHODS

### Patient Population

All examinations were conducted in accordance with the guidelines of The Ottawa Hospital for human research, and written informed consent was obtained from all participating subjects. From March 1, 2011, to December 31, 2013, 70 consecutive patients presenting at The Ottawa Hospital with a newly diagnosed brain lesion compatible with a glioma were asked to participate in this study. These patients were part of a diagnostic accuracy study on DCE- and DSC-MR imaging for glioma grading, which has been published previously.<sup>11</sup> Eleven patients were excluded due to the absence of a histopathologic diagnosis or the presence of an alternate histopathologic diagnosis: no biopsy ( $n = 2$ ), inconclusive biopsy ( $n = 1$ ), metastatic disease ( $n = 2$ ), lymphomas ( $n = 2$ ), glioneuronal tumors ( $n = 2$ ), meningioma ( $n = 1$ ), and neurosarcoïdosis ( $n = 1$ ). Nine patients with gliomas were excluded for technical reasons: inadequate bolus injection of contrast ( $n = 4$ ), hemorrhage within the glioblastoma causing extensive susceptibility artifacts ( $n = 3$ ), dynamic acquisition not centered over the tumor ( $n = 1$ ), and inadequate VIF for the DCE acquisition

( $n = 1$ ). Seven more patients were excluded because of a very small biopsy specimen or unspecific background CD34 staining.

### MR Imaging Acquisition Protocols

Conventional MR imaging was performed on a 3T scanner (Magnetom Trio; Siemens, Erlangen, Germany) by using axial T1-weighted precontrast (TR = 280 ms, TE = 2.51 ms, thickness = 3 mm), axial FLAIR (TR = 9710 ms, TE = 93 ms, TI = 2580 ms, thickness = 3 mm), axial T2-weighted (TR = 6910 ms, TE = 97 ms, thickness = 3 mm), axial T1 volumetric interpolated brain examination postcontrast (TR = 8.48 ms, TE = 3.21 ms, flip angle = 12°, thickness = 1 mm), and coronal T1-weighted postcontrast (TR = 280 ms, TE = 2.51 ms, thickness = 4 mm) images.

DCE-MR imaging was performed by using a 3D FLASH sequence (TR = 6.5 ms, TE = 1.7/3.9 ms, flip angle = 30°, thickness = 5 mm, 18 sections, temporal resolution = 3.5 seconds, duration = 440 seconds). This pulse sequence generated phase images in addition to the standard magnitude images. Both before and after the dynamic scan, two 3D volumetric interpolated brain examination sequences with different flip angles (TR = 20 ms, TE = 1.22 ms, flip angle = 4° and 25°, thickness = 5 mm, 18 sections) were acquired, which enabled calculation of the T1 maps.

In patients weighing between 50 and 100 kg, a fixed preloaded dose of 0.05 mmol (equivalent to 5 mL) of Gadovist 1.0 (Bayer Schering Pharma, Berlin, Germany) was injected at 2 mL/s for DCE imaging. This also served to decrease the T1 effects before a second injection of 0.05 mmol of contrast was performed for the DSC perfusion imaging. In patients weighing <50 kg or >100 kg, we used a dose of 0.05 mmol/kg.

The second injection of contrast agent was given 10 minutes after the first injection at 4 mL/s. DSC imaging was performed by using a T2\* EPI gradient recalled-echo sequence (TR = 2380 ms, TE = 54 ms, flip angle = 90°, thickness = 5 mm, 18 sections, temporal resolution = 2.5 seconds, duration = 125 seconds). Seven baseline measurements were obtained before contrast injection.

### Postprocessing of DCE Images

Two methods were used to process the DCE images. The extended Tofts model was used in both cases.

**Phase-Derived Vascular Input Function with Bookend T1 Correction.** Voxelwise maps of tissue contrast concentration across time were calculated by using pre- and post-DCE T1 maps combined with the tissue signal-intensity-versus-time curve.<sup>12</sup> Phase analysis was used to estimate the VIF from 1 section where the superior sagittal sinus ran approximately parallel with the main magnetic field and perpendicular to the section. A small ROI (2–4 pixels) was drawn at the center of the superior sagittal sinus, and the mean phase was measured as a function of time. The phase-versus-time curve was converted to a gadolinium-versus-time curve, which was then saved in a text file. This step was performed off-line by using in-house software written in IDL (Exelis Visual Information Solutions, Boulder, Colorado) and has been described in previous articles.<sup>10,11</sup> The gadolinium-versus-time curve was imported as the VIF in a kinetic modeling-analysis software (nordicICE software, Version 2; NordicNeuroLab, Bergen,

Norway) for a voxel-by-voxel estimation of plasma volume obtained from phase-derived vascular input function and bookend T1 mapping ( $Vp\_Φ$ ) and volume transfer constant obtained from phase-derived vascular input function and bookend T1 mapping ( $K^{trans}\_Φ$ ). Postprocessing parameters were the following: noise level = 0, spatial smoothing = off, vascular deconvolution = on, normalize kinetic parameters = on, autodetect VIF-tissue delay = on, hematocrit correction factor = 0.45.

**Magnitude-Derived Vascular Input Function with No T1 Correction.** DCE magnitude images were processed directly in NordicICE to generate maps of plasma volume obtained from magnitude-derived vascular input function ( $Vp\_SI$ ) and volume transfer constant obtained from magnitude-derived vascular input function ( $K^{trans}\_SI$ ). The signal intensity (SI) was converted to percentage relative change in signal intensity ( $relSI$ ) by using the expression:  $relSI(t) = 100 \times (S(t) - S_o)/S_o$ , where  $S$  is the SI at time  $t$  and  $S_o$  is the baseline SI. The  $relSI$  was assumed to be linearly related to concentration. The VIF was selected from a small ROI placed in the superior sagittal sinus directly from the DCE images. Signal conversion was set as SI to  $relSI(\%)$ . Other postprocessing parameters were similar to the analysis with phase-derived vascular input function and bookend T1 correction.

#### **Postprocessing of DSC Images**

DSC images were processed by using singular value decomposition and deconvolution as implemented in NordicICE. MR imaging signal intensity was converted to a T2 relaxation rate. An automated algorithm selected the most suitable pixels for VIF in a manually defined ROI covering the middle cerebral artery contralateral to the tumor. The SI was converted to relative change in R2 (ie,  $R2^* = 1/T2^*$ ) by using the standard expression:  $\Delta R2^*(t) = -\ln[S(t)/S_o]/TE$ , where  $S$  is the SI at time  $t$ ,  $S_o$  is the baseline SI, and TE is the echo time. Corrected CBV maps were generated. Correction for leakage in the CBV calculations was done by using preinjection of contrast agent and linear fitting to estimate the T1 contamination caused by extravasation of contrast agent.<sup>13</sup> Postprocessing parameters in NordicICE were the following: noise level = 0, no spatial smoothing, no temporal smoothing, signal conversion to  $\Delta R2^*$ , vascular deconvolution = on, apply contrast agent leakage correction = checked, detect both T1 and T2 leakage values = checked.

#### **Image Interpretation**

Two neuroradiologists (10 years of experience for C.H.T. and 12 years for S.C.) blinded to the histopathology determined the degree of tumoral contrast enhancement relative to the choroid plexus (none; mild [less than the choroid plexus]; moderate [equal to choroid plexus]; and marked [more than choroid plexus]). Axial T1-weighted postcontrast images were coregistered to the parametric maps. Because areas of highest values could vary between different parametric maps, a medical student traced 2 sets of ROIs: 1) 1 large "large-tumor" ROI over the solid component of the tumor for the section where the tumor was largest (identical ROI for all maps), and 2) 4 small "hot spot" ROIs (35 mm<sup>2</sup>) over the areas of highest values, which could vary in location between maps. For each parametric map, the mean pixel value inside each of the 5 ROIs was calculated. For the 4 small hot

spot ROIs, the 3 ROIs with the smallest values were discarded. Thus, for each parametric map, we recorded 2 values: 1 large-tumor value and 1 hot spot value. All ROIs were verified by a neuroradiologist to ensure that inadvertent placement on an adjacent vessel or hemorrhage was avoided. For DSC images, 2 sets of corrected CBV values were recorded for each patient: the unnormalized value (uCBV) and the value normalized to the contralateral white matter (rCBV).

#### **Histopathologic Analysis**

Following surgical resection or biopsy, histopathologic diagnosis was provided by neuropathologists (17 years of experience for J.W. and 21 years for G.H.J.) by using the 2007 World Health Organization classification. For each patient, a representative slide of the resected tumor tissue was selected by a neuropathologist (J.W.). Formalin-fixed, paraffin-embedded 4- $\mu$ m-thick sections of representative tumor were stained immunohistochemically by using an antibody to the endothelial marker CD34 (CD34, monoclonal clone QBEND/10, catalog number PA0212, "ready-to use" antibody; Leica Biosystems; <http://www.leicabiosystems.com>), following antigen retrieval with citrate buffer pH 6.0 for 20 minutes. Detection of bound antibody was achieved by using the automated bond platform from Leica Biosystems. Whole-section slide digitalization was performed at  $\times 20$  by using a MiraxMidi microscope (Carl Zeiss; [http://www.zeiss.com/corporate/en\\_de/home.html](http://www.zeiss.com/corporate/en_de/home.html)). On visual inspection, 3 fields (0.5–2.5 mm<sup>2</sup>) that appeared to have the darkest stain within the tumor were captured by using the software Panoramic Viewer 1.15 (3DHitech; [http://www.3dhitech.com/panoramic\\_viewer](http://www.3dhitech.com/panoramic_viewer)). Images were imported into a computer-assisted image-analysis software for calculation of the MVD (number of vessels/mm<sup>2</sup>) and MVA (vessel area/total field area) (Zen Blue 1.0; Carl Zeiss). For each patient, the highest MVD and MVA among the 3 fields were reported.

#### **Statistical Analysis**

Interobserver agreement on the degree of contrast enhancement was measured by using a  $\kappa$  statistic. Comparisons of immunohistochemical and DSC-/DCE-derived parameters according to the degree of contrast enhancement and tumor grade were performed by using the Kruskal-Wallis test and Mann-Whitney  $U$  test. Correlation analysis between DSC- and DCE-derived parameters with MVD and MVA was performed by using a Spearman rank correlation coefficient ( $r_s$ ). All data were analyzed by using MedCalc (Version 12; MedCalc Software, Ostend, Belgium).

## **RESULTS**

Forty-three patients with a new diagnosis of a glioma were included in this study. There were 10 patients with grade II gliomas (9 astrocytomas, 1 oligodendroglioma), 11 patients with grade III gliomas (6 astrocytomas, 4 oligoastrocytomas, 1 oligodendroglioma), and 22 patients with a glioblastoma (grade IV). Twenty-eight of these 43 patients were started on steroid therapy before their MR imaging examination. The mean age was 54 years (95% CI, 49.3–58.7 years). There were 21 men and 22 women.

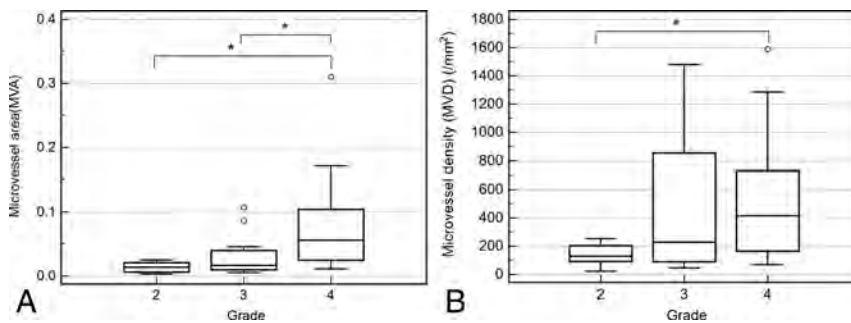


**FIGURE.** Box-and-whisker plots of microvessel area according to histopathologic grade (A) and microvessel density according to histopathologic grade (B). The asterisk indicates  $P < .05$ .

**Table 1: Median values of MVA, MVD, and DCE- and DSC-MRI parameters with interquartile range for low and high-grade gliomas<sup>a</sup>**

	Low-Grade (n = 10)	High-Grade (n = 33)	P Value
MVA (%)	1.4 (0.66–2.09)	3.2 (1.82–9.38)	.002
MVD (mm <sup>2</sup> )	129 (93–202)	376 (157–768)	.006
Large-tumor Vp_Φ (%)	0.098 (0.01–0.58)	1.45 (0.71–2.21)	.001
Large-tumor Vp_SI (%)	0.69 (0.27–2.20)	3.12 (1.37–6.72)	.04
Large-tumor uCBV (a.u.)	35.8 (16.9–62.8)	80.8 (57.3–152.5)	.01
Large-tumor rCBV	2.9 (1.53–4.19)	5.43 (3.19–8.21)	.02
Large-tumor K <sup>trans</sup> _Φ (min <sup>-1</sup> )	0.00016 (0.00001–0.00225)	0.019 (0.011–0.041)	.002
Large-tumor K <sup>trans</sup> _SI (min <sup>-1</sup> )	0.0012 (0.0004–0.0137)	0.05 (0.0118–0.0773)	.004
Hot spot Vp_Φ (%)	0.46 (0.02–1.04)	2.93 (1.85–4.42)	.0004
Hot spot Vp_SI (%)	1.84 (1.13–3.39)	8.51 (4.14–13.80)	.015
Hot spot uCBV (a.u.)	40.2 (16.8–181.3)	163 (142–274)	.002
Hot spot rCBV	2.85 (1.75–7.45)	11.6 (6.48–18.50)	.008
Hot spot K <sup>trans</sup> _Φ (min <sup>-1</sup> )	0.00054 (0.00017–0.01341)	0.047 (0.023–0.091)	.0006
Hot spot K <sup>trans</sup> _SI (min <sup>-1</sup> )	0.016 (0.002–0.067)	0.095 (0.044–0.162)	.02

**Note:**—a.u. indicates arbitrary units.

<sup>a</sup> Interquartile ranges are in parentheses.

**Table 2: Diagnostic accuracy of imaging and histopathologic parameters in differentiating grade III and IV astrocytomas using hot spot ROIs**

Parameters	AUC	95% CI	Cutoff Value	Sensitivity (%)	Specificity (%)
MVA	0.78	0.60–0.90	<2.32	77	73
MVD	0.62	0.44–0.78	<103	95	36
Hot spot Vp_Φ	0.81	0.64–0.92	<1.88	91	73
Hot spot Vp_SI	0.66	0.47–0.81	<4.2	91	64
Hot spot uCBV	0.80	0.63–0.92	<141	86	73
Hot spot rCBV	0.70	0.51–0.85	<9.88	68	73
Hot spot K <sup>trans</sup> _Φ	0.78	0.60–0.90	<0.024	86	64
Hot spot K <sup>trans</sup> _SI	0.72	0.53–0.86	<0.056	82	64
Combined Vp_Φ + K <sup>trans</sup> _Φ + MVA + uCBV	0.85	0.68–0.95	<0.67	77	82

**Note:**—AUC indicates area under the curve.

### Immunohistologic and Kinetic Parameters According to Tumor Grade

For all gliomas, there was a positive correlation between MVA and MVD ( $r_s = 0.74$ ; 95% CI, 0.57–0.85). For high-grade gliomas only, a similar positive correlation between MVA and MVD was found ( $r_s = 0.73$ ; 95% CI, 0.52–0.86). Histopathologic grade was a factor influencing MVA and MVD according to the Kruskal-Wallis test of independent samples ( $P < .05$ , Figure). Post hoc pair-wise comparisons according to the Mann-Whitney  $U$  test showed that median values of MVA for grades II and III were statistically lower than those for grade IV ( $P < .05$ ). Median MVA values were not statistically different between grades II and III ( $P = .21$ ). Median MVD values were statistically lower for grade II compared with grade IV ( $P = .02$ ) but were not statistically different between grades II

and III and between grades III and IV ( $P > .05$ ). MVA, MVD, DSC, and DCE parameters were significantly lower in low-grade-versus-high-grade gliomas (Table 1).

For differentiation between grade III and IV gliomas, there was a similar diagnostic accuracy between MVA (area under the curve = 0.78; 95% CI, 0.60–0.90), hot spot Vp\_Φ (area under the curve = 0.81; 95% CI, 0.64–0.92), hot spot K<sup>trans</sup>\_Φ (area under the curve = 0.78; 95% CI, 0.60–0.90) and hot spot uCBV (area under the curve = 0.80; 95% CI, 0.63–0.92; Table 2). Combining those 4 parameters slightly improved the diagnostic accuracy (area under the curve = 0.85; 95% CI, 0.68–0.95).

### MVA and MVD According to Tumor Enhancement

On postcontrast T1 images, there was excellent agreement between both radiologists in the assessment of gliomas that demonstrated no or mild enhancement versus those that demonstrated moderate or marked enhancement ( $\kappa = 0.95$ ; 95% CI, 0.86–1). There was only 1 disagreement, which was settled by a third neuro-radiologist. Among the 16 gliomas that had no or mild enhancement, 8 were low-grade, 7 were grade III, and 1 was grade IV. Among the 27 gliomas that demonstrated moderate or marked enhancement, there were 2 low-grade, 4 anaplastic grade III, and 21 grade IV gliomas. MVA and MVD were significantly higher in enhancing-versus-nonenhancing tumors or poorly enhancing tumors (Table 3).

### Relationship between MVA and DSC- or DCE-Derived Parameters

The strongest correlation was found between MVA and large-tumor Vp\_Φ ( $r_s = 0.74$ ; 95% CI, 0.57–0.85;  $P < .0001$ ;

Table 4). The second strongest correlation was between MVA and hot spot Vp\_Φ ( $r_s = 0.69$ ; 95% CI, 0.49–0.82;  $P < .0001$ ; Table 4). The correlation between MVA and hot spot uCBV ( $r_s = 0.68$ ; 95% CI, 0.48–0.82;  $P < .0001$ ) was stronger than that between MVA and hot spot rCBV ( $r_s = 0.55$ ; 95% CI, 0.30–0.73;  $P = .0001$ ). The correlation between MVA and large-tumor uCBV ( $r_s = 0.61$ ; 95% CI, 0.37–0.77;  $P < .0001$ ) was also stronger than that between MVA and large-tumor rCBV ( $r_s = 0.50$ ; 95% CI, 0.23–0.69;  $P = .0007$ ).

MVA correlated moderately with hot spot and large-tumor Vp\_SI ( $r_s = 0.44$ ; 95% CI, 0.16–0.65; and  $r_s = 0.52$ ; 95% CI, 0.26–0.71, respectively;  $P < .05$ ). MVA correlated moderately with hot spot and large-tumor K<sup>trans</sup> values from both acquisition techniques ( $r_s$  between 0.54 and 0.57;  $P \leq .0002$ ).

**Table 3: Median values for MVA and MVD with interquartile ranges for nonenhancing/poorly enhancing gliomas and moderately/strongly enhancing gliomas<sup>a</sup>**

Tumor Enhancement	MVA	MVD
None/poor ( <i>n</i> = 16)	1.4% (0.68%–2.16%)	187 mm <sup>2</sup> (92–255 mm <sup>2</sup> )
Moderate/strong ( <i>n</i> = 27)	4.9% (2.08%–10.19%)	408 mm <sup>2</sup> (156–842 mm <sup>2</sup> )
<i>P</i> value	.0002	.04

<sup>a</sup> Interquartile ranges are in parentheses.

**Table 4: Correlations (*r<sub>s</sub>*) among MVA, MVD, and DCE- and DSC-MRI parameters**

Parameter	MVA (95% CI)	<i>P</i> Value	MVD (95% CI)	<i>P</i> Value
Large-tumor Vp_Φ	0.74 (0.57–0.85)	<.0001	0.52 (0.26–0.71)	.0003
Large-tumor Vp_SI	0.52 (0.26–0.71)	.0003	0.29 (–0.14–0.54)	.06
Large-tumor uCBV	0.61 (0.37–0.77)	<.0001	0.42 (0.14–0.64)	.005
Large-tumor rCBV	0.50 (0.23–0.69)	.0007	0.45 (0.18–0.66)	.002
Large-tumor K <sup>trans</sup> _Φ	0.57 (0.33–0.75)	.0001	0.36 (0.07–0.60)	.02
Large-tumor K <sup>trans</sup> _SI	0.56 (0.32–0.74)	.0001	0.41 (0.13–0.63)	.006
Hot spot Vp_Φ	0.69 (0.49–0.82)	<.0001	0.46 (0.18–0.66)	.002
Hot spot Vp_SI	0.44 (0.16–0.65)	.033	0.20 (–0.11–0.47)	.2
Hot spot uCBV	0.68 (0.48–0.82)	<.0001	0.48 (0.21–0.68)	.001
Hot spot rCBV	0.55 (0.30–0.73)	.0001	0.47 (0.20–0.68)	.002
Hot spot K <sup>trans</sup> _Φ	0.56 (0.31–0.74)	.0001	0.37 (0.073–0.60)	.02
Hot spot K <sup>trans</sup> _SI	0.54 (0.29–0.73)	.0002	0.32 (0.024–0.57)	.04

### Relationship between MVD and DSC- or DCE-Derived Parameters

There was a moderate correlation between MVD and large-tumor Vp\_Φ ( $r_s = 0.52$ ; 95% CI, 0.26–0.71;  $P = .0003$ ; Table 4). MVD correlated moderately with normalized and unnormalized CBV for both hot spot and large-tumor ROIs ( $r_s$  between 0.42 and 0.48,  $P < .05$ ). MVD correlated weakly with hot spot and large-tumor K<sup>trans</sup> values ( $r_s$  between 0.32 and 0.41). No correlation was found between MVD and Vp\_SI values ( $P > .05$ ).

### DISCUSSION

Quantification of angiogenesis by using vessel counting or vessel area has been found to be important for prognostication of patients with gliomas.<sup>14,15</sup> DSC- and DCE-MR imaging–derived tumor blood volume has been reported to be a prognostic and predictive marker for patients with gliomas.<sup>1–5</sup> Maps of blood volume or vascular permeability can also be generated across the whole tumor, allowing the neurosurgeon to determine preoperatively the most appropriate target for biopsy and/or resection. Validation of MR imaging–derived blood volume with microvessel area and density from immunohistochemistry is important because absolute CBV measurement is more difficult with MR imaging compared with CT. The relationship between MR imaging signal intensity and contrast concentration is not always linear. Multiple acquisition and postprocessing techniques can influence DCE- and DSC-derived tumor blood volume measurements.<sup>5,6,13</sup> For DSC-MR imaging, gradient-echo sequences are sensitive to vessels of all sizes, whereas spin-echo sequences are mainly sensitive to capillaries. Gradient-echo DSC-MR imaging can have large-vessel contamination. We tried to avoid this latter problem by drawing ROIs that avoided large vessels. For DCE-MR imaging, measurements of the VIF from magnitude images can have large systematic errors, which could lead to the underestimation of the contrast medium concentration. Phase images can provide a more accurate quantification of the VIF because the relationship between phase and contrast concentration remains linear, even at high concentrations.

Using both DCE- and DSC-MR imaging, we have shown that high-grade gliomas have higher cerebral blood volume, plasma volume, and K<sup>trans</sup> compared with low-grade gliomas. This radiologic finding was confirmed by immunohistochemistry, which showed a higher microvessel density and microvessel area in high-grade gliomas versus low-grade gliomas. We also found that MVA correlated more with MR imaging–derived blood volume than MVD. Prior studies have shown a positive correlation between MVD and CBV obtained from perfusion CT or DCE-MR imaging in patients with gliomas.<sup>16–19</sup> In patients with recurrent high-grade gliomas, Hu et al<sup>20</sup> found that rCBV correlated strongly with MVA but weakly with MVD, in agreement with our study. Because high-

grade gliomas in humans can display very heterogeneous vessels in terms of size, MVA has been found to be a better marker for angiogenesis than MVD because it encompasses both the number and size of microvessels.<sup>14,20</sup>

For DCE-MR imaging, a stronger correlation was found between MVA and Vp with a more quantitative approach with phase-derived VIF and pre- and postcontrast T1 mapping, compared with a simpler approach with magnitude-derived VIF without T1 mapping. The measurement of the VIF from magnitude images can be challenging due to numerous problems such as signal saturation at high contrast concentration and inflow effects. The use of phase rather than the magnitude signal can circumvent those artifacts and provide a more robust measurement of the VIF. The T1 mapping enables voxelwise determination of contrast agent concentration-versus-time in tumor tissue, which should improve the accuracy and standardization.<sup>12</sup> A moderate correlation was found between K<sup>trans</sup> and MVA, regardless of the postprocessing techniques. This suggests that though K<sup>trans</sup> is a more indirect marker of angiogenesis than Vp, it might be less influenced by differences in postprocessing techniques. In rats bearing C6 xenografts, with a magnitude-derived VIF, Ng et al<sup>21</sup> found that between-rat variance of K<sup>trans</sup> measurements was lower than that for Vp. Jia et al<sup>18</sup> found a strong correlation between K<sup>trans</sup> and CD105 MVD.

For DSC-MR imaging, the correlation between MVA and CBV was slightly weaker than that between MVA and DCE-derived Vp\_Φ. The MVA-versus-CBV correlation was lower when CBV was normalized. For clinical applications, normalization of the CBV values against the contralateral white matter CBV has been recommended to obtain a relative CBV because for absolute quantification, the scaling factor converting signal intensity to contrast agent concentration is not known.<sup>22,23</sup> Normalization of CBV has been demonstrated to increase the repeatability of measurements, while arterial input function deconvolution may decrease it.<sup>6</sup> However, normalization also introduces noise in the measurements. An average coefficient of variation of 18% was

found for rCBV measurements of the normal-appearing white matter in 10 patients.<sup>24</sup> Some authors suggest using a median value of 3.2% for the normal-appearing white matter.<sup>25</sup> In our study, manual placement of the ROI in the contralateral white matter could have introduced an additional bias because the exact position might differ among patients. Hu et al<sup>20</sup> found excellent correlation between normalized CBV and MVA in recurrent gliomas. Their study differed from ours because they performed integration of the first-pass  $\Delta R2^*$  curve to obtain CBV (without deconvolution). Hu et al also performed coregistration of rCBV measurements with stereotactic biopsy locations.

The main limitation of this study is the lack of coregistration between the ROI location on the parametric maps and the biopsy/resection tumor site from which the immunohistologic parameters were derived. In glioblastomas with heterogeneous enhancement, the lack of coregistration could lead to a poor correlation between MR imaging parameters and histology. Another source of sampling bias is the selection of fields for vessel quantification because only 3 small fields in the whole tumor specimen were selected for each patient. Use of CD105 might be a superior immunohistochemical marker for angiogenesis compared with CD34.<sup>26</sup> CD34 is prone to background staining and is a marker of endothelial cells for both immature and normal vessels. Finally, we performed multiple statistical comparisons without performing a Bonferroni correction. This could have led to a type I error (finding a difference that does not exist).

## CONCLUSIONS

With DCE-MR imaging, use of a phase-derived VIF and bookend T1 mapping improves the correlation between immunohistochemistry and  $V_p$  (but not  $K^{trans}$ ). With DSC-MR imaging, normalization of CBV could decrease correlation with the microvessel area.

Disclosures: Thanh Binh Nguyen—RELATED: Grant: Bayer Healthcare,\* Comments: I received an investigator-initiated research grant; Consulting Fee or Honorarium: Bayer Healthcare, Comments: I have received consulting fees for my work with a perfusion expert panel; Support for Travel to Meetings for the Study or Other Purposes: Bayer Healthcare, Comments: I have received travel support from Bayer to cover hotel expenses to attend the perfusion imaging expert panel workshop; UNRELATED: Consultancy: Bayer Healthcare, Comments: I have acted as a consultant on a perfusion imaging panel; Payment for Development of Educational Presentations: Bayer Healthcare, Comments: I have participated in the development of a perfusion imaging syllabus. Kirstin Perdrizet—RELATED: Grant: Mach-Gaensslen Student Research Award,\* Comments: This award was paid to my institution (University of Ottawa) for my studentship. John Woulfe—UNRELATED: Grants/Grants Pending: Physicians Services Incorporated Foundation,\* Comments: For Parkinson disease research. \*Money paid to the institution.

## REFERENCES

- Law M, Young RJ, Babb JS, et al. Gliomas: predicting time to progression or survival with cerebral blood volume measurements at dynamic susceptibility weighted contrast-enhanced perfusion MR imaging. *Radiology* 2008;247:490–98 CrossRef Medline
- Hipp SJ, Steffen-Smith E, Hammoud D, et al. Predicting outcome of children with diffuse intrinsic pontine gliomas using multiparametric imaging. *Neuro Oncol* 2011;13:904–09 CrossRef Medline
- Hirai T, Murakami R, Nakamura H, et al. Prognostic value of perfusion MR imaging of high-grade astrocytomas: long-term follow-up study. *AJNR Am J Neuroradiol* 2008;29:1505–10 CrossRef Medline
- Mangla R, Singh G, Ziegelitz D, et al. Changes in relative cerebral blood volume 1 month after radiation-temozolomide therapy can help predict overall survival in patients with glioblastoma. *Radiology* 2010;256:575–84 CrossRef Medline
- Nguyen TB, Cron GO, Mercier JF, et al. Preoperative prognostic value of dynamic contrast-enhanced MRI-derived contrast transfer coefficient and plasma volume in patients with cerebral gliomas. *AJNR Am J Neuroradiol* 2015;36:63–69 CrossRef Medline
- Jafari-Khouzani K, Emblem KE, Kalpathy-Cramer J, et al. Repeatability of cerebral perfusion using dynamic susceptibility contrast MRI in glioblastoma patients. *Transl Oncol* 2015;8:137–46 CrossRef Medline
- Khalifa F, Soliman A, El-Baz A, et al. Models and methods for analyzing DCE-MRI: a review. *Med Phys* 2014;41:124301 CrossRef Medline
- van Osch MJ, Vonken EJ, Viergever MA, et al. Measuring the arterial input function with gradient echo sequences. *Magn Reson Med* 2003;49:1067–76 CrossRef Medline
- Korporaal JG, van den Berg CA, van Osch MJ, et al. Phase-based arterial input function measurements in the femoral arteries for quantification of dynamic contrast-enhanced (DCE) MRI and comparison with DCE-CT. *Magn Reson Med* 2011;66:1267–74 CrossRef Medline
- Footitt C, Cron GO, Hogan MJ, et al. Determination of the venous output function from MR signal phase: feasibility for quantitative DCE-MRI in human brain. *Magn Reson Med* 2010;63:772–81 CrossRef Medline
- Nguyen TB, Cron GO, Perdrizet K, et al. Comparison of the diagnostic accuracy of DSC- and dynamic contrast-enhanced MRI in the preoperative grading of astrocytomas. *AJNR Am J Neuroradiol* 2015;36:2017–22 CrossRef Medline
- Cron GO, Kelcz F, Santyr GE. Improvement in breast lesion characterization with dynamic contrast-enhanced MRI using pharmacokinetic modeling and bookend T(1) measurements. *Magn Reson Med* 2004;51:1066–70 CrossRef Medline
- Boxerman JL, Schmainda KM, Weisskoff RM. Relative cerebral blood volume maps corrected for contrast agent extravasation significantly correlate with glioma tumor grade, whereas uncorrected maps do not. *AJNR Am J Neuroradiol* 2006;27:859–67 Medline
- Korkolopoulou P, Patsouris E, Kavantzaz N, et al. Prognostic implications of microvessel morphometry in diffuse astrocytic neoplasms. *Neuropathol Appl Neurobiol* 2002;28:57–66 CrossRef Medline
- Wesseling P, van der Laak JA, Link M, et al. Quantitative analysis of microvascular changes in diffuse astrocytic neoplasms with increasing grade of malignancy. *Hum Pathol* 1998;29:352–58 CrossRef Medline
- Jain R, Gutierrez J, Narang J, et al. In vivo correlation of tumor blood volume and permeability with histologic and molecular angiogenic markers in gliomas. *AJNR Am J Neuroradiol* 2011;32:388–94 CrossRef Medline
- Haris H, Husain N, Singh A, et al. Dynamic contrast-enhanced derived cerebral blood volume correlates better with leak correction than with no correction for vascular endothelial growth factor, microvascular density, and grading of astrocytoma. *J Comput Assist Tomogr* 2008;32:955–65 CrossRef Medline
- Jia ZZ, Gu HM, Zhou XJ, et al. The assessment of immature microvascular density in brain gliomas with dynamic contrast-enhanced magnetic resonance imaging. *Eur J Radiol* 2015;84:1805–09 CrossRef Medline
- Sadeghi N, D'Haene N, Decaestecker C, et al. Apparent diffusion coefficient and cerebral blood volume in brain gliomas: relation to tumor cell density and tumor microvessel density based on stereotactic biopsies. *AJNR Am J Neuroradiol* 2008;29:476–82 CrossRef Medline
- Hu LS, Eschbacher JM, Dueck AC, et al. Correlations between perfusion MR imaging cerebral blood volume, microvessel quantification, and clinical outcome using stereotactic analysis in recurrent high-grade glioma. *AJNR Am J Neuroradiol* 2012;33:69–76 CrossRef Medline

21. Ng CS, Wei W, Bankson JA, et al. **Dependence of DCE-MRI biomarker values on analysis algorithm.** *PLoS One* 2015;10:e0130168 CrossRef Medline
22. Shiroishi M, Castellazzi G, Boxerman JL, et al. **Principles of T2\*-weighted dynamic susceptibility contrast MRI technique in brain tumor imaging.** *J Magn Reson Imaging* 2015;41:296–313 CrossRef Medline
23. Willats L, Calamante F. **The 39 steps: evading error and deciphering the secrets for accurate dynamic susceptibility contrast MRI.** *NMR Biomed* 2013;26:913–31 CrossRef Medline
24. Wetzel SG, Cha S, Johnson G, et al. **Relative cerebral blood volume measurements in intracranial mass lesions: interobserver and intraobserver reproducibility study.** *Radiology* 2002;224:797–803 CrossRef Medline
25. Kellner E, Breyer T, Gall P, et al. **MR evaluation of vessel size imaging of human gliomas: validation by histopathology.** *J Magn Reson Imaging* 2015;42:1117–25 CrossRef Medline
26. Nico B, Benagiano V, Mangieri D, et al. **Evaluation of microvascular density in tumors: pro and contra.** *Histol Histopathol* 2008;23:601–07 Medline

# Preradiotherapy MR Imaging: A Prospective Pilot Study of the Usefulness of Performing an MR Examination Shortly before Radiation Therapy in Patients with Glioblastoma

C. Majós, M. Cos, S. Castañer, A. Pons, M. Gil, A. Fernández-Coello, M. Macià, J. Bruna, and C. Aguilera



## ABSTRACT

**BACKGROUND AND PURPOSE:** Current protocols in patients with glioblastoma include performing an MR examination shortly after surgery and then 2–6 weeks after ending concomitant chemoradiotherapy. The assessment of this first postradiotherapy examination is challenging because the pseudoprogression phenomenon may appear. The aim of this study was to explore if performing an MR examination shortly before radiation therapy (preradiotherapy MR imaging) could improve the radiologic assessment of patients with glioblastoma.

**MATERIALS AND METHODS:** A preradiotherapy MR imaging examination was prospectively performed before the start of radiation therapy in 28 consecutive patients with glioblastoma who had undergone surgical resection. Tumor response to chemoradiotherapy was assessed twice: with the early postoperative MR examination as baseline and with the preradiotherapy MR imaging examination as baseline. In addition, tumor growth in the preradiotherapy MR imaging examination was evaluated, and its correlation with patient survival was assessed with Kaplan-Meier analysis and Cox regression.

**RESULTS:** Tumor progression after radiation therapy was found in 16 patients, corresponding to pseudoprogression in 7 of them (44%). Four assessments of pseudoprogression switched to partial response or stable disease when preradiotherapy MR imaging was the baseline examination, and the ratio of pseudoprogression was reduced to 25% (3 of 12). Significant differences in survival were found when patients were stratified according to the pattern of tumor growth on preradiotherapy MR imaging (median overall survival “no-growth,” 837 days; “focal-growth,” 582 days; “global-growth,” 344 days;  $P = .001$ ).

**CONCLUSIONS:** Performing a preradiotherapy MR imaging examination may improve the clinical management of patients with glioblastoma by reducing the ratio of pseudoprogression assessments and providing prognostic information.

**ABBREVIATIONS:** EPMP = early postoperative MR imaging; PRMR = preradiotherapy MR imaging

**G**lioblastoma is the most common and aggressive type of glioma.<sup>1</sup> The current standard of care for patients newly diagnosed with glioblastoma involves maximum safe surgical resec-

tion followed by radiation therapy plus concomitant and adjuvant temozolamide.<sup>2,3</sup> MR imaging plays a pivotal role in the follow-up of brain glioblastomas after treatment. Guidelines suggest performing an MR examination early after surgery to evaluate the extent of surgical resection, another examination 2–6 weeks after completion of concomitant treatment with radiation therapy and temozolamide to evaluate response, and then every 2–4 months for follow-up.<sup>4,5</sup> The examination performed 2–6 weeks after completion of radiation therapy represents a major challenge for multidisciplinary neuro-oncology units. This is because the pseudoprogression phenomenon may appear in this timeframe. It is well known that approximately half of the patients who show progressive disease on an MR examination performed up to 3 months after concomitant temozolamide–radiation therapy improve or stabilize on subsequent assessments without any change in therapy. This phenomenon is termed pseudoprogression.<sup>6</sup> Therefore, 2 possibilities should be taken into account when an enhancing-lesion enlargement is found in the first postradiation

Received April 15, 2016; accepted after revision July 1.

From the Departments of Radiology, Institut de Diagnòstic per la Imatge (C.M., M.C., S.C., A.P., C.A.), Medical Oncology, Institut Català d'Oncologia L'Hospitalet (M.G.), Neurosurgery (A.F.-C.), Radiotherapy Oncology, Institut Català d'Oncologia L'Hospitalet (M.M.), and Neurology (J.B.), Hospital Universitari de Bellvitge, L'Hospitalet de Llobregat, Spain; Centro de Investigación Red en Bioingeniería, Biomateriales y Nanomedicina (C.M., C.A.), Cerdanyola del Vallès, Spain; and Institut d'Investigació Biomèdica de Bellvitge, IDIBELL (J.B.), L'Hospitalet de Llobregat, Spain.

This work was supported in part by a grant from the Grupo Español de Investigación en Neurooncología (GEINO) and by the Centro de Investigación Red en Bioingeniería, Biomateriales y Nanomedicina (CIBER-BBN), which is an initiative of the VI National R&D&I Plan 2008–2011, CIBER Actions and financed by the Instituto de Salud Carlos III with assistance from the European Regional Development Fund.

Please address correspondence to Carles Majós, MD, Institut de Diagnòstic per la Imatge, Hospital Duran i Reynals, Gran Via de l'Hospitalet 199, 08908 L'Hospitalet de Llobregat, Barcelona, Spain; e-mail: cmajos@bellvitgehospital.cat

Indicates open access to non-subscribers at [www.ajnr.org](http://www.ajnr.org)

<http://dx.doi.org/10.3174/ajnr.A4917>

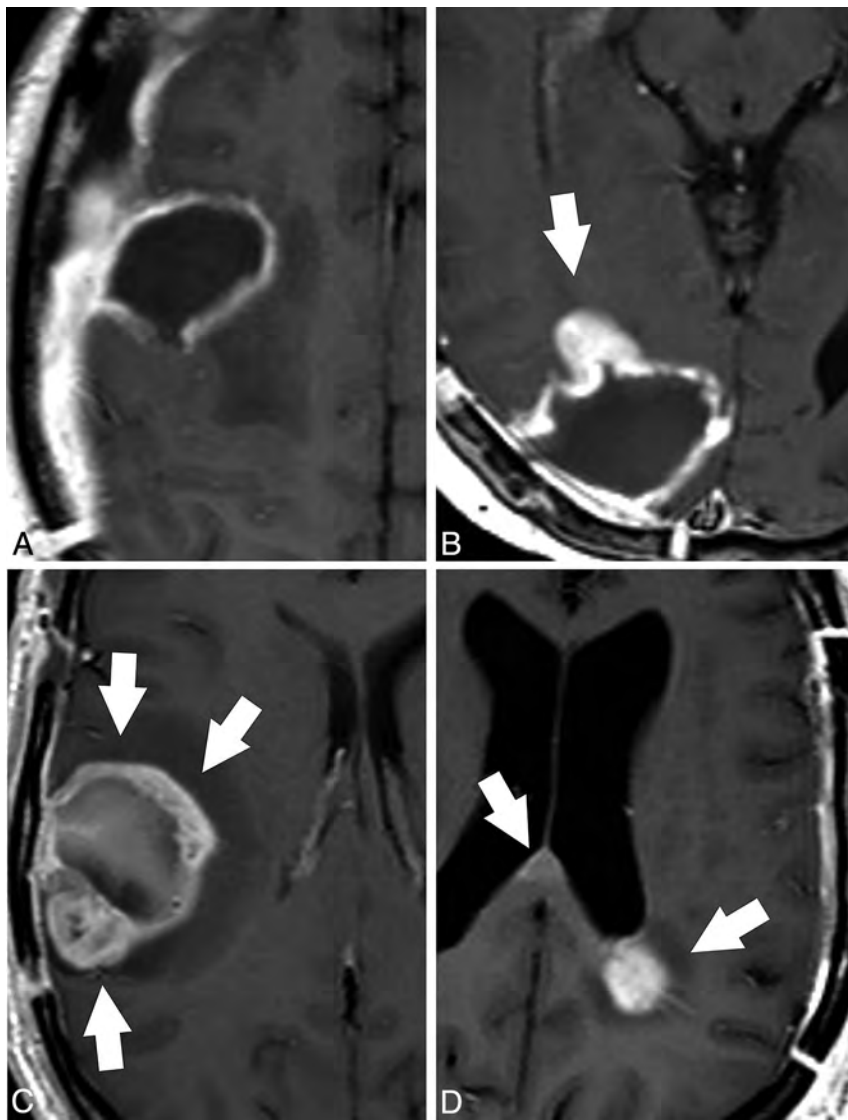


**FIG 1.** Patterns of tumor growth in the PRMR examination in patients with glioblastoma. Axial contrast-enhanced T1-weighted images. *A*, No growth. The MR examination shows a thin homogeneous enhancement in the wall of the surgical cavity that is considered normal evolution after surgery. *B*, Focal growth. A focal-enhancing nodule is found at the anterior margin of the surgical cavity in this study (arrow). *C*, Global growth. Thick irregular enhancement in the margins of the surgical cavity involving more than half of the surgical cavity (arrows). Note the presence of some hyperintense postsurgical material in the surgical cavity. *D*, Distant growth. Focal contrast enhancement is found in the juxtaventricular parietal lobe and in the splenium of the corpus callosum (arrows), distant to the surgical cavity (not shown), after resection of a left temporal lobe glioblastoma.

MR examination: true progression and pseudoprogression. Differentiation between the 2 entities has important clinical consequences. Patients with pseudoprogression will benefit from following adjuvant treatment with temozolamide, whereas an alternative treatment should be started as soon as possible in patients with true progression. Unfortunately, it is not currently possible to confidently discriminate between the 2 entities with MR imaging in this situation.<sup>7</sup>

Pseudoprogression has been related to vasodilation and disruption of the BBB caused by radiation toxicity, tumor necrosis caused by treatment effectiveness, and local tissue inflammatory reaction.<sup>6,8</sup> An additional possibility is that tumor growth between surgery and the start of radiation therapy plays a role in

this phenomenon. Radiation therapy should preferably be initiated into 6 weeks after surgery. Nevertheless, wound healing and the patient's clinical situation may require a delay in the start of treatment, and some recent studies have reported a time range up to 14 weeks from surgery to initiation of radiation therapy.<sup>9,10</sup> Glioblastoma is a highly proliferative tumor that may show relevant growth in this period of time.<sup>9</sup> However, the first postradiation examination is usually compared with the early postoperative MR imaging (EPMR) examination to assess tumor response, and tumor growth before starting treatment may be wrongly attributed to tumor progression.

Our intention in this study was to assess the impact of performing an MR examination shortly before the start of radiation therapy, hereafter referred to as the preradiation MR imaging (PRMR) examination, in the management of patients with glioblastoma who have undergone surgical resection of the tumor. Our hypothesis was that tumor growth before radiation therapy could play a role in some cases classified as pseudoprogression. If this is true, a number of patients who show contrast-enhancing lesion enlargement in the first postradiation MR examination compared with the EPMR examination, and who will be considered as experiencing pseudoprogression, could show stable disease or partial response when the examination is compared with the PRMR examination. Accordingly, the prevalence of pseudoprogression should decrease when PRMR is used as the baseline examination. Another aspect that we wanted to explore was whether the evolution of the tumor between

EPMR and PRMR could provide an assessment of the proliferative behavior of the tumor and if it could be of value in predicting the outcome after therapy. To do this, we evaluated the correlation between the pattern of tumor growth on the PRMR examination and patient overall survival.

## MATERIALS AND METHODS

### Patient Selection

This prospective study was approved by the ethics committee of Hospital Universitari de Bellvitge, and informed consent was obtained from all patients. The inclusion criteria for this study were as follows: surgical resection of a newly diagnosed tumor; histopathologic diagnosis of glioblastoma on the basis of the World

Health Organization criteria; EP MR available, including T1-weighted imaging, contrast-enhanced T1-weighted imaging, FLAIR imaging, and DWI; scheduled treatment with concomitant radiation therapy and temozolamide; and informed consent of the patient. Thirty consecutive patients studied in our hospital fulfilled the inclusion criteria and were prospectively included in the study between December 2012 and October 2014. Two patients showed quick clinical deterioration after surgery and did not start treatment with radiation therapy. These 2 patients were excluded from the study. The remaining 28 patients constituted the main body of the study.

### MR Imaging

All patients included in the study underwent MR imaging within 7 days before the start of radiation therapy. Follow-up MR imaging was performed 2–6 weeks after completion of radiation therapy in all patients and then every 2–4 months until the end of the study in February 2016.

All MR examinations were performed in a 1.5T MR unit (Achieva; Philips Healthcare, Best, the Netherlands) and included, at least, T1-weighted imaging, contrast-enhanced T1-weighted imaging, FLAIR imaging, and DWI sequences. T1-weighted images were acquired with TR, 500 ms; TE, 12 ms; FOV, 23 cm; acquisition matrix, 256 × 192 pixels; and section thickness, 5 mm with a 1-mm gap. FLAIR MR images were obtained

with TR, 11,000 ms; TE, 140 ms; TI, 2800 ms; FOV, 23 cm; acquisition matrix, 256 × 192 pixels; and section thickness, 5 mm with a 1-mm gap.

Three neuroradiologists (C.M., M.C., and S.C.) with 20, 12, and 13 years of experience in neuro-oncology MR imaging, respectively, blinded to survival data independently evaluated the MR examinations at 2 different times: in the early postoperative period (EP MR) and in the early preradiotherapy period (PRMR). Disagreements between readers were resolved by consensus.

The EP MR was assessed according to previously established criteria.<sup>11,12</sup> Patients were stratified into 3 groups according to the extent of tumor resection: total resection, subtotal resection between 95%–100%, and subtotal resection <95%.

Tumor growth in the PRMR was assessed by evaluating the enhancing component of the tumor. Four possibilities were envisaged: no growth, focal growth, global growth, and distant growth. Appearance of a thin homogeneous enhancement in the wall of the surgical cavity was considered to be the normal evolution after surgery, and “no growth” was considered. Abnormal growth of the enhancing component was considered focal when it involved less than half of the postsurgical cavity and global when it involved more than half of the wall. When new contrast-enhancement foci were found without contact with the surgical cavity, distant growth was considered (Fig 1). The findings of the PRMR examination were reported to the oncologist to evaluate the need for any change in the field of radiation therapy. Changes in treatment planning were reported.

Response to the treatment was assessed according to the Response Assessment in Neuro-Oncology criteria by comparing the first postradiation MR examination to the EP MR examination. Four possibilities were envisaged: complete response, partial response, stable disease, and progressive disease.<sup>7</sup> When progressive disease was found, we differentiated true progression from pseudoprogression by evaluating an MR examination performed more than 3 months after radiation therapy. If tumor growth was found in this examination, then the response was considered true progression. If the enhancing lesion was stable or decreased in size, then a diagnosis of pseudoprogression was made retrospectively. The same procedure was performed a second time using PRMR as the baseline examination, and the response was reassessed by comparing the first postradiation MR examination to the PRMR examination. Differences between the 2 assessments were reported.

### Statistical Analysis

Patient overall survival was defined as the time from surgery until death. For those patients who survived past the date of our analysis, survival was right censored in the survival analysis to the time the patient was last known to be alive. Two parameters were correlated to overall survival: the extent of the surgical resection evaluated in the EP MR examination and the pattern of tumor growth in the PRMR examination. Survival curves were constructed with the Kaplan-Meier method, and differences were evaluated with the log-rank

**Table 1: Clinical characteristics of the patients**

Characteristics	
Age (yr) (mean [range])	57 [26–73]
Sex (No. of patients)	
Men	19
Women	9
Karnofsky Performance Status (No. of patients)	
70–80	9
90–100	19
Time between surgery and EP MR (No. of patients)	
<24 h	2
24–48 h	15
48–72 h	11
Time between surgery and radiotherapy (d) (mean [range])	39 [27–64]
Time between PRMR and radiotherapy (No. of patients)	
1 d	8
2–3 d	9
4–5 d	9
6–7 d	2
Time between radiotherapy and follow-up with MRI (d) (mean [range])	28 [16–39]

**Table 2: Concordance among tumor response assessment performed 2–6 weeks after completion of radiotherapy with both EP MR and PRMR as baseline exams<sup>a</sup>**

PRMR as Baseline	EP MR as Baseline				Total
	True Progression <sup>b</sup>	Pseudoprogression <sup>b</sup>	Stable Disease	Partial Response	
True Progression <sup>b</sup>	9	0	0	0	9
Pseudoprogression <sup>b</sup>	0	3	0	0	3
Stable Disease	0	3	8	1	12
Partial Response	0	1	1	2	4
Total	9	7	9	3	28

<sup>a</sup> Patients: n = 28.

<sup>b</sup> Discrimination between true progression and pseudoprogression in patients showing progressive disease was performed by evaluating an MR exam performed more than 3 months after radiotherapy.

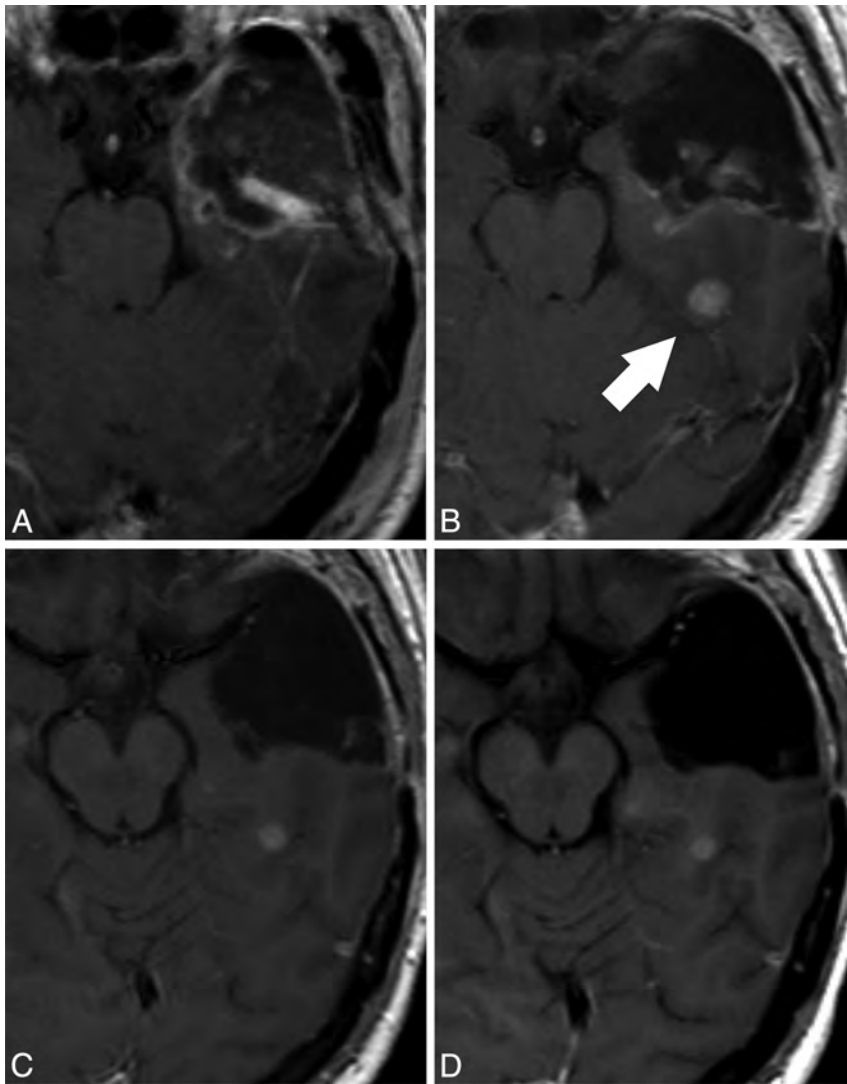


**FIG 2.** Representative case in which the response assessment is progressive disease (pseudoprogression) in reference to the EPMR examination and stable disease in reference to the PRMR examination. Contrast-enhanced T1-weighted images performed at A, 24 hours after surgery (EPMR), B, 3 days before radiation therapy (PRMR), C, 27 days after radiation therapy, and D, 135 days after radiation therapy. A contrast-enhancing nodule appears in the PRMR (arrow, B), distant to the surgical cavity. As a relevant consequence, the radiation therapy field design was modified to include the nodule in the target volume. The postradiation examination (C) shows a small decrease in the size of the nodule, which remains stable in an MR examination performed 4 months after radiation therapy (D). In this particular case, the PRMR provides evidence that the nodule appeared before treatment and remained stable after the treatment. The response assessment would be progressive disease compared with the EPMR (pseudoprogression because the nodule remained stable in the next follow-up MR examination performed 4 months after radiation therapy) and stable disease compared with the PRMR.

test. Multivariable analysis with the variables “extent of tumor resection” and “pattern of contrast enhancement growth” was performed by fitting the Cox proportional hazards models to test a possible dependence between both variables, and the hazard ratio for death was estimated for each variable. Finally, we tested differences in the time elapsed between surgery and PRMR among patterns of growth with the Kruskal-Wallis test. All statistics were computed with PASW Statistics 18 software (IBM, Armonk, New York). Significant differences were determined by using a level of  $P < .05$ .

## RESULTS

A summary of patient data and time elapsed between surgery, EPMR, PRMR, and radiation therapy can be found in Table 1. At the time of last assessment (February 2016), 8 patients were alive after 778 days of median follow-up (range, 637–945 days). Follow-up of deceased patients ranged between 78 and 1115 days (median, 444 days).

### Radiation Therapy Treatment Planning

The field of radiation therapy planned with the EPMR examination had to be redesigned in 4 patients on the basis of the PRMR findings. The reason for this change was distant growth in 3 patients and large local growth in 1 additional patient. Survival of these patients was 213, 286, 334, and 1115 days.

### Tumor Response Assessment

Tumor response to concomitant treatment with radiation therapy and temozolamide is shown in Table 2. The cross-table shows the correlation of the response assessment in the first postradiation MR examination when either the EPMR or the PRMR examinations were used as baseline. Sixteen patients showed progressive disease in the first postradiation examination when EPMR was used as baseline, corresponding to pseudoprogression in 7 patients and true progression in 9 (pseudoprogression ratio with EPMR as baseline examination, 7 of 16 = 44%; positive predictive value for true progression when tumor growth is found on the first postradiation MR examination, 9 of 16 = 56%). Then, the response was reassessed with PRMR as baseline examination. Four patients who were classified as pseudoprogression with EPMR as baseline were classified as stable disease or partial response with PRMR as baseline.

As a consequence, the number of patients who showed progressive disease was reduced to 12 when PRMR was used as baseline, corresponding to pseudoprogression in 3 patients and true progression in 9 patients (pseudoprogression ratio with PRMR as baseline, 3 of 12 = 25%; positive predictive value for true progression, 9 of 12 = 75%). Fig 2 shows a representative case in which tumor response was classified as pseudoprogression when the first postradiation MR examination was compared with the EPMR examination. In this case, PRMR showed that

**Table 3: Overall survival of patients stratified by the extent of resection evaluated on the EPMR and by the pattern of tumor growth on the PRMR**

Characteristic	Patients		Survival (d) (median; range)	Hazard Ratio (95% CI)	P Value
	Total	Alive			
Extent of resection evaluated on the EPMR					.002
Total	7	4	835; 169–961	0.099 (0.022–0.445)	
Between 95% and 100%	11	4	637; 213–1115	0.188 (0.060–0.591)	
Below 95%	10	0	386; 78–577	1 <sup>b</sup>	
Pattern of growth on the PRMR					.001
No growth	7	4	837; 508–961	0.047 (0.006–0.393)	
Focal	10	3	582; 279–758	0.294 (0.098–0.885)	
Global	8	1	344; 78–835	1 <sup>b</sup>	
Distant <sup>a</sup>	3	0	334; 286–1115	NE	

Note:—NE indicates not evaluated.

<sup>a</sup> Distant growth was not evaluated because of low number of cases.

<sup>b</sup> Used as reference category.

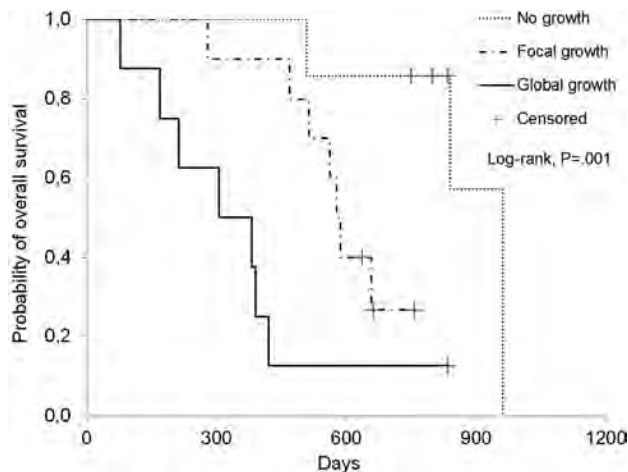


**FIG 3.** Survival curves of patients stratified according to the pattern of tumor growth in the PRMR. Patients with “no growth” in the PRMR showed significantly improved survival (median survival, 837 days) compared with patients with “focal growth” (median survival, 582 days) and “global growth” (median survival, 344 days;  $P = .001$ ).

distant enhancement growth occurred before starting radiation therapy, and the response was changed to stable disease when the postradiation MR examination was compared with the PRMR examination.

#### Tumor Growth Pattern in the PRMR

Data about extent of tumor resection, tumor growth on PRMR, and patient survival are shown in Table 3. Significant differences in survival were found among patterns of enhancement on PRMR (Fig 3). The multivariable analysis showed these differences to be independent of the extent of tumor resection. The most favorable situation for the patients was to show a “no growth” pattern (7 patients; 4 alive; hazard ratio = 0.047). The next favorable situation was to show a “focal growth” pattern (10 patients; 3 alive; hazard ratio = 0.294). Showing a “global growth” pattern was the least favorable situation (8 patients; 1 alive; used as a reference to calculate hazard ratio). Growth distant to the enhancements seen on the EPMR examination was found in 3 patients on the PRMR examination (all deceased after 286, 334, and 1115 days, respectively). We considered that a statistical analysis of survival in these 3 patients could not be performed because of the low number of cases. Nevertheless, we would like to note that 1) the median survival of patients in this group was similar to “global growth”; 2)

the longest surviving patient was included in this group; and 3) the volume targeted for radiation therapy had to be redesigned in all 3 patients.

No significant differences were found in time elapsed between surgery and PRMR among patterns of enhancement growth (median time [range] between surgery and PRMR: “no growth” pattern, 35 days [26–45 days]; “focal growth,” 36 days [28–42 days]; “global growth,” 37 days [22–59 days]; “distant growth,” 39 days [31–46 days];  $P = .827$ ).

#### DISCUSSION

Our results suggest that performing an MR examination shortly before the start of treatment with radiation therapy may be highly relevant in the management of patients with glioblastoma who have undergone surgical resection. In this prospective study, some patients showed tumor growth before radiation therapy that required an enlargement of the target volume. In addition, performing a PRMR examination may reduce the number of pseudoprogression classifications by identifying a sample of patients in whom enhancement growth found in the first postradiation examination occurs before starting the treatment and not as a reaction to it. A third aspect of interest is that PRMR may provide independent

prognostic information in patients with glioblastoma. In our study, the pattern of tumor growth on the PRMR examination satisfactorily correlated with patient survival, independent of the extent of surgical resection evaluated on the EPMR examination.

Glioblastoma is a very aggressive tumor with a high rate of proliferation and a dismal prognosis. MR imaging plays a very relevant role in the management of these tumors. An MR examination performed shortly after surgery, the EPMR, evaluates the extent of tumor resection and the presence of tumor remnant. This study is used to delineate the field for radiation therapy and will be the baseline examination to evaluate response to treatment. But unfortunately, glioblastoma may show relevant growth in short periods of time that could require enlarging the target volume of radiation therapy.<sup>9</sup> In this respect, some studies suggest performing an MR examination shortly before treatment to validate the field of radiation therapy.<sup>9,13</sup> However, to our knowledge, the impact of performing a PRMR examination has not been evaluated in depth, and current guidelines for glioblastoma management do not include performing PRMR.<sup>4,14</sup> According to our findings, this examination seems to have a very positive impact on patient management. Four patients in our study showed relevant

growth before radiation therapy that required enlarging the target volume.

Another relevant role of PRMR is related to the robustness of tumor follow-up. MR imaging plays a pivotal role in the detection of progressive disease in tumors that are not responding to treatment to provide the possibility of introducing an alternative treatment as soon as possible. Unfortunately, MR imaging assessments are not always totally accurate in detecting tumor progression. A paradigmatic example is the first postradiation MR examination, performed 2–6 weeks after treatment. In this examination, increased enhancement may be related to either true progression or pseudoprogression, and a reliable discrimination between these 2 entities cannot be performed by MR imaging alone. The pseudoprogression phenomenon has been considered to be induced by various nontumorous processes such as subacute radiation toxicity, treatment-related necrosis, and tissue inflammatory reaction.<sup>6,8</sup> We believe that an additional possibility might be that the enlargement of the contrast-enhancing area occurs before starting radiation therapy and not as a consequence of treatment. Enlargement of the contrast-enhancing area before radiation therapy could be attributed to either tumor growth, surgical injury, or a combination of both. In any case, the demonstration that the contrast-enhancement enlargement has occurred before the initiation of radiation therapy would suggest that the concomitant treatment has been effective and that it has to be continued with adjuvant temozolamide. In our study, enhancement growth in the first postradiation MR examination was related to enhancement growth before treatment in 4 patients. The identification of these 4 patients improved the positive predictive value for true progression in the first postradiation MR examination from 56% to 75%. This reduction in the number of cases classified as pseudoprogression would increase the robustness of the information that the radiologist brings to the multidisciplinary neuro-oncology unit to make the appropriate clinical decision when there is a precocious clinical deterioration of the patient.

Prognostic assessment of patients with glioblastoma is important by itself and may be relevant in deciding upon the best treatment to be offered in some particular cases. Some well-known prognostic factors are patient age, performance status, neurologic function, mental status, *MGMT* promoter methylation status, and extent of tumor resection.<sup>5,11,12,15–22</sup> The evolution of the tumor between EP MR and PRMR could provide information about proliferative behavior that might lead to additional predictive information about the outcome after therapy. Our study provides a positive argument for this possibility. We defined 4 patterns of tumor growth that satisfactorily correlated with patient survival. Showing no growth of the tumor was the most favorable option. In our study, patients with this pattern of growth survived longer (hazard ratio for death, 0.047) than patients showing a global growth of the enhancing tumor. An intermediate possibility was a focal pattern of growth (hazard ratio, 0.294).

Our study has several possible limitations. Distribution of the set of patients into 4 possibilities of tumor growth in the PRMR examination produced low numbers of patients in some groups. In particular, only 3 patients were included in the “distant growth” group. Although the survival of these patients was similar to the survival of patients with “global growth,” a statistical anal-

ysis could not be performed. Further studies could provide additional information about the clinical performance of this group of patients. Another consideration is the ranges of time elapsed between surgery and EP MR, between PRMR and radiation therapy, and between radiation therapy and follow-up with MR imaging. Shorter ranges of time could reduce the variability of the results and could provide more precise assessment of the parameters evaluated. However, all time ranges were within the standards considered in the diverse protocols, and time range did not influence the pattern of tumor growth found in the PRMR examination. A final concern is influence of a possible inflammatory component in the evolution found between EP MR and PRMR. To our knowledge, it is not possible to perform a precise analysis of the influence of an inflammatory component in the PRMR. We tried to avoid the uncertainty implicit in an association between a particular radiologic finding and a particular histologic situation by correlating our findings to patient survival and not to the presence or absence of tumor.

## CONCLUSIONS

On the basis of our findings, we believe that performing an MR examination shortly before the start of radiation therapy would have a positive impact on the management of patients with glioblastoma by improving the planning of radiation therapy, reducing the ratio of pseudoprogression assessments, and providing additional predictive information. However, further multicenter studies in a larger set of patients are required to validate our findings.

Disclosures: Carles Majós—RELATED: Grant: Grupo Español de Investigación en Neurooncología (GEINO)\* \*Money paid to the institution.

## REFERENCES

1. Ostrom QT, Gittleman H, Liao P, et al. **CBTRUS statistical report: primary brain and central nervous system tumors diagnosed in the United States in 2007–2011.** *Neuro Oncol* 2014;16(suppl 4):iv1–63 CrossRef Medline
2. Weller M, van den Bent M, Hopkins K, et al. **EANO guideline for the diagnosis and treatment of anaplastic gliomas and glioblastoma.** *Lancet Oncol* 2014;15:e395–403 CrossRef Medline
3. Stupp R, Mason WP, van den Bent MJ, et al. **Radiotherapy plus concomitant and adjuvant temozolomide for glioblastoma.** *N Engl J Med* 2005;352:987–96 CrossRef Medline
4. NCCN Guidelines. NCCN guidelines for treatment of cancer by site. Central Nervous System Cancers. National Comprehensive Cancer Network. [http://www.nccn.org/professionals/physician\\_gls/f\\_guidelines.asp#cns](http://www.nccn.org/professionals/physician_gls/f_guidelines.asp#cns). Updated 2015. Accessed December 9, 2015
5. Albert FK, Forsting M, Sartor K, et al. **Early postoperative magnetic resonance imaging after resection of malignant glioma: objective evaluation of residual tumor and its influence on regrowth and prognosis.** *Neurosurgery* 1994;34:45–60; discussion 60–61 CrossRef Medline
6. Brandsma D, Stalpers L, Taal W, et al. **Clinical features, mechanisms, and management of pseudoprogression in malignant gliomas.** *Lancet Oncol* 2008;9:453–61 CrossRef Medline
7. Wen PY, Macdonald DR, Reardon DA, et al. **Updated response assessment criteria for high-grade gliomas: response assessment in neuro-oncology working group.** *J Clin Oncol* 2010;28:1963–72 CrossRef Medline
8. Hygino da Cruz LC Jr, Rodriguez I, Domingues RC, et al. **Pseudoprogression and pseudoresponse: imaging challenges in the assess-**

- ment of posttreatment glioma. *AJNR Am J Neuroradiol* 2011;32:1978–85 CrossRef Medline
9. Pirzkall A, McGue C, Saraswathy S, et al. **Tumor regrowth between surgery and initiation of adjuvant therapy in patients with newly diagnosed glioblastoma.** *Neuro Oncol* 2009;11:842–52 CrossRef Medline
  10. Valdivieco I, Verger E, Bruna J, et al. **Impact of radiotherapy delay on survival in glioblastoma.** *Clin Transl Oncol* 2013;15:272–82 CrossRef Medline
  11. Ekinici G, Akpınar IN, Baltacıoğlu F, et al. **Early-postoperative magnetic resonance imaging in glial tumors: prediction of tumor regrowth and recurrence.** *Eur J Radiol* 2003;45:99–107 CrossRef Medline
  12. Majós C, Cos M, Castañer S, et al. **Early post-operative magnetic resonance imaging in glioblastoma: correlation among radiological findings and overall survival in 60 patients.** *Eur Radiol* 2016;26:1048–55 CrossRef Medline
  13. Essig M, Anzalone N, Combs SE, et al. **MR imaging of neoplastic central nervous system lesions: review and recommendations for current practice.** *AJNR Am J Neuroradiol* 2012;33:803–17 CrossRef Medline
  14. Stupp R, Tonn JC, Brada M, et al. **High-grade malignant glioma: ESMO Clinical Practice Guidelines for diagnosis, treatment and follow-up.** *Ann Oncol* 2010;21:90–93 CrossRef Medline
  15. Gorlia T, van den Bent MJ, Hegi ME, et al. **Nomograms for predicting survival of patients with newly diagnosed glioblastoma: prognostic factor analysis of EORTC and NCIC trial 26981-22981/CE.3.** *Lancet Oncol* 2008;9:29–38 CrossRef Medline
  16. Curran WJ Jr, Scott CB, Horton J, et al. **Recursive partitioning analysis of prognostic factors in three Radiation Therapy Oncology Group malignant glioma trials.** *J Natl Cancer Inst* 1993;85:704–10 CrossRef Medline
  17. Scott CB, Scarantino C, Urtasun R, et al. **Validation and predictive power of Radiation Therapy Oncology Group (RTOG) recursive partitioning analysis classes for malignant glioma patients: a report using RTOG90-06.** *Int J Radiat Oncol Biol Phys* 1998;40:51–55 CrossRef Medline
  18. Allahdini F, Amirjamshidi A, Reza-Zarei M, et al. **Evaluating the prognostic factors effective on the outcome of patients with glioblastoma multiformis: does maximal resection of the tumor lengthen the median survival?** *World Neurosurg* 2010;73:128–34 CrossRef Medline
  19. McGirt MJ, Chaichana KL, Gathinji M, et al. **Independent association of extent of resection with survival in patients with malignant brain astrocytoma.** *J Neurosurg* 2009;110:156–62 CrossRef Medline
  20. Lacroix M, Abi-Said D, Fourney DR, et al. **A multivariate analysis of 416 patients with glioblastoma multiforme: prognosis, extent of resection, and survival.** *J Neurosurg* 2001;95:190–98 CrossRef Medline
  21. Sanai N, Berger MS. **Glioma extent of resection and its impact on patient outcome.** *Neurosurgery* 2008;62:753–64; discussion 264–66 CrossRef Medline
  22. Smets T, Lawson TM, Grandin C, et al. **Immediate post-operative MRI suggestive of the site and timing of glioblastoma recurrence after gross total resection: a retrospective longitudinal preliminary study.** *Eur Radiol* 2013;23:1467–77 CrossRef Medline

# Computer-Extracted Texture Features to Distinguish Cerebral Radionecrosis from Recurrent Brain Tumors on Multiparametric MRI: A Feasibility Study

P. Tiwari, P. Prasanna, L. Wolansky, M. Pinho, M. Cohen, A.P. Nayate, A. Gupta, G. Singh, K.J. Hatanpaa, A. Sloan, L. Rogers, and A. Madabhushi



## ABSTRACT

**BACKGROUND AND PURPOSE:** Despite availability of advanced imaging, distinguishing radiation necrosis from recurrent brain tumors noninvasively is a big challenge in neuro-oncology. Our aim was to determine the feasibility of radiomic (computer-extracted texture) features in differentiating radiation necrosis from recurrent brain tumors on routine MR imaging (gadolinium T1WI, T2WI, FLAIR).

**MATERIALS AND METHODS:** A retrospective study of brain tumor MR imaging performed 9 months (or later) post-radiochemotherapy was performed from 2 institutions. Fifty-eight patient studies were analyzed, consisting of a training ( $n = 43$ ) cohort from one institution and an independent test ( $n = 15$ ) cohort from another, with surgical histologic findings confirmed by an experienced neuropathologist at the respective institutions. Brain lesions on MR imaging were manually annotated by an expert neuroradiologist. A set of radiomic features was extracted for every lesion on each MR imaging sequence: gadolinium T1WI, T2WI, and FLAIR. Feature selection was used to identify the top 5 most discriminating features for every MR imaging sequence on the training cohort. These features were then evaluated on the test cohort by a support vector machine classifier. The classification performance was compared against diagnostic reads by 2 expert neuro-radiologists who had access to the same MR imaging sequences (gadolinium T1WI, T2WI, and FLAIR) as the classifier.

**RESULTS:** On the training cohort, the area under the receiver operating characteristic curve was highest for FLAIR with 0.79; 95% CI, 0.77–0.81 for primary ( $n = 22$ ); and 0.79, 95% CI, 0.75–0.83 for metastatic subgroups ( $n = 21$ ). Of the 15 studies in the holdout cohort, the support vector machine classifier identified 12 of 15 studies correctly, while neuroradiologist 1 diagnosed 7 of 15 and neuroradiologist 2 diagnosed 8 of 15 studies correctly, respectively.

**CONCLUSIONS:** Our preliminary results suggest that radiomic features may provide complementary diagnostic information on routine MR imaging sequences that may improve the distinction of radiation necrosis from recurrence for both primary and metastatic brain tumors.

**ABBREVIATIONS:** AUC = area under receiver operating characteristic curve; Gd = gadolinium; mRmR = minimum redundancy and maximum relevance; RN = radiation necrosis; RT = radiation therapy; SVM = support vector machine

Treatment of malignant brain tumors involves a combined approach of surgical resection, radiation therapy (RT), and, depending on the histology, chemotherapy. Cerebral radiation necrosis (RN) is often an unavoidable complication of high-dose

focal RT that typically manifests 6–9 months post-RT and mimics the symptoms and MR imaging appearance of tumor recurrence, in both primary and metastatic brain tumor cases.<sup>1</sup> RN and tumor recurrence have substantially different treatment regimens and need to be identified expediently for determining prognosis, guiding subsequent therapy, and improving patient outcome.

Standard MR imaging<sup>2–4</sup> remains the technique of choice for posttreatment evaluation of patients with brain tumor. The Re-

Received April 12, 2016; accepted after revision July 16.

From the Department of Biomedical Engineering (P.T., P.P., G.S., A.M.), Case Western Reserve University, Cleveland, Ohio; University Hospitals Case Medical Center (A.P.N., A.G., L.W., M.C., A.S., L.R.), Cleveland, Ohio; and University of Texas Southwestern Medical Center (M.P., K.J.H.), Dallas, Texas.

Research reported in this publication was supported by the Coulter Translational Award; Ohio Third Frontier Technology Validation grant; National Science Foundation Innovation Corps; National Cancer Institute of the National Institutes of Health under award numbers R01CA136535-01, R01CA140772-01, and R21CA167811-01; National Institute of Biomedical Imaging and Bioengineering of the National Institutes of Health under award number R43EB015199-01; National Science Foundation under award number IIP-1248316; Clinical and Translational Science Collaborative Award ULTR 000439; and SOURCE Summer Research Program and Case Western Alumni Association.

The content is solely the responsibility of the authors and does not necessarily represent the official views of the National Institutes of Health.

Please address correspondence to Pallavi Tiwari, MD, Case Western University, 2103 Cornell Rd, Room 6131, Cleveland, OH 44106; e-mail: pallavi.tiwari@case.edu

Indicates open access to non-subscribers at www.ajnr.org

Indicates article with supplemental on-line appendix and tables.

Indicates article with supplemental on-line photos.

<http://dx.doi.org/10.3174/ajnr.A4931>

sponse Assessment in Neuro-Oncology (RANO; <http://radiopaedia.org/articles/rano-criteria-for-glioblastoma>) criteria recommend using 2D measurements (diameter) of contrast enhancement on posttreatment gadolinium-enhanced (Gd) T1-weighted MR imaging (with respect to pretreatment MR imaging) as the fundamentally quantifiable imaging criteria for assessment of response to treatment. However, due to a similar appearance on follow-up posttreatment Gd-T1WI MR imaging, differentiating RN and tumor recurrence by using 2D measurements of contrast enhancement (as manually identified by an expert) is clinically extremely challenging.<sup>5</sup> Recent studies have shown promise in using semi-quantitative MR imaging measures such as apparent diffusion coefficient ratios<sup>6</sup>; choline, creatine, and *N*-acetylaspartate ratios from MR spectroscopy<sup>7</sup>; and perfusion imaging<sup>6</sup> for differentiating RN from tumor recurrence. These techniques, however, may not be universally available, are often difficult to reproduce, and tend to increase the overall cost of the imaging examination. Hence, there is a need for identification of reliable noninvasive quantitative measurements on routinely acquired brain MR imaging (Gd-T1WI, T2WI, and fluid-attenuated inversion recovery) that can accurately distinguish RN from tumor recurrence.

The physiologic pathways leading to the development of RN and brain tumor recurrence are fundamentally different. Thus, there may be subtle variances in the morphologic appearance of the 2 conditions reflected as differences in the microarchitectural texture appearance embedded across Gd-T1WI, T2WI, and FLAIR, which might enable discrimination of RN from recurrent tumors.<sup>8</sup> Radiomic or computer-extracted texture features allow capture of higher order quantitative measurements (eg, co-occurrence matrix homogeneity, neighboring gray-level dependence matrix, multiscale Gaussian derivatives) for modeling macro- and microscale morphologic attributes within the lesion area for every MR imaging protocol. Some of these radiomic features may not be visually appreciable by a radiologist but may complement their ability to make a more reliable diagnosis of the disease. Of late, there has been interest in the use of radiomic features computed from treatment-naïve MR imaging to distinguish patients with glioblastoma with long-term and short-term survival.<sup>9</sup> Relatively little work, however, has focused on the use of radiomic analysis for distinguishing radiation necrosis from brain tumor recurrence on MR imaging.

The purpose of this study is to evaluate the feasibility of radiomic analysis on routine MR imaging sequences in identifying computer-extracted texture differences between RN and tumor recurrence that may not be visually appreciable on conventional MR imaging and to distinguish RN and recurrent cancer across primary and metastatic brain tumor studies. In this study, we identified a set of radiomic features that best distinguished RN from tumor recurrence on a training cohort across 3 routine multiparametric MR images (Gd-T1WI, T2WI, FLAIR). We then evaluated the validity of these radiomic features on a small holdout cohort and performed a head-to-head comparison of their performance against independent diagnostic reads by 2 expert neuroradiologists who were presented with the same routine MR imaging sequences as the classifier (Gd-T1WI, T2WI, and FLAIR). The ultimate goal of this work was to develop noninvasive techniques that can be used in conjunction with routine MR

**Table 1: Summary of study population**

Characteristic	Patient Cohort			
	Training		Holdout	
	Primary	Metastatic	Primary	Metastatic
No. of patients	22	21	11	4
Women	12	7	2	2
Men	9	15	9	2
Mean age (yr)	52.8	49.5	56.3	52
Age range (yr)	(33–75)	(37–65)	(43–75)	(43–58)

imaging protocols to complement a radiologist’s diagnosis of RN versus tumor recurrence for improving patient management both for primary and metastatic brain tumors.

## MATERIALS AND METHODS

### Study Population

The study population consisted of independent training and test cohorts obtained from the local (University Hospitals Case Medical Center) and the collaborating (University of Texas Southwestern Medical Center) institution and acquired for this institutional review board–approved and Health Insurance Portability and Accountability Act–compliant study. The 2 patient cohorts were identified by performing a retrospective review of neuropathology in all patients with brain tumor who underwent an operation for a recurrent or progressive Gd T1WI-enhancing lesion identified during follow-up at 9 months (or later) after the initial brain RT. Follow-up MR imaging scans within 0–21 days before the second resection or biopsy (for disease confirmation) were used for analysis. Inclusion criteria were that the pathology specimen be obtained by resection (preferably) or by multiple biopsies (>2) via stereotactic guidance. Single biopsies were not allowed because of the potential for sampling error. Histology was reviewed by a neuropathologist (M.C. at the local and K.J.H. at the collaborating institution) blinded to the original diagnosis and type of RT, to quantify the percentage of RN and recurrent tumors.

To avoid any training errors due to “mixed” pathologies on the same lesion, for the training cohort, we strictly defined the presence of RN as  $\geq 80\%$  RN and of recurrent tumor as  $\geq 80\%$  recurrent tumor (other “mixed” cases with varying proportions of RN and tumor recurrence were excluded). We identified 43 cases at the local institution from 2006 to 2014 that followed this strict inclusion criterion, consisting of 22 primary tumors (12 with recurrent tumor, 10 with RN) and 21 metastatic tumors (12 with recurrent tumor, 9 with RN). The test cohort consisted of 15 studies, 11 primary and 4 metastatic cases of patients who underwent an operation between 2009 and 2015 and were pathologically confirmed with either “predominant” or a mixture of RN and tumor recurrence in varying proportions on the same lesion as confirmed by pathology. Gd-T1WI scans were available for 10 of 15 studies; T2WI scans, for 7 of 15 studies; and FLAIR, for all 15 studies respectively. Table 1 shows the summary of the study population. The details on MR imaging protocol acquisition and pre-processing steps are provided in the On-line Appendix.

### Tumor Delineation and Segmentation

The ROI containing the lesion was manually segmented across contiguous sections on each Gd-T1WI, T2WI, and FLAIR se-

quence by an experienced radiologist (L.W.) with a hand-annotation tool in 3D Slicer (<http://www.slicer.org>). To assess the variability in features due to segmentation, we also segmented the ROI containing the lesion for every image with an automated brain tumor segmentation tool, BraTumIA (<http://istb-software.unibe.ch/bratumia/MIA/BraTumIA.html>).<sup>10</sup> The degree of overlap, computed as Dice Index, across manual and automated segmentation was recorded, and the variability of texture features across manual and automated segmentation was reported as box-plots (On-line Fig 1).

### **Radiomic Texture Features**

A total of 119 2D radiomic texture features on a per-voxel basis were extracted from every expert-annotated lesion on contiguous sections of a patient study. For every patient study, a median feature value was calculated from the feature responses of all voxels from across all sections associated with each annotated lesion. All feature calculations were performed by using in-house software implemented in the Matlab R 2014b platform (MathWorks, Natick, Massachusetts). A total of 13 Haralick, 25 Laws, 24 Laplacian pyramid features, and 20 Histogram of Gradient orientations features were computed in Matlab. A detailed description of a few representative radiomic features is provided in On-line Table 1.

### **Feature Selection and Classification on the Training Cohort**

To identify the most discriminating radiomic features across each of the MR imaging sequences on the training cohort, we used minimum redundancy and maximum relevance (mRmR)<sup>11</sup> feature-selection analysis in a sequential feed-forward fashion by using a Matlab R 2014b platform.<sup>12</sup> The sequential feed-forward algorithm is a bottom-up search approach, which starts from an empty feature set and gradually adds features selected via mRmR so that redundant features are removed while maximizing discrimination between the 2 classes (RN and tumor recurrence). Feed-forward mRmR feature selection was used in combination with a support vector machine (SVM) classifier,<sup>13</sup> and the performance metric was an area under the receiver operating characteristic curve (AUC). In our setup, we chose the top 5 most discriminative features from mRmR for each classification task (RN versus tumor recurrence in primary and metastatic subgroups, respectively). Inclusion of >5 features did not improve the AUC of the classifier within the training set. Hence, we limited inclusion of features to the classifier to just the top 5. To mitigate selection and classifier training bias, we used a 3-fold (1-fold held out for testing), patient-stratified, cross-validation scheme, which was repeated 100 times. The best 5 features were identified as the ones that most frequently appeared in the set of the top 5 most discriminative features across 100 runs of 3-fold cross-validation. The analysis was performed independently for every MR imaging sequence.

### **Classification on the Test Cohort**

The independent test cohort was evaluated within an SVM classifier by using the top 5 most discriminatory features identified during training, with evaluation being performed separately for the primary and metastatic subgroups. The radiomics classifier

output was obtained as a binary output in which an output of 1 represented tumor recurrence and zero represented RN for each of the studies in the test cohort. In cases in which >1 MR imaging sequence was available, a consensus (agreement of outcome in 2 of 2 or 2 of 3 sequences) across the binary classifier outputs was used as the final outcome of the radiomics classifier. For cases in which 2 sequences showed disagreement in diagnosis, the output of the sequence, identified as the most discriminating within the training cohort, was used to make the final decision. The final radiomics classifier output for every patient study was compared against the histopathologic findings to report the accuracy values.

### **Statistical Analysis**

Statistical analysis was performed by using a nonparametric Wilcoxon signed ranked test while comparing the differences in feature values across different feature sets for every MR imaging sequence for both the primary and metastatic cohorts independently. To further make the statistical significance test more stringent, the *P* value was appropriately adjusted at *P* = .00125 with a Bonferroni test to account for type I errors. All statistical analyses were implemented in the Matlab R2014b platform (MathWorks). All reported confidence intervals are over 95% confidence intervals.

### **Comparative Multireader Study**

Two board-certified neuroradiologists with 2 years of experience (A.P.N., A.G), blinded to the pathology reports, read the MR images (Gd-T1WI, T2WI, and FLAIR, as available) to diagnose the presence of RN or tumor recurrence on each of the holdout studies. The same sequence scans exposed to the SVM classifier were provided to the expert readers to avoid any comparison bias. Neither the machine-learning classifier nor the readers had access to the baseline, pretreatment scan. The only additional information to which the expert readers had access was the type of tumor (ie, oligodendroglioma, glioblastoma) for the primary brain tumor cohort and the location of primary disease for the metastatic brain tumor cohort. No additional clinical information (ie, age, sex, Karnofsky performance score) was provided. The readers were allowed to go back to the scans multiple times as required to make their final diagnosis. Both readers independently assigned a probability score (between 0.5 and 1 in increments of 0.1) for every study as belonging to either RN or tumor recurrence based on the confidence in their diagnostic call. A confidence of 0.5 denotes that the expert was uncertain of the diagnosis while a confidence of 1 denotes that the expert was completely confident in his or her diagnosis of RN or tumor recurrence. The probability scores and the resulting diagnosis for every threshold value for every study for the 2 experts are provided in On-line Table 3.

## **RESULTS**

### **RN versus Recurrent Tumors in the Primary Brain Tumor Subgroup**

**Feature Discovery and Classification on the Training Cohort.** Tumor delineation showed excellent agreement between the manual and automated segmentation (Dice Index range, 0.8–0.9). Differences in tumor volume and age across the 2 conditions were found to be statistically insignificant. The top radiomic features

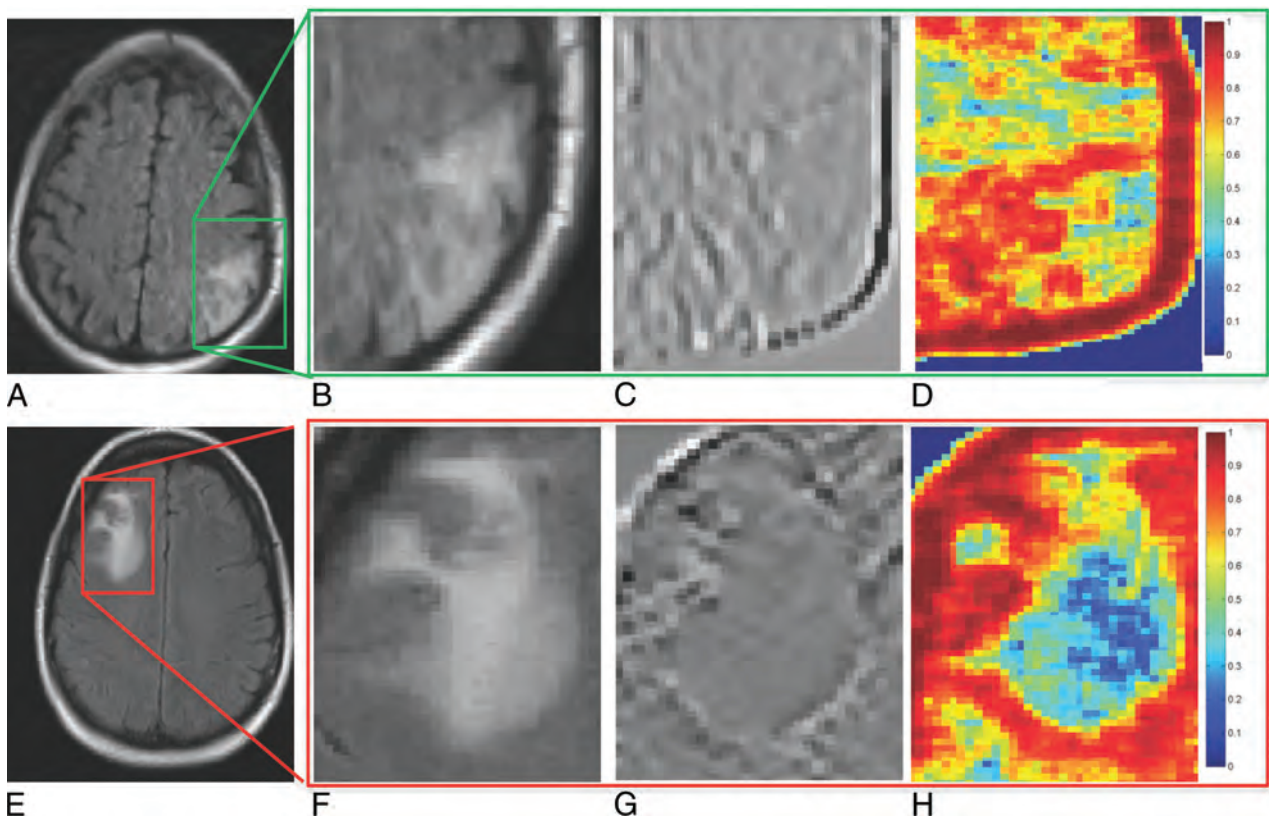


**FIG 1.** A representative 2D FLAIR section for RN (A) and tumor recurrence (E) shown for 2 different primary brain tumor studies. B and F, The original FLAIR images corresponding to RN (A) and tumor recurrence (E). C, D, G, and H, The top 2 texture features corresponding to RN (A) and tumor recurrence (E), respectively. Red represents high feature value, while blue represents a low feature value for a given pixel.

**Table 2: Classifier and blinded-reader detection accuracy on the holdout set using FLAIR or FLAIR, Gd-T1WI, and T2WI protocols when available<sup>a</sup>**

Detection Accuracy (Primary Cases, n = 11)			Detection Accuracy (Metastatic Cases, n = 4)			Overall Accuracy (n = 15)		
Expert 1	Expert 2	Radiomics Classifier	Expert 1	Expert 2	Radiomics Classifier	Expert 1	Expert 2	Radiomics Classifier
36%	54%	91%	50%	50%	50%	47%	53%	80%

<sup>a</sup> The ground truth was established on the basis of the true histopathologic diagnosis of the cases on the holdout set.

obtained by using mRmR for the primary brain tumor cohort are shown in On-line Table 2 and qualitatively represented in Fig 1. The average feature values for all 3 of the most discriminative features in the primary cohort were found to be statistically significantly different across RN and tumor recurrence ( $P < .001$ ). Correlation, energy, and Laws features (combination of level and edge filters [L5E5]) in the lower Laplacian scale space were consistently identified as the most discriminative ones in distinguishing the 2 classes across all 3 sequences.

The best performing feature sets in distinguishing RN and tumor recurrence were obtained for FLAIR, with reported AUC and accuracy values of  $0.79 \pm 0.05$ ; 95% confidence interval, 0.77–0.81; and  $0.75 \pm 0.05$ ; 95% CI, 0.73–0.77. This was followed by the feature set for T2WI with reported AUC and accuracy values of  $0.77 \pm 0.06$ ; 95% CI, 0.74–0.80; and  $0.72 \pm 0.08$ ; 95% CI, 0.69–0.75, respectively. Notably, Gd-T1-weighted MR imaging, a routinely used sequence in the clinic for response assessment, was ranked lowest in terms of accuracy ( $0.57 \pm 0.07$ ) and AUC ( $0.57 \pm 0.08$ ) across all 3 sequences for the primary brain tumor cohort.

**Classification of the Independent Test Cohort.** The accuracy of the classifier and the 2 expert readers for the holdout studies, both for primary and metastatic cases, are reported in Table 2. On-line Table 3 shows the results of the SVM classifier obtained on the test cohort by using the top 5 features identified via the mRmR feature-selection method. On the basis of the output of the classifier trained either on the FLAIR sequence alone (identified as best performing sequence on the training cohort) or by using the highest consensus (agreement in 2 of 2 or 2 of 3 sequences), 10 of 11 studies were correctly classified. For a threshold of  $>0.5$  in their confidence scores, radiologist 1 diagnosed 4 of 11 cases correctly and was unsure about 1 (study 10) (confidence score = 0.5), while radiologist 2 correctly identified 6 of the 11 cases. The overall accuracy for radiologist 1 was 54%, while for radiologist 2, it was 36%. One of the patient studies (study 7) comprised a “mixed” distribution of pathologies with 75% of RN and 25% of the tissue composing tumor recurrence. However, the patient was clinically treated as a case of recurrence leading to surgical resection; hence, the final diagnosis was a recurrence. Study 4 on the pathology report was identified as having equal (30%) proportions of RN

and tumor recurrence and was identified as having recurrence by the SVM classifier and the 2 expert readers.

### **RN versus Recurrent Tumors in Metastatic Brain Tumor Subgroup**

**Feature Discovery and Classification on the Training Cohort.** The top-ranked features in distinguishing RN and tumor recurrence as obtained from the mRmR feature-selection experiment for the metastatic brain tumor cohort are shown in On-line Tables 2 and 3. Difference variance (in the Laplacian pyramid domain), sum average (in Laplacian pyramid domain), correlation, and correlation (in Laplacian pyramid domain), along with Laws features, were consistently identified as key discriminative features across the 3 sequences. Several features were consistently identified as discriminative of RN and tumor recurrence across the 3 MR imaging sequences in both the primary and metastatic brain tumor cohorts. Unlike the primary brain tumor cohort, the *P* values for the 3 most discriminating feature sets obtained for the metastatic cohort were not found to be statistically significantly different between RN and tumor recurrence.

The 5 most discriminating features (identified via mRmR on the training cohort) for Gd-T1WI, T2WI, and FLAIR for the metastatic brain tumor cohort are listed in On-line Table 2. Similar to the primary brain tumor cohort, the most discriminative feature set was obtained for FLAIR with AUC and accuracy values of  $0.79 \pm 0.09$ ; 95% CI, 0.75–0.83; and  $0.75 \pm 0.06$ ; 95% CI, 0.72–0.78, respectively. This was followed by features extracted from the Gd-T1 sequence, which had AUC and accuracy values of  $0.69 \pm 0.08$ ; 95% CI, 0.66–0.72; and  $0.64 \pm 0.07$ ; 95% CI, 0.61–0.67, respectively. While Gd-T1 MR imaging was ranked lowest in terms of accuracy and AUC for the primary brain tumor cohort, T2-weighted MR imaging was identified as the sequence with the lowest accuracy and AUC in distinguishing the 2 classes in the metastatic brain tumor subgroup.

**Classification of the Independent Holdout Cohort.** As shown in On-line Table 3, 2 of 4 metastatic brain tumor recurrence cases (cases 2 and 3) in the holdout cohort were correctly identified by the SVM classifier (Table 2). Both neuroradiologists correctly and consistently identified 2 of the 4 cases (cases 1 and 3). Case 4 was incorrectly classified by the SVM classifier and the 2 expert readers.

## **DISCUSSION**

Differentiating RN from recurrent brain tumors is one of the most challenging clinical dilemmas in neuro-oncology due to the similar appearance of the 2 conditions on standard MR imaging. In this study, we investigated the feasibility of computerized texture features in distinguishing RN and tumor recurrence on Gd-T1WI, T2WI, and FLAIR across primary and metastatic brain tumor subgroups in a limited cohort of studies obtained from 2 different institutions.

A strength of this study is that the definition of RN versus recurrent tumor for our training cohort was stricter than that in many previously reported imaging studies, which have defined RN and recurrence on the basis of the suspicion of the disease on follow-up MRIs (with no histopathology confirmation).<sup>6,14</sup> To

evaluate the performance of our classifier across routinely seen clinical MR imaging studies, we allowed both mixed and predominant RN/tumor recurrence cases to be included within our holdout test cohort obtained from another institution (University of Texas Medical Center). The holdout test cohort was also independently analyzed by 2 expert readers who were blinded to the pathology reports and clinical findings. The visual traits for tumor recurrence that the 2 expert neuro-radiologists took into account while making the diagnosis included expansile lesion; solid, nodular, or ringlike well-defined enhancements; and internal hemorrhages (in primary tumors). Similarly, the experts identified feathery, geographic, and incomplete enhancements usually associated with predominantly radiation-induced effects.

Our study identified Laplacian pyramid texture features as being discriminative, possibly because this class of features emphasizes edge-related differences between RT and RN at lower resolutions. Similar to the visual features reported by our expert readers, Reddy et al<sup>15</sup> have previously reported meshlike diffuse enhancement and rim enhancement with feathery indistinct margins as characteristic of RN. Similarly, tumor recurrence is reported to have focal solid nodules and solid uniform enhancement with distinct margins.<sup>15</sup> Similarly, Laws features, which enable capture of a combination of different edge, level, and spot patterns within the lesion, were identified as being discriminative possibly because they implicitly model the so-called soap bubble and Swiss cheese patterns that have previously been suggested as associated with RN on Gd-T1WI. Additionally, it has been suggested that RN is associated with a diffuse pattern characterized by periventricular white matter changes,<sup>2</sup> while tumor recurrence has been suggested to be associated with hyper-/hypointensities indicative of hemorrhagic changes on Gd-T1WI, T2WI, and FLAIR MR imaging. Haralick texture features modeled on co-occurring intensity patterns and higher order image derivatives may be capturing these hemorrhagic changes on FLAIR and T2WI sequences.

Of the 3 MR imaging sequences (Gd-T1WI, T2WI, and FLAIR), FLAIR was identified as the most discriminative in the training cohort in terms of AUC and accuracy for both primary and metastatic brain tumor cohorts. FLAIR is highly sensitive, but not specific, for identifying coexisting tumor and edema.<sup>16</sup> In cases of invasive primary brain tumors, malignant tumor cells have been found up to 4 cm away from contrast-enhancing regions,<sup>17</sup> with >90% of the cases of recurrence occurring close to the tumor margin. Future studies could address the role of radiomic features obtained from peritumoral edema as complementary measurements to further improve the diagnosis of RN from tumor recurrence noninvasively.

A recent study<sup>14</sup> used Haralick and wavelet texture features on Gd-T1-weighted MR imaging to distinguish RN from metastatic brain tumor recurrence with a reported AUC of 94%. However, we believe that the results, reported on a per-section basis, may have been affected by the classifier being contaminated by sections from the same patient being used both in the training and testing sets during classification. Additionally, in most cases, the clinical diagnosis was assessed by clinical and radiologic follow-up (as opposed to a more reliable histologic confirmation).

Our study did have its limitations. As a feasibility study, the

reported results are preliminary because our study was limited by a relatively small sample size, both for the training and holdout cohorts. However, to the extent possible, a rigorous statistical analysis was performed to evaluate the classification results. Although the different image preprocessing steps performed did not explicitly account for varying signal-to-noise ratios due to different magnetic fields, this effect was largely mitigated because all the computerized image-based features were derived from cumulative statistics (median) of many pixels. The comparison between expert readers and the radiomics classifier was kept unbiased to the extent possible by ensuring that the expert readers were provided the same routine scans that were available to the classifier. However, the 2 expert readers who performed the analysis had only 2 years of experience as board-certified neuroradiologists. Additionally, the readers did not have access to all 3 sequences in some cases (due to those sequences not being available). While we attempted to control for heterogeneity in patient studies by separately assessing primary and metastatic tumor cohorts, a larger dataset is required to identify the influence of other variables on feature selection, such as treatment type and dose.

## CONCLUSIONS

In this feasibility study, we investigated the role of texture features in distinguishing radiation necrosis from recurrent brain tumors on Gd-T1WI, T2WI, and FLAIR sequences obtained from 2 different sites, across 2 subgroups of studies, primary and metastatic brain tumors. Our results suggest that radiomic analysis on routinely acquired MR imaging might enable discrimination of RN and tumor recurrence both for primary and metastatic brain tumors. Future work will focus on exploring the added value of texture features along with the diagnostic reads from expert radiologists as a part of a prospective clinical study. We will also prospectively validate the features identified in this study on a larger, multi-institutional cohort, in the context of differentiating both pseudoprogression and radiation necrosis from tumor recurrence.

Disclosures: Lee Wolansky—UNRELATED: Board Membership: Immunocellular Therapeutics, Comments: Data Monitoring Committee; Consultancy: BioClinica.\* Comments: consultant on brain tumor studies. Anant Madabhushi—UNRELATED: Board Membership: Inspirata; Consultancy: Inspirata; Grants/Grants Pending: Inspirata\*; Patents (planned, pending or issued): Inspirata.\* Elucid Bioimaging\*; Royalties: Inspirata, Elucid Bioimaging; Stock/Stock Options: Inspirata, Elucid Bioimaging.\*Money paid to the institution.

## REFERENCES

1. Verma N, Cowperthwaite MC, Burnett MG, et al. **Differentiating tumor recurrence from treatment necrosis: a review of neuro-oncologic imaging strategies.** *Neuro Oncol* 2013;15: 515–34 CrossRef Medline
2. Chan YL, Leung SF, King AD, et al. **Late radiation injury to the temporal lobes: morphologic evaluation at MR imaging.** *Radiology* 1999;213:800–07 Medline
3. Kumar AJ, Leeds NE, Fuller GN, et al. **Malignant gliomas: MR imaging spectrum of radiation therapy- and chemotherapy-induced necrosis of the brain after treatment.** *Radiology* 2000: 217:377–84 CrossRef Medline
4. Mullins ME, Barest GD, Schaefer PW, et al. **Radiation necrosis versus glioma recurrence: conventional MR imaging clues to diagnosis.** *AJNR Am J Neuroradiol* 2005;26:1967–72 Medline
5. Raimbault A, Cazals X, Lauvin MA, et al. **Radionecrosis of malignant glioma and cerebral metastasis: a diagnostic challenge in MRI.** *Diagn Interv Imaging* 2014;95:985–1000 CrossRef Medline
6. Pope WB, Kim HJ, Huo J, et al. **Recurrent glioblastoma multiforme: ADC histogram analysis predicts response to bevacizumab treatment.** *Radiology* 2009;252:182–89 CrossRef Medline
7. Catalaa I, Henry R, Dillon WP, et al. **Perfusion, diffusion and spectroscopy values in newly diagnosed cerebral gliomas.** *NMR Biomed* 2006;19:463–75 Medline
8. Prasanna P, Tiwari P, Madabhushi A. **Co-occurrence of local anisotropic gradient orientations (CoLIAGE): distinguishing tumor confounders and molecular subtypes on MRI.** *Med Image Comput Comput Assist Interv* 2014;17(Pt 3):73–80 CrossRef Medline
9. Yang D, Rao G, Martinez J, et al. **Evaluation of tumor-derived MRI-texture features for discrimination of molecular subtypes and prediction of 12-month survival status in glioblastoma.** *Med Phys* 2015; 42:6725–35 CrossRef Medline
10. Porz N, Bauer S, Pica A, et al. **Multi-modal glioblastoma segmentation: man versus machine.** *PLoS One* 2014;9:e96873 CrossRef Medline
11. Peng H, Long F, Ding C. **Feature selection based on mutual information: criteria of max-dependency, max-relevance, and min-redundancy.** *IEEE Trans Pattern Anal Mach Intell* 2005;27:1226–38 CrossRef Medline
12. Tan M, Pu J, B. Zheng B. **Optimization of breast mass classification using sequential forward floating selection (SFFS) and a support vector machine (SVM) model.** *Int J Comput Assist Radiol Surg* 2014; 9:1005–20 CrossRef Medline
13. Mundra PA, Rajapakse JC. **SVM-RFE with MRMR filter for gene selection.** *IEEE Trans Nanobioscience* 2010;9:31–37 CrossRef Medline
14. Larroza A, Moratal D, Paredes-Sánchez A, et al. **Support vector machine classification of brain metastasis and radiation necrosis based on texture analysis in MRI.** *J Magn Reson Imaging* 2015;42: 1362–68 CrossRef Medline
15. Reddy K, Westerly D, Chen C. **MRI patterns of T1 enhancing radiation necrosis versus tumour recurrence in high-grade gliomas.** *J Med Imaging Radiat Oncol* 2013;57:349–55 CrossRef Medline
16. Husstedt HW, Sickert M, Köstler H, et al. **Diagnostic value of the fast-FLAIR sequence in MR imaging of intracranial tumors.** *Eur Radiol* 2009;10:745–52 Medline
17. Silbergeld DL, Chicoine MR. **Isolation and characterization of human malignant glioma cells from histologically normal brain.** *J Neurosurg* 1997;86:525–31 Medline

## “Am I about to Lose my Job?!”: A Comment on “Computer-Extracted Texture Features to Distinguish Cerebral Radiation Necrosis from Recurrent Brain Tumors on Multiparametric MRI: A Feasibility Study”

After reading the accompanying article,<sup>1</sup> and especially the sensationalistic comments that will inevitably appear in the lay press, more than one neuroradiologist will ask the terrifying question, “If computers are now superior to human radiologists, am I about to lose my job?”

In this exceptionally interesting paper, the authors addressed a question that has vexed neuroradiologists since MR was first implemented: namely, how to differentiate recurrent brain tumors from radiation necrosis. The authors used a technique called machine learning. Their programs analyzed a set of 43 proved cases, from which they were able to discern specific characteristics that could distinguish between recurrent tumors and radiation necrosis. The authors then took a new set of 15 cases and matched the computer program and what it was able to “learn” from the test cases against 2 neuroradiologists. The computer won hands down: 12/15 correct for the computer versus 7/15 for neuroradiologist #1 and 8/15 for neuroradiologist #2. These results raise a very uncomfortable question for practicing radiologists: if computers are able to “discover” new imaging characteristics and act upon them to make a very difficult diagnosis, how long do we have until computers “learn” to make every other neuroradiologic diagnosis and make us obsolete?

Since the Industrial Revolution, automation has led to the creation of more (not fewer) jobs. An excellent example is the auto industry. Even though some jobs were lost (first in taking care of horses and later on the assembly line), in fact, ultimately, many more jobs were created.

In the past, the jobs that were eliminated tended to be repetitive, low-end jobs, which freed up human talent for more meaningful and creative endeavors. However, the advent of more sophisticated artificial intelligence has already led to computers doing the jobs that were previously the purview of the human intellectual elite. For example, many stock trades are now executed by computers. A recent sobering commentary by Wall Street analysts predicted the demise of their own field because of computer advances.<sup>2</sup>

Is the current paper a harbinger of our imminent demise? How can human radiologists survive in the world of advancing artificial intelligence? I do not believe that the prognosis is so grim. Clearly,

our profession will undergo substantial adjustments; however, this is a continuous process and has always been the case. In the following brief review, I hope to show that working with computers, rather than some apocalyptic struggle against them, will lead to optimal results for the patients we serve.

A recent thoughtful book by a specialist in advanced computer systems made a number of points apt to our discussion.<sup>3</sup> It is axiomatic that no system is perfect. This is also true of any computer system. Complex modern computer code is almost inevitably written upon much older code. Modern systems are so complicated that no single person understands them in their totality. Such complicated overlapping systems lead to unexpected results and failures, which are impossible to predict. Consequently, code is always being updated and needs to be evaluated “in the field” by human “users.” Think of the Galaxy 7 phone (Samsung, Suwon, South Korea). Inevitably unexpected problems or failures are detected, which require further debugging, updates, and patches. As programs get more complicated, things will probably get worse. A corollary point made by the author of *Overcomplicated* is that computers are not good at figuring out when they are wrong, which often entails the participation of another system or human intervention.<sup>3</sup>

“Augmentation, not automation” is the mantra of another book on this subject by Harvard Business School professor Thomas Davenport and Julia Kirby.<sup>4</sup> Their point is that even in the age of “smart machines,” the optimal result is when humans work together with a computer rather than one or the other separately. I see myself doing this all of the time now: looking up differential diagnoses on the Internet, using advanced analysis of perfusion, MRA, CTA, or fMRI data, using the PACS, etc. Could you image reviewing 3000 images (not an unusual number per case currently) on printed film? Can I use additional help now in my clinical practice? Absolutely! Examples include a reliable automated way to evaluate a patient with neurofibromatosis and dozens of irregularly shaped tumors or a patient with multiple MS lesions; an automated multiparametric way to evaluate the growth of a brain tumor; automated searches for additional metastases; and many, many more. Having a system that can auto-

mate routine work and check for my mistakes will allow me to work faster and more efficiently.

“Smart machines” are far from the only advances made in the field of radiology. Imaging technology is also progressing at an astounding pace, and there is no reason to suspect that things will slow down: PET-MR, hyperpolarized MR, resting-state fMRI, connectivity, molecular imaging, etc. Ultimately, these new technologies will need to be evaluated in human terms, which brings me to the crux of the argument: does “such-and-such” technique improve the lot of humanity? Using the example in the paper above, certainly the difference between tumor recurrence and radiation necrosis is important, but occasionally, the neurosurgeon will operate even when she or he believes that the diagnosis is radiation necrosis: for example, when the patient has become steroid-dependent.

In a recent interview, Freeman Dyson, a world-leading intellectual and physicist, emphasized the difficulty of establishing complementarity between the human (analog) and machine (digital) worlds.<sup>5</sup> It is hard to reduce a person to 1s and 0s. Yes, I realize that this is what we do in radiology, but we also have to understand that this is a rather substantial limitation of our field.

An example of the necessity of “human” input in image interpretation is the clinical history. We all realize that it is suboptimal to read films in a clinical vacuum. A telling example is from the preoperative assessment of language localization in patients with brain tumor by using fMRI. The American Society of Functional Neuroradiology explicitly endorses physical examination of the patient before the fMRI study. Why? Because one will interpret the exact same imaging findings differently based on the clinical examination: if a patient with a left inferior frontal gyrus glioma demonstrates right Broca area lateralization and clinically exhibits signs of expressive aphasia, I will strongly suggest that the result of my fMRI examination is a false-negative.<sup>6</sup> It would be impossible to make such a finding based on the imaging findings alone, no matter how sophisticated the image analysis.

Will computers come up with new and interesting ways to interpret imaging studies (like the present paper)? I am sure that

they will, just like they come up with eerily brilliant moves in chess. Will computers be able to assess seemingly unique human characteristics such as empathy or compassion some time in the future? Possibly, but probably not before I retire.

I would like to leave the reader with 2 final thoughts. Automated assembly lines for cars have existed for over a century. Yet, Rolls-Royce still makes cars by hand. Also, recently, Mercedes-Benz actually reverted from robots back to German workers because “robots can’t deal with the degree of individualization and the many variants that we have today.”<sup>7</sup> An interesting thought.

## REFERENCES

1. Tiwari P, Prasanna P, Wolansky L, et al. **Computer-extracted texture features to distinguish cerebral radionecrosis from recurrent brain tumors on multiparametric MRI: a feasibility study.** *AJNR Am J Neuroradiol* 2016 Sep 15. [Epub ahead of print] CrossRef Medline
2. Turner M. Wall Street analysts are predicting their own grim fate. <http://www.businessinsider.com/equity-research-analysts-face-uncertain-future-2016-8>. Accessed September 23, 2016
3. Arbesman S. *Overcomplicated: Technology at the Limits of Comprehension*. New York: Current; 2016
4. Davenport T, Kirby J. *Only Humans Need Apply: Winners and Losers in the Age of Smart Machines*. New York: Harper Business; 2016
5. Holodny E. Legendary physicist Freeman Dyson talks about math, nuclear rockets, and astounding things about the universe. <http://www.businessinsider.com/freeman-dyson-interview-2016-9>. Accessed September 23, 2016
6. Fraga de Abreu VH, Peck KK, Petrovich-Brennan NM, et al. **Brain tumors: the influence of tumor type and routine MR imaging characteristics at BOLD functional MR imaging in the primary motor gyrus.** *Radiology* 2016 Jul 7:151951. [Epub ahead of print] CrossRef Medline
7. Behrmann E, Rauwald C. Mercedes boots robots from the production line. <http://www.bloomberg.com/news/articles/2016-02-25/why-mercedes-is-halting-robots-reign-on-the-production-line>. Accessed September 23, 2016

**A.I. Holodny**

Department of Radiology  
Memorial Sloan-Kettering Cancer Center  
New York, New York

<http://dx.doi.org/10.3174/ajnr.A5002>

# CT Perfusion in Acute Lacunar Stroke: Detection Capabilities Based on Infarct Location

J.C. Benson, S. Payabvash, S. Mortazavi, L. Zhang, P. Salazar, B. Hoffman, M. Oswood, and A.M. McKinney

## ABSTRACT

**BACKGROUND AND PURPOSE:** Recent studies demonstrated superiority of CTP to NCCT/CTA at detecting lacunar infarcts. This study aimed to assess CTP's capability to identify lacunae in different intracranial regions.

**MATERIALS AND METHODS:** Over 5.5 years, 1085 CTP examinations were retrospectively reviewed in patients with acute stroke symptoms with CTP within 12 hours and MRI within 7 days of symptom onset. Patients had infarcts  $\leq 2$  cm or no acute infarct on DWI; patients with concomitant infarcts  $> 2$  cm on DWI were excluded. CTP postprocessing was automated by a delay-corrected algorithm. Three blinded reviewers were given patient NIHSS scores and symptoms; infarcts were recorded based on NCCT/CTA, CTP (CBF, CBV, MTT, and TTP), and DWI.

**RESULTS:** One hundred thirteen patients met inclusion criteria (53.1% female). On DWI, lacunar infarcts were present in 37 of 113 (32.7%), and absent in 76 of 113 (67.3%). On CTP, lacunar infarcts typically appeared as abnormalities larger than infarct size on DWI. Interobserver  $\kappa$  for CTP ranged from 0.38 (CBF) ( $P < .0001$ ) to 0.66 (TTP) ( $P < .0001$ ); interobserver  $\kappa$  for DWI was 0.88 ( $P < 0.0001$ ). In all intracranial regions, sensitivity of CTP ranged from 18.9% (CBV) to 48.7% (TTP); specificity ranged from 97.4% (CBF and TTP) to 98.7% (CBV and MTT). CTP's sensitivity was highest in the subcortical white matter with or without cortical involvement (21.7%–65.2%) followed by periventricular white matter (12.5%–37.5%); sensitivity in the thalami or basal ganglia was 0%.

**CONCLUSIONS:** CTP has low sensitivity and high specificity in identifying lacunar infarcts. Sensitivity is highest in the subcortical white matter with or without cortical involvement, but limited in the basal ganglia and thalami.

**ABBREVIATIONS:** CSWM = subcortical white matter with or without involvement of the cortex; PVWM = periventricular white matter

Lacunar infarcts are ischemic insults that predominantly result from the occlusion of single perforating arteries.<sup>1</sup> Typically, lacunae occur within the thalami, basal ganglia, brain stem, corona radiata, or internal capsule.<sup>2–4</sup> Although lacunar infarcts predominantly occur secondary to small vessel disease, other etiologies such as cardiac emboli and vasculitis also have been described.<sup>5</sup> Lacunar strokes are a common cause of morbidity and account for up to 25% of all ischemic strokes.<sup>6,7</sup> Classically, symp-

toms of lacunar infarcts include pure sensory syndrome, pure motor hemiparesis, sensorimotor stroke, ataxic hemiparesis, or dysarthria-clumsy hand syndrome.<sup>2,8</sup> Thrombolytic therapy has been shown to be effective in the treatment of acute lacunar stroke, making the timely and accurate diagnosis of lacunar infarcts of utmost importance.<sup>9</sup>

NCCT is less sensitive than DWI in the detection of lacunar strokes, with reported sensitivities ranging from 0%–35% for NCCT and 75%–95% for DWI.<sup>10–13</sup> Nevertheless, because CT remains more accessible than MR imaging in emergency settings, its optimization in the diagnosis of stroke continues to be vital.<sup>14</sup> Recently, CTP has been shown to be superior to NCCT and CTA in assessing for lacunar infarcts.<sup>4,15</sup> However, neither of the recent studies directly compared CTP with NCCT/CTA in the detection of lacunae: Rudilosso et al<sup>15</sup> assessed the use of CTP in patients with clinical lacunar syndrome, and Das et al<sup>4</sup> investigated the use of CTP as part of a multimodal approach in the setting of lacunar infarction, noting only that 61% of patients had an abnormality on CTP concordant with infarction on DWI. Furthermore, nei-

Received April 5, 2016; accepted after revision June 27.

From the Department of Radiology (J.C.B., S.P., S.M., A.M.M.) and Clinical and Translational Science Institute (L.Z., P.S.), University of Minnesota Medical Center, Minneapolis, Minnesota; Vital Images, a division of Toshiba Medical (B.H., M.O.), Minnetonka, Minnesota; and Department of Radiology (B.H., M.O.), Hennepin County Medical Center, Minneapolis, Minnesota.

Paper previously presented at: Annual Meeting of the American Society of Neuroradiology, May 23–26, 2016; Washington, DC.

All authors have participated sufficiently to take public responsibility for content.

Please address correspondence to John C. Benson, MD, University of Minnesota Medical Center, MMC 292, B-212 Mayo, 420 Delaware St SE, Minneapolis, MN 55455; e-mail: benso905@umn.edu

<http://dx.doi.org/10.3174/ajnr.A4904>

ther study investigated CTP's capability to detect lacunae within specific regions of the brain.

The purpose of this study was to compare the diagnostic performance of CTP with NCCT/CTA in the identification of acute lacunar infarcts and evaluate the diagnostic capabilities of CTP in the detection of lacunar strokes within different areas of the brain.

## MATERIALS AND METHODS

### Patient Selection

This study was completed at a level 1 trauma center and primary stroke center. Institutional review board approval was obtained for this study. A retrospective review of all patients who presented with symptoms of acute stroke between January 2006 and July 2011 was performed; 1085 patients with CTP examinations were identified. Patients were included if they underwent acute CTP imaging within 12 hours of symptom onset, as well as DWI within 7 days of presentation. One investigator manually measured the longest axial diameter of foci of restricted diffusion on DWI, if present. Patients were included if they had either 1) negative DWI or 2) one or more infarcts <20 mm in maximum diameter on DWI. The size of 20 mm as the uppermost criterion for lacunar infarcts was chosen based on prior studies implicating this as a clinically applicable measurement.<sup>4,16</sup> Exclusion criteria were: 1) infarct >20 mm in diameter, 2) lacunar stroke with coexisting large (>20 mm maximum diameter) infarct, 3) nonoptimal quality of either CTP or DWI (eg, technical problems such as motion), and 4) administration of intravenous tPA between the time of CTP and DWI acquisitions.

### DWI and CTP Acquisition and Postprocessing

MR imaging scans were performed on 2 different scanners (Ingenia 1.5T and Ingenia 3T MR scanners; Philips Medical Systems, Best, the Netherlands). On the 1.5T scanner, the sequence parameters were: TR = 3526, TE = 92, flip angle = 90°, EPI factor = 45, 2.4 acceleration (SENSE) factor, 3 directions of measurement, 16 cm FOV, 131 × 131 matrix, 5-mm section thickness. On the 3T scanner, the sequence parameters were: TR = 3832, TE = 84, flip angle = 90°, EPI factor = 51, 2.4 acceleration (SENSE) factor, 3 directions of measurement, 14 cm FOV, 152 × 121 matrix, 4-mm section thickness. Both scanners used 16-channel head coils. Foci of diffusion were measured in the longest axial axis. DWI b-value was  $b = 1000$  for all studies.

Every patient was imaged as part of the same protocol used for emergent strokes at our institution: an NCCT was immediately followed by multidetector CTA; CTP images were obtained <5 minutes later. For NCCT, FOV was 25 cm, with 512 × 512 matrix and 3-mm sections; for CTA, FOV was 22 cm, with 512 × 512 matrix and 0.9-mm sections. CTA is performed before CTP to minimize venous contamination on CTA scans; in several years' experience with this imaging protocol, the venous contamination noted on CTP images is minimal.<sup>17</sup> CTP images were not obtained if hemorrhage was visualized on the NCCT by the daytime hours staff, on-site radiology resident, or neuroradiology fellow; patients with hemorrhage did not meet the study's inclusion criteria.

A 64-section multidetector scanner was used to perform all CT scans (Brilliance CT; Philips Medical Systems). All CTP sequences

were completed by using 2 first-pass acquisitions of sequential 55–60 second dynamic injections/scans (1 image/s) with no delay between the acquisitions. Two acquisitions were completed because each included 40 mm of coverage; hence, 1 acquisition was set at the level of the basal ganglia, and the second was set at the level of the superior margin of the ventricles. According to the manufacturer, 55–60 second dynamic acquisitions were used based on several years' experience before this study of dynamic timing that minimized truncation effect. A truncation is applied to exclude the recirculation for the computation of CBV, with only the first-pass contrast taken into account for CBV. Each acquisition yielded 4 contiguous sections (25 cm FOV, 512 × 512 matrix, 10-mm section thickness, 32 × 1.25 mm collimation, 80 kV, 120 mAs), with a total of 40 mm of coverage. A bolus of 36–40 mL of nonionic contrast (iohexol [Omnipaque 350 mg/mL; GE Healthcare, Piscataway, New Jersey]) was intravenously administered for each acquisition via a power injector at a rate of 6.0 mL/s for a total of 72–80 mL of intravenous contrast for each CTP scan. A saline flush was administered between the acquisition of CTA and CTP imaging, but not between the 2 CTP acquisitions. Typically, the inferior margins of each CTP acquisition were the inferior margin of the basal ganglia and the midcentrum semiovale superiorly. The margins were occasionally adjusted if a suspected infarct was identified on the NCCT by the radiology resident or neuroradiology fellow.

CTP postprocessing was completed on a Vitrea workstation (Vital Images, Minnetonka, Minnesota). CTP postprocessing was automated by a delay-corrected singular value decomposition algorithm; the workstation's postprocessing software uses a deconvolution-based delay-corrected singular value decomposition algorithm via interhemispheric comparison (side-to-side). The interhemispheric comparison performed by the postprocessing software is done by using a multistep approach: 1) the midline of the brain is automatically located (but can be manually corrected, if necessary), 2) the affected side is automatically identified by using TTP maps, and 3) MTT, TTP, CBV, and CBF in the affected side are automatically compared with the corresponding parameters in the contralateral side by using relative differences between each voxel. Arterial input functions were selected from the anterior cerebral artery, and venous functions were selected from the posterior segment of the superior sagittal sinus; automatic selection was used, which was verified before the finalization of images.

### Image Review and Interpretation

Three staff neuroradiologists (2 with >10 years' experience, 1 with 1.5 years' experience), who had been blinded to the final results, independently reviewed the DWI, NCCT, CTA, and CTP images. Each reviewer was given the patient NIHSS score and symptoms at the time of presentation; the reviewers were otherwise blinded to the patient interpretative reports and the other reviewers' interpretations. The neuroradiologists assessed for the presence of stroke by using 4 different independent CTP parameters: CBF, CBV, MTT, and TTP. Presence or absence of stroke was then assessed on all imaging sequences; NCCT, CTA, and CTP images were reviewed first, and DWI was reviewed afterward to blind the review of CTA and perfusion data to the DWI results. Stroke locations were divided into the subcortical white matter

with or without involvement of the overlying cortex (CSWM), periventricular white matter (PVWM), basal ganglia and/or thalamus, cerebellum, and brain stem. Brain stem and cerebellar infarcts ( $n = 9$ ) were ultimately excluded because the CTP margins did not extend inferiorly enough to encompass strokes in those locations; 1 infarct in the PVWM was also excluded because the CTP images did not fully include the infarct. Interpretations were considered correct if 2 or more reviewers agreed on the results.

NCCT/CTA and CTP findings were subsequently compared with DWI. Using DWI as the “criterion standard,” findings were denoted as true-positive results if: 1) the abnormalities on NCCT/CTA corresponded with the same areas as the infarcts on DWI or 2) regional abnormalities on CTP included the area of lacunar infarction on DWI. Abnormalities on NCCT/CTA and CTP were marked as false-positives if: 1) no infarct was present on DWI or 2) the infarct on DWI was in a different location than that of the CTP. A single neuroradiologist graded the amount of chronic small vessel ischemic disease based on a grading scale: 1 (non-minimal), 2 (mild-moderate), 3 (moderate), 4 (moderate-severe), and 5 (severe).

### Statistical Analysis

Intra- and interobserver agreement was calculated by using the Cohen  $\kappa$ . The sensitivity and specificity of the NCCT/CTA and independent CTP parameters (CBF, CBV, MTT, and TTP) in each area of the brain (basal ganglia and/or thalamus, CSWM, PVWM) were calculated. A  $P$  value of  $<.05$  was considered statistically significant. Statistical analysis was performed by using

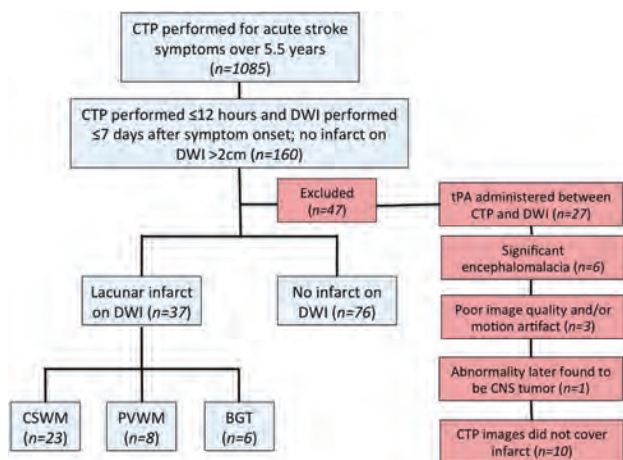


**FIG 1.** Flowchart of patient population. Infarcts in the cerebellum and brain stem were excluded because these were not adequately covered by the CTP images. BGT indicates basal ganglia and/or thalamus.

### Sensitivity, specificity, PPV, and NPV for NCCT/CTA and CTP (based on perfusion parameters) in the detection of acute lacunar infarct

Imaging Modality	Sensitivity	Specificity	PPV	NPV
NCCT/CTA	2.7% ( $P < .0001$ )	100.0% ( $P < .0001$ )	100.0% ( $P < .99$ )	68.1% ( $P < .0001$ )
CBF	24.3% ( $P < .003$ )	97.4% ( $P < .0001$ )	81.8% ( $P = .07$ )	72.8% ( $P < .0001$ )
CBV	18.9% ( $P = .0002$ )	98.7% ( $P < .0001$ )	87.5% ( $P = .07$ )	71.4% ( $P < .0001$ )
TTP	48.7% ( $P < .99$ )	97.4% ( $P < .0001$ )	90.0% ( $P = .0004$ )	80.0% ( $P < .0001$ )
MTT	35.1% ( $P = .10$ )	99.7% ( $P < .0001$ )	92.9% ( $P = .002$ )	76.0% ( $P < .0001$ )

**Note.**—NPV indicates negative predictive value; PPV, positive predictive value.

Statistical Analysis Software (SAS; SAS Institute, Cary, North Carolina). Charts were created in Microsoft PowerPoint Version 14.6 (Microsoft, Redmond, Washington).

## RESULTS

### Patient Population

One hundred sixty patients underwent CTP imaging within 12 hours and DWI within 7 days of symptom onset, with or without lacunar infarction on DWI. Of these, 27 were excluded because they received tPA between the CTP and DWI, 10 were excluded because the CTP images did not adequately involve the area of infarction (9 in the brain stem or cerebellum and 1 in the PVWM), 6 were excluded because of the presence of encephalomalacia (eg, from prior stroke), 3 were excluded because the examination was limited by motion and/or other types of artifact distortion, and 1 was excluded because the abnormality was later found to be a tumor (Fig 1). Thus, 113 patients were included for this study cohort; 37 (32.7%) had infarction on DWI, and 76 (67.3%) had no infarction. The average age at onset of symptoms was  $59.8 \pm 16.9$  years. Sixty (53.1%) of the included patients were women.

### Infarct Timing and Locations

The average time between symptom onset to CTP imaging was  $2.4 \pm 1.1$  hours for all patients; the average time between CTP and MR imaging was  $0.9 \pm 1.0$  days. The average degree/grade of chronic small vessel ischemic disease on NCCT was  $2.1 \pm 1.3$  for all patients, corresponding to approximately mild-to-moderate disease based on the grading scale used. Of the infarcts noted on DWI, 23 of 37 (62.2%) were located in the CSWM, 8 of 37 (21.6%) in the PVWM, and 6 of 37 (16.2%) in the basal ganglia and/or thalamus. The mean NIHSS score for all studied patients was  $4.0 \pm 5.0$  ( $3.9 \pm 5.6$  for patients with infarct and  $4.1 \pm 4.7$  for patients without infarct). Four patients received tPA before both CTP and MR imaging.

### Imaging Results

Regarding lacunar infarcts in all locations within the brain, CTP sensitivity for the detection of lacunae ranged from 18.9% (CBV) to 48.7% (TTP) depending on perfusion parameter. The sensitivity of NCCT/CTA was 2.7%. False-positive CTP interpretations, in which the consensus CTP was noted to be positive in a patient without infarct on DWI, were observed in all CTP sequences; no false-positive interpretation occurred in NCCT/CTA. Specificity of CTP ranged from 97.4% (CBF and TTP) to 98.7% (CBV and MTT); NCCT/CTA specificity was 100% (Table). Lacunar infarcts typically appeared on CTP images as regional abnormalities larger than the infarcts observed on DWI (Fig 2).

In all locations, the positive predictive value for CTP ranged from 81.8% (CBF) to 92.9% (MTT). The negative predictive value ranged from 71.4% (CBV) to 80.0% (TTP). Regarding interpretation of CTP images, interobserver  $\kappa$  ranged from 0.38 for CBF to 0.66 for TTP ( $P < .0001$  for all). Interobserver  $\kappa$  was 0.88 for DWI ( $P < .0001$ ) and 0.05 for NCCT/CTA ( $P = .18$ ).

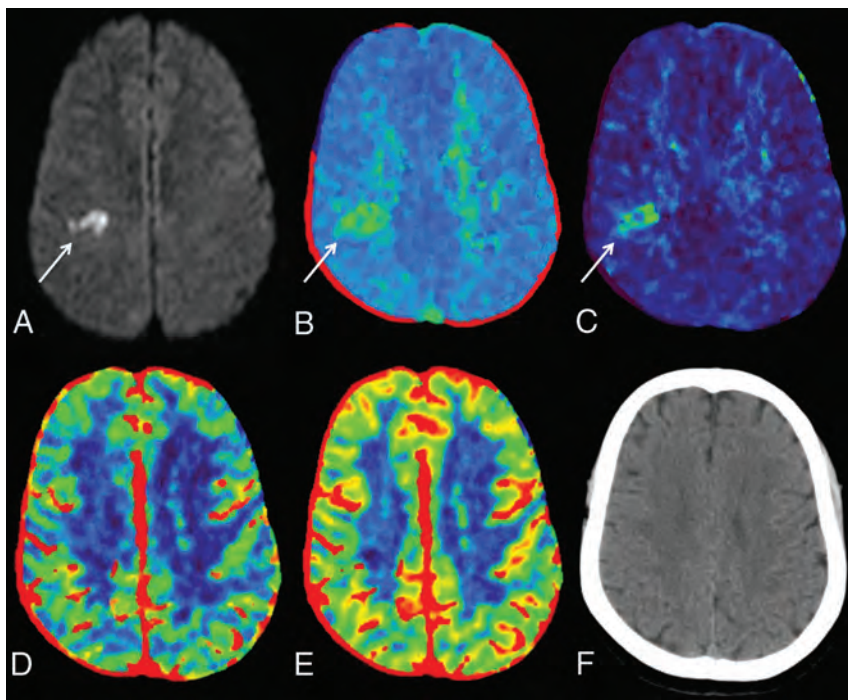


**FIG 2.** A 49-year-old woman who presented with left-sided facial weakness and dysarthria. Infarct within the right centrum semiovale on DWI (A, white arrow) corresponded with focal abnormalities on TTP (B) and MTT (C) images (white arrow on each); the abnormalities on TTP and MTT were slightly larger than the confirmed infarct on DWI. No abnormalities were identified on CBV (D), CBF (E), or NCCT (F).

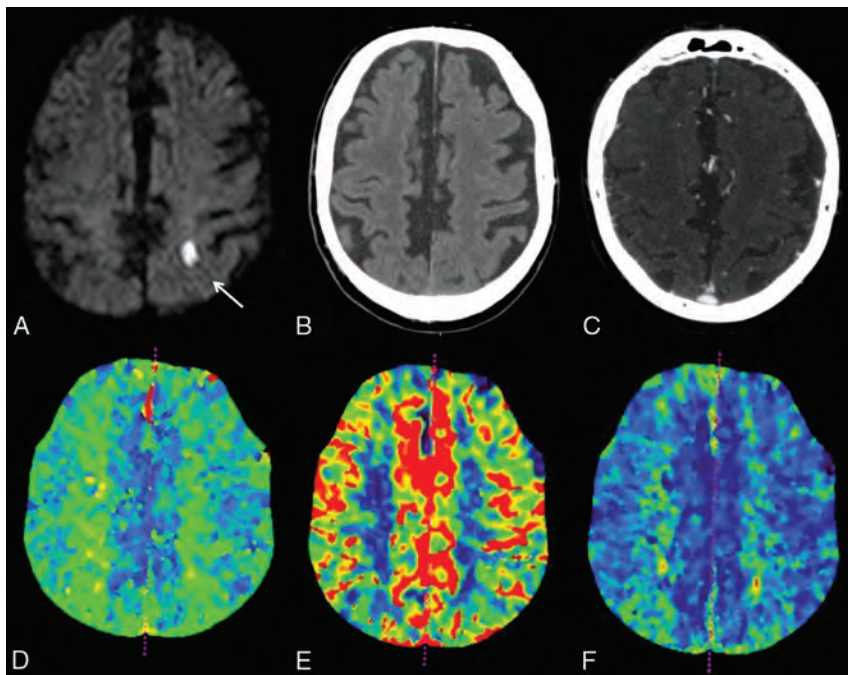


**FIG 3.** Example of a lacunar infarct not visualized on CTP images. A 74-year-old man who presented with right arm weakness. DWI confirmed a lacunar infarct in the left centrum semiovale (A, white arrow). No abnormalities were noted on NCCT (B), CTA (C), TTP (D), CBF (E), or CBV (F).

Conversely, regarding the capability of CTP to detect lacunar infarcts in different intracranial regions, the sensitivity of CTP was highest in the CSWM with TTP (65.2%). Within the PVWM, CTP sensitivity was highest with TTP and MTT (37.5% for both) and lowest with CBF (12.5%) (Fig 3). None of the lacunar infarcts

in the basal ganglia or thalamus were identified by using CTP (0/6). The sensitivity of NCCT/CTA for lacunar infarcts in the basal ganglia and/or thalamus was 16.7%; no lacunar infarcts were identified on NCCT/CTA in the CSWM or PVWM (0/23 and 0/8, respectively). The intracranial location with the highest positive predictive value was the CSWM with MTT (90.9%).

## DISCUSSION

This study set out to determine the capability of CTP to identify acute lacunar strokes. The results indicate that CTP has high specificity in the detection of lacunar strokes, though its sensitivity is low among all perfusion parameters. CTP is best able to detect infarcts in the CSWM, followed by the PVWM; lacunae were not accurately identified on CTP in the basal ganglia or thalamus. Overall, CTP outperformed NCCT/CTA in finding lacunar strokes. The sensitivities of TTP and MTT measured in this study were notably higher than those of CBF and CBV, consistent with past studies that have shown these parameters to be inferior to TTP and MTT as indicators of infarct.<sup>18</sup>

Over half of the lacunae noted on DWI in the present study were located in the subcortical white matter with or without involvement of the overlying cortex; the remaining infarcts were located in the PVWM, basal ganglia, and thalamus. Larger-scale studies have noted that most lacunar strokes occur in either the lentiform nuclei or thalamus.<sup>19</sup> The small number of lentiform and or thalamic lacunae in this study might be related to a relatively small cohort. Nevertheless, it is notable that none of the infarcts in the basal ganglia or thalamus were accurately identified on CTP. The cerebellum and brain stem were not adequately covered by the CTP images and consequently were not assessed in this study, which is a limitation.

A recent study by Das et al<sup>4</sup> indicated that CTP had added value to NCCT alone in the setting of lacunar infarcts.

However, reported sensitivities of CTP for detecting strokes < 2 cm have been quite variable; Mayer et al<sup>20</sup> stated that lacunar strokes were difficult to distinguish from artifact on CTP imaging, and other authors have cited sensitivities as low as 0% and as high as 47.4%–62.5%.<sup>10,15,21</sup> Furthermore, a systematic review by

Biesbroek et al<sup>22</sup> noted that approximately two-thirds of false-negative findings on CTP were lacunae, and a study by Eckert et al<sup>23</sup> noted that the most common cause of false-negative multimodal CT imaging was lacunar infarcts. Although the reason for this inconsistency among studies is not clear, it is likely that the variability is at least in part because of differences in the designs of the studies (eg, whether there was a known lacunar stroke and whether the reviewers were blinded). In addition, the parameters used in each study, such as time-to-maximum versus TTP, might have contributed to differences in reported sensitivities. The present study provided reviewers with patient NIHSS scores as well as presenting symptoms; thus, the results of this study might better reflect the sensitivity of lacunar infarct detection in a clinical setting.

In addition, differences in reported sensitivities of lacunar infarct detection might be attributed to the use of delay-sensitive singular value decomposition algorithms in some studies. Prior studies by Sasaki et al<sup>24</sup> and Kudo et al<sup>25</sup> have demonstrated the superior accuracy of delay-corrected singular value decomposition algorithms in CTP in acute infarcts. Delay-sensitive singular value decomposition algorithms have been shown to overestimate MTT prolongation and CBF reduction in acute stroke, thus falsely increasing their sensitivity to infarcts.<sup>24</sup> A recent study by Cao et al<sup>26</sup> also used delay-corrected singular value decomposition to assess for lacunar infarcts; the reviewers were similarly blinded to DWI results, but were aware of the patients' presenting symptoms. The authors of that study reported a superior sensitivity of MTT (56%) compared with the results of the current study, but similarly noted high specificities (100% for CBV, CBF, and MTT).

Although the presence of stroke on CTP appears to be fairly specific for infarction, the infarct size on CTP often did not correlate with the focus of restricted diffusion on DWI. In many patients, the defects on CTP appeared as regional abnormalities corresponding to, but larger than, the location of the lacunar stroke. In contrast, a recent study by Rudilosso et al<sup>15</sup> noted focal defects on CTP that more accurately estimated infarct size on DWI. The present study did not set specific CTP thresholds, which might have contributed to the mismatch in infarct sizes observed in CTP and DWI (ie, the area of restricted diffusion might have represented the infarct "core," whereas the observed abnormalities on CTP might have represented a wider zone of ischemia). Alternatively, abnormalities on CTP might have represented the cumulative effect of multiple lacunar infarcts within the same region; although patients with coexistent infarcts >2 cm were excluded, some patients had multiple lacunae that might have contributed to additional findings.

This study has limitations shared by any retrospective study. In addition, CTP sections did not adequately cover the brain stem or cerebellum, limiting our evaluation of its diagnostic capabilities in those regions. In addition, there was a temporal difference between the acquisition of CTP and DWI in some patients, which might have biased the results. Also, infarcts might have formed and/or increased in size between the acquisition of CTP and DWI. We sought to minimize any artifact differences by excluding patients who received tPA therapy between the 2 examinations. Next, as stated above, thresholds for CTP were not established for

this study. However, the purpose of this study was to assess CTP's ability to identify infarcts rather than measure CTP's capability to estimate infarct core. In addition, only a small number of subjects ( $n = 6$ ) had infarcts within the basal ganglia and/or thalamus, limiting the assessment of CTP capabilities within those regions. Finally, although this study assessed the use of CTP to visually detect positive lacunae based on decreased perfusion and increased delay, no specific measurement or threshold was used.

## CONCLUSIONS

This study found that CTP is superior to NCCT/CTA in the detection of acute lacunar infarcts. The specificity was high for lacunar infarct detection by using all of the studied perfusion parameters, but the sensitivity was lower than DWI. CTP is best able to delineate lacunae within the CSWM, followed by the PVWM, but did not accurately identify lacunar strokes within the basal ganglia or thalamus. Further work is necessary to determine which parameter (eg, TTP, MTT, time-to-maximum) best detects lacunae, and a prospective head-to-head comparison of such parameters might be useful.

Disclosures: Alexander McKinney—RELATED: Provision of Writing Assistance, Medicines, Equipment, or Administrative Support: Vital Images, Comments: provided equipment in 2013 that was used in this study; UNRELATED: Consultancy: Vital Images (a division of Toshiba Medical, Minnetonka, Minnesota), Comments: <\$5000 total in 2015–16; Expert Testimony: <\$10,000 legal consultancy in 2015–16. Pascal Salazar—Employment: Vital Images.

## REFERENCES

1. Micheli S, Corea F. **Lacunar versus non-lacunar syndromes.** *Front Neurol Neurosci* 2012;30:94–98 CrossRef Medline
2. Altmann M, Thommessen B, Rønning OM, et al. **Diagnostic accuracy and risk factors of the different lacunar syndromes.** *J Stroke Cerebrovasc Dis* 2014;23:2085–90 CrossRef Medline
3. Hommel M, Besson G, Le Bas JF, et al. **Prospective study of lacunar infarction using magnetic resonance imaging.** *Stroke* 1990;21:546–54 CrossRef Medline
4. Das T, Settecase F, Boulous M, et al. **Multimodal CT provides improved performance for lacunar infarct detection.** *AJNR Am J Neuroradiol* 2015;36:1069–75 CrossRef Medline
5. Caso V, Budak K, Georgiadis D, et al. **Clinical significance of detection of multiple acute brain infarcts on diffusion weighted magnetic resonance imaging.** *J Neurol Neurosurg Psychiatry* 2005;76:514–18 CrossRef Medline
6. Norrving B. **Long-term prognosis after lacunar infarction.** *Lancet Neurol* 2003;2:238–45 CrossRef Medline
7. Norrving B. **Evolving concept of small vessel disease through advanced brain imaging.** *J Stroke* 2015;17:94–100 CrossRef Medline
8. Arboix A, Martí-Vilalta JL. **Lacunar stroke.** *Expert Rev Neurother* 2009;9:179–96 CrossRef Medline
9. Pantoni L, Fierini F, Poggesi A. **Thrombolysis in acute stroke patients with cerebral small vessel disease.** *Cerebrovasc Dis* 2014;37:5–13 CrossRef Medline
10. Hana T, Iwama J, Yokosako S, et al. **Sensitivity of CT perfusion for the diagnosis of cerebral infarction.** *J Med Invest* 2014;61:41–45 CrossRef Medline
11. Chamorro A, Sacco RL, Mohr JP, et al. **Clinical-computed tomographic correlations of lacunar infarction in the Stroke Data Bank.** *Stroke* 1991;22:175–81 CrossRef Medline
12. Smajlović D, Sinanović O. **Sensitivity of the neuroimaging techniques in ischemic stroke.** *Med Arh* 2004;58:282–84 Medline
13. Lai PH, Li JY, Chang CY, et al. **Sensitivity of diffusion-weighted magnetic resonance imaging in the diagnosis of acute lacunar infarcts.** *J Formos Med Assoc* 2001;100:370–76 Medline

14. Wintermark M, Bogousslavsky J. **Imaging of acute ischemic brain injury: the return of computed tomography.** *Curr Opin Neurol* 2003; 16:59–63 CrossRef Medline
15. Rudilosso S, Urra X, San Román L, et al. **Perfusion deficits and mismatch in patients with acute lacunar infarcts studied with whole-brain CT perfusion.** *AJNR Am J Neuroradiol* 2015;36:1407–12 CrossRef Medline
16. Potter GM, Marlborough FJ, Wardlaw JM. **Wide variation in definition, detection, and description of lacunar lesions on imaging.** *Stroke* 2011;42:359–66 CrossRef Medline
17. Leiva-Salinas C, Provenzale JM, Wintermark M. **Responses to the 10 most frequently asked questions about perfusion CT.** *AJR Am J Roentgenol* 2011;196:53–60 CrossRef Medline
18. Tomandl BF, Klotz E, Handschu R, et al. **Comprehensive imaging of ischemic stroke with multisection CT.** *Radiographics* 2003;23: 565–92 CrossRef Medline
19. Longstreth WT Jr, Bernick C, Manolio TA, et al. **Lacunar infarcts defined by magnetic resonance imaging of 3660 elderly people: the Cardiovascular Health Study.** *Arch Neurol* 1998;55:1217–25 CrossRef Medline
20. Mayer TE, Hamann GF, Baranczyk J, et al. **Dynamic CT perfusion imaging of acute stroke.** *AJNR Am J Neuroradiol* 2000;21:1441–49 Medline
21. Maruya J, Yamamoto K, Ozawa T, et al. **Simultaneous multi-section perfusion CT and CT angiography for the assessment of acute ischemic stroke.** *Acta Neurochir (Wien)* 2005;147:383–91; discussion 391–92 CrossRef Medline
22. Biesbroek JM, Niesten JM, Dankbaar JW, et al. **Diagnostic accuracy of CT perfusion imaging for detecting acute ischemic stroke: a systematic review and meta-analysis.** *Cerebrovasc Dis* 2013;35:493–501 CrossRef Medline
23. Eckert B, Küsel T, Leppien A, et al. **Clinical outcome and imaging follow-up in acute stroke patients with normal perfusion CT and normal CT angiography.** *Neuroradiology* 2011;53:79–88 CrossRef Medline
24. Sasaki M, Kudo K, Ogasawara K, et al. **Tracer delay-insensitive algorithm can improve reliability of CT perfusion imaging for cerebrovascular steno-occlusive disease: comparison with quantitative single-photon emission CT.** *AJNR Am J Neuroradiol* 2009;30:188–93 CrossRef Medline
25. Kudo K, Sasaki M, Ogasawara K, et al. **Difference in tracer delay-induced effect among deconvolution algorithms in CT perfusion analysis: quantitative evaluation with digital phantoms.** *Radiology* 2009;251:241–49 CrossRef Medline
26. Cao W, Yassi N, Sharma G, et al. **Diagnosing acute lacunar infarction using CT perfusion.** *J Clin Neurosci* 2016;29:70–72 CrossRef Medline

# Comparison of High-Resolution MR Imaging and Digital Subtraction Angiography for the Characterization and Diagnosis of Intracranial Artery Disease

 N.J. Lee,  M.S. Chung,  S.C. Jung,  H.S. Kim,  C.-G. Choi,  S.J. Kim,  D.H. Lee,  D.C. Suh,  S.U. Kwon,  D.-W. Kang, and  J.S. Kim



## ABSTRACT

**BACKGROUND AND PURPOSE:** High-resolution MR imaging has recently been introduced as a promising diagnostic modality in intracranial artery disease. Our aim was to compare high-resolution MR imaging with digital subtraction angiography for the characterization and diagnosis of various intracranial artery diseases.

**MATERIALS AND METHODS:** Thirty-seven patients who had undergone both high-resolution MR imaging and DSA for intracranial artery disease were enrolled in our study (August 2011 to April 2014). The time interval between the high-resolution MR imaging and DSA was within 1 month. The degree of stenosis and the minimal luminal diameter were independently measured by 2 observers in both DSA and high-resolution MR imaging, and the results were compared. Two observers independently diagnosed intracranial artery diseases on DSA and high-resolution MR imaging. The time interval between the diagnoses on DSA and high-resolution MR imaging was 2 weeks. Interobserver diagnostic agreement for each technique and intermodality diagnostic agreement for each observer were acquired.

**RESULTS:** High-resolution MR imaging showed moderate-to-excellent agreement (interclass correlation coefficient = 0.892–0.949;  $\kappa$  = 0.548–0.614) and significant correlations ( $R$  = 0.766–0.892) with DSA on the degree of stenosis and minimal luminal diameter. The interobserver diagnostic agreement was good for DSA ( $\kappa$  = 0.643) and excellent for high-resolution MR imaging ( $\kappa$  = 0.818). The intermodality diagnostic agreement was good ( $\kappa$  = 0.704) for observer 1 and moderate ( $\kappa$  = 0.579) for observer 2, respectively.

**CONCLUSIONS:** High-resolution MR imaging may be an imaging method comparable with DSA for the characterization and diagnosis of various intracranial artery diseases.

**ABBREVIATIONS:** HR-MR = high-resolution MR imaging; ICAD = intracranial artery disease; ICC = interclass correlation coefficient

Intracranial artery disease (ICAD) is one of the major causes of ischemic stroke and neurologic symptoms.<sup>1–3</sup> ICAD generally presents with intracranial artery stenosis on luminal evaluation, even though it includes various ICADs, such as atherosclerosis,

dissection, Moyamoya disease, and vasculitis. The degree of stenosis has been the most common and important characteristic for evaluating ICAD and determining the treatment options.<sup>4,5</sup>

Luminal angiography, such as digital subtraction angiography, CT angiography, and MR angiography, has been widely used and has functioned successfully for the evaluation of stenosis and the diagnosis of ICAD. Among these methods, DSA is thought to be the criterion standard tool compared with the other modalities because it depicts luminal geometric shapes and hemodynamic information with higher resolution.<sup>6–8</sup> However, DSA has several limitations. It only depicts the luminal morphology and not the vessel walls directly, and many diseases share nonspecific luminal findings. Because DSA is also an invasive procedure with the risk of neurologic complications and radiation exposure, it is not suitable for screening or serial examinations.<sup>9–11</sup> Accordingly, CTA and MRA have been commonly used as the minimally invasive method to diagnose and differentiate intracranial artery disease in the clinical field, though they have more drawbacks in the luminal evaluation to DSA.

Received April 7, 2016; accepted after revision July 22.

From the Department of Radiology and Research Institute of Radiology (N.J.L., M.S.C., S.C.J., H.S.K., C.-G.C., S.J.K., D.H.L., D.C.S.) and Department of Neurology (S.U.K., D.-W.K., J.S.K.), University of Ulsan College of Medicine, Asan Medical Center, Seoul, Korea.

The authors declare no relationships with any companies whose products or services may be related to the subject matter of the article.

This work was supported by a grant from the Korea Healthcare Technology R&D Project, Ministry for Health, Welfare, and Family Affairs, Republic of Korea (H112C1847).

Paper previously presented orally at: Annual Meeting of the European Congress of Radiology, March 2–6, 2016; Vienna, Austria.

Please address correspondence to Seung Chai Jung, MD, PhD, Department of Radiology and Research Institute of Radiology, University of Ulsan College of Medicine, Asan Medical Center, 86 Asanbyeongwon-Gil, Songpa-Gu, Seoul 138–736, Republic of Korea; e-mail: dynamics79@gmail.com

 Indicates open access to non-subscribers at [www.ajnr.org](http://www.ajnr.org)

 Indicates article with supplemental on-line photo.

<http://dx.doi.org/10.3174/ajnr.A4950>

High-resolution MR imaging (HR-MR) has recently been introduced as a minimally invasive and promising advanced imaging technique for directly depicting the intracranial arterial wall.<sup>12,13</sup>

Although HR-MR evaluates and differentiates various ICADs with the direct depiction of arterial walls and multicontrast images<sup>6,14-20</sup> that may correlate with luminal angiography,<sup>8,21,22</sup> the usefulness and value of HR-MR compared with luminal angiography are still unclear. Only a few studies presented a comparison or correlation between DSA and HR-MR,<sup>8,13,23</sup> and these studies showed a good correlation regarding the degree of stenosis<sup>8,23</sup> and HR-MR features beyond DSA.<sup>13</sup> However, the observations were based on single vascular pathology or a single cerebral artery (middle cerebral artery, basilar artery) or a small sample size ( $n = 9$ ).

In our study, we compared HR-MR with DSA in the characterization and diagnosis of various ICADs. We hypothesized that HR-MR may be an imaging method comparable with DSA for the characterization and diagnosis of ICAD.

## MATERIALS AND METHODS

This retrospective study was approved by our institutional review board, and patient informed consent was waived. The stipulation regarding obtaining informed consent from study patients was waived. Patient information was anonymized and de-identified before the assessment.

### Patients

From August 2011 to April 2014, 79 patients underwent both DSA and HR-MR in our hospital. Of them, 42 patients were excluded because the imaging was performed for aneurysms and extracranial artery disease and had time intervals beyond 1 month between the 2 imaging methods. Finally, 37 patients were retrospectively enrolled. These patients were admitted to our hospital with intracranial artery disease. DSA and HR-MR were performed within 1 month. There were 18 male and 19 female patients with a mean age of 51 years (range, 17–74 years of age); 44 intracranial arteries were included in our study. These included the middle cerebral artery ( $n = 31$ ), vertebral artery ( $n = 7$ ), basilar artery ( $n = 2$ ), internal carotid artery ( $n = 1$ ), anterior cerebral artery ( $n = 1$ ), posterior inferior cerebellar artery ( $n = 1$ ), and multiple cerebral arteries ( $n = 1$ ). Seven patients had bilateral middle cerebral artery disease. The patients were admitted with ischemic symptoms ( $n = 21$ ), headache or neck pain ( $n = 8$ ), dizziness ( $n = 4$ ), headache with ischemia ( $n = 3$ ), and no symptoms ( $n = 1$ ).

### Imaging Protocol

HR-MR was performed with 3D proton-density imaging and 2D proton-density, T1-weighted, T2-weighted, and contrast-enhanced T1-weighted imaging with planes perpendicular to the arterial course by using a 3T scanner with an 8-channel head coil (Achieva; Philips Healthcare, Best, the Netherlands). The 3D proton-density imaging with turbo spin-echo sequences was performed with the following parameters: TR, 2000 ms; TE, 30.7 ms; flip angle, 90°; matrix, 640 × 640; FOV, 180 × 180 mm; section thickness, 0.6 mm; and NEX, 1. The 2D proton-density imaging was performed on the basis of turbo spin-echoes. The protocols

for proton-density imaging were as follows: TR, 2000 ms; TE, 32.7 ms; flip angle, 90°; matrix, 336 × 336; FOV, 100 × 100 mm; section thickness, 1 mm; NEX, 2. For T1-weighted imaging, the parameters were as follows: TR, 1533.2 ms; TE, 8.4 ms; flip angle, 90°; matrix, 512 × 512; FOV, 100 × 100 mm; section thickness, 1 mm; NEX, 2. For T2-weighted imaging, the parameters were as follows: TR, 3178.2 ms; TE, 80 ms; flip angle, 90°; matrix, 512 × 512; FOV, 100 × 100 mm; section thickness, 1 mm; and NEX, 4. Contrast-enhanced T1-weighted imaging was performed after intravenous administration of gadoterate meglumine (Dotarem; Guerbet, Aulnay-sous-Bois, France) at a dose of 0.1 mmol/kg of body weight.

DSA was performed in 4 vessels by using a biplane system, including high-resolution 3D rotational angiography (Artis zee; Siemens, Erlangen, Germany). Transfemoral access was used, and selective injection of contrast medium, iodixanol (320 mg of iodine/mL, Visipaque; GE Healthcare, Piscataway, New Jersey), was performed at a rate of 2.5 mL per second by using an injector (Mark V ProVis; Medrad, Medrad, Indianola, Pennsylvania). The parameters were as follows: matrix, 1024 or 2048; FOV, 320 mm.

### Imaging Analysis

The degree of stenosis and the minimal luminal diameter of an ICAD were independently measured by 2 observers on the basis of the PACS workstation and in-house analysis software based on ImageJ, a public domain, Java-based image-processing program developed at the National Institutes of Health, Bethesda, Maryland, for both DSA and HR-MR. The measurement was performed on the basis of the manual thresholding. The degree of stenosis was assessed on the basis of the Warfarin-Aspirin Symptomatic Intracranial Disease (WASID) trial<sup>24</sup> by measuring the diameter of the residual lumen at the maximal narrowing site by using the formula  $[1 - (\text{diameter of stenosis} / \text{diameter of normal}) \times 100]$  (Fig 1). The normal arterial luminal diameter was measured distal or proximal to the maximal narrowing site.<sup>25</sup> The minimal luminal diameter referred to the measurement at the maximal narrowing site. The degree of stenosis was classified into 3 groups: <50%, 50%–70%, and >70%. In the measurements, 4 arteries were excluded because they were not steno-occlusive lesions (ie, normal variation, aneurysm).

### Diagnosis

Two neuroradiologists independently diagnosed various ICADs on DSA and HR-MR. The clinical information, such as patient age, sex, symptoms, onset of symptoms, examination date of DSA and HR-MR, medical background (ie, hypertension; diabetes mellitus; hyperlipidemia; smoking; alcohol; previous medical history, including heart disease, stroke, trauma, and medication; laboratory findings including hemoglobin A1c, lipid battery, blood pressure, homocysteine, and body mass index), and the number of vascular risk factors for atherosclerosis, was provided to the observers. DSA and HR-MR were respectively reviewed with a 2-week interval for prevention of recall bias. Interobserver agreement for each technique was respectively obtained. For each observer, intermodality agreement was acquired respectively, and agreement and disagreement between the 2 modalities were analyzed.

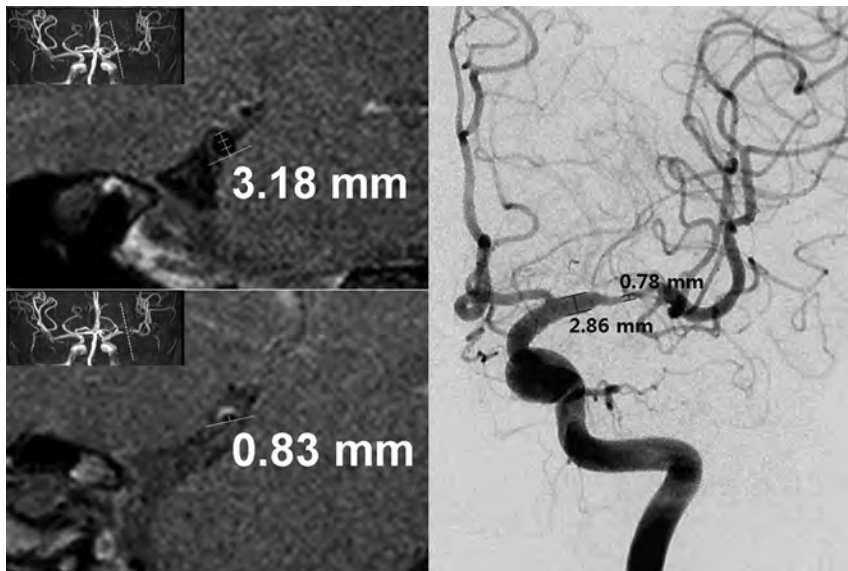


**FIG 1.** Measurements of the degree of stenosis and minimal luminal diameter in both DSA and HR-MR. The degree of stenosis is 73.9% on HR-MR (normal luminal diameter, 3.18 mm; minimal luminal diameter, 0.83 mm) and 72.7% on DSA (normal luminal diameter, 2.86 mm; minimal luminal diameter, 0.78 mm).

### **Atherosclerosis**

Atherosclerosis was diagnosed according to the following criteria: 1) radiologic findings: atherosclerotic stenosis or occlusion (DSA) and eccentric wall thickening (HR-MR) of arteries in the corresponding vascular territory of acute infarction; 2) clinical findings:  $\geq 2$  vascular risk factors according to patient age (men older than 50 years, women older than 60 years), hypertension, diabetes mellitus, hyperlipidemia, obesity, and smoking; and 3) exclusion criteria: cardioembolism,  $> 50\%$  stenosis of extracranial arteries proximal to the symptomatic intracranial stenosis, nonatherosclerotic vasculopathy such as vasculitis, or Takayasu arteritis.<sup>15,26</sup>

### **Dissection**

Dissection was classified as a definite or suspected case according to the Strategies against Stroke Study for Young Adults in Japan criteria.<sup>27</sup> Intimal flap and double lumen were considered definite dissection findings. Suspected dissection included the string of pearls sign, tapered occlusion (DSA), intramural hematoma, and aneurysmal dilation (HR-MR).<sup>27</sup>

### **Moyamoya Disease**

Moyamoya disease is defined as stenosis or occlusion at the terminal portions of the internal carotid artery or the proximal portions of the anterior or middle cerebral artery with abnormal vascular networks.<sup>28-31</sup> According to the guidelines of the Research Committee on Spontaneous Occlusion of the Circle of Willis, Moyamoya disease was classified as definite Moyamoya disease with bilateral lesions or probable Moyamoya syndrome with a unilateral lesion.<sup>30,31</sup> For HR-MR, we added the following diagnostic criteria: severe decrease in the outer diameter relative to the normal artery, thin vessel wall, and mild and diffuse concentric enhancement.<sup>15,18</sup>

### **Vasculitis**

Vasculitis is diagnosed in an exclusive process considering its clinical and radiologic features. Therefore, there is no definite evidence of the presence of other intracranial artery diseases, including atherosclerosis, dissection, and Moyamoya disease. Alternating lesions of stenosis, dilation, and occlusion were suggested as the classic DSA features.<sup>32</sup> Smooth and concentric wall thickening with enhancement in the involved vessels was considered the HR-MR feature.<sup>17,19,26,33</sup>

### **Miscellaneous Diagnoses**

In patients with DSA or HR-MR demonstrating hypoplasia, fenestration, and a tortuous course of the normal artery, normal variation was diagnosed. Localized and blood-filled outward bulging of the arterial wall without a vessel arising from the apex and with surrounding hemorrhage was diagnosed as a ruptured aneurysm.

### **Undetermined Diagnosis**

When a patient could not be diagnosed on the basis of the aforementioned criteria, the diagnosis was classified as undetermined.

### **Statistical Analysis**

Commercially available software (MedCalc for Windows, Version 11.1.1.0; MedCalc Software, Mariakerke, Belgium) was used for the analysis. The Kolmogorov-Smirnov test was used to determine whether the values were normally distributed. For all statistical analyses, a 2-tailed  $P$  value  $< .05$  was considered indicative of a statistically significant difference. The degree of stenosis and minimal luminal diameter were compared by using the paired Wilcoxon signed rank test, and interobserver agreement was assessed by using the interclass correlation coefficient (ICC). Intermodality agreement regarding the measurements between DSA and HR-MR was assessed by using the ICC (continuous values) and Cohen  $\kappa$  (classified stenosis groups,  $< 50\%$ ,  $50\% - 70\%$ ,  $> 70\%$ ), and the Spearman  $R$  was calculated regarding the relationship between DSA and HR-MR. Interobserver and intermodality diagnostic agreement regarding ICAD was analyzed by using the Cohen  $\kappa$ . The proportions of undetermined diagnoses were compared between DSA and HR-MR by using the McNemar test. The strength of agreement of the ICC and  $\kappa$  values was categorized as follows:  $< 0.20$ , poor;  $0.21 - 0.40$ , fair;  $0.41 - 0.60$ , moderate;  $0.61 - 0.80$ , good; and  $0.81 - 1.00$ , excellent.

## **RESULTS**

### **Comparison of the Degree of Stenosis and the Minimal Luminal Diameter**

The information about the degree of stenosis and the minimal luminal diameter is presented in Table 1. The minimal luminal

**Table 1: Comparison of the degree of stenosis and the minimal luminal diameter**

	Degree of Stenosis (%)		Minimal Luminal Diameter (mm)	
	Observer 1	Observer 2	Observer 1	Observer 2
DSA <sup>a</sup>	71.72 ± 21.21 <sup>b</sup>	70.64 ± 23.18 <sup>b</sup>	0.50 ± 0.40 <sup>c</sup>	0.51 ± 0.42 <sup>c</sup>
Interobserver agreement	0.930 (0.868–0.963)		0.916 (0.838–0.956)	
HR-MR <sup>a</sup>	74.27 ± 20.39 <sup>b</sup>	70.42 ± 23.12 <sup>b</sup>	0.61 ± 0.49 <sup>c</sup>	0.59 ± 0.48 <sup>c</sup>
Interobserver agreement	0.909 (0.828–0.952)		0.915 (0.836–0.956)	
Agreement				
Continuous values <sup>d</sup>	0.937 (0.882–0.967)	0.943 (0.892–0.970)	0.892 (0.791–0.944)	0.949 (0.902–0.974)
Classified stenosis <sup>e</sup>	0.548 (0.310–0.785)	0.614 (0.403–0.825)		
Correlation				
Continuous values <sup>f</sup>	0.861 ( <i>P</i> < .001)	0.892 ( <i>P</i> < .001)	0.816 ( <i>P</i> < .001)	0.879 ( <i>P</i> < .001)
Classified stenosis <sup>f</sup>	0.773 ( <i>P</i> < .001)	0.766 ( <i>P</i> < .001)		

<sup>a</sup> Data indicate the mean ± SD.

<sup>b</sup> There were no significant differences between DSA and HR-MR (*P* > .05).

<sup>c</sup> There were significant differences between DSA and HR-MR (*P* < .05).

<sup>d</sup> Agreement refers to the interclass correlation coefficients between DSA and HR-MR, and data in parentheses indicate 95% confidence intervals.

<sup>e</sup> Agreement refers to the  $\kappa$  values between DSA and HR-MR, and data in parentheses indicate 95% confidence intervals.

<sup>f</sup> Correlation refers to the Spearman *R* values between DSA and HR-MR.

**Table 2: Interobserver and intermodality diagnostic agreement**

	Diagnostic Agreement <sup>a</sup>	Agreement Ratio <sup>b</sup>	Disagreement Ratio <sup>b</sup>	Undetermined Diagnosis <sup>c</sup>
DSA <sup>d</sup>	0.643 (0.458–0.828)	73.0% (27/37)	27.0% (10/27)	5.41%/16.22%
HR-MR <sup>d</sup>	0.818 (0.670–0.966)	86.5% (32/37)	13.5% (5/37)	2.70%/5.41%
Observer 1 <sup>e</sup>	0.704 (0.528–0.881)	78.4% (29/37)	21.6% (8/37)	
Observer 2 <sup>e</sup>	0.579 (0.390–0.768)	67.6% (25/37)	32.4% (12/37)	

<sup>a</sup> Agreement refers to  $\kappa$  values between DSA and HR-MR, and data in parentheses indicate 95% confidence intervals.

<sup>b</sup> Data in parentheses indicate the numbers of agreed or disagreed cases compared with the total number of cases in the diagnosis.

<sup>c</sup> The proportions of undetermined diagnosis for observer 1/observer 2.

<sup>d</sup> Interobserver agreement between observer 1 and observer 2.

<sup>e</sup> Intermodality agreement between DSA and HR-MR.

diameter had a significant difference (*P* = .026, .014), whereas the degree of stenosis did not have a significant difference (*P* = .070, 0.708) between DSA and HR-MR. Interobserver agreement for the measurements was excellent (ICC = 0.909–0.930). Intermodality agreement for the measurements was excellent (ICC = 0.937–0.943); moderate to good ( $\kappa$  = 0.548–0.614) for the degree of stenosis; and excellent (ICC = 0.892–0.949) for the minimal luminal diameter. The correlation coefficients were 0.766–0.892 (Spearman *R*, *P* < .001) for the degree of stenosis and 0.816–0.879 (Spearman *R*, *P* < .001) for the minimal luminal diameter.

### Comparison of Diagnoses

**Interobserver Diagnostic Agreement.** On DSA images, both observers agreed as to the diagnosis in 27 of the 37 the patients (73.0%), and the interobserver diagnostic agreement was good ( $\kappa$  = 0.643; 95% confidence interval, 0.458–0.828). For HR-MR, 2 observers were in agreement with regard to the diagnosis of ICAD in 32 of the 37 patients (86.5%), thus resulting in excellent agreement ( $\kappa$  = 0.818; 95% confidence interval, 0.670–0.966) (Table 2 and On-line Figure).

**Intermodality Diagnostic Agreement.** For the diagnoses for DSA and HR-MR, there was agreement in 29 of the 37 patients (78.4%) and disagreement in 8 patients (21.6%) for observer 1. For observer 2, in 25 of the 37 patients (67.6%), there was agreement in the diagnoses, and in 12 patients (32.4%), there was disagreement. There was also good and moderate agreement between the 2 imaging modalities with  $\kappa$  values of 0.704

(95% confidence interval, 0.528–0.881) and 0.579 (95% confidence interval, 0.390–0.768), respectively. The percentages of undetermined diagnoses did not show significant differences between DSA and HR-MR, even though HR-MR showed lower percentages than DSA (observer 1: 5.41% versus 2.70%, *P* = 1.000; observer 2: 16.22% versus 5.41%, *P* = .125) (Table 2 and On-line Figure).

### DISCUSSION

In our study, HR-MR showed greater than or equal to moderate agreement (ICC = 0.892–0.949;  $\kappa$  = 0.548–0.614) and significant correlations (Spearman *R* = 0.766–0.892, *P* < .001) with DSA regarding the degree of stenosis and the minimal luminal diameter. There was no significant difference in the degree of stenosis, whereas the minimal luminal diameter was significantly higher on HR-MR than on DSA. Both interobserver diagnostic agreements were higher on HR-MR than on DSA. The percentages of undetermined diagnoses were similar on HR-MR compared with DSA. HR-MR may, therefore, be a useful imaging option comparable with DSA for the characterization of stenosis and the diagnosis of various ICADs.

Although many studies have reported the diagnostic usefulness of HR-MR, they focused on the radiologic findings of pathologic vessel walls for the diagnosis or differentiation of ICADs.<sup>3,15–17,21,34,35</sup> However, those studies lacked information regarding the comparison between luminal angiography and HR-MR, which may lead to disputes and confusion regarding the usefulness of HR-MR as an imaging method. Only a few studies have attempted to reveal the usefulness of HR-MR compared with DSA.<sup>8,13,18,23</sup> However, these observations were limited regarding only single vascular pathology (atherosclerosis, Moyamoya disease) or single cerebral artery (middle cerebral artery, basilar artery) or the small patient sample size (*n* = 9). In particular, although these studies acknowledged that HR-MR presents additional information, such as the direct depiction of vessel walls beyond the luminal evaluation, HR-MR was evaluated

by using DSA as the reference standard. We performed an independent evaluation and diagnosis for each technique and compared DSA and HR-MR in various ICADs with the largest patient populations in all of the published studies, to our knowledge.

Liu et al<sup>8</sup> showed a significant correlation (Spearman  $R = 0.68$ ;  $P < .01$ ) and no significant difference ( $P > .05$ ) in the degree of stenosis detected by both DSA and HR-MR. Our study also demonstrated the significant correlation (Spearman  $R = 0.766-0.892$ ;  $P < .001$ ) without a significant difference ( $P > .05$ ) in the degree of stenosis. Our results also included the significant correlation (Spearman  $R = 0.816-0.879$ ;  $P < .001$ ) in the minimal luminal diameter. Liu et al only evaluated the degree of stenosis in the middle cerebral artery, whereas our results were based on various intracranial arteries, which may contribute to a wide application of HR-MR with its results comparable with those of DSA.

The degree of stenosis did not have a significant difference between DSA and HR-MR, whereas the minimal luminal diameter measured significantly higher in HR-MR than in DSA (0.50–0.51 versus 0.59–0.61). The discrepancy may suggest the overestimation of the luminal diameter on HR-MR or the underestimation on DSA. According to the previously mentioned studies, DSA may underestimate the diameter of intracranial arteries due to its limited number of projections.<sup>36,37</sup> Of 80 arteries (both observers 1 and 2), 18 demonstrated a discrepancy in the classification of the stenosis (<50%, 50%–70%, >70%) between DSA and HR-MR. However, of those arteries, 15 showed that the differences from the margins of the degree of stenosis (50% or 70%) were within 5%; thus, the discrepancy may be within the measurement error.

Katsuno and Kobayashi<sup>38</sup> compared the diagnoses of DSA and basiparallel anatomic scanning MR imaging, showing only the outer lumen of the vessels, in 22 patients with severe headache and neck pain. They focused on dissection and atherosclerosis, which had good agreement ( $\kappa = 0.636$ ; 95% confidence interval, 0.314–0.959) between DSA and basiparallel anatomic scanning MR imaging.<sup>38</sup> In this study, the intermodality diagnostic agreement was 0.579–0.704, even in various ICADs.

In our study, HR-MR showed higher interobserver diagnostic agreement and lower proportions of undetermined diagnosis than DSA. Although the higher interobserver diagnostic agreement and the lower proportions of undetermined diagnoses were unclear as to their statistical significance and may not indicate higher diagnostic performance, HR-MR may not only be a useful imaging technique regarding the diagnosis but may also contribute to solving problem cases on luminal angiography due to the additional information beyond the luminal characterization. Hui et al<sup>13</sup> also postulated that DSA is inferior to HR-MR in vessel wall evaluation, though stenosis and occlusion may appear similar in all kinds of ICADs. Although DSA is still the criterion standard in ICAD, other types of luminal angiography, such as CTA and MRA with their minimal invasiveness, have widened the scope because DSA is an invasive study with complication risks, including morbidity and mortality.<sup>8-10</sup> However, we should be concerned about the balance between the risks of an incorrect diagnosis and the association with an imaging procedure. HR-MR is a minimally invasive imaging technique that showed superior diagnostic performance over CTA or MRA.<sup>8,21</sup> Therefore, HR-MR may be an

alternative to luminal angiography for both characterization and diagnosis.

DSA can present hemodynamic information and anatomic luminal changes, whereas HR-MR can offer direct anatomic information regarding a vascular wall or plaque as well as luminal change. In addition, parenchymal information regarding the area corresponding to the vascular abnormality can be demonstrated by HR-MR.<sup>12</sup> Therefore, HR-MR may present information different from that of DSA, allowing it to function as a comparable imaging method with different indications in ICAD.

Our study has a number of limitations. First, it was a retrospective study and enrolled only a small number of patients, which may result in limitations in its statistical significance and selection bias. Second, we did not perform comparisons of HR-MR with 3D rotational angiography, which may be a solution to the discrepancies in the minimal luminal diameter and degree of stenosis. Third, the diagnoses in our study may be insufficient because they were made according to the aforementioned diagnostic criteria and the conclusive diagnosis with pathologic confirmation in ICAD was not acquired. Therefore, ICAD was usually diagnosed on the basis of the clinical, laboratory, and radiologic information without the pathologic confirmation, and physicians sometimes must diagnose challenging cases in the real clinical field. The enrolled patients were also challenging cases for both DSA and HR-MR, which may introduce a selection bias and result in an imbalance of analyzed arterial segments. However, we believe that our study substantially reflects actual clinical practice despite these limitations. Fourth, there was no correlation with the treatment options or prognosis between DSA and HR-MR. We hope that our study contributes to further study regarding the comparisons between HR-MR and DSA as imaging methods used to guide treatment or prognosis.

## CONCLUSIONS

HR-MR may be an imaging method comparable with DSA in the characterization and diagnosis of various ICADs.

Disclosures: Seung Chai Jung—RELATED: Grant: Korea Healthcare Technology R&D Project, Ministry for Health, Welfare, and Family Affairs, Republic of Korea (H112C1847). Sun U. Kwon—UNRELATED: Grants/Grants Pending: Korea Healthcare Technology R&D Project, Ministry of Health and Welfare, Republic of Korea (H110C2020). \* \*Money paid to the institution.

## REFERENCES

1. Bang OY. **Intracranial atherosclerosis: current understanding and perspectives.** *J Stroke* 2014;16:27–35 CrossRef Medline
2. Sacco RL, Boden-Albala B, Gan R, et al. **Stroke incidence among white, black, and Hispanic residents of an urban community: the Northern Manhattan Stroke Study.** *Am J Epidemiol* 1998;147:259–68 CrossRef Medline
3. Li ML, Xu WH, Song L, et al. **Atherosclerosis of middle cerebral artery: evaluation with high-resolution MR imaging at 3T.** *Atherosclerosis* 2009;204:447–52 CrossRef Medline
4. Warfarin-Aspirin Symptomatic Intracranial Disease (WASID) Trial Investigators. **Design, progress and challenges of a double-blind trial of warfarin versus aspirin for symptomatic intracranial arterial stenosis.** *Neuroepidemiology* 2003;22:106–17 CrossRef Medline
5. Chimowitz MI, Lynn MJ, Howlett-Smith H, et al; Warfarin-Aspirin Symptomatic Intracranial Disease Trial Investigators. **Comparison of warfarin and aspirin for symptomatic intracranial arterial stenosis.** *N Engl J Med* 2005;352:1305–16 CrossRef Medline

6. Wang Y, Lou X, Li Y, et al. **Imaging investigation of intracranial arterial dissecting aneurysms by using 3 T high-resolution MRI and DSA: from the interventional neuroradiologists' view.** *Acta Neurochir (Wien)* 2014;156:515–25 CrossRef Medline
7. Leng X, Wong KS, Liebeskind DS. **Evaluating intracranial atherosclerosis rather than intracranial stenosis.** *Stroke* 2014;45:645–51 CrossRef Medline
8. Liu Q, Huang J, Degnan AJ, et al. **Comparison of high-resolution MRI with CT angiography and digital subtraction angiography for the evaluation of middle cerebral artery atherosclerotic steno-occlusive disease.** *Int J Cardiovasc Imaging* 2013;29:1491–98 CrossRef Medline
9. Kaufmann TJ, Huston J 3rd, Mandrekar JN, et al. **Complications of diagnostic cerebral angiography: evaluation of 19,826 consecutive patients.** *Radiology* 2007;243:812–19 CrossRef Medline
10. Chung TS, Joo JY, Lee SK, et al. **Evaluation of cerebral aneurysms with high-resolution MR angiography using a section-interpolation technique: correlation with digital subtraction angiography.** *AJNR Am J Neuroradiol* 1999;20:229–35 Medline
11. Soize S, Bouquigny F, Kadziolka K, et al. **Value of 4D MR angiography at 3T compared with DSA for the follow-up of treated brain arteriovenous malformation.** *AJNR Am J Neuroradiol* 2014;35:1903–09 CrossRef Medline
12. Xu WH, Li ML, Niu JW, et al. **Intracranial artery atherosclerosis and lumen dilation in cerebral small-vessel diseases: a high-resolution MRI study.** *CNS Neurosci Ther* 2014;20:364–67 CrossRef Medline
13. Hui FK, Zhu X, Jones SE, et al. **Early experience in high-resolution MRI for large vessel occlusions.** *J Neurointerv Surg* 2015;7:509–16 CrossRef Medline
14. Mandell DM, Matouk CC, Farb RI, et al. **Vessel wall MRI to differentiate between reversible cerebral vasoconstriction syndrome and central nervous system vasculitis: preliminary results.** *Stroke* 2012;43:860–62 CrossRef Medline
15. Kim YJ, Lee DH, Kwon JY, et al. **High resolution MRI difference between moyamoya disease and intracranial atherosclerosis.** *Eur J Neurol* 2013;20:1311–18 CrossRef Medline
16. Zhu XJ, Du B, Lou X, et al. **Morphologic characteristics of atherosclerotic middle cerebral arteries on 3T high-resolution MRI.** *AJNR Am J Neuroradiol* 2013;34:1717–22 CrossRef Medline
17. Obusec EC, Hui F, Hajj-Ali RA, et al. **High-resolution MRI vessel wall imaging: spatial and temporal patterns of reversible cerebral vasoconstriction syndrome and central nervous system vasculitis.** *AJNR Am J Neuroradiol* 2014;35:1527–32 CrossRef Medline
18. Ryoo S, Cha J, Kim SJ, et al. **High-resolution magnetic resonance wall imaging findings of Moyamoya disease.** *Stroke* 2014;45:2457–60 CrossRef Medline
19. Mossa-Basha M, Hwang WD, De Havenon A, et al. **Multicontrast high-resolution vessel wall magnetic resonance imaging and its value in differentiating intracranial vasculopathic processes.** *Stroke* 2015;46:1567–73 CrossRef Medline
20. Choi YJ, Jung SC, Lee DH. **Vessel wall imaging of the intracranial and cervical carotid arteries.** *J Stroke* 2015;17:238–55 CrossRef Medline
21. Kim YS, Lim SH, Oh KW, et al. **The advantage of high-resolution MRI in evaluating basilar plaques: a comparison study with MRA.** *Atherosclerosis* 2012;224:411–16 CrossRef Medline
22. Qiao Y, Anwar Z, Intrapromkul J, et al. **Patterns and implications of intracranial arterial remodeling in stroke patients.** *Stroke* 2016;47:434–40 CrossRef Medline
23. Lou X, Ma N, Shen H, et al. **Noninvasive visualization of the basilar artery wall and branch ostia with high-resolution three-dimensional black-blood sequence at 3 Tesla.** *J Magn Reson Imaging* 2014;39:911–16 CrossRef Medline
24. Chimowitz MI, Kokkinos J, Strong J, et al. **The Warfarin-Aspirin Symptomatic Intracranial Disease Study.** *Neurology* 1995;45:1488–93 Medline
25. Huang J, Degnan AJ, Liu Q, et al. **Comparison of NASCET and WASID criteria for the measurement of intracranial stenosis using digital subtraction and computed tomography angiography of the middle cerebral artery.** *J Neuroradiol* 2012;39:342–45 CrossRef Medline
26. Swartz RH, Bhuta SS, Farb RI, et al. **Intracranial arterial wall imaging using high-resolution 3-Tesla contrast-enhanced MRI.** *Neurology* 2009;72:627–34 CrossRef Medline
27. Maruyama H, Nagoya H, Kato Y, et al. **Spontaneous cervicocephalic arterial dissection with headache and neck pain as the only symptom.** *J Headache Pain* 2012;13:247–53 CrossRef Medline
28. Suzuki J, Takaku A. **Cerebrovascular “moyamoya” disease: disease showing abnormal net-like vessels in base of brain.** *Arch Neurol* 1969;20:288–99 CrossRef Medline
29. Fukui M. **Guidelines for the diagnosis and treatment of spontaneous occlusion of the circle of Willis (‘moyamoya’ disease): Research Committee on Spontaneous Occlusion of the Circle of Willis (Moyamoya Disease) of the Ministry of Health and Welfare, Japan.** *Clin Neurol Neurosurg* 1997;99(suppl 2):S238–40 Medline
30. Kuroda S, Houkin K. **Moyamoya disease: current concepts and future perspectives.** *Lancet Neurol* 2008;7:1056–66 CrossRef Medline
31. Scott RM, Smith ER. **Moyamoya disease and moyamoya syndrome.** *N Engl J Med* 2009;360:1226–37 CrossRef Medline
32. Gomes LJ. **The role of imaging in the diagnosis of central nervous system vasculitis.** *Curr Allergy Asthma Rep* 2010;10:163–70 CrossRef Medline
33. Hajj-Ali RA, Calabrese LH. **Diagnosis and classification of central nervous system vasculitis.** *J Autoimmun* 2014;48–49:149–52 CrossRef Medline
34. Kwak HS, Hwang SB, Chung GH, et al. **High-resolution magnetic resonance imaging of symptomatic middle cerebral artery dissection.** *J Stroke Cerebrovasc Dis* 2014;23:550–53 CrossRef Medline
35. Bley TA, Uhl M, Carew J, et al. **Diagnostic value of high-resolution MR imaging in giant cell arteritis.** *AJNR Am J Neuroradiol* 2007;28:1722–27 CrossRef Medline
36. Choi CG, Lee DH, Lee JH, et al. **Detection of intracranial atherosclerotic steno-occlusive disease with 3D time-of-flight magnetic resonance angiography with sensitivity encoding at 3T.** *AJNR Am J Neuroradiol* 2007;28:439–46 Medline
37. BouSSION N, Soulez G, De Guise JA, et al. **Geometrical accuracy and fusion of multimodal vascular images: a phantom study.** *Med Phys* 2004;31:1434–43 CrossRef Medline
38. Katsuno M, Kobayashi S. **Diagnosis of vertebral artery dissection with basiparallel anatomical scanning magnetic resonance imaging.** *J Nippon Med Sch* 2011;78:367–73 CrossRef Medline

# A Simplified Model for Intravoxel Incoherent Motion Perfusion Imaging of the Brain

J. Conklin, C. Heyn, M. Roux, M. Cerny, M. Wintermark, and C. Federau



## ABSTRACT

**BACKGROUND AND PURPOSE:** Despite a recent resurgence, intravoxel incoherent motion MRI faces practical challenges, including limited SNR and demanding acquisition and postprocessing requirements. A simplified approach using linear fitting of a subset of higher b-values has seen success in other organ systems. We sought to validate this method for evaluation of brain pathology by comparing perfusion measurements using simplified linear fitting to conventional biexponential fitting.

**MATERIALS AND METHODS:** Forty-nine patients with gliomas and 17 with acute strokes underwent 3T MRI, including DWI with 16 b-values (range, 0–900 s/mm<sup>2</sup>). Conventional intravoxel incoherent motion was performed using nonlinear fitting of the standard biexponential equation. Simplified intravoxel incoherent motion was performed using linear fitting of the log-normalized signal curves for subsets of b-values >200 s/mm<sup>2</sup>. Comparisons between ROIs (tumors, strokes, contralateral brain) and between models (biexponential and simplified linear) were performed by using 2-way ANOVA. The root mean square error and coefficient of determination ( $R^2$ ) were computed for the simplified model, with biexponential fitting as the reference standard.

**RESULTS:** Perfusion maps using simplified linear fitting were qualitatively similar to conventional biexponential fitting. The perfusion fraction was elevated in high-grade ( $n = 33$ ) compared to low-grade ( $n = 16$ ) gliomas and was reduced in strokes compared to the contralateral brain ( $P < .001$  for both main effects). Decreasing the number of b-values used for linear fitting resulted in reduced accuracy (higher root mean square error and lower  $R^2$ ) compared with full biexponential fitting.

**CONCLUSIONS:** Intravoxel incoherent motion perfusion imaging of common brain pathology can be performed by using simplified linear fitting, with preservation of clinically relevant perfusion information.

**ABBREVIATIONS:**  $D$  = diffusion coefficient;  $D^*$  = pseudo-diffusion coefficient;  $f$  = perfusion fraction; IVIM = intravoxel incoherent motion; rCBV = relative cerebral blood volume

Initially proposed by Le Bihan et al in the 1980s,<sup>1,2</sup> the intravoxel incoherent motion (IVIM) model enables simultaneous evaluation of diffusion and perfusion through a multi-b-value diffusion-weighted MRI acquisition. This approach offers theoretical

advantages over other perfusion imaging strategies; namely, it is inherently quantitative, provides intrinsic coregistration between perfusion and diffusion parameters, and does not rely on intravenous contrast injection or estimation of an arterial input function. While early investigations were hampered by various technical limitations,<sup>3</sup> advances in field strength, gradient hardware, and echo-planar and parallel imaging technology have led to a resurgent interest in IVIM for a wide range of clinical applications.<sup>4–18</sup>

Brain imaging with IVIM is particularly challenging due to the low blood volume fractions of cerebral tissues<sup>19–21</sup> and CSF partial volume contamination.<sup>22</sup> Nonetheless, IVIM has now been validated for quantitative evaluation of brain perfusion using clinically available hardware and pulse sequences.<sup>23</sup> Recent work in neuro-oncology has shown the potential for IVIM in differentiating tumor recurrence from posttreatment effects,<sup>9,10</sup> in the preoperative evaluation of tumor grade,<sup>6,18</sup> and in differentiating primary CNS lymphoma from glioblastoma.<sup>16</sup> IVIM has also been applied in the setting of acute stroke,<sup>7,24,25</sup> where

Received January 14, 2016; accepted after revision July 16.

From the Department of Medical Imaging (J.C., C.H.), Sunnybrook Health Sciences Centre and University of Toronto, Toronto, Ontario, Canada; Department of Diagnostic and Interventional Radiology (M.R., M.C., C.F.), Centre Hospitalier Universitaire Vaudois and University of Lausanne, Lausanne, Switzerland; Department of Radiology (M.W.), University of Virginia, Charlottesville, Virginia; and Department of Radiology (M.W., C.F.), Stanford University, Stanford, California.

C. Federau received support from the Swiss National Science Foundation.

Related abstract previously presented at: Annual Meeting of the American Society of Neuroradiology and the Foundation of the ASNR Symposium, May 21–26, 2016, Washington, DC.

Please address correspondence to Christian Federau, MD, MSc, Department of Radiology, Division of Neuroradiology, Stanford University, 300 Pasteur Dr, Stanford, CA 94305-5105; e-mail christian.federau@gmail.com

Indicates open access to non-subscribers at www.ajnr.org

<http://dx.doi.org/10.3174/ajnr.A4929>

perfusion imaging without gadolinium is of particular interest given the association between cerebrovascular disease and renal insufficiency.<sup>26</sup>

Despite these promising advancements, practical issues such as low SNR and demanding acquisition and postprocessing requirements may impede more widespread adoption of IVIM in clinical and research settings. Conventional IVIM requires acquisition of a large number of b-values (from 10 to 36),<sup>27</sup> including low b-values sensitive to microcirculatory blood flow (ie, pseudodiffusion) and high b-values in the regime where true molecular diffusion dominates. A biexponential fit is then performed over the full range of b-values using a nonlinear fitting procedure.<sup>11,23</sup>

In contrast, an alternate solution to the IVIM equation can be obtained by performing a linear fit of the log-transformed data, using only a subset of higher b-values. This simplified procedure, also referred to as asymptotic fitting,<sup>19,27</sup> offers potential advantages over biexponential fitting, including shorter acquisition protocols, computational simplicity, and reduced uncertainty in the setting of low SNR.<sup>19</sup> In principle, this method allows estimation of IVIM parameters using as few as 2 nonzero b-values. Linear fitting has been applied for imaging of the liver,<sup>13</sup> kidneys,<sup>15</sup> pancreas,<sup>5</sup> prostate,<sup>12</sup> and breast,<sup>4</sup> and in the evaluation of head and neck malignancies.<sup>14,17</sup> To our knowledge, there has been no systematic comparison of simplified linear fitting with standard biexponential fitting for the evaluation of brain pathology.

Therefore, the purpose of this study was: 1) to compare the perfusion fraction (*f*) estimates obtained using simplified linear fitting with those of conventional biexponential fitting, and 2) to examine the effect of reducing the number of b-values on the quality of the resulting perfusion maps. We performed this analysis in 2 common clinical scenarios, namely, evaluation of brain gliomas and acute strokes.

## MATERIALS AND METHODS

### Subjects

Subjects were participants in a study of IVIM for the evaluation of brain gliomas at the University of Lausanne from May 2011 to July 2014 and a bicentric study of IVIM for evaluation of acute stroke at the University of Lausanne and the University of Virginia from February 2011 to August 2013. Institutional ethics review board approval at both institutions was obtained, and patient consent was waived. This retrospective analysis includes subject overlap with 2 previously published studies, which applied conventional IVIM methodology for the evaluation of gliomas<sup>6</sup> and strokes,<sup>7</sup> respectively. Inclusion criteria for patients with gliomas were: 1) preoperative imaging, including 16 b-value IVIM acquisition, without corruption by motion artifacts; 2) no relevant treatment history at the time of imaging, including chemotherapy, radiation therapy, or antiangiogenic therapy; and 3) histopathologic tumor diagnosis and grading according to the World Health Organization criteria. Due to the relatively low number of patients with histopathologically confirmed low-grade gliomas (*n* = 10), 6 additional patients with diagnosis of low-grade glioma on radiologic criteria alone were included in the analysis.<sup>6</sup> Inclusion criteria for patients with stroke were: 1) MRI

within 5 days of symptom onset, including successful 16-b-value IVIM acquisition, without corruption by motion artifacts; 2) supratentorial diffusion-restricting infarct of >0.5 cm in minimal diameter; and 3) no hemorrhagic transformation at the time of imaging.

### MRI Acquisition

All imaging was performed on 3T MRI systems (Magnetom Skyra, Verio, or Trio; Siemens, Erlangen, Germany) using 32-channel phased array receiver coils. The IVIM acquisition consisted of a Stejskal-Tanner diffusion-weighted EPI spin-echo pulse sequence,<sup>28</sup> with diffusion-weighting obtained along 3 orthogonal directions using 16 different b-values (*b* = 0, 10, 20, 40, 80, 110, 140, 170, 200, 300, 400, 500, 600, 700, 800, 900 s/mm<sup>2</sup>). Images were acquired in the axial plane, with nominal in-plane resolution = 1.2 × 1.2 mm<sup>2</sup>, section thickness = 4 mm, NEX = 1, acceleration factor = 2, bandwidth = 1086–1106 Hz/pixel, TR = 4000 ms, TE = lowest achievable for each scanner (89–102 ms). For patients with tumors, DSC perfusion MRI was performed using a T2\*-weighted gradient-echo EPI pulse sequence (nominal in-plane resolution = 1.8 × 1.8 mm<sup>2</sup>, section thickness = 6 mm, TR = 1950 ms, TE = 43 ms) sequentially acquired after IV injection of gadoterate meglumine (Dotarem; Guerbet, Aulnay-sous-Bois, France) with a dose of 0.2 mL/kg and a rate of 3 mL/s. Additional conventional images were obtained according to the institutional brain tumor and stroke imaging protocols.

### Conventional IVIM Model

The standard 2-compartment model of diffusion proposed by Le Bihan et al<sup>2</sup> was assumed, described by the biexponential equation:

$$1) \quad \frac{S(b)}{S_0} = f \times e^{-bD^*} + (1 - f) \times e^{-bD},$$

where the first term represents intravascular signal loss due to blood flow in the microvasculature, characterized by the pseudodiffusion coefficient *D*<sup>\*</sup>, and the second term represents extravascular signal loss due to molecular diffusion of water, characterized by the diffusion coefficient *D*. The perfusion fraction *f* represents the proportion of MR-visible water contained within the microcirculation (ie, the intravascular or “fast” diffusion compartment).

For the conventional IVIM calculation, a voxelwise fitting of Equation 1 was performed using a 2-step procedure as previously described.<sup>6,23</sup> Briefly, the *S(b) / S<sub>0</sub>* curve was fitted for *b* > 200 s/mm<sup>2</sup> to solve for the parameter *D*, under the assumption that *D*<sup>\*</sup> ≫ *D* so that pseudodiffusion effects can be ignored for higher b-values.<sup>29</sup> A nonlinear fit of Equation 1 was then performed over all 16 b-values to solve for *f* and *D*<sup>\*</sup> while holding *D* constant, using the Levenberg-Marquardt algorithm<sup>30</sup> (Matlab, Optimization Toolbox; MathWorks, Natick, Massachusetts). This 2-step procedure has been shown to provide robust parameter estimates under biologic conditions.<sup>23</sup> The perfusion fraction calculated using this method was defined as *f*<sub>biexponential</sub>.

### Simplified IVIM Model

Under the assumptions that  $D^* \gg D$ ,<sup>29</sup> the first term of Equation 1 (corresponding to the intravascular compartment) has a negligible contribution to the signal  $S(b)$  for higher b-values. Taking the natural logarithm of Equation 1, this allows for the following simplification<sup>2</sup>:

$$2) \quad \ln\left(\frac{S(b)}{S_0}\right) = -bD + \ln(1 - f).$$

Equation 2 provides a linear relationship with slope  $-D$  and intercept  $\ln(1 - f)$ , which can be solved for  $f$  and  $D$  using as few as

**Table 1: Combinations of b-values used for linear fitting**

No. of Nonzero b-Values	b-Values (sec × mm <sup>-2</sup> )
7	300, 400, 500, 600, 700, 800, 900
4	300, 500, 700, 900
3	300, 600, 900
2	300, 900

2 nonzero b-values, provided they are selected from the regime in which pseudodiffusion effects are negligible. Voxelwise linear least squares regression was applied to solve Equation 2 using different combinations of b-values of  $>200$  s/mm<sup>2</sup> (Table 1). The perfusion fraction calculated using this simplified linear fitting method was defined as  $f_{\text{linear}}$ . Note that this approach does not allow estimation of the pseudo-diffusion coefficient,  $D^*$ .

### DSC Reconstruction

Leakage-corrected CBV maps were reconstructed from T2\*-weighted gradient-echo images using a Boxerman-Weiskoff correction for contrast agent extravasation,<sup>31</sup> implemented using the Dynamic Susceptibility Contrast MR Analysis plug-in for ImageJ (DSCoMAN, Version 1.0, <https://sites.duke.edu/dblab/dsco-man>). Successful DSC perfusion imaging was obtained in 40 of the 49 patients with brain tumors included in this study.

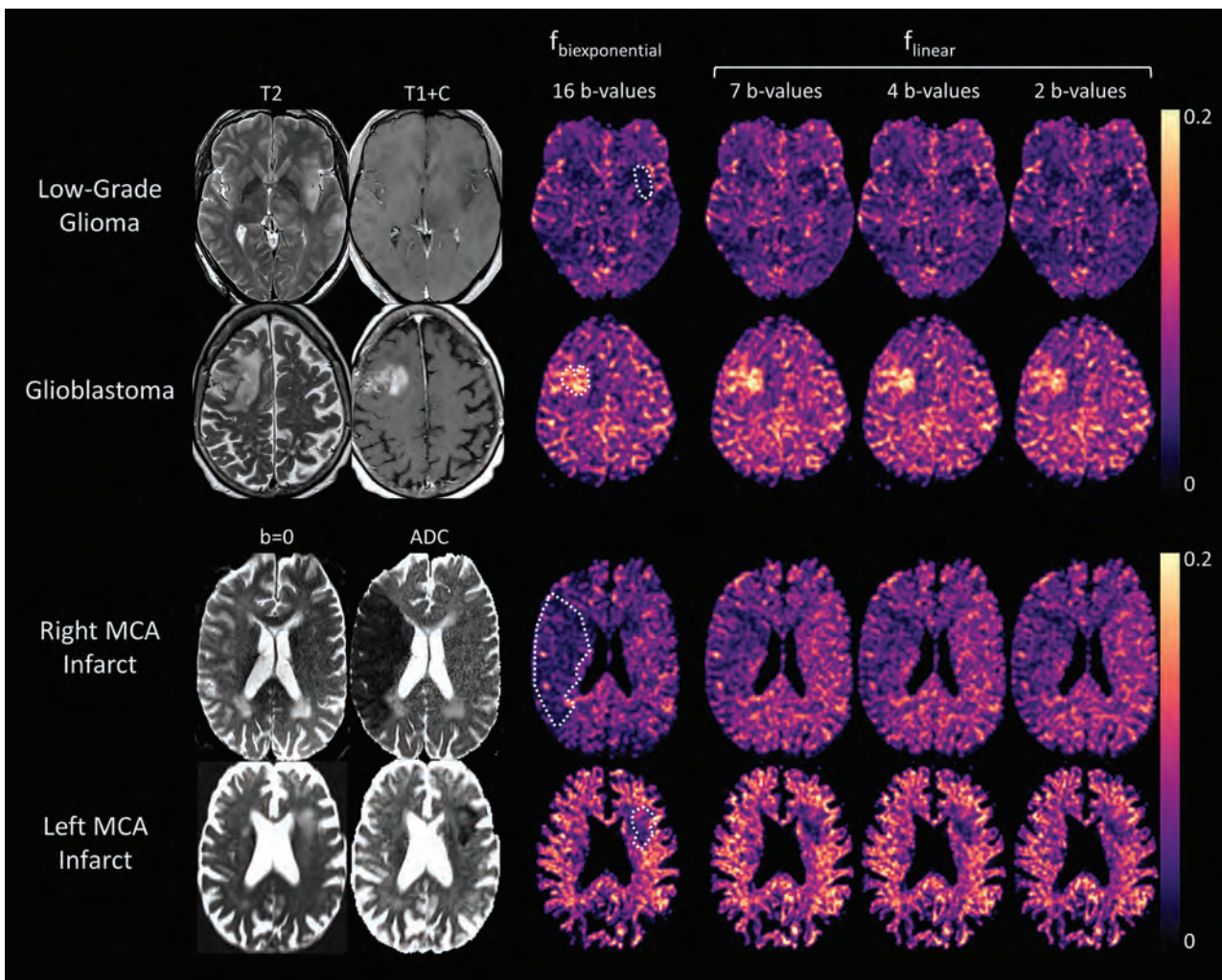


**FIG 1.** Anatomic images and IVIM perfusion maps for 4 clinical cases.  $f_{\text{bixponential}}$  is the perfusion fraction estimate of the conventional biexponential fit (16 b-values) and  $f_{\text{linear}}$  is the perfusion fraction estimate of the simplified linear fit using 2–7 nonzero b-values. *Upper row:* T2-weighted image, postgadolinium T1-weighted image, and perfusion maps for a patient with a histopathologically confirmed low-grade glial tumor (World Health Organization grade II). A subtle T2-hyperintense, hypoenhancing lesion in the left insular cortex corresponds to a focal region of low perfusion fraction on all perfusion maps. *Second row:* T2-weighted image, postgadolinium T1-weighted image, and perfusion maps for a patient with histopathologically confirmed glioblastoma (World Health Organization grade IV). A solid enhancing right frontal mass corresponds to a region of increased perfusion fraction on all perfusion maps. *Third row:*  $b=0$  (ie, T2-weighted) image, ADC map, and perfusion maps for a patient with a large acute right MCA territory infarct, demonstrating a wedge-shaped area of decreased perfusion fraction corresponding to the area of restricted diffusion (infarct core). *Lower row:* Similar findings in a different patient with a smaller left MCA territory infarct. ROIs for tumors and strokes are shown overlaid on the conventional  $f_{\text{bixponential}}$  perfusion maps (dotted white lines).

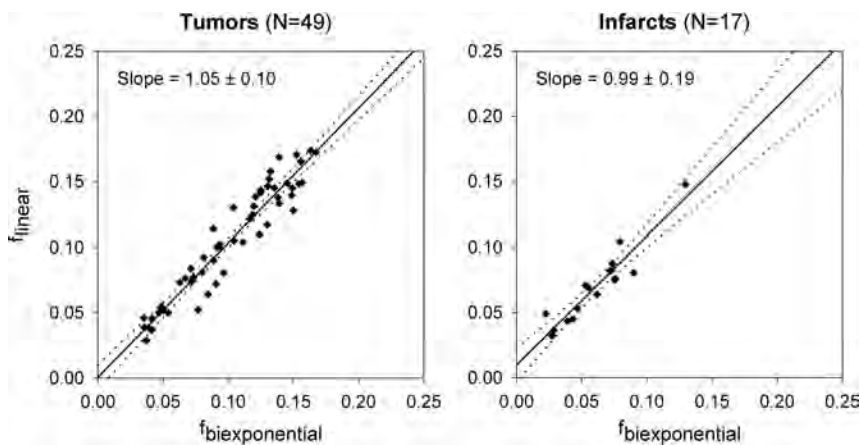


**FIG 2.** Plots comparing the perfusion fraction estimated using the conventional 16 b-value biexponential fit ( $f_{\text{biexponential}}$ ) with those using simplified linear fitting of 7 nonzero b-values ( $f_{\text{linear}}$ ) for tumors (left) and infarcts (right). Solid line indicates the least squares optimal linear regression; dotted lines indicate the 95% confidence interval for the line of best fit. The slope and its 95% confidence interval are also provided for each regression line.

### ROI Analysis

Voxels with  $D > 2.5 \times 10^{-3}$  (approximately 1 SD below the mean diffusion coefficient for CSF)<sup>32</sup> were presumed to contain predominantly CSF and were excluded from the analysis. Voxels with  $f < 0$  or  $f > 0.3$  were considered nonphysiologic (likely contaminated by image noise or volume averaging with flowing CSF)<sup>23</sup> and were also excluded. For patients with gliomas, ROIs were manually placed within the tumor encompassing the region of maximum perfusion fraction by the consensus of 2 neuroradiologists. Regions of intratumoral hemorrhage and necrosis were excluded through close reference to conventional imaging sequences. To evaluate interobserver reliability, an additional radiologist independently retraced all tumor ROIs using an identical procedure, without reference to the initial ROIs or clinical data. To evaluate intraobserver reliability, one radiologist retraced these ROIs during a separate review session, without reference to the initial ROI results. Intraclass correlation coefficients were calculated for interobserver and intraobserver reliability. For patients with DSC perfusion imaging, ROIs were manually copied onto the CBV maps with close reference to anatomic landmarks, and an ROI was placed in the contralateral deep WM to permit normalization and calculation of relative CBV (rCBV). For patients with stroke, a semiautomated procedure was used to define an ROI encompassing the infarct core, by applying a threshold to the diffusion coefficient map under supervision of a single neuro-radiologist. A homologous ROI was manually traced within the contralateral hemisphere.

The mean perfusion fraction estimated using the biexponential model ( $f_{\text{biexponential}}$ ) and the simplified linear model ( $f_{\text{linear}}$ ) was calculated for each ROI. A linear least squares regression of  $f_{\text{linear}}$  on  $f_{\text{biexponential}}$  was then performed for tumors ( $n = 49$ ) and infarcts ( $n = 17$ ). The coefficient of determination ( $R^2$ ) and root mean square error for  $f_{\text{linear}}$  compared with  $f_{\text{biexponential}}$  were calculated for each ROI. This procedure was repeated for estimates of  $f_{\text{linear}}$  using each of the b-value combinations listed in Table 1.

All calculations were performed on a Dell PC (Intel Core i5–2300 CPU at 2.8 GHz, 6 GB of RAM; www.dell.com).

### Statistical Analysis

Statistical analysis was performed using SPSS, Version 16.0 (IBM, Armonk, New York). For tumors, a 2-way mixed ANOVA was performed with perfusion fraction as the dependent variable, tumor grade (low or high) as a between-subjects factor, and IVIM model ( $f_{\text{biexponential}}$  using 16 b-values or  $f_{\text{linear}}$  using 2, 3, 4, or 7 nonzero b-values) as a within-subjects factor. For strokes, a 2-way repeated-measures ANOVA was performed with perfusion fraction as the dependent variable and tissue type (stroke or contralateral brain) and IVIM model as within-subjects factors. For each ANOVA, the threshold for statistical significance was set as  $.05/3 = .017$ —that is, Bonferroni correction for 3 comparisons (2 possible main effects and 1 possible interaction).

The Mauchly test was used to evaluate the assumption of sphericity, and  $dfs$  were corrected according to the Greenhouse-Geisser (for  $\epsilon < 0.75$ ) or Huynh-Feldt (for  $\epsilon > 0.75$ ) method as appropriate. If either ANOVA demonstrated a significant main effect for the IVIM model in the absence of a significant interaction term, post hoc pair-wise comparisons were performed between  $f_{\text{biexponential}}$  and each of the 4 linear IVIM models (4 comparisons) using the Bonferroni correction.

### RESULTS

Perfusion fraction maps created using the simplified linear model ( $f_{\text{linear}}$ ) were qualitatively similar to those obtained using the conventional biexponential model ( $f_{\text{biexponential}}$ ) for low- and high-grade gliomas and for acute infarcts, even when as few as 2 nonzero b-values were used in the fitting procedure (Fig 1). Interobserver reliability for ROI measurements was “substantial” (intraclass correlation coefficient = 0.78) and intraobserver reliability was “almost perfect” (intraclass correlation coefficient = 0.89) according to the standard interpretation of Landis and Koch.<sup>33</sup> Quantitative comparisons of the perfusion fraction for each pathology and IVIM model are provided in Figs 2 and 3.

For tumors, ANOVA demonstrated significant main effects for tumor grade (elevated perfusion fraction in high-grade tumors) and IVIM model (both  $P < .001$ ). The interaction term was not statistically significant, indicating that the observed differences in perfusion fraction between low- and high-grade gliomas did not depend on the choice of IVIM model. In paired post hoc comparisons between IVIM models,  $f_{\text{linear}}$  calculated using 2 nonzero b-values was significantly lower than  $f_{\text{biexponential}}$  ( $P < .001$ ). There were no significant differences between  $f_{\text{biexponential}}$  and  $f_{\text{linear}}$  calculated using 3, 4, or 7 nonzero b-values.

For strokes, ANOVA demonstrated significant main effects for tissue type (decreased perfusion fraction in acute infarcts) and IVIM model (both  $P < .001$ ). The interaction term was not statistically significant, indicating that the observed differences in perfusion fraction between infarcts and contralateral brain did

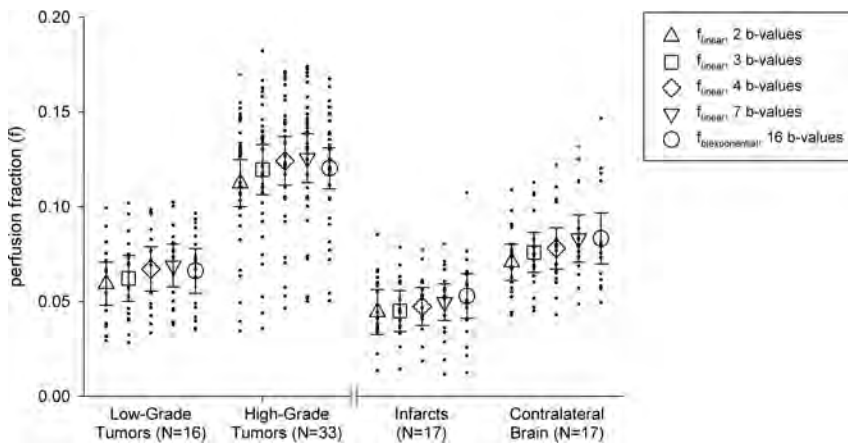


**FIG 3.** Comparison of the perfusion fraction between low- and high-grade tumors (left) and between acute infarcts and contralateral brain tissue (right). Triangle, square, diamond, and inverted triangle markers indicate the mean perfusion fraction calculated by the simplified linear method using 2, 3, 4, and 7 nonzero b-values, respectively (Table 1). Circle markers indicate the mean perfusion fraction calculated using the conventional 16 b-value biexponential method. Error bars indicate 95% confidence intervals.

**Table 2: Measurements of fit and error for  $f_{\text{linear}}$  compared with  $f_{\text{biexponential}}$**

No. of Nonzero b-Values <sup>a</sup>	ROI			
	Tumors (n = 49)		Infarcts (n = 17)	
	R <sup>2</sup>	RMSE	R <sup>2</sup>	RMSE
7	0.913	0.0131	0.887	0.0128
4	0.890	0.0140	0.871	0.0113
3	0.870	0.0152	0.749	0.0139
2	0.853	0.0164	0.719	0.0144

**Note:**—R<sup>2</sup> indicates coefficient of determination for linear regression of  $f_{\text{linear}}$  on  $f_{\text{biexponential}}$ ; RMSE, root mean square error.

<sup>a</sup>Indicates the total number of nonzero b-values used in the estimation of  $f_{\text{linear}}$  (specific b-values are provided in Table 1).

not depend on the choice of the IVIM model. In paired post hoc comparisons between IVIM models,  $f_{\text{linear}}$  calculated using 2 nonzero b-values was significantly lower than  $f_{\text{biexponential}}$  ( $P < .005$ ). There were no significant differences between  $f_{\text{biexponential}}$  and  $f_{\text{linear}}$  calculated using 3, 4, or 7 nonzero b-values.

The effect of the decreasing number of b-values on the accuracy of  $f_{\text{linear}}$  is shown in Table 2, which provides the R<sup>2</sup> and root mean square error for  $f_{\text{linear}}$  calculated using each of the b-value combinations listed in Table 1. Decreasing the number of b-values was associated with reduced accuracy, reflected by decreasing R<sup>2</sup> and increasing root mean square error.

For patients with gliomas, the relationship between the IVIM perfusion fraction and DSC-derived rCBV is shown in Fig 4. A moderate correlation was observed between rCBV and each of the IVIM models considered in this study, with correlation coefficients  $r = 0.49$  for  $f_{\text{biexponential}}$  and  $r = 0.48, 0.50, 0.50,$  and  $0.48$  for  $f_{\text{linear}}$  with 7, 4, 3, and 2 nonzero b-values, respectively.

Time to reconstruct a complete perfusion fraction dataset for a single patient was approximately 2 minutes for  $f_{\text{linear}}$  compared with 36 minutes for  $f_{\text{biexponential}}$ .

## DISCUSSION

Our results demonstrate that clinically relevant perfusion information can be obtained using a simplified IVIM methodology

based on linear (asymptotic) fitting of as few as 2 nonzero b-values. We validated this method for 2 commonly encountered clinical scenarios: evaluation of brain gliomas and acute strokes. Perfusion maps constructed using the simplified fitting procedure were qualitatively similar to those obtained with conventional biexponential fitting.

As expected, reducing the number of b-values in the estimation of  $f_{\text{linear}}$  came at a cost of reduced accuracy in the resulting perfusion maps compared with full biexponential fitting. However, clinically meaningful differences in the perfusion fraction (between high- and low-grade tumors and between ischemic and healthy brain tissue) were observed independent of the choice of model and number of b-values used in the fit. For both gliomas

and strokes,  $f_{\text{linear}}$  underestimated  $f_{\text{biexponential}}$  when only 2 nonzero b-values were used. Given the assumptions of the simplified model, this underestimation may be due to high values of  $f$  (as seen in high-grade tumors) and/or low values of the product  $bD^*$ , resulting in pseudodiffusion effects that are not negligible for  $b > 200$  s/mm<sup>2</sup>. In addition, reducing the number of b-values resulted in increased variability (lower R<sup>2</sup>) in the estimated perfusion fraction. This variability may be more problematic in the evaluation of strokes than in tumors because the large perfusion fraction observed in high-grade gliomas would be easier to detect than the small differences in the perfusion fraction between ischemic and normal brain tissue. On the basis of these results and the data presented in Table 2, we propose a recommended minimum of 4 nonzero b-values for clinical application of the simplified IVIM procedure. Although admittedly arbitrary, this threshold provides acceptable root mean square error ( $<0.015$ ) and R<sup>2</sup> ( $>0.85$ ) across all the ROIs considered.

The simplified linear fitting procedure has been applied in other organ systems.<sup>4,5,12,13,15</sup> However, only 2 very limited studies have applied this method to brain imaging.<sup>25,27</sup> In the first,  $f_{\text{linear}}$  was compared with  $f_{\text{biexponential}}$  for normal brain tissue but not for clinical pathology.<sup>27</sup> Interestingly, the authors found that  $f_{\text{linear}}$  correlated more closely than  $f_{\text{biexponential}}$  to CBV measured by DSC perfusion imaging, possibly due to greater uncertainty associated with biexponential fitting in the setting of low SNR.<sup>19</sup> In the second study,  $f_{\text{linear}}$  was evaluated in a small number of patients with acute stroke; however, no comparison with  $f_{\text{biexponential}}$  could be performed due to the limited range of b-values obtained.<sup>25</sup> The present study is the first to systematically compare  $f_{\text{linear}}$  with  $f_{\text{biexponential}}$  for the evaluation of brain pathology.

With respect to gliomas, results using simplified linear fitting are in agreement with prior studies using conventional IVIM methods,<sup>6,18</sup> suggesting that the perfusion fraction obtained by either fitting procedure is valuable in the preoperative evaluation of tumor grade. Interestingly, a recent study did not show a significant association between IVIM and conventional DSC perfusion parameters,<sup>34</sup> while the present study and another study with partial subject over-

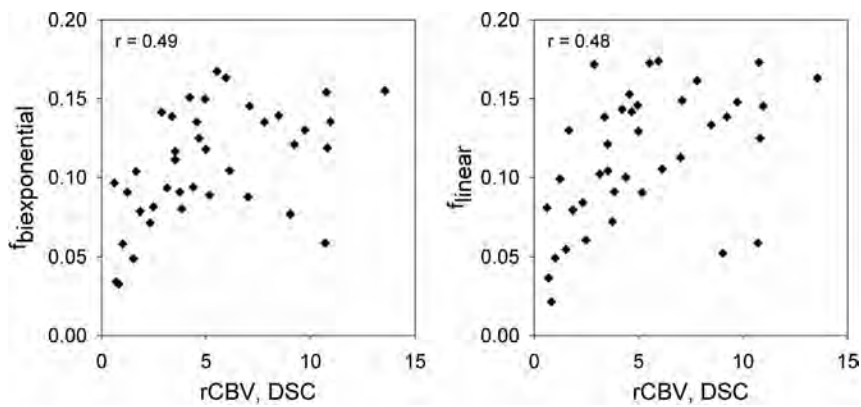


**FIG 4.** Correlation between IVIM perfusion fraction ( $f$ ) and DSC-derived relative CBV for patients with brain gliomas. The relationship between  $f$  and rCBV is shown for conventional biexponential fitting (*left panel*) and for simplified linear fitting of 7 nonzero b-values (*right panel*). Plotted values indicate the mean perfusion fraction and rCBV over the tumor ROI for  $n = 40$  patients. The correlation coefficient ( $r$ ) for each relationship is also provided.

lap<sup>6</sup> showed only a moderate correlation. The data in Fig 4 suggest that this relationship may depend on the value of rCBV, with stronger correlation for lower rCBV and an apparent plateau for higher rCBV values. Our results are consistent with the hypothesis that IVIM parameters may contain slightly different information than classically defined perfusion measurements, as has been previously postulated on theoretical grounds.<sup>6,35</sup>

One explanation for the difference between IVIM and DSC perfusion may be the inherent sensitivity of IVIM to flow in the microcirculation, with a lower contribution from larger arteries and veins which contain faster blood flow. The weighting of the IVIM perfusion fraction toward the capillary network is supported by immunohistochemical measurements of microvessel density in animal models.<sup>36,37</sup> IVIM parameters could therefore provide complementary information to conventional perfusion measurements, and the ability to obtain this information rapidly using an easily implemented protocol may be of great interest to the broader neuro-oncology community. For example, a recent study found that the IVIM perfusion fraction was prognostic for 2-year survival in a small cohort of patients with gliomas.<sup>38</sup>

IVIM in acute stroke has been less well-studied.<sup>24,25</sup> In our study,  $f_{\text{linear}}$  and  $f_{\text{biexponential}}$  were both capable of differentiating between ischemic and contralateral healthy brain tissues. The ability to rapidly obtain simultaneous diffusion and perfusion information using a simplified linear fitting procedure may prove useful in the setting of acute stroke. Beyond obvious advantages such as lack of dependence on gadolinium administration or estimation of an arterial input function, the local nature of IVIM perfusion measurements may make them more sensitive to flow from leptomeningeal collaterals, which is a known challenge for other MR perfusion methods.<sup>39</sup> Further, the intrinsic coregistration between perfusion and diffusion maps provided by IVIM may enable more precise assessment of diffusion-perfusion mismatch.<sup>40</sup> These areas require further investigation.

Our study has several limitations. First, the simplified fitting methodology does not allow estimation of the pseudo-diffusion coefficient  $D^*$ . However, the interpretation of  $D^*$  itself is challenging, and experimental evidence suggests that signal decay in the low b-value regime is likely multicompartamental, with distinct

arterial and venous contributions.<sup>41</sup> Further, there is good theoretical evidence that  $D$  and  $f$  can be more reliably measured than  $D^*$ ,<sup>19</sup> and a recent investigation using Monte Carlo simulations demonstrated significant limitations on the uncertainty in  $D^*$  that could reasonably be achieved in a clinical examination.<sup>42</sup> In contrast, the interpretation of  $f$  is more straightforward, and recent studies suggest that  $f$  may be the most clinically important of the IVIM parameters.<sup>6,16,18</sup> Other limitations include the retrospective nature of our analysis and the inclusion of data from only 2 centers using a single hardware platform. Further evaluation at multiple institutions using a variety of hardware configurations is required

to demonstrate the broader applicability of the simplified IVIM methodology for brain imaging. Finally, while it appears that IVIM provides clinically valuable information regarding the cerebral microcirculation, the underlying physiologic interpretation of IVIM perfusion parameters requires further study.<sup>34</sup>

## CONCLUSIONS

IVIM perfusion information for common brain pathology can be obtained using simplified linear fitting of as few as 2 nonzero b-values. Decreasing the number of b-values comes at a cost of reduced accuracy in the resulting perfusion maps, and we have proposed a recommended minimum of 4 nonzero b-values when applying linear fitting for quantitative evaluation of clinical pathology. The reduced acquisition times and simple postprocessing requirements of this technique may facilitate more widespread adoption of IVIM for brain imaging in clinical and research settings.

Disclosures: Max Wintermark—UNRELATED: Board membership: GE National Football League advisory board. Christian Federau—RELATED: Grant: Swiss National Science Foundation

## REFERENCES

1. Le Bihan D, Breton E, Lallemand D, et al. MR imaging of intravoxel incoherent motions: application to diffusion and perfusion in neurologic disorders. *Radiology* 1986;161:401–07 CrossRef Medline
2. Le Bihan D, Breton E, Lallemand D, et al. Separation of diffusion and perfusion in intravoxel incoherent motion MR imaging. *Radiology* 1988;168:497–505 CrossRef Medline
3. Le Bihan D. Intravoxel incoherent motion perfusion MR imaging: a wake-up call. *Radiology* 2008;249:748–52 CrossRef Medline
4. Cho GY, Moy L, Zhang JL, et al. Comparison of fitting methods and b-value sampling strategies for intravoxel incoherent motion in breast cancer. *Magn Reson Med* 2015;74:1077–85 CrossRef Medline
5. Concia M, Sprinkart AM, Penner AH, et al. Diffusion-weighted magnetic resonance imaging of the pancreas: diagnostic benefit from an intravoxel incoherent motion model-based 3 b-value analysis. *Invest Radiol* 2014;49:93–100 CrossRef Medline
6. Federau C, Meuli R, O'Brien K, et al. Perfusion measurement in brain gliomas with intravoxel incoherent motion MRI. *AJNR Am J Neuroradiol* 2014;35:256–62 CrossRef Medline
7. Federau C, Sumer S, Becce F, et al. Intravoxel incoherent motion

- perfusion imaging in acute stroke: initial clinical experience. *Neuroradiology* 2014;56:629–35 CrossRef Medline
8. Iima M, Le Bihan D. **Clinical intravoxel incoherent motion and diffusion MR imaging: past, present, and future.** *Radiology* 2016;278:13–32 CrossRef Medline
  9. Kim DY, Kim HS, Goh MJ, et al. **Utility of intravoxel incoherent motion MR imaging for distinguishing recurrent metastatic tumor from treatment effect following gamma knife radiosurgery: initial experience.** *AJNR Am J Neuroradiol* 2014;35:2082–90 CrossRef Medline
  10. Kim HS, Suh CH, Kim N, et al. **Histogram analysis of intravoxel incoherent motion for differentiating recurrent tumor from treatment effect in patients with glioblastoma: initial clinical experience.** *AJNR Am J Neuroradiol* 2014;35:490–97 CrossRef Medline
  11. Luciani A, Vignaud A, Cavet M, et al. **Liver cirrhosis: intravoxel incoherent motion MR imaging—pilot study.** *Radiology* 2008;249:891–99 CrossRef Medline
  12. Pang Y, Turkbey B, Bernardo M, et al. **Intravoxel incoherent motion MR imaging for prostate cancer: an evaluation of perfusion fraction and diffusion coefficient derived from different b-value combinations.** *Magn Reson Med* 2013;69:553–62 CrossRef Medline
  13. Patel J, Sigmund EE, Rusinek H, et al. **Diagnosis of cirrhosis with intravoxel incoherent motion diffusion MRI and dynamic contrast-enhanced MRI alone and in combination: preliminary experience.** *J Magn Reson Imaging* 2010;31:589–600 CrossRef Medline
  14. Sasaki M, Sumi M, Eida S, et al. **Simple and reliable determination of intravoxel incoherent motion parameters for the differential diagnosis of head and neck tumors.** *PLoS One* 2014;9:e112866 CrossRef Medline
  15. Sigmund EE, Vivier PH, Sui D, et al. **Intravoxel incoherent motion and diffusion-tensor imaging in renal tissue under hydration and furosemide flow challenges.** *Radiology* 2012;263:758–69 CrossRef Medline
  16. Suh CH, Kim HS, Lee SS, et al. **Atypical imaging features of primary central nervous system lymphoma that mimics glioblastoma: utility of intravoxel incoherent motion MR imaging.** *Radiology* 2014;272:504–13 CrossRef Medline
  17. Sumi M, Nakamura T. **Head and neck tumors: assessment of perfusion-related parameters and diffusion coefficients based on the intravoxel incoherent motion model.** *AJNR Am J Neuroradiol* 2013;34:410–16 CrossRef Medline
  18. Togao O, Hiwatashi A, Yamashita K, et al. **Differentiation of high-grade and low-grade diffuse gliomas by intravoxel incoherent motion MR imaging.** *Neuro Oncol* 2016;18:132–41 CrossRef Medline
  19. Pekar J, Moonen CT, van Zijl PC. **On the precision of diffusion/perfusion imaging by gradient sensitization.** *Magn Reson Med* 1992;23:122–29 CrossRef Medline
  20. Kim T, Kim SG. **Quantification of cerebral arterial blood volume and cerebral blood flow using MRI with modulation of tissue and vessel (MOTIVE) signals.** *Magn Reson Med* 2005;54:333–42 CrossRef Medline
  21. Ito H, Kanno I, Iida H, et al. **Arterial fraction of cerebral blood volume in humans measured by positron emission tomography.** *Ann Nucl Med* 2001;15:111–16 CrossRef Medline
  22. Federau C, O'Brien K. **Increased brain perfusion contrast with T<sub>2</sub>-prepared intravoxel incoherent motion (T2prep IVIM) MRI.** *NMR Biomed* 2015;28:9–16 CrossRef Medline
  23. Federau C, Maeder P, O'Brien K, et al. **Quantitative measurement of brain perfusion with intravoxel incoherent motion MR imaging.** *Radiology* 2012;265:874–81 CrossRef Medline
  24. Suo S, Cao M, Zhu W, et al. **Stroke assessment with intravoxel incoherent motion diffusion-weighted MRI.** *NMR Biomed* 2016;29:320–28 CrossRef Medline
  25. Wirestam R, Brockstedt S, Lindgren A, et al. **The perfusion fraction in volunteers and in patients with ischaemic stroke.** *Acta Radiol* 1997;38:961–64 CrossRef Medline
  26. Toyoda K, Ninomiya T. **Stroke and cerebrovascular diseases in patients with chronic kidney disease.** *Lancet Neurol* 2014;13:823–33 CrossRef Medline
  27. Wirestam R, Borg M, Brockstedt S, et al. **Perfusion-related parameters in intravoxel incoherent motion MR imaging compared with CBV and CBF measured by dynamic susceptibility-contrast MR technique.** *Acta Radiol* 2001;42:123–28 CrossRef Medline
  28. Turner R, Le Bihan D, Maier J, et al. **Echo-planar imaging of intravoxel incoherent motion.** *Radiology* 1990;177:407–14 CrossRef Medline
  29. Le Bihan D, Turner R, MacFall JR. **Effects of intravoxel incoherent motions (IVIM) in steady-state free precession (SSFP) imaging: application to molecular diffusion imaging.** *Magn Reson Med* 1989;10:324–37 CrossRef Medline
  30. Seber GA, Wild CJ. *Nonlinear Regression.* Hoboken: Wiley; 2003
  31. Boxerman JL, Schmainda KM, Weisskoff RM. **Relative cerebral blood volume maps corrected for contrast agent extravasation significantly correlate with glioma tumor grade, whereas uncorrected maps do not.** *AJNR Am J Neuroradiol* 2006;27:859–67 Medline
  32. Helenius J, Soinne L, Perkiö J, et al. **Diffusion-weighted MR imaging in normal human brains in various age groups.** *AJNR Am J Neuroradiol* 2002;23:194–99 Medline
  33. Landis JR, Koch GG. **The measurement of observer agreement for categorical data.** *Biometrics* 1977;33:159–74 CrossRef Medline
  34. Bisdas S, Braun C, Skardelly M, et al. **Correlative assessment of tumor microcirculation using contrast-enhanced perfusion MRI and intravoxel incoherent motion diffusion-weighted MRI: is there a link between them?** *NMR Biomed* 2014;27:1184–91 CrossRef Medline
  35. Le Bihan D, Turner R. **The capillary network: a link between IVIM and classical perfusion.** *Magn Reson Med* 1992;27:171–78 CrossRef Medline
  36. Iima M, Reynaud O, Tsurugizawa T, et al. **Characterization of glioma microcirculation and tissue features using intravoxel incoherent motion magnetic resonance imaging in a rat brain model.** *Invest Radiol* 2014;49:485–90 CrossRef Medline
  37. Lee HJ, Rha SY, Chung YE, et al. **Tumor perfusion-related parameter of diffusion-weighted magnetic resonance imaging: correlation with histological microvessel density.** *Magn Reson Med* 2014;71:1554–58 CrossRef Medline
  38. Federau C, Cerny M, Roux M, et al. **IVIM perfusion fraction is prognostic for survival in brain glioma.** *Clin Neuroradiol* 2016 Apr 26. [Epub ahead of print] CrossRef Medline
  39. Calamante F, Willats L, Gadian DG, et al. **Bolus delay and dispersion in perfusion MRI: implications for tissue predictor models in stroke.** *Magn Reson Med* 2006;55:1180–85 CrossRef Medline
  40. Schaefer PW, Hunter GJ, He J, et al. **Predicting cerebral ischemic infarct volume with diffusion and perfusion MR imaging.** *AJNR Am J Neuroradiol* 2002;23:1785–94 Medline
  41. Duong TQ, Kim SG. **In vivo MR measurements of regional arterial and venous blood volume fractions in intact rat brain.** *Magn Reson Med* 2000;43:393–402 Medline
  42. Zhang Q, Wang YX, Ma HT, et al. **Cramér-Rao bound for intravoxel incoherent motion diffusion weighted imaging fitting.** *Conf Proc IEEE Eng Med Biol Soc* 2013;2013:511–14 CrossRef Medline

# Vascular Dysfunction in Leukoaraiosis

 K. Sam,  A.P. Crawley,  J. Poubanc,  J. Conklin,  O. Sobczyk,  D.M. Mandell,  J. Duffin, L. Venkatraghavan,  J.A. Fisher,  S.E. Black, and  D.J. Mikulis



## ABSTRACT

**BACKGROUND AND PURPOSE:** The pathogenesis of leukoaraiosis has long been debated. This work addresses a less well-studied mechanism, cerebrovascular reactivity, which could play a leading role in the pathogenesis of this disease. Our aim was to evaluate blood flow dysregulation and its relation to leukoaraiosis.

**MATERIALS AND METHODS:** Cerebrovascular reactivity, the change in the blood oxygen level–dependent 3T MR imaging signal in response to a consistently applied step change in the arterial partial pressure of carbon dioxide, was measured in white matter hyperintensities and their contralateral spatially homologous normal-appearing white matter in 75 older subjects (age range, 50–91 years; 40 men) with leukoaraiosis. Additional quantitative evaluation of regions of leukoaraiosis was performed by using diffusion ( $n = 75$ ), quantitative T2 ( $n = 54$ ), and DSC perfusion MRI metrics ( $n = 25$ ).

**RESULTS:** When we compared white matter hyperintensities with contralateral normal-appearing white matter, cerebrovascular reactivity was lower by a mean of  $61.2\% \pm 22.6\%$ , fractional anisotropy was lower by  $44.9\% \pm 6.9\%$ , and CBF was lower by  $10.9\% \pm 11.9\%$ . T2 was higher by  $61.7\% \pm 13.5\%$ , mean diffusivity was higher by  $59.0\% \pm 11.7\%$ , time-to-maximum was higher by  $44.4\% \pm 30.4\%$ , and TTP was higher by  $6.8\% \pm 5.8\%$  (all  $P < .01$ ). Cerebral blood volume was lower in white matter hyperintensities compared with contralateral normal-appearing white matter by  $10.2\% \pm 15.0\%$  ( $P = .03$ ).

**CONCLUSIONS:** Not only were resting blood flow metrics abnormal in leukoaraiosis but there is also evidence of reduced cerebrovascular reactivity in these areas. Studies have shown that reduced cerebrovascular reactivity is more sensitive than resting blood flow parameters for assessing vascular insufficiency. Future work is needed to examine the sensitivity of resting-versus-dynamic blood flow measures for investigating the pathogenesis of leukoaraiosis.

**ABBREVIATIONS:** BOLD = blood oxygen level–dependent; CVR = cerebrovascular reactivity; MD = mean diffusivity; NAWM = normal-appearing white matter;  $P_{ET}CO_2$  = end-tidal partial pressure of carbon dioxide;  $P_{ET}O_2$  = end-tidal partial pressure of oxygen; WMH = white matter hyperintensities

Age-related changes in the cerebral white matter are apparent on MR imaging. They appear as bright regions on T2-weighted images and are called white matter hyperintensities (WMH) if they are presumed to be of vascular origin. These areas are characterized by myelin pallor, reactive astrogliosis, and loss

of oligodendrocytes, axons, and myelin fibers.<sup>1</sup> This rarefaction of white matter tissue is the origin of the term “leukoaraiosis,” derived from the Greek words “leuko-” for white and “araios” for rarefied.<sup>2</sup> As many as 95% of individuals older than 50 years of age demonstrate these white matter changes, particularly in the periventricular and deep white matter.<sup>3,4</sup> Once thought to represent benign age-related changes, studies during the past 25 years have shown that WMH are associated with morbidity, including cognitive impairment<sup>5</sup> and disability.<sup>6–8</sup>

Substantial evidence indicates that age-related vascular changes may lead to WMH, including increased vessel tortuosity,<sup>9</sup>

Received November 20, 2015; accepted after revision June 7, 2016.

From the Departments of Physiology (K.S., J.D., J.A.F.) and Medical Imaging (A.P.C., D.J.M.), University of Toronto, Toronto, Ontario, Canada; Division of Neuroradiology (K.S., A.P.C., J.P., J.C., O.S., D.M.M., D.J.M.), Joint Department of Medical Imaging, University Health Network, Toronto, Ontario, Canada; Department of Anesthesiology (J.D., L.V., J.A.F.), University Health Network and The University of Toronto, Toronto, Ontario, Canada; and LC Campbell Cognitive Neurology Research Unit (S.E.B.), Sunnybrook Health Sciences Centre, Toronto, Ontario, Canada.

This work was supported by the Canadian Stroke Network and the Ontario Research Fund (RE 02-002) for Kevin Sam, Adrian P. Crawley, Julien Poubanc, John Conklin, Olivia Sobczyk, James Duffin, Daniel M. Mandell, Joseph A. Fisher, Sandra E. Black, and David J. Mikulis. This study was also supported by the Alternative Funding Plan for the Academic Health Sciences Centres of Ontario Innovation fund. Dr Black also acknowledges support for the Sunnybrook BrainLab from the Heart and Stroke Foundation Canadian Partnership for Stroke Recovery and the LC Campbell Foundation.

Please address correspondence to David John Mikulis, MD, Toronto Western Hospital, Joint Department of Medical Imaging, McLaughlin Pavilion, 3rd Floor, Room 431, 399 Bathurst St, Toronto, ON M5T 2S8, Canada; e-mail: mikulis@uhnres.utoronto.ca

 Indicates open access to non-subscribers at [www.ajnr.org](http://www.ajnr.org)

<http://dx.doi.org/10.3174/ajnr.A4888>

increased stringed vessels (remnants of capillaries with no endothelial cells), and vessel basement membrane thickening.<sup>10</sup> Histopathologic analysis of abnormal white matter shows venular intramural collagen deposition leading to wall-thickening stenosis.<sup>11</sup> The vascular anatomy of the white matter provides an intrinsically higher vascular resistance compared with the cortex.<sup>12</sup> Interestingly, white matter areas with excellent collateral blood supply, such as the subcortical U-fibers, do not usually show age-related WMH.<sup>13</sup> Collectively, these findings suggest an association between vascular dysfunction and leukoaraiosis.

In the present study, we sought to further characterize the vascular pathophysiology of WMH by evaluating cerebrovascular reactivity (CVR). CVR is defined as the change in cerebral blood flow induced by a vasoactive stimulus. Reduced CVR, normally found in the white matter of young healthy individuals,<sup>14</sup> has been shown to spatially correspond with predilection maps of age-related leukoaraiosis development.<sup>15</sup> CVR reductions are associated with cortical thinning,<sup>16</sup> the risk of future ischemic stroke,<sup>17</sup> cognitive decline,<sup>18</sup> and abnormal diffusion tensor imaging metrics.<sup>19</sup> WMH are associated with increased mean diffusivity (MD) and decreased fractional anisotropy, likely representing axonal destruction and glial proliferation.<sup>20</sup> Previous studies have found a relationship between impaired CVR and abnormal diffusion metrics in the white matter of patients with Moyamoya disease<sup>19</sup> and steno-occlusive carotid disease,<sup>21</sup> suggesting that chronic hypoperfusion is associated with pathologic changes to white matter microstructure. Moreover, vascular dysfunction in the form of blood-brain barrier leakage in WMH is also associated with increased MD.<sup>22</sup>

We evaluated CVR in regions of WMH and normal-appearing white matter (NAWM) by measuring the change in blood oxygen level-dependent (BOLD) MR imaging in response to a standard CO<sub>2</sub> challenge. To characterize the hemodynamic properties and microstructure of WMH, we obtained additional MR images and performed DTI and DSC perfusion MR imaging. We hypothesized that both CVR and these additional MR imaging metrics would differ between leukoaraiosis and NAWM.

## MATERIALS AND METHODS

### Subject Recruitment

Seventy-five older adults with age-related leukoaraiosis (age range, 50–91 years; 40 men) were recruited from outpatient neurology clinics at the Toronto Western Hospital and Sunnybrook Health Sciences Centre. Reasons for clinical referral included the following: chronic imbalance, gait disturbances, transient episodes of paresthesia, syncopal episodes, headaches, cognitive decline, or memory impairment. Informed consent and institutional research ethics board approval were obtained. All patients had undergone prior MRA or CTA and T2-weighted FLAIR imaging, which were screened by experienced neuroradiologists (D.M.M. and D.J.M.) before inclusion in the study.

Because no direct histologic confirmation could be obtained, the diagnosis of leukoaraiosis was based on the exclusion of other diseases that can generate MR imaging T2-weighted hyperintensities (subsequently listed). Clinical and imaging-based inclusion criteria were as follows: 1) a previous neurologic event involving

the white matter >3 months from presentation; 2) older than 50 years of age; 3) MRI white matter disease burden greater than Fazekas grade 2<sup>23</sup>; 4) no hemodynamically significant (ie, >50%) stenosis of the ICAs, vertebral arteries, or basilar artery on CTA or MRA; 5) no evidence of dissection; 6) no evidence of pulmonary or cardioembolic disease; and 7) no known history of CADASIL, multiple sclerosis, primary malignancy, previous CNS infection, or head trauma. Subjects with significant motion artifacts on BOLD images were excluded.

Forty-three patients from the Toronto Western Hospital (age range, 50–87 years; 23 men and 20 women), and 32 patients from Sunnybrook Health Sciences Centre (age range, 51–91 years; 17 men and 15 women) met the inclusion criteria and were considered in subsequent analysis. Age, Montreal Cognitive Assessment score,<sup>24</sup> gray matter volume, and white matter volume were collected as continuous variables. History of stroke, TIA, coronary artery disease, smoking, hypertension, diabetes mellitus, dyslipidemia, hypercholesterolemia, and obstructive sleep apnea were collected as binary variables.

### MR Imaging Acquisition

Subjects underwent MR imaging on a 3T system (Signa HDx platform; GE Healthcare, Milwaukee, Wisconsin) at the Toronto Western Hospital and a 3T Achieva system (Philips Healthcare, Best, the Netherlands) at Sunnybrook Health Sciences Centre by using an 8-channel phased array head coil. Subjects were asked to refrain from heavy exercise and drinking alcohol on the day of each scan. The imaging acquisition parameters were as follows:

T1-weighted 3D spoiled gradient-echo sequence: section thickness = 1.2–1.5 mm, matrix size = 256 × 256, FOV = 22 × 22 cm, flip angle = 8° to 20°, TE = 2.3–3 ms, TR = 7.8–9.5 ms; BOLD sequence was a T2\*-weighted echo-planar imaging gradient-echo sequence: section thickness = 3.0–5.0 mm, FOV = 24 × 24 cm, matrix size = 64 × 64, flip angle = 85° to 90°, TE = 30 ms, TR = 2000 ms; conventional FLAIR images: section thickness = 3 mm, 36 to 52 sections per volume, no intersection gap, matrix size = 256 × 224 to 240 × 240, FOV = 22 × 22 cm, flip angle = 90°, TE = 125 to 165 ms, TR = 9000 to 9145 ms, TI = 2200 to 2800 ms; diffusion tensor imaging with an echo-planar imaging spin-echo sequence: section thickness = 3 mm, matrix size = 76 × 62 to 128 × 128, FOV = 22 × 22 cm,  $b = 1000$  s/mm<sup>2</sup>, 23 diffusion-encoding gradients, 2 non-diffusion-weighted B0 images, TE = 55–80 ms, TR = 9150–14,500 ms; proton-density/T2-weighted images using fast spin-echo: section thickness = 3 mm, matrix size = 128 × 128 to 256 × 209, FOV = 22 × 22 cm, flip angle = 90°, TE = 11.1/90–11/102 ms, TR = 2500–7200 ms; multiecho T2 mapping using a fast spin-echo: section thickness = 3 mm, no intersection gap, matrix size = 256 × 192, FOV = 230 × 184 to 22 × 22 cm, TE = 13, 26, 39, 52, 65, 78, 91, 104, 117, 130, 143, 156 ms, TR = 5000–6000 ms; and DSC perfusion imaging using a gradient-multiphase-echo echo-planar imaging sequence: section thickness = 5 mm, matrix size = 128 × 128, FOV = 27 × 27 cm, flip angle = 90°, TE = 31.5 ms, TR = 1725 ms, 50 sections per location, during which a single bolus of 0.1 mmol/kg of gadolinium contrast agent was injected at a rate of 5 mL/s.

### **Vasodilatory Stimulus**

CVR was assessed by measuring the change in BOLD MR imaging in response to a standardized change in end-tidal (ie, end-expiratory) partial pressure of carbon dioxide ( $P_{ET}CO_2$ ) as the vasodilatory stimulus.<sup>25</sup>  $P_{ET}CO_2$  and end-tidal partial pressure of oxygen ( $P_{ET}O_2$ ) were targeted independently of each other and of the subjects' minute ventilation and breathing pattern by using an automated gas blender and sequential gas delivery breathing circuit (RespirAct; Thornhill Research, Toronto, Canada). Targeting  $P_{ET}CO_2$  and  $P_{ET}O_2$  was achieved by administering blends of gases according to previously described algorithms.<sup>26</sup> The targeting sequence used in this study was the following: 1) baseline  $P_{ET}CO_2$  of 40 mm Hg for 60 seconds (normocapnia); 2) hypercapnic step change to  $P_{ET}CO_2$  of 50 mm Hg for 90 seconds; 3) return to baseline for 90 seconds; and 4) a second hypercapnic step for 120 seconds with a final return to baseline.<sup>27</sup> All steps were implemented while maintaining normoxia ( $P_{ET}O_2 \sim 110$  mm Hg). CVR was calculated as  $\Delta\%$  BOLD/ $P_{ET}CO_2$ . CVR maps were displayed on a blue-to-red color scale, with regions of negative CVR (representative of steal physiology) in blue.

### **Image Reconstruction**

The acquired BOLD MR imaging and  $P_{ET}CO_2$  data were imported to a freeware program for analysis, Analysis of Functional Neuro Images (AFNI; <http://afni.nimh.nih.gov/afni>).<sup>28</sup> The BOLD time-series at each voxel was orthogonalized to 6 translational and rotational rigid body motion estimates by using the AFNI volume registration procedure to minimize any influence of hypercapnia-related head motion. BOLD images were section time-corrected and aligned to axial anatomic T1-weighted images. T1- and T2-weighted images were reviewed to identify regions of parenchymal infarction and prior hemorrhage. Masks of each parenchymal lesion were manually traced in AFNI and excluded from the CVR maps, which were calculated according to previously validated methods.<sup>29</sup> T1-weighted anatomic images were segmented into CSF, gray matter, and white matter by using SPM8 software (<http://www.fil.ion.ucl.ac.uk/spm/>). CSF was masked from the CVR maps.

Maps of the traverse relaxation time (T2) were calculated to confirm tissue dysfunction in the cerebral white matter. T2 reflects white matter water content and myelination and was calculated in AFNI by using methods previously described.<sup>30</sup> To calculate fractional anisotropy and MD maps, we imported diffusion-weighted images into FSL 4.1.8 (<http://www.fmrib.ox.ac.uk/fsl>).<sup>31</sup> Preprocessing included eddy current and motion artifact correction by using the FMRIB Diffusion Toolbox (<http://fsl.fmrib.ox.ac.uk/fsl/fslwiki/FDT>).<sup>32</sup> Individual brain masks were created by using the FSL Brain Extraction Tool (<http://fsl.fmrib.ox.ac.uk/fsl/fslwiki/BET>).<sup>33</sup> The preprocessed images were then fitted with a diffusion tensor model by using DTIFit ([http://fsl.fmrib.ox.ac.uk/fsl/fsl-4.1.9/fdt/fdt\\_dtifit.html](http://fsl.fmrib.ox.ac.uk/fsl/fsl-4.1.9/fdt/fdt_dtifit.html)),<sup>31</sup> and parametric maps of fractional anisotropy and MD were calculated for each subject.

The time-signal attenuation curves obtained from perfusion-weighted T2\* images were converted to time-concentration curves by using PerfTool,<sup>34</sup> which uses a delay-insensitive reformulated singular value decomposition approach to deconvolu-

tion of the time-concentration curves.<sup>35</sup> The arterial input function was selected from an ROI placed on the middle cerebral artery. These preprocessed perfusion-weighted images were used to generate maps of cerebral blood flow, relative cerebral blood volume, mean transit time, time-to-maximum, and time-to-peak by using PerfTool.<sup>34</sup>

### **Generating CVR Maps**

$P_{ET}CO_2$  data were first synchronized to the whole-brain average BOLD signal by using Matlab software (MathWorks, Natick, Massachusetts) to compensate for delays in breath sample analysis and the transit delay of blood flow from the pulmonary to cerebral circulation. A voxel-by-voxel linear least-squares fit of the BOLD signal time-series to the  $P_{ET}CO_2$  was performed, and the slope of the regression was taken as the CVR. CVR values are expressed as the percentage MR signal change per millimeter of mercury of  $P_{ET}CO_2$ .

### **Generating ROIs of WMH and NAWM**

The Lesion Explorer processing pipeline (available for download at <http://sabre.brainlab.ca>) was used to segment WMH and obtain measures of supratentorial total intracranial volume (total brain tissue and CSF).<sup>36,37</sup> All T1-weighted images were transformed into Montreal Neurological Institute space by using SPM8. The transformation matrix was applied to all quantitative MR imaging maps to perform the transformation to standard space while retaining the native structure. AFNI was used to identify NAWM contralateral to WMH. In brief, a diamond-shaped structuring element was used to erode the white matter in 5 iterations at the resolution of the T1-weighted image to prevent partial voluming effects. The WMHs were subtracted after erosion to give rise to a NAWM mask contralateral to the WMH ROI.

### **Accounting for the Confounding Factor of Spatial Location**

One important confounding factor that may produce differences between WMH and NAWM is spatial location. For example, WMH tend to develop in the periventricular white matter, and CVR may be lower in these areas. Therefore, CVR measurements in NAWM may be overestimated because CVR values in these regions tend to be higher. To account for this possibility, a second NAWM ROI was generated, including only those NAWM regions that are contralateral and spatially homologous to the regions of WMH (Fig 1).

### **Statistical Analyses**

Statistical analysis was performed with SPSS 21.0 (IBM, Armonk, New York). To assess the relationship between CVR and cognitive function, we performed a univariate general linear regression between CVR (within NAWM or WMH) and Montreal Cognitive Assessment scores, while controlling for age, sex, vascular risk factors, and total gray and white matter volume.

The relationship between each vascular risk factor and CVR was assessed with univariate regression analyses by using the CVR within each ROI (namely, WMH or NAWM, Fig 1G) as the dependent variable and either age, sex, Montreal Cognitive Assessment score, vascular risk factors (listed in Table 1), total gray

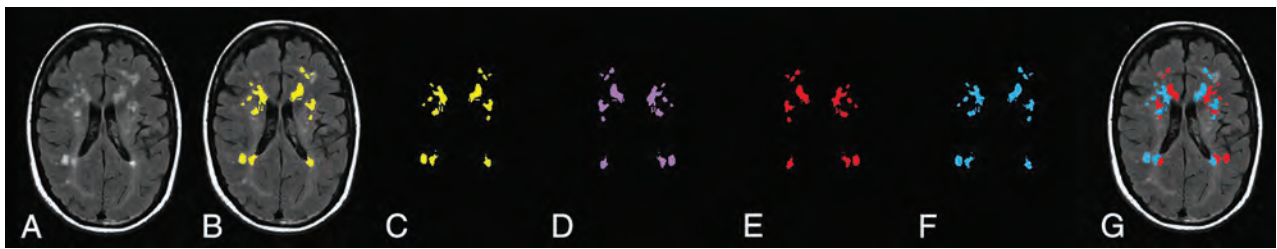


**FIG 1.** Calculation of ROIs used to control for differences in the spatial location of MR imaging metrics. *A*, Representative FLAIR image of a patient with periventricular and deep white matter hyperintensities. *B*, WMH are highlighted in yellow and overlaid on the FLAIR image. *C*, WMH (yellow) with the underlying FLAIR image removed. *D*, The WMH are left-right flipped about the y-axis (pink). This transformation is in Montreal Neurological Institute coordinates but retains the native structure (no warping of the brain). *E*, WMH (*C*) is subtracted from contralateral NAWM (pink). This is the final NAWM mask used in the statistical comparison between WMH and contralateral NAWM. *F*, Contralateral NAWM is left-right flipped and combined with the initial WMH ROI (*C*) by using a logical “and” operation; the resulting WMH mask includes only those voxels that have homologous NAWM in the contralateral hemisphere. This is the final WMH mask used in statistical comparisons between WMHs and contralateral NAWM. *G*, Final masks (*E* and *F*) overlaid on a FLAIR image.

**Table 1: Baseline characteristics of subjects**

Parameter	Value (N = 75)
<b>Demographics</b>	
Age (yr) (mean) (SD)	74 (9.7)
Men (No.) (%)	40 (53)
Baseline WMH volume (mL) (mean) (SD)	26.7 (23.5)
MoCA (mean) (SD) <sup>a</sup>	24 (5)
<b>Vascular risk factors (No.) (%)</b>	
Ischemic stroke	26 (35)
TIA	14 (19)
CAD	11 (15)
Dyslipidemia	39 (52)
Hypertension	47 (63)
Diabetes mellitus	10 (13)
Current smoking	4 (5)
Obstructive sleep apnea	6 (8)

**Note:**—CAD indicates coronary artery disease; MoCA = Montreal Cognitive Assessment.

<sup>a</sup> Six missing values.

matter volume, WMH volume, or NAWM volume as the independent variable. Partial  $\eta^2$  effect sizes were calculated for significant between-group results (ie, the presence-versus-absence of each vascular risk factor).

To assess the relationship between CVR, diffusion, and perfusion metrics, we calculated the Pearson linear correlation coefficient for each comparison between metrics, by using the difference in each parameter value between WMH and NAWM.

Statistical comparisons of CVR, DTI, and perfusion parameter differences between WMH and NAWM were performed by using a paired Student *t* test. Results were considered significant at  $\alpha = .05$ .

## RESULTS

The 75 subjects had a mean WMH volume of  $26.7 \pm 23.5$  mL per subject (range, 0.3–93.9 mL). Table 1 provides their demographics. Table 2 shows comparisons between WMH and the contralateral NAWM. Comparisons between these 2 ROIs for each metric are provided in Fig 2.

CVR, fractional anisotropy, and CBF were reduced in WMH compared with NAWM, while T2, MD, and time-to-maximum were increased in WMH compared with NAWM (all,  $P < .01$ ). CBV was reduced in WMH compared with NAWM ( $P = .03$ ). MTT values were not significantly different between WMH and NAWM. There was no correlation between CVR and the other

diffusion and perfusion metrics for any of the ROIs considered (WMH, NAWM, and total white matter); and there was no relationship between CVR and Montreal Cognitive Assessment scores (mean,  $24/30 \pm 4.8$ ). Previous stroke was associated with lower CVR in WMH ( $P < .05$ ;  $\eta^2 = 0.07$  moderate effect size). There was no significant association between CVR and the remaining vascular risk factors listed in Table 1.

## DISCUSSION

Our results provide evidence for vascular dysfunction in regions of leukoaraiosis, characterized by quantitative changes in multiple MR imaging parameters. Compared with the contralateral NAWM, the increased MD and decreased fractional anisotropy in leukoaraiosis are consistent with the findings in previous studies<sup>38,39</sup> and indicate that white matter structural integrity has been compromised and water is able to diffuse more freely through areas of demyelination and axonal degeneration.<sup>40</sup> Quantitative T2 values were higher in leukoaraiosis, which is to be expected because this indicates increased water content due to loss in tissue structure.<sup>41</sup> CBF was reduced; this change indicated a reduction in blood supply,<sup>22</sup> CBV was also reduced; this change suggested decreased density of the local microvasculature.<sup>42</sup> Finally, time-dependent MR imaging metrics such as time-to-maximum and TTP were prolonged in leukoaraiosis; this finding demonstrates a delay in the blood supply to areas of leukoaraiosis. Collectively, these abnormal MR imaging metrics provide evidence for vascular dysfunction in areas of leukoaraiosis in our cohort of patients.

We also found that CVR in regions of leukoaraiosis was significantly lower than in NAWM. These results are similar to findings from a previous study by Uh et al<sup>22</sup> reporting lower CVR values in leukoaraiosis. However, the approach to CVR quantification in the present study is more accurate. Inhalation of 5% CO<sub>2</sub> (as performed by Uh et al) produces a variable PaCO<sub>2</sub> stimulus that depends on the subject’s minute ventilation and breathing pattern, which can lead to inaccurate CVR quantitation.<sup>43</sup> Our ability to maintain a standardized extended period of hypercapnia (independent of minute ventilation) provides greater confidence in the accuracy of our CVR measurements.

Reduced CVR suggests a role for endothelial dysfunction in the development of leukoaraiosis and is consistent with the findings of Hassan et al,<sup>44</sup> who demonstrated upregulated markers of endothelial activation and damage in leukoaraiosis. By account-

**Table 2: Measurements of CVR, FA, MD, T2, and perfusion metrics in WMH and contralateral homologous NAWM**

	WMH (Contralateral to NAWM), Mean (SD)	NAWM (Contralateral to WMH), Mean (SD)	Paired Differences			
			Mean (SD)	95% CI Difference	t-Score	df
CVR (% BOLD/mm Hg)	0.05 (0.07)	0.13 (0.03)	0.06 (0.03)	0.05–0.07	14.8 <sup>a</sup>	74
FA (unitless)	0.28 (0.07)	0.50 (0.11)	0.18 (0.04)	1.72–1.91	38.2 <sup>a</sup>	74
MD ( $\times 10^{-3}$ mm <sup>2</sup> /s)	1.37 (0.11)	0.84 (0.03)	0.51 (0.11)	0.48–0.54	40.7 <sup>a</sup>	74
T2 (ms)	136.7 (14.4)	84.9 (4.9)	51.6 (11.8)	48.5–54.8	32.3 <sup>a</sup>	53
CBF (mL/100 g/min)	18.2 (3.5)	21.0 (4.4)	1.9 (4.3)	0.16–3.7	2.8 ( <i>P</i> = .01)	24
rCBV (AU) <sup>b</sup>	103.9 (10.1)	117.5 (9.3)	8.9 (19.7)	0.8–17.7	2.3 ( <i>P</i> = .03)	24
MTT (s)	4.6 (0.5)	4.1 (0.3)	0.3 (1.1)	–0.1–0.8	1.5 ( <i>P</i> = .15)	24
Tmax (s)	3.5 (0.3)	2.4 (0.2)	1.1 (0.8)	0.8–1.2	6.8 <sup>a</sup>	24
TTP (s)	22.3 (1.3)	20.8 (1.0)	1.6 (1.2)	1.1–2.1	6.7 <sup>a</sup>	24

**Note:**—FA indicates fractional anisotropy; rCBV, relative CBV; Tmax, time-to-maximum; AU, arbitrary units.

<sup>a</sup> *P* < .001 compared with contralateral WMH.

<sup>b</sup> These arbitrary units indicate that WMH are reduced compared to contralateral NAWM by 10.2%.

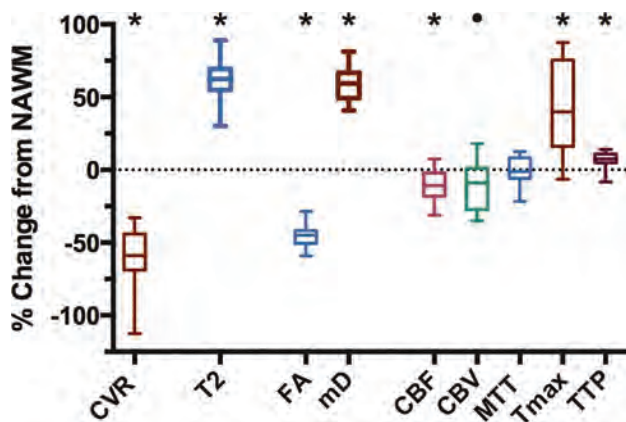


**FIG 2.** Relative values of MR imaging metrics in WMH compared with contralateral NAWM. The values of each MR imaging metric are given as a percentage change from NAWM. The ROIs used for these measurements are taken from Fig 1G. CVR, fractional anisotropy, CBF, and relative CBV values are significantly lower in WMH compared with NAWM, while MD, T2, MTT, time-to-maximum, and TTP are significantly higher in WMH compared with NAWM (asterisk, *P* < .01, compared with NAWM, and circle, *P* < .05, compared with NAWM). Bars indicate minimum and maximum; boxes, the interquartile range; and the line within each box, the median. FA indicates fractional anisotropy; Tmax, time-to-maximum; MD, mean diffusivity.

ing for spatial location, we point out that the areas with diminished CVR were colocalized with diffusion and perfusion abnormalities, which were seen only in WMH and not in the contralateral NAWM. Furthermore, the subjects who presented with strokes had a decreased CVR in WMH. Together, these findings support our hypothesis that vascular dysfunction, with loss in blood flow control, exacerbates white matter damage in areas of WMH.

Our results are consistent with those in other studies reporting CBF reductions in leukoaraiosis compared with NAWM,<sup>22,45–47</sup> but they are not in agreement for CBV. We found a reduction in CBV, possibly due to a loss of vascular density, whereas another study showed no difference in CBV between leukoaraiosis and NAWM.<sup>46</sup> These observations of reduced perfusion metrics and CVR in leukoaraiosis are also in agreement with predilection maps demonstrating that regions of white matter with lower perfusion have a higher frequency of leukoaraiosis.<sup>45,48</sup> Finally, we found prolonged time-dependent perfusion measures in leukoaraiosis. Prolonged TTP and time-to-maximum values have

also been reported in the infarct core of patients with acute stroke, by using CT perfusion.<sup>49</sup>

CVR may be more sensitive than resting blood flow metrics for the following reasons: CBF measures can be normal due to the action of vascular autoregulation, CBV is difficult to quantitate accurately, and transit time measures can be increased but with normal CVR, with collaterals that maintain normal resting blood flow.<sup>50</sup>

Our study is limited in several respects. First, our measure of CVR is based on the percentage BOLD change per millimeter of mercury  $P_{ET}CO_2$ . The BOLD signal does not measure blood flow directly but represents an interaction of arterial partial pressure of oxygen, cerebral blood flow, cerebral blood volume, hematocrit, and cerebral metabolic rate of oxygen.<sup>51</sup> However, we have previously shown that the BOLD MR imaging signal response to hypercapnia is well-correlated with CBF measurements obtained by using arterial spin-labeling in patients with steno-occlusive disease.<sup>52</sup> Second, only a subset of subjects underwent quantitative T2 measurements (54 of 75 subjects) and perfusion measurements (25 of 75 subjects). Third, we report only limited cognitive measures; only the Montreal Cognitive Assessment score was collected, which did not provide a detailed profile of each subject's cognitive status. In this respect, our study was not designed to assess the relationship between impaired CVR and cognitive function. An extensive neuropsychological battery would have been needed for this purpose. Finally, we acknowledge that the criterion standard of histopathologic diagnosis was not obtained in our patient cohort.

## CONCLUSIONS

WMH demonstrate abnormal hemodynamic parameters in a pattern consistent with diminished blood flow regulation and increased vulnerability to transient ischemia compared with NAWM. It remains to be determined whether impaired CVR is a causative and/or predictive factor in the pathogenesis of leukoaraiosis versus a secondary response to the reduced metabolic activity of leukoaraiotic tissue. Whether the impaired reactivity in white matter precedes white matter tissue injury or vice versa remains unclear, and a 1-year follow-up study in this cohort of patients is planned to better address this question. Nevertheless, our findings support the hypothesis that vascular dysfunction in cerebrovascular regulation is an important factor in the pathophysiology of white matter disease.

## ACKNOWLEDGMENTS

We are grateful to the Toronto Western Hospital and Sunnybrook Health Sciences Centre RespirAct technologists, Anne Battisti-Charbonney and Diem Pham, and the MR imaging technologists, Keith Ta and Eugen Hlasny. We also thank David Crane (MacIntosh laboratory manager) and Anoop Ganda (psychometrist/research coordinator) for enabling the Sunnybrook data acquisition, which required availability after hours and on weekends. Last, we greatly appreciate the assistance of Alicia McNeely and Courtney Berezuk, Sunnybrook BrainLab imaging analysts, for identifying areas of white matter hyperintensities and lacunes for the Sunnybrook dataset, and to Christopher Scott, Sunnybrook BrainLab manager, for facilitating training and analysis by using the Lesion Explorer pipeline.

Disclosures: Kevin Sam—*RELATED: Grant:* Research funding was provided by the Canadian Stroke Network from 2010 to 2014.\* *Olivia Sobczyk—UNRELATED: Consultancy:* Thornhill Research Inc, *Comments:* for the RespirAct device, but not in relation to the submitted work. *James Duffin—UNRELATED: Employment:* I am the senior scientist at Thornhill Research. *Joseph A. Fisher—UNRELATED: Other:* I am one of the inventors of the RespirAct used in the study. I also have shares in and sit on the board of the company. Thornhill Research is a spinoff from the University Health Network, part of the University of Toronto. The RespirAct is a research tool and not a commercial product. Should it ever become one, I would stand to profit\*. *OTHER:* coinventor of the RespirAct, a device used in this study. I also hold shares and serve as a director of Thornhill Research Inc, a University of Toronto/University Health Network-related company, which retains an ownership position and will receive royalties should the RespirAct become a commercial product. *Sandra E. Black—RELATED: Grant:* Canadian Stroke Network (2010–2014)\*; *UNRELATED: Grants/Grants Pending:* Elan,\* Roche,\* GE Healthcare,\* Eli Lilly,\* Pfizer,\* Lundbeck,\* Glaxo-SmithKline,\* Transition Therapeutics,\* Biogen Idec,\* *Comments:* contract research to the institution; *Payment for Lectures (including service on Speakers Bureaus):* Continuing Medical Education lectures for Novartis, Eisai, Pfizer; *OTHER:* received compensation in the past 2 years for ad hoc consulting with Boehringer Ingelheim and Novartis and honoraria from the Rehabilitation Institute of Chicago, the Heart and Stroke/Richard Lewar Centre of Excellence in Cardiovascular Research, Eisai Korea, and Novartis. My research unit is receiving research funding from Roche, GE Healthcare, Lilly Avid, Pfizer, Lundbeck, and Transition Therapeutics. I also receive research funding from the Canadian Institutes of Health Research, National Institutes of Health, Heart and Stroke Foundation of Canada, Alzheimer Drug Discovery Foundation, Weston Foundation, Brain Canada, University of Toronto Department of Medicine, and the Ontario Brain Institute. *David J. Mikulis—RELATED: Grant:* Canadian Institutes of Health Research\*; *UNRELATED:* Canadian Institutes of Health Research,\* GE Healthcare,\* Physician's Services Incorporated Foundation; *Stock/Stock Options:* stock (<2% equity in Thornhill Research Inc, the vendor of the RespirAct); *OTHER:* I am coinventor of the RespirAct, a device used in this study and hold a minor equity position in Thornhill Research Inc and have received research support from GE Healthcare, Siemens, Toshiba, and the Ontario Research Fund. \*Money paid to the institution.

## REFERENCES

1. Simpson JE, Fernando MS, Clark L, et al; MRC Cognitive Function and Ageing Neuropathology Study Group. **White matter lesions in an unselected cohort of the elderly: astrocytic, microglial and oligodendrocyte precursor cell responses.** *Neuropathol Appl Neurobiol* 2007;33:410–19 CrossRef Medline
2. Hachinski VC, Potter P, Merskey H. **Leuko-araiosis: an ancient term for a new problem.** *Can J Neurol Sci* 1986;13(4 suppl):533–34 Medline
3. de Leeuw FE, de Groot JC, Achten E, et al. **Prevalence of cerebral white matter lesions in elderly people: a population based magnetic resonance imaging study—the Rotterdam Scan Study.** *J Neurol Neurosurg Psychiatry* 2001;70:9–14 CrossRef Medline
4. Launer LJ, Berger K, Breteler MM, et al. **Regional variability in the prevalence of cerebral white matter lesions: an MRI study in 9 European countries (CASCADE).** *Neuroepidemiology* 2006;26:23–29 Medline
5. Verdelho A, Madureira S, Moleiro C, et al; LADIS Study. **White matter changes and diabetes predict cognitive decline in the elderly: the LADIS study.** *Neurology* 2010;75:160–67 CrossRef Medline
6. Whitman GT, Tang Y, Lin A, et al. **A prospective study of cerebral white matter abnormalities in older people with gait dysfunction.** *Neurology* 2001;57:990–94 CrossRef Medline
7. Ogama N, Sakurai T, Shimizu A, et al. **Regional white matter lesions predict falls in patients with amnesic mild cognitive impairment and Alzheimer's disease.** *J Am Med Dir Assoc* 2014;15:36–41 CrossRef Medline
8. Malmstrom TK, Morley JE. **The frail brain.** *J Am Med Dir Assoc* 2013;14:453–55 CrossRef Medline
9. Moody DM, Santamore WP, Bell MA. **Does tortuosity in cerebral arterioles impair down-autoregulation in hypertensives and elderly normotensives? A hypothesis and computer model.** *Clin Neurosurg* 1991;37:372–87 Medline
10. Farkas E, de Vos RA, Donka G, et al. **Age-related microvascular degeneration in the human cerebral periventricular white matter.** *Acta Neuropathol* 2006;111:150–57 CrossRef Medline
11. Moody DM, Brown WR, Challa VR, et al. **Periventricular venous collagenosis: association with leukoaraiosis.** *Radiology* 1995;194:469–76 CrossRef Medline
12. Moody DM, Brown WR, Challa VR, et al. **Cerebral microvascular alterations in aging, leukoaraiosis, and Alzheimer's disease.** *Ann N Y Acad Sci* 1997;826:103–16 CrossRef Medline
13. Henry-Feugeas MC. **Alzheimer's disease in late-life dementia: a minor toxic consequence of devastating cerebrovascular dysfunction.** *Med Hypotheses* 2008;70:866–75 CrossRef Medline
14. Mandell DM, Han JS, Poulblanc J, et al. **Selective reduction of blood flow to white matter during hypercapnia corresponds with leukoaraiosis.** *Stroke* 2008;39:1993–98 CrossRef Medline
15. Sachdev P, Wen W, Chen X, et al. **Progression of white matter hyperintensities in elderly individuals over 3 years.** *Neurology* 2007;68:214–22 CrossRef Medline
16. Fierstra J, Poulblanc J, Han JS, et al. **Steal physiology is spatially associated with cortical thinning.** *J Neurol Neurosurg Psychiatry* 2010;81:290–93 CrossRef Medline
17. Markus H, Cullinane M. **Severely impaired cerebrovascular reactivity predicts stroke and TIA risk in patients with carotid artery stenosis and occlusion.** *Brain* 2001;124(pt 3):457–67 CrossRef Medline
18. Balucani C, Viticchi G, Falsetti L, et al. **Cerebral hemodynamics and cognitive performance in bilateral asymptomatic carotid stenosis.** *Neurology* 2012;79:1788–95 CrossRef Medline
19. Conklin J, Fierstra J, Crawley AP, et al. **Impaired cerebrovascular reactivity with steal phenomenon is associated with increased diffusion in white matter of patients with Moyamoya disease.** *Stroke* 2010;41:1610–16 CrossRef Medline
20. Helenius J, Soenne L, Salonen O, et al. **Leukoaraiosis, ischemic stroke, and normal white matter on diffusion-weighted MRI.** *Stroke* 2002;33:45–50 CrossRef Medline
21. Conklin J, Fierstra J, Crawley AP, et al. **Mapping white matter diffusion and cerebrovascular reactivity in carotid occlusive disease.** *Neurology* 2011;77:431–38 CrossRef Medline
22. Uh J, Yezhuvath U, Cheng Y, et al. **In vivo vascular hallmarks of diffuse leukoaraiosis.** *J Magn Reson Imaging* 2010;32:184–90 CrossRef Medline
23. Fazekas F, Kleinert R, Offenbacher H, et al. **Pathologic correlates of incidental MRI white matter signal hyperintensities.** *Neurology* 1993;43:1683–89 CrossRef Medline
24. Nasreddine ZS, Phillips NA, Bedirian V, et al. **The Montreal Cognitive Assessment, MoCA: a brief screening tool for mild cognitive impairment.** *J Am Geriatr Soc* 2005;53:695–99 CrossRef Medline
25. Han JS, Mikulis DJ, Mardimae A, et al. **Measurement of cerebrovascular reactivity in pediatric patients with cerebral vasculopathy using blood oxygen level-dependent MRI.** *Stroke* 2011;42:1261–69 CrossRef Medline
26. Slessarev M, Han J, Mardimae A, et al. **Prospective targeting and control of end-tidal CO<sub>2</sub> and O<sub>2</sub> concentrations.** *J Physiol* 2007;581(pt 3):1207–19 CrossRef Medline

27. Vesely A, Sasano H, Volgyesi G, et al. **MRI mapping of cerebrovascular reactivity using square wave changes in end-tidal PCO<sub>2</sub>.** *Magn Reson Med* 2001;45:1011–13 CrossRef Medline
28. Cox RW. **AFNI: software for analysis and visualization of functional magnetic resonance neuroimages.** *Comput Biomed Res* 1996; 29:162–73 CrossRef Medline
29. Poubanc J, Crawley AP, Sobczyk O, et al. **Measuring cerebrovascular reactivity: the dynamic response to a step hypercapnic stimulus.** *J Cereb Blood Flow Metab* 2015;35:1746–56 CrossRef Medline
30. Miller AJ, Joseph PM. **The use of power images to perform quantitative analysis on low SNR MR images.** *Magn Reson Imaging* 1993; 11:1051–56 CrossRef Medline
31. Smith SM, Jenkinson M, Woolrich MW, et al. **Advances in functional and structural MR image analysis and implementation as FSL.** *Neuroimage* 2004;23(suppl 1):S208–19 CrossRef Medline
32. Jenkinson M, Bannister P, Brady M, et al. **Improved optimization for the robust and accurate linear registration and motion correction of brain images.** *Neuroimage* 2002;17:825–41 CrossRef Medline
33. Smith SM. **Fast robust automated brain extraction.** *Hum Brain Mapp* 2002;17:143–55 CrossRef Medline
34. Kosior JC, Frayne R. **PerfTool: a software platform for investigating bolus-tracking perfusion imaging quantification strategies.** *J Magn Reson Imaging* 2007;25:653–59 CrossRef Medline
35. Smith MR, Lu H, Trochet S, et al. **Removing the effect of SVD algorithmic artifacts present in quantitative MR perfusion studies.** *Magn Reson Med* 2004;51:631–34 CrossRef Medline
36. Ramirez J, Scott CJ, McNeely AA, et al. **Lesion Explorer: a video-guided, standardized protocol for accurate and reliable MRI-derived volumetrics in Alzheimer's disease and normal elderly.** *J Vis Exp* 2014;(86) doi: 10.3791/50887 CrossRef Medline
37. Ramirez J, Gibson E, Qudus A, et al. **Lesion Explorer: a comprehensive segmentation and parcellation package to obtain regional volumetrics for subcortical hyperintensities and intracranial tissue.** *Neuroimage* 2011;54:963–73 CrossRef Medline
38. Bastin ME, Clayden JD, Pattie A, et al. **Diffusion tensor and magnetization transfer MRI measurements of periventricular white matter hyperintensities in old age.** *Neurobiol Aging* 2009;30:125–36 CrossRef Medline
39. Maniega SM, Valdés Hernández MC, Clayden JD, et al. **White matter hyperintensities and normal-appearing white matter integrity in the aging brain.** *Neurobiol Aging* 2015;36:909–18 CrossRef Medline
40. Feldman HM, Yeatman JD, Lee ES, et al. **Diffusion tensor imaging: a review for pediatric researchers and clinicians.** *J Dev Behav Pediatr* 2010;31:346–56 CrossRef Medline
41. Haller S, Kövari E, Herrmann FR, et al. **Do brain T2/FLAIR white matter hyperintensities correspond to myelin loss in normal aging? A radiologic-neuropathologic correlation study.** *Acta Neuropathol Commun* 2013;1:14 CrossRef Medline
42. Lin CY, Chang C, Cheung WM, et al. **Dynamic changes in vascular permeability, cerebral blood volume, vascular density, and size after transient focal cerebral ischemia in rats: evaluation with contrast-enhanced magnetic resonance imaging.** *J Cereb Blood Flow Metab* 2008;28:1491–501 CrossRef Medline
43. Sobczyk O, Battisti-Charbonney A, Fierstra J, et al. **A conceptual model for CO<sub>2</sub>-induced redistribution of cerebral blood flow with experimental confirmation using BOLD MRI.** *Neuroimage* 2014;92: 56–68 CrossRef Medline
44. Hassan A, Hunt BJ, O'Sullivan M, et al. **Markers of endothelial dysfunction in lacunar infarction and ischaemic leukoaraiosis.** *Brain* 2003;126(pt 2):424–32 CrossRef Medline
45. Brickman AM, Zahra A, Muraskin J, et al. **Reduction in cerebral blood flow in areas appearing as white matter hyperintensities on magnetic resonance imaging.** *Psychiatry Res* 2009;172:117–20 CrossRef Medline
46. Marstrand JR, Garde E, Rostrup E, et al. **Cerebral perfusion and cerebrovascular reactivity are reduced in white matter hyperintensities.** *Stroke* 2002;33:972–76 CrossRef Medline
47. O'Sullivan M, Lythgoe DJ, Pereira AC, et al. **Patterns of cerebral blood flow reduction in patients with ischemic leukoaraiosis.** *Neurology* 2002;59:321–26 CrossRef Medline
48. Holland CM, Smith EE, Csapo I, et al. **Spatial distribution of white-matter hyperintensities in Alzheimer disease, cerebral amyloid angiopathy, and healthy aging.** *Stroke* 2008;39:1127–33 CrossRef Medline
49. Campbell BC, Christensen S, Levi CR, et al. **Cerebral blood flow is the optimal CT perfusion parameter for assessing infarct core.** *Stroke* 2011;42:3435–40 CrossRef Medline
50. Leoni RF, Mazzetto-Betti KC, Silva AC, et al. **Assessing cerebrovascular reactivity in carotid steno-occlusive disease using MRI BOLD and ASL techniques.** *Radiol Res Pract* 2012;2012:268483 CrossRef Medline
51. Ogawa S, Lee TM, Barrere B. **The sensitivity of magnetic resonance image signals of a rat brain to changes in the cerebral venous blood oxygenation.** *Magn Reson Med* 1993;29:205–10 CrossRef Medline
52. Mandell DM, Han JS, Poubanc J, et al. **Mapping cerebrovascular reactivity using blood oxygen level-dependent MRI in patients with arterial steno-occlusive disease: comparison with arterial spin labeling MRI.** *Stroke* 2008;39:2021–28 CrossRef Medline

# Comparison of Quantitative Cerebral Blood Flow Measurements Performed by Bookend Dynamic Susceptibility Contrast and Arterial Spin-Labeling MRI in Relapsing-Remitting Multiple Sclerosis

R.M. D'Ortenzio, S.P. Hojjat, R. Vitorino, C.G. Cantrell, L. Lee, A. Feinstein, P. O'Connor, T.J. Carroll, and R.I. Aviv



## ABSTRACT

**BACKGROUND AND PURPOSE:** Quantitative CBF usage as a biomarker for cognitive impairment and disease progression in MS is potentially a powerful tool for longitudinal patient monitoring. Dynamic susceptibility contrast perfusion with bookend TI-calibration (bookend technique) and pseudocontinuous arterial spin-labeling have recently been used for CBF quantification in relapsing-remitting MS. The noninvasive nature of pseudocontinuous arterial spin-labeling is advantageous over gadolinium-based techniques, but correlation between the techniques is not well-established in the context of MS.

**MATERIALS AND METHODS:** We compared pseudocontinuous arterial spin-labeling CBF with the bookend technique in a prospective cohort of 19 healthy controls, 19 subjects with relapsing-remitting MS without cognitive impairment, and 20 subjects with relapsing-remitting MS with cognitive impairment on a voxelwise and Brodmann region basis. The linear Pearson correlation, SNR, and coefficient of variation were quantified.

**RESULTS:** Voxelwise paired *t* tests revealed no significant CBF differences between techniques after normalization of global mean intensities. The highest Pearson correlations were observed in deep GM structures (average  $r = 0.71$  for the basal ganglia and  $r = 0.65$  for the thalamus) but remained robust for cortical GM, WM, and white matter lesions (average  $r = 0.51, 0.53, 0.54$ , respectively). Lower Pearson correlations were observed for cortical lesions (average  $r = 0.23$ ). Brodmann region correlations were significant for all groups. All correlations were maintained in healthy controls and in patients with relapsing-remitting multiple sclerosis. The highest SNR was present in bookend perfusion, while the highest coefficient of variation was present in white matter lesions.

**CONCLUSIONS:** Agreement between pseudocontinuous arterial spin-labeling and bookend technique CBF measurements is demonstrated in healthy controls and patients with relapsing-remitting MS.

**ABBREVIATIONS:** BG = basal ganglia; CL = cortical lesion; CV = coefficient of variation; HC = healthy controls; pCASL = pseudocontinuous arterial spin-labeling; RRMS = relapsing-remitting MS; RRMS-I = RRMS with cognitive impairment cohort; RRMS-NI = RRMS not cognitively impaired cohort; TH = thalamus; WML = white matter lesion

Multiple sclerosis is the most common nontraumatic cause of neurologic disability in young and middle-aged adults.<sup>1</sup> In addition to physical disability, cognitive impairment is an important contributor to functional disability in patients with MS and increasingly recognized as an important contributor to quality of

life.<sup>2</sup> Cerebral hypoperfusion has been well-described in MS, initially with PET and recently with MR imaging.<sup>3-6</sup> The etiology is likely multifactorial<sup>7</sup>; primary and secondary hypoperfusion, metabolic dysfunction, and primary cerebrovascular abnormality are all posited.<sup>8</sup>

Few studies have evaluated the role of deep gray matter or cortical perfusion in cognition. Recently, quantitative CBF perfusion imaging has been shown to correlate strongly with cognitive impairment in relapsing-remitting multiple sclerosis.<sup>9-11</sup> A pseudocontinuous arterial spin-labeling (pCASL) study demonstrated a 7% reduction in cortical CBF in early relapsing-remitting

Received May 14, 2016; accepted June 23.

From the Departments of Psychiatry (A.F.), Neurology (L.L.), and Medical Imaging (S.P.H., R.V., R.I.A.), Sunnybrook Health Sciences Centre, Toronto, Ontario, Canada; University of Toronto (R.M.D., P.O.C., L.L., A.F., R.I.A.), Toronto, Ontario, Canada; and Departments of Biomedical Engineering (C.G.C., T.J.C.) and Radiology (T.J.C.), Northwestern University, Chicago, Illinois.

R.M. D'Ortenzio and S.P. Hojjat contributed equally to this work.

Robert D'Ortenzio was supported by the Comprehensive Research Experience for Medical Students program at University of Toronto. Dr Aviv was supported by a Canadian Institute of Health Research operating grant. Drs Aviv and Hojjat are supported by a Biogen fellowship funding award. Charles Cantrell is supported by the American Heart Association (14PRE20380310). Dr Carroll is supported by a National Institutes of Health grant (1R21EB017928-01A1).

Please address correspondence to Seyed-Parsa Hojjat, PhD, Sunnybrook Health Sciences Centre, 2075 Bayview Ave, Room AB-204, Toronto, ON, M4N 3M5, Canada; e-mail: r.dortenzio@mail.utoronto.ca

Indicates open access to non-subscribers at www.ajnr.org

<http://dx.doi.org/10.3174/ajnr.A4939>

ting MS (RRMS) compared with healthy controls (HC), with cortical CBF reduction associated with lower memory scores in the RRMS group.<sup>9</sup> Another pCASL study demonstrated focal cerebral hypoperfusion in functionally important areas in cognitively impaired RRMS groups compared with HC and cognitively preserved RRMS groups.<sup>10</sup> Similar results were shown by using the bookend perfusion technique in RRMS and patients with secondary-progressive MS, in which hypoperfusion explained ~7%–20% of cognitive impairment, respectively, after correction for confounding factors.<sup>11,12</sup> Most important, hypoperfusion was present in the patients with cognitive impairment compared those without impairment in RRMS in the absence of structural differences. Cortical CBV reduction in MS was independently associated with overall cognitive impairment and correlated highly with individual cognitive tests.<sup>13</sup> Data are also available from studies evaluating deep gray matter perfusion. Inglese et al<sup>14</sup> reported a significant CBV reduction in deep GM perfusion in primary-progressive MS compared with relapsing-remitting MS. Deep GM CBV correlated with the Color-Word Interference Test (Delis-Kaplan Executive Function System).<sup>14</sup> These results demonstrate the apparently independent role that cortical hypoperfusion plays in cognition in MS, suggesting utility as a biomarker of cortical disease severity.

The bookend perfusion technique, which uses unique “bookend” calibration scans on either side of a conventional DSC sequence, is validated against H<sub>2</sub> [<sup>15</sup>O] PET and demonstrates high test-retest repeatability.<sup>15</sup> Most important, the technique demonstrates reproducible CBF measurements in both HC and disease states, providing both GM and WM perfusion metrics and demonstrating high signal to noise by exploiting the T2\* effects of gadolinium.<sup>16,17</sup> The acquisition and processing are vendor-neutral and can be implemented by using sequences already available on most MR imaging scanners. Disadvantages include the need for gadolinium administration, with a potential for increased adverse events, stimulating a growing interest in noncontrast-based perfusion sequences such as pCASL.<sup>18</sup> pCASL exploits magnetically polarized protons in water molecules in arterial blood as an endogenous tracer and, therefore, does not require contrast administration.<sup>19,20</sup> Quantitative CBF is achieved with good success, especially in the GM of healthy individuals.<sup>21–23</sup> Disadvantages include the inherently low SNR and longer transit times associated with WM, rendering WM CBF signal unreliable.<sup>24</sup> Last, pCASL is mostly limited to larger research centers, with limited routine clinical use compared with DSC sequences.

Given the options available for quantitative imaging and the potential role for longitudinal cognitive impairment monitoring in MS via perfusion measurements, we sought to compare the pCASL and bookend perfusion techniques in HC and an RRMS not cognitively impaired cohort (RRMS-NI) and an RRMS with cognitive impairment cohort (RRMS-I) to assess their correlation coefficient of variation (CV) and SNR in the healthy and disease states. We hypothesized that good correlation would be seen between the 2 techniques in the context of an RRMS study cohort but that the SNR would be higher in bookend CBF measurements.

## MATERIALS AND METHODS

### Patient Cohorts

This study was approved by the Sunnybrook Ethics Review Board, and informed consent was obtained for all patients. Patients with RRMS were prospectively recruited during 1 year from 2 tertiary referral MS clinics by a senior neurologist with specialist practice in MS (20 years' experience). The Montreal Cognitive Assessment screening<sup>25</sup> was initially used to identify 20 patients with RRMS-I followed by 19 age- and sex-matched patients with RRMS-NI and 19 HC. Exclusion criteria were a history of drug/alcohol abuse, MS disease activity or steroid use within the past 3 months, pre-morbid (ie, pre-MS) psychiatric history, head injury with loss of consciousness, concurrent medical diseases (eg, cerebrovascular disease), and contraindications to MR imaging/gadolinium (eg, impaired renal function).

### Cognitive Testing

Briefly, cognitive testing was performed by using a comprehensive test validated for use in MS (the Minimal Assessment of Cognitive Function In Multiple Sclerosis), testing processing speed, working and visuospatial memory (Paced Auditory Serial Addition Test, Symbol Digit Modalities Test), executive function (Delis-Kaplan Executive Function System), verbal fluency (California Verbal Learning Test-Second Edition, Brief Visuospatial Test-Revised), visuospatial perception and spatial processing (Judgment of Line Orientation Test), and verbal fluency (Controlled Oral Word Association Test).<sup>26</sup> Consistent with convention, patients scoring >1.5 SDs below normative data on ≥2 tests were defined as being cognitively impaired.<sup>12</sup> The Expanded Disability Status Scale and Hospital Anxiety and Depression Scales were evaluated for each patient.

### Image Acquisition

MR images were obtained by using a 3T scanner (Achieva; Philips Healthcare, Best, the Netherlands) by using an 8-channel phased array head coil receiver. Acquisitions included a volumetric T1 turbo field echo (TR/TE/flip angle = 9.5 ms/2.3 ms/12°, matrix size = 256 × 219, FOV = 24 cm, section thickness = 1.2 mm) and a proton-density/T2 sequence (TR/TE/flip angle = 2500 ms/10.7 ms/90°, matrix size = 256 × 263, FOV = 23 cm, section thickness = 3 mm). Bookend perfusion included an echo-planar DSC sequence: TR/TE/flip angle = 1633 ms/30 ms/60°, matrix size = 96 × 93, FOV = 22 cm, in-plane voxel size = 2.3 × 2.4 mm, no gap, bandwidth = 1260 Hz/pixel, sections = 24, section thickness = 4 mm following 10 mL of gadobutrol (1 mmol/mL) (Gadovist; Bayer Schering Pharma, Berlin, Germany) injected at a rate of 5 mL/s (Medrad-Spectris Solaris; Bayer) immediately followed by a 25-mL bolus of saline at 5 mL/s. Sixty acquisitions were performed at 1.6-second intervals, with gadobutrol administration on the fifth sequence. A segmented inversion recovery Look-Locker EPI sequence was performed immediately before and after the DSC sequence: TR/TE/flip angle = 29 ms/14 ms/20°, matrix size = 128 × 126, FOV = 22 cm, 15 lines in *k*-space per acquisition, section thickness = 4 mm, scan time = 73 seconds, 60 time points. To facilitate longitudinal magnetization recovery, we used a 3-second delay after the last imaging time point.<sup>20</sup> pCASL images were acquired similar to the manner of Shirzadi et al,<sup>27</sup> with

the following parameters: TR/TE = 4000/9.7 ms, matrix size = 64 × 64 × 18, voxel size = 3 × 3 × 5 mm<sup>3</sup>, label offset = 80 mm, first section postlabel delay = 1600 ms, label duration (middle section) = 1800 ms, scan duration = 248 seconds (30-tag control pair). Reference arterial spin-labeling images for absolute quantification of CBF were acquired (TR/TE = 10,000/9.7 ms, matrix = 64 × 64 × 18, resolution = 3 × 3 × 5 mm<sup>3</sup>, scan duration = 40 seconds).<sup>28</sup>

### Perfusion Processing

Bookend perfusion uses pre- and postgadolinium WM T1 values relative to T1 changes in the blood pool to carefully model the effects of intravascular-to-extravascular water exchange and quantify quantitative cerebral blood volume, in WM, independent of an arterial input function.<sup>17</sup> CBV and CBF quantification account for compartmentalization effects, average brain density, and hematocrit differences between large arteries and capillaries.<sup>29</sup> Deconvolution of tissue concentration–time curves by the arterial input function with singular value decomposition is used to calculate rCBF, while the ratio of area under the curve of the tissue concentration–time curve and arterial input function represents the relative CBV. Finally, CBF is calculated as the product of relative CBF, quantitative cerebral blood volume, and relative CBV.<sup>30</sup>

pCASL quantitative CBF calculations are completed by using the image-processing pipeline developed by Shirzadi et al.<sup>27</sup> Briefly, masks are created by automatic segmentation of GM voxels from the T1 image by using the FAST tool (FMRIB Automated Segmentation Tool; <http://poc.vl-e.nl/distribution/manual/fsl-3.2/fast/index.html>).<sup>31</sup> T1 images with tissue masks are then registered to arterial spin-labeling coordinate space. CBF calculations are then optimized by determining the point of maximum GM detectability with only differences in control and labeled images contributing to this peak level, included by using an aligning/sorting/discarding/refining pipeline.<sup>27</sup> Finally CBF is defined by using the following equation:

$$\text{CBF} = 60 \times 100 \times \frac{\Delta M}{2 \times \alpha \times T_{1,b} \times M_0} \times e^{\frac{\text{PLD} + \Delta t_z \times (Z - 1)}{T_{1,b}}} \times e^{\frac{\text{TE}}{T_{2,t}}}$$

where  $\Delta M$  represents the mean signal in the difference (reference tag) image,  $M_0$  represents the equilibrium magnetization signal extracted from the reference scan,  $\alpha = 0.85$  represents labeling efficiency,  $T_{1,b} = 1.68$  seconds represents the longitudinal recovery time of arterial blood, postlabeling delay (PLD) is 1.6 seconds,  $\Delta t_z$  is the acquisition time for each axial section, TE represents the TE of the reference scan, and  $T_{2,t}^* = 0.06$  seconds represents the transverse tissue relaxation time.<sup>27</sup>

### Image Processing

The reference pCASL control and pregadolinium DSC image acquisitions were normalized to Montreal Neurological Institute 152 space in SPM8 software (<http://www.fil.ion.ucl.ac.uk/spm>), creating 2 study-specific Montreal Neurological Institute 152 templates. Each individual's averaged pCASL control and pregadolinium DSC images were then registered to their study-specific Montreal Neurological Institute template by using a linear registration tool (FMRIB Linear Image Registration Tool, FLIRT; <http://www.fmrib.ox.ac.uk/>) followed by nonlinear intensity

modulation and multiresolution nonlinear registration with 4 subsampling levels (FMRIB Nonlinear Registration Tool, FNIRT; <http://fsl.fmrib.ox.ac.uk/fsl/fslwiki/FNIRT>). To better guide the alignment at each resolution level, we smoothed the images by using a full width at half maximum Gaussian kernel. Basal ganglia (BG) and thalamus (TH) regions were manually traced for each subject by an experienced neuroradiologist (10 years' experience) from T1-weighted images in native space. Similarly, WM, cortical lesions, and T1 black holes were manually traced with Analyze 8.0 (Biomedical Imaging Resource, Mayo Clinic, Rochester, Minnesota) on proton-density/T2 and volumetric T1, respectively. These ROIs were coregistered to Montreal Neurological Institute space as above and were removed from GM and WM regions but were independently analyzed. The resulting Montreal Neurological Institute images were 91 × 109 × 91 voxels, with each voxel measuring 2 × 2 × 2 mm.

pCASL and bookend modalities were correlated on a voxel-wise basis blinded to patient group, after constructing mean images by averaging the CBF intensity of each corresponding voxel over subjects within each cohort. A 7 × 7 voxel grid was created for each axial section of the CBF maps, and the mean CBF value within each grid section was calculated; this process yielded a wide range of CBF values.<sup>29</sup> To account for anatomic ROI variations occurring during average image construction, we included only nonzero CBF values in average calculations, thereby ensuring that only overlapping voxels from each subject were considered. ROIs were subsegmented into GM and WM by using subject-specific masks generated by using the “Segment” function in SPM8. GM was thresholded to have a minimum probability of 80% to reduce GM/WM overlap and partial volume effects. GM CBF intensities were also correlated on a Brodmann region basis. Brodmann areas were selected individually from average CBF maps for each subject group by using a standard mask template in Montreal Neurological Institute 152 space. GM CBF values were averaged over voxels contained within each Brodmann region, and average values were plotted.

### Statistical Analysis

Baseline demographic data were compared between patients with and without impairment and HC by using univariate general linear regression for age and logistic regression for sex. Age and sex were expressed as mean ± SD and proportions, respectively. Paired *t* tests were performed between pCASL and bookend mean CBF intensities for both whole-brain CBF maps to evaluate statistically significant spatial intensity differences between sequences for each of GM, WM, BG, and TH. To account for global overestimation of bookend CBF,<sup>29</sup> we normalized mean intensities before paired *t* test analysis. The *T* value maps were thresholded at a false discovery rate corrected to  $P < .05$ , with a minimum cluster size of 20 voxels.<sup>32</sup>

Voxel-by-voxel linear correlation was performed with the Pearson coefficient method by using mean CBF intensity masked as WM, GM, BG, TH, white matter lesion (WML), and cortical lesion (CL) ROIs. To allow comparison of subject groups and ROIs, accounting for differences in voxel number, we calculated Fischer *Z* scores and converted them to standard *z* scores by dividing by the standard error ( $1/\sqrt{\nu - 3}$ ) where  $\nu$  = number of

**Table 1: Demographic and clinical characteristics of HC and patients with RRMS<sup>a</sup>**

Parameter	Healthy Controls (n = 19)	RRMS-NI (n = 19)	RRMS-I (n = 20)
Age (yr)	49.0 ± 7.1	46.4 ± 7.2	48.1 ± 4.7
Women (No.) (%)	14 (73.68)	15 (78.95)	12 (60)
Education (yr)	16.9 ± 2.9 <sup>b</sup>	16.1 ± 1.3	14.6 ± 1.9 <sup>b</sup>
Disease duration (yr)	NA	11.8 ± 5.4	11.6 ± 4.9
HADS-A (log; median [IQR])	3 (1, 6) <sup>b,c</sup>	6 (5, 7) <sup>c</sup>	8 (7, 10)
HADS-D (log; median [IQR])	2.3 ± 2.3 <sup>b</sup>	3.5 ± 3.2 <sup>d</sup>	7.6 ± 2.9 <sup>b,d</sup>
EDSS (median [IQR])	NA	1.5 (1, 2) <sup>d</sup>	2.5 (2, 3) <sup>d</sup>
Cognitive tests (z score)			
BVMT-R_IR	0.37 ± 1.15 <sup>b</sup>	-0.07 ± 1.04 <sup>d</sup>	-1.68 ± 1.34 <sup>b,d</sup>
BVMT-R_DR	0.40 ± 1.14 <sup>b</sup>	0.42 ± 0.77 <sup>d</sup>	-1.62 ± 1.48 <sup>b,d</sup>
COWAT_FAS	-0.67 ± 0.83	-0.26 ± 1.06 <sup>d</sup>	-1.16 ± 0.89 <sup>d</sup>
CVLT-II_IR	-0.25 ± 1.05 <sup>b</sup>	-0.23 ± 1.04 <sup>d</sup>	-1.94 ± 1.36 <sup>b,d</sup>
CVLT-II_DR	-0.11 ± 0.66 <sup>b</sup>	0.21 ± 0.92 <sup>d</sup>	-2.20 ± 1.61 <sup>b,d</sup>
PASAT-2	-0.21 ± 0.88 <sup>b</sup>	-0.26 ± 0.66 <sup>d</sup>	-1.80 ± 0.57 <sup>b,d</sup>
JLO	0.98 ± 0.19 <sup>b</sup>	0.83 ± 0.59	0.40 ± 0.67 <sup>b</sup>
SDMT	-0.14 ± 0.92 <sup>b</sup>	0.02 ± 0.75 <sup>d</sup>	-1.80 ± 1.17 <sup>b,d</sup>
DK-EFS	0.51 ± 0.73 <sup>b</sup>	0.26 ± 0.61	-0.20 ± 1.25 <sup>b</sup>

**Note:**—BVMT-R\_IR indicates Brief Visuospatial Test-Revised\_Immediate Recall; BVMT-R\_DR, Brief Visuospatial Test-Revised\_Delayed Recall; HADS-A, Hospital Anxiety; HADS-D, Hospital Depression; IQR, interquartile range; NA, not applicable; EDSS, Expanded Disability Status Scale; COWAT\_FAS, Controlled Oral Word Association Test\_Word Recall; CVLT-II\_IR, California Verbal Learning Test-Second Edition\_Immediate Recall; CVLT-II\_DR, California Verbal Learning Test-Second Edition\_Delayed Recall; PASAT-2, Paced Auditory Serial Addition-Part 2; JLO, Judgment of Line Orientation Test; SDMT, Symbol Digit Modalities Test; DK-EFS, Delis-Kaplan Executive Function System.

<sup>a</sup> Clinical demographics of participating patients. Significance  $P < .05$ . All values are mean ± SD unless specified.

<sup>b</sup> HC vs RRMS-I.

<sup>c</sup> HC vs RRMS-NI.

<sup>d</sup> RRMS-NI vs RRMS-I.

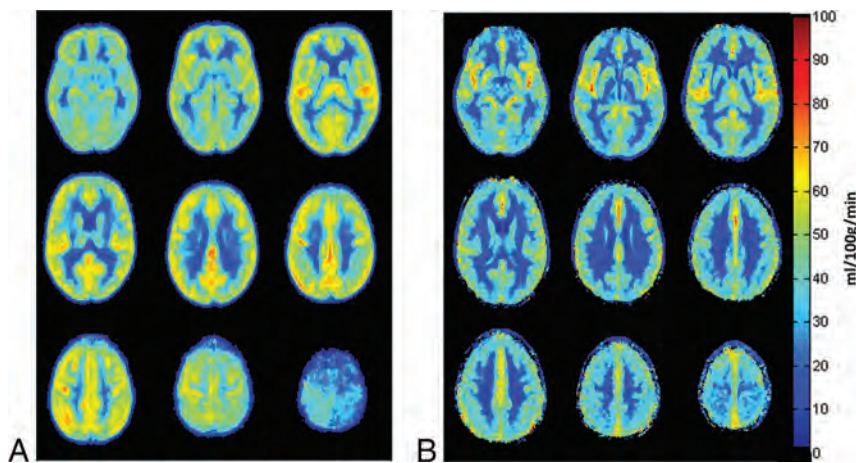


**FIG 1.** Average CBF maps for 19 HC registered to a standard Montreal Neurological Institute template for pCASL (A) and bookend (B) techniques. Images are presented in sequential axial sections from the skull base to vertex.

voxels. Last, the Brodmann region rather than voxelwise linear correlation was conducted by using the Pearson correlation for each hemisphere.  $P < .05$  was considered significant.

Dispersion between CBF imaging techniques was assessed by using Bland-Altman techniques.<sup>33</sup> The coefficient of variation, a standard measure of dispersion [ $CV = (SD/\mu) \times 100$ ], in which  $\mu$  is the mean CBF value across both modalities and  $SD$  represents the SD of the difference of voxelwise CBF values between imaging modalities, was calculated for mean CBF images in all subject groups. Noise was estimated as the mean of 100 randomly selected voxels outside the brain parenchyma from unsmoothed images. These voxels were plotted as a histogram of signal intensities and fitted with a Gaussian distribution. To ensure that the noise esti-

mation had not been affected by processing, we compared the SD with the mean of the noise distribution.<sup>34</sup> SNR was then defined as the ratio between the mean noise estimation to the mean GM CBF. All statistical analyses were completed by using Matlab software (MathWorks, Natick, Massachusetts).

## RESULTS

A summary of clinical data is presented in Table 1. There were no significant differences in age or sex between group cohorts (all  $P > .05$ ). Average ages were  $49.0 \pm 7.1$ ,  $46.4 \pm 7.2$ , and  $48.1 \pm 4.7$  years for the HC, RRMS-NI, and RRMS-I groups, respectively. Similarly, the percentages of female sex were 73.7% (14/19), 79% (15/19), and 60% (12/20), respectively.

### Paired T Test Comparison

CBF measurements demonstrated greater global intensity by using the pCASL technique compared with the bookend technique. No significant difference in regional voxel-by-voxel CBF signal intensities for any of the WM, GM, BG, and TH regions was present in paired  $t$  tests between pCASL and bookend perfusion for HC, RRMS-I, and RRMS-NI groups after normalization of global mean intensities. Representative axial sections of both sequences are demonstrated in Fig 1.

### Voxelwise Correlation

Results of the mean CBF linear correlation are summarized in Table 2 and illustrated for HC in Fig 2A. There was no significant difference in correlation strengths among any groups. Although there was proportionally large scatter in voxelwise intensities, correlation  $r$  values were strong for HC, RRMS-NI, and

RRMS-I (average over ROIs,  $r = 0.62$ ,  $0.64$ , and  $0.59$  respectively). Correlations were stronger for deep GM ROIs (average  $r = 0.71$  for the BG, and  $r = 0.65$  for the TH) compared with cortical GM, WM, and WML regions (average  $r = 0.51$ ,  $0.53$ ,  $0.54$ , respectively). Correlation was weakest in CL regions (average  $r = 0.21$ ). Slope values were all  $< 1$  (average =  $0.51$ ), indicating that in general, pCASL-derived CBF values were of overall higher magnitude compared with bookend CBF values.

### Coefficient of Variation and Signal-to-Noise Ratio

CV calculations demonstrate that on average, WML, CL followed by WM show greatest dispersion between bookend and pCASL modalities (average CV = 38.0%, 37.4%, and 30.1%, respec-

tively), whereas the lowest dispersion was seen within the GM (average CV = 25.9%). Bland-Altman plots (Fig 2B) demonstrated good agreement of mean voxelwise CBF values among perfusion modalities. Bland-Altman plots of WM showed mean differences significantly greater than zero in WM (13.7 mL/100 g/min for HC). The estimated SNR was higher for bookend measurements (mean SNR = 6.6) compared with pCASL CBF measurements (mean SNR = 4.3). SDs of noise dis-

tributions were the same order of magnitude as the mean (mean noise pCASL  $\approx 3.2 \times SD$ ; mean noise bookend  $\approx 2.0 \times SD$ ). CV and SNR values are presented in Table 3.

### GM Brodmann Region-Based Correlation

The results of the Brodmann correlation are detailed in Table 4. Figure 3 shows a scatterplot of Brodmann region-wise analysis for the right hemisphere of the RRMS-I group. Each data point represented the average CBF within 1 Brodmann area. CBF intensities showed significant correlation for all test groups (at  $P < .05$ , Table 4), with a maximum correlation of  $r = 0.68$  in the right hemisphere of the RRMS-I group between pCASL and bookend modalities. No Brodmann area fell beyond 2 SDs of the linear fit, indicating regional consistency among perfusion modalities. Slope values were  $< 1$  for all subject groups (average slope = 0.36).

**Table 2: Voxelwise Pearson correlation<sup>a</sup>**

		Corr. Slope	Coef. ( <i>r</i> )	SE of <i>r</i> ( $\pm$ )	No. of Voxels	Fischer Z	P Value
HC	GM	0.56	0.56	0.02	4678	0.64	<.0001
	WM	0.37	0.50	0.02	4421	0.57	<.0001
	BG	0.90	0.73	0.04	392	0.98	<.0001
	TH	0.56	0.61	0.08	197	0.75	<.0001
RRMS-NI	GM	0.57	0.57	0.02	4521	0.70	<.0001
	WM	0.43	0.55	0.02	4324	0.66	<.0001
	BG	0.70	0.65	0.05	356	0.82	<.0001
	TH	0.76	0.70	0.06	192	0.90	<.0001
	WML	0.61	0.60	0.03	1515	0.69	<.0001
	CL	0.28	0.43	0.24	34	0.47	.005
RRMS-I	GM	0.41	0.46	0.02	4717	0.54	<.0001
	WM	0.35	0.54	0.02	4501	0.64	<.0001
	BG	0.64	0.68	0.05	367	0.86	<.0001
	TH	0.43	0.59	0.08	204	0.70	<.0001
	WML	0.48	0.65	0.03	1800	0.77	<.0001
	CL	0.19	0.35	0.16	95	0.37	.0002

**Note:**—Corr. Coef. indicates correlation coefficient; SE, standard error of correlation coefficients.

<sup>a</sup> Summary of Pearson correlation coefficient, standard error of correlation coefficients, z scores, and P values for all subject groups and ROIs, for voxelwise analysis.

### DISCUSSION

We have demonstrated moderate correlation between bookend perfusion and pCASL on a voxelwise and Brodmann region basis. The highest correlation was seen within the deep GM structures, but a strong cortical GM, WM, and WML correlation was also demonstrated. CL demonstrated a low correlation and a higher coefficient of variation. Correlation was maintained both in HC and in patients with RRMS. pCASL CBF values were consistently higher than bookend values with absolute difference maps showing the largest deviations within CLs, WMLs, and WM. SNR estimations were expectedly better in bookend perfusion than in pCASL. The SD of the noise distribution was confirmed to be the same order of magnitude as the mean noise value for both modalities, indicating that noise estimations were not greatly affected by image processing.<sup>3,4</sup>

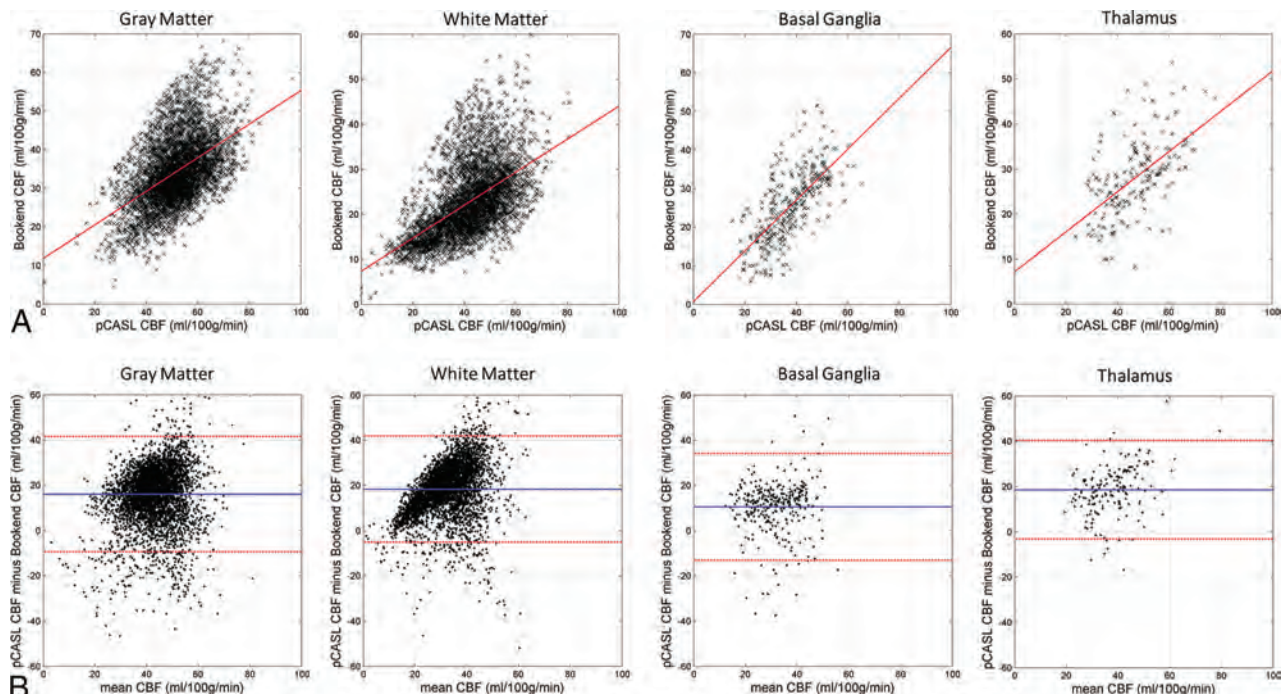


**FIG 2.** A, Upper Row: voxelwise comparison of ROIs of pCASL versus bookend techniques by using Pearson correlations for mean HC CBF. Red lines indicate linear Pearson correlation fits. B, Lower row: Bland-Altman plots for each ROI. Horizontal axis shows the means of pCASL and bookend measurements in milliliters per 100 g per minute, and pCASL CBF minus bookend CBF is shown on the vertical axis in milliliters per 100 g per minute. The red horizontal lines represent the mean difference  $\pm 2$  SDs. The blue horizontal solid line represents the mean difference.

**Table 3: Coefficient of variation and SNR<sup>a</sup>**

	Mean Difference (mL/100 g/min)	CV (%)	SNR
HC			
GM	8.1	27.9	Bookend = 6.81 pCASL = 4.7
WM	13.7	31.7	
BG	5.0	26.2	
TH	5.4	35.4	
RRMS-NI			
GM	16.0	24.9	Bookend = 6.5 pCASL = 4.2
WM	14.0	30.1	
BG	5.2	28.0	
TH	10.0	22.9	
WML	1.79	41.6	
CL	-0.13	33.3	
RRMS-I			
GM	16.0	24.9	Bookend = 7.4 pCASL = 4.1
WM	18.3	28.4	
BG	10.5	31.9	
TH	18.6	23.1	
WML	5.6	34.3	
CL	4.21	41.4	

<sup>a</sup> Summary of mean difference of pCASL CBF minus bookend CBF (Bland-Altman plots, Fig. 2B), CV, and estimated SNR for all subject groups and ROIs.

**Table 4: Brodmann area Pearson correlation<sup>a</sup>**

	Slope	Corr. Coef. ( <i>r</i> )	SE of <i>r</i> ( $\pm$ )	Fischer Z	Standard Z	P Value
HC						
Right	0.40	0.67	0.13	0.81	5.71	<.0001
Left	0.36	0.64	0.14	0.76	5.38	<.0001
RRMS-NI						
Right	0.44	0.67	0.13	0.80	5.67	<.0001
Left	0.33	0.55	0.17	0.61	4.34	<.0001
RRMS-I						
Right	0.33	0.68	0.12	0.83	5.89	<.0001
Left	0.33	0.57	0.16	0.65	4.57	<.0001

<sup>a</sup> Pearson correlation coefficients for Brodmann regional analysis separated by cerebral hemisphere and subject group.

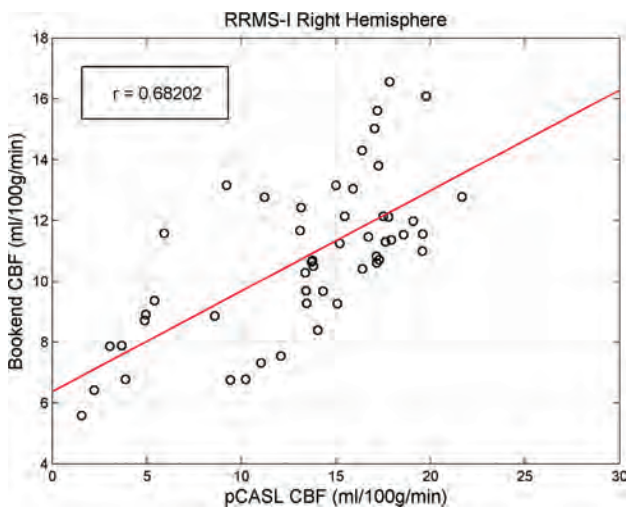


**FIG 3.** An example of a Brodmann area Pearson correlation for the right hemisphere of the RRMS-NI subject group. Each data point represents the average CBF intensity within 1 Brodmann area.

It is estimated that ~44% of patients with RRMS have cognitive impairment, an important factor in quality of life.<sup>35</sup> Cerebral hypoperfusion associated with MS is widely documented, yet the pathophysiologic mechanisms are not well-understood.<sup>7</sup> Con-

tributing factors such as neuronal loss, primary vascular abnormality, and metabolic dysregulation have been implicated.<sup>4,5,7,12</sup> Perfusion imaging provides insight into the pathophysiology and disease severity of MS<sup>13</sup> and correlates with cognitive impairment in patients with secondary-progressive MS.<sup>12</sup> The finding of hypoperfused, structurally normal GM in MS demonstrates the shortcomings of current clinical MR imaging methods.<sup>9,36</sup> The potential for CBF imaging to be used as a clinical biomarker for disease severity in MS could improve monitoring of disease progression and the detection of early disease activity.

Regional variations in the rate of arterial blood flow, brain function, and tissue health play an important role in perfusion signal intensity of all types.<sup>7</sup> Thus, WM differences between perfusion techniques (mean differences in Table 2), though not statistically significant in our study, are clinically important, requiring further consideration. pCASL is an inherently low SNR technique that shows good reliability in healthy adults<sup>10,11</sup> but is particularly susceptible to slower flow rates present in normal WM and the disease state.<sup>37</sup> Indeed, CL, WML, and WM regions showed marginally greater dispersion (CV in Table 2) than other ROIs, consistent with previous literature,<sup>37,38</sup> though most voxels fell within 2 SDs of the mean difference. Similarly, the low correlation for cortical lesions is likely due to the summative effect of a small ROI size and low cortical lesion blood flow as previously demonstrated.<sup>39</sup> Despite the known confounding effect of arterial transit time changes in disease, especially for pCASL,<sup>40</sup> excluding CL, a moderate-to-strong overall correlation between the pCASL and bookend technique was seen. We did not find significant reduction in correlation between the 2 techniques within HC or patients with RRMS with and without impairment. These results indicate that both modalities will give quantitatively comparable estimates of CBF for all patient cohorts, especially on a regional basis. The strongest correlation and lowest dispersion were seen in the deep GM structures. This finding may be attributed to higher pCASL SNR in GM and a lower likelihood of GM voxel contamination by WM tissue from partial volume effects, despite minimizing partial volume effects in cortical GM by applying an 80% probability threshold to the GM masks. The moderate but relatively weaker voxelwise correlations for GM and WM suggest that these techniques may not optimally correlate in studies requiring voxelwise analyses, similar to a recent voxel-based morphometric study.<sup>39</sup>

Brodmann regions correlated strongly without outlying areas, indicating high regional consistency between pCASL and bookend perfusion techniques. This finding is clinically important in the context of prior studies demonstrating localization of perfusion reduction to common regions in secondary-progressive MS. In particular, patients with secondary-progressive MS with cognitive impairment demonstrated localized reduction in the superior medial frontal cortex and bilateral superior frontal gyri corresponding to Brodmann regions 6, 8, and 9.<sup>12</sup> Perfusion correlations, though imperfect, therefore appear sufficiently robust to support using either perfusion technique when studying regional/Brodmann hypoperfusion in RRMS. The study therefore extends the findings of Carroll et al<sup>17</sup> by demonstrating meaningful regional correlations for both GM and WM between pCASL and bookend perfusion in HC and patients with RRMS.

While providing quantitative CBF measurements, bookend and pCASL rely on very different methods requiring either gadolinium injection or endogenous tagged blood water, respectively. Pearson correlation slope values for both voxelwise and Brodmann region analysis were both significantly  $<1$ , consistent with previous studies showing that the bookend and pCASL technique under-<sup>29</sup> and overestimate<sup>41</sup> CBF compared with H<sub>2</sub> [<sup>15</sup>O] PET, respectively. We observed generally the smallest slopes in Pearson correlations for WM (Table 2) regions, which is consistent with our observation of mean differences (Table 3) being largest in WM. Recent work by Lindgren et al<sup>42</sup> comparing bookend and pCASL techniques in healthy controls demonstrated similar ROI CBF values after sequence calibration, but lower Pearson correlation coefficients despite achieving similar results on Bland-Altman analysis. The correlation difference may be due to postprocessing techniques because we included an automatic rejection of intermediate CBF images affected by patient head motion, which was shown to increase SNR relative to other techniques.<sup>27</sup> In addition, Lindgren et al suggested that their pCASL measurements may have been compromised by poor radiolabeling, which was not an issue encountered in the present study.

Limitations of the study include the statistical method of generating average CBF images for each subject group. All voxelwise correlations are likely underestimations of true values because only overlapping parts of each ROI were considered. Because all zero CBF values were excluded from voxelwise averaging, the greater the anatomic variation between subjects or imperfect anatomic registration (resulting in less voxelwise overlap of ROIs), the further the correlation values will be decreased. This method of zero exclusion ensures that average CBF map intensities are not diluted by background voxels, which would result in erroneous overestimation of Pearson correlations. Our correlation values were moderate to strong; this result might be interpreted as insufficient to recommend pCASL as a reasonable technique to longitudinally monitor CBF changes in comparison with bookend DSC. However, moderate correlation strengths are partially due to the exclusion of nonzero values, which would otherwise artificially elevate the correlation coefficient without accurately reflecting meaningful CBF comparisons. Repeatability is a known problem with all perfusion techniques, including pCASL.<sup>43</sup> The repeatability of H<sub>2</sub> [<sup>15</sup>O] PET CBF has been recorded at 8% in WM and 10% in GM during a 2-day interval between measurements.<sup>44</sup> Such variations are unlikely to have accounted for correlation differences, given that the pCASL and bookend image acquisitions were performed minutes apart. Variability can be mitigated to some extent for pCASL by using postprocessing techniques that eliminate spurious voxels caused by small amounts of head motion.<sup>27</sup> Ideally, we would perform perfusion techniques in random order; however, pCASL was acquired, by necessity, before the bookend technique for every subject because of deleterious gadolinium effects on the pCASL signal. We did not use background suppression for the pCASL sequence primarily because of our interest in identifying outlier volume as judged by the raw arterial spin-labeling images.<sup>27</sup> Finally, the relatively small sample size of this study (total 58 subjects) may limit the correlation strength of average CBF images between pCASL and bookend techniques.

## CONCLUSIONS

We have demonstrated that pCASL correlates with bookend perfusion in HC and RRMS diseased states, strongest in deep GM structures and on a Brodmann basis. pCASL shows promise as a noninvasive tool for CBF measurement both in healthy and diseased states such as RRMS.

Disclosures: Liesly Lee—UNRELATED: Consultancy: Genzyme Canada, Novartis Canada, Biogen Canada, Roche Canada, Comments: Advisory Board member; Grants/Grants Pending: Genzyme Canada, Novartis Canada, Biogen Canada, Comments: clinical trial participation; Payment for Development of Educational Presentations: Biogen Canada, Comments: review article publication. Anthony Feinstein—UNRELATED: Expert Testimony: MS Society of Canada\*; Payment for Lectures (including service on Speakers Bureaus): Teva Neuroscience, Merck-Serono, Novartis, Biogen Idec. Timothy Carroll—UNRELATED: Grants/Grants Pending: National Institutes of Health,\* Comments: I have research grants, not directly related to the subject matter of this work; Patents (planned, pending or issued): I have a number of US patents not related to this work.\* Richard I. Aviv—RELATED: Grant: Canadian Institute of Health Research,\* Comments: peer-reviewed grant held by research institute. \*Money paid to the institution.

## REFERENCES

1. Goldenberg MM. **Multiple sclerosis review.** *P T* 2012;37:175–84 Medline
2. Rao SM, Leo GJ, Bernardin L, et al. **Cognitive dysfunction in multiple sclerosis, I: frequency, patterns, and prediction.** *Neurology* 1991; 41:685–91 CrossRef Medline
3. Sun X, Tanaka M, Kondo S, et al. **Clinical significance of reduced cerebral metabolism in multiple sclerosis: a combined PET and MRI study.** *Ann Nucl Med* 1998;12:89–94 CrossRef Medline
4. Swank RL, Roth JG, Woody DC Jr. **Cerebral blood flow and red cell delivery in normal subjects and in multiple sclerosis.** *Neurol Res* 1983;5:37–59 CrossRef Medline
5. Lycke J, Wikkelso C, Bergh AC, et al. **Regional cerebral blood flow in multiple sclerosis measured by single photon emission tomography with technetium-99m hexamethylpropyleneamine oxime.** *Eur Neurol* 1993;33:163–67 Medline
6. Brooks DJ, Leenders KL, Head G, et al. **Studies on regional cerebral oxygen utilisation and cognitive function in multiple sclerosis.** *J Neurol Neurosurg Psychiatry* 1984;47:1182–91 CrossRef Medline
7. D'Haeseleer M, Cambron M, Vanopdenbosch L, et al. **Vascular aspects of multiple sclerosis.** *Lancet Neurol* 2011;10:657–66 CrossRef Medline
8. De Keyser J, Steen C, Mostert JP, et al. **Hypoperfusion of the cerebral white matter in multiple sclerosis: possible mechanisms and pathophysiological significance.** *J Cereb Blood Flow Metab* 2008;28: 1645–51 CrossRef Medline
9. Debernard L, Melzer TR, Van Stockum S, et al. **Reduced grey matter perfusion without volume loss in early relapsing-remitting multiple sclerosis.** *J Neurol Neurosurg Psychiatry* 2014;85:544–51 CrossRef Medline
10. Hojjat SP, Cantrell CG, Vitorino R, et al. **Regional reduction in cortical blood flow among cognitively impaired adults with relapsing-remitting multiple sclerosis patients.** *Mult Scler* 2016 Jan 11. [Epub ahead of print] Medline
11. Hojjat S, Cantrell C, Carroll T, et al. **Perfusion reduction in the absence of structural differences in cognitively impaired versus unimpaired RRMS patients.** *Mult Scler* 2016 Feb 4. [Epub ahead of print] Medline
12. Aviv RI, Francis PL, Tenenbein R, et al. **Decreased frontal lobe gray matter perfusion in cognitively impaired patients with secondary-progressive multiple sclerosis detected by the bookend technique.** *AJNR Am J Neuroradiol* 2012;33:1779–85 CrossRef Medline
13. Francis PL, Jakubovic R, O'Connor P, et al. **Robust perfusion deficits in cognitively impaired patients with secondary-progressive multiple sclerosis.** *AJNR Am J Neuroradiol* 2013;34:62–67 CrossRef Medline
14. Inglese M, Adhya S, Johnson G, et al. **Perfusion magnetic resonance**

- imaging correlates of neuropsychological impairment in multiple sclerosis. *J Cereb Blood Flow Metab* 2008;28:164–71 CrossRef Medline
15. Shin W, Cashen TA, Horowitz SW, et al. **Quantitative CBV measurement from static T1 changes in tissue and correction for intravascular water exchange.** *Magn Reson Med* 2006;56:138–45 CrossRef Medline
  16. Shin W, Horowitz S, Ragin A, et al. **Quantitative cerebral perfusion using dynamic susceptibility contrast MRI: evaluation of reproducibility and age- and gender-dependence with fully automatic image postprocessing algorithm.** *Magn Reson Med* 2007;58:1232–41 CrossRef Medline
  17. Carroll TJ, Horowitz S, Shin W, et al. **Quantification of cerebral perfusion using the “bookend technique”: an evaluation in CNS tumors.** *Magn Reson Imaging* 2008;26:1352–59 CrossRef Medline
  18. Petersen ET, Zimine I, Ho YC, et al. **Non-invasive measurement of perfusion: a critical review of arterial spin labelling techniques.** *Br J Radiol* 2006;79:688–701 CrossRef Medline
  19. Detre JA, Wang J, Wang Z, et al. **Arterial spin-labeled perfusion MRI in basic and clinical neuroscience.** *Corr Opin Neurol* 2009;22:348–55 CrossRef Medline
  20. Detre JA, Leigh JS, Williams DS, et al. **Perfusion imaging.** *Magn Reson Med* 1992;23:37–45 CrossRef
  21. Chen Y, Wang DJ, Detre JA. **Test-retest reliability of arterial spin labeling with common labeling strategies.** *J Magn Reson Imaging* 2011;33:940–49 CrossRef Medline
  22. Wu WC, Jiang SF, Yang SC, et al. **Pseudocontinuous arterial spin-labeling perfusion magnetic resonance imaging: a normative study of reproducibility in the human brain.** *Neuroimage* 2011;56:1244–50 CrossRef Medline
  23. Jain VI, Duda J, Avants B, et al. **Longitudinal reproducibility and accuracy of pseudo-continuous arterial spin-labeled perfusion MR imaging in typically developing children.** *Radiology* 2012;263:527–36 CrossRef Medline
  24. Adams CW, Poston RN, Buk SJ, et al. **Inflammatory vasculitis in multiple sclerosis.** *J Neurol Sci* 1985;69:269–83 CrossRef Medline
  25. Nasreddine ZS, Phillips NA, Bédirian V, et al. **The Montreal Cognitive Assessment, MoCA: a brief screening tool for mild cognitive impairment.** *J Am Geriatr Soc* 2005;53:695–99 CrossRef Medline
  26. Benedict RH, Fischer JS, Archibald CJ, et al. **Minimal neuropsychological assessment of MS patients: a consensus approach.** *Clin Neuropsychol* 2002;16:381–97 CrossRef Medline
  27. Shirzadi Z, Crane DE, Robertson AD, et al. **Automated removal of spurious intermediate cerebral blood flow volumes improves image quality among older patients: a clinical arterial spin labeling investigation.** *J Magn Reson Imaging* 2015;42:1377–85 CrossRef Medline
  28. Alsop DC, Detre JA, Golay X, et al. **Recommended implementation of arterial spin-labeled perfusion MRI for clinical applications: a consensus of the ISMRM perfusion study group and the European consortium for ASL in dementia.** *Magn Reson Med* 2015;73:102–16 CrossRef Medline
  29. Vakil P, Lee JJ, Mouannes-Srouf JJ, et al. **Cerebrovascular occlusive disease: quantitative cerebral blood flow using dynamic susceptibility contrast MR imaging correlates with quantitative H<sub>2</sub>[15O] PET.** *Radiology* 2013;266:879–86 CrossRef Medline
  30. Srouf JM, Shin W, Shah S, et al. **SCALE-PWI: a pulse sequence for absolute quantitative cerebral perfusion imaging.** *J Cereb Blood Flow Metab* 2011;31:1272–82 CrossRef Medline
  31. Zhang Y, Brady M, Smith S. **Segmentation of brain MR images through a hidden Markov random field model and the expectation-maximization algorithm.** *IEEE Trans Med Imaging* 2001;20:45–57 CrossRef Medline
  32. Cha YH, Jog MA, Kim YC, et al. **Regional correlation between resting state FDG PET and pCASL perfusion MRI.** *J Cereb Blood Flow Metab* 2013;33:1909–14 CrossRef Medline
  33. Bland JM, Altman DG. **Statistical methods for assessing agreement between two methods of clinical measurement.** *Lancet* 1986;1:307–10 Medline
  34. Constantinides CD, Atalar E, McVeigh ER. **Signal-to-noise measurements in magnitude images from NMR phased arrays.** *Magnetic Reson Med* 1997;38:852–57 CrossRef Medline
  35. Amato MP, Zipoli V, Portaccio E. **Multiple sclerosis-related cognitive changes: a review of cross-sectional and longitudinal studies.** *J Neurol Sci* 2006;245:41–46 CrossRef Medline
  36. Roosendaal SD, Moraal B, Pouwels PJ, et al. **Accumulation of cortical lesions in MS: relation with cognitive impairment.** *Mult Scler* 2009;15:708–14 CrossRef Medline
  37. van Gelderen P, de Zwart JA, Duyn JH. **Pitfalls of MRI measurement of white matter perfusion based on arterial spin labeling.** *Magn Reson Med* 2008;59:788–95 CrossRef Medline
  38. van Osch MJ, Teeuwisse WM, van Walderveen MA, et al. **Can arterial spin labeling detect white matter perfusion signal?** *Magn Reson Med* 2009;62:165–73 CrossRef Medline
  39. Hojjat SP, Kincal M, Vitorino R, et al. **Cortical perfusion alteration in normal-appearing gray matter is most sensitive to disease progression in relapsing-remitting multiple sclerosis.** *AJNR Am J Neuroradiol* 2016 Mar 24. [Epub ahead of print] Medline
  40. Chalela JA, Alsop DC, Gonzalez-Atavales JB, et al. **Magnetic resonance perfusion imaging in acute ischemic stroke using continuous arterial spin labeling.** *Stroke* 2000;31:680–87 CrossRef Medline
  41. Zhang K, Herzog H, Mauler J, et al. **Comparison of cerebral blood flow acquired by simultaneous [15O]water positron emission tomography and arterial spin labeling magnetic resonance imaging.** *J Cereb Blood Flow Metab* 2014;34:1373–80 CrossRef Medline
  42. Lindgren E, Wirestam R, Markenroth Bloch K, et al. **Absolute quantification of perfusion by dynamic susceptibility contrast MRI using bookend and VASO steady-state CBV calibration: a comparison with pseudo-continuous ASL.** *MAGMA* 2014;27:487–99 CrossRef Medline
  43. Mutsaerts HJ, van Osch MJ, Zelaya FO, et al. **Multi-vendor reliability of arterial spin labeling perfusion MRI using a near-identical sequence: implications for multi-center studies.** *Neuroimage* 2015;113:143–52 CrossRef Medline
  44. Carroll TJ, Teneggi V, Jobin M, et al. **Absolute quantification of cerebral blood flow with magnetic resonance, reproducibility of the method, and comparison with H<sub>2</sub>(15)O positron emission tomography.** *J Cereb Blood Flow Metab* 2002;22:1149–56 Medline

# Metabolic Abnormalities in the Hippocampus of Patients with Schizophrenia: A 3D Multivoxel MR Spectroscopic Imaging Study at 3T

E.J. Meyer, I.I. Kirov, A. Tal, M.S. Davitz, J.S. Babb, M. Lazar, D. Malaspina, and O. Gonen



## ABSTRACT

**BACKGROUND AND PURPOSE:** Schizophrenia is well-known to be associated with hippocampal structural abnormalities. We used <sup>1</sup>H-MR spectroscopy to test the hypothesis that these abnormalities are accompanied by NAA deficits, reflecting neuronal dysfunction, in patients compared with healthy controls.

**MATERIALS AND METHODS:** Nineteen patients with schizophrenia (11 men; mean age, 40.6 ± 10.1 years; mean disease duration, 19.5 ± 10.5 years) and 11 matched healthy controls (5 men; mean age, 33.7 ± 10.1 years) underwent MR imaging and multivoxel point-resolved spectroscopy (TE/TR, 35/1400 ms) <sup>1</sup>H-MRS at 3T to obtain their hippocampal GM absolute NAA, Cr, Cho, and mIns concentrations. Unequal variance *t* tests and ANCOVA were used to compare patients with controls. Bilateral volumes from manually outlined hippocampal masks were compared by using unequal variance *t* tests.

**RESULTS:** Patients' average hippocampal GM Cr concentrations were 19% higher than that of controls, 8.7 ± 2.2 versus 7.4 ± 1.2 mmol/L (*P* < .05); showing no differences, concentrations in NAA were 8.8 ± 1.6 versus 8.7 ± 1.2 mmol/L; in Cho, 2.3 ± 0.7 versus 2.1 ± 0.3 mmol/L; and in mIns, 6.1 ± 1.5 versus 5.2 ± 0.9 (all *P* > .1). There was a positive correlation between mIns and Cr in patients (*r* = 0.57, *P* = .05) but not in controls. The mean bilateral hippocampal volume was ~10% lower in patients: 7.5 ± 0.9 versus 8.4 ± 0.7 cm<sup>3</sup> (*P* < .05).

**CONCLUSIONS:** These findings suggest that the hippocampal volume deficit in schizophrenia is not due to net loss of neurons, in agreement with histopathology studies but not with prior <sup>1</sup>H-MR spectroscopy reports. Elevated Cr is consistent with hippocampal hypermetabolism, and its correlation with mIns may also suggest an inflammatory process affecting some cases; these findings may suggest treatment targets and markers to monitor them.

**ABBREVIATIONS:** CSI = chemical shift imaging; <sup>1</sup>H-MRSI = 3D multivoxel <sup>1</sup>H-MRS imaging; SZ = schizophrenia

Schizophrenia (SZ) is a chronic psychiatric disorder that profoundly alters a person's perception, cognition, and behavior. Due to its high prevalence (~1%), early onset, and the limited efficacy of existing treatments, SZ exacts enormous personal and economic tolls.<sup>1</sup> The characteristic "positive" symptoms of SZ psychosis (delusions, hallucinations, disorganized speech, and

behavior) are accompanied by cognitive decline and "negative" symptoms, including diminished emotional expression and avolition.<sup>2</sup> Despite recognition as fundamental to the disorder as early as 1919, cognitive and negative symptoms were largely ignored once relatively effective pharmacologic treatments for the positive symptoms emerged in the 1950s.<sup>3</sup> In recent years, the development of sophisticated investigative techniques has rekindled interest in the neurobiologic substrate underlying SZ so that therapy may be developed to target the full range of symptoms and alter the clinical course.

This surge of effort has resulted in the development of a plurality of sometimes competing, sometimes overlapping theories of SZ pathophysiology, from the classic neurotransmitter-based theories to genetic-, immune-, synapse-, and network-based the-

Received March 31, 2016; accepted after revision June 3.

From the Department of Radiology (E.J.M., I.I.K., M.S.D., J.S.B., M.L., O.G.), Center for Advanced Imaging Innovation and Research, Bernard and Irene Schwartz Center for Biomedical Imaging, and Department of Psychiatry (D.M.), Institute for Social and Psychiatric Initiatives, New York University School of Medicine, New York, New York; and Department of Chemical Physics (A.T.), Weizmann Institute of Science, Rehovot, Israel.

This work was supported by National Institutes of Health grants: RC1MH088843, 2K24MH00169, MH108962, EB011639, EB01015, NS081772, NS090417, NS097494; and the Center for Advanced Imaging Innovation and Research ([www.cai2r.net](http://www.cai2r.net)), a National Institute of Biomedical Imaging and Bioengineering Biomedical Technology Resource Center (NIH P41 EB017183) and CTSI UL1TR000038 (New York University). Assaf Tal acknowledges the support of the Monroy-Marks Career Development Fund, the Carolito Stiftung Fund, the Leona M. and Harry B. Helmsley Charitable Trust, and the historic generosity of the Harold Perlman Family. This research was supported by a research grant from the Sylvia Schaefer Alzheimer's Research Fund.

Please address correspondence to Oded Gonen, PhD, Department of Radiology, New York University School of Medicine, 660 First Ave, 4th Floor, New York, NY 10016; e-mail: [oded.gonen@med.nyu.edu](mailto:oded.gonen@med.nyu.edu)

Indicates open access to non-subscribers at [www.ajnr.org](http://www.ajnr.org)

<http://dx.doi.org/10.3174/ajnr.A4886>

**Table 1: Demographics for controls and patients**

Subject	Status	Age (yr)/Sex	Disease	
			Duration (yr)	Psychotropic Medication
1	C	45/M	NA	NA
2	C	31/M	NA	NA
3	C	29/F	NA	NA
4	C	36/M	NA	NA
5	C	43/M	NA	NA
6	C	24/F	NA	NA
7	C	55/F	NA	NA
8	C	26/F	NA	NA
9	C	29/F	NA	NA
10	C	22/M	NA	NA
11	C	31/F	NA	NA
12	P	41/M	22	Fluphenazine
13	P	44/F	27	Quetiapine
14	P	43/M	18	Haloperidol, quetiapine
15	P	52/M	32	Citalopram
16	P	51/F	15	Gabapentin, lithium, ziprasidone
17	P	23/M	3	Risperidone
18	P	47/M	31	Fluoxetine, risperidone, valproic acid, trazodone
19	P	44/M	26	Clozapine, valproic acid
20	P	26/M	8	Ziprasidone
21	P	29/F	8	Bupropion, aripiprazole, fluphenazine
22	P	42/F	23	Ziprasidone, bupropion, eszopiclone
23	P	22/M	4	Clozapine
24	P	48/M	23	Quetiapine
25	P	34/M	5	Risperidone
26	P	30/F	10	Risperidone
27	P	49/F	31	Aripiprazole
28	P	51/F	35	NA
29	P	43/F	20	Aripiprazole, escitalopram, fluphenazine
30	P	52/M	30	Aripiprazole, valproic acid, hydroxyzine, paroxetine, trazodone

**Note:**—NA indicates not applicable; C, controls; P, patients.

ories. The hippocampus is implicated in many of these theories. SZ is known to be associated with reduced hippocampal volume, increased basal perfusion, decreased activation during certain memory tasks, decreased neurogenesis in the dentate gyrus, and reduced connectivity with cortical and subcortical regions.<sup>4-9</sup> Recent findings show that conversion to psychosis in high-risk subjects is predicted by hypermetabolism in the hippocampal CA1 subregion.<sup>4</sup> Psychosis may be conceptualized as a disruption in learning and memory involving impaired habituation and “run-away” pattern completion due to hippocampal hyperactivity.<sup>4,10,11</sup> The mechanism underlying these hippocampal abnormalities remains unclear. The absence of gliosis on postmortem histopathology and reduced volume in prodromal and first-episode cases has fomented a shift from neurodegenerative to neurodevelopmental hypotheses.<sup>12</sup> Lack of classic neurodegeneration with gliosis, however, does not imply the absence of subtler progressive damage and inflammation. Mounting genetic and epidemiologic data suggest a role for aberrant immune function and inflammation in SZ.<sup>13</sup>

<sup>1</sup>H-MR spectroscopy measures metabolites used as markers for underlying physiologic processes, most prominently: NAA (NAA and *N*-acetyl aspartylglutamate) for neuronal integrity, Cr (creatinine and phosphocreatine) for energy metabolism, Cho (phosphocholine, choline, and glycerophosphocholine) for membrane turnover, and mIns (myo-inositol) for astroglial proliferation.<sup>14</sup> Most previous hippocampal <sup>1</sup>H-MR spectroscopy

studies in SZ reported lower NAA<sup>15</sup>; one found increased Cr and Cho.<sup>15</sup> None of 10 others that measured Cho, 7 that measured Cr, or 8 that measured mIns, found changes.<sup>16</sup> Difficulty interpreting results may stem from diagnostic heterogeneity within and between studies, insufficiently powered samples, and methodologic variation.<sup>16</sup>

This study compares absolute hippocampal GM NAA, Cr, Cho, and mIns levels, obtained with 3D multivoxel <sup>1</sup>H-MR spectroscopy imaging (<sup>1</sup>H-MRSI) at 3T, between patients with SZ and controls, to test the hypothesis that patients with SZ have decreased hippocampal GM NAA, reflecting neuronal damage. Higher field strength and <sup>1</sup>H-MRSI (compared with single-voxel spectroscopy) yield better coverage of the irregular shape of the hippocampus and better SNR and spatial resolution.

## MATERIALS AND METHODS

### Human Subjects

The patients with SZ or schizoaffective disorders were recruited from the outpatient clinics of New York University Langone Medical Center and Bellevue Hospital, diagnosed on the basis of the Diagnostic Interview for Genetic Studies conducted by clinicians trained for reliability, and had ongoing assessments.<sup>17</sup> All were taking stable doses of medications and had no other psychiatric or neurologic disorders. Age-matched controls recruited from hospital postings met the criteria of no personal or family history of psychosis, no axis I disorder in the past 2 years, and no known neurologic disorder. Exclusion criteria for both patients and controls included uncontrolled medical illness, MR imaging contraindication or inability to tolerate an MR imaging examination, and substance (except tobacco) use in the past 6 months. Substance use history of the patients was the following: Six of 19 reported current or past tobacco use; 6/19, past cannabis use; 9/19, past cocaine use; and 7/19, past alcohol use. All participant demographics are compiled in Table 1, and all gave institutional review board–approved written consent.

ability, and had ongoing assessments.<sup>17</sup> All were taking stable doses of medications and had no other psychiatric or neurologic disorders. Age-matched controls recruited from hospital postings met the criteria of no personal or family history of psychosis, no axis I disorder in the past 2 years, and no known neurologic disorder. Exclusion criteria for both patients and controls included uncontrolled medical illness, MR imaging contraindication or inability to tolerate an MR imaging examination, and substance (except tobacco) use in the past 6 months. Substance use history of the patients was the following: Six of 19 reported current or past tobacco use; 6/19, past cannabis use; 9/19, past cocaine use; and 7/19, past alcohol use. All participant demographics are compiled in Table 1, and all gave institutional review board–approved written consent.

### MR Imaging Data Acquisition

All experiments were performed at 3T in a whole-body MR imaging scanner (Magnetom Trio; Siemens, Erlangen Germany) with a transmit-receive head coil (TEM3000; MR Instruments, Minneapolis, Minnesota). For anatomic reference, tissue segmentation, and <sup>1</sup>H-MRSI VOI guidance, T1-weighted 3D MPRAGE images were obtained from each subject: TE/TI/TR, 2.6/800/1360 ms; matrix, 256 × 256; FOV, 256 × 256 mm<sup>2</sup>; 160 sections, 1-mm-thick each. These were reformatted into 192 axial, sagittal, and coronal sections at 1-mm<sup>3</sup> isotropic resolution.

Our noniterative, B0 map–based, BOLERO (B0 Loop-Encoded

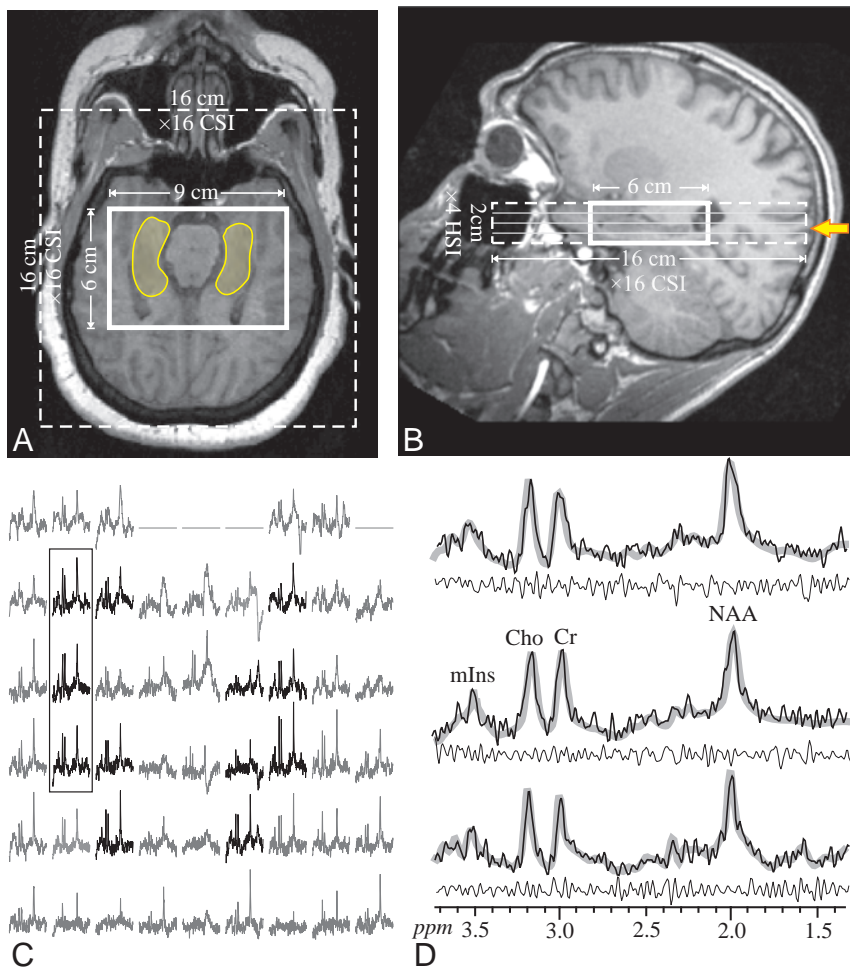


**FIG 1.** Upper: Axial (A) and sagittal (B) T1-weighted MR imaging from a 23-year-old male patient (17 in Table 1) superimposed on the  $9 \times 6 \times 2 \text{ cm}^3$  (left-right  $\times$  anteroposterior  $\times$  inferior-superior) VOI,  $16 \times 16 \text{ cm}^2$  axial CSI FOV (solid and dashed lines), and the hippocampal outline (transparent yellow on A). The yellow arrow in B indicates the level of A, C, and D. Lower left: C, Real part of the  $9 \times 6$  axial (left-right  $\times$  anteroposterior)  $^1\text{H}$  spectra matrix from the VOI section shown in A and marked with the solid yellow arrow on B. Spectra within the hippocampus in A are black, while the remaining ones (not included in the analyses) are gray. All are on a common frequency (parts per million) and intensity scale. The 3 spectra in the black frame over the right hippocampus are expanded on the right (D) for greater detail. Note that the hippocampi do not include voxels at the edges of the VOI (that may have relative VOI chemical shift displacement); note also the good SNR and excellent spectral resolution ( $8.1 \pm 3.0 \text{ Hz}$  linewidth) from the high spatial resolution ( $0.5 \text{ cm}^3$ ) voxels. Right: D, The 3 spectra from the solid frame on C (black line) overlaid on the spectral fit (thick gray lines) and the residual (experimental - fit) underneath (thin black line). Note the spectral resolution and fidelity of the fit, reflected by the residual.

ReadOut) in-house software adjusted the first- and second-order shims of the scanner to optimize the magnetic field homogeneity over the hippocampi in 3–5 minutes.<sup>18</sup> A 6-cm anteroposterior  $\times$  9-cm left-right  $\times$  2-cm inferior-superior =  $108\text{-cm}^3$  parallelepiped  $^1\text{H}$ -MRSI VOI was then image-guided over the bilateral hippocampus, as shown in Fig 1. This VOI was excited by using point-resolved spectroscopy (TE/TR, 35/1400 ms) with 2 second-order Hadamard-encoded slabs (4 sections) interleaved along the inferior-superior direction at every TR, as shown in Fig 1B, for optimal SNR and spatial coverage.<sup>19</sup> Interleaving also enabled strong, 9 mT/m, Hadamard section-selection gradients, reducing the NAA  $\rightarrow$  mIns chemical shift displacement to  $\sim 0.13 \text{ mm}$ ,  $\sim 3\%$  of the section thickness.<sup>20</sup> Thin sections were also chosen to reduce broadening from susceptibility gradients in the inferior-su-

perior direction from the air-tissue interface with the maxillary sinuses just below, as seen in Fig 1A.

The 4 Hadamard section planes were encoded with  $16 \times 16$  2D chemical shift imaging (CSI) over a  $16 \times 16 \text{ cm}^2$  (left-right  $\times$  anteroposterior) FOV to form  $1.0 \times 1.0 \times 0.5 \text{ cm}^3$  voxels. (Note that the actual voxel size [full width at half maximum of the point spread function] for such uniform 2D phase encoding is  $1.12 \times 1.12 \times 0.5 = 0.63 \text{ cm}^3$ ,<sup>21,22</sup> because in the Hadamard direction, the nominal equals the actual voxel size<sup>23</sup>). The VOIs were defined in their planes by two 11.2-ms numerically optimized  $180^\circ$  radiofrequency pulses (4.8-kHz bandwidth) under 1.8 and 1.2 mT/m in the anteroposterior and left-right directions, to yield  $9 \times 6 \times 4 = 216$  voxels (Fig 1C). Such gradients lead the NAA VOI to experience a relative section in-plane chemical shift displacement of 2.3 mm in the anteroposterior and 3.5 mm in the left-right directions<sup>24</sup> (ie, of the  $6 \times 9 \times 2 \text{ cm}^3$  anteroposterior  $\times$  left-right  $\times$  inferior-superior nominal VOIs, at least  $5.7 \times 8.6 \times 2 \text{ cm}^2$  [93.4%] is common for all metabolites).<sup>25</sup> Note that Cho and Cr have even smaller relative displacements; the CSI localization grid does not experience this displacement.<sup>26</sup> Because it is a relative shift, this error is encountered only at the VOI edges,<sup>25</sup> and it is smaller than the  $1 \times 1 \text{ cm}^2$  in-plane CSI resolution. Therefore, to avert it for all metabolites, we chose the in-plane VOI size large enough,  $9 \times 6 \text{ cm}^2$ , to have these displacement-error prone voxels at the VOI edges completely outside the hippocampus, as shown in Figs 1A and 2A. The MR spectroscopy signals were acquired for 256

ms at  $\pm 1\text{-kHz}$  bandwidth. At 2 averages, the  $^1\text{H}$ -MR spectroscopy was  $\sim 25$  minutes, and the examination took under an hour.

### MR Spectroscopy Postprocessing

The MR spectroscopy data were processed off-line by using in-house software. Residual water was removed from the MR signals in the time domain<sup>27</sup>; the data was static-field drift-corrected,<sup>28</sup> voxel-shifted to align the CSI grid with the NAA VOI, Fourier transformed in the temporal, anteroposterior, and left-right directions, and Hadamard reconstructed along the inferior-superior direction. Spectra were automatically corrected for frequency and zero-order phase shifts in reference to the NAA peak in each voxel.

Relative levels of the  $i$ th ( $i = \text{NAA, Cr, Cho, mIns}$ ) metabolite in the  $j$ th ( $j = 1..216$ ) voxel of the  $k$ th ( $k = 1..30$ ) subject were

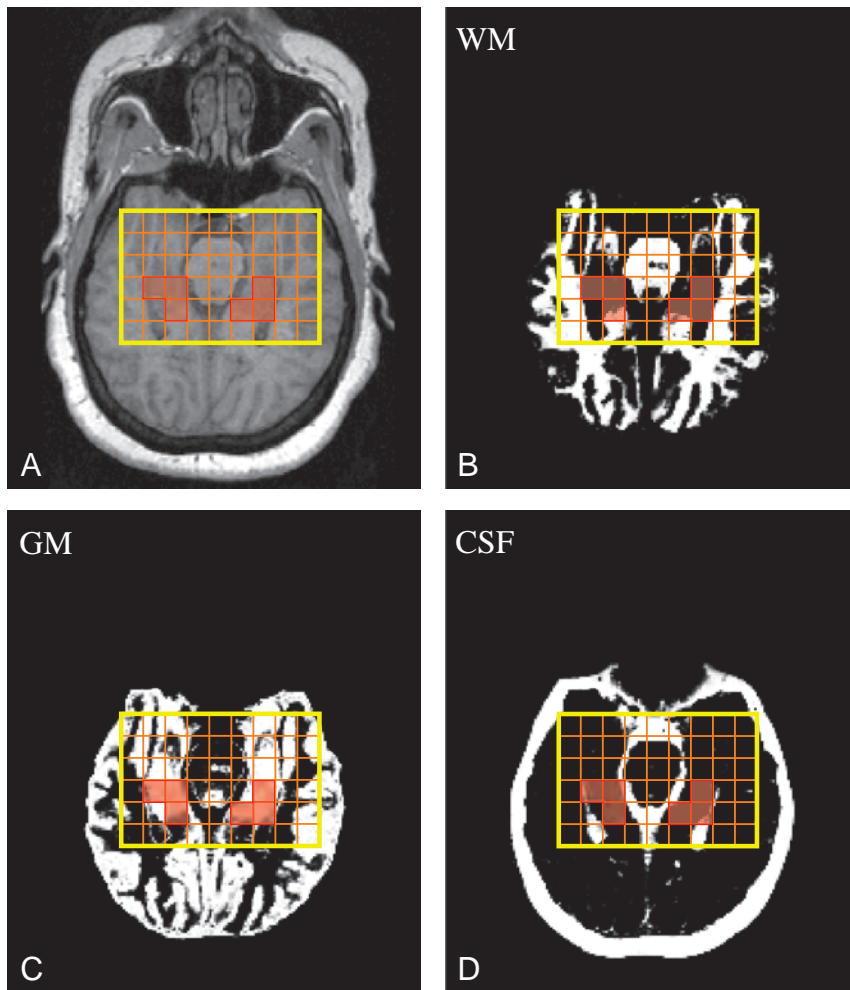


**FIG 2.** Upper: A, Axial MPRAGE image from a 51-year-old female patient (16 in Table 1) superimposed on the VOI (in yellow). Orange lines show the  $9 \times 6$  voxel CSI grid; voxels that passed the selection criteria to calculate the NAA concentration are highlighted in transparent red. B–D, SPM12-generated WM (B), GM (C), and CSF (D) masks also superimposed on the VOI CSI grid and selected voxels. Note the  $n \geq 2$  voxels that “passed” the selection criteria described in the “Materials and Methods” section.

estimated from their peak area,  $S_{ijk}$ , by using parametric spectral modeling,<sup>29</sup> with Glx, Cho, Cr, mIns, NAA, and taurine model functions, as shown in Fig 1D. The  $S_{ijk}$  was scaled into absolute concentration,  $C_{ijk}$ , relative to a 2 L reference sphere of  $C_i^{\text{vitro}} = 12.5, 10.0, 3.0,$  and  $7.5$ -mmol/L of NAA, Cr, Cho, and mIns in water at physiologic ionic strength:

$$C_{ijk} = C_i^{\text{vitro}} \times \frac{S_{ijk}}{S_{ijR}} \times \frac{V_k^{180^\circ}}{V_R^{180^\circ}} \times \frac{1}{F_{jk}} \times f_i,$$

where  $S_{ijR}$  is the metabolite signals of the phantom;  $V_k^{180^\circ}$  and  $V_R^{180^\circ}$  are subject and reference radiofrequency voltages for nonselective 1-ms  $180^\circ$  pulses; and  $F_{jk}$  is the tissue fraction of that voxel, estimated from the WM-, GM-, and CSF-segmented MPRAGE images, as described below. The  $f_i$  corrects  $C_{ijk}$  for in vivo ( $T_1^{\text{vivo}}, T_2^{\text{vivo}}$ ) assuming small patient-control differences) and in vitro ( $T_1^{\text{vitro}}, T_2^{\text{vitro}}$ ) relaxation time differences.<sup>30</sup>

$$f_i = \frac{\exp(-TE/T_2^{\text{vitro}})}{\exp(-TE/T_2^{\text{vivo}})} \times \frac{1 - \exp(-TR/T_1^{\text{vitro}})}{1 - \exp(-TR/T_1^{\text{vivo}})}$$

by using the  $T_1^{\text{vivo}} = 1.4, 1.3, 1.1,$  and  $1.2$  seconds and  $T_2^{\text{vivo}} = 343, 172, 248,$  and  $200$  ms reported for NAA, Cr, Cho, and mIns at  $3T^{31-33}$ ;  $T_1^{\text{vitro}} = 605, 336, 235,$  and  $319$  ms and  $T_2^{\text{vitro}} = 483, 288, 200,$  and  $233$  ms in the reference phantom.

Bilateral hippocampi masks were manually traced on the axial MPRAGE images on the basis of an MR imaging atlas,<sup>34</sup> as shown in Fig 1A, and visually verified on sagittal and coronal planes. The axial MR images were segmented into CSF and gray and white matter masks by using SPM12 software (<http://www.fil.ion.ucl.ac.uk/spm/software/spm12>),<sup>35</sup> as shown in Fig 2B–D. An in-house program (Matlab 14; MathWorks, Natick, Massachusetts) calculated the fraction of each tissue mask inside each voxel,<sup>36</sup> from which  $F_{jk} = (\text{GM volume} + \text{WM volume}) / (\text{voxel volume})$  for Equation 1 was obtained. We retained only voxels with at least 30% of their volume within the hippocampus mask. To minimize inclusion of degraded signals, we retained only voxels that also had the following: 1)  $F_{jk} > 70\%$  (ie, contained  $<30\%$  of CSF), 2) Cramer-Rao lower bounds of  $<20\%$  for a given metabolite; and 3)  $4 \text{ Hz} < \text{line-widths} < 13 \text{ Hz}$ , as shown in Fig 2. The software then estimated the global GM and WM concentrations of each metabolite in the retained  $n \geq 2$  hippocampal voxels by using linear regression, as described previously.<sup>36</sup> This approach

overcomes the GM/WM partial volume issue encountered by single-voxel MR spectroscopy. Note that although metabolic gradients are reported along the long axis of the hippocampus<sup>37,38</sup> and because the entire structure is taken here as a whole and the intra-subject gradients of these metabolites are reported to be quite similar, our average concentration reported here is nevertheless a useful intersubject comparison metric.

### Statistical Analyses

Exact Mann-Whitney and unequal variance  $t$  tests were used to compare the groups in terms of age, the volume measure, and each metabolite concentration without adjustment for age and sex. ANOVA was used to compare the groups in terms of the volume and each metabolite concentration adjusted for age and sex. ANOVA for each measure allowed the error variance to differ across subject groups to avoid an assumption of variance equality.  $F$  and Levene tests were used to compare the groups in terms of the variance of the volume measure and each metabolite concentration. All tests were conducted at the 5% significance level.

**Table 2: Means, number of subjects from whom the data was derived (in parentheses), and P values (from unequal variance t tests) of the absolute NAA, Cr, Cho, and mIns hippocampal GM concentrations and the volumes of the bilateral hippocampi in controls and patients<sup>a</sup>**

Metabolite	Controls	Patients	P Value
NAA (mM)	8.7 ± 1.2 (n = 11)	8.8 ± 1.6 (n = 16)	.876
Cr (mM)	7.4 ± 1.2 (n = 10) <sup>b</sup>	8.7 ± 2.2 (n = 19) <sup>b</sup>	.035 <sup>b</sup>
Cho (mM)	2.1 ± 0.3 (n = 10)	2.3 ± 0.7 (n = 18)	.189
mIns (mM)	5.2 ± 0.9 (n = 10)	6.1 ± 1.5 (n = 12)	.161
Volume (cm <sup>3</sup> )	8.4 ± 0.5 (n = 11) <sup>b</sup>	7.5 ± 0.9 (n = 19) <sup>b</sup>	.003 <sup>b</sup>

<sup>a</sup> Note the elevation of Cr and the reduction in volume in patients compared with controls.

<sup>b</sup> Significant difference.

## RESULTS

Nineteen patients and 11 controls were included in the analyses, as shown in Table 1. The groups were not different with respect to age ( $P = .119$ ). The BOLERO shim procedure yielded metabolite linewidths of  $8.1 \pm 3.0$  Hz across all 216 VOI voxels for patients and controls, as shown in Fig 1. The mean number of voxels that passed the selection criteria described above and were used to estimate metabolite concentrations was  $10.5 \pm 3.4$  in patients and  $14.5 \pm 5.4$  in controls for NAA;  $8.3 \pm 3.4$  and  $11.3 \pm 4.9$  for Cho;  $8.0 \pm 3.5$  and  $12.8 \pm 4.4$  for Cr; and  $4.8 \pm 1.7$  and  $7.0 \pm 3.8$  for mIns. Average hippocampal GM metabolite concentrations and the volumes of the bilateral hippocampi, as shown in Fig 1A, are given in Table 2. Note that because the analysis was performed independently for each metabolite, different numbers of subjects are included for each on the basis of how many had at least 2 voxels that passed the exclusion criteria.

Patients had 19% ( $P < .05$ ) higher hippocampal GM Cr levels than controls, even after adjusting for age and sex, as shown in Table 2 and Fig 3. NAA, Cho, and mIns were not significantly different. The variance of the Cho levels was larger in patients than in controls ( $P = .05$ ) and trended that way for Cr ( $P = .06$ ). There was a positive correlation between mIns and Cr levels in patients ( $r = 0.57, P = .05$ ) but not in controls ( $r = 0.42, P = .26$ ). Other metabolites were not significantly correlated. Bilateral hippocampal volume was  $\sim 10\%$  ( $P < .05$ ) lower in patients.

## DISCUSSION

Most surprising, our findings do not support the hypothesis that patients with SZ exhibit decreased hippocampal GM NAA (due to neuronal dysfunction) compared with healthy controls, as generally reported.<sup>16</sup> They are, however, concordant with neuropathology studies that consistently find reduced hippocampal volume without a net loss of neurons, but with neuronal architectural disarray and molecular alterations (eg, changes in receptor density and deficits in the inhibitory interneurons that compose 10% of hippocampal neurons).<sup>12</sup>

Our finding of elevated hippocampal GM Cr in SZ may suggest either altered hippocampal energy metabolism or an increased proportion of glial cells. The Cr <sup>1</sup>H-MR spectroscopy peak is a composite of free creatine and phosphocreatine that interconvert to regenerate adenosine triphosphate, thus acting as a short-term energy “buffer” for the cell. Cr elevation may, therefore, reflect altered energy metabolism, likely hypermetabolism because a more metabolically active cell reasonably requires greater capacity to regenerate adenosine triphosphate (decreased

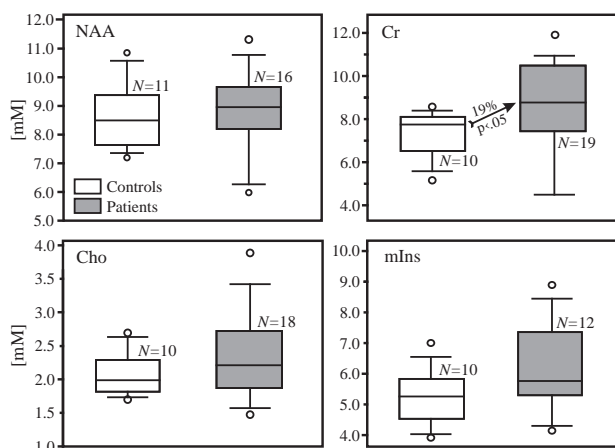


**FIG 3.** Boxplots showing the first, second (median), and third quartiles; 5th and 95th percentiles (*whiskers*); and outliers (*dots*) of the distribution of the bilateral hippocampal NAA, Cr, Cho, and mIns concentrations (millimolar) in the patient (shaded) and control (white) boxes. Numbers of controls and patients included in the analyses for each metabolite, N, are listed. Note that the NAA, Cho, and mIns concentrations do not differ significantly between patients and controls (Table 2), whereas the Cr concentration is 19% higher in the bilateral hippocampi of patients than in controls (arrow).

Cr has similarly been interpreted as hypometabolism).<sup>10,39</sup> Indeed, an increase in energy metabolism is consistent with the hippocampal hyperactivity model of SZ, supported by evidence from animal models, neuroimaging, and histopathology studies.<sup>40</sup> Nuclear imaging studies show increased basal perfusion,<sup>41</sup> which correlates with psychotic symptoms and is normalized by D2 antagonists,<sup>42</sup> while resting-state fMRI shows hyperactivity correlated with cognitive deficits and negative symptoms.<sup>43</sup> Hippocampal hyperactivity may be mediated by increased glutamatergic activity, which has been found in the hippocampus of unmedicated patients with SZ and is associated with reduced hippocampal volume and worse executive functioning and global clinical state.<sup>44</sup> Furthermore, a reciprocal pathway between the hippocampus and dopaminergic neurons in the midbrain supports a link to the dopamine hypothesis of SZ.<sup>40</sup>

Cho and mIns are elevated alongside Cr in astrogliosis, reflecting their higher levels in glial cells than neurons.<sup>14</sup> Although we did not find significant elevations in hippocampal GM Cho or mIns, the correlation between Cr and mIns in patients (but not controls) suggests that in at least some cases, elevation in Cr may reflect astrogliosis, a response to inflammation. Evidence supporting an immune or inflammatory component in SZ continues to accumulate. This includes the increased risk of SZ after exposure to certain maternal viruses in utero; the increased expression in the hippocampus of genes related to the immune response identified by messenger RNA sequencing; the significant associations with inflammatory-related genes identified in genome-wide association meta-analyses (including in the human leukocyte antigen complex, of which a recent study suggests that increased expression of a complement component gene may mediate excessive synaptic pruning); and the increase in proinflammatory cytokines, including interleukin-6 and tumor necrosis factor- $\alpha$  in patients with psychosis.<sup>45,46</sup>

That histopathology studies do not show glial cell proliferation in SZ does not rule out the possibility that a subset of patients

might undergo astrogliosis.<sup>12</sup> This notion is consistent with the emerging concept of the clinical syndrome of SZ as composed of a group of separate conditions differing in relevant pathophysiologicals, termed “SZ and related psychoses.” Consistent with the idea of etiologic heterogeneity, patients exhibited greater coefficients of variation than controls for both Cho (28% versus 16%,  $P = .05$ ) and Cr (25% versus 16%,  $P = .06$ ). A subset of patients may undergo an inflammatory process, causing elevated Cho, Cr, and mIns through astrogliosis or subtler inflammation that damages glial cells and/or myelin.

The reduced hippocampal volume seen in patients is consistent with prior reports. Along with the prefrontal cortex, the hippocampus is consistently observed to undergo volume loss in SZ.<sup>4</sup> A recent collaborative analysis of brain volumes by using imaging data from 2028 individuals with SZ and 2540 healthy controls found the largest patient control effect size for the hippocampus of any subcortical area, with a mean 4.10% volume decrease compared with controls.<sup>47</sup> The lack of correlation between hippocampal volume and NAA levels in our study suggests that the lower volume in patients is not due to neuronal loss from progression of a pathogenic process and may, therefore, be suggestive of a developmental trait.

There may be several reasons for the discordance between our findings and most previous studies. First, clinical heterogeneity (disease duration, symptomatology, medications) both between and within studied populations is known to affect <sup>1</sup>H-MR spectroscopy results.<sup>16</sup> Second, methodology differences are well-known to affect results. Our 3D technique yields better spatial resolution (0.5 versus 3.5 cm<sup>3</sup> or larger) and delineation of the irregular shape, with less inclusion of neighboring WM than single voxels, even accounting for partial WM and CSF volume. Third, studies that found lower NAA in patients had, on average, longer TEs, making them more sensitive to quantification errors due to T2-weighting variations, than our short TE = 35 ms acquisition.<sup>48</sup> Fourth, some studies used Cr as an “internal reference” and reported its ratios with other metabolites. This approach magnifies errors and is further complicated by findings that Cr is altered in several brain regions in SZ.<sup>16</sup> Finally, as others have pointed out, there is a publication bias in favor of NAA deficit reports as opposed to a finding of “no change.”<sup>16</sup>

Admittedly, our study also has several limitations. First, our sample comprised patients with varying disease durations, medication regimens, and histories of substance use at insufficient numbers to distinguish the effects of these variables. Second, a relatively small sample size may have limited the power to detect small differences (eg, Cho or mIns elevations in patients). Third, even our improved spatial resolution is insufficient to resolve hippocampal subfields that may be differentially affected in SZ.<sup>4</sup> Fourth, the regressions used to obtain metabolite concentrations relied on relatively few, 8–14, voxels per individual, because a balance was struck among the 3D <sup>1</sup>H-MRSI spatial resolution, measurement time, and hippocampal volume. While the number of voxels in the hippocampus may be improved at higher fields, at 3T, this is likely nearly as good as can be achieved. Fifth, because of the anatomic milieu (deep in the brain, irregularly shaped, near air-filled sinuses), it is difficult to obtain adequate SNR to quantify hippocampal glutamate and glutamine levels. Finally, our in-

terpretation of elevated Cr is limited by the inability of 3T <sup>1</sup>H-MR spectroscopy to distinguish Cr from phosphocreatine resonances, and our proposals of altered energy metabolism and astrogliosis are here supported by inference and existing literature rather than direct measurement.

## CONCLUSIONS

Decreased volume without GM NAA decline in the hippocampus of patients with SZ suggests a process that preserves neuronal integrity and could represent a developmental rather than pathologic disruption. Increased hippocampal GM Cr suggests hypermetabolism and/or possibly astrogliosis in a subset of patients. These findings may have implications for both the pathogenesis and treatment of SZ by supporting the hippocampal hyperactivity model. In some patients, an inflammatory process (possibly involving astrogliosis) may be a treatment target in addition to the antidopaminergic treatments. Indeed, there is growing recognition that the efficacy of antipsychotics may be mediated, in part, through anti-inflammatory action, and there is ongoing effort with promising results for anti-inflammatory agents, including aspirin, COX-2 inhibitors, and N-acetylcysteine as adjuvant therapies.<sup>49</sup> Therefore, we propose <sup>1</sup>H-MRSI as both a probe to identify patient subgroups and a method to monitor therapies.

Disclosures: Emma J. Meyer—RELATED: National Institutes of Health.\* Ivan I. Kirov—UNRELATED: Travel/Accommodations/Meeting Expenses Unrelated to Activities Listed: North American Brain Injury Society, Comments: for travel to their annual meeting to give a lecture on proton MR spectroscopy in traumatic brain injury. Mariana Lazar—RELATED: Grant: National Institute of Mental Health.\* Comments: This work was funded, in part, by a grant from the National Institute of Mental Health. Dolores Malaspina—RELATED: Grant: National Institute of Mental Health\*; UNRELATED: Expert Testimony: Provided “expert opinion” over 10,000 times, Comments: As a psychiatrist, I consult on issues such as psychiatric diagnoses of mass shooters and possible mental illness in transportation agents; Grants/Grants Pending: National Institute of Mental Health.\* \*Money paid to the institution.

## REFERENCES

1. Wu EQ, Birnbaum HG, Shi L, et al. **The economic burden of schizophrenia in the United States in 2002.** *J Clin Psychiatry* 2005;66:1122–29 CrossRef Medline
2. American Psychiatric Association. American Psychiatric Association. DSM-5 Task Force. *Diagnostic and Statistical Manual of Mental Disorders: DSM-5.* Washington, DC: American Psychiatric Association; 2013
3. Malaspina D, Walsh-Messinger J, Gaebel W, et al. **Negative symptoms, past and present: a historical perspective and moving to DSM-5.** *Eur Neuropsychopharmacol* 2014;24:710–24 CrossRef Medline
4. Tamminga CA, Stan AD, Wagner AD. **The hippocampal formation in schizophrenia.** *Am J Psychiatry* 2010;167:1178–93 CrossRef Medline
5. Adriano F, Caltagirone C, Spalletta G. **Hippocampal volume reduction in first-episode and chronic schizophrenia: a review and meta-analysis.** *Neuroscientist* 2012;18:180–200 CrossRef Medline
6. Steen RG, Mull C, McClure R, et al. **Brain volume in first-episode schizophrenia: systematic review and meta-analysis of magnetic resonance imaging studies.** *Br J Psychiatry* 2006;188:510–18 CrossRef Medline
7. Iritani S. **Neuropathology of schizophrenia: a mini review.** *Neuropathology* 2007;27:604–08 CrossRef Medline
8. Samudra N, Ivleva EI, Hubbard NA, et al. **Alterations in hippocampal connectivity across the psychosis dimension.** *Psychiatry Res* 2015;233:148–57 CrossRef Medline

9. Kirov II, Hardy CJ, Matsuda K, et al. **In vivo 7 Tesla imaging of the dentate granule cell layer in schizophrenia.** *Schizophr Res* 2013;147:362–67 CrossRef Medline
10. Wood SJ, Berger G, Velakoulis D, et al. **Proton magnetic resonance spectroscopy in first episode psychosis and ultra-high-risk individuals.** *Schizophr Bull* 2003;29:831–43 CrossRef Medline
11. Schobel SA, Lewandowski NM, Corcoran C, et al. **Differential targeting of the CA1 subfield of the hippocampal formation by schizophrenia and related psychotic disorders.** *Arch Gen Psychiatry* 2009;66:938–46 CrossRef Medline
12. Harrison PJ. **The hippocampus in schizophrenia: a review of the neuropathological evidence and its pathophysiological implications.** *Psychopharmacology (Berl)* 2004;174:151–62 Medline
13. Najjar S, Pearlman DM, Alper K, et al. **Neuroinflammation and psychiatric illness.** *J Neuroinflammation* 2013;10:43 CrossRef Medline
14. Zhu H, Barker PB. **MR spectroscopy and spectroscopic imaging of the brain.** *Methods Mol Biol* 2011;711:203–26 CrossRef Medline
15. Lutkenhoff ES, van Erp TG, Thomas MA, et al. **Proton MRS in twin pairs discordant for schizophrenia.** *Mol Psychiatry* 2010;15:308–18 CrossRef Medline
16. Schwerk A, Alves FD, Pouwels PJ, et al. **Metabolic alterations associated with schizophrenia: a critical evaluation of proton magnetic resonance spectroscopy studies.** *J Neurochem* 2014;128:1–87 CrossRef Medline
17. Nurnberger JI Jr, Blehar MC, Kaufmann CA, et al. **Diagnostic Interview for Genetic Studies: rationale, unique features, and training.** *Arch Gen Psychiatry* 1994;51:849–59; discussion 863–64 CrossRef Medline
18. Hetherington HP, Chu WJ, Gonen O, et al. **Robust fully automated shimming of the human brain for high-field 1H spectroscopic imaging.** *Magn Reson Med* 2006;56:26–33 CrossRef Medline
19. Goelman G, Liu S, Hess D, et al. **Optimizing the efficiency of high-field multivoxel spectroscopic imaging by multiplexing in space and time.** *Magn Reson Med* 2006;56:34–40 CrossRef Medline
20. Goelman G, Liu S, Fleysher R, et al. **Chemical-shift artifact reduction in Hadamard-encoded MR spectroscopic imaging at high (3T and 7T) magnetic fields.** *Magn Reson Med* 2007;58:167–73 CrossRef Medline
21. Mareci TH, Brooker HR. **Essential considerations for spectral localization using indirect gradient encoding of spatial information.** *J Magn Reson* 1991;92:229–46 CrossRef
22. Brooker HR, Mareci TH, Mao JT. **Selective Fourier transform localization.** *Magn Reson Med* 1987;5:417–33 CrossRef Medline
23. Goelman G, Liu S, Gonen O. **Reducing voxel bleed in Hadamard-encoded MRI and MRS.** *Magn Reson Med* 2006;55:1460–65 CrossRef Medline
24. de Graaf RA. *In Vivo NMR Spectroscopy: Principles and Techniques.* 2nd ed. Chichester, UK: John Wiley & Sons; 2007
25. Barker PB, Bizzi A, Stefano ND, et al. **Spectral analysis methods, quantitation and common artifacts.** In: *Clinical MR Spectroscopy Techniques and Applications.* Cambridge: Cambridge University Press; 2010:34–50
26. Brown TR, Kincaid BM, Ugurbil K. **NMR chemical shift imaging in three dimensions.** *Proc Natl Acad Sci U S A* 1982;79:3523–26 CrossRef Medline
27. Marion D, Ikura M, Bax A. **Improved solvent suppression in one- and two-dimensional NMR spectra by convolution of time-domain data.** *J Magn Reson* 1989;84:425–30 CrossRef
28. Tal A, Gonen O. **Localization errors in MR spectroscopic imaging due to the drift of the main magnetic field and their correction.** *Magn Reson Med* 2013;70:895–904 CrossRef Medline
29. Soher BJ, Young K, Govindaraju V, et al. **Automated spectral analysis III: application to in vivo proton MR spectroscopy and spectroscopic imaging.** *Magn Reson Med* 1998;40:822–31 CrossRef Medline
30. Kirov I, George IC, Jayawickrama N, et al. **Longitudinal inter- and intra-individual human brain metabolic quantification over 3 years with proton MR spectroscopy at 3 T.** *Mag Reson Med* 2012;67:27–33 CrossRef Medline
31. Träber F, Block W, Lamerichs R, et al. **1H metabolite relaxation times at 3.0 Tesla: measurements of T1 and T2 values in normal brain and determination of regional differences in transverse relaxation.** *J Magn Reson Imaging* 2004;19:537–45 CrossRef Medline
32. Kirov I, Fleysher L, Fleysher R, et al. **Age dependence of regional proton metabolites T2 relaxation times in the human brain at 3 T.** *Magn Reson Med* 2008;60:790–95 CrossRef Medline
33. Posse S, Otazo R, Caprihan A, et al. **Proton echo-planar spectroscopic imaging of J-coupled resonances in human brain at 3 and 4 Tesla.** *Mag Reson Med* 2007;58:236–44 CrossRef Medline
34. Oishi K. *MRI Atlas of Human White Matter.* Amsterdam: Elsevier/Academic Press; 2011
35. Ashburner J, Friston KJ. **Unified segmentation.** *Neuroimage* 2005;26:839–51 CrossRef Medline
36. Tal A, Kirov I, Grossman RI, et al. **The role of gray and white matter segmentation in quantitative proton MR spectroscopic imaging.** *NMR Biomed* 2012;25:1392–400 CrossRef Medline
37. King KG, Glodzik L, Liu S, et al. **Anteroposterior hippocampal metabolic heterogeneity: three-dimensional multivoxel proton 1H MR spectroscopic imaging—initial findings.** *Radiology* 2008;249:242–50 CrossRef Medline
38. Vermathen P, Laxer KD, Matson GB, et al. **Hippocampal structures: anteroposterior N-acetylaspartate differences in patients with epilepsy and control subjects as shown with proton MR spectroscopic imaging.** *Radiology* 2000;214:403–10 CrossRef Medline
39. Mazgaj R, Tal A, Goetz R, et al. **Hypo-metabolism of the rostral anterior cingulate cortex associated with working memory impairment in 18 cases of schizophrenia.** *Brain Imaging Behav* 2016;10:115–23 CrossRef Medline
40. Heckers S, Konradi C. **GABAergic mechanisms of hippocampal hyperactivity in schizophrenia.** *Schizophr Res* 2015;167:4–11 CrossRef Medline
41. Malaspina D, Storer S, Furman V, et al. **SPECT study of visual fixation in schizophrenia and comparison subjects.** *Biol Psychiatry* 1999;46:89–93 CrossRef Medline
42. Lahti AC, Holcomb HH, Weiler MA, et al. **Functional effects of antipsychotic drugs: comparing clozapine with haloperidol.** *Biol Psychiatry* 2003;53:601–08 CrossRef Medline
43. Tregellas JR, Smucny J, Harris JG, et al. **Intrinsic hippocampal activity as a biomarker for cognition and symptoms in schizophrenia.** *Am J Psychiatry* 2014;171:549–56 CrossRef Medline
44. Poels EM, Kegeles LS, Kantrowitz JT, et al. **Glutamatergic abnormalities in schizophrenia: a review of proton MRS findings.** *Schizophr Res* 2014;152:325–32 CrossRef Medline
45. Sekar A, Bialas AR, de Rivera H, et al. **Schizophrenia risk from complex variation of complement component 4.** *Nature* 2016;530:177–83 CrossRef Medline
46. Hwang Y, Kim J, Shin JY, et al. **Gene expression profiling by mRNA sequencing reveals increased expression of immune/inflammation-related genes in the hippocampus of individuals with schizophrenia.** *Transl Psychiatry* 2013;3:e321 CrossRef Medline
47. van Erp TG, Hibar DP, Rasmussen JM, et al. **Subcortical brain volume abnormalities in 2028 individuals with schizophrenia and 2540 healthy controls via the ENIGMA consortium.** *Mol Psychiatry* 2016;21:585 CrossRef Medline
48. Bracken BK, Rouse ED, Renshaw PF, et al. **T2 relaxation effects on apparent N-acetylaspartate concentration in proton magnetic resonance studies of schizophrenia.** *Psychiatry Res* 2013;213:142–53 CrossRef Medline
49. Sommer IE, van Westrhenen R, Begemann MJ, et al. **Efficacy of anti-inflammatory agents to improve symptoms in patients with schizophrenia: an update.** *Schizophr Bull* 2014;40:181–91 CrossRef Medline

# Are Anatomic Results Influenced by WEB Shape Modification? Analysis in a Prospective, Single-Center Series of 39 Patients with Aneurysms Treated with the WEB

 D. Herbreteau,  R. Bibi,  A.P. Narata,  K. Janot,  C. Papagiannaki,  S. Soize, and  L. Pierot



## ABSTRACT

**BACKGROUND AND PURPOSE:** Endovascular treatment with the flow-disrupter Woven EndoBridge aneurysm embolization system (WEB) is an innovative treatment for wide-neck bifurcation aneurysms. Prospective, multicenter studies have shown the high safety of this technique. Stability of aneurysm occlusion in long-term follow-up has been rarely studied. Moreover the “compression” phenomenon has been reported and seems to be associated with poor anatomic results. This prospective, single-center series analyzes the safety and efficacy of the WEB device in long-term follow-up in relation to WEB shape modification.

**MATERIALS AND METHODS:** All patients with aneurysms treated with the WEB were prospectively included in a data base. Demographics, aneurysm characteristics, adverse events, and anatomic results were retrospectively analyzed. Anatomic results and modification of the WEB shape on the follow-up examinations were independently evaluated by a core laboratory.

**RESULTS:** Thirty-nine patients were included. We observed few complications: intraoperative rupture in no patients (0.0%) and thromboembolic events in 3 patients (7.7%) with a permanent deficit in 1 (2.6%). At short-term, midterm, and long-term follow-up, adequate occlusion was obtained in 86.8%, 83.3%, and 87.5%, respectively. Retreatment rates were low (5.1%). At 6 months, WEB shape modification (compression/retraction) was observed in 31.6% of patients but was not associated with a lower rate of adequate occlusion.

**CONCLUSIONS:** This prospective, single-center series with WEB devices used in 39 patients during 3.5 years confirms data from previous multicenter studies. Treatment can be accomplished with good safety and efficacy, with a high rate of adequate occlusion. Anatomic results were not worse in case of WEB shape modification.

**ABBREVIATIONS:** AcomA = anterior communicating artery; DL = Dual-Layer; PcomA = posterior communicating artery; SL = Single-Layer; SLS = Single-Layer Sphere; WEB = Woven EndoBridge; WEBCAST = WEB Clinical Assessment of IntraSaccular Aneurysm Therapy

Wide-neck intracranial aneurysms occurring at vascular bifurcations are very challenging for endovascular therapies.<sup>1</sup> Due to the width of the neck, deposition of coils into the aneurysm without protruding into the parent vessel is difficult, even with the help of the remodeling technique.<sup>2</sup> Stent placement is a potential option for this kind of aneurysm; however, Y-stent placement is often necessary and the need for dual antiplatelet treatment limits its use to unruptured aneurysms.<sup>3</sup> A similar problem is encountered with flow diverters, which can only be

used for unruptured aneurysms.<sup>1,4</sup> Moreover, the efficacy of flow diverters in the treatment of wide-neck bifurcation aneurysms has not been established, and there is a potential risk of occlusion or a decrease in the size of the bifurcation branches covered by the flow diverter.<sup>1,5,6</sup> Flow disrupters are intrasaccular devices that disrupt the flow at the aneurysm neck, inducing intra-aneurysmal thrombosis. The WEB device (Woven EndoBridge aneurysm embolization system; Sequent Medical, Aliso Viejo, California) is currently the flow disrupter available for clinical use that has been most widely evaluated in multiple multicenter studies showing its safety and efficacy for the treatment of these complex aneurysms.<sup>7-13</sup>

However mid- and long-term anatomic results remain uncertain. In a recent small series, Cognard and Januel<sup>14</sup> reported the so-called “compression phenomenon” associated with relatively poor anatomic outcome in mid- and long-term results. Even if this series is small and self-evaluated and the change of the WEB shape is probably related to retraction rather than compression, the potential clinical importance of this phenomenon should not

Received April 21, 2016; accepted after revision July 7.

From the Department of Neuroradiology (D.H., R.B., A.P.N., K.J.), Bretonneau Hospital, University of Tours, Tours, France; University François-Rabelais (D.H.), Tours, France; Department of Neuroradiology (C.P.), Charles Nicole Hospital, University of Rouen, Rouen, France; and Department of Neuroradiology (S.S., L.P.), Centre Hospitalier Universitaire Reims, University Reims-Champagne-Ardenne, Reims, France.

Please address correspondence to Denis Herbreteau, MD, Neuroradiology Department, Hôpital Bretonneau, Université François Rabelais, 2 Boulevard Tonnelé, 37044 Tours, France; e-mail: denis.herbreteau@univ-tours.fr

 Indicates article with supplemental on-line table.

<http://dx.doi.org/10.3174/ajnr.A4918>

be neglected and should be further analyzed.<sup>15</sup> A retrospective European series also analyzing mid- and long-term anatomic results showed stable adequate occlusion in 81.1% and 89.7%, respectively, but potential modification of the device was not analyzed.<sup>16,17</sup>

To further evaluate this important question, we analyzed mid- and long-term anatomic follow-up in a prospective single-center series.

## **MATERIALS AND METHODS**

### **Study Population**

Institutional review board approval was obtained, and informed consent was waived according to the design of the study.

From July 2012 (when the first patient was treated with the WEB in the department) to December 2015, patients treated at our institution (University Hospital, Tours) with the WEB were prospectively included in a data base. The decision for treatment and its technique (surgery or endovascular treatment) was decided on a case-by-case basis by a multidisciplinary team that included neurosurgeons and interventional neuroradiologists.

The decision for treatment with the WEB was made by the interventional neuroradiologists on the basis of aneurysm characteristics (location, size, and neck size).

### **WEB Devices**

The WEB is a self-expanding, retrievable, electrothermally detachable device with nitinol braids placed within the aneurysm sac; it induces a flow disruption at the level of the neck and subsequently an intra-aneurysmal thrombosis. Several WEB devices were available at the time of this study. The WEB-Dual Layer (DL), initially used, has a second nitinol braid that is proximally placed inside the first nitinol braid.

From November 2013, the WEB-DL was no longer used and was replaced by WEB-Single-Layer (SL) and WEB-Single-Layer Sphere (SLS), which represent an evolution of the MicroBraid technology (Sequent Medical). The WEB-SL has a barrel shape, and the WEB-SLS is spheric. The WEB-SL and SLS are available in an expanded range of diameters between 4 and 11 mm and in heights between 3 and 9 mm.

The most recent evolution of the device is the enhanced-visualization (WEB-EV), which incorporates composite wire made from nitinol and platinum.

Parallel to this evolution, the microcatheters used to deliver these devices had changed. Initially, the WEB-DL used Rebar 27 (Covidien, Irvine, California), Headway 27 (MicroVention, Tustin, California), and DAC 038 (Stryker, Kalamazoo, Michigan) according to the size of the device. Sequent Medical developed specific microcatheters for WEB treatment, including VIA 27 and VIA 33. Recently, the VIA 21 was introduced for WEB sizes between 4 and 7 mm.

### **Procedural Modalities**

Treatment with the WEB was performed in a manner similar to aneurysm coil treatment, with general anesthesia, intraoperative intravenous heparin, and a single femoral approach.

Several pre-, intra-, and postoperative antiplatelet therapy protocols were used according to aneurysm rupture status and

alternative treatment options. For ruptured aneurysms, no antiplatelet treatment was administered during or after the procedure. In unruptured aneurysms, aspirin was given during the procedure and for 3 months after. When stent placement was used during the procedure, additional treatment with clopidogrel or ticagrelor was prescribed for 3 months, and aspirin, for at least 12 months.

Triaxial access was usually used with a long introducer sheath placed in the internal carotid artery or vertebral artery. A distal access catheter was placed in the intracranial portion of the ICA or vertebral artery, and a microcatheter was placed in the aneurysm.

Careful measurements of the aneurysm (transverse diameter and height) were performed in 2 orthogonal projections on 3D DSA. The mean transverse diameter and height were calculated to determine the appropriate sizing of the device. During the initial period, the size of the WEB device was chosen to fit the aneurysm sac. With increasing experience, we oversized the device in the transverse diameter by approximately 1 mm and undersized it in height by approximately 1 mm (the rule of +1 mm/−1 mm).

The WEB device was then carefully deployed in the aneurysmal sac. After deployment, a control angiogram was performed to check the position of the device and evaluate flow stagnation inside the aneurysm. If needed, the device was resheathed and repositioned. In case of inappropriate sizing, the device was removed and another device was deployed.

### **Data Collection**

For each patient, we collected the following data: patient age, sex, and aneurysm status and aneurysm characteristics, including location, transverse diameter, height and neck size, type of device used (DL/SL/SLS), perioperative antiplatelet treatment, occurrence of complications during or after procedure, and the use of additional devices during procedure.

The preoperative World Federation of Neurosurgical Societies score was obtained in cases of ruptured aneurysms.<sup>18</sup> The modified Rankin Scale score was obtained before treatment in patients with unruptured aneurysms and at 1 month.

Follow-up images were obtained and included MR imaging at 3 months, DSA at 6 months, MR imaging at 1 year, DSA at 2 years, and MR imaging every year afterward.

### **Data Analysis**

All adverse events occurring during the procedure, hospital stay, and until the last follow-up were reported and analyzed, including thromboembolic events and intraoperative rupture. Morbidity was defined as mRS of >1 when the preoperative mRS was ≤1 (or in case of ruptured aneurysm) and as an increase of 1 point when the preoperative mRS was >1.

A core laboratory evaluated anatomic results independently. Aneurysm occlusion was evaluated by using the 3-grade scale (complete occlusion, neck remnant, aneurysm remnant) immediately at the end of the procedure and during follow-up. Adequate occlusion was defined as complete occlusion or neck remnant. The core laboratory also evaluated potential modification of the WEB device, which was classified into 2 groups: no noticeable modification of the WEB shape and modification of the WEB shape. Modifications were evaluated by comparing, in similar angiographic views, the dis-

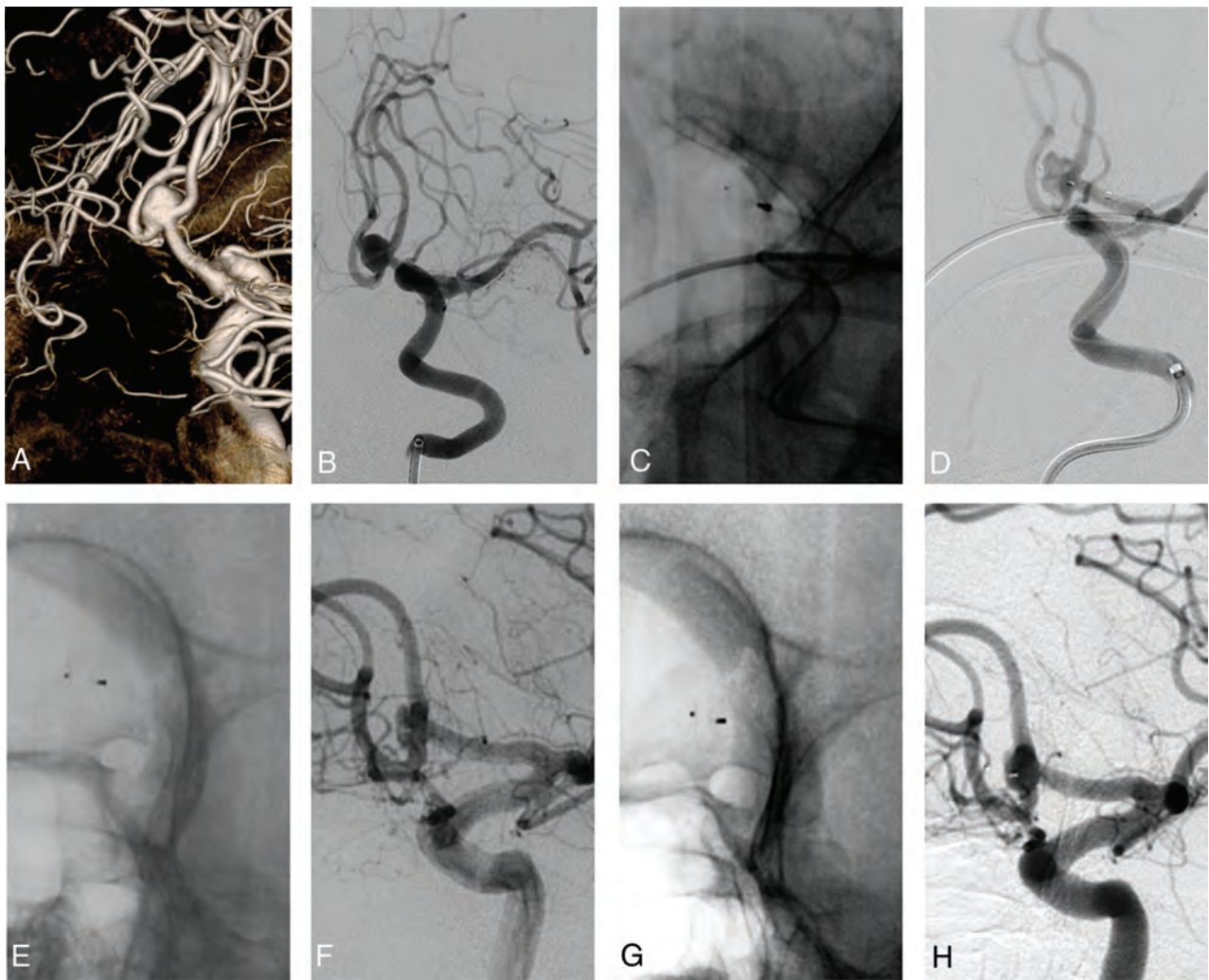


**FIG 1.** An unruptured AcomA aneurysm in a 78-year-old woman (patient 21). Preoperative views: 3D-DSA (A) and oblique view (B). Operative views: WEB in place in the aneurysm, not detached (C), and subtracted view (D), showing contrast in the aneurysm. Six-month DSA: no change of the WEB shape (E) and neck remnant (F). Eighteen-month DSA: WEB shape modification (G) and unchanged neck remnant (H).

tance between the distal and proximal markers of the device and evaluating the concavity of the distal and proximal surfaces. No quantitative evaluation was performed.

Anatomic results and WEB shape modification were analyzed according to device sizing, which was classified into 2 groups according to the rule of +1 mm/−1 mm. The device was undersized when its transverse diameter was not at least 0.5 mm greater compared with the mean transverse diameter of the aneurysm, and it was appropriately sized when the device diameter was at least 0.5 mm greater than the mean transverse diameter of the aneurysm.

Anatomic results were also evaluated in relation to shape modification.

#### Statistical Analysis

Continuous variables were described as mean  $\pm$  SD, with extreme values and categorical variables as a number and percentage. Categorical variables were compared by using the  $\chi^2$  or Fisher exact tests, as appropriate. A *P* value of .05 was considered significant. Analyses were conducted by using MedCalc statistical software for Windows (Version 11.4.3.0; MedCalc Software, Mariakerke, Belgium).

## RESULTS

### Study Population

Among >650 patients treated between July 2012 and December 2015 in our department, 39 patients (6.0%) with 39 aneurysms were treated with the WEB device.

Of this population, 6 patients were included in the French Observatory study<sup>10</sup>; 5 patients, in the WEB Clinical Assessment of IntraSaccular Aneurysm Therapy (WEBCAST) study;<sup>11</sup> and 3 patients, in WEBCAST 2.

Mean patient age was  $58.5 \pm 20$  years. Twenty-three (59.0%) patients were women. Thirty-five (89.7%) aneurysms were unruptured. No aneurysm was previously treated. Aneurysms were located at the MCA bifurcation in 21/39 (53.8%), the anterior communicating artery (AcomA) in 9/39 (23.1%), the basilar tip in 5/39 (12.8%), the ICA terminus in 2/39 (5.1%), the pericallosal artery in 1/39 (2.6%), and the posterior communicating artery (PcomA) in 1/39 (2.6%). Aneurysm width (mean diameter) ranged from 4.3 to 9.5 mm; 11/39 (28.2%) were <5-mm average width, and 28/39 (71.8%) were  $\geq$ 5-mm average width. Neck size was <4 mm in 7/39 aneu-

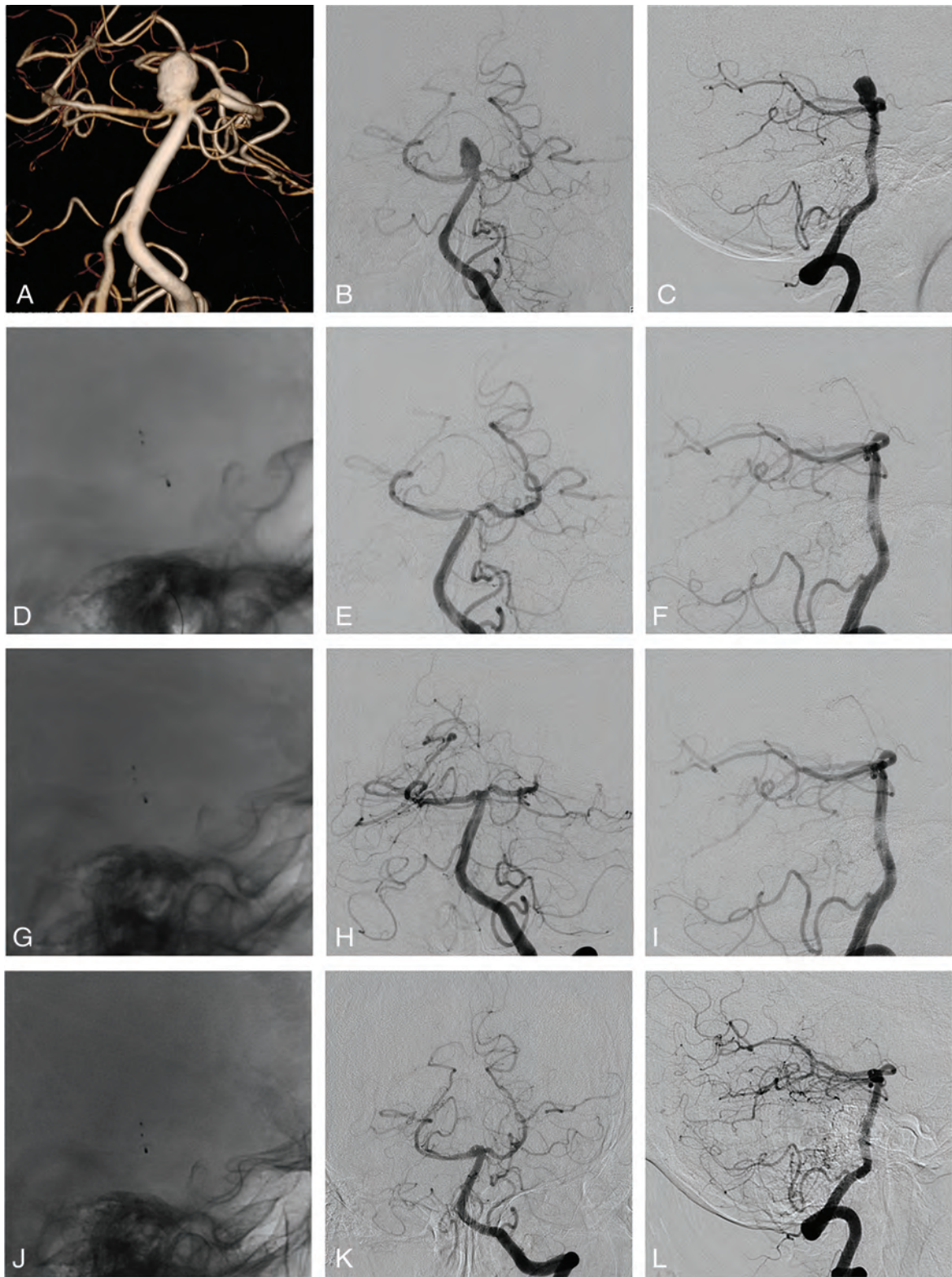


**FIG 2.** Unruptured basilar artery aneurysm in a 69-year-old women (patient 11). Preoperative views: 3D-DSA (A) and frontal (B), and lateral views (C). Operative views: lateral, unsubtracted view showing the WEB (D) and frontal (E) and lateral (F) views showing complete aneurysm occlusion. Six-month DSA: lateral, unsubtracted view showing the WEB change (G) and frontal (H) and lateral (I) views showing complete aneurysm occlusion. Eighteen-month DSA: lateral, unsubtracted view showing the WEB change (J) and frontal (K) and lateral (L) views showing complete aneurysm occlusion.

rysms (17.9%) and  $\geq 4$  mm in 32/39 (82.1%). All except 1 (38/39, 97.4%) met the definition of wide-neck bifurcation aneurysms by either a neck size of  $\geq 4$  mm or a dome/neck ratio

of  $< 2$ . Sixteen patients (41.0%) were treated by using the WEB-DL; 18 (46.2%), with the WEB-SL; and 5, (12.8%) with the WEB-SLS.

### **Treatment Feasibility**

Technical success (deployment of the WEB in the target aneurysm) was achieved in 39/39 (100%). Adjunctive stent placement was performed in 2 patients (5.1%) due to WEB protrusion. In both cases, the WEB was sized according to the rule of +1 mm/−1 mm.

### **Adverse Events**

There was no intraoperative aneurysm rupture. Thromboembolic events occurred in 3/39 (7.7%) patients, with no clinical deficit in 2 and a permanent deficit related to stent placement in 1 (2.6%). There were no delayed adverse events. Modified Rankin scale scores at 30 days were available for 39 patients: mRS was 0 in 37/39 (94.8%), 2 in 1/39 (2.6%, this patient experienced an ischemic event after stent placement), and 4 in 1/39 (2.6%, this patient was already mRS 4 due to SAH). Procedure- and device-related mortality was 0%. Procedure-related morbidity (mRS 2) was 2.6%.

### **Aneurysm Occlusion and Retreatment**

Short-term follow-up (3–6 months) data were available for 38 patients (1 was lost to follow-up). Complete aneurysm occlusion was obtained in 23/38 aneurysms (60.5%), whereas neck and aneurysm remnants were observed in 10/38 (26.3%) and 5/38 (13.2%), respectively, leading to a rate of adequate occlusion of 86.8%. At midterm follow-up (1 year), complete occlusion was obtained in 12/24 aneurysms (50.0%); neck remnant, in 8/24 (33.3%); and aneurysm remnant, in 4/24 (16.7%), with adequate occlusion in 83.3%. At long-term follow-up ( $\geq 18$  months), complete occlusion was obtained in 13/24 aneurysms (54.2%); neck remnant, in 8/24 (33.3%); and aneurysm remnant, in 3/24 aneurysms (12.5%), with adequate occlusion in 87.5%.

Two of 39 aneurysms (5.1%) were retreated during the follow-up period. One (patient 22) had a 7.1 mm, unruptured, AcomA aneurysm treated with an undersized WEB, retreated at 8 months with stent placement and coiling. The other (patient 8) had a 6.0-mm, unruptured, MCA aneurysm treated with an appropriately sized WEB. An aneurysm remnant was depicted at midterm follow-up without WEB shape modification and was retreated at 14 months.

### **WEB Sizing, Shape Modification, and Aneurysm Occlusion**

According to the rule of +1 mm/−1 mm (see above), the WEB device was undersized in 11/39 patients (28.2%) and appropriately sized in 28/39 patients (71.8%). Among the 38 patients with short-term angiographic follow-up, 10 had an undersized WEB (26.3%), and 28, an appropriately sized WEB (73.7%).

WEB shape modification was observed in 12/38 patients (31.6%) with short-term follow-up. It was observed in similar percentages in patients with an undersized WEB (3/10, 30.0%) and an appropriately sized WEB (9/28, 32.1%) ( $P = .99$ ). At long-term follow-up, the shape of the device was not modified in the 12 patients who already had a shape modification at short-term follow-up, and 1 additional patient had WEB shape modification.

In patients with an undersized WEB, short-term anatomic results were complete occlusion in 5/10 aneurysms (50.0%), neck remnant in 2/10 (20.0%), and aneurysm remnant in 3/10 (30.0%). In patients with an appropriately sized WEB, complete

occlusion was observed in 18/28 aneurysms (64.3%); neck remnant, in 8/28 (28.6%); and aneurysm remnant, in 2/28 (7.1%). The rate of complete occlusion was not significantly different between both groups ( $P = .67$ ). Adequate occlusion (complete occlusion or neck remnant) was observed in 7/10 aneurysms with an undersized WEB (70.0%) and in 26/28 aneurysms with an appropriately sized WEB (92.9%) ( $P = .10$ ).

At short-term follow-up, in the group of patients with WEB shape modification, anatomic results were complete occlusion in 3/12 (25.0%), neck remnant in 7/12 (58.3%), and aneurysm remnant in 2/12 (16.7%). In the group of patients without WEB shape modification, anatomic results were complete occlusion in 20/26 (76.9%), neck remnant in 3/26 (11.5%), and aneurysm remnant in 3/26 (11.5%). The rate of complete occlusion was significantly different between both groups ( $P = .004$ ). Adequate occlusion was observed in 10/12 aneurysms with WEB shape modification (83.3%) and in 24/26 aneurysms without WEB shape modification (92.3%) ( $P = .64$ ). The percentage of neck remnants was significantly different between both groups ( $P = .004$ ).

## **DISCUSSION**

This series reports the initial experience with the WEB device in aneurysm treatment. It explains the relatively low percentage of patients treated with this technique (6.0%) because indications at the beginning were limited to selected cases with wide-neck bifurcation aneurysms difficult to treat with other techniques.

As demonstrated in previous Good Clinical Practice series, treatment with the WEB was highly feasible with no failures in this series.<sup>7–13</sup> Most aneurysms were bifurcation aneurysms located at the MCA, basilar artery, ICA, and AcomA. More atypical locations were also treated, including the PcomA and pericallosal artery. Some aneurysm locations (AcomA, PcomA, pericallosal artery) proved more challenging to treat. In addition, aneurysms with excessive angulation versus the parent artery sometimes proved more difficult. Recent improvements to the WEB delivery system (0.021 profile and VIA 21) facilitate treatment of these aneurysms. The WEB is a safe and efficient alternative to balloon-remodeling treatment, stent placement, flow diversion, or clipping. The single-balloon remodeling technique is less efficacious and more difficult in bifurcation aneurysms.<sup>2</sup> Moreover, the double-balloon technique can be used, but it is technically more challenging. Stent-assisted coiling and flow diversion are typically reserved for patients with unruptured aneurysms because double antiplatelet treatment is required and is more limited in bifurcation aneurysms (especially with flow diversion). Moreover, the anatomic evolution (possible stenosis) of a small vessel such as the MCA filled with 2 intermingled stents remains unknown. The use of intraluminal flow diverters for the treatment of bifurcation aneurysms is also not simple because 1 or several bifurcation branches will be covered by the flow diverter with the potential risk of occlusion.<sup>5,6</sup>

In our series, all except 4 patients were treated for unruptured aneurysms, mostly due to the logistic organization (devices not available at all times on-site in our department), and antiplatelet therapy was conducted according to our routine protocol for unruptured aneurysms. Because no pre- or intraoperative antiplatelet treatment is needed for WEB treatment and because a rapid

restriction of flow is observed at the level of the aneurysm dome, we recently used the WEB device for ruptured aneurysms.<sup>19,20</sup> Larger series are needed to confirm the initial good results in this subgroup of patients.

Safety was good with no mortality and low treatment-related morbidity (1 patient, 2.6%). There was no intraoperative rupture and a limited number of thromboembolic events (3/39 patients, 7.7%), 2 without any clinical worsening. There was also an ischemic event in a complex case in which the placement of a stent was necessary due to WEB protrusion. A postoperative decrease of blood pressure led to this ischemic lesion with clinical worsening (mRS 2). Due to the small number of patients and events, it is not possible to compare safety in patients treated with the WEB-DL versus the WEB-SL/SLS. These results are in line with data from the Good Clinical Practice studies, despite this series including the first cases treated with this new technique (thus, the learning curve).<sup>10-13</sup>

The increasing use of coiling for aneurysm treatment has been associated with a depiction of recanalization as one of the limitations of the endovascular approach. Therefore, long-term stability of aneurysm treatment is a critical issue after endovascular treatment, especially for wide-neck aneurysms, which are prone to recurrence. From the literature, recanalization occurs for 8%–33.6% of aneurysms treated with coils, with 7%–10% retreatment.<sup>21-23</sup> These rates have led to the development of new tools, including the flow disrupter.

Data regarding the stability of WEB aneurysm treatment are still relatively limited. Animal studies conducted in the rabbit elastase aneurysm model showed that treatment with the WEB device was associated with high rates of immediate- and long-term aneurysm occlusion.<sup>24</sup> In the recent analysis of the cumulated population of 2 Good Clinical Practice studies, adequate occlusion (complete occlusion and neck remnant) was obtained in 82% of aneurysms at 1-year follow-up.<sup>13</sup> In a retrospective European series, adequate occlusion was observed in 81.1% in short-term follow-up (median, 6 months) and 89.7% in midterm follow-up (median, 13 months).<sup>16</sup> In the same series, long-term follow-up was analyzed in a subgroup of 26 aneurysms, showing adequate occlusion in 84.2%, with stability of aneurysm occlusion between midterm and long-term in all cases.<sup>17</sup> Similar results were obtained in the present series. Adequate occlusion was obtained in 86.8% (33/38) at short-term follow-up (6 months), 83.3% (20/24) at midterm follow-up (1 year), and 87.5% (21/24) at long-term follow-up ( $\geq 18$  months). The rate of adequate occlusion was similar at different follow-up intervals.

Two aneurysms were retreated with stent-assisted coiling (retreatment rate: 5.1%) during the follow-up period: 1 between 6 months and 1 year and 1 between 12 and 18 months. The retreatment rate was similar to that reported in the cumulated populations of the WEBCAST and French Observatory studies (3.6%).

A recent small series reported disappointing anatomic results potentially related to WEB compression.<sup>14</sup> Adequate occlusion was observed in 71.5% of cases at short-term follow-up and 57.2% of cases at long-term follow-up. For the authors, these poor results were related to WEB compression. The potential phenomenon of so-called WEB compression is a decrease in the height of the device owing to the deepening of the proximal and distal con-

cave device recesses during follow-up. Because both the proximal marker (near the aneurysm neck) and the distal marker (near the aneurysm apex) move toward the center of the device with time, one hypothesis is that the mechanism responsible for this phenomenon is likely associated with clot organization/retraction.<sup>15</sup> The present series provides important insights into this phenomenon. The phenomenon is relatively frequent (31.6%) and, at least in this series, is not related to WEB sizing. The phenomenon is observed in similar percentages in patients treated with undersized and appropriately sized WEBs (30.0% and 32.1%, respectively). On the other hand, adequate occlusion is more frequent but not significant when there is no WEB shape modification (92.3% compared with 83.3% in case of WEB shape modification). Moreover, the rate of complete aneurysm occlusion is significantly lower in case of WEB shape modification (25.0%) compared with cases with no modification (76.9%) due to a higher rate of neck remnants (58.3% and 11.5%, respectively). Adequate occlusion is also more often obtained when the device is appropriately sized (92.9%) than when an undersized device is used (70.0%), but this result is not statistically significant due to the small number of patients in the groups.

This study has several limitations. First, it is a single-center, retrospectively analyzed series. Because cases were prospectively collected, it gives a precise idea of the good safety of the device; all cases included were also those treated at the beginning of our clinical experience with the WEB (learning curve). Moreover, it gives the opportunity to precisely analyze the anatomic results with several follow-up angiograms for some patients. Second, it was not a randomized study, and direct comparison with other techniques is difficult. However, in the absence of a reference technique for the treatment of wide-neck bifurcation, a randomized trial is difficult to design and probably not ethical. Third, the series is relatively small (39 patients), but long-term follow-up was obtained in a large number of patients, which permits analyzing precisely the stability of aneurysm occlusion with the WEB. However, the small number of patients in this single-center series limits the interpretation of WEB sizing and WEB shape modification on anatomic results. Fourth, the WEB shape modification was studied semiquantitatively by comparing the shape of the device postoperatively and at follow-up directly. It is important to conduct a quantitative study in a large series of patients, but it is beyond the scope of this study.

## CONCLUSIONS

This prospective, single-center series with WEB devices in 39 patients, during a 3.5-year period, confirms data from previous multicenter studies. Treatment can be accomplished with a high degree (100%) of technical success and safety. Efficacy is also good, with adequate occlusion in 83.3% at midterm follow-up and 87.0% at long-term follow-up in these difficult-to-treat wide-neck bifurcation aneurysms. In this series, WEB shape modification was observed in 31.6% at 6 months and is associated with a significantly lower percentage of complete aneurysm occlusion and a higher percentage of neck remnants, with a similar rate of adequate occlusion.

Disclosures: Denis Herbreteau—UNRELATED: Consultancy; Sequent Medical; Travel/Accommodations/Meeting Expenses Unrelated to Activities Listed; Stryker, Codman, ev3. Richard Bibi—UNRELATED: Travel/Accommodations/Meeting Expenses Unrelated to Activities Listed; Sequent Medical invitation to Congress. Ana Paula Narata—UNRELATED: Consultancy; Sequent Medical.\* Laurent Pierot—RELATED: Consulting Fee or Honorarium; Sequent Medical; Payment for Writing or Reviewing the Manuscript; Sequent Medical; UNRELATED: Consultancy; Blockade Medical, Medtronic, MicroVention, Neuravi, Penumbra, Sequent Medical. \*Money paid to the institution.

## REFERENCES

- Pierot L, Biondi A. **Endovascular techniques for the management of wide-neck intracranial bifurcation aneurysms: a critical review of the literature.** *J Neuroradiol* 2016;43:167–75 CrossRef Medline
- Pierot L, Cognard C, Spelle L, et al. **Safety and efficacy of balloon remodeling technique during endovascular treatment of intracranial aneurysms: critical review of the literature.** *AJNR Am J Neuro-radiol* 2012;33:12–15 CrossRef Medline
- Pierot L, Wakhloo A. **Endovascular treatment of intracranial aneurysms: current status.** *Stroke* 2013;44:2046–54 CrossRef Medline
- Pierot L. **Flow diverter stents in the treatment of intracranial aneurysms: Where are we?** *J Neuroradiol* 2011;38:40–46 CrossRef Medline
- Gawlitza M, Januel AC, Tall P, et al. **Flow diversion treatment of complex bifurcation aneurysms beyond the circle of Willis: a single center series with special emphasis on covered cortical branches and perforating arteries.** *J NeuroIntervent Surg* 2016;8:481–87 CrossRef Medline
- Caroff J, Neki H, Mihalea C, et al. **Flow-diverter stents for the treatment of saccular middle cerebral artery bifurcation aneurysms.** *AJNR Am J Neuroradiol* 2016;37:279–84 CrossRef Medline
- Pierot L, Liebig T, Sychra V, et al. **Intrasaccular flow-disruption treatment of intracranial aneurysms: preliminary results of a multicenter clinical study.** *AJNR Am J Neuroradiol* 2012;33:1232–38 CrossRef Medline
- Pierot L, Klisch J, Cognard C, et al. **Endovascular WEB flow disruption in middle cerebral artery aneurysms: preliminary feasibility, clinical, and anatomical results in a multicenter study.** *Neurosurgery* 2013;73: 27–34; discussion 34–35 CrossRef Medline
- Papagiannaki C, Spelle L, Januel AC, et al. **WEB intrasaccular flow disruptor-prospective, multicenter experience in 83 patients with 85 aneurysms.** *AJNR Am J Neuroradiol* 2014;35:2006–11 CrossRef Medline
- Pierot L, Moret J, Turjman F, et al. **WEB treatment of intracranial aneurysms: indications, feasibility, complications, and 1-month safety results with the WEB-DL and WEB-SL/SLS in the French Observatory.** *AJNR Am J Neuroradiol* 2015;36:922–27 CrossRef Medline
- Pierot L, Costalat V, Moret J, et al. **Safety and efficacy of aneurysm treatment with WEB: results of WEBCAST Study.** *J Neurosurg* 2016; 124:1250–66 CrossRef Medline
- Pierot L, Moret J, Turjman F, et al. **WEB treatment of intracranial aneurysms: clinical and anatomic results in the French Observatory.** *AJNR Am J Neuroradiol* 2016;37:655–59 CrossRef Medline
- Pierot L, Spelle L, Molyneux A, et al. **Clinical and anatomical follow-up in patients with aneurysms treated with the WEB device: 1-year follow-up report in the cumulated population of 2 prospective, multicenter series (WEBCAST and French Observatory).** *Neurosurgery* 2016;78:133–41 CrossRef Medline
- Cognard C, Januel AC. **Remnants and recurrences after the use of the WEB intrasaccular device in large-neck bifurcation aneurysms.** *Neurosurgery* 2015;76:522–30; discussion 530 CrossRef Medline
- Pierot L. **Letter: WEB aneurysm treatment—occlusion stability and “compression.”** *Neurosurgery* 2015;77:E666–67 CrossRef Medline
- Lubicz B, Klisch J, Gauvrit JY, et al. **WEB-DL endovascular treatment of wide-neck bifurcation aneurysms: short- and midterm results in a European study.** *AJNR Am J Neuroradiol* 2014;35:432–38 CrossRef Medline
- Pierot L, Klisch J, Liebig T, et al. **WEB-DL endovascular treatment of wide-neck bifurcation aneurysms: long-term results in a European series.** *AJNR Am J Neuroradiol* 2015;36:2314–19 CrossRef Medline
- Teasdale GM, Drake CG, Hunt W, et al. **A universal subarachnoid hemorrhage scale: report of a committee of the World Federation of Neurosurgical Societies.** *J Neurol Neurosurg Psychiatry* 1988;51:1457 CrossRef Medline
- Caroff J, Mihalea C, D’Argento F, et al. **Woven Endobridge (WEB) device for endovascular treatment of ruptured intracranial wide-neck aneurysms: a single-center experience.** *Neuroradiology* 2014; 56:755–61 CrossRef Medline
- Liebig T, Kabbasch C, Strasilla C, et al. **Intrasaccular flow disruption in acutely ruptured aneurysms: a multicenter retrospective review of the use of the WEB.** *AJNR Am J Neuroradiol* 2015;36:1721–27 CrossRef Medline
- Gallas S, Januel AC, Pasco A, et al. **Long-term follow-up of 1036 cerebral aneurysms treated by bare coils: a multicentric cohort treated between 1998 and 2003.** *AJNR Am J Neuroradiol* 2009;30: 1986–92 CrossRef Medline
- Benaissa A, Barbe C, Pierot L. **Analysis of Recanalization after Endovascular Treatment of intracranial Aneurysm (ARETA trial): presentation of a prospective multicenter trial.** *J Neuroradiol* 2015; 42:80–85 CrossRef Medline
- Ferns SP, Sprengers ME, van Rooij WJ, et al. **Coiling of intracranial aneurysms: a systematic review on initial occlusion and reopening and retreatment rates.** *Stroke* 2009;40:e523–29 CrossRef Medline
- Ding YH, Dai D, Schroeder D, et al. **Experimental testing of the dual-layer Woven EndoBridge device using an elastase-induced aneurysm model in rabbits.** *Interv Neuroradiol* 2016;22:299–303 CrossRef Medline

# Efficacy and Safety of the Woven EndoBridge (WEB) Device for the Treatment of Intracranial Aneurysms: A Systematic Review and Meta-Analysis

S. Asnafi, A. Rouchaud, L. Pierot, W. Brinjikji, M.H. Murad, and D.F. Kallmes



## ABSTRACT

**BACKGROUND AND PURPOSE:** Intracranial flow diverters are increasingly being used in the treatment of wide-neck and bifurcation aneurysms. We performed a systematic review and meta-analysis of existing literature on the Woven EndoBridge device in the treatment of intracranial aneurysms.

**MATERIALS AND METHODS:** A comprehensive literature search was performed through October 1, 2015. We extracted information on baseline aneurysm and patient characteristics. Outcomes studied included immediate and midterm (>3 month) angiographic outcomes (complete occlusion as well as adequate occlusion, defined as complete occlusion or neck remnant), aneurysm retreatment, intraoperative rupture, perioperative morbidity and mortality, thromboembolic complications, and treatment failure. Meta-analysis was performed by using the random-effects model.

**RESULTS:** Fifteen uncontrolled series were included in this analysis, including 565 patients with 588 aneurysms, of which 127 were ruptured. Initial complete and adequate occlusion rates were 27% (95% CI, 15%–39%) and 59% (95% CI, 39%–78%), respectively. Midterm complete and adequate occlusion rates after a median of 7 months were 39% (95% CI, 26%–52%) and 85% (95% CI, 78%–91%), respectively. Perioperative morbidity and mortality rates were 4% (95% CI, 1%–8%) and 1% (95% CI, 0%–2%), respectively. Midterm adequate occlusion rates for ruptured aneurysms were 85% (95% CI, 67%–98%), compared with 84% (95% CI, 72%–94%) for unruptured aneurysms ( $P = .89$ ). Patients with ruptured aneurysm had similar rates of perioperative morbidity to patients with unruptured aneurysm (2%; 95% CI, 0%–26% versus 2%; 95% CI, 0%–6%, respectively;  $P = .35$ ).

**CONCLUSIONS:** Early evidence derived from uncontrolled studies suggests that Woven EndoBridge treatment has a good safety profile and promising rates of adequate occlusion, especially given the complexity of aneurysms treated. Further prospective clinical trials are needed to confirm these results and better define the risks and benefits of use of the Woven EndoBridge device in treating wide-neck and wide-neck bifurcation aneurysms.

**ABBREVIATION:** WEB = Woven EndoBridge

With the advent of stent-assisted and balloon-assisted coiling, wide-neck and wide-neck bifurcation intracranial aneurysms are increasingly treated with endovascular techniques. Both stent-assisted and balloon-assisted coiling have been shown safe and effective in treating these aneurysms by allowing for increased packing and lower rates of parent artery occlusion com-

pared with conventional coiling alone.<sup>1–7</sup> However, because of less than satisfactory occlusion rates with coil embolization of wide-neck and wide-neck bifurcation aneurysms, there has been a push toward treating these lesions with intrasaccular and intraluminal flow diverters.

The Woven EndoBridge (WEB; Sequent Medical, Aliso Viejo, California) is a nitinol braided-wire intravascular device designed to disrupt blood flow at the aneurysmal neck. This device is specifically designed for the treatment of wide-neck bifurcation aneurysms.<sup>8,9</sup> To date, several case series have demonstrated that the WEB device is both safe and effective in treatment of wide-neck and wide-neck bifurcation aneurysms.<sup>10–13</sup> We present the results of a systematic review and meta-analysis examining outcomes of endovascular treatment of wide-neck and wide-neck bifurcation aneurysms with the WEB device. The aim of our study was to assess both angiographic and clinical outcomes.

Received April 4, 2016; accepted after revision June 24.

From the Department of Radiology (S.A., A.R., W.B., D.F.K.) and Center for the Science of Healthcare Delivery (M.H.M.), Mayo Clinic, Rochester, Minnesota; and Department of Neuroradiology (L.P.), Maison Blanche Hospital, University of Reims Champagne-Ardenne, Reims, France.

Please address correspondence to Waleed Brinjikji, MD, Department of Radiology, Mayo Clinic, 200 First St SW, Rochester, MN 55905; e-mail: brinjikji.waleed@mayo.edu; @wbrinjikji

Indicates article with supplemental on-line table.

<http://dx.doi.org/10.3174/ajnr.A4900>

## MATERIALS AND METHODS

### Literature Search

A comprehensive literature search of 3 data bases (PubMed, Ovid MEDLINE, and Ovid EMBASE) was designed and conducted by an experienced librarian with input from the authors. The keywords “intracranial aneurysm,” “cerebral aneurysm,” “aneurysm,” “wide-neck,” “bifurcation,” “WEB device,” and “intraluminal flow diverter” were used in both “AND” and “OR” combinations. The search was limited to articles published from January 1, 2010, to October 1, 2015, and was supplemented by contacting experts in the field for any additional studies. All studies reporting patients with aneurysms treated with the WEB device were included. Inclusion criteria were the following: 1) English language, 2) study reporting a consecutive series of aneurysms treated with the WEB device, and 3) series of at least 5 patients reporting angiographic and/or clinical outcomes. Review articles, comments, guidelines, technical notes, and editorials were excluded. Two of the authors selected the included studies. A third author arbitrated in cases of disagreement.

### Outcomes and Data Extraction

For each study, we extracted the following baseline information: number of patients, aneurysm rupture status, patient sex, mean age, use of core lab in assessing angiographic outcomes, number of aneurysms treated, mean aneurysm size, mean aneurysm neck size, length of clinical follow-up, and length of angiographic follow-up.

Outcomes studied included immediate and midterm (>3 month) angiographic outcomes (complete occlusion and adequate occlusion, which was defined as complete occlusion or neck remnant), aneurysm retreatment, intraoperative rupture, perioperative morbidity and mortality, thromboembolic complication, and treatment failure. Treatment failure was defined as a failed attempt at WEB device placement. Outcomes were calculated for the overall patient population with subgroup analysis by rupture status (ruptured versus unruptured). Morbidity was defined as mRS score >1. There were variable classification scales to assess aneurysm occlusion used in this study. For studies that used the WEB Occlusion Scale, complete occlusion was defined as no contrast opacification of the aneurysm with or without contrast opacification of the proximal recess of the device. Earlier studies that did not use the WEB Occlusion Scale and used the Raymond scale instead often classified contrast opacification of the proximal recess of the device as a neck remnant or did not specify recess opacification rates. Thus, for the purposes of this meta-analysis, we report adequate occlusion, which was defined as complete occlusion or neck remnant (complete occlusion with opacification of the neck).

### Study Risk of Bias

We modified the Newcastle-Ottawa Quality Assessment Scale for Case Control Studies to assess the risk of bias of the studies included in this meta-analysis. This tool is designed for use in comparative studies; however, because none of the included studies were controlled, we assessed study risk of bias based on selected items from the tool, focusing on the following questions: 1) did the study include all patients or consecutive patients versus a selected sample?; 2) was the study retrospective or prospective?; 3) was angio-

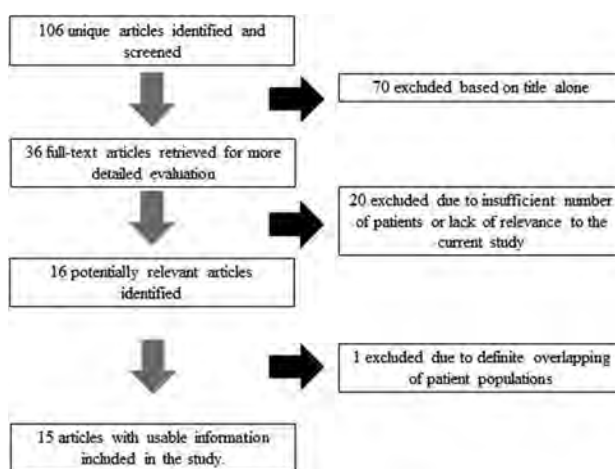


FIG 1. Search strategy results.

graphic and clinical follow-up satisfactory, thus allowing for ascertainment of all outcomes?; 4) were outcomes clearly reported?; and, 5) were the interventionalists treating the patients the same as those who assessed angiographic and clinical outcomes?

### Statistical Analysis

We estimated from each study the cumulative incidence (event rate at the end of the study) and 95% CI. Because we anticipated marked heterogeneity in the populations and interventions across the various included studies, a random-effects model was used to pool incidence rates across studies.<sup>14</sup> Variance was estimated by using the Freeman-Tukey double arcsine method.<sup>15</sup> The  $I^2$  statistic was used to express the proportion of inconsistency that is not attributable to chance.<sup>16</sup> Analysis was conducted by using STATA Statistical Software: Release 14 (StataCorp, College Station, Texas).

## RESULTS

### Study Selection and Characteristics

The initial literature search yielded 106 articles. Upon review of the abstracts and titles, 90 articles were excluded. Sixteen articles were selected for full-text screening. In total, 15 studies including 565 patients with 588 aneurysms were included. Of these, 127 aneurysms (22%) were ruptured and 461 aneurysms (78%) were unruptured; in no case was the rupture status unknown. There were 470 aneurysms (80%) in the anterior circulation and 118 (20%) in the posterior circulation. Seventy-three aneurysms (12.0%) were treated with adjunctive coiling, stent placement, or stent-assisted coiling. Type of pre- and postoperative antiplatelet therapy varied widely between studies.

Of the 15 studies, 6 had a low risk of bias, 3 had a high risk of bias, and 6 had a moderate risk of bias. The smallest study had 6 patients with 6 aneurysms, and the largest study had 90 patients with 98 aneurysms. Eleven studies had angiographic follow-up at 6 months or longer. A summary of included studies is provided in the On-line Table. Flow chart for study selection is provided in Fig 1.

### Overall Outcomes

The WEB treatment outcomes are presented in Table 1. Initial complete occlusion rates and adequate occlusion rates were 27% (95% CI, 15%–39%) and 59% (95% CI, 39%–78%), respectively.

Midterm complete occlusion rates after a median of 7 months were 39% (95% CI, 26%–52%) and midterm adequate occlusion rates were 85% (95% CI, 78%–91%) (Fig 2). Treatment failure occurred in 3% of cases (95% CI, 1%–6%). Perioperative morbidity and mortality rates were 4% (95% CI, 1%–8%) and 1% (95% CI, 0%–2%), respectively. The rate of thromboembolic complications was 8% (95% CI, 5%–12%). Midterm good neurologic outcome rates are provided in Fig 3.

### Angiographic and Clinical Outcomes by Rupture Status

The rate of midterm complete occlusion was 45% (95% CI, 25%–65%) for the ruptured group and 22% (11%–33%) for the unruptured group ( $P = .008$ ). The rate of midterm adequate occlusion for ruptured aneurysms was 85% (95% CI, 67%–98%), compared

with 84% (95% CI, 72%–94%) for unruptured aneurysms ( $P = .89$ ). Data on initial occlusion by rupture status were not consistently reported, and no meta-analysis could be performed for this outcome.

Patients with ruptured aneurysms had similar rates of perioperative morbidity as those with unruptured aneurysms (2%; 95% CI, 0%–6% versus 2%; 95% CI, 0%–6%, respectively;  $P = .35$ ). Rates of intraoperative rupture in ruptured and unruptured aneurysms were 6% (95% CI, 0%–11%) and 1% (95% CI, 0%–3%), respectively ( $P = .08$ ). Treatment failure occurred at a higher rate for unruptured aneurysms (6%; 95% CI, 3%–9%) compared with the ruptured aneurysms (0%; 95% CI, 0%–4%) ( $P = .04$ ). These results are presented in Table 2.

**Table 1: Summary of outcomes**

Outcome	Event Rate (%) (95% CI)	Raw Proportion
Initial complete occlusion	27 (15–39) <sup>a</sup>	76/277
Initial adequate occlusion	59 (39–78) <sup>a</sup>	132/277
Midterm complete occlusion	39 (26–52) <sup>a</sup>	168/362
Midterm adequate occlusion	85 (78–91)	209/261
Midterm good neurologic outcome	96 (94–98)	328/346
Intraoperative rupture	1 (0–2)	12/556
Perioperative morbidity	4 (1–8) <sup>a</sup>	29/449
Perioperative mortality	1 (0–2)	13/517
Thromboembolic complication	8 (5–12)	56/556
Retreatment	6 (1–12) <sup>a</sup>	37/501
Treatment failure	3 (1–6)	27/543

<sup>a</sup> Indicates  $I^2$  value above 50% (substantial heterogeneity).

### DISCUSSION

This systematic review and meta-analysis of 15 uncontrolled studies demonstrated that treatment of wide-neck bifurcation aneurysms with the WEB device was achieved with high rates of technical success and low rates of complications. Initial adequate occlusion rate was nearly 60%, and adequate occlusion rate at follow-up was 85%. There were no substantial differences in outcomes by rupture status. These findings are important because they suggest that the WEB device might be a valuable tool in the treatment of wide-neck bifurcation aneurysms regardless of rupture status.

As demonstrated by this meta-analysis, a number of prior studies have examined the safety and efficacy of the WEB device. In a systematic review of 6 studies by Armoiry et al,<sup>17</sup> the authors reported high rates of treatment feasibility (93%–100%) with ad-

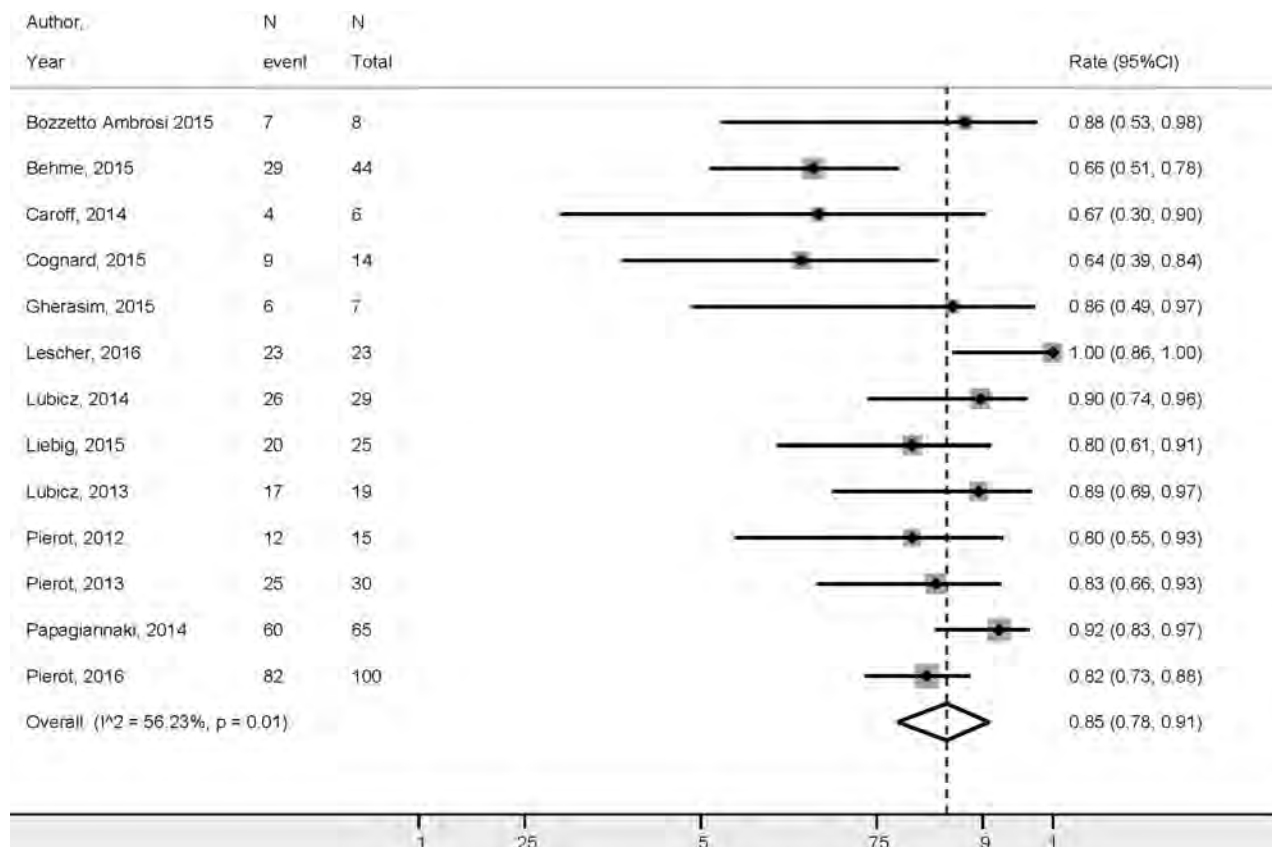


**FIG 2.** Midterm adequate occlusion rates overall.

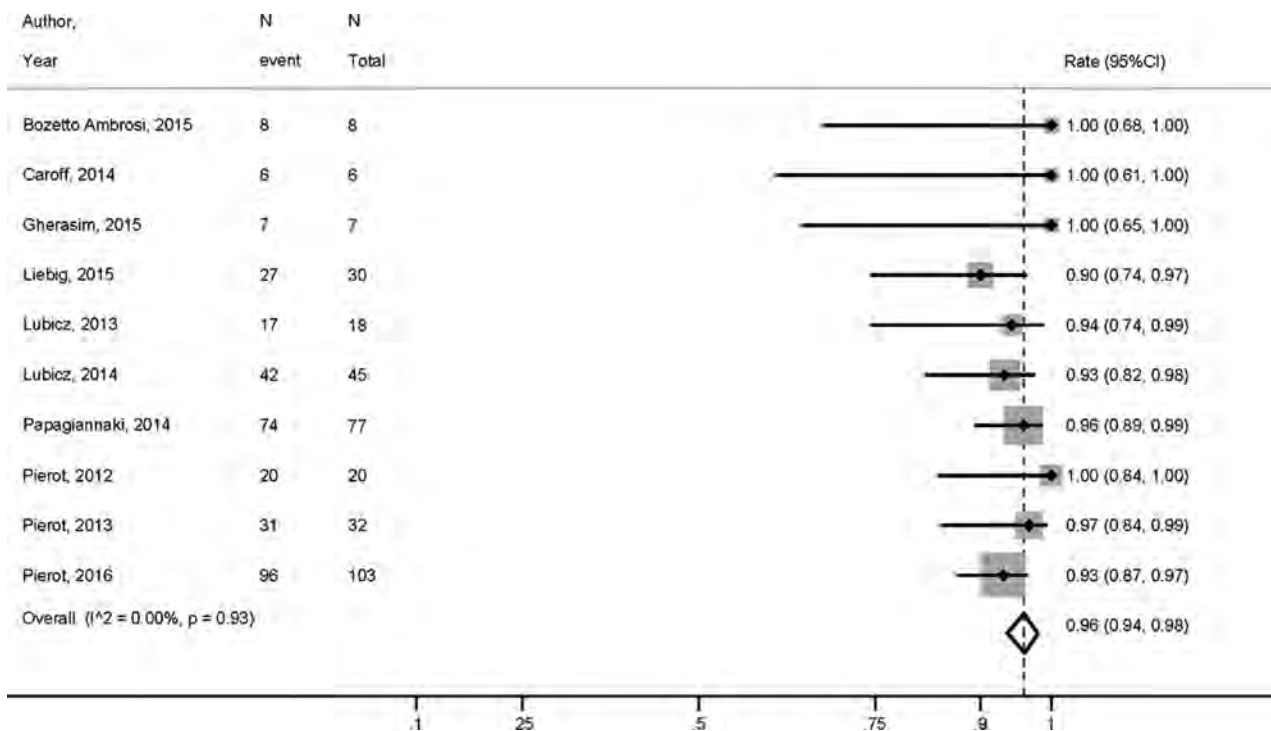


FIG 3. Midterm good neurologic outcome rates.

Table 2: Outcomes by rupture status

Outcome	Ruptured Group Event Rate (%) (95% CI)	Raw Proportion	Unruptured Group Event Rate (%) (95% CI)	Raw Proportion	P Value
Initial adequate occlusion	100 (57–100)	4/4	70 (44–91)	49/73	.24
Midterm complete occlusion	45 (25–65)	18/35	22 (11–33)	22/89	.008
Midterm adequate occlusion	85 (67–98)	33/44	84 (72–94)	76/118	.89
Intraoperative rupture	6 (0–11)	4/79	1 (0–3)	3/220	.08
Perioperative morbidity	2 (0–26) <sup>a</sup>	14/70	2 (0–6)	5/145	.35
Perioperative mortality	15 (7–23)	11/69	0 (0–3)	0/122	<.0001
Thromboembolic complication	21 (0–56) <sup>a</sup>	10/79	5 (2–10)	17/220	.07
Retreatment	4 (0–20)	7/66	7 (0–25) <sup>a</sup>	17/171	.71
Treatment failure	0 (0–3.9)	0/79	6 (3–9)	18/274	.04
Midterm good neurologic outcome	100 (97–100)	36/39	99 (94–100)	80/82	.21

<sup>a</sup> Indicates I<sup>2</sup> value above 50% (substantial heterogeneity).

equate occlusion rates between 65% and 85% at midterm follow-up. Permanent morbidity rates ranged from 2%–7% depending on the series, and mortality ranged from 0%–17%. Our study differs from the systematic review performed by Armoiry et al<sup>17</sup> in that we conducted a formal meta-analysis and were able to pool data from 15 studies including over 550 patients. By doing so, we were able to report efficacy and complication rates with narrow confidence intervals and provide important subgroup analyses of outcomes by rupture status.

Midterm occlusion rates with the WEB device were slightly higher than those reported for stent-assisted coil treatment of wide-neck bifurcation intracranial aneurysms. Typical long-term complete or near-complete occlusion rates for coiling of wide-neck and bifurcation aneurysms is generally on the order of 70%.<sup>18–20</sup> One recently published meta-analysis of over 2000 patients undergoing stent-assisted coiling of wide-neck bifurcation aneurysms found long-term occlusion rates of 73%.<sup>21</sup> Meanwhile, our study found a long-term adequate occlusion rate of 80%. Initial occlusion rates were approximately 60% with the

WEB device, compared with 54% for stent-assisted coiling of wide-neck bifurcation aneurysms. In addition to improved occlusion rates, a distinct advantage of treatment with the WEB device compared with stent-assisted coiling is the fact that pre- and/or intraoperative antiplatelet therapy is generally not required for WEB treatment. This is particularly important in the treatment of ruptured aneurysms.

Given the short length of follow-up available in many of the included studies (median of 7 months), the angiographic outcomes of the WEB device are generally similar to flow diversion. Complete occlusion rates in studies reporting 6–12 month follow-up for flow diversion typically range from 70%–93%.<sup>22–26</sup> One large meta-analysis of 1451 patients with 1654 aneurysms treated with flow diverters found complete occlusion rates of 76%, with a vast amount of studies reporting follow-up after less than 12 months, similar to our results. In general, occlusion rates with flow diversion improve with increased follow-up as studies with 24 months or more of follow-up report occlusion rates over 90%.<sup>26–28</sup> Similar to flow-diversion therapy, occlusion rates with

the WEB device generally increase with time because the healing process after placement of an intra-aneurysmal flow diverter involves a complex process of loose connective tissue deposition followed by endothelialization of the device–neck interface. Given the lack of consistent long-term (ie, >12 months) follow-up in the studies included in this meta-analysis, it is possible that we are in fact underestimating long-term occlusion rates.

This systematic review also demonstrated that complication rates associated with the WEB device were relatively low. Among unruptured aneurysms, perioperative morbidity rates were less than 3% despite a thromboembolic and iatrogenic rupture rate of 9%. Ruptured aneurysms had higher complication rates, which are likely due in part to preoperative morbidity and aneurysm complexity. Perioperative morbidity and mortality rates for stent-assisted coiling of unruptured aneurysms are similar, ranging from 3%–5% depending on the study.<sup>29,30</sup> One recently published meta-analysis of stent-assisted coiling of wide-neck and bifurcation aneurysms found procedure-related morbidity and mortality rates of 3% and 1%, respectively.<sup>21</sup> However, these conventional techniques are associated with poorer long-term angiographic outcomes and are hampered by the need for perioperative dual antiplatelet therapy, a factor that is particularly important in the treatment of ruptured aneurysms.<sup>31,32</sup> Permanent morbidity and mortality rates related to flow-diverter treatment range from 8%–10%.<sup>33</sup> Thus, our findings suggest that the WEB device has a safety profile similar to flow diversion.

### Limitations

The main limitation of this meta-analysis is that all the included studies were uncontrolled and many were retrospective. Many were also single-center and reported a wide variety of aneurysm morphologies and patient scenarios. There also might be variability in practice patterns and operator and medical center expertise. This is evident by the wide range of antiplatelet therapy regimens that were administered to patients before and after WEB treatment. There remains the possibility that there could be overlap in patients among studies. Although we were careful to exclude studies that had overlapping patient populations by examining the time periods studied and institutions where the patients were treated, in some cases, articles were not clear as to whether patients included in their studies were included in prior publications or in larger registries. The mean length of follow-up in the reviewed literature was modest. Another limitation is the lack of stratification of outcomes based on important variables such as type and size of the WEB device in many of the included studies. Publication bias is quite likely, and the role of the device manufacturer in the research is not fully clear. Lastly, we do not have data on baseline patient morbidity. Thus, we are unable to determine what proportion of patients with poor neurologic function at follow-up developed this after the procedure. Therefore, the overall certainty in the evidence at present is rated very low.<sup>34</sup>

### CONCLUSIONS

Our meta-analysis of 15 studies including over 500 patients with over 500 aneurysms treated with the WEB device demonstrated

that the WEB device has a safety profile similar to other endovascular devices such as coils and flow diverters. Furthermore, the WEB device is associated with satisfactory midterm angiographic adequate occlusion rates. These findings are particularly important given the complexity of aneurysms treated. Further prospective clinical trials, including clinical trials comparing WEB device treatment with conventional endovascular and surgical techniques, are needed to confirm these results and better define the risks and benefits of using the WEB device in treatment of wide-neck and wide-neck bifurcation aneurysms.

Disclosures: Laurent Pierot—RELATED: Consulting Fee or Honorarium: Sequent; UNRELATED: Consultancy: Blockade, Medtronic, Microvention, Neural, Penumbra. David F. Kallmes—UNRELATED: Board Membership: GE Healthcare.\* Comments: cost-effectiveness board; Consultancy: Medtronic,\* Comments: clinical trials planning and implementation; Grants/Grants Pending: Sequent Medical,\* Microvention,\* Codman,\* Medtronic,\* NeuroSigma,\* Surmodics,\* Comments: preclinical research and clinical trials support; Travel/Accommodations/Meeting Expenses Unrelated to Activities Listed: Medtronic,\* Comments: presentation at FDA panel meeting. \*Money paid to the institution.

### REFERENCES

1. Moret J, Cognard C, Weill A, et al. The “remodelling technique” in the treatment of wide neck intracranial aneurysms: angiographic results and clinical follow-up in 56 cases. *Interv Neuroradiol* 1997;3: 21–35 Medline
2. Nakahara T, Hidaka T, Kutsuna M, et al. Intraaneurysmal embolization for wide-necked aneurysms: remodeling technique, combined neck-clipping and coiling therapy, scaffolding technique. *Interv Neuroradiol* 2000;6(suppl 1):95–101 Medline
3. Biondi A, Janardhan V, Katz JM, et al. Neuroform stent-assisted coil embolization of wide-neck intracranial aneurysms: strategies in stent deployment and midterm follow-up. *Neurosurgery* 2007;61: 460–68; discussion 468–69 CrossRef Medline
4. Mu SQ, Yang XJ, Li YX, et al. Endovascular treatment of wide-necked intracranial aneurysms using of “remodeling technique” with the HyperForm balloon. *Chin Med J (Engl)* 2008;121:725–29 Medline
5. Lee JY, Seo JH, Cho YD, et al. Endovascular treatment of wide-neck intracranial aneurysms using a microcatheter protective technique: results and outcomes in 75 aneurysms. *AJNR Am J Neuroradiol* 2011;32:917–22 CrossRef Medline
6. Pierot L, Cognard C, Spelle L, et al. Safety and efficacy of balloon remodeling technique during endovascular treatment of intracranial aneurysms: critical review of the literature. *AJNR Am J Neuroradiol* 2012;33:12–15 CrossRef Medline
7. Pierot L, Wakhloo AK. Endovascular treatment of intracranial aneurysms: current status. *Stroke* 2013;44:2046–54 CrossRef Medline
8. Ding YH, Lewis DA, Kadirvel R, et al. The Woven EndoBridge: a new aneurysm occlusion device. *AJNR Am J Neuroradiol* 2011;32:607–11 CrossRef Medline
9. Pierot L, Liebig T, Sychra V, et al. Intrasaccular flow-disruption treatment of intracranial aneurysms: preliminary results of a multicenter clinical study. *AJNR Am J Neuroradiol* 2012;33:1232–38 CrossRef Medline
10. Lubicz B, Klisch J, Gauvrit JY, et al. WEB-DL endovascular treatment of wide-neck bifurcation aneurysms: short- and midterm results in a European study. *AJNR Am J Neuroradiol* 2014;35:432–38 CrossRef Medline
11. Papagiannaki C, Spelle L, Januel AC, et al. WEB intrasaccular flow disruptor—prospective, multicenter experience in 83 patients with 85 aneurysms. *AJNR Am J Neuroradiol* 2014;35:2106–11 CrossRef Medline
12. Liebig T, Kabbasch C, Strasilla C, et al. Intrasaccular flow disruption in acutely ruptured aneurysms: a multicenter retrospective review of the use of the WEB. *AJNR Am J Neuroradiol* 2015;36:1721–27 CrossRef Medline

13. Pierot L, Moret J, Turjman F, et al. **WEB treatment of intracranial aneurysms: clinical and anatomic results in the French observatory.** *AJNR Am J Neuroradiol* 2016;37:655–69 CrossRef Medline
14. DerSimonian R, Laird N. **Meta-analysis in clinical trials.** *Control Clin Trials* 1986;7:177–88 CrossRef Medline
15. Barendregt JJ, Doi SA, Lee YY, et al. **Meta-analysis of prevalence.** *J Epidemiol Community Health* 2013;67:974–78 CrossRef Medline
16. Higgins JP, Thompson SG, Deeks JJ, et al. **Measuring inconsistency in meta-analyses.** *BMJ* 2003;327:557–60 CrossRef Medline
17. Armoiry X, Turjman F, Hartmann DJ, et al. **Endovascular treatment of intracranial aneurysms with the WEB device: a systematic review of clinical outcomes.** *AJNR Am J Neuroradiol* 2016;37:868–72 CrossRef Medline
18. Pierot L, Spelle L, Vitry F. **Immediate anatomic results after the endovascular treatment of unruptured intracranial aneurysms: analysis of the ATENA series.** *AJNR Am J Neuroradiol* 2010;31:140–44 CrossRef Medline
19. Pierot L, Cognard C, Ricolfi F, et al. **Immediate anatomic results after the endovascular treatment of ruptured intracranial aneurysms: analysis in the CLARITY series.** *AJNR Am J Neuroradiol* 2010;31:907–11 CrossRef Medline
20. Brinjikji W, Murad MH, Lanzino G, et al. **Endovascular treatment of intracranial aneurysms with flow diverters: a meta-analysis.** *Stroke* 2013;44:442–47 CrossRef Medline
21. Zhao B, Yin R, Lanzino G, et al. **Endovascular coiling of wide-neck and wide-neck bifurcation aneurysms: a systematic review and meta-analysis.** *AJNR Am J Neuroradiol* 2016 Jun 2. [Epub ahead of print] CrossRef Medline
22. Puffer RC, Piano M, Lanzino G, et al. **Treatment of cavernous sinus aneurysms with flow diversion: results in 44 patients.** *AJNR Am J Neuroradiol* 2014;35:948–51 CrossRef Medline
23. Moon K, Albuquerque FC, Ducruet AF, et al. **Resolution of cranial neuropathies following treatment of intracranial aneurysms with the Pipeline embolization device.** *J Neurosurg* 2014;121:1085–92 CrossRef Medline
24. Szikora I, Berentei Z, Kulcsar Z, et al. **Treatment of intracranial aneurysms by functional reconstruction of the parent artery: the Budapest experience with the Pipeline embolization device.** *AJNR Am J Neuroradiol* 2010;31:1139–47 CrossRef Medline
25. Lylyk P, Miranda C, Ceratto R, et al. **Curative endovascular reconstruction of cerebral aneurysms with the Pipeline embolization device: the Buenos Aires experience.** *Neurosurgery* 2009;64:632–42; discussion 642–43; quiz N6 CrossRef Medline
26. Nelson PK, Lylyk P, Szikora I, et al. **The Pipeline embolization device for the intracranial treatment of aneurysms trial.** *AJNR Am J Neuroradiol* 2011;32:34–40 CrossRef Medline
27. Briganti F, Napoli M, Leone G, et al. **Treatment of intracranial aneurysms by flow diverter devices: long-term results from a single center.** *Eur J Radiol* 2014;83:1683–90 CrossRef Medline
28. Saatci I, Yavuz K, Ozer C, et al. **Treatment of intracranial aneurysms using the Pipeline flow-diverter embolization device: a single-center experience with long-term follow-up results.** *AJNR Am J Neuroradiol* 2012;33:1436–46 CrossRef Medline
29. Ryu CW, Park S, Shin HS, et al. **Complications in stent-assisted endovascular therapy of ruptured intracranial aneurysms and relevance to antiplatelet administration: a systematic review.** *AJNR Am J Neuroradiol* 2015;36:1682–88 CrossRef Medline
30. Hong Y, Wang YJ, Deng Z, et al. **Stent-assisted coiling versus coiling in treatment of intracranial aneurysm: a systematic review and meta-analysis.** *PLoS One* 2014;9:e82311 CrossRef Medline
31. Pierot L, Spelle L, Vitry F. **Immediate clinical outcome of patients harboring unruptured intracranial aneurysms treated by endovascular approach: results of the ATENA study.** *Stroke* 2008;39:2497–504 CrossRef Medline
32. Cognard C, Pierot L, Anxionnat R, et al. **Results of embolization used as the first treatment choice in a consecutive nonselected population of ruptured aneurysms: clinical results of the Clarity GDC study.** *Neurosurgery* 2011;69:837–41; discussion 842 CrossRef Medline
33. Kallmes DF, Hanel R, Lopes D, et al. **International retrospective study of the Pipeline embolization device: a multicenter aneurysm treatment study.** *AJNR Am J Neuroradiol* 2015;36:108–15 CrossRef Medline
34. Murad MH, Montori VM, Ioannidis JP, et al. **How to read a systematic review and meta-analysis and apply the results to patient care: users' guides to the medical literature.** *JAMA* 2014;312:171–79 CrossRef Medline
35. Behr D, Berlis A, Weber W. **Woven EndoBridge intrasaccular flow disrupter for the treatment of ruptured and unruptured wide-neck cerebral aneurysms: report of 55 cases.** *AJNR Am J Neuroradiol* 2015; 36:1501–06 CrossRef Medline
36. Bozzetto Ambrosi P, Gory B, Sivan-Hoffmann R, et al. **Endovascular treatment of bifurcation intracranial aneurysms with the WEB SL/SLS: 6-month clinical and angiographic results.** *Interv Neuroradiol* 2015;21:462–69 CrossRef Medline
37. Caroff J, Mihalea C, Dargento F, et al. **Woven Endobridge (WEB) device for endovascular treatment of ruptured intracranial wide-neck aneurysms: a single-center experience.** *Neuroradiology* 2014; 56:755–61 CrossRef Medline
38. Caroff J, Mihalea C, Klisch J, et al. **Single-Layer WEBs: intrasaccular flow disrupters for aneurysm treatment—feasibility results from a European study.** *AJNR Am J Neuroradiol* 2015;36:1942–46 CrossRef Medline
39. Cognard C, Januel AC. **Remnants and recurrences after the use of the WEB intrasaccular device in large-neck bifurcation aneurysms.** *Neurosurgery* 2015;76:522–30; discussion 530 CrossRef Medline
40. Gherasim DN, Gory B, Sivan-Hoffmann R, et al. **Endovascular treatment of wide-neck anterior communicating artery aneurysms using WEB-DL and WEB-SL: short-term results in a multicenter study.** *AJNR Am J Neuroradiol* 2015;36:1150–54 CrossRef Medline
41. Lubicz B, Mine B, Collignon L, et al. **WEB device for endovascular treatment of wide-neck bifurcation aneurysms.** *AJNR Am J Neuroradiol* 2013;34:1209–14 CrossRef Medline
42. Pierot L, Klisch J, Cognard C, et al. **Endovascular WEB flow disruption in middle cerebral artery aneurysms: preliminary feasibility, clinical, and anatomical results in a multicenter study.** *Neurosurgery* 2013;73:27–34; discussion 34–35 CrossRef Medline
43. Pierot L, Spelle L, Molyneux A, et al. **Clinical and anatomical follow-up in patients with aneurysms treated with the WEB device: 1-year follow-up report in the cumulated population of 2 prospective, multicenter series (WEBCAST and French Observatory).** *Neurosurgery* 2016;78:133–41 CrossRef Medline
44. Pierot L, Costalat V, Moret J, et al. **Safety and efficacy of aneurysm treatment with WEB: results of the WEBCAST study.** *J Neurosurg* 2016;1250–56 CrossRef Medline
45. Lescher S, du Mesnil de Rochemont R, Berkefeld J. **Woven Endobridge (WEB) device for endovascular treatment of complex unruptured aneurysms: a single center experience.** *Neuroradiology* 2016;58:383–90 CrossRef Medline

# Does Arterial Flow Rate Affect the Assessment of Flow-Diverter Stent Performance?

H.G. Morales, O. Bonnefous, A.J. Geers, O. Brina, V.M. Pereira, L. Spelle, J. Moret, and I. Larrabide

## ABSTRACT

**BACKGROUND AND PURPOSE:** Our aim was to assess the performance of flow-diverter stents. The pre- and end-of-treatment angiographies are commonly compared. However, the arterial flow rate may change between acquisitions; therefore, a better understanding of its influence on the local intra-aneurysmal hemodynamics before and after flow-diverter stent use is required.

**MATERIALS AND METHODS:** Twenty-five image-based aneurysm models extracted from 3D rotational angiograms were conditioned for computational fluid dynamics simulations. Pulsatile simulations were performed at different arterial flow rates, covering a wide possible range of physiologic flows among 1–5 mL/s. The effect of flow-diverter stents on intra-aneurysmal hemodynamics was numerically simulated with a porous medium model. Spatiotemporal-averaged intra-aneurysmal flow velocity and flow rate were calculated for each case to quantify the hemodynamics after treatment. The short-term flow-diverter stent performance was characterized by the relative velocity reduction inside the aneurysm.

**RESULTS:** Spatiotemporal-averaged intra-aneurysmal flow velocity before and after flow-diverter stent use is linearly proportional to the mean arterial flow rate (minimum  $R^2 > 0.983$  of the linear regression models for untreated and stented models). Relative velocity reduction asymptotically decreases with increasing mean arterial flow rate. When the most probable range of arterial flow rate was considered (3–5 mL/s), instead of the wide possible flow range, the mean SD of relative velocity reduction was reduced from 3.6% to 0.48%.

**CONCLUSIONS:** Both intra-aneurysmal aneurysm velocity and flow-diverter stent performance depend on the arterial flow rate. The performance could be considered independent of the arterial flow rates within the most probable range of physiologic flows.

**ABBREVIATIONS:** CFD = computational fluid dynamics;  $m$  = ratio between the aneurysm velocity and the arterial flow;  $\bar{Q}$  = mean arterial flow rate;  $Q_{\min}$  = minimum arterial flow rate required to have a distinguishable velocity inside the aneurysm;  $s$  = stented;  $u$  = untreated;  $vel_{red}$  = relative velocity reduction;  $vel_{sa}$  = spatiotemporal-averaged flow velocity

Flow diverters are low-porosity stents designed to reduce the blood flow inside the aneurysm cavity. They also serve as a scaffold for neointima formation at the aneurysm ostium.<sup>1,2</sup> To evaluate the potential occlusion performance by intrasaccular

thrombus formation, one must conduct middle- and long-term observations. However, to foresee these future conditions and to assess potential short-term complications, one must evaluate immediate posttreatment hemodynamic features using the end-of-treatment angiography.<sup>3–5</sup>

Qualitative, angiography-based metrics of short-term hemodynamics have been proposed, such as the SMART (simple measurement of aneurysm residual after treatment) scale or grading of the intrasaccular contrast flow speed.<sup>6,7</sup> Additionally, more complex quantitative techniques have been introduced by processing the pre- and posttreatment angiograms.<sup>8</sup> In most of these techniques, information about the contrast propagation is directly compared between pre- and posttreatment angiograms without paying attention to the potential arterial flow rate changes between image acquisitions and its impact on aneurysmal hemodynamics. It has been reported that change in 30%–50% of

Received November 19, 2015; accepted after revision July 20, 2016.

From Medisys-Philips Research (H.G.M., O.Bonnefous), Paris, France; Centre for Cardiovascular Science (A.J.G.), University of Edinburgh, Edinburgh, Scotland; Department of Information and Communication Technologies (A.J.G.), Universitat Pompeu Fabra, Barcelona, Spain; Department of Information Neuroradiology (O.Brina), University Hospital of Geneva, Geneva, Switzerland; Department of Medical Imaging and Department of Surgery (V.M.P.), University Health Network, Toronto, Ontario, Canada; Interventional Neuroradiology (L.S., J.M.), Beaujon University Hospital, Clichy, France; Paris Diderot University (L.S.), Paris, France; and PLADEMA-CONICET (I.L.), Universidad Nacional del Centro de la Provincia de Buenos Aires, Tandil, Argentina.

Please address correspondence to Hernán G. Morales, PhD, 33 Rue de Verdun, 92156 Suresnes, France; e-mail: hernan.morales@philips.com

<http://dx.doi.org/10.3174/ajnr.A4933>

the mean arterial flow rate could lead to a 30%–80% variation of hemodynamic quantities, such as mean flow velocity, aneurysm inflow, or wall shear stress.<sup>9</sup>

The purpose of this study was to evaluate the role of the arterial flow rate on flow-diverter stent performance. Because patient-specific flow measurements are not unique and depend on the instance at which a medical examination is performed, a wide range of flow rates was considered.

## MATERIALS AND METHODS

Twenty-five aneurysms from different patients were investigated. 3D rotational angiography images of the aneurysms and their surrounding vasculature were acquired with an x-ray system (Allura Xper FD20; Philips Healthcare, Best, the Netherlands). All aneurysms were located between the siphon of the internal carotid artery and its downstream bifurcation. Medical data were collected by 2 departments of interventional neuroradiology: University Hospitals of Geneva, Geneva, Switzerland, and Beaujon University Hospital, France.

From these images, a surface mesh was extracted by image segmentation. The surface meshes were cleaned and smoothed. Hexahedral meshes inside each vascular model were generated with a cell size of 0.2 mm at the wall, 0.1 mm in the porous medium, and 0.2 mm elsewhere, with 4 cells between sizes. The total number of elements ranged between  $2.08 \times 10^5$  and  $6.44 \times 10^5$ . For a given case, the same mesh was used for both untreated and stented models. More details about the mesh strategies can be found elsewhere.<sup>10–12</sup>

In these volumetric meshes, governing equations of flow motion were solved by using the open-source computational fluid dynamics (CFD) package OpenFOAM 2.2.1 (www.openfoam.org). Arterial walls were considered rigid and nonslippery (flow velocity = 0). Blood was modeled as a Newtonian and incompressible fluid, with the knowledge that changes in blood viscosity due to increments in shear strain rates can be neglected.<sup>13</sup> A parabolic profile was set at the inlet of each vascular model as a spatial condition, which changes in time according to the pulsatile waveform (temporal variation). Zero-pressure conditions were imposed at all outlets. Details of this methodology can be found elsewhere.<sup>10</sup>

### Arterial Flow Rates

To single out the effect of the mean arterial flow rate,  $\bar{Q}$ , the same shape of the flow waveform was used for all simulations, which was scaled to achieve the desired  $\bar{Q}$  (Fig 1). The waveform was originally extracted from a DSA sequence of a patient by using valid optical flow techniques.<sup>14–16</sup> Per case, 9 pulsatile flow simulations were created. Five of those flows were set within the most probable range (3 mL/s to 5 mL/s),<sup>17,18</sup> every 0.5 mL/s. To cover lower flows, which occurs according to a possible range among 1 mL/s to 5 mL/s, we used both the inlet-area flow condition<sup>19</sup> and the 1.5-Pa wall shear stress condition at the inlet. In case those strategies provided a value within 3 mL/s to 5 mL/s, flow rate values were imposed at 1.0, 1.5, 2.0, and 2.5 mL/s.<sup>10</sup> With this configuration, the highest simulated flow rate has a systolic value of 7.56 mL/s, which is below the highest values measured in patients (>11 mL/s).<sup>17</sup>

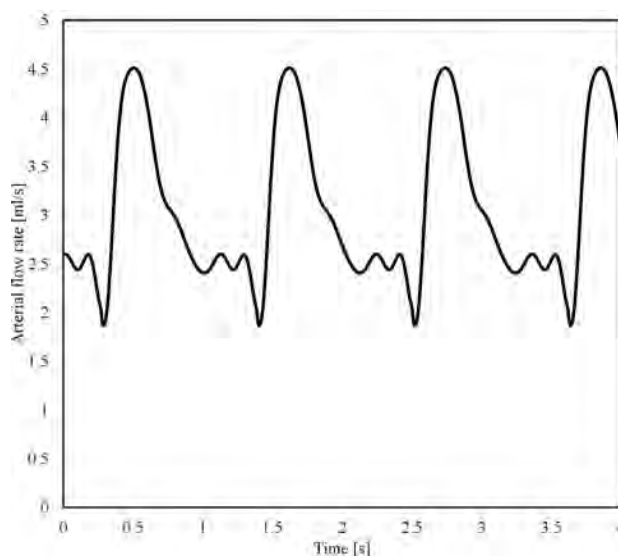


FIG 1. Waveform ( $\bar{Q} = 3$  mL/s).

### Virtual Stent Placement

To model the influence of a flow-diverter stent on the intra-aneurysmal hemodynamics, we placed a porous medium at the aneurysm ostium. This medium locally imposes an additional hydraulic resistance to flow and has been previously used.<sup>11,20–23</sup> The Darcy-Forchheimer law was used in the porous medium, which includes both viscous- and inertia-related pressure losses. The parameters of this medium used were  $k = 8.7 \times 10^{-7}$  (viscosity term) and  $F = 8.1 \times 10^4$  (inertia term), and an equivalent porosity of around 70% was imposed. Details of the volumetric porous medium approach can be found elsewhere.<sup>11</sup>

### Data Analysis

The following analysis was conducted to characterize the flow-diverter stent performance at different arterial flow rates.

Inside the aneurysm, the spatiotemporal-averaged flow velocity,  $\overline{vel}_{sa}$ , was calculated, which has been shown to be independent of the waveform shape.<sup>12,24</sup> Per case, linear regression models were applied to the untreated and stented datasets. The goal was to confirm that  $\overline{vel}_{sa}$  can be characterized as a linear function of  $\bar{Q}$  (see Equation 1) for untreated aneurysms<sup>12</sup> and to extend this characterization of the  $\overline{vel}_{sa}$  after treatment under the hypothesis that this relationship should be preserved.

$$1) \quad \overline{vel}_{sa}(\bar{Q}) = m \cdot (\bar{Q} - Q_{\min})$$

In Equation 1, the parameters  $m$  and  $Q_{\min}$  are given by the linear regression models applied on the results of the CFD simulations, but they can also be derived from measurements by using functional image analysis.<sup>14,15</sup>  $Q_{\min}$  can be interpreted as the minimum arterial flow rate required to have a distinguishable velocity inside the aneurysm. The parameter  $m$  represents the ratio between the aneurysm velocity and the arterial flow.

Afterward, the flow-diverter stent performance was characterized by the relative velocity reduction,  $vel_{red}$ :

$$2) \quad vel_{red} = 1 - \frac{\overline{vel}_{sa,s}}{\overline{vel}_{sa,u}}$$

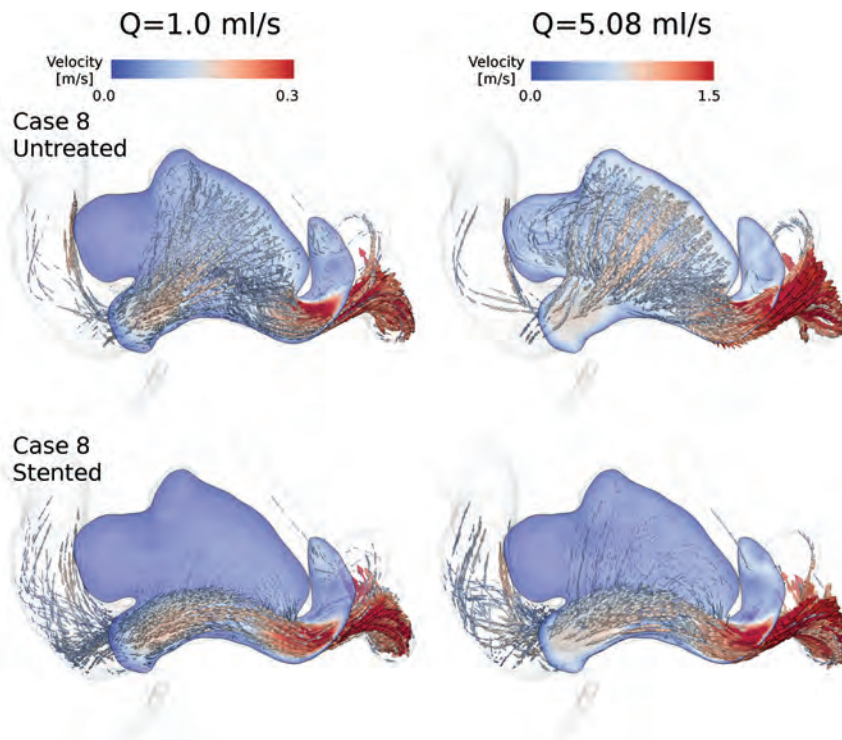


**FIG 2.** Peak systolic instantaneous streamlines of velocity and an aneurysmal cut plane for case 8 at 2 arterial flow rates. Untreated and stented models are in the upper and lower rows, respectively.

**Linear regressions for untreated and stented conditions for all aneurysm models**

Case	Untreated			Stented		
	<i>m</i>	<i>Q</i> <sub>min</sub>	<i>R</i> <sup>2</sup>	<i>m</i>	<i>Q</i> <sub>min</sub>	<i>R</i> <sup>2</sup>
1	0.025	0.484	1.000	0.006	0.929	0.997
2	0.037	0.395	1.000	0.010	0.816	0.994
3	0.053	0.588	0.999	0.012	0.770	0.996
4	0.047	0.330	1.000	0.018	0.605	0.997
5	0.070	0.508	0.999	0.015	0.762	0.994
6	0.043	0.325	1.000	0.011	0.895	0.992
7	0.075	0.477	0.995	0.024	0.891	0.983
8 <sup>a</sup>	0.069	0.451	1.000	0.019	0.461	0.999
9	0.067	0.664	0.997	0.015	1.062	0.990
10	0.026	0.255	0.998	0.008	0.744	0.993
11 <sup>a</sup>	0.091	0.356	1.000	0.022	0.368	0.999
12	0.047	0.484	1.000	0.016	1.075	0.983
13	0.030	0.591	0.998	0.011	1.053	0.991
14	0.048	0.394	1.000	0.022	0.588	0.997
15	0.104	0.364	1.000	0.030	0.677	0.992
16	0.041	0.580	0.999	0.014	0.764	0.996
17	0.051	0.676	0.999	0.013	1.038	0.983
18	0.060	0.353	1.000	0.017	0.672	0.998
19	0.047	0.365	1.000	0.007	0.946	0.990
20	0.078	0.540	0.999	0.015	0.974	0.990
21	0.038	0.231	1.000	0.009	0.473	1.000
22 <sup>a</sup>	0.112	0.282	1.000	0.058	0.333	1.000
23	0.040	0.454	1.000	0.025	0.706	0.996
24	0.067	0.439	0.999	0.027	0.745	0.994
25	0.025	0.201	1.000	0.011	0.679	0.999

<sup>a</sup> Cases in the row have  $\Delta Q_{\min} \leq 0.05$  mL/s.

where the indexes *u* and *s* stand for untreated and stented, respectively. By placing Equation 1 inside Equation 2 for both untreated and stented conditions, defining the slope ratio  $r_m = m_s / m_u$ , and making  $\bar{Q}_s = \bar{Q}_u = \bar{Q}$ , Equation 2 becomes:

$$3) \quad vel_{red} = 1 - r_m \cdot \frac{(\bar{Q} - Q_{\min,s})}{(\bar{Q} - Q_{\min,u})}$$

To evaluate when  $vel_{red}$  becomes independent of the flow rate, Equation 3 was derived with respect to  $\bar{Q}$  and set to zero:

$$4) \quad \frac{\partial(vel_{red})}{\partial \bar{Q}} = \frac{-r_m \cdot \Delta Q_{\min}}{(\bar{Q} - Q_{\min,u})^2} = 0,$$

where  $\Delta Q_{\min} = Q_{\min,s} - Q_{\min,u}$ . Equation 4 is satisfied under 2 conditions:

- The ratio  $r_m$  is zero, meaning that the slope after stent placement ( $m_s$ ) is zero or “tiny” with respect to the slope before treatment ( $m_u$ ), ie,  $m_u \gg m_s$ .
- $\Delta Q_{\min} = 0$ , meaning that the  $Q_{\min}$  before and after stent placement are the same ( $Q_{\min,s} \approx Q_{\min,u}$ ).

A less-evident third condition may occur in the case that both,  $Q_{\min,s}$  and  $Q_{\min,u}$  (in Equation 3), are small compared with  $\bar{Q}$ . In this situation, equation 3 becomes

$$5) \quad vel_{red} = 1 - r_m.$$

**RESULTS**

In all cases, flow direction was changed after treatment. The porous medium produced an additional hydraulic resistance to flow near the aneurysm ostium, thus reducing the amount of flow that penetrates the aneurysm. Figure 2 shows examples of the flow patterns that can be obtained after flow diversion by using a porous medium. These results are similar to those using explicit stent models.<sup>25-27</sup> In general, it seems that the flow patterns were unaltered when  $\bar{Q}$  was changed.

$\overline{vel}_{sa}$  linearly increased when  $\bar{Q}$  goes up before and after treatment for all cases (minimum  $R^2 > 0.995$  for untreated and  $R^2 > 0.983$  for stented cases). The Table presents the results of the linear regressions that were applied for each case before and after treatment. Moreover for all cases, the slope  $m$  was reduced ( $r_m < 1$ ) and  $Q_{\min,s} > Q_{\min,u}$  ( $\Delta Q > 0$ ) after flow-diverter stent placement. Figure 3 depicts the  $\overline{vel}_{sa}$  as a function of  $\bar{Q}$  for cases 1 and 8 as a visual example of these results. Using these linear regressions, we calculated  $vel_{red}$  (Equation 3) and plotted it in Fig 4 by using the range (1–6 mL/s).

In general,  $vel_{red}$  decreased with an increasing arterial flow rate (Fig 4A). However in cases 8, 11, and 22 (footnoted in the Table), almost a constant reduction was observed. In those cases,  $\Delta Q_{\min}$  was relatively small (mean = 0.024 mL/s, maximum  $\leq 0.05$  mL/s) compared with the rest of the cases (mean = 0.37 mL/s, minimum  $\geq 0.18$  mL/s). These results can also be visualized in Fig 4B, where the standard deviation of  $vel_{red}$  is presented for each case. When the most probable flow range is taken into account at 3–5 mL/s,<sup>17,18</sup> the mean SD of  $vel_{red}$  was reduced from 3.6% (Fig 4B) to 0.48% (Fig 4C).

## DISCUSSION

In this study, the intra-aneurysmal hemodynamics were investigated before and after flow-diverter stent placement for different arterial flow rates in 25 aneurysm models. As was expected,  $\overline{vel}_{sa}$  increases when the arterial flow rate goes up (Fig 3). However, the increment is linear and can be simply represented by 2 coefficients:  $m$  and  $Q_{min}$ . When the short-term flow-diverter stent performance is characterized by the relative reduction of the aneurysm flow velocity,  $vel_{red}$  (Equation 3), the flow-diverter stent was relatively “more effective” at lower flow rates than at higher ones (Fig 4). To better understand these findings, we performed the following analyses.

### Linear Law

It was confirmed in untreated aneurysm models that the  $\overline{vel}_{sa}$  linearly depends on  $\overline{Q}$  ( $R^2 > 0.995$ ),<sup>12</sup> and this linear relationship was extended for stented aneurysms ( $R^2 > 0.983$ ). Indeed, from a hemodynamic point of view, a stented aneurysm is like another aneurysm with a particular resistance near the ostium (obtained by the stent), and this law is preserved. This relationship is very useful for characterizing aneurysm flow velocities because the influence of the arterial flow rate is included. Other variables such as wall shear stress or pressure can be also represented as functions of  $\overline{Q}$ , but a quadratic relation seems to be more appropriate according to previous studies.<sup>12,24</sup> These characterizations go beyond any hemodynamic assessment by using patient-specific measure-

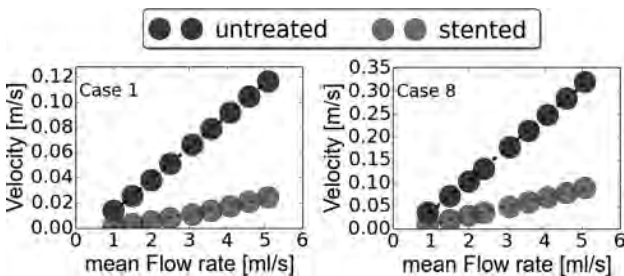


**FIG 3.**  $\overline{vel}_{sa}$  for cases 1 and 8 before and after flow-diverter stent placement. Points were derived from CFD simulations, and the curves represent the linear regressions that were applied on each point set.

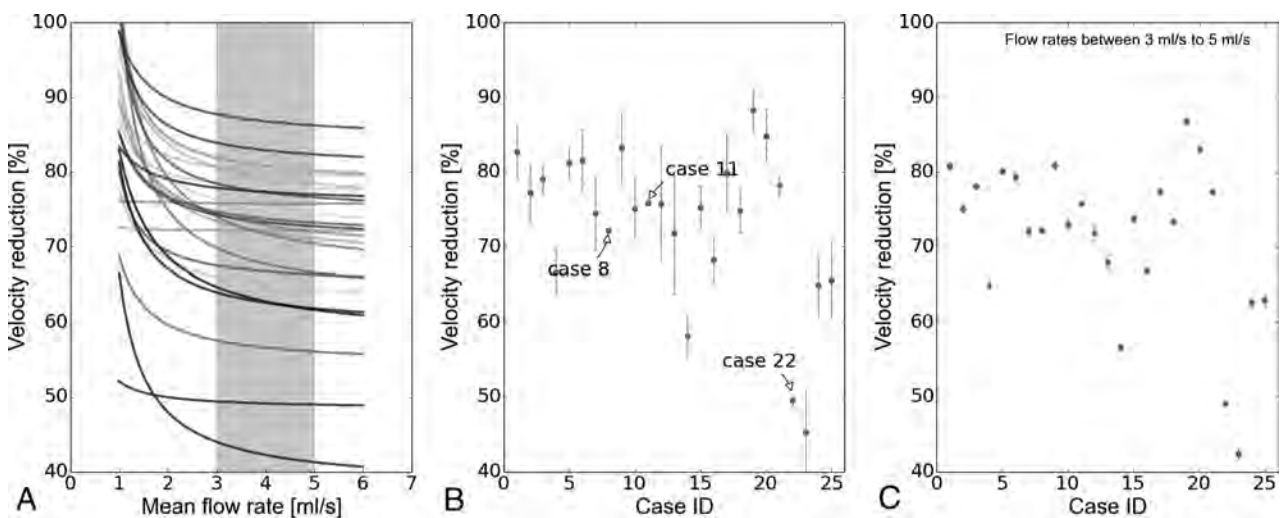


**FIG 4.** A,  $vel_{red}$  as function of  $\overline{Q}$ , where the gray region represents the most probable arterial flow range (3–5 mL/s). B, Mean and SD of  $vel_{red}$  per case. C, Mean and SD of  $vel_{red}$  per case but only considering the most probable arterial flow range.  $vel_{red}$  is presented as a percentage.

ments (either from CFD simulations or from image processing), because those evaluations are limited to flow conditions during recording, which change with time.

This linear law describes the intra-aneurysmal velocity at any flow rate in terms of the slope  $m$  and  $Q_{min}$  (both positive). If the endovascular device reduced the aneurysmal velocity, 2 changes were observed in these curves. First, the slope after treatment must be smaller than before (yet still positive), making  $r_m < 1$ . This ratio is a direct indication that the blood flow speed is decreased after treatment, with the benefit of being independent of the arterial flow rate. For example,  $r_m$  can be used to compare devices for a given aneurysm because it is related to the untreated condition, and a lower  $r_m$  means that the implanted device will produce a higher velocity reduction inside the aneurysm. On the contrary,  $r_m > 1$  means that the treatment is actually increasing the velocity inside the aneurysm, which could be harmful and may increase the risk of rupture.

The slopes can also be used to compare cases because they quantify the hemodynamics of each aneurysm, independent of the arterial flow rate. For example, a standardized “critical slope” after flow diversion can be identified, in which aneurysm thrombosis would be expected. Nevertheless, further investigation is required to find this critical slope in a larger dataset with clinical follow-up information. Still, if these curves are used for this purpose or another one such as aneurysm rupture, then the specific arterial flow rate at which those aneurysms were evaluated becomes irrelevant because the flow rate is implicitly considered when using this approach.

The second change in the curves is that  $Q_{min}$  increases after stent placement; this change makes a positive  $\Delta Q_{min}$  ( $Q_{min,s} - Q_{min,u}$ ). As discussed by Morales and Bonnefous,<sup>12</sup>  $Q_{min}$  is given by the regressions and does not necessarily represent a physical phenomenon (zero velocity for a given nonzero flow rate), though it can be seen as the minimum arterial flow rate required to have a distinguishable flow motion inside the aneurysm cavity.  $Q_{min}$  increases after stent placement because the blood flow needs more energy (a higher  $Q_{min}$ ) to overcome the additional hydraulic

resistance produced by the flow-diverter stent and then to generate this distinguishable flow motion.

The validity of the linear model is only within the possible flow rate range studied here, which includes the most probable physiologic range. For flow rates between 0 and 1.0 mL/s, a quadratic model crossing the origin would be more appropriate. Nevertheless, the interest in such a low range is arguable because it will not be a physiologic condition and other phenomena, such as blood coagulation, may arise. Moreover, because the flow rate range covered here is based on the variability among patients,<sup>19</sup> a shorter patient-specific flow range should be within this wide range without affecting the presented relationships for that patient.

#### **Flow-Diverter Stent Performance and Arterial Flow Rate**

In this study, the short-term flow-diverter stent performance was characterized by  $vel_{red}$ .

As presented in Equation 3 and confirmed in Fig 4,  $vel_{red}$  is higher when the arterial flow rate is low. This finding indicates that the arterial flow rate should be taken into account to fairly compare the performance of endovascular devices by any approach (in vivo, in vitro, or in silico). Using the same Reynolds number would not be fair for comparing the hemodynamics of 2 (or more) aneurysms because this number depends on the local arterial caliber; therefore, if 2 cases have the same number, the one with the higher arterial caliber will have a lower flow rate. This lower arterial flow rate benefits the device performance as shown in Fig 4A.

The weakening of the stent performance when increasing the arterial flow rate (and vice versa) is because the hydraulic resistance of the flow-diverter stent decreases when increasing the Reynolds number (proportional to the flow rate). This phenomenon is well-known in classic fluid mechanics and has been thoroughly studied for high-porosity stent placement in cerebral aneurysms.<sup>25</sup>

Previously, Larrabide et al<sup>26</sup> performed CFD simulations by using an explicit representation of the flow-diverter stents to investigate the velocity variation during the cardiac cycle as a mean to quantify the device performances. They found that the pulsatility of the aneurysmal velocity increases after treatment. Similarly, Peach et al<sup>27</sup> investigated the influence of several flow-diverter stent designs (different porosities and pore sizes) on hemodynamics, and the lowest flow reductions were seen at peak systole, when parent vessel flow is at its highest. These studies show that the stent performance is “weaker” at systole than at diastole (higher-versus-lower arterial flow rates); this finding is congruent with our findings when increasing the arterial flow rates.

Additionally, Mut et al<sup>9</sup> varied the flow rate conditions before and after flow-diverter stent placement. It was found that a change in 30%–50% of the mean arterial flow could lead to a variation between 30% and 80% of some hemodynamic quantities. This is similar to the presentation in Fig 3—that is, variations of  $\bar{Q}$  do change  $\overline{vel}_{sa}$ . Besides, the authors concluded that this variation can lead to misleading interpretations when clinical information is used, in particular, when pre- and posttreatment conditions are compared because flow conditions may vary

among image acquisitions. The results presented here are in accordance with this statement, and the authors stress that caution is needed when comparing the 2 situations (either experimental or clinical) in which the arterial flow rates are known.

#### **Flow Rate–Free Performance**

The first condition that satisfies Equation 4 was not found in our study because it means flow cessation inside the aneurysm after treatment ( $m_s = 0$ ), which can be achieved after several months due to the formation of intrasaccular thrombus. The second condition was observed in 3 cases. There,  $\Delta Q_{min}$  was very small ( $\leq 0.05$  mL/s) compared with the rest of the cases (minimum  $\geq 0.018$  mL/s).

The third condition that makes  $vel_{red}$  independent of  $\bar{Q}$  is the one derived from Equation 5. The largest variations in  $vel_{red}$  were observed at the lower end of the possible flow range, which are outside the most probable range at the ICA (gray region in Fig 4A). Nevertheless, further investigation is required in a larger population to see for which cases this assumption is plausible, by measuring the SD of  $vel_{red}$ , for example. A possible case stratification could be based on morphologic features such as aneurysm size and shape.

#### **Potential Clinical Translation**

Equation 5 is a plausible way to transfer these findings into clinical practice. However, this equation assumes that  $\bar{Q}_s = \bar{Q}_u = \bar{Q}$  and that  $\bar{Q} \gg Q_{min}$  (for untreated and stented conditions).

To overcome the first limitation, (ie,  $\bar{Q}_s \neq \bar{Q}_u$ ), a more general expression should be used:

$$6) \quad vel_{red} = 1 - r_m \cdot \frac{\bar{Q}_s}{\bar{Q}_u}$$

Equation 6 states that  $vel_{red}$  can be obtained by knowing  $r_m$ , the arterial flow rate before ( $\bar{Q}_u$ ) and after treatment ( $\bar{Q}_s$ ) and that those  $\bar{Q}$ 's should be higher to neglect the influence of each  $Q_{min}$ . These quantities can be obtained from either CFD simulations or image analysis. For the latter, medical images can be processed by using optical flow techniques to retrieve both the arterial and aneurysm flows.<sup>14–16</sup>

From a more generic perspective, this study reveals the importance of the arterial flow rate when evaluating aneurysm hemodynamics. As a consequence, qualitative evaluations such as the SMART scale or the grading of contrast flow speed should be avoided because no distinction can be made between variations in contrast due to either the implanted device or a reduction in the arterial flow rate. This advice is very important when comparing pre- and posttreatment angiograms of the same patient, but also when comparing among subjects. Additionally, this study proposes a simple quantification approach in which the arterial flow rate is considered to properly quantify aneurysm hemodynamics.

#### **Limitations**

Arterial walls were considered a rigid wall though it is known that the arteries are flexible structures and radial dilations occur due to pressure changes. Nevertheless, it is expected that main flow structures will be preserved.<sup>28</sup> As in both numeric and experimental studies, the vascular morphology was not altered after flow-

diverter stent placement. Indeed, the placement of a stent could locally change the artery shape. Unfortunately, it is not possible to overcome this limitation due to the lack of information regarding the mechanical properties of the artery and implanted devices, as well as the surrounding tissue and organs that could influence the final morphology after stent placement.

## CONCLUSIONS

Spatiotemporal-averaged intra-aneurysmal velocity can be characterized by a linear function of the arterial flow rate before and after flow-diverter stent placement. This characterization provides a simple way to study intra-aneurysmal hemodynamics that goes beyond any patient-specific flow measurements. By using this linear relationship, it was found that the arterial flow rate affects the short-term flow-diverter stent performance. However, the device performance can be considered independent of the arterial flow rates within (and above) the physiologic flow range.

## ACKNOWLEDGMENTS

We thank the units of interventional neuroradiology of the Department of Medical Imaging and Information Sciences, University Hospitals of Geneva, Switzerland, and of Beaujon University Hospital, Clichy, France, for providing the medical images from which the vascular models were extracted.

Disclosures: Vitor Mendes Pereira—UNRELATED: Grant: Philips Healthcare.\* Comments: grant to pay for a technician for 2 years for a related research project. Laurent Spelle—UNRELATED: Consulting Fee or Honorarium: Medtronic, Stryker, Sequent Medical, Jacques Moret—UNRELATED: Consultancy: Covidien, Microvention, Stryker. Ignacio Larrabide—UNRELATED: Consultancy: Galgo Medical S.L.; Employment: CONICET and UNICEN; Patents (planned, pending or issued): WO 2015063352 A1. \*Money paid to the institution.

## REFERENCES

1. Durso PI, Lanzino G, Cloft HJ, et al. **Flow diversion for intracranial aneurysms: a review.** *Stroke* 2011;42:2363–68 CrossRef Medline
2. Pierot L. **flow diverter stents in the treatment of intracranial aneurysms: where are we?** *J Neuroradiol* 2011;38:40–46 CrossRef Medline
3. Byrne JV, Beltechi R, Yarnold JA, et al. **Early experience in the treatment of intra-cranial aneurysms by endovascular flow diversion: a multicentre prospective study.** *PLoS One* 2010;5:1–8 CrossRef Medline
4. Szikora I, Berentei Z, Kulcsar Z, et al. **Treatment of intracranial aneurysms by functional reconstruction of the parent artery: the Budapest experience with the Pipeline embolization device.** *AJNR Am J Neuroradiol* 2010;31:1139–47 CrossRef Medline
5. Lylyk P, Miranda C, Ceratto R, et al. **Curative endovascular reconstruction of cerebral aneurysms with the Pipeline embolization device: the Buenos Aires experience.** *Neurosurgery* 2009;64:632–42; discussion 642–43; quiz N6 CrossRef Medline
6. Grunwald IQ, Kamran M, Corkill RA, et al. **Simple measurement of aneurysm residual after treatment: the SMART scale for evaluation of intracranial aneurysms treated with flow diverters.** *Acta Neurochir (Wien)* 2012;154:21–26; discussion 26 CrossRef Medline
7. Ionita CN, Paciorem AM, Dohatcu A, et al. **The asymmetric vascular stent efficacy in a rabbit aneurysm model.** *Stroke* 2009;40:959–65 CrossRef Medline
8. Benz T, Kowarschik M, Endres J, et al. **A Fourier-based approach to the angiographic assessment of flow diverter efficacy in the treatment of cerebral aneurysms.** *IEEE Trans Med Imaging* 2014;33:1788–802 CrossRef Medline
9. Mut F, Ruijters D, Babic D, et al. **Effects of changing physiologic**

- conditions on the in vivo quantification of hemodynamic variables in cerebral aneurysms treated with flow diverting devices.** *Int J Numer Method Biomed Eng* 2014;30:135–42 CrossRef Medline
10. Morales HG, Bonnefous O. **Peak systolic or maximum intra-aneurysmal hemodynamic condition? Implications on normalized flow variables.** *J Biomech* 2014;47:2362–70 CrossRef Medline
11. Morales HG, Bonnefous O. **Modeling hemodynamics after flow diverter with a porous medium.** In: *Proceedings of the International Symposium on Biomedical Imaging*, Beijing, China. April 29 to May 2, 2014
12. Morales HG, Bonnefous O. **Unraveling the relationship between arterial flow and intra-aneurysmal hemodynamics.** *J Biomech* 2015;48:585–91 CrossRef Medline
13. Morales HG, Larrabide I, Geers AJ, et al. **Newtonian and non-Newtonian blood flow in coiled cerebral aneurysms.** *J Biomech* 2013;46:2158–64 CrossRef Medline
14. Bonnefous O, Pereira VM, Ouared R, et al. **Quantification of arterial flow using digital subtraction angiography.** *Med Phys* 2012;39:6264–75 CrossRef Medline
15. Pereira VM, Bonnefous O, Ouared R, et al. **A DSA-based method using contrast-motion estimation for the assessment of the intra-aneurysmal flow changes induced by flow diverter stents.** *AJNR Am J Neuroradiol* 2013;34:808–15 CrossRef Medline
16. Pereira VM, Ouared R, Brina O, et al. **Quantification of internal carotid artery flow with digital subtraction angiography: validation of an optical flow approach with Doppler ultrasound.** *AJNR Am J Neuroradiol* 2014;35:156–63 CrossRef Medline
17. Ford MD, Alperin N, Lee SH, et al. **Characterization of volumetric flow rate waveforms in the normal internal carotid and vertebral arteries.** *Physiol Meas* 2005;26:477–88 CrossRef Medline
18. Hoi Y, Wasserman BA, Xie YJ, et al. **Characterization of volumetric flow rate waveforms at the carotid bifurcations of older adults.** *Physiol Meas* 2010;31:291–302 CrossRef Medline
19. Cebral JR, Castro MA, Putman CM, et al. **Flow-area relationship in internal carotid and vertebral arteries.** *Physiol Meas* 2008;29:585–94 CrossRef Medline
20. Fernández MA, Gerbeau J, Martin V. **Numerical simulation of blood flows through a porous interface.** *ESAIM: Mathematical Modelling and Numerical Analysis* 2008;42:961–90 CrossRef
21. Augsburger L, Reymond P, Rufenacht DA, et al. **Intracranial stents being modeled as a porous medium: flow simulation in stented cerebral aneurysms.** *Ann Biomed Eng* 2011;39:850–63 CrossRef Medline
22. Zhang Y, Chong W, Qian Y. **Investigation of intracranial aneurysm hemodynamics following flow diverter stent treatment.** *Med Eng Phys* 2013;35:608–15 CrossRef Medline
23. Levitt MR, McGah PM, Aliseda A, et al. **Cerebral aneurysms treated with flow-diverting stents: computational models with intravascular blood flow measurements.** *AJNR Am J Neuroradiol* 2014;35:143–48 CrossRef Medline
24. Geers AJ, Larrabide I, Morales HG, et al. **Approximating hemodynamics of cerebral aneurysms with steady flow simulations.** *J Biomech* 2014;47:178–85 CrossRef Medline
25. Kim M, Taulbee DB, Tremmel M, et al. **Comparison of two stents in modifying cerebral aneurysm hemodynamics.** *Ann Biomed Eng* 2008;36:726–41 CrossRef Medline
26. Larrabide I, Geers AJ, Morales HG, et al. **Change in aneurysmal flow pulsatility after flow diverter treatment.** *Comput Med Imaging Graph* 2016;50:2–8 CrossRef Medline
27. Peach TW, Ngoepe M, Spranger K, et al. **Personalizing flow diverter intervention for cerebral aneurysms: from computational hemodynamics to biochemical modeling.** *Int J Numer Method Biomed Eng* 2014;30:1387–407 CrossRef Medline
28. Dempere-Marco L, Oubel E, Castro MA, et al. **CFD analysis incorporating the influence of wall motion: application to intracranial aneurysms.** *Med Image Comput Comput Assist Interv* 2006;9(pt 2):438–45 Medline

# Yield of Repeat 3D Angiography in Patients with Aneurysmal-Type Subarachnoid Hemorrhage

R.S. Bechan, W.J. van Rooij, J.P. Peluso, and M. Sluzewski



## ABSTRACT

**BACKGROUND AND PURPOSE:** Aneurysmal-type subarachnoid hemorrhage is a serious disease with high morbidity and mortality. When no aneurysm is found, the patient remains at risk for rebleeding. Negative findings for SAH on angiography range from 2% to 24%. Most previous studies were based on conventional 2D imaging. 3D rotational angiography depicts more aneurysms than 2D angiography. The purpose of this study was to evaluate the yield of repeat 3D rotational angiography in patients with aneurysmal-type SAH with negative initial 3D rotational angiography findings and to classify the initial occult aneurysms.

**MATERIALS AND METHODS:** Between March 2013 and January 2016, 292 patients with SAH and an aneurysmal bleeding pattern were admitted. Of these 292 patients, 30 (10.3%; 95% CI, 7.3%–14.3%) had initial negative 3D rotational angiography findings within 24 hours. These patients underwent a second 3D rotational angiography after 7–10 days.

**RESULTS:** In 8 of 30 patients (26.7%; 95% CI, 14.0%–44.7%) with initial negative 3D rotational angiography findings, a ruptured aneurysm was found on repeat 3D rotational angiography. Three of 8 initial occult aneurysms were very small (1–2 mm), 2 were supraclinoid carotid artery dissecting aneurysms (2 and 8 mm), 2 were small (1 and 3 mm) basilar perforator aneurysms, and 1 was a 3-mm vertebral artery dissecting aneurysm.

**CONCLUSIONS:** In 10% of patients with aneurysmal-type SAH, initial 3D rotational angiography findings were negative, and in 1 in 4, repeat 3D rotational angiography demonstrated a ruptured aneurysm. Initial occult aneurysms were dissecting aneurysms of perforators or main arteries or were very small (1–2 mm) or both. Our results indicate that repeat 3D rotational angiography is mandatory in patients with initial 3D rotational angiography findings negative for aneurysmal-type SAH.

**ABBREVIATIONS:** aSAH = aneurysmal-type SAH; 3DRA = 3D rotational angiography

Subarachnoid hemorrhage with an aneurysmal bleeding pattern (aSAH) is a serious disease with high morbidity and mortality. In 80%–90% of patients with aSAH, an aneurysm can be found as the cause of hemorrhage,<sup>1</sup> and early repair is advocated to prevent recurrent hemorrhage.

The incidence of angiograms negative for aSAH has been reported to range from 2% to 24% in various studies.<sup>2,3</sup> In some of these patients, the source of the hemorrhage is an occult aneurysm, but intracranial artery dissections, dural arteriovenous malformations, micro-AVMs, trauma, bleeding disorders, substance abuse, or other causes should also be considered. Even though no

aneurysm is found, these patients are at risk for early rebleed with an inherent risk of morbidity and death.<sup>4</sup> An aneurysm is not depicted on first angiography for several reasons: very small aneurysms, small aneurysms with an intraluminal thrombus, aneurysms on arterial dissections, suboptimal image quality due to technical reasons or in uncooperative patients, and a missed diagnosis of an aneurysm.

Repeat angiography is advocated to avoid missing a treatable cause of aSAH. Previous studies have demonstrated that repeat angiography after 7–10 days can depict an aneurysm in up to one-third of patients with initial negative angiography findings.<sup>5–8</sup> 3D rotational angiography (3DRA) has been proved to depict more aneurysms than 2D DSA.<sup>9,10</sup> In our institution, diagnostic work-up of patients with aSAH now consists of 3DRA of all vessels within 24 hours. With negative findings, 3DRA is repeated. In this study, we evaluated the yield of repeat 3DRA in patients with aSAH with negative initial 3DRA findings. In addition, we classified the initial occult aneurysms.

Received March 27, 2016; accepted after revision July 8.

From the Department of Radiology, Sint Elisabeth Ziekenhuis, Tilburg, the Netherlands.

Please address correspondence to Willem Jan van Rooij, MD, Department of Radiology, Sint Elisabeth Ziekenhuis, Hilvarenbeekseweg 60, 5022GC Tilburg, the Netherlands; e-mail: wjvanrooij@gmail.com

<http://dx.doi.org/10.3174/ajnr.A4942>

### Types of aneurysms found on repeat 3DRA in patients with aSAH

	Age (yr)/Sex	Aneurysm Location	Size
1	61, M	Dissecting aneurysm of perforator of the basilar tip	3 mm
2	60, M	Superior cerebellar artery	1 mm
3	65, M	Dissecting aneurysm of the supraclinoid internal carotid artery	2 mm
4	62, F	Dissecting aneurysm of the supraclinoid internal carotid artery	8 mm
5	46, F	Dissecting aneurysm of the V4 segment	3 mm
6	62, F	A1–A2 junction	1 mm
7	70, M	A1	1 mm
8	65, M	Dissecting aneurysm of perforator of the basilar tip	1 mm

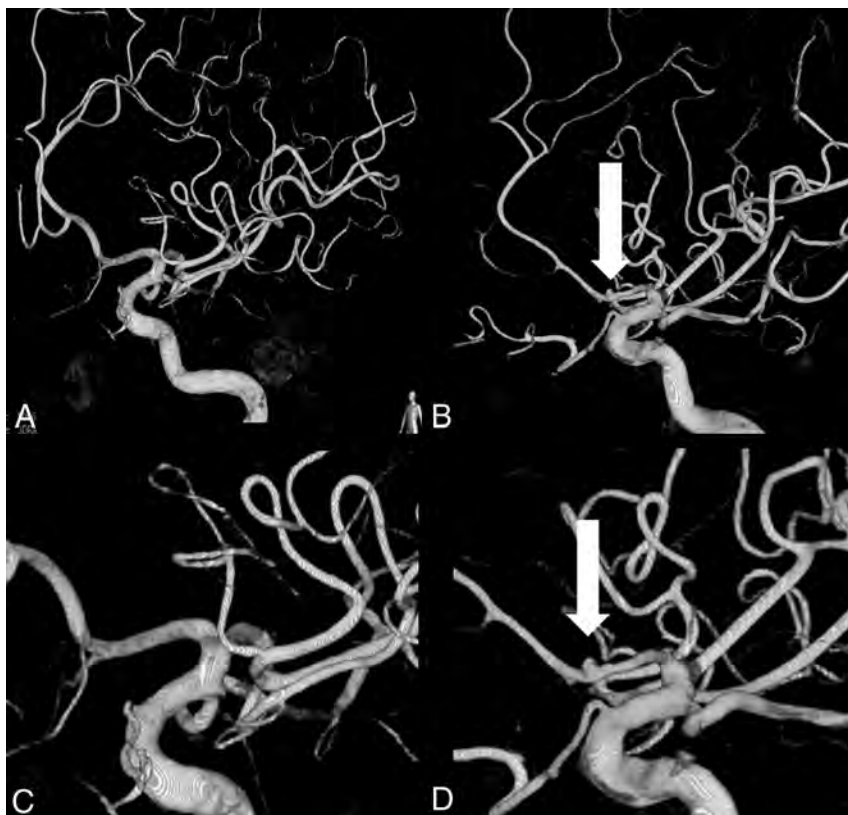


**FIG 1.** A 65-year-old man with initial negative findings on 3DRA. A, 3DRA within 24 hours after SAH shows no aneurysm. B, Repeat 3DRA after 10 days shows a very small (2 mm) A1 aneurysm. C and D, Magnification images of the A1 segment and an A1 aneurysm.

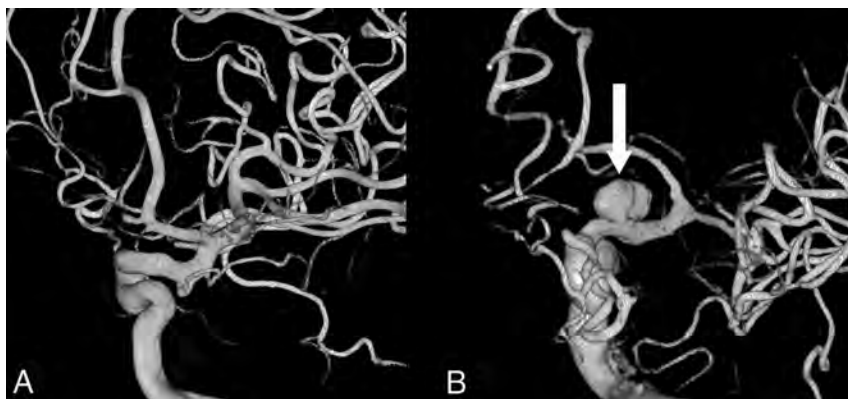


**FIG 2.** A 62-year-old woman with initial negative findings on 3DRA. A, 3DRA within 24 hours after SAH shows no aneurysm. B, Repeat 3DRA after 10 days shows an 8-mm supraclinoid internal artery dissecting aneurysm.

### MATERIALS AND METHODS

#### Patients

This observational study with prospectively collected data was compliant with the institutional privacy policy. The institutional review board gave exempt status for approval and informed consent. Between March 2013 and January 2016, 292 patients with aSAH were admitted. The diagnosis of aSAH was established with CT. All 292 patients had 3DRA of all vessels within 24 hours. When the first 3DRA had negative findings, patients underwent a repeat 3DRA after 7–10 days.

#### Analysis of 3D Rotational Angiography

The protocol for 3D angiography has been described previously.<sup>11</sup> 3D angiography examinations were reviewed by an experienced interventional neuroradiologist (W.J.v.R., with 27 years of experience) to determine the presence of a causative vascular abnormality. After review of the catheter angiograms, the presence of a causative vascular abnormality for the SAH was established by consensus of a panel comprising experienced interventional neuroradiologists and vascular neurosurgeons. Treatment decisions were also reached by consensus of this panel.

#### Statistical Analysis

Descriptive statistics were used for the presence, size, and locations of aneurysms. Quantitative variables were expressed with descriptive statistics, and categorical variables were expressed as frequencies or percentages with 95% CIs. Statistical analysis was performed with MedCalc statistical software, Version 14.12.0 for Windows (MedCalc Software, Mariakerke, Belgium).

### RESULTS

Of 292 patients admitted with aSAH on a native CT scan, in 30 patients (10.3%, 95% CI, 7.3%–14.3%), no aneurysm was detected on 3DRA within 24 hours. In 8 of these 30 patients (27%), an aneurysm was found on repeat 3DRA after 10 days. Qualification of these aneurysms is shown in the Table. Three of 8 initial occult aneurysms were very small (1–2 mm), 2 were supraclinoid carotid artery dissecting aneurysms (2 and 8 mm)

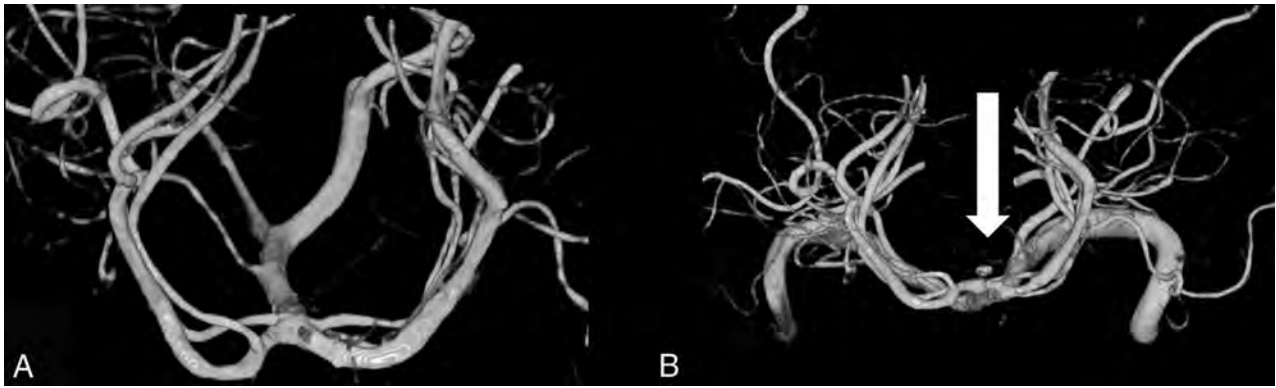


**FIG 3.** A 61-year-old man with initial negative findings on 3DRA. A, 3DRA (head-tail projection) within 24 hours after SAH shows no aneurysm. B, Repeat 3DRA (head-tail projection) after 10 days shows a very small basilar tip perforator dissecting aneurysm.

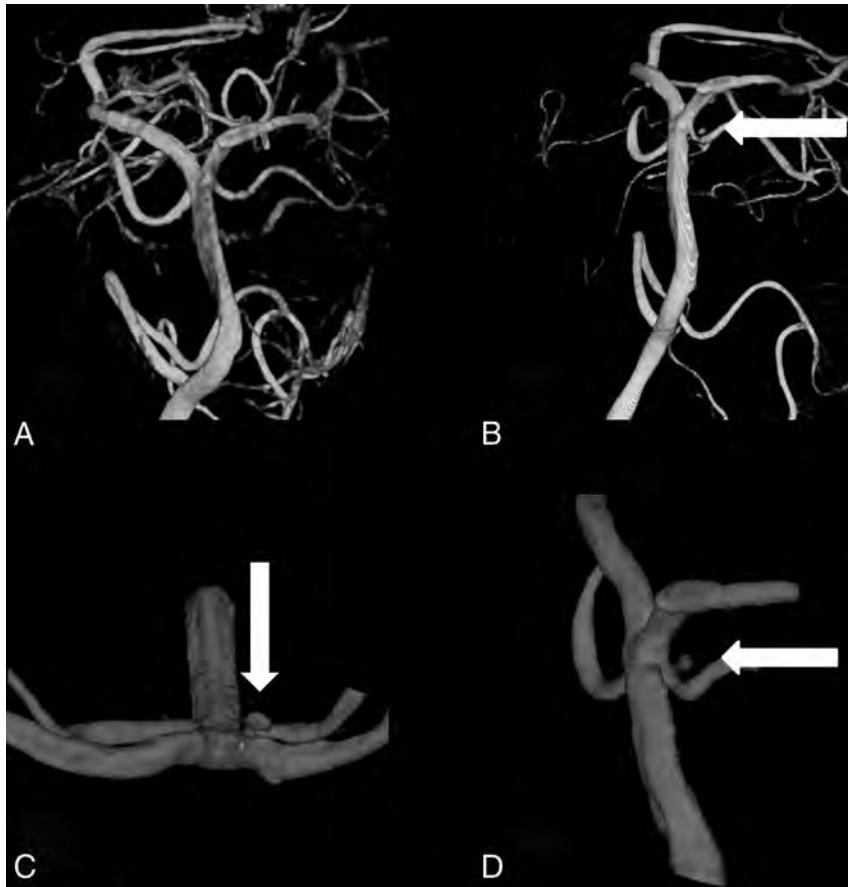


**FIG 4.** A 65-year-old man with initial negative findings on 3DRA. A, 3DRA within 24 hours after SAH shows no aneurysm. B, Repeat 3DRA after 10 days shows a very small basilar tip perforator dissecting aneurysm. C, Magnification image of a basilar tip perforator dissecting aneurysm (head-tail projection). D, Magnification image of basilar tip perforator dissecting aneurysm (lateral projection).

(Figs 1 and 2), 2 were small (1 and 3 mm) basilar perforator aneurysms (Figs 3 and 4), and 1 was a 3-mm vertebral artery dissecting aneurysm (Fig 5). In retrospect, only one 1-mm A1 aneurysm was missed on initial 3DRA; the other aneurysms were not present at the time of first 3DRA.

## DISCUSSION

The main cause of aSAH with an aneurysmal bleeding pattern is aneurysmal rupture, and angiography with false-negative

findings to detect an aneurysm may result in poor patient outcome. Repeat imaging for the initial angiogram negative for aSAH is controversial because of the various diagnostic modalities and lack of a clear consensus on yield.

In a previous study, we demonstrated that selective 3DRA in addition to standard multiprojection 2D angiography yielded an aneurysm in almost 80% of patients (18 of 23) with 2D angiography negative for aSAH. The advantage of 3DRA over DSA is obvious: free rotation of high-resolution images in any projection without overprojecting bony structures. With 2D imaging, a small aneurysm may be obscured by overprojecting adjacent vessels in the limited number of available projections.<sup>10</sup> Therefore, previous data of the yield of repeat 2D DSA cannot be compared with results of the yield of repeat 3DRA. To our knowledge, this is the first study using 3DRA for both initial and repeat angiography.

In the present study, we used 3DRA of all cerebral vessels as a standard diagnostic work-up. Despite this optimal vascular imaging, in 10% of patients (30 of 292) with aSAH, this was negative for aneurysms; and in 8 of these 30 patients (27%), an aneurysm

was found on repeat 3DRA. Not surprising, most initial occult aneurysms were very small, and most of them were, in retrospect, not visible on the initial 3DRA. Dissecting aneurysms of either a parent vessel or a perforator branch of the basilar artery composed the other types of aneurysms, which were probably not present on the initial 3DRA. Perforator artery aneurysms of the basilar trunk are rarely described in the literature. A recent literature review found 12 patients with basi-



**FIG 5.** A 46-year-old woman with initial negative findings on 3DRA. **A**, 3DRA within 24 hours after SAH shows no aneurysm. **B**, Repeat 3DRA after 10 days shows a V4 dissecting aneurysm.

lar perforator artery aneurysms. All aneurysms arose from the middle or rostral basilar perforator arteries.<sup>12</sup> The incidence of ruptured basilar perforator artery aneurysms in our study population was 2 of 270 ruptured aneurysms (0.7%). Because many physicians are unfamiliar with these types of aneurysms, treatment poses a technical challenge.

A number of possible factors leading to no visualization of a structural lesion, when it is actually present, have been mentioned in the literature. These include thrombus inside the aneurysmal sac; compression by surrounding hematoma; focal arterial spasm, which may lead to a temporary obliteration of the aneurysm neck; and technical and interpretation factors.<sup>3,13,14</sup>

The timing of repeat angiography remains controversial. Randomized controlled trials do not exist to support any imaging protocol in the initial angiography negative for subarachnoid hemorrhage. However, data from large retrospective series provide useful information from the experience of a high-volume neurovascular center.<sup>15</sup> In our hospital, repeat angiography is performed 7–10 days after the initial ictus, when the patient is still in the hospital. A study by Fontanella et al<sup>2</sup> reported that the incidence of rebleed was 5% and all the episodes occurred within 17 days after the initial ictus. Some authors advocate that repeat angiography be delayed 4–6 weeks after the initial ictus.<sup>15,16</sup> The arguments in favor of delayed repeat angiography are that by this time, radiologic vasospasm has recovered and hematoma around the vessel and any thrombus inside the proximal vessel or aneurysm sac have also resolved, thus making visualization of the aneurysm easier. There are also authors who advocate even a third angiography; a large retrospective study reported a yield of 8% from a third angiography.<sup>15</sup> In these previous studies, not all patients had a 3D reconstruction of the cerebral vessels. A large prospective study assessed the yield of repeat conventional angiography in patients with SAH and initial catheter angiograms with negative findings. The results of this study showed an overall yield of 4.2% for conventional angiography performed 7 days after presentation and 0% for conventional angiography performed 3 months after presentation.<sup>17</sup> In our hospital, we decided not to do a third 3DRA.

## CONCLUSIONS

Angiograms negative for aSAH are a very important clinical entity; the primary aim in management of these patients is to ensure that there is no structural lesion underlying the bleed, primarily aneurysms. The optimal imaging technique for depicting intracranial aneurysms is 3DRA. With this imaging quality, 10% of patients had an initial 3DRA with negative findings, and repeat 3DRA after 10 days revealed an aneurysm in 1 of 4. These aneurysms were either very small or were dissecting aneurysms of either a large vessel or a perforator branch. Our results indicate that repeat 3DRA is mandatory in patients with initial negative findings.

## REFERENCES

- Byyny RL, Mower WR, Shum N, et al. Sensitivity of noncontrast cranial computed tomography for the emergency department diagnosis of subarachnoid hemorrhage. *Ann Emerg Med* 2008;51:697–703 CrossRef Medline
- Fontanella M, Rainero I, Panciani PP, et al. Subarachnoid hemorrhage and negative angiography: clinical course and long-term follow-up. *Neurosurg Rev* 2011;34:477–84 CrossRef Medline
- Jung JY, Kim YB, Lee JW, et al. Spontaneous subarachnoid haemorrhage with negative initial angiography: a review of 143 cases. *J Clin Neurosci* 2006;13:1011–17 CrossRef Medline
- Rinkel GJ, Wijdicks EF, Hasan D, et al. Outcome in patients with subarachnoid haemorrhage and negative angiography according to pattern of haemorrhage on computed tomography. *Lancet* 1991;338:964–68 CrossRef Medline
- Yu DW, Jung YJ, Choi BY, et al. Subarachnoid hemorrhage with negative baseline digital subtraction angiography: is repeat digital subtraction angiography necessary? *J Cerebrovasc Endovasc Neurosurg* 2012;14:210–15 CrossRef Medline
- Khan N, Schuknecht B, Yonekawa Y. Presentation and management of patients with initial negative 4-vessel cerebral angiography in subarachnoid hemorrhage. *Acta Neurochir Suppl* 2002;82:71–81 Medline
- Topcuoglu MA, Ogilvy CS, Carter BS, et al. Subarachnoid hemorrhage without evident cause on initial angiography studies: diagnostic yield of subsequent angiography and other neuroimaging tests. *J Neurosurg* 2003;98:1235–40 CrossRef Medline
- Ishihara H, Kato S, Akimura T, et al. Angiogram-negative subarachnoid hemorrhage in the era of three dimensional rotational angiography. *J Clin Neurosci* 2007;14:252–55 CrossRef Medline
- van Rooij WJ, Sprengers ME, de Gast AN, et al. 3D rotational angiography: the new gold standard in the detection of additional intracranial aneurysms. *AJNR Am J Neuroradiol* 2008;29:976–79 CrossRef Medline
- van Rooij WJ, Peluso JP, Sluzewski M, et al. Additional value of 3D rotational angiography in angiographically negative aneurysmal subarachnoid hemorrhage: how negative is negative? *AJNR Am J Neuroradiol* 2008;29:962–66 CrossRef Medline
- Bechan RS, van Rooij SB, Sprengers ME et al. CT angiography versus 3D rotational angiography in patients with subarachnoid hemorrhage. *Neuroradiology* 2015;57:1239–46 CrossRef Medline
- Gross BA, Puri AS, Du R. Basilar trunk perforator artery aneurysms: case report and literature review. *Neurosurg Rev* 2013;36:163–68; discussion 168 CrossRef Medline
- Houben MP, van Rooij WJ, Sluzewski M, et al. Subarachnoid hem-

- orrhage without aneurysm on the angiogram: the value of repeat angiography [in Dutch]. *Ned Tijdschr Geneesk* 2002;146:804–08 Medline
14. Kumar R, Kanti Das K, Sahu RK, et al. **Angio negative spontaneous subarachnoid hemorrhage: is repeat angiogram required in all cases?** *Surg Neurol Int* 2014;5:125 CrossRef Medline
15. Dalyai R, Chalouhi N, Theofanis T, et al. **Subarachnoid hemorrhage with negative initial catheter angiography: a review of 254 cases evaluating patient clinical outcome and efficacy of short- and long-term repeat angiography.** *Neurosurgery* 2013;72:646–52; discussion 651–52 CrossRef Medline
16. Gupta SK, Gupta R, Khosla VK, et al. **Nonaneurysmal nonperimesencephalic subarachnoid hemorrhage: is it a benign entity?** *Surg Neurol* 2009;71:566–67; discussion 571–72 CrossRef Medline
17. Delgado Almandoz JE, Jagdeesan BD, Refai D, et al. **Diagnostic yield of repeat catheter angiography in patients with catheter and computer tomography angiography negative subarachnoid hemorrhage.** *Neurosurgery* 2012;70:1135–42 CrossRef Medline

# Porcine In Vivo Validation of a Virtual Contrast Model: The Influence of Contrast Agent Properties and Vessel Flow Rates

T.W. Peach, Y. Ventikos, J.V. Byrne, and Z. You



## ABSTRACT

**BACKGROUND AND PURPOSE:** Accurately and efficiently modeling the transport of angiographic contrast currently offers the best method of verifying computational fluid dynamics simulations and, with it, progress toward the lofty goal of prediction of aneurysm treatment outcome a priori. This study specifically examines the influence of estimated flow rate and contrast properties on such in silico predictions of aneurysm contrast residence and decay.

**MATERIALS AND METHODS:** Four experimental sidewall aneurysms were created in swine, with aneurysm contrast flow patterns and decay rates observed under angiography. A simplified computational fluid dynamics model of the experimental aneurysm was constructed from 3D angiography and contrast residence predicted a priori. The relative influence of a number of estimated model parameters (contrast viscosity, contrast density, and blood flow rate) on contrast residence was then investigated with further simulations.

**RESULTS:** Contrast infiltration and washout pattern were accurately predicted by the a priori computational fluid dynamics model; however, the contrast decay rate was underestimated by ~25%. This error was attributed to the estimated parent vessel flow rate alone, and the effects of contrast viscosity and density on the decay rate were found to be inconsequential. A linear correlation between the parent vessel flow rate and the corresponding contrast decay rate was observed.

**CONCLUSIONS:** In experimental sidewall aneurysms, contrast fluid properties (viscosity and density) were shown to have a negligible effect on variation in the modeled contrast decay rate. A strong linear correlation was observed between parent vessel flow rate and contrast decay over a physiologically reasonable range of flow rates.

**ABBREVIATIONS:** CFD = computational fluid dynamics; Q = flow rate (mL/min); Re = Reynolds number

The complex hemodynamic environment in and around a cerebral aneurysm has been linked to the initiation, development, and possible rupture of the lesion.<sup>1-3</sup> Observing angiographic contrast in the dome of an aneurysm remains the primary means a clinician uses to obtain a high-resolution and real-time assessment of both the quantity and quality of aneurysmal blood flow. These in vivo observations may be complemented by computational fluid dynamics (CFD) simulations, which elucidate properties that cannot be measured clinically, such as wall shear

stress, and provide a predictive capacity and the possibility of virtual treatment planning.<sup>4,5</sup>

The role of CFD in the field of neuroradiology is controversial and has become the focus of much fruitful discussion.<sup>6-8</sup> A key point in this discussion is the need to bring the disciplines closer by combining the merits of computational and bench testing with those of animal models and clinical cases, to move toward a sophisticated model of intracranial aneurysm as a disease.<sup>9,10</sup> Angiographic contrast transport is the only property common to both simulated hemodynamic measures and the complex biochemical environment that may be observed clinically. Hence, the need for accurately modeling contrast in silico is clear: CFD simulations may begin to be verified with the clinical criterion standard, and the quantification of aneurysm contrast/blood residence times has the potential to provide a direct link to models of intracranial aneurysm remodelling and thrombus formation.<sup>11-13</sup>

Implementations of such virtual contrast models, which approximate contrast as a dye-like scalar, are relatively simple.<sup>11,14-16</sup> Although these simulations produce physically mean-

Received January 13, 2016; accepted after revision June 2.

From the Department of Mechanical Engineering (T.W.P., Y.V.), University College London, London, UK; Department of Neuroradiology (J.V.B.), John Radcliffe Hospital, Oxford, UK; and Department of Engineering Science (Z.Y.), University of Oxford, Oxford, UK.

This study was funded by a grant from the Wellcome Trust (WT 088877/Z/09Z).

Please address correspondence to Y. Ventikos, PhD, Department of Mechanical Engineering, University College London, London WC1E 7JE, UK; e-mail: y.ventikos@ucl.ac.uk

Indicates open access to non-subscribers at www.ajnr.org

<http://dx.doi.org/10.3174/ajnr.A4884>

ingful contrast washout behavior, inaccuracies remain that are attributed to not explicitly modeling contrast properties (density and viscosity) or variations in patient-specific vessel flow rates.<sup>14,15,17</sup> Some models in the literature have shown very accurate replication of contrast infiltration and washout curves by directly matching properties estimated from angiography a posteriori (heart rate, flow rate, contrast bolus profile, and so forth).<sup>15</sup> However, the clinical usefulness and predictive strength of such a result are limited.

This study was instead conducted by using a generalist approach; only the aneurysm and parent vessel 3D geometry were extracted from angiography with all other simulation parameters estimated. A range of parameters were modeled, including the parent vessel flow rate and both the viscosity and density of the angiographic contrast medium, with the relative influence of each parameter on contrast decay quantified. The surgically created aneurysm model, with known dimensions, allowed any variation in results due to angiographic reconstruction to be controlled for, unlike in previous studies.<sup>11,14-16</sup> Such an approach makes advances toward accurate a priori prediction of contrast washout, requiring only a 3D reconstruction of the aneurysm in question, which may be obtained from any imaging technique.

## MATERIALS AND METHODS

### Experimental Setup

Experimental aneurysms were created in a porcine animal model by using 2 female Large White pigs of 60–65 kg and adopting the method described by German and Black.<sup>18</sup> Each sidewall aneurysm was formed surgically by vein graft by using the jugular vein cut at 45°, forming an anastomosis on the common carotid artery with continuous 8/0 stitching. One aneurysm was formed on each common carotid artery in both animals, with a total of 4 experimental aneurysms of near-identical size and shape. The common carotid artery was observed to have a diameter of approximately 4 mm in both animals, and the resulting sidewall aneurysms had a 5-mm diameter, 15-mm length, and 7-mm neck diameter. After creation, the aneurysms healed for 3 weeks to allow any local swelling to dissipate and for endothelialization at the anastomosis site to stabilize. Both animals were administered dual antiplatelet therapy following the surgical procedure.

Three weeks postcreation, each animal was catheterized via the femoral artery, and angiography was performed on an Innova 4100 system (GE Healthcare; Milwaukee, Wisconsin). 3D rotational angiography was used to accurately reconstruct the vessel and aneurysm geometry, while 2D angiography was used to verify the patency of each aneurysm and observe angiographic contrast washout in the aneurysm dome. A single series of 2D DSA acquisitions in the coronal plane was made for each of the 4 experimental aneurysms. Additionally, sagittal plane imaging was performed to verify complete and uniform contrast filling in each aneurysm. The 3D rotational runs were performed at a rotation speed of 20° per second with a 20-mL contrast injection delivered at 2 mL/s, and the 2D runs were conducted at 7.5 frames per second with a 10-mL contrast injection delivered at 7.5 mL/s. In all imaging, the catheter tip was located ~100 mm (25 vessel diameters) proximal to the aneurysm, and good contrast mixing was observed across the entire vessel lumen.

Ethics approval was obtained from the Oxford institutional ethics committee. Both animals were subsequently implanted with a flow-diverter device and formed part of a larger unrelated study, which is not reported in this article.

### Postprocessing

DICOM postprocessing was completed in OsiriX Imaging Software, Version 7.5.1 (<http://www.osirix-viewer.com>), where 3D geometries were segmented and the resulting vascular surfaces were exported as STereoLithograph files. Good correspondence was seen among a number of metrics (vessel diameter, aneurysm diameter, aneurysm neck diameter, and aneurysm length) measured at both the surgical creation and on the 3D reconstruction created from angiography 3 weeks postcreation. Visually, the flow patterns among the 4 experimental aneurysms appeared identical, with contrast entering the aneurysm neck distally and circulating around the whole aneurysm dome, forming 1 large vortex.

The 2D DICOM images were exported and segmented in Matlab (MathWorks, Natick, Massachusetts). A segmentation window isolating the aneurysm dome from the parent vessel was created manually for each experimental aneurysm, and the mean gray-scale value in the aneurysm dome was calculated for each DICOM in the time-series.

### Experimental Calibration

To verify the direct correspondence between pixel gray-scale value and contrast concentration, we performed a brief calibration experiment. A number of 10-mL syringes were filled with a mixture of saline and contrast medium in varying concentrations (0%–50% contrast by volume) and were imaged by using a standard neck/cerebral DSA protocol. After we subtracted background values, the mean gray-scale value of each syringe was found to vary linearly with contrast concentration.

### CFD Simulations

Given the similarity in vessel size, aneurysm size, and aneurysm flow pattern among the 4 experimental aneurysms and in the interest of increasing computational efficiency, the 3D geometry of only 1 aneurysm was selected for the computational study. The aneurysm geometry was imported into CFD-VisCART (ESI Group, Paris, France) and meshed; unstructured meshing was completed with a minimum mesh density of 4000 elements/mm<sup>3</sup>, resulting in a total mesh size of 4,290,000 elements.

Contrast was modeled computationally as an independent scalar quantity introduced at the simulation inlet and transported in the bulk flow, similar to dye particles. Although this method is a major simplification of what is, in reality, a 2-fluid mixing problem, the reduction in both computational cost and the complexity required to characterize true 2-fluid flow are considerable. The modeled contrast does not alter the simulated blood density or viscosity and has a diffusivity in blood of  $1.0 \times 10^{-7}$  mm<sup>2</sup>/s, an order of magnitude estimate based on the diffusivity of tracer particles in blood.<sup>19</sup> A uniform contrast bolus was prescribed at the geometry inlet with a duration of 1 cardiac cycle. Thus, the total contrast transport seen virtually can be considered analogous to the experimental transport averaged over the cardiac cycle.

The computational mesh was imported into the multiphysics

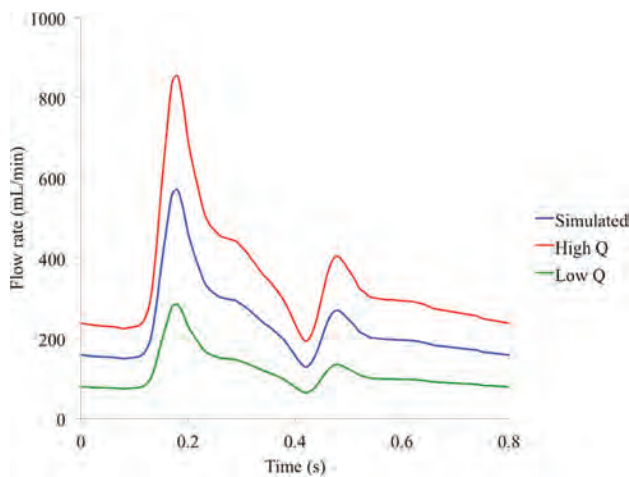


**FIG 1.** Parent vessel flow rate profiles based on the human ICA.

suite CFD-ACE+ (ESI Group). Blood flow was modeled as an incompressible fluid with unsteady 3D Navier-Stokes governing equations, with second-order interpolations in space and time, a time-step of 0.01 second, a rigid arterial wall, a fluid density of  $1000 \text{ kg/m}^3$ , and a dynamic viscosity of  $0.004 \text{ Pa} \times \text{s}$ . We adopted a Newtonian fluid model, assuming that non-Newtonian flow effects are small in both the aneurysm dome and arteries with a diameter of  $>0.5 \text{ mm}$ .<sup>20,21</sup> We ignored gravitational effects, assuming that the experimental aneurysms remained located, as created, in the approximate horizontal (coronal) plane.

The transient simulation was run with a time-varying inflow based on the profile of flow in the human ICA, derived from a 1D model of the vasculature, as depicted in Fig 1.<sup>22</sup> Because an accurate profile of flow in a porcine common carotid artery was not available to the authors, we concluded that the similarity in flow rate, artery diameter, and distance from the heart between the porcine common carotid artery and the human ICA made this assumption reasonable. This assumption is interrogated further in the discussion that follows. A radially symmetric inlet velocity profile was prescribed at the inlet and scaled to give a mean flow rate of  $230 \text{ mL/min}$ .

The simulation was run on thirty-two 2.93-GHz cores, with each time-step converging to 5 orders of magnitude residual reduction in around 50–100 iterations in a typical solution time of 30 minutes per time-step. The contrast bolus of 0.8-second duration was introduced after 2 full cardiac cycles (1.60 seconds real time) to reduce the influence of initial transient flow effects. The simulation was run for a further 4 cardiac cycles after the contrast bolus was first introduced, giving a total simulation time of 6 cardiac cycles (4.80 seconds real time). The absolute value of contrast residing in the aneurysm dome of the simulated geometry was then exported at every fourth time-step.

Virtual angiography was generated by aligning the simulation geometry into the same plane as that seen experimentally before the simulated contrast concentration distribution was then discretized into a  $100 \times 150$  grid of pixels (approximately matching the experimental imaging resolution of  $0.2 \times 0.2 \text{ mm}$ ).

**Table 1: Contrast media properties**

Contrast Agent	Density	Viscosity
Omnipaque 180	$1164 \text{ kg/m}^3$	$0.0015 \text{ Pa} \times \text{s}$
Omnipaque 350	$1410 \text{ kg/m}^3$	$0.0204 \text{ Pa} \times \text{s}$

**Table 2: Contrast-blood mixture properties**

	Density	Viscosity	Modified Re
High Re (Omnipaque 180)	$1080 \text{ kg/m}^3$	$0.00275 \text{ Pa} \times \text{s}$	+70%
Low Re (Omnipaque 350)	$1200 \text{ kg/m}^3$	$0.0122 \text{ Pa} \times \text{s}$	-40%

### Accounting for Contrast Properties

A second set of simulations was conducted to quantify the influence of contrast properties. In the absence of a true 2-fluid model, flow effects arising from the local gradient in viscosity and density between blood and contrast could not be modeled explicitly. Instead, we ran simulations, assuming a working fluid equivalent to a perfect 50:50 mixture of blood and contrast, which was transported through the geometry for the entire simulation (ie, before, during, and after the virtual contrast bolus was introduced).

In an attempt to quantify the overall influence of contrast properties, 2 media were chosen that represented the greatest overall change in fluid properties. Specifically, contrast media with the highest and lowest ratios of density to viscosity were chosen (as summarized in Table 1), which correspondingly increase and decrease the simulation Reynolds number (Re) to the greatest degree.

The density, viscosity, and equivalent change in inlet Reynolds number for the simulations incorporating the properties of each contrast agent (assuming a 50:50 mix of contrast and blood) are summarized in Table 2. For comparison, the equivalent mixture of blood and the contrast agent used experimentally (iohexol, Omnipaque 240; GE Healthcare, Piscataway, New Jersey) would result in an effective increase in the Re of 23%. Both simulations (high Re and low Re) were run with the same parameters and postprocessed in the same manner as described in the previous section.

### Accounting for Parent Vessel Flow Rate

Approximating the average and instantaneous parent vessel flow rate is an additional source of error in simulated contrast washout behavior that is often reported in the literature. To quantify this variation, we conducted a third and final set of CFD simulations with altered mean parent vessel flow rates corresponding to a 50% increase ( $345 \text{ mL/min}$ ) and 50% decrease ( $115 \text{ mL/min}$ ) compared with the mean human ICA rate ( $230 \text{ mL/min}$ ) used in previous simulations. The overall shape of the flow profile in time was unaltered and was only scaled to achieve an altered flow rate, as indicated in Fig 1.

The 50% increased flow rate was chosen as an approximation to the flow rate of a human common carotid artery, which could also be considered an upper estimate of the flow rate in the experimental porcine common carotid artery. The 50% decreased flow rate was selected as an order-of-magnitude estimate based on previous experiments conducted by the authors, which quantified flow rate reduction in a vessel cross-section partially occluded by a catheter lumen. Hence, it was assumed that the range of mean flow rates considered ( $115\text{--}345 \text{ mL/min}$ ) encompassed that likely to be seen experimentally. Both simulations with altered flow

rate (Q) (low Q and high Q) were run with solver settings and postprocessing procedures identical to simulations discussed previously.

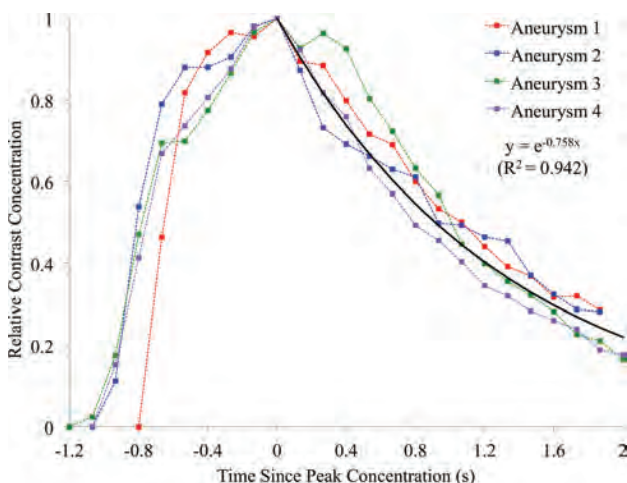


**FIG 2.** Experimental contrast residence curves for all 4 experimental aneurysms and the fitted exponential decay curve.

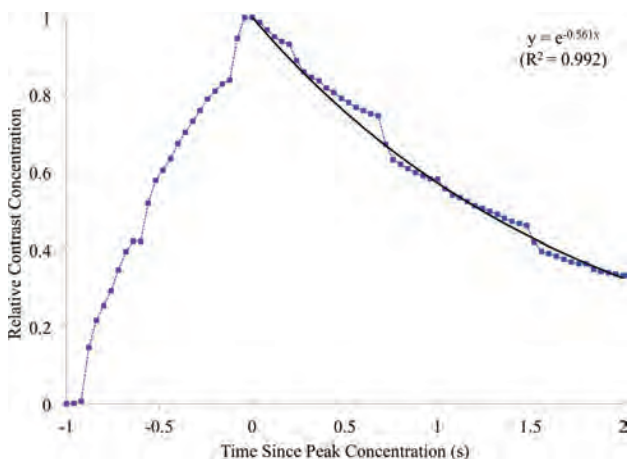


**FIG 3.** Simulated contrast residence curve and the fitted exponential decay curve.

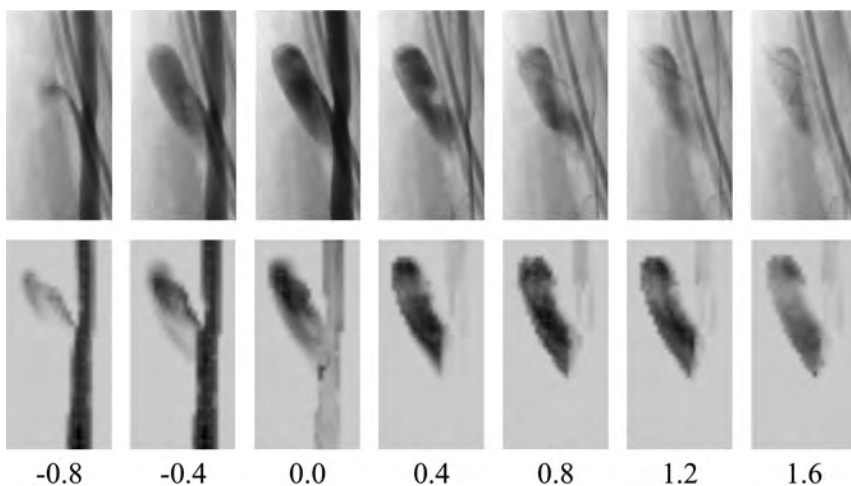


**FIG 4.** Experimental (upper) and virtual (lower) DSA. Images are separated by 0.40-second intervals and aligned at 0.0 seconds to peak aneurysm contrast concentration.

### Inferring Experimental Flow Rate

Finally, by tracking the contrast-front transport in consecutive DICOM images, we calculated an estimate of the true experimental parent vessel flow rate, assuming a Poiseuille velocity profile. The velocity of the contrast-front was recorded for 2 consecutive 0.133-second intervals in each experimental aneurysm, which resulted in 8 separate estimates of the instantaneous parent vessel flow rate.

### RESULTS

Contrast concentration, averaged over the aneurysm dome, for each experimental aneurysm is summarized in Fig 2. The contrast curves are aligned to peak relative contrast concentration, at  $t = 0$  seconds. Assuming a capacitor-based model of contrast residence, we fitted an exponential decay curve to the decay portion of the experimental data with a decay constant of  $0.758 \text{ second}^{-1}$ . Simulated contrast residence is shown in Fig 3, with a corresponding exponential curve fitted and a decay constant of  $0.561 \text{ second}^{-1}$ . Experimental and virtual angiography is shown in Fig 4, where the same convention of aligning the peak contrast concentration to 0.0 seconds is adopted.

The contrast decay curves for the simulations conducted at altered Reynolds numbers and parent vessel flow rates are displayed in Figs 5 and 6, respectively. These decay curves are plotted alongside both the initial simulated contrast concentration and the experimental results. The corresponding exponential decay constants for the experimental results and each of the 5 simulations are summarized in Table 3. In Fig 7, the exponential decay constants of the simulations conducted at the initial, high, and low flow rates are plotted against mean flow rate, with a linear trend line fitted, assuming direct proportionality.

Finally, the 8 instantaneous parent vessel flow rates that were extracted from the experimental angiography are found to correspond to a mean parent vessel flow rate of  $296 \text{ mL/min}$  with a range of  $202\text{--}516 \text{ mL/min}$ .

### DISCUSSION

The global contrast transport in the experimental aneurysm dome is well-described by the exponential decay model proposed in Fig 2, with little variation seen across all 4 experimental aneurysms. In agreement with the observations of others in the literature, the modeling of contrast agent in this study as an independent scalar transported in simulated fluid flow accurately replicates the behavior seen experimentally.<sup>14-16</sup>

The overall contrast infiltration and washout patterns are similar for the experimental and simulated cases (Figs 2 and 3), but the simulated contrast decay constant is 26% lower than the experimental value. As such, after 2.0 seconds, approximately 25% of the total contrast volume remains in the aneurysm in the experimental case, but 35% of the simulated contrast remains. This underestimation of the simulated contrast decay constant ( $0.560 \text{ second}^{-1}$ ) is beyond the range of scatter seen in the experimental

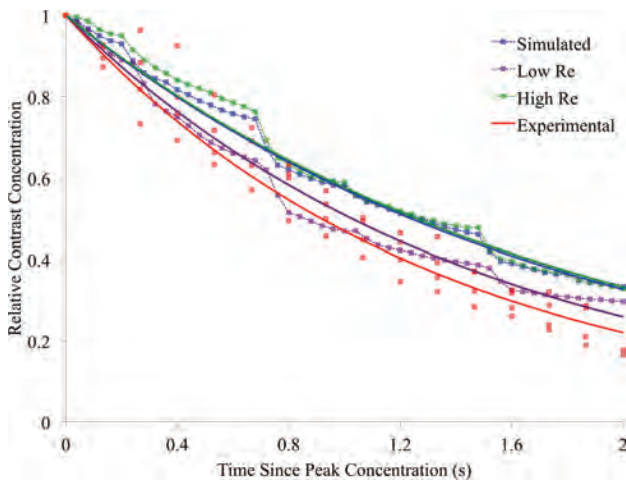


**FIG 5.** Simulated and experimental contrast decay incorporating variation in simulated contrast density and viscosity.

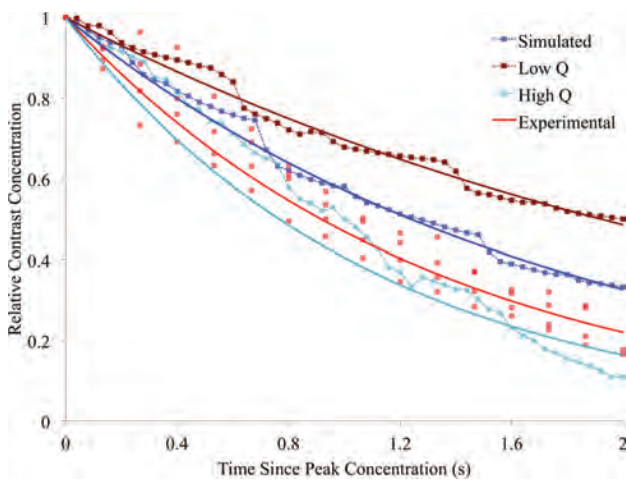


**FIG 6.** Simulated and experimental contrast decay incorporating variation in the simulated parent vessel flow rate.

**Table 3: Summary of experimental and simulated contrast decay constants**

	Contrast Decay Constant
Experimental	0.758 second <sup>-1</sup>
Initial simulation	0.560 second <sup>-1</sup>
High Re simulation	0.552 second <sup>-1</sup>
Low Re simulation	0.677 second <sup>-1</sup>
High Q simulation	0.903 second <sup>-1</sup>
Low Q simulation	0.362 second <sup>-1</sup>

data, where curves fitted to individual experimental aneurysm decay traces show decay constants of 0.68–0.859 second<sup>-1</sup>. The physical distribution of contrast within the aneurysm dome is well-predicted by the simulation, with similar areas of infiltration, circulation, and washout visible in the experimental and simulated angiography of Fig 4. However, the lower rate of contrast decay in the simulated case results in increased aneurysm contrast residence and a noticeably darker angiogram.

The range in simulated contrast decay constant seen over the high Re and low Re simulations is small and of the order of the scatter seen in the experimental data in Fig 5. Additionally, the range of decay constants across the 2 simulations (0.552–0.677 second<sup>-1</sup>) does not

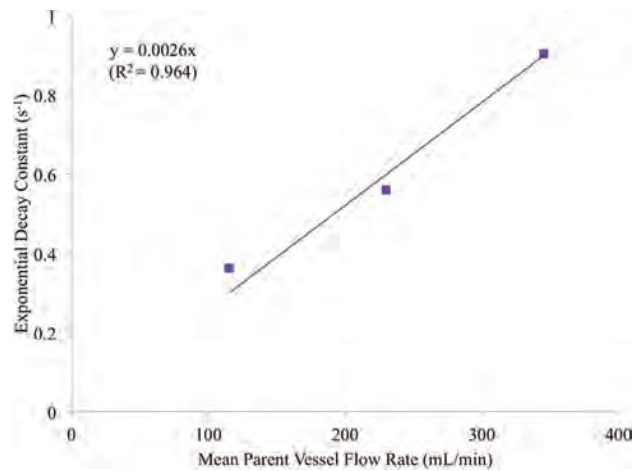


**FIG 7.** Simulated contrast decay constant and mean parent vessel flow rate.

encompass the experimental value (0.758 second<sup>-1</sup>). Such a result suggests that the differences between blood and contrast fluid properties alone are unlikely to account for the discrepancy in the predicted contrast decay rate seen in the original simulation (Fig 3). This assumption is further reinforced by the highly asymmetric spread of the high Re and low Re curves in Fig 5, with no discernible difference between the initial and high Re simulations and the experimental contrast agent used, corresponding to a slight increase (23%) in the simulation Reynolds number.

As indicated in both Fig 6 and Table 3, the range in decay constant seen for the high Q and low Q simulations is both more substantial than the range seen in Fig 5 and encompasses the decay seen experimentally. Hence, a discrepancy between the experimental flow rate and the flow rate assumed a priori in the original CFD simulation is the most likely cause of the poor experimental contrast decay rate prediction.

The spread of the high Q and low Q simulation decay curves about the original simulation in Fig 6 is relatively symmetric, unlike the previous simulations of Fig 5. However, the high Q contrast curve is not as well-approximated to an exponential decay as the other simulation results; this outcome is likely due to the low degree of flow recirculation observed in the simulation, where flow streamlines traced the perimeter of the aneurysm dome before immediately exiting.

From the decay curves in Fig 6, it appears that a simulation adopting a parent vessel flow rate between the mean human ICA rate of the original simulation and the mean human common carotid artery rate of the high Q case would result in a contrast decay curve similar to that obtained experimentally. When the simulation flow rate and contrast decay rate for the high Q, low Q, and original simulations are plotted in Fig 7, a linear and directly proportional trend line may be fitted to the data. Thus, if one assumes this linear relationship between the decay and flow rates and an experimental cardiac profile similar to that in the human ICA/common carotid artery, a simulated mean parent vessel flow rate of approximately 290 mL/min would mimic the contrast decay rate of the in vivo model (0.758 second<sup>-1</sup>). Such a mean flow rate is both reasonable and only 2% lower than the mean flow rate of 296 mL/min that was estimated from experimental angiography.

## Study Limitations

As previously discussed, the simplified contrast model implemented does not explicitly model the mixing of 2 fluids; hence, local gradients of contrast and blood fluid properties are not captured. However, given the rapid and fairly complete degree of blood and contrast mixing seen experimentally and the fundamental design of the contrast medium being highly diffusive, such a phenomenon is likely insignificant.

The experimental 2D DSA frame rate of 7.5 frames per second was chosen to approximately match the temporal resolution frequently used in the clinical setting. Although some flow effects may not be fully resolved temporally at such a frame rate, the relatively smooth curves and lack of any aliasing in Fig 2 suggest that the global aneurysm flow effects are adequately resolved. Additionally, the flow features observed in the simulated results (with an effective frame rate of 100 frames per second) did not show any high-frequency variations.

Over the range of flow rates considered (115–345 mL/min), there appears to be a simple linear relation between the parent vessel flow rate and aneurysm contrast decay rate. However, it is unclear whether a similar relationship would hold for other aneurysm geometries under similar flow rates. More generally, this study focused only on a sidewall aneurysm model, so any conclusions are unlikely to hold true in the drastically different flow environment of bifurcation aneurysms.

Finally, this study only focused on the global contrast concentration within the aneurysm dome. Local variation in contrast concentration, both in and out of the 2D DSA plane, was not quantified for simplicity and brevity, but a strong qualitative similarity was seen between experimental and simulated local contrast concentration patterns. The use of 4D angiographic technology in any future study would allow the time-varying 3D distribution of contrast in the aneurysm dome to be fully captured and the effect of contrast and flow properties on contrast distributions to be interrogated more completely.

## CONCLUSIONS

Good correspondence was seen between a CFD contrast transport model and experimental results. Aneurysm flow patterns and contrast decay mechanisms were accurately predicted by simulation and may have the potential to offer clinical insight in treatment planning.

Modeled contrast fluid properties (viscosity and density) were shown to have a negligible effect on the aneurysm contrast decay rate, compared with assuming properties identical to a Newtonian blood model. Mismatch between the experimental and simulated contrast decay rate was attributed to an initial underestimate of the simulated parent vessel flow rate, later verified by angiography. This influence of patient-specific vessel flow rates remains a major challenge to a priori prediction of aneurysm contrast residence and treatment outcomes.

## ACKNOWLEDGMENTS

All authors would like to thank Dr M. Megahed of the ESI Group for allowing the use of the CFD-ACE suite.

Disclosures: Thomas Peach, Yiannis Ventikos, Zhong You—RELATED: Grant: Wellcome Trust/Engineering and Physical Sciences Research Council (grant WT 088877/Z/09Z).\* James Byrne—RELATED: Grant: Wellcome Trust (grant WT 088877/Z/09Z).\* Support for Travel to Meetings for the Study or Other Purposes: Wellcome Trust (grant WT 088877/Z/09Z). \*Money paid to the institution.

## REFERENCES

1. Brisman JL, Song JK, Newell DW. **Cerebral aneurysms.** *N Engl J Med* 2006;355:928–39 CrossRef Medline
2. Sforza DM, Putman CM, Cebral JR. **Hemodynamics of cerebral aneurysms.** *Annu Rev Fluid Mech* 2009;41:91–107 CrossRef Medline
3. Xu J, Yu Y, Wu X, et al. **Morphological and hemodynamic analysis of mirror posterior communicating artery aneurysms.** *PLoS One* 2013;8:e55413 CrossRef Medline
4. Steinman D, Milner JS, Norley CJ, et al. **Image-based computational simulation of flow dynamics in a giant intracranial aneurysm.** *AJNR Am J Neuroradiol* 2003;24:559–66 Medline
5. Chung B, Cebral JR. **CFD for evaluation and treatment planning of aneurysms: review of proposed clinical uses and their challenges.** *Ann Biomed Eng* 2015;43:122–38 CrossRef Medline
6. Kallmes DF. **Point: CFD—computational fluid dynamics or confounding factor dissemination.** *AJNR Am J Neuroradiol.* 2012;33:395–96 CrossRef Medline
7. Cebral JR, Meng H. **Counterpoint: realizing the clinical utility of computational fluid dynamics—closing the gap.** *AJNR Am J Neuroradiol* 2012;33:396–98 CrossRef Medline
8. Ventikos Y. **Resolving the issue of resolution.** *AJNR Am J Neuroradiol* 2014;35:544–45 CrossRef Medline
9. Robertson AM, Watton PN. **Computational fluid dynamics in aneurysm research: critical reflections, future directions.** *AJNR Am J Neuroradiol* 2012;33:992–95 CrossRef Medline
10. Strother CM, Jiang J. **Intracranial aneurysms, cancer, x-rays, and computational fluid dynamics.** *AJNR Am J Neuroradiol* 2012;33:991–92 CrossRef Medline
11. Sadasivan C, Cesar L, Seong J, et al. **An original flow diversion device for the treatment of intracranial aneurysms: evaluation in the rabbit elastase-induced model.** *Stroke* 2009;40:952–58 CrossRef Medline
12. Cebral JR, Vazquez M, Sforza DM, et al. **Analysis of hemodynamics and wall mechanics at sites of cerebral aneurysm rupture.** *J Neurointerv* 2015;7:530–36 CrossRef Medline
13. Gester K, Lüchtfeld I, Büsen M, et al. **In vitro evaluation of intra-aneurysmal, flow-diverter-induced thrombus formation: a feasibility study.** *AJNR Am J Neuroradiol* 2016;37:490–96 CrossRef Medline
14. Ford MD, Stuhne GR, Nikolov HN, et al. **Virtual angiography for visualization and validation of computational models of aneurysm hemodynamics.** *IEEE Trans Med Imaging* 2005;24:1586–92 CrossRef Medline
15. Endres J, Kowarschik M, Redel T, et al. **A workflow for patient-individualized virtual angiogram generation based on CFD simulation.** *Comput Math Methods Med* 2012;2012:306765 CrossRef Medline
16. Cebral JR, Pergolizzi RS Jr, Putman CM. **Computational fluid dynamics modeling of intracranial aneurysms: qualitative comparison with cerebral angiography.** *Acad Radiol* 2007;14:804–13 CrossRef Medline
17. Wang ZJ, Hoffmann KR, Wang Z, et al. **Contrast settling in cerebral aneurysm angiography.** *Phys Med Biol* 2005;50:3171–81 CrossRef Medline
18. German W, Black S. **Experimental production of carotid aneurysms.** *N Engl J Med* 1954;250:104–06 CrossRef Medline
19. Saadatmand M, Ishikawa T, Matsuki N, et al. **Fluid particle diffusion through high-hematocrit blood flow within a capillary tube.** *J Biomech* 2011;44:170–75 CrossRef Medline
20. Perktold K, Resch M, Florian H. **Pulsatile non-Newtonian flow characteristics in a three-dimensional human carotid bifurcation model.** *J Biomech Eng* 1991;113:464–75 CrossRef Medline
21. Valencia AA, Guzmán AM, Finol EA, et al. **Blood flow dynamics in saccular aneurysm models of the basilar artery.** *J Biomech Eng* 2006;128:516–26 CrossRef Medline
22. Raymond P, Vardoulis O, Stergiopoulos N. **Generic and patient-specific models of the arterial tree.** *J Clin Monit Comput* 2012;26:375–82 CrossRef Medline

# Cognitive Impairment and Basal Ganglia Functional Connectivity in Vascular Parkinsonism

V. Dunet, J. Deverduin, C. Charrout, E. Le Bars, F. Molino, S. Menjot de Champfleury, F. Maury, M. Charif, X. Ayrygnac, P. Labauge, G. Castelnovo, F. Pinna, A. Bonafe, C. Geny, and N. Menjot de Champfleury



## ABSTRACT

**BACKGROUND AND PURPOSE:** Patients with vascular parkinsonism have higher cognitive decline and more basal ganglia lesions. We aimed to evaluate the relationship of cognitive impairment with functional connectivity between the basal ganglia and cingulate cortex in vascular parkinsonism.

**MATERIALS AND METHODS:** Thirty patients (8 with vascular parkinsonism and 22 with Parkinson disease) and 23 controls were enrolled. The Mattis Dementia Rating Scale and the Stroop Task were used to assess cognitive decline. MR imaging examinations included T1-MPRAGE, FLAIR, and resting-state fMRI sequences. MPRAGE was segmented to obtain basal ganglia and cingulate cortex volumes. FLAIR was segmented to obtain white matter hyperintensity lesion volume. Resting-state fMRI sequences were used to compare basal ganglia functional connectivity with the cingulate cortex between patients and controls.

**RESULTS:** Patients with vascular parkinsonism exhibited impaired attention, resistance to interference, and inhibitory control and an increased number of errors on the Stroop Task. They also had higher caudate nucleus and white matter hyperintensity lesion volumes, which were positively correlated ( $\rho = 0.75, P < .0001$ ). Caudate nucleus functional connectivity with the perigenual anterior cingulate cortex was increased in patients with vascular parkinsonism compared with controls and patients with Parkinson disease, and it was positively correlated with the caudate nucleus volume ( $\rho = 0.44, P = .016$ ). Caudate nucleus functional connectivity with the posterior cingulate cortex was decreased in patients with vascular parkinsonism compared with controls and negatively correlated with the number of errors on the Stroop test ( $\rho = -0.51, P = .0003$ ).

**CONCLUSIONS:** In patients with vascular parkinsonism, cognitive decline could be related to changes of caudate nucleus functional connectivity with the cingulate cortex at resting-state, which may be induced by ischemia-related remodelling.

**ABBREVIATIONS:** BOLD = blood oxygen level–dependent; MNI = Montreal Neurological Institute; PD = Parkinson disease; VP = vascular parkinsonism; rsfMRI = resting-state fMRI; WMHL = white matter hyperintensity lesions

Brain lesions related to small-vessel disease may affect the white matter and basal ganglia and can lead to parkinsonism features.<sup>1</sup> Vascular parkinsonism (VP) has thus emerged as a second-

ary parkinsonism subtype that occurs in 3.2/100,000 individuals per year and 2 times more frequently in men than in women.<sup>2</sup> Clinically, patients with VP more frequently present with lower body parkinsonism, urinary incontinence, and abnormal pyramidal response.<sup>3</sup> Compared with age-matched patients with Parkinson disease (PD) and healthy controls, they also have significantly

Received January 28, 2016; accepted after revision June 5.

From the Departments of Neuroradiology (V.D., J.D., C.C., E.L.B., F.P., A.B., N.M.d.C.) and Neurology (F.Maury, M.C., X.A., P.L., F.P., C.G.), Montpellier University Hospital Center, Gui de Chauliac Hospital, Montpellier, France; Institut d'Imagerie Fonctionnelle Humaine, I2FH (V.D., J.D., C.C., E.L.B., F.P., A.B., N.M.d.C.), Hôpital Gui de Chauliac, Centre Hospitalier Régional Universitaire de Montpellier, Montpellier, France; Department of Diagnostic and Interventional Radiology (V.D.), Lausanne University Hospital, Lausanne, Switzerland; Laboratoire Charles Coulomb (J.D., F.Molino), Centre National de la Recherche Scientifique Unite Mixte de Recherche 5221, Montpellier University, Montpellier, France; Intracense (J.D.), Montpellier, France; Neuropsychiatry: Epidemiological and Clinical Research (C.C.), Institut National de la Santé et de la Recherche Médicale, U1061, Montpellier University, La Colombiere Hospital, Montpellier, France; Institut National de la Santé et de la Recherche Médicale (C.C.), U1198, Montpellier University, Montpellier, France; Institut de Genomique Fonctionnelle (F.Molino), UMR 5203, Institut National de la Santé et de la Recherche Médicale, U661, Montpellier University, Montpellier, France; Clinique du Parc (S.M.d.C.), Service d'imagerie, Castenau-Le-Lez, France;

Departments of Neurology (G.C.) and Medical Imaging (N.M.d.C.), Caremeau University Hospital Center, Nimes, France; Team "Plasticity of Central Nervous System, Stem Cells and Glial Tumors" (A.B., N.M.d.C.), U1051, Institut of Neurosciences of Montpellier, Saint Eloi Hospital, Montpellier, France; EuroMov (C.G.), Montpellier, France; and Movement to Health (C.G.), Montpellier University, Montpellier, France.

This work was supported by grants from the Centre Hospitalier Regional Universitaire of Montpellier, which was not involved in any step of the study.

Please address correspondence to Vincent Dunet, MD, BSc, Department of Neuroradiology, Montpellier University Hospital Center, Gui de Chauliac Hospital, 80 Ave Augustin Fliche, 34295 Montpellier Cedex 5, France; e-mail: vincent.dunet@chuv.ch

Indicates article with supplemental on-line table.

<http://dx.doi.org/10.3174/ajnr.A4889>

higher cognitive decline with impaired attention and resistance to interference and reduced inhibitory control.<sup>4</sup> Regarding brain morphology, patients with VP are characterized by more frequent basal ganglia lesions<sup>5-7</sup> compared with patients with PD and controls. Because attention, resistance to interference, and inhibitory control were related to cingulate cortex function, we hypothesized that basal ganglia functional connectivity with the cingulate cortex could be modified in patients with VP.

Resting-state fMRI (rsfMRI) provides information regarding the functional connectivity of brain structures. This relies on temporal correlation of activity estimated by measuring the blood oxygen level-dependent (BOLD) signal. Seed-driven functional connectivity MR imaging allows determining correlation coefficients between the time course of a seed ROI and the time course of others voxels (seed-to-voxel analysis) or determining correlations between each pair of seed areas (ROI-to-ROI analysis).

We thus aimed to determine whether alteration of basal ganglia functional connectivity with the cingulate cortex could be involved in the cognitive impairment of patients with VP compared with those with PD and healthy controls by using both seed-to-voxel and ROI-to-ROI analyses of rsfMRI sequences.

## MATERIALS AND METHODS

### Study Population

Between December 2011 and December 2014, 35 patients (mean age,  $79 \pm 5$  years; male/female ratio, 25:10) with parkinsonism and 27 healthy age-matched controls (mean age,  $78 \pm 3$  years; male/female ratio, 19:8) were prospectively enrolled and underwent brain MR imaging. Inclusion criteria for patients were the following: between 70 and 90 years of age, symptoms of parkinsonism starting after 70 years of age, and a diagnosis of VP or PD. Controls were chosen to match the age distribution of the patients. Exclusion criteria were the same for all subjects (controls and patients) and included the following: a history of head injury, stroke, intracranial bleeding, exposure to neuroleptic drugs, psychiatric comorbidity, and contraindications to MR imaging. A neuroradiologist who was not involved in MR imaging data processing analyzed previous brain MR imaging or CT examinations available on the institutional PACS system before inclusion as well as MR images obtained during the study to rule out stroke and intracranial bleeding sequelae.

### Ethics Approval

The institutional review board gave its approval for this study. The experiments were undertaken with the understanding and written informed consent of each subject, and the study complied with the World Medical Association Declaration of Helsinki.

### Clinical Assessment

All patients underwent a neurologic evaluation the day of the brain MR imaging examination. Diagnoses were established by an experienced neurologist according to the UK Parkinson's Disease Society Brain Bank criteria<sup>8</sup> for idiopathic PD. For VP, the clinical criteria of Zijlmans et al<sup>9</sup> (hypokinesia/bradykinesia predominantly affecting the lower body with frontal gait disorder; muscular rigidity; postural instability not caused by visual, vestibular, cerebellar or proprioceptive dysfunction; and resting tremor)

were used along with minimal or absent levodopa response and multiple vascular risk factors. Patients were thus classified in 2 groups: 8 patients met the criteria for VP (mean age,  $78 \pm 2$  years; male/female ratio, 7:1) and 27 patients met those of idiopathic PD (mean age,  $80 \pm 5$  years; male/female ratio, 18:9).

The severity of the parkinsonian symptoms was assessed by using the Hoehn and Yahr scale (range, 0–5), the Schwab and England Activities of Daily Living scale (range, 0%–100%), the Movement Disorder Society Unified Parkinson's Disease Rating Scale (range, 0–199),<sup>10</sup> and the Short Motor Disability Scale<sup>11</sup> (range, 0–17). The educational attainment was also recorded.

Global cognitive efficiency was assessed by the Mini-Mental State Examination score (range, 0–30) and the Mattis Dementia Rating Scale (range, 0–144), involving 5 items (attention, initiation, construction, conceptualization, and memory). To assess executive function, we performed a Victoria Stroop Task.<sup>12</sup> It involved 3 conditions: color naming, word reading, and interference, in which a color name is written in a different color. Four colors, red, yellow, blue, and green, were used. Z scores of color naming; word reading; interference; weak interference index (word reading time/color-naming time), which reflects inhibitory abilities when the interference produced by an inappropriate answer is weak; and strong interference index (interference time/color naming time), which reflects inhibitory abilities when the interference produced by an inappropriate answer is strong (ie, classic "Stroop effect"); and the number of errors were recorded.

### MR Imaging Protocol

The morning after the clinical assessment, all participants underwent a brain MR imaging on a 3T scanner (Magnetom Skyra; Siemens, Erlangen, Germany). The protocol included a T1-weighted MPRAGE sequence (TR = 1690 ms, TE = 2.54 ms, flip angle =  $9^\circ$ , section thickness = 1 mm, 176 sections, isotropic voxel size =  $1 \text{ mm}^3$ ), a FLAIR sequence (TR = 5000 ms, TE = 384 ms, TI = 1800 ms, flip angle =  $120^\circ$ , section thickness = 0.9 mm, 160 sections, voxel size =  $0.4 \times 0.4 \times 0.9 \text{ mm}^3$ ), and a BOLD sensitive functional sequence (TR = 2660 ms, TE = 30 ms, echo-train length = 36, flip angle =  $90^\circ$ , section thickness = 3 mm, in-plane resolution =  $2.39 \times 2.39 \text{ mm}$ , 44 sections, no intersection gap, interleaved acquisition, 200 volumes, acquisition time = 8 minutes). For rsfMRI, acquisitions were started 10 minutes after participants were asked to lie still and awake with their eyes closed.

### Structural Data Processing

A neuroradiologist blinded to the patients' clinical diagnoses processed structural T1-MPRAGE data by using SPM8 (<http://www.fil.ion.ucl.ac.uk/spm/>) running on Matlab 2014a (MathWorks, Natick, Massachusetts). The preprocessing pipeline included the following steps: realignment, segmentation (gray matter, white matter, CSF), normalization in Montreal Neurological Institute (MNI) space, and smoothing with default settings. ROIs around the basal ganglia (caudate nucleus, putamen, and pallidum) were automatically delineated on the average normalized T1-MPRAGE template of all subjects by using the Anatomical Automatic Labeling (SPM8) atlas in MNI space.

At the patient level, we also extracted normalized volume [Normalized Volume in Percentages =  $100 \times (\text{Brain Structure}$

Absolute Volume in Milliliters/Total Intracranial Volume in Milliliters)] of the caudate nucleus, putamen, pallidum, and cingulate cortex from native T1-MPRAGE by using the algorithm MorphoBox.<sup>13</sup> White matter hyperintensity lesions (WMHL) were also semiautomatically delineated on FLAIR images by using MRICron software (<https://www.nitrc.org/projects/mricron>) to obtain WMHL volume, which was also normalized according to total intracranial volume.

### Resting-State Data Processing

All rsfMRI ( $n = 53$ ) was preprocessed by a neuroradiologist, blinded to the patients' clinical diagnoses, with SPM8 running on Matlab 2014a. For each participant, the first 5 volumes were discarded to allow equilibration of the magnetic field and the participants' adaptation to the scanning noise.<sup>14</sup> The preprocessing pipeline included the following steps: section timing, realignment, coregistration, normalization in MNI-space, and smoothing by using a Gaussian filter with a full width at half maximum of 8 mm. Preprocessed rsfMRI data, structural T1-MPRAGE data, and predefined ROIs were imported in the toolbox Conn ([www.nitrc.org/projects/conn](http://www.nitrc.org/projects/conn)). Additional preprocessing included de-noising with voxelwise removal of linear trends over each patient's rsfMRI dataset and temporal low-pass filtering ( $0.009 \text{ Hz} < f < 0.08 \text{ Hz}$ ) to retain low-frequency fluctuations. The BOLD signal of white matter and CSF and movement parameters were used as covariates to remove unwanted physiologic and motion artifact effects.<sup>15</sup> First-level analyses (within subjects) then used a weighted General Linear Model for estimation of the Fisher-transformed bivariate correlation coefficients between the seed time-series and each voxel time-series. Functional connectivity measures were tested at the second level (between subjects) by using random effects analyses on a seed-to-voxel basis by using the ROIs defined above. Contrasts among groups (controls, VP, and PD) were generated as 2-tailed  $t$  tests with a combination of a voxelwise threshold (uncorrected  $P < .001$ ) and a cluster-extent threshold (family-wise error rate-corrected  $P < .05$ ), while controlling for age.<sup>16</sup> To explore the potential effect of basal ganglia volumes on functional connectivity, we used normalized basal ganglia volumes secondarily as covariates.

Because Stroop Task performance was related to activity of the anterior cingulate cortex,<sup>17</sup> we also performed an ROI-to-ROI analysis between the basal ganglia and the anterior cingulate cortex subregions (subgenual, perigenual, and supragenual). Subregions were segmented on the anterior cingulate cortex AAL atlas region on the basis of the parcellation proposed by Vogt.<sup>18</sup> Contrasts between groups were generated as 2-tailed  $t$  tests with a combination of a voxelwise threshold (uncorrected  $P < .001$ ) and a cluster-extent threshold (false-discovery rate-corrected  $P < .05$ ), while controlling for age.<sup>16</sup>

### Statistical Analysis

Continuous variables are presented as mean  $\pm$  SD. Three groups were defined according to clinical evaluation: VP, PD, and controls. Patient characteristics were compared by using a nonparametric Kruskal-Wallis test for continuous variables and a Fisher exact test for categorical variables. The Wilcoxon signed rank test was used for post hoc analysis. A  $P$  value  $< .05$  was considered

statistically significant. The potential relation between clinical scores and MR volumetry or rsfMRI results was assessed by a 2-sided Spearman correlation coefficient ( $\rho$ ). All statistics were performed with STATA 13.1 software (StataCorp, College Station, Texas).

## RESULTS

### Study Population Clinical and Volumetric Characteristics

None of the participants were reported to have fallen asleep during the rsfMRI sequence. Of the 62 participants, 4 controls and 5 patients with PD did not remain lying down during the whole rsfMRI sequence due to back pain and/or uncontrolled head motion and were thus excluded from the analysis. In total, we analyzed 53 individual datasets: 23 controls (mean age,  $78 \pm 2$  years; male/female ratio, 17:6), 8 patients with VP (mean age,  $78 \pm 2$  years; male/female ratio, 7:1), and 22 patients with PD (mean age,  $80 \pm 5$  years; male/female ratio, 15:7).

Clinical and MR imaging volumetric characteristics of subjects included in the rsfMRI analysis ( $n = 53$ ) are reported in the Online Table. Regarding the Mattis Dementia Rating Scale, patients with VP had significantly lower scores for attention and a lower total score than controls. Regarding the Victoria Stroop Task, patients with VP had significantly lower scores for color naming and word reading and a higher number of errors than controls. Patients with VP also had lower scores for color naming than patients with PD. MR imaging volumetry demonstrated caudate nucleus hypertrophy and higher WMHL volumes in patients with VP, but similar cingulate cortex volumes compared with patients with PD and controls. Caudate nucleus and WMHL volumes were highly correlated ( $n = 53$ ,  $\rho = 0.75$ ,  $P < .0001$ ). There was no significant correlation between the caudate nucleus volume and neuropsychological metrics.

### Increased Functional Connectivity in Patients with Vascular Parkinsonism

MNI coordinates of regions with increased functional connectivity from the basal ganglia to the cingulate cortex in patients with VP, on seed-to-voxel analysis, are reported in the Table. Functional connectivity of both the left and right caudate nuclei to the anterior cingulate cortex was increased in patients with VP compared with controls as well as functional connectivity of the right caudate nucleus to the anterior cingulate cortex compared with patients with PD (Fig 1A–C). On ROI-to-ROI analysis, only right caudate nucleus functional connectivity with the bilateral perigenual but not the supragenual anterior cingulate cortex was increased in patients with VP compared with those with PD. Both on seed-to-voxel and ROI-to-ROI analyses, the increased functional connectivity of the right caudate nucleus disappeared when controlling for caudate volume. Indeed, the caudate nucleus volume positively correlated ( $\rho = 0.44$ ,  $P = .016$ ) with the functional connectivity between the right caudate nucleus and the perigenual anterior cingulate cortex (Fig 1D).

We did not find any significant correlation between neuropsychological metrics and the right caudate nucleus to perigenual anterior cingulate cortex functional connectivity (all  $P$  values  $> .11$ ).

### Basal ganglia functional connectivity with the cingulate cortex in patients with VP

Seeds	Regions	Cluster MNI Coordinates			Cluster Size (Voxels)	Cluster Uncorrected P Value	Cluster FWE-Corrected P Value
		X	Y	Z			
Functional connectivity significantly increased in patients with VP							
Comparison with controls							
Right caudate	Anterior cingulate gyrus	6	22	12	54	<.0001	<.0001
Left caudate	Anterior cingulate gyrus	-18	10	32	15	.000003	.00004
Comparison with patients with PD							
Right caudate	Anterior cingulate gyrus, right paracingulate gyrus, left paracingulate gyrus	2	44	2	226	.0019	.026
Functional connectivity significantly decreased in patients with VP							
Comparison with controls							
Right caudate	Posterior cingulate gyrus, precuneus cortex	2	-42	36	658	.000004	.00006
Left caudate	Posterior cingulate gyrus, precuneus cortex	2	-60	52	520	.00002	.0002

Note:—FWE indicates family-wise error.

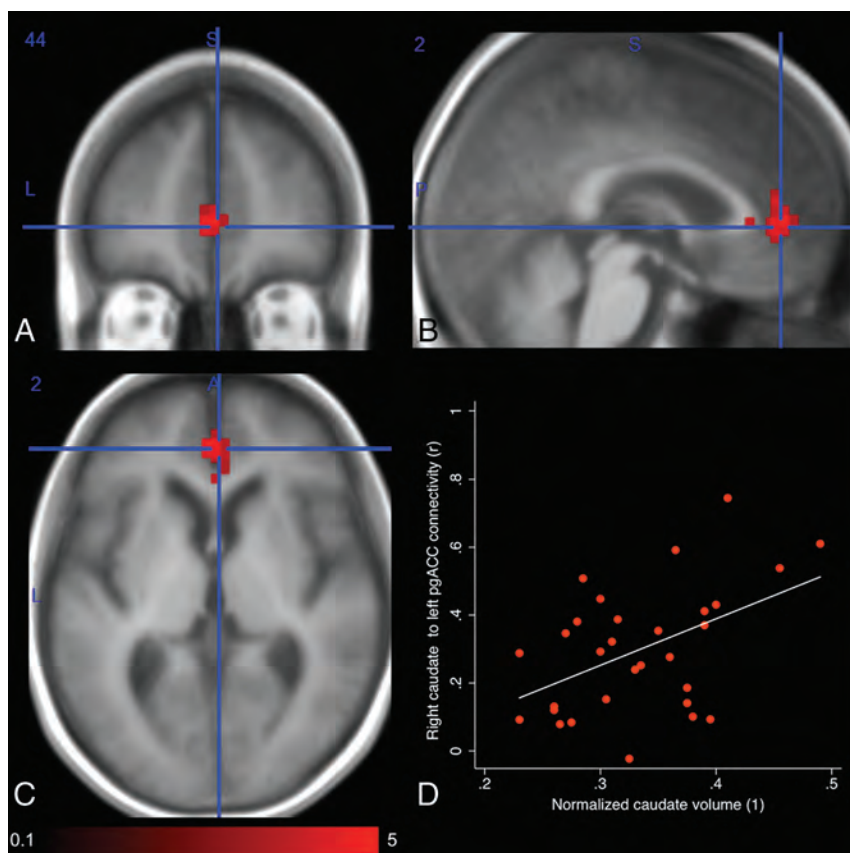


**FIG 1.** Comparison of the functional connectivity of the right caudate nucleus between patients with vascular parkinsonism and those with Parkinson disease. Contrast is generated as a 2-tailed  $t$  test (scale:  $t = 0.1-5$ ) with a combination of a voxelwise threshold (uncorrected  $P < .001$ ) and a cluster-extent threshold (family-wise error rate-corrected  $P < .05$ ), while controlling for age. Increased functional connectivity of the right caudate nucleus to the perigenual anterior cingulate cortex (MNI coordinates:  $x = 2, y = 44, z = 2$ ) in axial (A), sagittal (B), and coronal (C) planes is observed. Functional connectivity of the right caudate nucleus to the perigenual anterior cingulate cortex positively correlates with normalized caudate nucleus volumes (D).

#### Decreased Functional Connectivity in Patients with Vascular Parkinsonism

MNI coordinates of regions with decreased functional connectivity from the basal ganglia to the cingulate cortex in patients with VP are reported in the Table. Right and left caudate nuclei functional connectivity with the posterior cingulate cortex and ipsilat-

eral precuneus cortex was decreased in patients with VP compared with controls (Fig 2A–C). The difference did not disappear when controlling for caudate volume. Caudate nucleus functional connectivity with the posterior cingulate cortex was not correlated with the caudate volume ( $\rho = -0.12, P = .50$ ).

Right caudate nucleus functional connectivity with the posterior cingulate cortex was negatively correlated with the number of errors on the Victoria Stroop Task ( $\rho = -0.51, P = .0003$ ) (Fig 2D).

#### DISCUSSION

The main findings in patients with VP may be summarized as follows: 1) They have impaired attention, resistance to interference, and inhibitory control and an increased number of errors on the Stroop Task; 2) caudate nucleus functional connectivity with the perigenual anterior cingulate cortex was increased, and caudate nucleus functional connectivity with the posterior cingulate cortex was decreased; and 3) caudate nucleus functional connectivity with the perigenual anterior cingulate cortex positively correlated with caudate nucleus volume.

#### Cognitive Impairment in Vascular Parkinsonism

Vascular parkinsonism is commonly described as a secondary parkinsonism subtype, morphologically characterized

by more white matter and basal ganglia lesions than age-matched patients with Parkinson disease.<sup>7</sup> However, these unspecific brain lesions may also be encountered in patients with no parkinsonian syndrome, especially in the elderly population. Whether these lesions contribute to parkinsonism or are only concomitant is still unclear; this uncertainty leads to persistent controversy on the

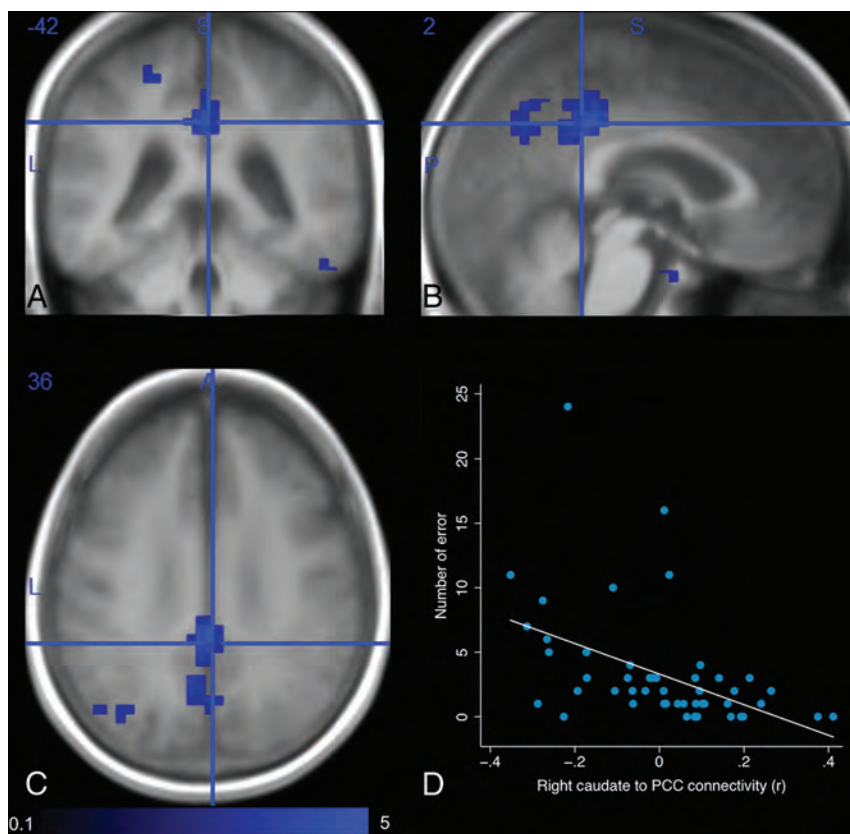


**FIG 2.** Comparison of the functional connectivity of the right caudate nucleus between patients with vascular parkinsonism and controls. Contrast is generated as a 2-tailed *t* test (scale:  $t = 0.1-5$ ) with a combination of a voxelwise threshold (uncorrected  $P < .001$ ) and a cluster-extent threshold (family-wise error rate-corrected  $P < .05$ ), while controlling for age. Decreased functional connectivity of the right caudate nucleus to the posterior cingulate cortex (MNI coordinates:  $x = 2$ ,  $y = -42$ ,  $z = 36$ ) in the axial (A), sagittal (B), and coronal (C) planes is observed. Functional connectivity of the right caudate nucleus to the posterior cingulate cortex negatively correlates with the number of errors during the Stroop Task (D).

reality of this syndrome.<sup>19</sup> Clinically, severe cognitive decline has been described as a hallmark in patients with so-called vascular parkinsonism.<sup>4,20-22</sup> In agreement, we observed that patients with VP had lower total scores on the Mattis Dementia Rating Scale than healthy controls of similar educational attainment level, reflecting global cognitive impairment. On the Victoria Stroop Task, they specifically had impaired attention and resistance to interference, reduced inhibitory control, and an increased number of errors, findings also concordant with recent studies.<sup>3,4</sup> The number of patients receiving levodopa, the dose of levodopa, and the time between last intake and clinical assessment were similar between patients with VP and those with PD. This finding suggests that levodopa medication did not influence cognitive status, as previously reported,<sup>23-25</sup> and that it may not account for functional imaging differences in our study.

#### **Caudate Nucleus Functional Connectivity and Relation to Volume**

Caudate nucleus functional connectivity with the anterior cingulate cortex has been reported,<sup>16,26-28</sup> especially with the perigenual anterior cingulate cortex.<sup>26,29</sup> In the present study, we found that caudate nuclei functional connectivity with the perigenual anterior cingulate cortex was increased in patients with VP

compared with controls and patients with PD. Caudate nucleus functional connectivity with the posterior cingulate cortex was also decreased in patients with VP compared with controls. While cingulate cortex volumes were similar across study groups, patients with VP exhibited higher caudate volumes. The increased functional connectivity between the caudate nucleus and the perigenual anterior cingulate cortex, moreover, disappeared when controlling for caudate nucleus volume. Rauch et al<sup>30</sup> demonstrated that lesions of the anterior cingulate cortex created for treatment of obsessive-compulsive disorder induced caudate nucleus atrophy, which confirmed structural interaction. Inversely, caudate hypertrophy was observed in patients during the subacute phase of ischemic corticostriatal stroke.<sup>31</sup> Thus, we observed that the caudate volume was positively correlated with the WMHL volume, a marker of the severity of brain small-vessel disease.<sup>1</sup> This correlation seems to indicate that repeat ischemic events observed in patients with VP could induce caudate hypertrophy, which may lead to increased caudate nucleus functional connectivity with the perigenual anterior cingulate cortex at resting-state. The time course of caudate hypertrophy and resting-state

functional connectivity increase following ischemic events, however, remains unknown and could be evaluated by longitudinal morphologic and rsfMRI studies.

#### **Relation between Cognitive Impairment and Functional Connectivity Changes**

At resting-state, in patients with VP, caudate nucleus functional connectivity with the perigenual anterior cingulate cortex and posterior cingulate cortex was altered, with both the perigenual anterior cingulate cortex and posterior cingulate cortex being part of the default mode network.<sup>32</sup> Patients with VP also had concomitant impaired attention on the Mattis Dementia Rating Scale and impaired resistance to interference and inhibitory control as well as an increased number of errors on the Stroop Task.

Concerning attention, increased perigenual anterior cingulate cortex activation has been associated with attentional lapses in healthy subjects.<sup>32</sup> Moreover, in normal aging, reduced resting-state connectivity of the posterior cingulate cortex has been correlated with less effective executive function and processing speed.<sup>33</sup> Lin et al<sup>34</sup> also recently reported that high resting-state posterior cingulate cortex connectivity within the default mode network was associated with low reaction time during atten-

tional tasks. In agreement, we observed that resting-state caudate nucleus functional connectivity with the perigenual anterior cingulate cortex was increased and resting-state caudate nucleus functional connectivity with the posterior cingulate cortex was decreased in patients with VP, both of which could contribute to impaired attention on the Mattis Dementia Rating Scale.

With regard to resistance to interference and inhibitory control, the perigenual anterior cingulate cortex has also been described as a task-negative region in which a deactivation is observed in response to a specific cognitive task. During the Stroop Task,<sup>17</sup> a negative BOLD response in the perigenual anterior cingulate region is induced with concomitant increased activity in the supragenual anterior cingulate region.<sup>35</sup> Stroop performance was thus negatively correlated with BOLD signal-intensity change in the perigenual anterior cingulate cortex. In patients with VP, increased functional connectivity between the caudate nucleus and the perigenual anterior cingulate cortex at resting-state was observed with concomitant impaired inhibitory control and resistance to interference on the Stroop Task. This finding may suggest incomplete deactivation of the perigenual anterior cingulate cortex during the Stroop Task. Abnormally increased resting-state activity may thus not be sufficiently suppressed during the task, which could result in impaired inhibitory control and resistance to interference.

With regard to response errors, we observed an increased number of errors on the Stroop Task in patients with VP. Increased resting-state default mode network activation was described before response errors.<sup>36</sup> Two studies also showed that stop-signal errors are preceded by greater resting-state activity in the perigenual anterior cingulate cortex.<sup>37</sup> Although we observed a concomitant increased number of errors on the Stroop Task and increased caudate nucleus functional connectivity to the perigenual anterior cingulate cortex, we did not find any significant correlation between them and could thus not confirm any causal link in patients with VP. However, the number of errors on the Stroop task was negatively correlated with functional connectivity of the caudate nucleus to the posterior cingulate cortex. As discussed above, resting-state connectivity of the posterior cingulate cortex was positively correlated with attentional task performance.<sup>34</sup> This correlation suggests that the higher number of errors could be due rather to attention impairment in patients with VP, but it needs confirmatory studies.

### Study Limitations

We have to address some limitations in our study. First, we report results in a small population of patients with VP due to the low incidence of the disease, the focus on an elderly population, and the application of restrictive inclusion criteria to limit confounding factors such as exposure to neuroleptic drugs, brain traumatic injury, or stroke. While the observed functional connectivity differences were highly significant and are concordant with brain spatial distribution of cognitive function reported in the literature, correlations with clinical scores were weak. This outcome might be due to underpowered analysis, but cognitive decline could also result from impairment of functional connectivity between structures other than the basal ganglia and cingulate cortex. Second, because we focused on subjects older than 70 years of age,

similar study should be performed to confirm these results in younger patients. Third, the correlation between caudate volume and caudate nucleus functional connectivity with the posterior cingulate cortex was insignificant. The posterior cingulate cortex sits at the crossing of multiple connectivity networks,<sup>38</sup> with a relatively low contribution from the caudate nucleus.<sup>27</sup> Beyond analysis underpowering, low connectivity with the caudate nucleus and interference from other networks could explain why the impact of the caudate nucleus hypertrophy was insignificant or masked. Fourth, we found concomitant increased caudate nucleus functional connectivity with the perigenual anterior cingulate cortex at resting-state and impaired resistance to interference and inhibitory control in patients with VP, which suggest abnormal deactivation during the Stroop Task. This finding should be confirmed by a task fMRI study including pre-, per-, and post-task acquisitions. Finally, we demonstrated that increased caudate nucleus functional connectivity with the perigenual anterior cingulate cortex was related to caudate nucleus hypertrophy in patients with VP. The time course of caudate hypertrophy and increased resting-state connectivity after ischemic events should be evaluated by longitudinal studies.

### CONCLUSIONS

In patients with VP, cognitive impairment could be related to increased caudate nucleus functional connectivity with the perigenual anterior cingulate cortex and decreased caudate nucleus functional connectivity with the posterior cingulate cortex at resting-state. Increased caudate nucleus–perigenual anterior cingulate cortex functional connectivity positively correlated with caudate nucleus hypertrophy, which was related to WMHL volume, a marker of small-vessel disease. These findings suggest that ischemia-related remodelling may contribute to cognitive decline in patients with VP.

### REFERENCES

1. van der Holst HM, van Uden IW, Tuladhar AM, et al. **Cerebral small vessel disease and incident parkinsonism: the RUN DMC study.** *Neurology* 2015;85:1569–77 CrossRef Medline
2. Caslake R, Taylor K, Scott N, et al. **Age-, and gender-specific incidence of vascular parkinsonism, progressive supranuclear palsy, and parkinsonian-type multiple system atrophy in North East Scotland: the PINE study.** *Parkinsonism Relat Disord* 2014;20:834–39 CrossRef Medline
3. Vale TC, Caramelli P, Cardoso F. **Clinicoradiological comparison between vascular parkinsonism and Parkinson's disease.** *J Neurol Neurosurg Psychiatry* 2015;86:547–53 CrossRef Medline
4. Benitez-Rivero S, Lama MJ, Huertas-Fernandez I, et al. **Clinical features and neuropsychological profile in vascular parkinsonism.** *J Neurol Sci* 2014;345:193–97 CrossRef Medline
5. Demirkiran M, Bozdemir H, Sarica Y. **Vascular parkinsonism: a distinct, heterogeneous clinical entity.** *Acta Neurol Scand* 2001;104:63–67 CrossRef Medline
6. Rampello L, Alvano A, Battaglia G, et al. **Different clinical and evolutionary patterns in late idiopathic and vascular parkinsonism.** *J Neurol* 2005;252:1045–49 CrossRef Medline
7. Zijlmans JC, Thijssen HO, Vogels OJ, et al. **MRI in patients with suspected vascular parkinsonism.** *Neurology* 1995;45:2183–88 CrossRef Medline
8. Gibb WR, Lees AJ. **The significance of the Lewy body in the diagno-**

- sis of idiopathic Parkinson's disease. *Neuropathol Appl Neurobiol* 1989;15:27–44 CrossRef Medline
9. Zijlmans JC, Daniel SE, Hughes AJ, et al. **Clinicopathological investigation of vascular parkinsonism, including clinical criteria for diagnosis.** *Mov Disord* 2004;19:630–40 CrossRef Medline
  10. Goetz CG, Tilley BC, Shaftman SR, et al; Movement Disorder Society UPDRS Revision Task Force. **Movement Disorder Society-sponsored revision of the Unified Parkinson's Disease Rating Scale (MDS-UPDRS): scale presentation and clinimetric testing results.** *Mov Disord* 2008;23:2129–70 CrossRef Medline
  11. Bensimon G, Ludolph A, Agid Y, et al. **Riluzole treatment, survival and diagnostic criteria in Parkinson plus disorders: the NNIPPS study.** *Brain* 2009;132:156–71 CrossRef Medline
  12. Spreen O, Strauss E, eds. *A Compendium of Neuropsychological Tests: Administration, Norms, and Commentary.* New York: Oxford University Press; 1991
  13. Schmitter D, Roche A, Maréchal B, et al; Alzheimer's Disease Neuroimaging Initiative. **An evaluation of volume-based morphometry for prediction of mild cognitive impairment and Alzheimer's disease.** *Neuroimage Clin* 2015;7:7–17 CrossRef Medline
  14. Wang L, Zang Y, He Y, et al. **Changes in hippocampal connectivity in the early stages of Alzheimer's disease: evidence from resting state fMRI.** *Neuroimage* 2006;31:496–504 CrossRef Medline
  15. Behzadi Y, Restom K, Liu J, et al. **A component based noise correction method (CompCor) for BOLD and perfusion based fMRI.** *Neuroimage* 2007;37:90–101 CrossRef Medline
  16. Manza P, Zhang S, Hu S, et al. **The effects of age on resting state functional connectivity of the basal ganglia from young to middle adulthood.** *Neuroimage* 2015;107:311–22 CrossRef Medline
  17. Gruber SA, Rogowska J, Holcomb P, et al. **Stroop performance in normal control subjects: an fMRI study.** *Neuroimage* 2002;16:349–60 CrossRef Medline
  18. Vogt BA. **Pain and emotion interactions in subregions of the cingulate gyrus.** *Nat Rev Neurosci* 2005;6:533–44 CrossRef Medline
  19. Vizcarra JA, Lang AE, Sethi KD, et al. **Vascular Parkinsonism: deconstructing a syndrome.** *Mov Disord* 2015;30:886–94 CrossRef Medline
  20. Korczyn AD. **Vascular contribution to dementia in Parkinson's disease.** *Neurodegener Dis* 2010;7:127–30 CrossRef Medline
  21. Chen YF, Tseng YL, Lan MY, et al. **The relationship of leukoaraiosis and the clinical severity of vascular Parkinsonism.** *J Neurol Sci* 2014;346:255–59 CrossRef Medline
  22. Santangelo G, Vitale C, Trojano L, et al. **Differential neuropsychological profiles in Parkinsonian patients with or without vascular lesions.** *Mov Disord* 2010;25:50–56 CrossRef Medline
  23. Poletti M, Bonuccelli U. **Acute and chronic cognitive effects of levodopa and dopamine agonists on patients with Parkinson's disease: a review.** *Ther Adv Psychopharmacol* 2013;3:101–13 CrossRef Medline
  24. Molloy SA, Rowan EN, O'Brien JT, et al. **Effect of levodopa on cognitive function in Parkinson's disease with and without dementia and dementia with Lewy bodies.** *J Neurol Neurosurg Psychiatry* 2006;77:1323–28 CrossRef Medline
  25. Kulisevsky J, García-Sánchez C, Berthier ML, et al. **Chronic effects of dopaminergic replacement on cognitive function in Parkinson's disease: a two-year follow-up study of previously untreated patients.** *Mov Disord* 2000;15:613–26 Medline
  26. Torta DM, Cauda F. **Different functions in the cingulate cortex, a meta-analytic connectivity modeling study.** *Neuroimage* 2011;56:2157–72 CrossRef Medline
  27. Beckmann M, Johansen-Berg H, Rushworth MF. **Connectivity-based parcellation of human cingulate cortex and its relation to functional specialization.** *J Neurosci* 2009;29:1175–90 CrossRef Medline
  28. Hacker CD, Perlmutter JS, Criswell SR, et al. **Resting state functional connectivity of the striatum in Parkinson's disease.** *Brain* 2012;135:3699–711 CrossRef Medline
  29. Margulies DS, Kelly AM, Uddin LQ, et al. **Mapping the functional connectivity of anterior cingulate cortex.** *Neuroimage* 2007;37:579–88 CrossRef Medline
  30. Rauch SL, Kim H, Makris N, et al. **Volume reduction in the caudate nucleus following stereotactic placement of lesions in the anterior cingulate cortex in humans: a morphometric magnetic resonance imaging study.** *J Neurosurg* 2000;93:1019–25 CrossRef Medline
  31. Abela E, Seiler A, Missimer JH, et al. **Grey matter volumetric changes related to recovery from hand paresis after cortical sensorimotor stroke.** *Brain Struct Funct* 2015;220:2533–50 CrossRef Medline
  32. Weissman DH, Roberts KC, Visscher KM, et al. **The neural bases of momentary lapses in attention.** *Nat Neurosci* 2006;9:971–78 CrossRef Medline
  33. Damoiseaux JS, Beckmann CF, Arigita EJ, et al. **Reduced resting-state brain activity in the "default network" in normal aging.** *Cereb Cortex* 2008;18:1856–64 CrossRef Medline
  34. Lin P, Yang Y, Jovicich J, et al. **Static and dynamic posterior cingulate cortex nodal topology of default mode network predicts attention task performance.** *Brain Imaging Behav* 2016;10:212–25 CrossRef Medline
  35. Leung HC, Skudlarski P, Gatenby JC, et al. **An event-related functional MRI study of the Stroop color word interference task.** *Cereb Cortex* 2000;10:552–60 CrossRef Medline
  36. Eichele T, Debener S, Calhoun VD, et al. **Prediction of human errors by maladaptive changes in event-related brain networks.** *Proc Natl Acad Sci U S A* 2008;105:6173–78 CrossRef Medline
  37. Li CS, Yan P, Bergquist KL, et al. **Greater activation of the "default" brain regions predicts stop signal errors.** *Neuroimage* 2007;38:640–48 CrossRef Medline
  38. Leech R, Sharp DJ. **The role of the posterior cingulate cortex in cognition and disease.** *Brain* 2014;137:12–32 CrossRef Medline

# Prognostic Value of Labyrinthine 3D-FLAIR Abnormalities in Idiopathic Sudden Sensorineural Hearing Loss

J.I. Lee, R.G. Yoon, J.H. Lee, J.W. Park, M.H. Yoo, J.H. Ahn, J.W. Chung, and H.J. Park

## ABSTRACT

**BACKGROUND AND PURPOSE:** According to recent research, modern MR imaging can detect the presence of abnormalities on labyrinthine. Our aim was to report the patterns and prognostic role of abnormal findings on labyrinthine imaging in patients with sudden sensorineural hearing loss.

**MATERIALS AND METHODS:** This study comprised 113 patients who were diagnosed with unilateral sudden sensorineural hearing loss and underwent 3T MR imaging, including pre-/postcontrast 3D fluid-attenuated inversion recovery and T1-weighted imaging. We analyzed abnormalities on MR imaging and correlated them with audiometric results.

**RESULTS:** Thirty-one (27%) patients showed abnormal findings on labyrinthine MR imaging in the affected ear. The initial/final hearing levels of the MRI+ group ( $91 \pm 25/73 \pm 27$  dB hearing loss) were significantly worse than those of the MRI- group ( $69 \pm 30/48 \pm 24$  dB hearing loss). The incidence of abnormalities on labyrinthine MR imaging was significantly lower (3 of 40, 8%) in 40 patients with initial mild-to-moderate hearing loss than in those with profound hearing loss (16 of 34, 47%). Considering hearing improvement by the Siegel criteria, the rate of complete or partial recovery was significantly higher in the MRI- group (34%) than in the MRI+ group (10%). In patients with initial severe or profound hearing loss, the MRI- group showed greater hearing improvement ( $38 \pm 21$  dB) than the MRI+ group ( $23 \pm 22$  dB).

**CONCLUSIONS:** Abnormalities on labyrinthine MR imaging were found in 27% of patients with sudden sensorineural hearing loss. The initial hearing loss was worse in the MRI+ group than in the MRI- group. In patients with initial severe and profound hearing loss, the presence of abnormalities on labyrinthine MR imaging indicated a poor prognosis.

**ABBREVIATIONS:** DPOAE = distortion product otoacoustic emissions; HL = hearing loss; PTA = pure-tone average; SSNHL = sudden sensorineural hearing loss

Sudden sensorineural hearing loss (SSNHL) is caused by a variety of pathophysiologic mechanisms and can occur when cochlea or neural function or both are impaired. Viral infection and traumatic, neoplastic, immunologic, toxic, circulatory, and neurologic causes are well-known etiologic factors in 10%–15% of patients with SSNHL, but the cause is unknown in most cases.<sup>1</sup> Although there are many causes of SSNHL, temporal bone histopathologic evidence indicates that SSNHL could be caused by

viral cochleitis or cochlear neuritis, and these lesions are unlike those resulting from known vascular causes.<sup>2</sup>

MR imaging is frequently performed to evaluate patients with SSNHL, traditionally to identify brain lesions or retrocochlear lesions such as vestibular schwannoma.<sup>3</sup> Several studies reported that new MR imaging sequences can evaluate labyrinthine abnormalities (the presence of intracellular and extracellular methemoglobin or increased protein content in the membranous fluid) by using 3D fluid-attenuated inversion recovery in patients with SSNHL<sup>4-10</sup> and can distinguish endolymphatic hydrops by volumetric quantification of MR imaging.<sup>11</sup> These abnormal findings may also be a novel prognostic factor for SSNHL, but there are conflicting results about the prognostic value of abnormalities on labyrinthine MR imaging.<sup>6,9</sup>

The purpose of this study was to report the incidence of abnormalities on labyrinthine MR imaging in 113 patients with SSNHL and to evaluate the prognostic value of these abnormalities.

Received December 21, 2015; accepted after revision June 16, 2016.

From the Departments of Otolaryngology (J.I.L., J.W.P., J.H.A., J.W.C., H.J.P.) and Radiology (J.H.L.), Asan Medical Center, University of Ulsan College of Medicine, Seoul, Korea; Department of Radiology (R.G.Y.), Catholic Kwandong University International St. Mary's Hospital, Catholic Kwandong University College of Medicine, Incheon, Korea; and Department of Otolaryngology (M.H.Y.), College of Medicine, Kyungpook National University, Daegu, Korea.

J.I.L. and R.G.Y. contributed equally to this article.

Please address correspondence to Hong Ju Park, MD, PhD, Department of Otolaryngology, Asan Medical Center, University of Ulsan College of Medicine, 86 Asanbyeongwon-gil, Songpa-gu, Seoul, Korea 138-736; e-mail: dzness@amc.seoul.kr

<http://dx.doi.org/10.3174/ajnr.A4901>

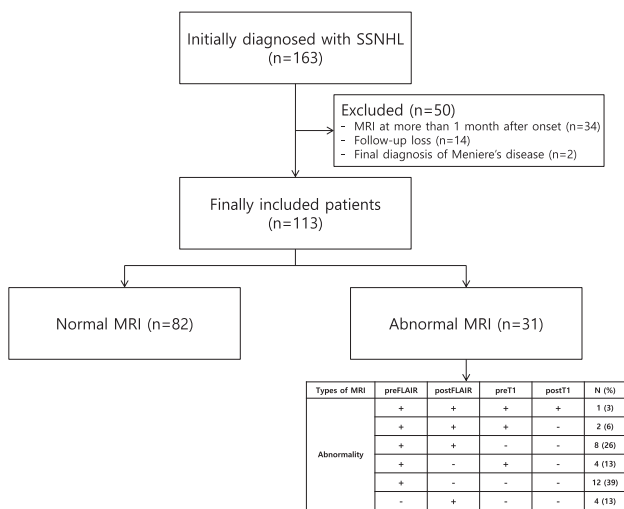


**FIG 1.** Study population excluded and enrolled in this study.

## MATERIALS AND METHODS

### Patients

From July 2011 to June 2013, 163 patients were diagnosed with unilateral SSNHL and underwent 3T MR imaging, including pre-/postcontrast 3D-FLAIR and T1-weighted imaging. The criteria used to define SSNHL were the presence of unilateral sensorineural hearing loss of  $\geq 30$  dB over at least 3 contiguous audiometric frequencies developed during a period of a few hours up to 3 days, without any obvious cause.<sup>12</sup> We excluded 34 patients who underwent MR imaging after  $>1$  month from onset, 14 patients with loss to follow-up, and 2 patients diagnosed with Menière disease during follow-up. Finally, 113 patients were included in this study (Fig 1). The protocol was approved by the institutional review board of Asan Medical Center.

### Audiologic Evaluation and MR Imaging

All patients underwent a physical examination; an otologic assessment, including an endoscopic examination of the tympanic membrane; and both pure-tone and speech audiometry. Hearing levels were evaluated with pure-tone audiometry (Madsen Orbiter 922; GN Otometrics, Taastrup, Denmark) in a sound-isolated chamber. Hearing loss (HL) was defined by the pure-tone average (PTA), calculated by using thresholds at 0.5, 1.0, 2.0, and 4.0 kHz. Audiometric assessments were performed at the time of diagnosis, 1 month later, and then after steroid treatment; the last audiometric findings obtained  $4.3 \pm 4.1$  months (median, 3.0 months) after steroid treatment were considered the definitive posttreatment result.

The severity of the initial hearing loss was classified as mild (26–40 dB), moderate (41–55 dB), moderately severe (56–70 dB), severe (71–90 dB), or profound ( $>90$  dB). If the patient did not respond to the maximum sound level, we defined the threshold as the maximum level plus 5 dB. After at least 1 month, the PTA was determined again for evaluation of the therapeutic effects. The degree of recovery was evaluated according to the Siegel criteria,<sup>13</sup> as follows: complete recovery = final hearing  $< 25$  dB HL; partial recovery = gain  $>15$  dB and a final hearing of 25 to 45 dB HL; slight improvement = gain  $>15$  dB and a final hearing of

$>45$  dB HL; and no improvement = gain  $<15$  dB and a final hearing of  $>75$  dB HL. All patients were treated with oral methylprednisolone, 48 mg/day for 9 days, and then tapered during 5 days. Intratympanic steroid injections were administered to patients experiencing insufficient hearing gains after intraoral methylprednisolone therapy.

MR imaging was performed by using a 3T MR imaging system (Achieva; Philips Healthcare, Best, the Netherlands) with an 8-channel head coil. The protocols included coronal T1- and T2-weighted turbo spin-echo, axial 3D T2-weighted, pre-/postcontrast 3D-FLAIR, and postcontrast T1-weighted imaging. For enhancement, Gd-DOTA (Dotarem; Guerbet, Aulnay-sous-Bois, France) at 0.2 mmol/kg of body weight was used, and axial 3D-FLAIR images were acquired with a time delay of 7 minutes. The delay between SSNHL onset and MR imaging was  $9.7 \pm 8.0$  days (range, 1–30 days).

Axial 3D T2-weighted imaging was performed with the following parameters: TR = 2000 ms; TE<sub>eff</sub> = 250 ms; flip angle = 90°; number of signal averages = 2; echo-train length = 70; number of encoding steps = 300; FOV = 180 × 180 mm; matrix = 300 × 300 (reconstruction matrix = 512 × 512); voxel size = 0.6 × 0.6 × 0.6 mm; slab number = 1; slab thickness = 40 mm; section thickness = 1.2 mm; spacing between sections = 0.6 mm; acquisition time = 4 minutes 58 seconds; and sensitivity encoding factor = 2.

Axial pre-/postcontrast 3D-FLAIR MR imaging was performed with the following parameters: TR = 8000 ms; TE<sub>eff</sub> = 280 ms; flip angle = 90°; number of signal averages = 1; TI = 2400 ms; fat saturation = spectral adiabatic inversion recovery; flip angle = 90°; echo-train length = 80; number of encoding steps = 300; FOV = 180 × 180 mm; matrix = 300 × 300 (reconstruction matrix = 512 × 512); voxel size = 0.6 × 0.6 × 0.6 mm; slab number = 1; slab thickness = 40 mm; section thickness = 1.2 mm; spacing between sections = 0.6 mm; acquisition time = 8 minutes 48 seconds; and sensitivity encoding factor = 2.

Axial postcontrast T1-weighted imaging was performed with the following parameters: TR = 25 ms; TE<sub>eff</sub> = 4.6 ms; flip angle = 30°; number of signal averages = 2; echo-train length = 70; number of encoding steps = 300; FOV = 180 × 180 mm; matrix = 300 × 300 (reconstruction matrix = 512 × 512); voxel size = 0.6 × 0.6 × 0.6 mm; slab number = 1; slab thickness = 40 mm; section thickness = 1.2 mm; spacing between sections = 0.6 mm; acquisition time = 3 minutes 57 seconds; and sensitivity encoding factor = 2.

Two neuroradiologists (R.G.Y. and J.H.L.) reviewed pre-/postcontrast 3D FLAIR images and pre-/postcontrast T1-weighted images to determine the presence of abnormalities on labyrinthine MR imaging in both labyrinths. They were blinded to the patient medical histories. The presence of any signal changes for the cochlea, vestibule, and semicircular canals was visually assessed and recorded separately as positive or negative (Fig 2). If there was any discrepancy between the decisions for the signal changes noted by the 2 readers, a consensus was achieved by discussion. The presence of contrast enhancement was defined as positive when comparisons of the pre- and post-contrast-enhanced 3D FLAIR images and T1-weighted images showed a distinct linear or dotlike area of increased signal intensity within the cochlea, vestibule, or semicircular canals after contrast material injection. The presence of any signal changes in

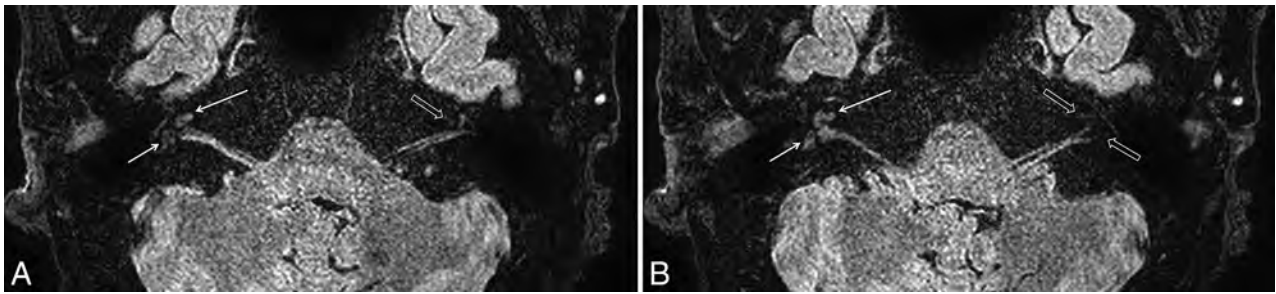


**FIG 2.** Precontrast axial scans of 3D-FLAIR MR imaging in right inner ear of a 63-year-old man with right sudden sensorineural hearing loss with vertigo. Bright signals (arrows) are visible only in the right cochlea and vestibule at the level of the basal turn (A) and midturn (B) of the cochlea and vestibule, not in the left healthy cochlea and vestibule (open arrows).

**Table 1: Clinical and demographic characteristics of patients with SSNHL**

	All (N = 113)	MRI- Group (n = 82)	MRI+ Group (n = 31)	P Value
Mean age (yr)	53 ± 14	53 ± 14	55 ± 14	.634
Sex (male/female)	51:62	38:44	13:18	.675
DM (No.) (%)	11 (10)	7 (9)	4 (13)	.490
HTN (No.) (%)	27 (24)	20 (24)	7 (23)	.840
Vertigo (No.) (%)	30 (27)	21 (26)	9 (29)	.713
Tinnitus (No.) (%)	82 (73)	61 (74)	21 (68)	.480
Ear fullness (No.) (%)	53 (47)	39 (48)	14 (45)	.820
Initial visit after onset (days)	7 ± 10	7 ± 10	9 ± 9	.076
MRI after onset (days)	10 ± 8	10 ± 8	9 ± 6	.804
ITSI before MRI (No.) (%)	16 (14)	11 (13)	5 (16)	.713

**Note:**—DM indicates diabetes mellitus; HTN, hypertension; ITSI, intratympanic steroid injection.

**Table 2: Initial and final audiologic results and classification by Siegel criteria in MRI+ and MRI- groups**

	All Cases (N = 113)	MRI- Group (n = 82)	MRI+ Group (n = 31)	P Value
Initial audiogram (mean) (dB HL)	75 ± 30	69 ± 30	91 ± 25	<.001
Severity of initial HL (No.) (%)				.005
Mild	16 (14)	15 (18)	1 (3)	
Moderate	24 (21)	22 (27)	2 (6)	
Moderately severe	15 (13)	10 (12)	5 (16)	
Severe	24 (21)	17 (21)	7 (23)	
Profound	34 (30)	18 (22)	16 (52)	
Additional ITSI (No.) (%)	79 (70)	50 (61)	29 (94)	.001
Final audiogram (mean) (dB HL)	55 ± 27	48 ± 24	73 ± 27	<.001
Improvement of hearing (ΔPTA, dB)	20 ± 24	21 ± 23	18 ± 24	.964
Improvement by Siegel criteria (No.) (%)				.003
No improvement	50 (44)	38 (46)	12 (39)	
Slight improvement	32 (28)	16 (20)	16 (52)	
Partial recovery	18 (16)	17 (21)	1 (3)	
Complete recovery	13 (12)	11 (13)	2 (6)	

**Note:**—ΔPTA indicates difference of mean pre- and posttreatment PTA; ITSI, intratympanic steroid injection.

the labyrinth was considered MRI+, and the absence of any high signal was considered MRI-.

### Statistical Analysis

The results of audiologic findings in patients with MRI+ and MRI- were compared by using the Mann-Whitney *U* test for continuous variables and the Pearson  $\chi^2$  test for categorical variables. A *P* value < .05 was considered statistically significant. Statistical analyses were conducted by using SPSS software (Version 14.0 for Windows; IBM, Armonk, New York).

### RESULTS

Thirty-one (27%) of 113 patients with SSNHL showed abnormalities on labyrinthine MR imaging in the affected ears. Between the

MRI+ and MRI- groups, there were no significant differences in age, sex, underlying disease (diabetes mellitus, hypertension), or associated symptoms (Table 1). The average period from onset to initial visit and from onset to MR imaging examination of all patients was  $7 \pm 10$  and  $10 \pm 8$  days, respectively, which was also not significantly different between the 2 groups. In the MRI+ group, 27 patients showed high signal intensity in the affected inner ears on precontrast 3D-FLAIR images, 11 of whom also showed high signal intensity on gadolinium-enhanced 3D-FLAIR images in the affected ear. Moreover, 7 of 27 patients who were MRI+ in precontrast 3D-FLAIR images also showed high signals on precontrast T1-weighted images, one of whom exhibited high signals on both pre- and postcontrast T1-weighted images. High signals on only postcontrast 3D-FLAIR images were observed in 4 patients. No patients exhibited high signals in the contralateral intact ear. Twenty-nine patients showed high signals in the cochleae, and 20 of them showed high signals in the vestibule. Two patients exhibited high signals only in the vestibule or semicircular canal (1 each).

Patients were classified into 5 categories on the basis of PTA: 16 patients with mild HL, 24 with moderate HL, 15 with moderately severe HL, 24 with severe HL, and 34 profound HL. The incidence of abnormalities on labyrinthine MR imaging was analyzed according to the initial hearing levels (Table 2). The abnormal rate was significantly lower (8%, 3 of 40) in patients with initial mild-to-moderate HL than in patients with initial profound HL (47%, 16 of 34).

The initial/final hearing levels ( $91 \pm 25/73 \pm 27$  dB HL) of the MRI+ group were significantly worse than those ( $69 \pm 30/48 \pm 24$  dB HL) of the MRI- group (Table 2). When one considers hearing improvement according to the Siegel criteria, the rate of complete or partial recovery in the MRI- group (34%) was significantly higher than that (10%) of the MRI+ group (Fig 3); however, the overall

hearing improvement of the MRI+ group ( $18 \pm 24$  dB) was not significantly worse than that of the MRI- group ( $21 \pm 23$  dB).

When analyzing the data from the patients with SSNHL with the initial severe and profound HL ( $n = 58$ ), the MRI+ group showed a significantly reduced improvement compared with that of the MRI- group. The degree of hearing improvement in patients in the MRI+ group ( $23 \pm 24$  dB) was significantly lower than that of patients in the MRI- group ( $38 \pm 27$  dB). Moreover, the final PTA of the MRI+ group ( $80 \pm 27$  dB HL) was significantly higher than that of the MRI- group ( $60 \pm 23$  dB HL) (Fig 4).

Ten patients showed low-frequency hearing loss at the initial PTA, according to the classification of Mazzoli et al.<sup>14</sup> Only 1 patient (10%) showed an MRI+ finding. By the Siegel criteria,

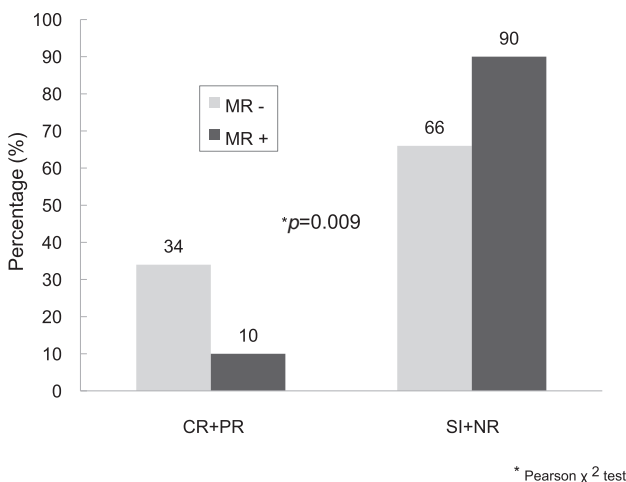


**FIG 3.** Hearing improvement according to the Siegel criteria in the MRI+ and MRI- groups. CR indicates complete recovery; PR, partial recovery; SI, slight improvement; NR, no recovery.

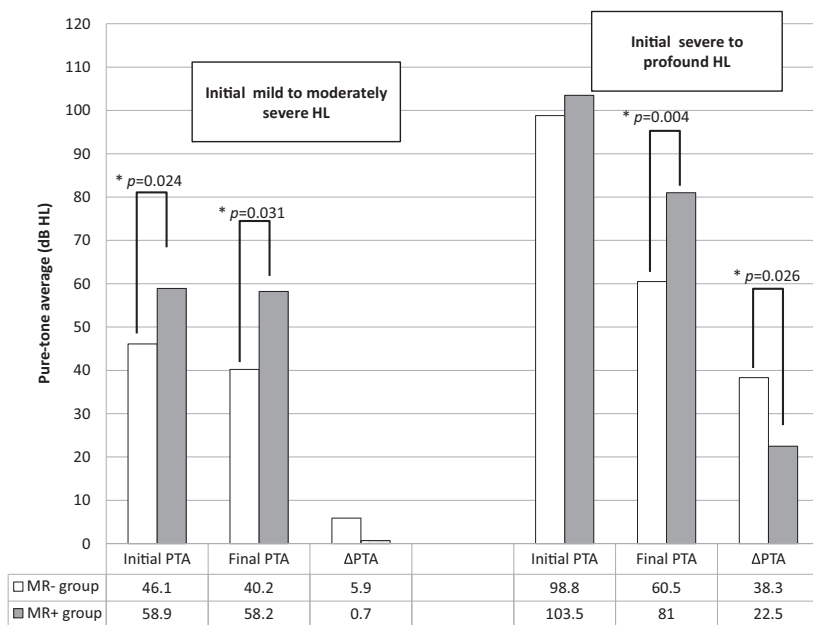


**FIG 4.** Initial pretreatment and final posttreatment audiologic findings and the improvement of hearing ( $\Delta$ PTA) in the MRI- and MRI+ groups according to the initial hearing loss.  $\Delta$ PTA indicates the difference of mean pre- and posttreatment.

7 (70%) recovered completely or partially, and another 3 (30%) showed no improvement. Patients with the low-frequency type showed a low incidence of abnormal findings on MR imaging and a better prognosis compared with patients with other types.

## DISCUSSION

Although contrast-enhanced MR imaging has been used to rule out retrocochlear lesions in patients with SSNHL, modern MR imaging can also detect the presence of abnormalities on labyrinthine MR imaging. It was previously reported that increased protein concentrations are characterized by high signal intensity on 3D-FLAIR imaging,<sup>5,8,10,15</sup> which was reported to be more sensitive than T1- and T2-weighted MR imaging.<sup>6,7</sup> Moreover, 3D-FLAIR imaging can detect the breakdown of the blood-labyrinth barrier as an enhancement of fluid signal in the inner ear and/or nerve signal after gadolinium injection, owing to its high sensitivity to magnetic susceptibility.<sup>8,9</sup> Typically, the perilymph and endolymph are isointense to CSF on all MR imaging sequences. It was reported that healthy subjects did not exhibit high signal intensity in the inner ear with or without gadolinium enhancement on 3D-FLAIR images until 10 minutes after gadolinium injection.<sup>16</sup>

In our study, 3D-FLAIR provided a diagnostic sensitivity for 27% (31 of 113) of patients with SSNHL who were otherwise healthy. We observed high signal intensity in the affected ears only, not in the contralateral intact ears, confirming the high reliability of 3D-FLAIR MR imaging. Our abnormality rate on labyrinthine MR imaging (27%) was similar to those (26%–34%) of previous reports,<sup>9,17</sup> though others reported high abnormality rates (57%–65%).<sup>6,7</sup> We speculate that both inflammation and hemorrhage might increase the protein content, resulting in positive findings on 3D-FLAIR. Temporal bone histopathologic evidence indicated that SSNHL may be caused by viral cochleitis or cochlear neuritis rather than vascular etiologies.<sup>2</sup>

Intralabyrinthine hemorrhage might be differentiated from increased protein content when high signal intensities are observed in both T1 and 3D-FLAIR imaging.<sup>6,18</sup> According to these criteria, intralabyrinthine hemorrhage could be suspected in 6% (7 of 113) of patients in this study. Whether the abnormalities on labyrinthine MR imaging indicate increased protein content induced by an inflammatory process or intralabyrinthine hemorrhage requires further clarification.

In the current study, initial hearing levels in the MRI+ group ( $91 \pm 25$  dB HL) were significantly worse than those of the MRI- group ( $69 \pm 30$  dB HL); this finding suggests that extensive damage to the inner ear structures correlates with a positive result on 3D-FLAIR. The incidence of abnormalities on labyrinthine MR imaging was low (3, 8%) in 40 patients with initial mild-to-moderate

HL and increased to 47% (16 of 34) in patients with profound HL, which was a significant difference. These findings are comparable with those of previous reports in which the initial PTA exhibited a good correlation with 3D-FLAIR MR imaging findings and 3D-FLAIR hyperintensity significantly correlated with vertigo, suggesting extensive inner ear damage<sup>6</sup>; however, other studies reported no significant differences in the initial PTA findings, regardless of abnormalities on MR imaging.<sup>7,9</sup> Differences in study populations, time intervals between SSNHL onset and MR imaging, and masking effects induced by steroid treatment could explain these differences.<sup>6</sup> Objective criteria for the presence of high signal intensity on MR images also need to be determined to mitigate any potential differences arising from this issue.

Regarding the prognostic value of abnormalities on labyrinthine MR imaging, recent studies show inconsistent results. Investigations of 3D-FLAIR demonstrated that high signal intensities in the cochlea on precontrast 3D-FLAIR images are associated with a poor prognosis for hearing<sup>7,9</sup>; however, another study showed that hyperintense signals on 3D FLAIR or gadolinium-enhanced MR imaging were not significantly correlated with hearing improvement or posttreatment PTA.<sup>6</sup>

In our study, 3D-FLAIR MR imaging findings closely correlated with the severity of hearing loss. Furthermore, posttreatment hearing levels in the MRI+ group were worse than those of the MRI- group. Moreover, the rate of complete or partial recovery in the MRI- group (34%) was significantly higher than that of the MRI+ group (10%) when hearing improvement was defined according to the Siegel criteria; however, the MRI+ group might have experienced poor hearing outcomes because they had poorer initial hearing levels than the MRI- group, and patients with a high level of initial HL exhibited a poorer hearing prognosis.<sup>7,9</sup> Our findings, in which the overall hearing improvement of the MRI+ group (18 ± 24 dB) was not significantly worse than that of the MRI- group (21 ± 23 dB), support this hypothesis; thus, we analyzed the hearing improvement according to the initial hearing levels and observed that the hearing improvement of the MRI+ group (23 ± 24 dB) was significantly less than that of the MRI- group (38 ± 27 dB) when the initial hearing loss was severe or profound (Fig 4). Our findings demonstrate that patients with SSNHL with mild or moderate initial HL rarely exhibited abnormalities on labyrinthine MR imaging (8%, 3 of 40), which were without any significant prognostic value. By contrast, patients with SSNHL with initial severe or profound HL frequently exhibited abnormalities on labyrinthine MR imaging (40%, 23 of 58), which were significantly associated with a poor prognosis.

Similar findings were reported by using distortion product otoacoustic emissions (DPOAE) in patients with SSNHL.<sup>19</sup> The function of the outer hair cells as measured by DPOAE, which indicates intact labyrinthine function, was relatively preserved in patients with initial mild-to-moderate HL, and their hearing recovery was not associated with the DPOAE results. This finding is analogous to our findings in which labyrinthine involvement was rare and not related to hearing improvement in patients with initial mild-to-moderate HL; however, patients with preserved DPOAE and initial moderately severe-to-profound HL, who would be analogous to patients with initial severe-or-profound HL in the MRI- group in our study, had a good prognosis.

A large-scale quantitative study involving additional tests, including pure-tone audiometry and DPOAE, may help provide a detailed understanding of the pathophysiology of SSNHL and determine the prognostic value of abnormalities on labyrinthine MR imaging. In this study, we could not correlate MR imaging involvement of different inner ear structures with clinical symptoms because of the small study population.

## CONCLUSIONS

Abnormalities on labyrinthine MR imaging were found in 27% of patients with SSNHL. Notably, the initial HL in the MRI+ group was worse than that of the MRI- group. In patients with initial severe and profound hearing loss, the presence of an abnormality on labyrinthine MR imaging was a poor prognostic factor. Further studies with a larger study population are needed to clarify the distribution of specific patterns of abnormalities on MR imaging and their clear relationship with hearing improvement.

## REFERENCES

- Hughes GB, Freedman MA, Haberkamp TJ, et al. **Sudden sensorineural hearing loss.** *Otolaryngol Clin North Am* 1996;29:393–405 Medline
- Schuknecht HF, Donovan ED. **The pathology of idiopathic sudden sensorineural hearing loss.** *Arch Otorhinolaryngol* 1986;243:1–15 CrossRef Medline
- Aarnisalo AA, Suoranta H, Ylikoski J. **Magnetic resonance imaging findings in the auditory pathway of patients with sudden deafness.** *Otol Neurotol* 2004;25:245–49 CrossRef Medline
- Weissman JL, Curtin HD, Hirsch BE, et al. **High signal from the otic labyrinth on unenhanced magnetic resonance imaging.** *AJNR Am J Neuroradiol* 1992;13:1183–87 Medline
- Cervantes SS, Barrs DM. **Sudden sensorineural hearing loss associated with intralabyrinthine hemorrhage.** *Otol Neurotol* 2015;36:e134–35 CrossRef Medline
- Berrettini S, Seccia V, Fortunato S, et al. **Analysis of the 3-dimensional fluid-attenuated inversion-recovery (3D-FLAIR) sequence in idiopathic sudden sensorineural hearing loss.** *JAMA Otolaryngol Head Neck Surg* 2013;139:456–64 CrossRef Medline
- Yoshida T, Sugiura M, Naganawa S, et al. **Three-dimensional fluid-attenuated inversion recovery magnetic resonance imaging findings and prognosis in sudden sensorineural hearing loss.** *Laryngoscope* 2008;118:1433–37 CrossRef Medline
- Sugiura M, Naganawa S, Teranishi M, et al. **Three-dimensional fluid-attenuated inversion recovery magnetic resonance imaging findings in patients with sudden sensorineural hearing loss.** *Laryngoscope* 2006;116:1451–54 CrossRef Medline
- Lee HY, Jung SY, Park MS, et al. **Feasibility of three-dimensional fluid-attenuated inversion recovery magnetic resonance imaging as a prognostic factor in patients with sudden hearing loss.** *Eur Arch Otorhinolaryngol* 2012;269:1885–91 CrossRef Medline
- Kim DY, Lee JH, Goh MJ, et al. **Clinical significance of an increased cochlear 3D fluid-attenuated inversion recovery signal intensity on an MR imaging examination in patients with acoustic neuroma.** *AJNR Am J Neuroradiol* 2014;35:1825–29 CrossRef Medline
- Gürkov R, Berman A, Dietrich O, et al. **MR volumetric assessment of endolymphatic hydrops.** *Eur Radiol* 2015;25:585–95 CrossRef Medline
- Wilson WR, Byl FM, Laird N. **The efficacy of steroids in the treatment of idiopathic sudden hearing loss: a double-blind clinical study.** *Arch Otolaryngol* 1980;106:772–76 CrossRef Medline
- Siegel LG. **The treatment of idiopathic sudden sensorineural hearing loss.** *Otolaryngol Clin North Am* 1975;8:467–73 Medline
- Mazzoli M, Van Camp G, Newton V, et al. **Recommendations for the description of genetic and audiological data for families with non-**

- syndromic hereditary hearing impairment. *Audiol Med* 2003;1:148–50 CrossRef
15. Melhem ER, Jara H, Eustace S. **Fluid-attenuated inversion recovery MR imaging: identification of protein concentration thresholds for CSF hyperintensity.** *AJR Am J Roentgenol* 1997;169:859–62 CrossRef Medline
16. Naganawa S, Komada T, Fukatsu H, et al. **Observation of contrast enhancement in the cochlear fluid space of healthy subjects using a 3D-FLAIR sequence at 3 Tesla.** *Eur Radiol* 2006;16:733–37 CrossRef Medline
17. Ryu IS, Yoon TH, Ahn JH, et al. **Three-dimensional fluid-attenuated inversion recovery magnetic resonance imaging in sudden sensorineural hearing loss: correlations with audiologic and vestibular testing.** *Otol Neurotol* 2011;32:1205–09 CrossRef Medline
18. Noguchi K, Seto H, Kamisaki Y, et al. **Comparison of fluid-attenuated inversion-recovery MR imaging with CT in a simulated model of acute subarachnoid hemorrhage.** *AJNR Am J Neuroradiol* 2000;21:923–27 Medline
19. Park H, Lee Y, Park M, et al. **Short-term changes of hearing and distortion product otoacoustic emissions in sudden sensorineural hearing loss.** *Otol Neurotol* 2010;31:862–66 CrossRef Medline

# Prospective Validation of Two 4D-CT–Based Scoring Systems for Prediction of Multigland Disease in Primary Hyperparathyroidism

S. Sho, M. Yilma, M.W. Yeh, M. Livhits, J.X. Wu, J.K. Hoang, and A.R. Sepahdari

## ABSTRACT

**BACKGROUND AND PURPOSE:** Patients with multigland primary hyperparathyroidism are at higher risk for missed lesions on imaging and failed parathyroidectomy. The purpose of this study was to prospectively validate the ability of previously derived predictive score systems, the composite multigland disease score, and the multiphase multidetector contrast-enhanced CT (4D-CT) composite multigland disease score, to identify patients with a high likelihood of multigland disease.

**MATERIALS AND METHODS:** This was a prospective study of 71 patients with primary hyperparathyroidism who underwent 4D-CT and successful parathyroidectomy. The size and number of lesions identified on 4D-CT, serum calcium levels, and parathyroid hormone levels were collected. A composite multigland disease score was calculated from 4D-CT imaging findings and the Wisconsin Index (the product of the serum calcium and parathyroid hormone levels). A 4D-CT multigland disease score was obtained by using the CT data alone.

**RESULTS:** Twenty-eight patients with multigland disease were compared with 43 patients with single-gland disease. Patients with multigland disease had a significantly smaller lesion size ( $P < .01$ ) and a higher likelihood of having either  $\geq 2$  or 0 lesions identified on 4D-CT ( $P < .01$ ). Composite multigland disease scores of  $\geq 4$ ,  $\geq 5$ , and 6 had specificities of 72%, 86%, and 100% for multigland disease, respectively. 4D-CT multigland disease scores of  $\geq 3$  and 4 had specificities of 74% and 88%.

**CONCLUSIONS:** Predictive scoring systems based on 4D-CT data, with or without laboratory data, were able to identify a subgroup of patients with a high likelihood of multigland disease in a prospectively accrued population of patients with primary hyperparathyroidism. These scoring systems can aid in surgical planning.

**ABBREVIATIONS:** 4D-CT = multiphase multidetector contrast-enhanced CT; MGD = multigland disease; PTH = parathyroid hormone; SGD = single-gland disease; WIN = Wisconsin Index

Primary hyperparathyroidism is characterized by excessive parathyroid hormone production resulting in hypercalcemia. Surgical resection remains the only definitive cure. In recent years, preoperative localization of the abnormal parathyroid gland is routinely performed and plays an integral part in operative guidance.<sup>1–3</sup> Most cases of primary hyperparathyroidism are caused by a single parathyroid adenoma; however, 10%–30% of patients are known to have multigland disease (MGD).<sup>4,5</sup> These patients pose a considerable challenge in preoperative localization

because the performance of technetium Tc99m sestamibi scanning and sonography is inferior in patients with MGD compared with patients with single-gland disease (SGD).<sup>6,7</sup> The decision to perform minimally invasive parathyroidectomy or 4-gland exploration relies heavily on preoperative imaging findings. Accurate preoperative identification of abnormal parathyroid lesions promotes effective operative planning and patient counseling, and can prevent a failed operation.<sup>3,8–10</sup> For example, reliable preoperative determination of SGD allows a surgeon to perform minimally invasive unilateral parathyroidectomy, which minimizes the incision length and reduces the risk of bilateral recurrent laryngeal nerve injury.

Multiphase multidetector contrast-enhanced CT (4D-CT) has emerged in recent years as a new technique of preoperative localization of an abnormal parathyroid gland. 4D-CT has been shown to successfully localize abnormal parathyroid glands that have been missed by scintigraphy and sonography. Furthermore, multiple studies have shown the superior sensitivity of 4D-CT in identifying abnormal parathyroid glands in patients with both SGD

Received April 3, 2016; accepted after revision June 11.

From the Department of Surgery (S.S., M.Y., M.W.Y., M.L., J.X.W.), Section of Endocrine Surgery, and Department of Radiological Sciences (A.R.S.), David Geffen School of Medicine, University of California, Los Angeles, Los Angeles, California; and Department of Radiology (J.K.H.), Duke University Medical Center, Durham, North Carolina.

Please address correspondence to Ali R. Sepahdari, MD, Department of Radiological Sciences, David Geffen School of Medicine, University of California, Los Angeles, 757 Westwood Plaza, Suite 1621D, Los Angeles, CA 90095; e-mail: ali.sepahdari@gmail.com; @alispahdari

<http://dx.doi.org/10.3174/ajnr.A4948>

and MGD.<sup>6-8</sup> However, the sensitivity of 4D-CT for MGD remains low at 32%–53%, compared with its sensitivity for SGD (88%–93%).<sup>6-8</sup>

To improve identification of patients with a high likelihood of MGD, Sepahdari et al<sup>11</sup> developed a composite MGD score based on 4D-CT imaging and biochemical data derived from a retrospective review of 155 patients. Variables included in this scoring system were the following: 1) the size of the largest lesion identified on 4D-CT, 2) the number of lesions identified on 4D-CT, and 3) the Wisconsin Index (product of serum calcium and parathyroid hormone levels). Scores of  $\geq 4$ ,  $\geq 5$ , and 6 had specificities of 81%, 93%, and 98%, respectively, for the identification of MGD.<sup>11</sup> Although promising, this MGD scoring system was derived solely from a retrospective review and therefore was limited due to biases inherent to its study design. The aim of the current study was to evaluate the performance of the MGD scoring system for predicting MGD by applying it to a prospectively accrued patient population.

## MATERIALS AND METHODS

### Study Subjects

Institutional review board approval was obtained for this study, which was performed with a waiver of informed consent and a waiver of Health Insurance Portability and Accountability Act authorization. All subjects having 4D-CT for primary hyperparathyroidism were accrued in a prospective manner during the 12 months between January 2014 and January 2015 in a single academic institution (University of California Los Angeles). Subjects were identified at the time of the initial scan. Clinical data and CT-derived data were recorded. Periodic chart review was then performed to track clinical outcomes. Subjects who went on to have successful parathyroidectomy, defined as an intraoperative parathyroid hormone (PTH) drop of 50% and/or at least 6 months of postoperative eucalcemia, were included for further analysis.

### 4D-CT Technique

Imaging was performed on either a 64–detector row scanner (Somatom Definition; Siemens, Erlangen, Germany) or a 256–detector row scanner (Somatom Definition Flash; Siemens). Scanning included noncontrast, arterial phase, and delayed-phase images from the hard palate to the carina. The parameters for all 3 phases were the following: section thickness, 0.6 mm; tube rotation time, 0.5 seconds; pitch factor, 1; FOV, 24 cm; 120 kVp; 230 reference mAs with automated tube current modulation (CARE Dose4D; Siemens). Arterial phase images were obtained 25 seconds following the initiation of a 100- to 120-mL IV bolus of iohexol, 350 mg of iodine/mL, injected through either a 20- or 22-ga antecubital catheter at either 4 or 3 mL/s. The delayed phase was acquired 30 seconds after the arterial phase ended. All images were reconstructed at 1-mm section thickness in the axial, coronal, and sagittal planes and reviewed in the PACS.

### Lesion Localization

All parathyroid lesions were classified as correctly or incorrectly localized on 4D-CT by correlating the operative notes with the original radiology reports and by using anatomic landmarks re-

**Table 1: MGD scores<sup>a</sup>**

Criterion	Scoring
No. of candidate lesions identified on 4D-CT	Single lesion: 0 Multiple lesions: 2 No lesions: 2
Maximum diameter of largest lesion on 4D-CT	>13 mm: 0 7–13 mm: 1 <7 mm or no lesions: 2
WIN	>1600: 0 800–1600: 1 <800: 2

<sup>a</sup> The composite MGD score is based on all 3 components in Table 1 and ranges from 0 to 6. The 4D-CT MGD score does not include the WIN and ranges from 0 to 4.

ported in both the operative and radiology reports. Lesions were described by using a system based on the anteroposterior location relative to the course of the recurrent laryngeal nerve. Lesions posterior to the expected course of the nerve were defined as superior parathyroid glands, and those anterior to the recurrent laryngeal nerve were defined as inferior parathyroid glands. The location along a superior-inferior axis was also described with the thyroid isthmus and the lower edge of the thyroid gland as landmarks. Lesions lying outside these typical locations were described as ectopic. Radiology reports were generated by a subspecialty-certified neuroradiologist with 10 years' experience in CT interpretation, including 5 years' experience in interpretation of 4D-CT. Sensitivities for lesion localization were based on these original radiology reports.

### Predictors of Multigland Disease

4D-CT imaging and biochemical predictors of MGD were originally proposed by Sepahdari et al<sup>11</sup> on the basis of prior surgical literature.<sup>12,13</sup> 4D-CT imaging predictors were the number of lesions identified on the original radiology report and the size of the largest lesion (maximum diameter in any plane). Laboratory data included serum calcium levels (milligram/deciliter), serum PTH levels (picogram/milliliter), and the Wisconsin Index (WIN). The WIN is the product of the serum calcium levels (milligram/deciliter) and PTH levels (picogram/milliliter) and was shown to help discriminate MGD and SGD in prior studies.<sup>11,12</sup>

A composite MGD score was derived from variables of lesion size on 4D-CT, the number of prospectively detected lesions on 4D-CT, and the WIN. Each variable contributed up to 2 points to the MGD scores (Table 1). The cutoff values used to assign points in the score were determined in a previous study by Sepahdari et al,<sup>11</sup> on the basis of prior literature for lesion size and ranges of biochemical markers. Maximum lesion size of >13 mm, 7–13 mm, and <7 mm were assigned scores of 0, 1, and 2. A single prospectively identified candidate lesion was assigned a score of zero versus a score of 2 for multiple candidate lesions or no candidate lesion. WINs of >1600, 800–1600, and <800 were assigned scores of 0, 1, and 2, respectively. A second scoring system, the 4D-CT MGD score, was based only on the 4D-CT imaging variables of lesion size and the number of prospectively detected lesions on 4D-CT. The composite MGD score ranged from 0 to 6. The 4D-CT MGD score ranged from 0 to 4. For both scoring systems, a higher score more strongly favored MGD.

**Table 2: Characteristics of patients with MGD and SGD<sup>a</sup>**

	All Subjects	MGD	SGD	P Value
<b>Patient characteristics</b>				
No. of patients	71	28	43	
No. of glands	120	77	43	
Mean age (yr)	62 (range, 21–88)	62.4	62.4	.99
Female	58 (82%)	26 (93%)	32 (74%)	.15
<b>4D-CT characteristics</b>				
Mean size of abnormal glands (mm)	9.6 (6.2)	7.5 (3.3)	11.2 (7.4)	.003
Median size of abnormal glands (mm)	9	7	10	
<b>Preoperatively detected lesions</b>				
1	33 (46%)	6 (21%)	27 (63%)	.003
≥2	28 (39%)	16 (58%)	12 (28%)	
None	10 (14%)	6 (21%)	4 (9.3)	
<b>Biochemical markers</b>				
Serum calcium level (mg/dL)	10.6 (0.6)	10.4 (0.6)	10.7 (0.6)	.08
Serum parathyroid hormone level (pg/mL)	93 (43)	87 (41)	97 (44)	.34
WIN	989 (484)	910 (453)	1040 (501)	.27
<b>MGD scores</b>				
Composite MGD score	3.4 (1.6)	4.3 (1.5)	2.7 (1.4)	<.001
4D-CT MGD score	2.1 (1.4)	2.9 (1.1)	1.5 (1.5)	<.001
<b>4D-CT sensitivity</b>				
Detection of lesions	82 (69%)	43 (56%)	39 (91%)	
Detection of all lesions in individual patients	47 (67%)	8 (29%)	39 (91%)	
<b>Parathyroid adenoma localization</b>				
≥1 Incorrectly localized or missed adenomas	24 (33%)	20 (71%)	4 (9%)	
All adenomas localized correctly	47 (67%)	8 (29%)	39 (91%)	

<sup>a</sup> Values are expressed as mean (SD) except as specified.

### Data Analysis

The characteristics of MGD were compared with those of SGD for individual variables and the scoring system. The  $\chi^2$  test was used to assess differences in patients with MGD and SGD for categorical data. The Student *t* test was used to assess differences between MGD and SGD for continuous variables. Receiver operating characteristic analysis was performed to determine the sensitivity and specificity of each feature for predicting MGD.  $P < .05$  was the threshold used for statistical significance for all tests. The data were entered into an Excel spreadsheet (2007 Version; Microsoft, Redmond, Washington). Statistical analyses were performed by using SAS Enterprise Guide (Version 4.2; SAS Institute, Cary, North Carolina).

## RESULTS

### Study Subjects

One-hundred four patients with primary hyperparathyroidism were imaged with 4D-CT during the study period from January 2014 to January 2015. Twenty-nine patients had no record of parathyroidectomy and therefore were excluded due to an inability to definitively categorize them as having either SGD or MGD on the basis of operative diagnoses. Two had failed parathyroidectomy, 1 had parathyroid carcinoma, and 1 patient died of an unrelated cause before the operation. The final analysis group included 71 patients (Table 2). Failed parathyroidectomies were defined as a lack of persistent eucalcemia for 6 months postoperatively and likely indicate that the abnormal parathyroid adenoma responsible for hyperparathyroidism was not removed in these patients. Therefore, it is unclear whether these patients had a single abnormal adenoma that was missed or had MGD and not all of the abnormal adenomas were removed. Therefore, these 2 patients were removed from analysis because we could not definitively place them in either the SGD or MGD group. Of these

patients, 28 had MGD and 43 had SGD. There were 77 abnormal glands among the 28 patients with MGD, with 120 abnormal glands identified surgically. There were no statistically significant differences between the SGD and MGD groups with regard to age and sex.

### Lesion Localization

Among the 28 patients with MGD, 43 of 77 abnormal glands (56%) were identified preoperatively by using 4D-CT. For 8 of 28 patients (29%), all of the abnormal glands in an individual patient could be identified preoperatively with 4D-CT alone. Of the 43 patients with SGD, 39 (91%) lesions were identified preoperatively with 4D-CT.

### Imaging Findings and Biochemical Factors

Patients with MGD had a smaller mean lesion size of 7.5 mm compared with patients with SGD, 11.2 mm ( $P = .003$ ). There was also a significant difference

between patients with MGD and SGD in the number of lesions identified with 4D-CT (Table 2). A single candidate lesion was identified in 63% of patients with SGD on 4D-CT compared with 21% of those with MGD ( $P = .003$ ). There was no statistically significant difference in mean calcium, PTH, and the Wisconsin Index between the 2 groups (Table 2).

Although notable differences were observed between MGD and SGD with regard to gland size and the number of lesions identified on 4D-CT, these factors individually did not serve as reliable predictors of MGD. Identification of either multiple or no abnormal glands was only 63% specific for MGD and 79% sensitive (Table 3). A lesion size of  $\leq 7$  mm had a specificity of 79% for MGD with a sensitivity of 50%. A WIN of  $< 800$  had a 93% specificity for MGD but only a 25% sensitivity.

### Performance of Composite MGD and 4D-CT MGD Scores

The mean composite MGD score was significantly higher among patients with MGD at 4.3 compared with those with SGD at 2.7 ( $P < .001$ ). Similar findings were noted for the 4D-CT MGD score (2.9 versus 1.5, respectively;  $P < .001$ ) (Table 2). Composite MGD scores of  $\geq 4$ ,  $\geq 5$ , and 6 had high specificities of 72%, 86%, and 100%, respectively, for multigland disease (Table 4). When applied to the current prospective patient population, the calculated area under the receiver operating characteristic curve was 0.78 (Figure). The 4D-CT MGD scores of  $\geq 3$  and 4 were similarly effective in predicting MGD, with specificities of 74% and 88%, respectively (Table 4), and with an area under the receiver operating characteristic curve of 0.78 (Fig 1B).

## DISCUSSION

Preoperative localization of abnormal parathyroid glands plays an integral role in surgical planning. 4D-CT has improved localiza-

**Table 3: Performance of individual components of MGD score system for predicting multigland disease**

	No. of Patients	Sensitivity	Specificity	Positive Predictive Value
No. of glands: $\geq 2$ or no lesion on 4D-CT	22	79%	63%	58%
Size of gland: $< 7$ mm or no lesion on 4D-CT	14	50%	79%	61%
WIN: $< 800$	7	25%	93%	70%

**Table 4: Performance of the composite and 4D-CT MGD scores for predicting multigland disease**

	No. of Patients	Sensitivity	Specificity	Positive Predictive Value
Composite MGD score				
$\geq 1$	28	100%	5%	41%
$\geq 2$	26	93%	16%	42%
$\geq 3$	24	86%	51%	53%
$\geq 4$	22	79%	72%	65%
$\geq 5$	13	46%	86%	68%
6	6	21%	100%	100%
4D-CT MGD score				
$\geq 0$	28	100%	0%	39%
$\geq 1$	28	100%	26%	47%
$\geq 2$	23	82%	60%	58%
$\geq 3$	21	75%	74%	66%
4	9	32%	88%	64%

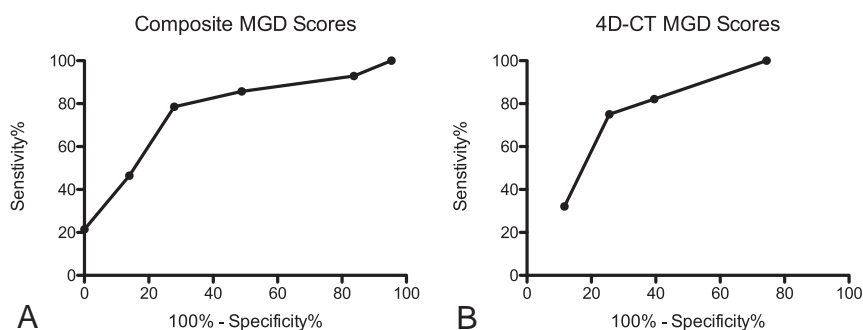


**FIGURE.** Receiver operating characteristic curves showing performance in predicting MGD with the composite MGD score (A) and the 4D-CT MGD score (B). The area under the curve is 0.78 for both methods.

tion ability in both MGD and SGD compared with ultrasound and sestamibi scans, but the sensitivity of 4D-CT for MGD remains low at 32%–53% compared with its sensitivity for SGD at 88%–93%.<sup>6–8</sup> The composite MGD score and the 4D-CT MGD score systems proposed by Sepahdari et al<sup>11</sup> suggested that a multifactorial system using 4D-CT information, with or without laboratory information, could effectively categorize patients into subsets with a very high likelihood for MGD, a very high likelihood for SGD, or intermediate likelihood of either MGD or SGD. The major limitation of that study is that it was based on a retrospectively derived sample, without a separate validation cohort. In our current study, we applied the composite MGD and 4D-CT MGD score systems to a prospective cohort and confirmed that these score systems could be used to predict MGD with high specificity.

The retrospectively derived MGD score systems by Sepahdari et al<sup>11</sup> performed equally well in our prospective setting. Using a retrospective patient population, Sepahdari et al observed high specificities of 81%, 93%, and 98% in predicting multigland dis-

ease for composite MGD scores of  $\geq 4$ ,  $\geq 5$ , and 6, respectively. In our current prospective study, similarly high specificities of 72%, 86%, and 100% were observed for composite MGD scores of  $\geq 4$ ,  $\geq 5$ , and 6, respectively. This finding was also true for the 4D-CT score system. 4D-CT scores of  $\geq 3$  and 4 yielded specificities of 81% and 96% in the retrospective population, compared with 74% and 88% in the current prospective population. Last, areas under the receiver operating characteristic curves of MGD predictive score systems were also similar between the retrospective and prospective patient cohorts (0.82 and 0.83 for composite and 4D-CT MGD scores in the retrospective cohort compared with 0.78 for both techniques in the prospective cohort). Our prospective cohort validated the retrospectively derived system of Sepahdari et al, achieving results nearly identical to those of the retrospective cohort.

Our study also shows that the number of candidate lesions identified on 4D-CT alone is not sufficient for distinguishing MGD from SGD. In clinical practice, radiologists may rely on detecting multiple glands as the best sign of MGD. However, we showed that identification of  $\geq 2$  lesions on 4D-CT is neither sensitive nor specific for MGD. Among patients with SGD, 12 of 43 (28%) were noted to have  $\geq 2$  suspected lesions (false-positive), and 6 of 28 (21%) patients with MGD had only 1 suspected lesion (false-negative). These findings illustrate the need for additional data regarding lesion size and biochemical information to better estimate the risk for MGD.

The composite and 4D-CT MGD score systems should serve as evidence-based foundations for communicating certainty and uncertainty in the diagnosis of abnormal parathyroid glands. They should maximize the clinically actionable information available from imaging. These scoring systems are valuable in giving objective probabilities of MGD versus SGD. In clinical practice, a radiologist can advise surgeons that a composite MDG score of  $\geq 5$  or a 4D-CT MGD score of 4 is highly likely to represent MGD. Surgeons can then use these objective data to better plan operative approaches and counsel patients accordingly. For instance, given a high preoperative probability of MGD, surgeons may decide to avoid minimally invasive unilateral parathyroidectomy, which risks failing to identify abnormal glands during the operation, and instead opt for a 4-gland exploration to identify multiple abnormal parathyroid glands.

Several limitations exist in our study. Although this study was performed in a prospective manner, it remains a single-institu-

tion study with studies interpreted by a single neuroradiologist, who also participated in the original retrospective study. The composite MGD predictive score system is largely dependent on the 4D-CT findings, and imaging interpretation may vary in a systematic way among different radiologists. However, previous studies have shown high concordance in 4D-CT interpretations between neuroradiologists, suggesting that assignment of MGD scores is likely to be highly reproducible.<sup>14,15</sup> Last, a patient population presenting to a single institution may represent inherent bias. Thus, the applicability of the MGD predictive score system should also be prospectively validated in a multi-institution setting. Notably, the previous study by Sepahdari et al,<sup>11</sup> in which the MGD predictive score system was developed, was performed in 2 academic institutions with 2 different interpreting neuroradiologists. Rates of lesion identification were similar between the 2 institutions and the MGD score system was developed on the basis of patients from both institutions.

## CONCLUSIONS

The composite MGD score and 4D-CT MGD score performed well in a prospective setting, identifying patients with a high likelihood of MGD by using 4D-CT data and biochemical information. Use of these scores preoperatively to identify patients at risk for MGD may play an important role in operative planning.

## REFERENCES

- Sosa JA, Udelsman R. **Minimally invasive parathyroidectomy.** *Surg Oncol* 2003;12:125–34 CrossRef Medline
- Siperstein A, Berber E, Mackey R, et al. **Prospective evaluation of sestamibi scan, ultrasonography, and rapid PTH to predict the success of limited exploration for sporadic primary hyperparathyroidism.** *Surgery* 2004;136:872–80 CrossRef Medline
- McGreal G, Winter DC, Sookhai S, et al. **Minimally invasive, radio-guided surgery for primary hyperparathyroidism.** *Ann Surg Oncol* 2001;8:856–60 CrossRef Medline
- Cayo AK, Sippel RS, Schaefer S, et al. **Utility of intraoperative PTH for primary hyperparathyroidism due to multigland disease.** *Ann Surg Oncol* 2009;16:3450–54 CrossRef Medline
- Ruda JM, Hollenbeak CS, Stack BC Jr. **A systematic review of the diagnosis and treatment of primary hyperparathyroidism from 1995 to 2003.** *Otolaryngol Head Neck Surg* 2005;132:359–72 CrossRef Medline
- Rodgers SE, Hunter GJ, Hamberg LM, et al. **Improved preoperative planning for directed parathyroidectomy with 4-dimensional computed tomography.** *Surgery* 2006;140:932–40; discussion 940–41 CrossRef Medline
- Cheung K, Wang TS, Farrokhyar F, et al. **A meta-analysis of preoperative localization techniques for patients with primary hyperparathyroidism.** *Ann Surg Oncol* 2012;19:577–83 CrossRef Medline
- Kukar M, Platz TA, Schaffner TJ, et al. **The use of modified four-dimensional computed tomography in patients with primary hyperparathyroidism: an argument for the abandonment of routine sestamibi single-positron emission computed tomography (SPECT).** *Ann Surg Oncol* 2015;22:139–45 CrossRef Medline
- Harari A, Zarnegar R, Lee J, et al. **Computed tomography can guide focused exploration in select patients with primary hyperparathyroidism and negative sestamibi scanning.** *Surgery* 2008;144:970–76; discussion 976–79 CrossRef Medline
- Cham S, Sepahdari AR, Hall KE, et al. **Dynamic parathyroid computed tomography (4DCT) facilitates reoperative parathyroidectomy and enables cure of missed hyperplasia.** *Ann Surg Oncol* 2015; 22:3537–42 CrossRef Medline
- Sepahdari AR, Bahl M, Harari A, et al. **Predictors of multigland disease in primary hyperparathyroidism: a scoring system with 4D-CT imaging and biochemical markers.** *AJNR Am J Neuroradiol* 2015;36: 987–92 CrossRef Medline
- Mazeh H, Chen H, Leverson G, et al. **Creation of a “Wisconsin index” nomogram to predict the likelihood of additional hyperfunctioning parathyroid glands during parathyroidectomy.** *Ann Surg* 2013;257:138–41 CrossRef Medline
- Siperstein A, Berber E, Barbosa GF, et al. **Predicting the success of limited exploration for primary hyperparathyroidism using ultrasound, sestamibi, and intraoperative parathyroid hormone: analysis of 1158 cases.** *Ann Surg* 2008;248:420–28 Medline
- Sepahdari AR, Yeh MW, Rodrigues D, et al. **Three-phase parathyroid 4-dimensional computed tomography initial experience: inexperienced readers have high accuracy and high interobserver agreement.** *J Comput Assist Tomogr* 2013;37:511–17 CrossRef Medline
- Bahl M, Sepahdari AR, Sosa JA, et al. **Parathyroid adenomas and hyperplasia on four-dimensional CT scans: three patterns of enhancement relative to the thyroid gland justify a three-phase protocol.** *Radiology* 2015;277:454–62 CrossRef Medline

# Intravoxel Incoherent Motion in Normal Pituitary Gland: Initial Study with Turbo Spin-Echo Diffusion-Weighted Imaging

 K. Kamimura,  M. Nakajo,  Y. Fukukura,  T. Iwanaga,  T. Saito,  M. Sasaki,  T. Fujisaki,  A. Takemura,  T. Okuaki, and  T. Yoshiura

## ABSTRACT

**BACKGROUND AND PURPOSE:** DWI with conventional single-shot EPI of the pituitary gland is hampered by strong susceptibility artifacts. Our purpose was to evaluate the feasibility of intravoxel incoherent motion assessment by using DWI based on TSE of the normal anterior pituitary lobe.

**MATERIALS AND METHODS:** The intravoxel incoherent motion parameters, including the true diffusion coefficient ( $D$ ), the perfusion fraction ( $f$ ), and the pseudo-diffusion coefficient ( $D^*$ ), were obtained with TSE-DWI in 5 brain regions (the pons, the WM and GM of the vermis, and the genu and splenium of the corpus callosum) in 8 healthy volunteers, and their agreement with those obtained with EPI-DWI was evaluated by using the intraclass correlation coefficient. The 3 intravoxel incoherent motion parameters in the anterior pituitary lobe were compared with those in the brain regions by using the Dunnett test.

**RESULTS:** The agreement between TSE-DWI and EPI-DWI was moderate (intraclass correlation coefficient = 0.571) for  $D$ , substantial (0.699) for  $f$ , but fair (0.405) for  $D^*$ .  $D$  in the anterior pituitary lobe was significantly higher than in the 5 brain regions ( $P < .001$ ). The  $f$  in the anterior pituitary lobe was significantly higher than in the 5 brain regions ( $P < .001$ ), except for the vermian GM. The pituitary  $D^*$  was not significantly different from that in the 5 brain regions.

**CONCLUSIONS:** Our results demonstrated the feasibility of intravoxel incoherent motion assessment of the normal anterior pituitary lobe by using TSE-DWI. High  $D$  and  $f$  values in the anterior pituitary lobe were thought to reflect its microstructural and perfusion characteristics.

**ABBREVIATIONS:**  $D$  = true diffusion coefficient;  $D^*$  = pseudo-diffusion coefficient;  $f$  = perfusion fraction; ICC = intraclass correlation coefficient; IVIM = intravoxel incoherent motion

Intravoxel incoherent motion (IVIM) imaging is an advanced DWI technique that allows a separate quantitative evaluation of all the microscopic random motion that contributes to DWI, which is essentially represented by molecular diffusion and blood microcirculation (perfusion).<sup>1</sup> Currently, DWI based on single-shot EPI is most commonly used for IVIM imaging.<sup>2,3</sup> However, EPI-DWI is associated with strong susceptibility artifacts, which cause image degradation in the skull base,<sup>4</sup> making it difficult, if not impossible, to accurately measure the IVIM parameters in the anterior pituitary lobe. DWI based on TSE has been reported to mitigate such prob-

lems in the skull base.<sup>5</sup> To our knowledge, perfusion of the normal pituitary gland has not yet been evaluated by imaging modalities. Therefore, the purpose of this study was to evaluate the feasibility of IVIM assessment based on TSE-DWI in the normal pituitary gland.

## MATERIALS AND METHODS

The study was conducted with approval of the Kagoshima University Hospital review boards. Written informed consent was obtained from each participant. First, we performed an in vitro experiment on a phantom for validation of TSE-DWI sequences. Second, the IVIM measurement by using TSE-DWI was validated in the in vivo human brain by comparing it with conventional EPI-DWI. Finally, IVIM parameters in the anterior pituitary lobe were measured and compared with those in the brain parenchyma.

## MR Imaging Parameters

All MR imaging was performed by using a 3T system (Ingenia; Philips Healthcare, Best, the Netherlands) and a 15-channel receiver head coil. The imaging parameters for the TSE-DWI were

Received April 5, 2016; accepted after revision July 16.

From the Department of Radiology (K.K., M.N., Y.F., T.Y.), Kagoshima University Graduate School of Medical and Dental Sciences, Kagoshima, Japan; Department of Radiological Technology (T.I., T.S., M.S., T.F.), Kagoshima University Hospital, Kagoshima, Japan; Philips Electronics Japan (A.T.), Tokyo, Japan; and Philips Healthcare (T.O.), Tokyo, Japan.

Please address correspondence to Takashi Yoshiura, MD, PhD, Department of Radiology, Kagoshima University Graduate School of Medical and Dental Sciences, 8-35-1 Sakuragaoka, Kagoshima 890-8544, Japan; e-mail: yoshiura@m3.kufm.kagoshima-u.ac.jp

<http://dx.doi.org/10.3174/ajnr.A4930>

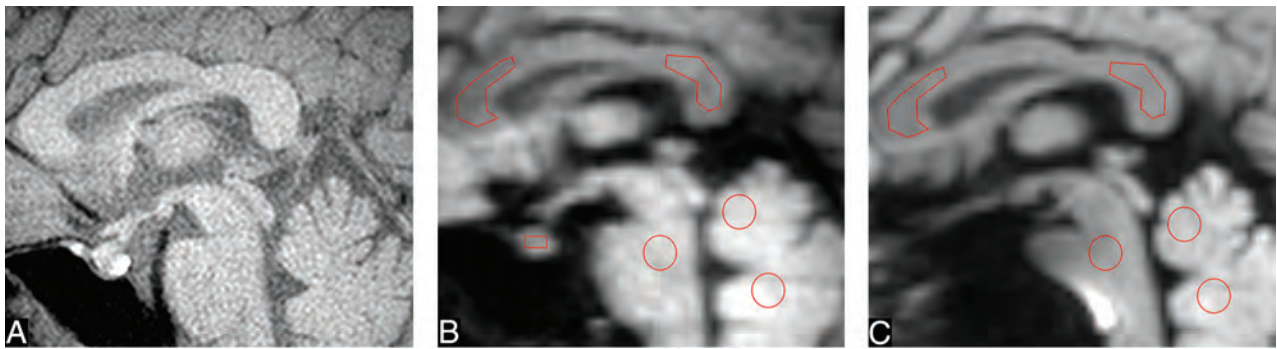


**FIG 1.** Sagittal fat-suppressed T1-weighted image (A), TSE-DWI ( $b = 1000 \text{ s/mm}^2$ ) (B), and EPI-DWI ( $b = 1000 \text{ s/mm}^2$ ) (C) of a healthy volunteer. The normal pituitary gland is clearly visualized with minimal image degradation on TSE-DWI (B), while it is not identifiable on EPI-DWI (C). Five ROIs are placed in the pons, the WM and GM regions of the vermis, and the genu and splenium of the corpus callosum (B and C). On TSE-DWI, an additional ROI is placed in the anterior pituitary lobe (B).

as follows: TR/TE = 3000/52 ms; flip angle =  $90^\circ$ ; echo-train length = 60; sensitivity encoding factor = none; FOV = 180 mm; acquisition matrix =  $100 \times 100$  (reconstructed into  $112 \times 112$ ); voxel size =  $1.8 \times 1.8 \times 3.0 \text{ mm}^3$  ( $1.6 \times 1.6 \times 3.0 \text{ mm}^3$  after reconstruction); NEX = 6. The motion-probing gradient was applied in 3 orthogonal directions. For the human studies, peripheral pulse gating was used to reduce possible signal variability due to CSF pulsation, resulting in a TR ranging from 2400 to 3000 ms and an imaging time from 8 minutes 52 seconds to 11 minutes 6 seconds. We used 13 different b-values (0, 10, 20, 30, 50, 80, 100, 200, 300, 400, 600, 800, and  $1000 \text{ s/mm}^2$ ). The imaging parameters for the EPI-DWI were as follows: TR/TE = 3000/56 ms; flip angle =  $90^\circ$ ; EPI factor = 61; sensitivity encoding factor = 2; FOV = 180 mm; NEX = 3. The imaging matrix and the motion-probing gradient settings, including the b-values, were the same as those for TSE-DWI. The imaging time was 5 minutes 39 seconds. T1-weighted spin-echo images with fat suppression were also obtained for anatomic reference (TR/TE = 500/6.9 ms; imaging matrix =  $240 \times 226$ ).

### Phantom Study

A plastic bottle with a 10-cm diameter filled with Gd-DTPA-doped (0.3-mmol/L) water at  $22^\circ\text{C}$  was used for the in vitro experiment. Images were obtained at a 3-mm-thick midsagittal plane by using TSE-DWI and EPI-DWI with the 13 b-values (0, 10, 20, 30, 50, 80, 100, 200, 300, 400, 600, 800, and  $1000 \text{ s/mm}^2$ ). A board-certified radiologist (K.K., with 17 years of experience) measured the signal intensity at different b-values within a manually drawn, circular ROI with an area of  $92 \text{ mm}^2$  on a PACS workstation.

### Human Studies

Volunteers were eligible for study inclusion if they met the following conditions: 1) They were at least 20 years of age to, at most, 40 years of age, 2) were not pregnant, 3) had no neurologic diseases, 4) had no endocrine diseases, 5) had no history of head injury, and 6) had no contraindications to MR imaging (eg, noncompatible biometallic implants or claustrophobia). IVIM imaging was performed by using both TSE-DWI and EPI-DWI sequences on a 3-mm-thick midsagittal plane, including the pituitary gland.

### Visual Assessment of Image Quality

The isotropic diffusion-weighted images ( $b = 1000 \text{ s/mm}^2$ ) from TSE-DWI and EPI-DWI were reviewed by a radiologist (K.K.), and the visibility of the pituitary gland was rated as either good (visible with minimal degradation), acceptable (visible with acceptable degradation), poor (visible with serious degradation), or undetectable, with the corresponding T1-weighted image as a reference.

### IVIM Data Analysis

The IVIM analysis was performed by using a standard 2-compartment diffusion model with a capillary perfusion component and a nonvascular compartment.<sup>1</sup> Signal decay was estimated by using the following biexponential equation:

$$1) \quad SI/SI_0 = (1 - f) \times \exp(-bD) + f \times \exp(-bD^*),$$

where  $D$  and  $D^*$  are the true diffusion coefficient and the pseudo-diffusion coefficient, respectively;  $SI$  and  $SI_0$  are the signal intensity at a given b-value and at  $b = 0 \text{ s/mm}^2$ , respectively; and  $f$  is the volume fraction within a voxel of water flowing in perfusion capillaries. The pseudo-diffusion coefficient  $D^*$  represents the incoherent molecular translation of water within flowing blood when that blood flow changes capillary segments several times during the TE and thereby mimics the random walk of the diffusion process.<sup>1</sup> The signal decay was fitted in a step on a voxel-by-voxel basis to create each parameter map of  $D$ ,  $f$ , and  $D^*$  by using an Interactive Data Language-based software (Philips Research Integrated Development Environment; Philips Healthcare).

### Quantitative Analysis

Two independent radiologists (K.K. and M.N., with 17 and 11 years of experience, respectively) manually drew 5 ROIs (range,  $31.0\text{--}222 \text{ mm}^2$ ; Fig 1) in the pons, the WM and GM regions of the vermis, and the genu and splenium of the corpus callosum. The ROIs were first drawn on the  $D$  map derived from the TSE-DWI and then were copied automatically onto the corresponding  $f$  and  $D^*$  maps. The same ROIs were also copied to the parametric maps from EPI-DWI, but subsequent manual adjustments of their positions were needed because of image distortion. For TSE-DWI,

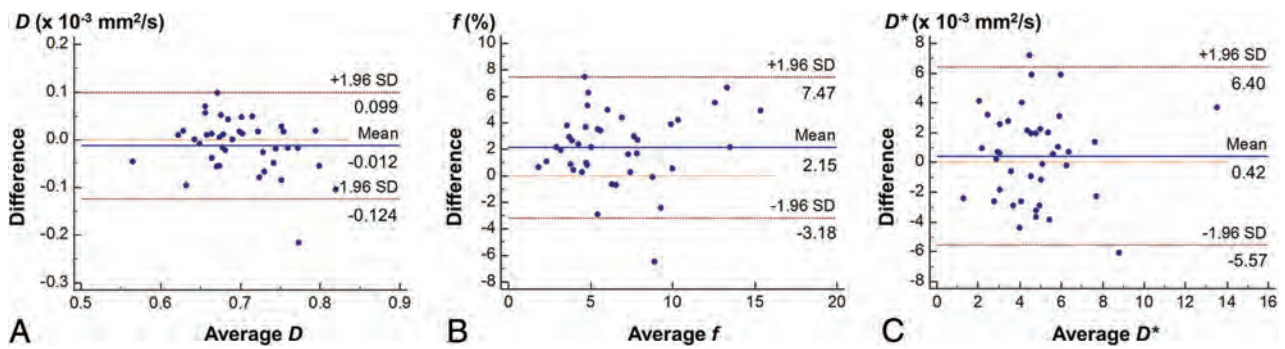


**FIG 2.** Bland-Altman plots of  $D$  (A),  $f$  (B), and  $D^*$  (C) assessing the intermodality agreement between TSE-DWI and EPI-DWI.

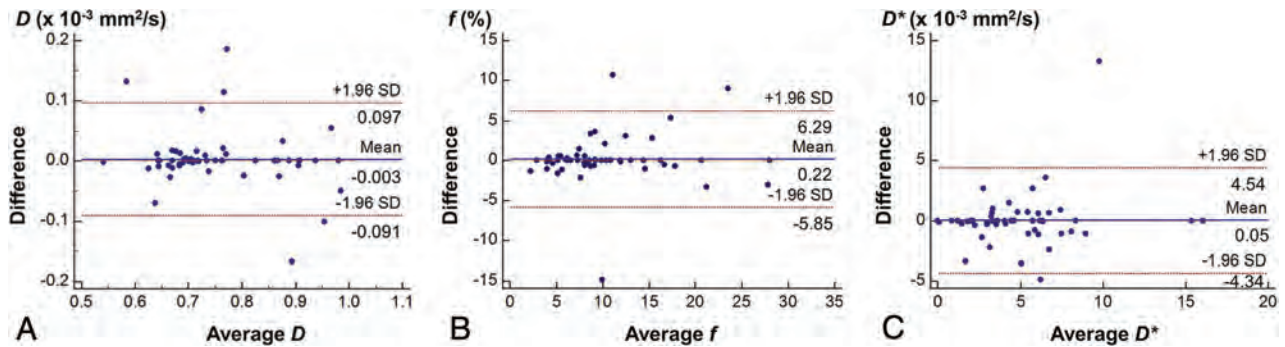


**FIG 3.** Bland-Altman plots of  $D$  (A),  $f$  (B), and  $D^*$  (C) obtained with TSE-DWI, assessing the interobserver agreement.

the ROI was also placed in the anterior pituitary lobe (range, 20.7–31.0 mm<sup>2</sup>; Fig 1) by using the corresponding T1-weighted image as a reference.

### Statistical Analysis

The signal decay (relative signal intensity to the baseline) according to the increasing b-values in the phantom was compared between TSE-DWI and EPI-DWI by using the intraclass correlation coefficient (ICC). The intermodality agreement of the 3 IVIM parameters ( $D$ ,  $f$ , and  $D^*$ ) between TSE-DWI and EPI-DWI within the 5 ROIs in the brain parenchyma was evaluated by using the ICC and Bland-Altman plot. The interobserver agreement of the IVIM measurements was evaluated with respect to the 5 ROIs for EPI-DWI and 6 ROIs (including the pituitary gland) for TSE-DWI by using the ICC and Bland-Altman plot. The IVIM parameters in the anterior pituitary lobe were compared with those in the 5 ROIs in the brain parenchyma by using the Dunnett test. For the human studies, the measured values from the 2 observers were averaged to represent each ROI. Statistical analyses were performed by using commercially available software packages (GraphPad Prism 6, Version 6.07; GraphPad Software, San Diego, California; and MedCalc statistical software, Version 15.10.0; MedCalc Software, Mariakerke, Belgium).  $P$  values < .05 were considered significant.

## RESULTS

### Phantom Study

The phantom experiment revealed almost perfect accordance in the signal decay between TSE-DWI and EPI-DWI (ICC = 1.0).

### Human Studies

**Study Participants.** According to the inclusion criteria, 8 healthy, young adult volunteers (2 men and 6 women; age range, 22–35 years; median age, 28 years) participated in the study.

**Visual Assessment.** In all subjects, the pituitary gland was clearly visualized with a minimal degree of distortion on the isotropic TSE-DWI and was rated as good. On the other hand, the pituitary gland was undetectable due to severe susceptibility artifacts with EPI-DWI in all subjects (Fig 1).

**Intermodality Agreement.** The intermodality agreement for the IVIM parameters was moderate (ICC = 0.571) for  $D$ , substantial (ICC = 0.699) for  $f$ , and fair (ICC = 0.405) for  $D^*$ . The Bland-Altman analysis showed that the 95% limits of agreement between the 2 methods were  $-0.124, 0.099 \times 10^{-3}$  mm<sup>2</sup>/s for  $D$ ;  $-3.18\%, 7.47\%$  for  $f$ ; and  $-5.57, 6.40 \times 10^{-3}$  mm<sup>2</sup>/s for  $D^*$  (Fig 2). The  $f$  was slightly overestimated in TSE-DWI compared with EPI-DWI. No obvious systematic bias was shown for the other 2 parameters.

**Interobserver Agreement.** Our evaluation of the interobserver agreement for the IVIM parameters showed almost perfect agreement for  $D$  (ICC = 0.907) and  $f$  (ICC = 0.872) and substantial agreement (ICC = 0.786) for  $D^*$ . The Bland-Altman analysis showed that the 95% limits of agreement between the 2 observers were  $-0.091, 0.097 \times 10^{-3}$  mm<sup>2</sup>/s for  $D$ ;  $-5.85\%, 6.29\%$  for  $f$ ; and  $-4.34, 4.45 \times 10^{-3}$  mm<sup>2</sup>/s for  $D^*$  (Fig 3). No obvious systematic bias was shown for any parameter. The evaluation of interobserver agreement for EPI-DWI resulted in almost perfect agreement for each IVIM parameter: ICC = 0.876, 0.907, and

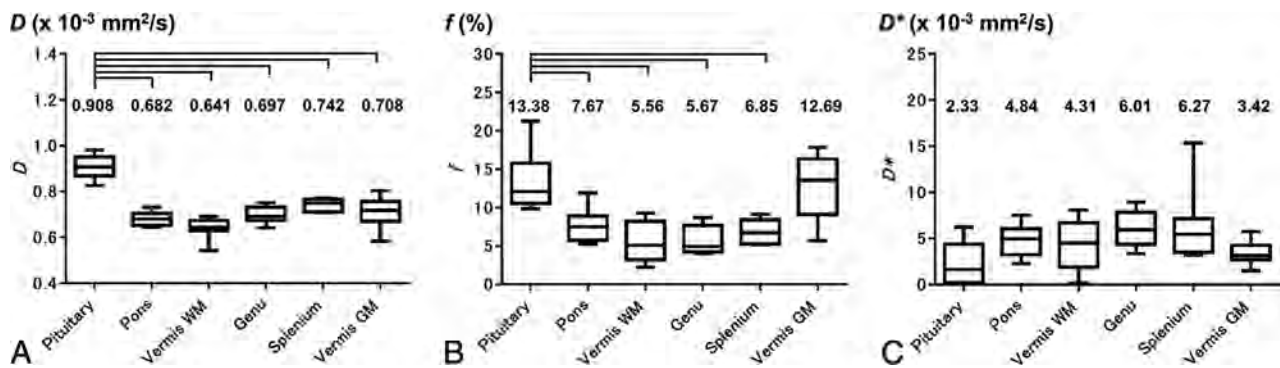


**FIG 4.** IVIM parameters in the anterior pituitary lobe compared with those in 5 brain regions (pons, GM and WM of vermis, and genu and splenium of corpus callosum): *D* (A), *f* (B), *D\** (C). Brackets indicate a significant difference ( $P < .001$ ).

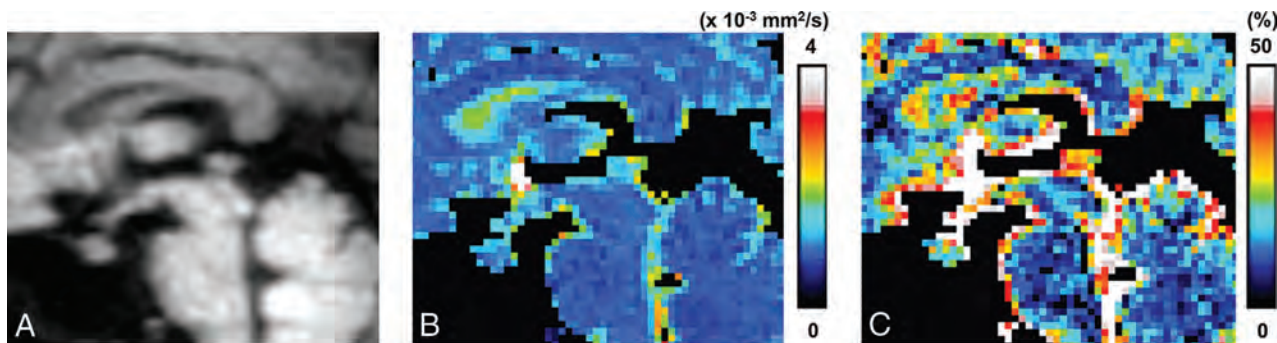


**FIG 5.** Representative example of TSE-DWI ( $b = 1000 \text{ s/mm}^2$ ) of the pituitary gland (A) and corresponding maps of *D* (B) and *f* (C).

0.853 for *D*, *f*, and *D\**, respectively. The Bland-Altman analysis showed no obvious systematic bias in any parameter, and the 95% limits of interobserver agreement were  $-0.092, 0.098 \times 10^{-3} \text{ mm}^2/\text{s}$ ;  $-3.92\%, 4.10\%$ ; and  $-4.23, 3.62 \times 10^{-3} \text{ mm}^2/\text{s}$  for *D*, *f*, and *D\**, respectively.

**IVIM Parameters in the Anterior Pituitary Lobe.** The mean *D* in the normal anterior pituitary lobe was  $0.908 \pm 0.050 \times 10^{-3} \text{ mm}^2/\text{s}$ , which was significantly higher than that in the pons ( $0.682 \pm 0.030 \times 10^{-3} \text{ mm}^2/\text{s}$ ); the vermian WM ( $0.641 \pm 0.045 \times 10^{-3} \text{ mm}^2/\text{s}$ ) and GM ( $0.708 \pm 0.067 \times 10^{-3} \text{ mm}^2/\text{s}$ ); and the genu ( $0.697 \pm 0.036 \times 10^{-3} \text{ mm}^2/\text{s}$ ) and splenium ( $0.742 \pm 0.027 \times 10^{-3} \text{ mm}^2/\text{s}$ ) of the corpus callosum (all comparisons,  $P < .001$ ). The mean *f* in the normal anterior pituitary lobe was  $13.38\% \pm 3.85\%$ , which was significantly higher than that in the pons ( $7.67\% \pm 2.14\%$ ), the vermian WM ( $5.56\% \pm 2.63\%$ ), and the genu ( $5.67\% \pm 1.84\%$ ) and splenium ( $6.85\% \pm 1.58\%$ ) of the corpus callosum ( $P < .001$ ), while it was not significantly different from that in the vermian GM ( $12.69\% \pm 4.21\%$ ). The mean *D\** in the normal anterior pituitary lobe ( $2.33 \pm 2.29 \times 10^{-3} \text{ mm}^2/\text{s}$ ) was not significantly different from that in the pons ( $4.84 \pm 1.74 \times 10^{-3} \text{ mm}^2/\text{s}$ ), the vermian WM ( $4.31 \pm 2.85 \times 10^{-3} \text{ mm}^2/\text{s}$ ) and GM ( $3.42 \pm 1.29 \times 10^{-3} \text{ mm}^2/\text{s}$ ), and the genu ( $6.01 \pm 1.93 \times 10^{-3} \text{ mm}^2/\text{s}$ ) and splenium ( $6.27 \pm 3.98 \times 10^{-3} \text{ mm}^2/\text{s}$ ) of the corpus callosum (Fig 4). The *D* and *f* maps of a representative subject are shown in Fig 5.

## DISCUSSION

As we expected, the normal pituitary gland was clearly visualized with minimal degradation with TSE-DWI, while severe suscepti-

bility artifacts were noted in conventional EPI-DWI. Due to distortion and signal loss, quantitative evaluation of the pituitary gland was extremely difficult with EPI-DWI. Thus, previous studies with EPI-DWI have been mainly limited to pituitary macroadenomas, apoplexy, abscesses, or other parasellar lesions.<sup>6-9</sup> To overcome image degradation, other researchers have applied non-EPI-DWI, such as single-shot fast spin-echo,<sup>10</sup> line scan,<sup>11</sup> and periodically rotated overlapping parallel lines with enhanced reconstruction DWI for sellar and parasellar lesions.<sup>12</sup> However, none of these studies aimed at evaluation or IVIM analysis of the normal pituitary gland. Recently, Hiwatashi et al<sup>13</sup> evaluated the ADC of the normal anterior pituitary lobe by 3D turbo field echo with diffusion-sensitized driven-equilibrium preparation, a novel high-resolution 3D, non-EPI-DWI technique. They validated the ADC measurement with diffusion-sensitized driven-equilibrium preparation by comparing it with conventional EPI-DWI. To our knowledge, theirs is the only report to demonstrate the feasibility of quantitative diffusion measurement of the normal pituitary gland. However, IVIM of the normal pituitary gland has never been evaluated.

To date, IVIM has been used mainly for assessment in non-central nervous system organs. For example, it has been used to evaluate liver cirrhosis, assess the vascularity of abdominal tumors, and detect early responses to anticancer therapy.<sup>14,15</sup> Applications for intracranial and head and neck diseases have also been increasingly reported.<sup>3,16</sup> In these studies, an EPI-based DWI sequence was almost invariably used. However, as mentioned above, EPI-DWI can have susceptibility artifacts in the skull base and head-and-neck regions. Sakamoto et al<sup>17</sup> reported

IVIM imaging, based on a non-EPI-DWI technique, HASTE-DWI, in head-and-neck tumors. In their study, however, validation of their imaging technique was not attempted. In our study, IVIM assessment based on TSE-DWI was compared with that based on conventional EPI-DWI, and it was shown that TSE-DWI can provide a  $D$  and  $f$  that are similar to those based on EPI-DWI. On the other hand, limited agreement was noted for  $D^*$ . This may be due to the high variability in the  $D^*$  measurement, as shown in previous reports.<sup>14</sup>

Moreover, our results demonstrated acceptable interobserver reproducibility in IVIM measurements with TSE-DWI.

Our results show that  $D$  in the normal anterior pituitary lobe was significantly higher than that in the pons, the GM and WM vermis, and the corpus callosum. This finding is consistent with the report by Hiwatashi et al<sup>13</sup> that the ADC in the anterior pituitary lobe was significantly higher than that in the pons and the vermis; though unlike  $D$ , the ADC represented both the true diffusion and the capillary perfusion. As they speculated, lack of myelination may contribute to the higher  $D$  value in comparison with that in the brain parenchyma.<sup>13</sup> Our results also show that the  $f$  in the anterior pituitary lobe was significantly higher than that in the pons, the vermian WM, and the genu and splenium of the corpus callosum, while it was comparable with that in the vermian GM. Theoretically,  $f$  is considered proportional to cerebral blood volume.<sup>18</sup> Measurement of perfusion parameters in the anterior pituitary lobe has never been reported, to our knowledge; thus, there are no previous imaging results to use as a reference. Nevertheless, this finding is consistent with previously documented high-histologic vascular density.<sup>19</sup> Future studies based on noninvasive perfusion methods, such as dynamic contrast-enhanced perfusion MR imaging, are necessary to further confirm our findings. No significant difference was shown in  $D^*$  between the anterior pituitary lobe and the brain parenchyma. This may be attributable to the known high variability in the  $D^*$  measurement.<sup>20</sup>

Our results suggest that IVIM is applicable to pituitary lesions such as pituitary adenomas. Currently, MR imaging evaluation of pituitary lesions requires contrast-enhanced imaging, typically dynamic contrast-enhanced studies.<sup>21</sup> IVIM based on TSE-DWI may serve as an alternative imaging method to characterize pituitary lesions for patients with impaired renal function or allergic reactions to contrast agents. Moreover, perfusion assessment of the anterior pituitary lobe could be relevant to functional pituitary diseases. A previous article suggested that pituitary hormone deficiency is closely related to perfusion abnormalities in the adenohypophysis.<sup>22</sup>

This study has several limitations. Our TSE-DWI IVIM sequence had limited spatial resolution. In most previous studies on brain IVIM imaging, a high number of b-values (typically >10) were used to ensure the accuracy and reproducibility of the measurement.<sup>2,3</sup> We decided to use 13 b-values to remain conservative in terms of b-value settings in this feasibility study. In a given imaging time, this choice resulted in low spatial resolution, in which the number of voxels covering the anterior pituitary lobe was limited (8–12 voxels). Recent studies have proposed simplified IVIM techniques with reduced numbers of b-values and acceptable measurement precision.<sup>23</sup> Introduction of such methods

would allow pituitary IVIM imaging with higher spatial resolution. Our subjects were limited to a small number of healthy young adults with relatively large pituitary glands for this feasibility study. For imaging smaller pituitary glands in elderly individuals and for small pituitary lesions, we may need to improve the spatial resolution. Because we used healthy volunteers, we could not show histologic evidence for IVIM parametric differences between the pituitary gland and brain parenchyma.

## CONCLUSIONS

Our results demonstrated the feasibility of IVIM parameters, specifically  $D$  and  $f$ , of the normal anterior pituitary lobe by using the TSE-DWI technique.  $D$  in the anterior pituitary lobe was significantly higher than that in the brain parenchyma, while  $f$  was comparable with that in the cerebellar GM. These findings likely reflect the structural and perfusion characteristics of the anterior pituitary lobe at the microscopic level.

## REFERENCES

1. Le Bihan D, Breton E, Lallemand D, et al. **MR imaging of intravoxel incoherent motions: application to diffusion and perfusion in neurologic disorders.** *Radiology* 1986;161:401–07 CrossRef Medline
2. Federau C, O'Brien K, Meuli R, et al. **Measuring brain perfusion with intravoxel incoherent motion (IVIM): initial clinical experience.** *J Magn Reson Imaging* 2014;39:624–32 CrossRef Medline
3. Togao O, Hiwatashi A, Yamashita K, et al. **Differentiation of high-grade and low-grade diffuse gliomas by intravoxel incoherent motion MR imaging.** *Neuro Oncol* 2016;18:132–41 CrossRef Medline
4. Le Bihan D, Poupon C, Amadon A, et al. **Artifacts and pitfalls in diffusion MRI.** *J Magn Reson Imaging* 2006;24:478–88 CrossRef Medline
5. Raya JG, Dietrich O, Reiser MF, et al. **Methods and applications of diffusion imaging of vertebral bone marrow.** *J Magn Reson Imaging* 2006;24:1207–20 CrossRef Medline
6. Rogg JM, Tung GA, Anderson G, et al. **Pituitary apoplexy: early detection with diffusion-weighted MR imaging.** *AJNR Am J Neuroradiol* 2002;23:1240–45 Medline
7. Yamasaki F, Kurisu K, Satoh K, et al. **Apparent diffusion coefficient of human brain tumors at MR imaging.** *Radiology* 2005;235:985–91 CrossRef Medline
8. Takao H, Doi I, Watanabe T. **Diffusion-weighted magnetic resonance imaging in pituitary abscess.** *J Comput Assist Tomogr* 2006;30:514–16 CrossRef Medline
9. Boxerman JL, Rogg JM, Donahue JE, et al. **Preoperative MRI evaluation of pituitary macroadenoma: imaging features predictive of successful transphenoidal surgery.** *AJR Am J Roentgenol* 2010;195:720–28 CrossRef Medline
10. Kunii N, Abe T, Kawamo M, et al. **Rathke's cleft cysts: differentiation from other cystic lesions in the pituitary fossa by use of single-shot fast spin-echo diffusion-weighted MR imaging.** *Acta Neurochir (Wien)* 2007;149:759–69; discussion 769 CrossRef Medline
11. Suzuki C, Maeda M, Hori K, et al. **Apparent diffusion coefficient of pituitary macroadenoma evaluated with line-scan diffusion-weighted imaging.** *J Neuroradiol* 2007;34:228–35 CrossRef Medline
12. Mahmoud OM, Tominaga A, Amatya VJ, et al. **Role of PROPELLER diffusion-weighted imaging and apparent diffusion coefficient in the evaluation of pituitary adenomas.** *Eur J Radiol* 2011;80:412–17 CrossRef Medline
13. Hiwatashi A, Yoshiura T, Togao O, et al. **Evaluation of diffusivity in the anterior lobe of the pituitary gland: 3D turbo field echo with diffusion-sensitized driven-equilibrium preparation.** *AJNR Am J Neuroradiol* 2014;35:95–98 CrossRef Medline
14. Lewis S, Dyvorne H, Cui Y, et al. **Diffusion-weighted imaging of the**

- liver: techniques and applications.** *Magn Reson Imaging Clin N Am* 2014;22:373–95 CrossRef Medline
15. De Robertis R, Tinazzi Martini P, Demozzi E, et al. **Diffusion-weighted imaging of pancreatic cancer.** *World J Radiol* 2015;7:319–28 CrossRef Medline
  16. Sumi M, Nakamura T. **Head and neck tumors: assessment of perfusion-related parameters and diffusion coefficients based on the intravoxel incoherent motion model.** *AJNR Am J Neuroradiol* 2013;34:410–16 CrossRef Medline
  17. Sakamoto J, Imaizumi A, Sasaki Y, et al. **Comparison of accuracy of intravoxel incoherent motion and apparent diffusion coefficient techniques for predicting malignancy of head and neck tumors using half-Fourier single-shot turbo spin-echo diffusion-weighted imaging.** *Magn Reson Imaging* 2014;32:860–66 CrossRef Medline
  18. Le Bihan D, Turner R. **The capillary network: a link between IVIM and classical perfusion.** *Magn Reson Med* 1992;27:171–78 CrossRef Medline
  19. Vidal S, Scheithauer BW, Kovacs K. **Vascularity in nontumorous human pituitaries and incidental microadenomas: a morphometric study.** *Endocr Pathol* 2000;11:215–27 CrossRef Medline
  20. Pekar J, Moonen CT, van Zijl PC. **On the precision of diffusion/perfusion imaging by gradient sensitization.** *Magn Reson Med* 1992;23:122–29 CrossRef Medline
  21. Miki Y, Matsuo M, Nishizawa S, et al. **Pituitary adenomas and normal pituitary tissue: enhancement patterns on gadopentetate-enhanced MR imaging.** *Radiology* 1990;177:35–38 CrossRef Medline
  22. Wang CY, Chung HW, Cho NY, et al. **Idiopathic growth hormone deficiency in the morphologically normal pituitary gland is associated with perfusion delay.** *Radiology* 2011;258:213–21 CrossRef Medline
  23. Conklin J, Heyn C, Roux M, et al. **A simplified model for intravoxel incoherent motion MRI of the brain: clinical validation for perfusion imaging of gliomas and acute strokes.** In: *Proceedings of the 54th Annual Meeting of the American Society of Neuroradiology and the Foundation of the ASNR Symposium*, Washington, DC. May 21–26, 2016

# CT and MR Imaging in the Diagnosis of Scleritis

M.C. Diogo, M.J. Jager, and T.A. Ferreira



## ABSTRACT

**SUMMARY:** Scleritis is a rare, underdiagnosed vision-threatening condition that can occur isolated or in association with other orbital abnormalities. The etiology of scleritis is mainly inflammatory noninfectious, either idiopathic or in the context of systemic disease. Ultrasonography remains the criterion standard in diagnostic imaging of this condition but might prove insufficient, and studies on the diagnostic value of CT and MR imaging are lacking. We retrospectively analyzed 11 cases of scleritis in which CT and/or MR imaging were performed during the active phase of disease and assessed the diagnostic utility of these techniques. The most important imaging findings of scleritis were scleral enhancement, scleral thickening, and focal periscleral cellulitis. MR imaging is the recommended imaging technique, though posterior scleritis also can be accurately diagnosed on CT. It is important for the radiologist to be acquainted with these findings because being able to diagnose scleritis is of clinical significance and might be vision-saving.

**ABBREVIATIONS:** CECT = contrast-enhanced CT; IOID = idiopathic orbital inflammatory disease

Scleritis is a rare but often treatable vision-threatening condition that can occur isolated or in association with other orbital abnormalities.<sup>1,2</sup> The most common etiology is inflammatory (noninfectious, 90% of patients), either idiopathic in the spectrum of idiopathic orbital inflammatory disease (IOID)/pseudotumor or in the context of a systemic disease.<sup>3</sup> Infectious scleritis is rare (7% of cases) and is associated with predisposing factors such as surgery or trauma.<sup>3,4</sup>

Although the diagnosis of scleritis is usually based on clinical assessment and ultrasonography,<sup>3,5</sup> the variable clinical presentation, variable ultrasonography findings, and unfamiliarity with the diagnosis account for posterior scleritis being one of the most underdiagnosed conditions in ophthalmology.<sup>6</sup>

Improvements in CT and MR techniques have led to important progress in ophthalmologic imaging.<sup>7</sup> However, detailed studies concerning imaging of scleritis, especially MR imaging, are few and contain only small numbers of patients.<sup>5,6,8-11</sup>

This article considers the role of CT and MR imaging in the diagnosis of scleritis, emphasizing the array of imaging findings in 11 cases.

## CASE SERIES

We describe a series of 11 cases of scleritis in 10 different patients. All cases had CT and/or MR imaging performed during the active phase of disease. Scleritis was confirmed by an experienced ophthalmologist by using clinical and imaging criteria and by the therapeutic response in doubtful cases.

CT was performed in 8 cases of unilateral scleritis and MR imaging in 6 unilateral and 1 bilateral case of scleritis.

Table 1 lists the clinical and diagnostic information for the 10 patients who form the basis of this report. All patients underwent laboratory testing to determine the presence of infectious and systemic inflammatory diseases.

### Patient 1

A 50-year-old woman with Down syndrome presented with a 5-month history of ocular pain, proptosis, and periorbital swelling on the right orbit and low-grade fever. Contrast-enhanced CT (CECT) showed signs of pre- and postseptal cellulitis and scleritis of the right eye (Fig 1A). Infectious cellulitis was diagnosed and antibiotic therapy started. After a lack of improvement, an inflammatory etiology (IOID) was suspected and nonsteroidal anti-inflammatory drugs were initiated. Complete resolution of symptoms was subsequently achieved with systemic corticosteroids.

Eighteen months later, the same patient re-presented with similar complaints related to the left eye. Clinically, it was again thought to be infectious orbital cellulitis. On CECT, imaging findings on the left orbit were identical to the previous

Received December 20, 2015; accepted after revision June 14, 2016.

From the Department of Neuroradiology (M.C.D.), Centro Hospitalar de Lisboa Central, Lisbon, Portugal; and Departments of Ophthalmology (M.J.J.) and Radiology (T.A.F.), Leiden University Medical Center, Leiden, the Netherlands.

Please address correspondence to Mariana Cardoso Diogo, MD, Departamento de Neuroradiologia, Hospital de São José, Rua José António Serrano, 1150 – Lisboa, Portugal; e-mail: mariana.cardoso.diogo@gmail.com

<http://dx.doi.org/10.3174/ajnr.A4890>

**Table 1: Clinical data of patients with scleritis analyzed by CT and/or MR imaging**

Pt	Duration of Symptoms <sup>a</sup>	US Performed, Diagnosis	Clinical Diagnosis <sup>b</sup>	Imaging Modality	Systemic Disease	Final Diagnosis
1	5 mo	No	Infectious cellulitis	CT	Down syndrome	IOID with scleritis
1	2 mo	No	Infectious cellulitis	CT	Down syndrome	IOID with scleritis
2	3 mo	Yes, disc edema	Optic neuritis	MRI	Not found	Bilateral idiopathic scleritis
3	2 mo	No	Intraorbital mass	CT	Not found	Idiopathic scleritis
4	2 mo	Yes, uveal mass	Choroidal melanoma	CT	Not found	Nodular idiopathic scleritis
5	Acute	No	Infectious cellulitis	CT, MRI	DRM; Colon carcinoma	Infectious orbital disease with panophthalmitis
6	6 mo	No	Infectious cellulitis	CT, MRI	Down syndrome	IOID with sclerouveitis
7	1 mo	Yes, scleritis	Scleritis or tumor	MRI	Granulomatosis with polyangiitis	Autoimmune orbital inflammation with scleritis
8	2 mo	No	Uveitis	CT, MRI	JIA	Autoimmune sclerouveitis
9	3 wk	Yes, inconclusive	Optic pathway condition	CT, MRI	None	Idiopathic scleritis
10	4 wk	No	Optic pathway condition	MRI	None	Idiopathic scleritis

**Note:**—DRM indicates dermatomyositis; JIA, juvenile idiopathic arthritis; Pt, patient; US, ultrasonography.

<sup>a</sup>Duration of symptoms refers to the time elapsed between onset of symptoms of scleritis (pain, vision disturbances) and the time of imaging.

<sup>b</sup>Diagnosis after ophthalmologic evaluation and ultrasound and before CT and/or MRI.

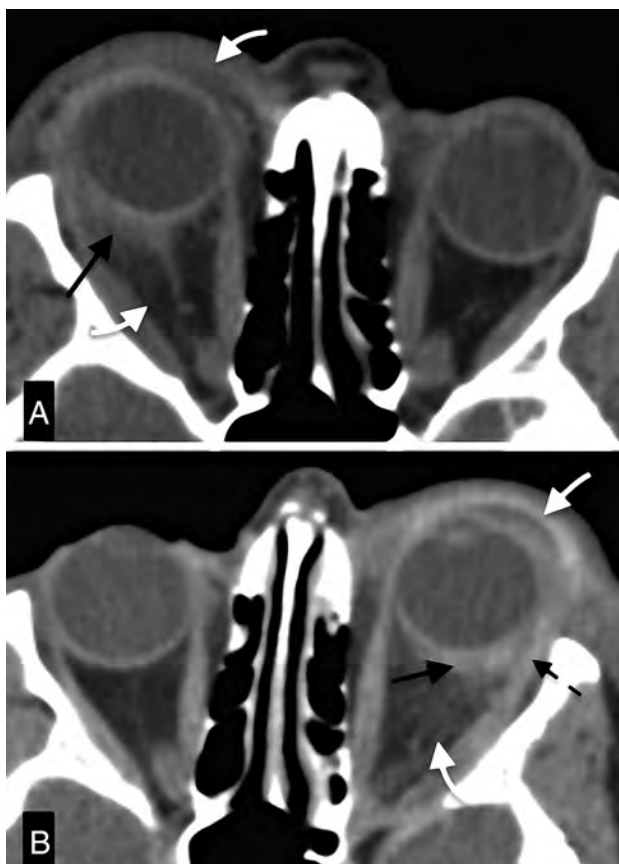


**FIG 1.** Asynchronous IOID with scleritis. *A*, CECT depicts outward, eccentric thickening and enhancement of the right globe wall with focal periscleral cellulitis (*black arrow*), compatible with posterior scleritis. There is associated pre- and postseptal cellulitis (*white arrow*) and proptosis. *B*, CECT 18 months after examination (*A*) shows almost identical findings in the left orbit. *Black* and *white arrows* point to the scleritis and cellulitis, respectively. Notice the complete resolution of the alterations of the right orbit. Also, notice involvement of the tendon of the lateral rectus anteriorly (*dashed arrow*).

findings on the right side (Fig 1*B*). Because of the presence of scleritis and a history of pseudotumor, recurrent IOID (with scleritis) was diagnosed and corticosteroids started, with total recovery.



**FIG 2.** Bilateral inflammatory isolated scleritis: axial MR images. *A*, Post-Gd-DTPA T1-weighted image with fat saturation shows bilateral enhancement of the outer aspect of the sclera (*white arrows*) extending to the optic nerve sheath, depicting scleritis. There is also focal periscleral cellulitis. Notice the absence of ocular anomalies on the precontrast T1WI (*B*).

#### **Patient 2**

An 11-year-old girl presented with 3 months of severe headaches that progressed to bilateral orbital pain and blurry vision. She had a history of recurrent peripheral articular pain. Ultrasonography revealed bilateral disc edema, and optic neuropathy was suspected. Gadolinium-enhanced MR imaging showed bilateral posterior scleritis (Fig 2*B*). In the absence of infectious parameters, an inflammatory idiopathic etiology was assumed and systemic cor-

ticosteroids started, with improvement. Follow-up MR imaging showed no anomalies.

### Patient 3

A 68-year-old woman presented with a 2-month history of proptosis and ocular pain on the left eye. Suspecting a retrobulbar mass, CECT was performed, depicting scleritis with periscleral cellulitis. Diagnosis of inflammatory idiopathic scleritis was made, and the patient was started on nonsteroidal anti-inflammatory drugs, with clinical improvement.

### Patient 4

A 41-year-old woman was referred for enucleation by an ophthalmologist with the diagnosis of uveal melanoma. She had a 2-month history of vision loss and pain in the left eye. Fundoscopy and ultrasonography findings were compatible with a mass, but because of clinical uncertainty, including the presence of pain, a CECT was performed. It showed a scleral mass displacing the choroid anteriorly, with periscleral cellulitis (Fig 3). Given the cellulitis, sparing of the choroid, and the presence of pain, a diagnosis of inflammatory idiopathic nodular scleritis was suggested. Systemic corticosteroids were started, with complete resolution of symptoms, confirming the diagnosis.



**FIG 3.** Nodular inflammatory scleritis mimicking uveal melanoma. CECT depicts a posterior globe wall mass (black arrow) deviating the choroid-retinal layer internally (white arrow), and hence, most probably arising from the sclera. Also notice the presence of slight periscleral cellulitis.

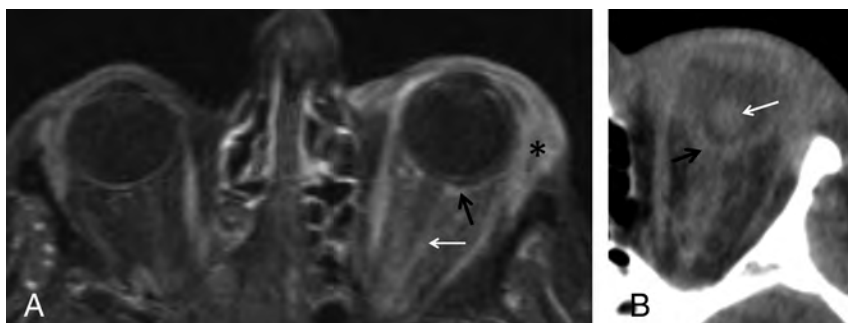


**FIG 4.** Infectious orbital process with scleritis followed by panophthalmitis. Post-Gd-DTPA axial T1-weighted spectral presaturation with inversion recovery image of the orbit (A) depicts scleral enhancement (black arrow) and extensive pre- and postseptal cellulitis, with involvement of the optic nerve sheath (white arrow) and dacryoadenitis (asterisk). CECT performed 48 hours later (B) shows lens luxation (white arrow) and inward folding of the globe wall with volume loss (black arrow), depicting globe rupture.

### Patient 5

A 66-year-old woman under immunosuppression for dermatomyositis presented with sudden onset of vision loss on the left, headache, proptosis, fever, and elevated infectious parameters. MR imaging depicted pre- and postseptal cellulitis, scleritis, and dacryoadenitis (Fig 4A). An orbital infection was suspected, and the patient was started on antibiotics. Despite treatment, infection progressed to panophthalmitis, and a subsequent CT showed globe rupture (Fig 4B). Cultures isolated *Clostridium septicum*.

### Patient 6

A 56-year-old woman with Down syndrome complained of progressive right eyelid swelling and proptosis. Infectious cellulitis was suspected and the patient started on antibiotics, without improvement. An inflammatory idiopathic etiology was suspected and MR imaging performed, demonstrating pre- and postseptal cellulitis, scleritis, and uveitis, with choroidal and retinal detachments. Therapy with corticosteroids was initiated, with resolution of all ocular complaints.

### Patient 7

An 80-year-old woman with granulomatosis with polyangiitis (Wegener) presented with a history of left ocular pain and 1 month of left eyelid swelling. Ultrasonography identified left posterior scleritis, but because of lack of improvement on nonsteroidal anti-inflammatory drugs, MR imaging was performed to exclude malignancy. It showed left scleritis (Fig 5), dacryoadenitis, and cellulitis. The findings were consistent with inflammatory autoimmune orbital disease, and corticosteroids were started. Resolution of symptoms was achieved after adding cyclophosphamide.

### Patient 8

A 10-year-old boy with a history of idiopathic juvenile arthritis presented with ocular pain and diminished visual acuity of the left eye. Fundoscopy showed optic disc edema and signs of posterior uveitis, and orbital MR imaging depicted scleritis (Fig 6). Inflammatory autoimmune sclerouveitis was diagnosed, and corticosteroids and immunosuppressive medication were started, with clinical improvement.

### Patient 9

A 47-year-old man presented with a 3-week history of headaches and blurred vision. Ultrasonography was inconclusive. CECT depicted posterior scleritis, confirmed by MR imaging (Fig 7). Assuming an inflammatory idiopathic etiology, nonsteroidal anti-inflammatory drugs were started, with complete resolution of symptoms.

### Patient 10

An 8-year-old boy, with headaches for 4 weeks, presented with diminished visual acuity on the right eye. An optic neuropathy was suspected, and MR imaging

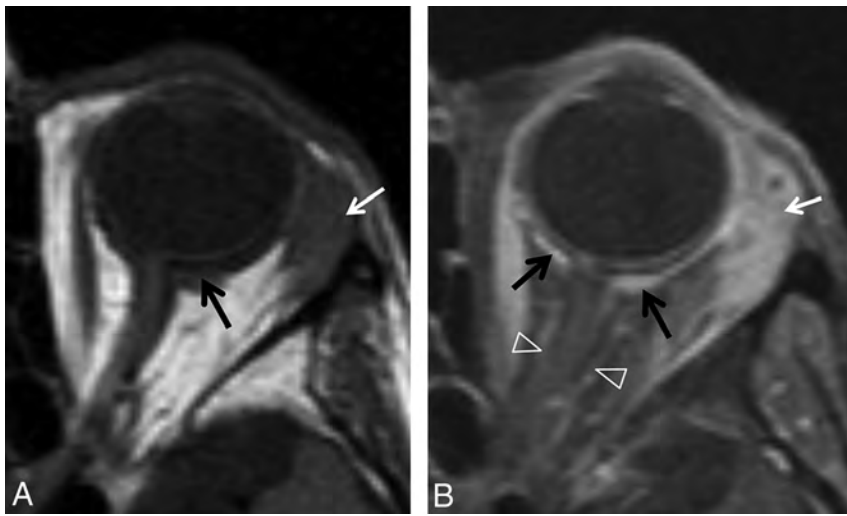


**FIG 5.** Orbital inflammation with scleritis in patient with granulomatosis with polyangiitis (Wegener). TIWI (A) shows eccentric focal thickening of the sclera (black arrow), with coexisting enlargement of the lacrimal gland (white arrow), both enhancing on the post-Gd-DTPA T1-weighted spectral presaturation with inversion recovery image (B). Enhancement extends to the optic nerve sheath (open arrow heads). This illustrates posterior scleritis with optic perineuritis, cellulitis, and dacryoadenitis.

was performed, showing scleritis and focal periscleral cellulitis. An inflammatory idiopathic etiology was suspected and the patient started on corticosteroids and methotrexate, with visual recovery.

## DISCUSSION

Although clinically scleritis is classified according to an anterior or posterior location and subdivided into diffuse or nodular (focal) forms,<sup>12,13</sup> there has been no defined classification applied to imaging studies. Inflammation or infection of the sclera as observed on CT or MR imaging is generally referred to as “scleritis” independent of location or etiology. Anterior scleritis is the most common form, readily diagnosed on direct observation without the need for imaging.<sup>2,12</sup> Posterior scleritis accounts for 2%–12% of cases and is widely underdiagnosed because of its rarity, variable clinical findings, and unfamiliarity with this condition of the general ophthalmologist and radiologist.<sup>2,6</sup> The etiology of scleritis is most often inflammatory noninfectious, occurring either as an idiopathic condition (43%) or as a manifestation of a systemic disease (48%),<sup>7,12,14</sup> most often autoimmune. Rheumatoid arthritis and granulomatosis with polyangiitis are the most common underlying conditions. Idiopathic inflammatory scleritis might occur isolated or associated with extraocular anomalies and, we believe, as suggested by other authors,<sup>10,11,15–17</sup> is part of the IOID/pseudotumor spectrum. We identified a systemic disease in 2 patients (granulomatosis with polyangiitis, juvenile idiopathic arthritis). In addition, 2 patients had Down syndrome, which to our knowledge has not been specifically associated with scleritis; both patients presented with extensive IOID. Infectious scleritis is rare, particularly in the absence of predisposing factors.<sup>3,4</sup> In our series, 1 case was identified in an immunosuppressed patient.

The most distinctive clinical feature of scleritis is orbital pain, present in around 60% of patients.<sup>3</sup> Orbital pain occurred in 7 of our 11 cases. From the remaining 4 cases, 3 presented with head-

aches. Decreased vision has been described to occur in up to 31% of patients, 3% developing permanent visual loss.<sup>1</sup> We found visual symptoms in 6 cases, 5 of which resolved completely with treatment. Fever is a feature in infectious scleritis. Treatment depends on etiology and, excluding infectious causes, involves nonsteroidal anti-inflammatory drugs, corticosteroids, and immunosuppressive drugs.<sup>3,18</sup>

Correctly diagnosing scleritis is important given the potential for complications and the frequent association with systemic disease, of which scleritis might be the presenting manifestation.<sup>2,3,14</sup> Because the posterior sclera cannot be directly visualized, imaging methods are needed to make or confirm the diagnosis in clinically challenging cases. Sonography is the most widely used imaging technique, but often fails to show pathognomonic findings and is

of limited value in evaluating other intraorbital structures.<sup>2,19</sup> Scleritis is frequently part of a more extensive inflammatory process, which might involve other orbital structures. In our series, sonography was performed by a specialized ophthalmologist in 4 patients and was diagnostic in 1 patient. Sonography was not performed in the remaining patients because scleritis was not clinically suspected.

MR imaging has excellent soft tissue contrast and the ability to image the entire orbit. On T2-weighted sequences, the posterior globe wall appears as a single hypointense ring, whereas on T1-weighted sequences, the sclera can be individualized as the outer hypointense rim of the globe. A distinct hyperintense and enhancing rim can be seen internal to the sclera, corresponding to the choroid, and, at least partially, to the retina (Fig 2B).

Direct signs of scleritis on imaging are scleral enhancement, scleral thickening, and focal periscleral cellulitis. Our most consistent finding was scleral enhancement, present in 100% of contrast-enhanced examinations. Enhancement might involve the whole sclera (Fig 1B) or be preferentially peripheral (Fig 2), perhaps illustrating different degrees of inflammation, starting from the vascularized outer aspect of the sclera. It also might extend along the optic nerve sheath (Fig 5), representing optic perineuritis. Scleral enhancement is always abnormal and should not be confused with choroidal enhancement, a physiologic finding. Use of contrast is critical because scleral enhancement might be the only positive finding (Fig 2).<sup>5</sup> On MR imaging, postcontrast T1WI should be acquired with fat saturation because the fat signal might mask scleral enhancement. Another sign of scleritis is scleral thickening, present in 83% of our patients and easily identified on MR imaging. On CT, though the globe layers cannot be separated, we found eccentric globe wall thickening and peripheral enhancement in all patients, making CT a useful tool in the diagnosis of scleritis.<sup>6,11,20</sup> Periscleral cellulitis, described as the “ring sign” by Chaques et al,<sup>11</sup> is also an important sign of scleritis,

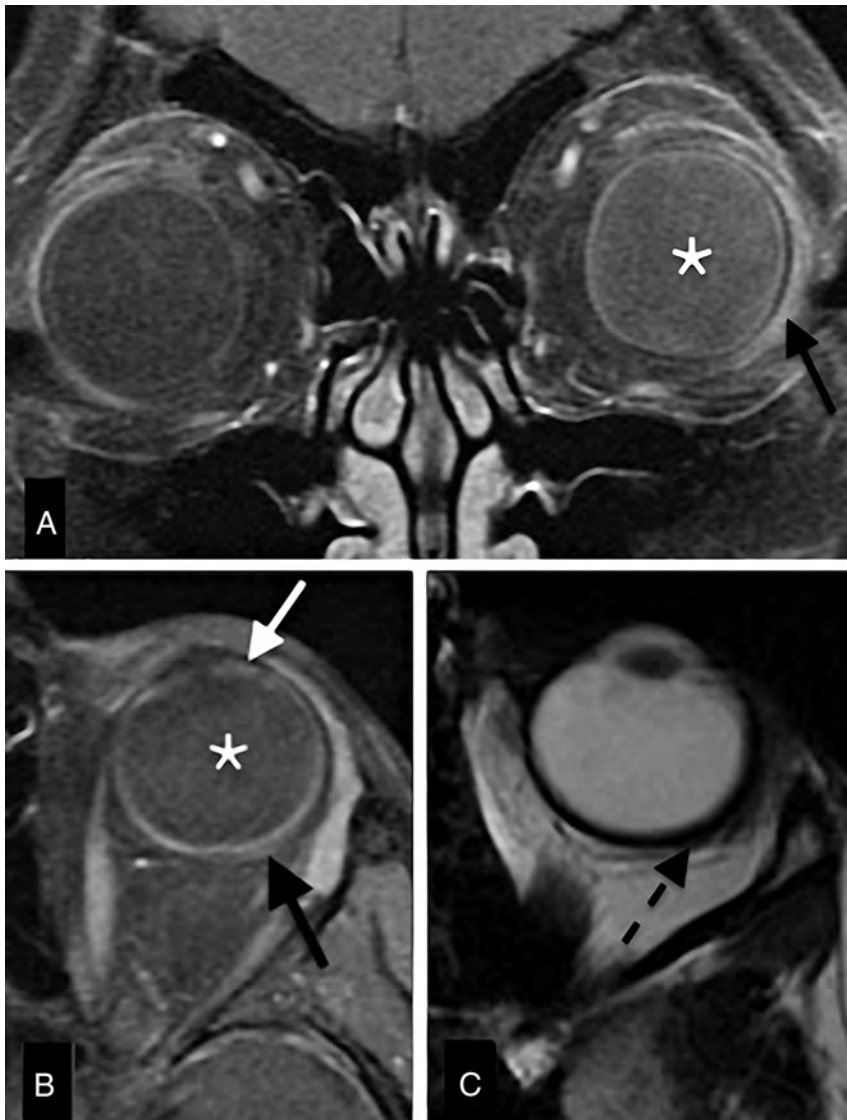


**FIG 6.** Scleritis with vitritis and uveitis. Enhanced coronal (A) and axial (B) T1-weighted spectral presaturation with inversion recovery images and axial T2WI (C) with a sclerouveitis. There is increased signal intensity of the vitreous on the left (vitritis; A, B, asterisk), with slight focal enhancement of the iris/ciliary body (uveitis; white arrow) and concurrent slight focal scleral outward thickening (C, black dashed arrow) and enhancement (B, black solid arrow).

found in 42% of our patients. Imaging findings are summarized in Table 2.

Indirect signs of scleritis include retinal and choroidal detachment and effusion in the suprachoroidal or Tenon spaces.<sup>6</sup> There might be associated uveitis,<sup>18,21</sup> which can be differentiated from scleritis, particularly on MR imaging.

Scleritis also might be associated with extraocular orbital abnormalities, as seen in 5 of our cases, such as pre- and postseptal cellulitis, myositis, or dacryoadenitis. When scleritis occurs with anterior cellulitis, the clinical picture is often mistaken for infectious orbital cellulitis. Because extension of an orbital infection to the sclera is extremely rare in immunocompetent patients, coexistence of cellulitis and scleritis on imaging should raise suspicion of an inflammatory noninfectious etiology.<sup>3</sup> Other clues pointing to an inflammatory etiology include sub-

acute/chronic complaints and absence of fever, infectious parameters, or sinusitis.

The differential diagnosis of scleritis on imaging mainly is tumor, particularly with nodular scleritis, with published cases of globe tumors misdiagnosed as scleritis<sup>14</sup> and scleritis mimicking a choroidal mass.<sup>8,9</sup> In the diffuse form of scleritis, posterior uveitis, diffuse melanoma, and lymphoma are the most relevant differential diagnoses. CT and MR imaging have proved useful in distinguishing these entities.<sup>20</sup> In challenging cases, a therapeutic trial (with nonsteroidal anti-inflammatory drugs or steroids)<sup>15</sup> and/or histopathologic confirmation might be warranted because misdiagnoses of scleritis have been described to lead to inadvertent enucleations.<sup>9</sup> In the presented case with melanoma as the presumptive diagnosis (patient 4), imaging and treatment with corticosteroids led to resolution of the mass, making a biopsy unnecessary. Clues to the inflammatory (versus neoplastic) nature of the process include the presence of pain, cellulitis as seen on imaging, and the specific scleral location, though some intraocular tumors might also involve the sclera. Additional MR sequences, such as DWI, might be of benefit,<sup>22</sup> particularly in lymphoma, which often demonstrates restricted diffusion.<sup>23</sup> Neither DWI nor other advanced imaging sequences were routinely performed in our patients.

Although we present a small group of patients, they illustrate a wide range of direct and indirect imaging findings in scleritis. CT and MR imaging provided useful information and influenced

clinical decision-making. MR imaging is the most useful examination in the diagnosis of scleritis,<sup>5,9</sup> differentiating the sclera from the other ocular layers. In our experience and as ascertained by previous studies,<sup>6,11,20</sup> CT is also able to diagnose scleritis, showing eccentric outward globe wall thickening and enhancement, frequently associated with periscleral cellulitis. Both techniques are more informative than ultrasonography for assessment of extraocular extension of disease.

We suggest that in cases when clinical evaluation and ultrasonography do not suffice in the diagnosis of scleritis, or when associated ailments are suspected, MR imaging be performed. When MR imaging is not available, or when there are contraindications, CT can be of diagnostic value.

The results of our study are limited by its retrospective nature, the small number of patients, and the lack of a standardized pro-

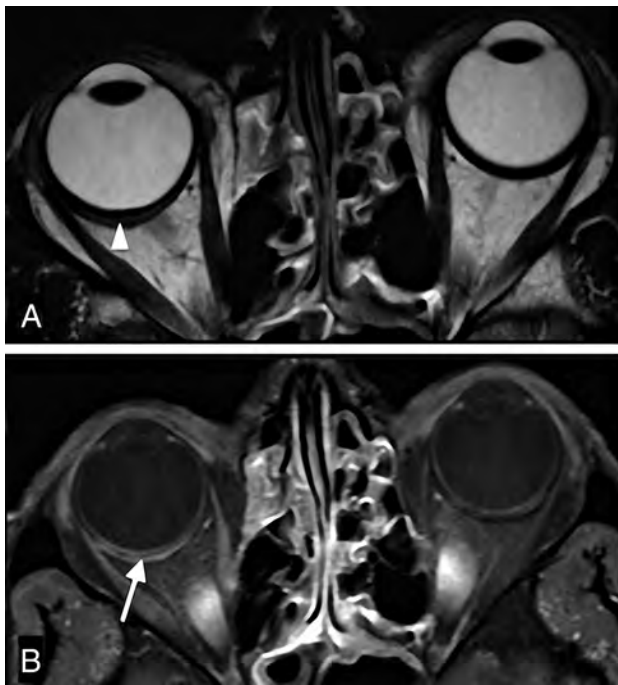


**FIG 7.** Isolated inflammatory scleritis: orbital MR imaging. T2-weighted (A) and Gd-DTPA enhanced T1-weighted spectral presaturation with inversion recovery (B) images depict scleral thickening and enhancement (B, white arrow). There is a linear hyperintense (fluid) collection between the sclera and the choroid/retina, representing a suprachoroidal effusion (A, white arrowhead).

**Table 2: Imaging findings in 11 cases with scleritis on CT (n = 8) and MRI (n = 8)**

Imaging Modality	Imaging Finding	No. (%)
CT	Eccentric enhancement of the globe wall	8 (100)
	Eccentric thickening of the sclerouveal rim	8 (100)
	Periscleral cellulitis	6 (75)
	Pre/postseptal cellulitis	4 (50)
	Nodular scleral thickening	1 (13)
MR	Scleral enhancement	8 (100)
	Scleral thickening	6 (75)
	Focal periscleral cellulitis	4 (50)
	Pre/postseptal cellulitis	2 (25)
	Scleral thinning	1 (13)
	Dacryoadenitis	1 (13)
	Uveitis	2 (25)
	Suprachoroidal effusion	1 (13)
	Retinal detachment	1 (13)
	Choroidal detachment	1 (13)

tol. Despite this, we believe that this article contributes to the current knowledge on imaging signs of scleritis on CT and MR imaging. To the best of our knowledge, this is the largest series of MR imaging in scleritis analyzed to date.

## CONCLUSIONS

Scleritis is an underdiagnosed, treatable condition, almost invariably of inflammatory noninfectious etiology—idiopathic, in the spectrum of IOID, or in the context of a systemic disease. Imaging findings on CT and particularly on MR imaging are quite distinct and include scleral enhancement, scleral thickening, and focal periscleral cellulitis. To the radiologist, familiarization with these findings is important to recognize this diagnosis.

Disclosures: Martine Jäger—UNRELATED: Travel/Accommodations/Meeting Expenses Unrelated to Activities Listed: Costs made for travel as visiting professor have been repaid by universities.

## REFERENCES

- McCluskey PJ, Watson PG, Lightman S, et al. **Posterior scleritis: clinical features, systemic associations, and outcome in a large series of patients.** *Ophthalmology* 1999;106:2380–86 CrossRef Medline
- Benson WE. **Posterior scleritis.** *Surv Ophthalmol* 1988;32:297–316 CrossRef Medline
- Biber J, Schwam B, Raizman M. **Scleritis.** In: Krachmer J, Mannis M, Holland E, eds. *Cornea*. 3rd ed. St Louis: Mosby; 2011
- Ho YF, Yeh LK, Tan HY, et al. **Infectious scleritis in Taiwan—a 10-year review in a tertiary-care hospital.** *Cornea* 2014;33:838–43 CrossRef Medline
- Cordero-Coma M, García-Morán A, Yilmaz T, et al. **Adjunctive globe magnetic resonance imaging in the diagnosis of posterior scleritis.** *Can J Ophthalmol* 2011;46:329–32 CrossRef Medline
- Biswas J, Mittal S, Ganesh SK, et al. **Posterior scleritis: clinical profile and imaging characteristics.** *Indian J Ophthalmol* 1998;46:195–202 Medline
- Mafee MF, Karimi A, Shah J, et al. **Anatomy and pathology of the eye: role of MR imaging and CT.** *Radiol Clin N Am* 2006;44:135–57 CrossRef
- Osman Saatci A, Saatci I, Kocak N, et al. **Magnetic resonance imaging characteristics of posterior scleritis mimicking choroidal mass.** *Eur J Radiol* 2001;39:88–91 CrossRef Medline
- Maggioni F, Ruffatti S, Viaro F, et al. **A case of posterior scleritis: differential diagnosis of ocular pain.** *J Headache Pain* 2007;8:123–26 CrossRef Medline
- Johnson MH, DeFilipp GJ, Zimmerman RA, et al. **Scleral inflammatory disease.** *AJNR Am J Neuroradiol* 1987;8:861–65 Medline
- Chaque VJ, Lam S, Tessler HH, et al. **Computed tomography and magnetic resonance imaging in the diagnosis of posterior scleritis.** *Ann Ophthalmol* 1993;25:89–94 Medline
- Okhravi N, Odufuwa B, McCluskey P, et al. **Scleritis.** *Surv Ophthalmol* 2005;50:351–63 CrossRef Medline
- Watson PG, Hayreh SS. **Scleritis and episcleritis.** *Br J Ophthalmol* 1976;60:163–91 CrossRef Medline
- Kalkala C, Daoud YJ, Paredes I, et al. **Masquerade scleritis.** *Ocul Immunol Inflamm* 2005;13:479–82 CrossRef Medline
- Gordon LK. **Orbital inflammatory disease: a diagnostic and therapeutic challenge.** *Eye (Lond)* 2006;20:1196–206 CrossRef Medline
- Uehara F, Ohba N. **Diagnostic imaging in patients with orbital cellulitis and inflammatory pseudotumor.** *Int Ophthalmol Clin* 2002;42:133–42 CrossRef Medline
- Ding ZX, Lip G, Chong V. **Idiopathic orbital pseudotumour.** *Clin Radiol* 2011;66:886–92 CrossRef Medline
- Wieringa WG, Wieringa JE, ten Dam-van Loon NH, et al. **Visual outcome, treatment results, and prognostic factors in patients with scleritis.** *Ophthalmology* 2013;120:379–86 CrossRef Medline
- Benson WE, Shields JA, Tasman W, et al. **Posterior scleritis. A cause of diagnostic confusion.** *Arch Ophthalmol* 1979;97:1482–86 CrossRef Medline
- Dorey SE, Clark BJ, Christopoulos VA, et al. **Orbital lymphoma misdiagnosed as scleritis.** *Ophthalmology* 2002;109:2347–50 CrossRef Medline
- Cheung CM, Chee SP. **Posterior scleritis in children: clinical features and treatment.** *Ophthalmology* 2012;119:59–65 CrossRef Medline
- Kapur R, Sepahdari AR, Mafee MF, et al. **MR imaging of orbital inflammatory syndrome, orbital cellulitis, and orbital lymphoid lesions: the role of diffusion-weighted imaging.** *AJNR Am J Neuroradiol* 2009;30:64–70 Medline
- Razek AA, Elkhamary S, Mousa A. **Differentiation between benign and malignant orbital tumors at 3-T diffusion MR-imaging.** *Neuroradiology* 2011;53:517–22 CrossRef Medline

# Pediatric Patients Demonstrate Progressive T1-Weighted Hyperintensity in the Dentate Nucleus following Multiple Doses of Gadolinium-Based Contrast Agent

 D.R. Roberts,  A.R. Chatterjee,  M. Yazdani,  B. Marebwa,  T. Brown,  H. Collins,  G. Bolles,  J.M. Jenrette,  P.J. Nietert, and  X. Zhu



## ABSTRACT

**BACKGROUND AND PURPOSE:** While there have been recent reports of brain retention of gadolinium following gadolinium-based contrast agent administration in adults, a retrospective series of pediatric patients has not previously been reported, to our knowledge. We investigated the relationship between the number of prior gadolinium-based contrast agent doses and increasing T1 signal in the dentate nucleus on unenhanced T1-weighted MR imaging. We hypothesized that despite differences in pediatric physiology and the smaller gadolinium-based contrast agent doses that pediatric patients are typically administered based on weighted-adjusted dosing, the pediatric brain would also demonstrate dose-dependent increasing T1 signal in the dentate nucleus.

**MATERIALS AND METHODS:** We included children with multiple gadolinium-based contrast agent administrations at our institution. A blinded reader placed ROIs within the dentate nucleus and adjacent cerebellar white matter. To eliminate reader bias, we also performed automated ROI delineation of the dentate nucleus, cerebellar white matter, and pons. Dentate-to-cerebellar white matter and dentate-to-pons ratios were compared with the number of gadolinium-based contrast agent administrations.

**RESULTS:** During 20 years at our institution, 280 patients received at least 5 gadolinium-based contrast agent doses, with 1 patient receiving 38 doses. Sixteen patients met the inclusion/exclusion criteria for ROI analysis. Blinded reader dentate-to-cerebellar white matter ratios were significantly associated with gadolinium-based contrast agent doses ( $r_s = 0.77, P = .001$ ). The dentate-to-pons ratio and dentate-to-cerebellar white matter ratios based on automated ROI placement were also significantly correlated with gadolinium-based contrast agent doses ( $t = 4.98, P < .0001$  and  $t = 2.73, P < .02$ , respectively).

**CONCLUSIONS:** In pediatric patients, the number of prior gadolinium-based contrast agent doses is significantly correlated with progressive T1-weighted dentate hyperintensity. Definitive confirmation of gadolinium deposition requires tissue analysis. Any potential clinical sequelae of gadolinium retention in the developing brain are unknown. Given this uncertainty, we suggest taking a cautious stance, including the use, in pediatric patients, of higher stability, macrocyclic agents, which in both human and animal studies have been shown to be associated with lower levels of gadolinium deposition, and detailed documentation of dosing. Most important, a patient should not be deprived of a well-indicated contrasted MR examination.

**ABBREVIATIONS:** DN/C = dentate-to-cerebellar white matter; DN/P = dentate-to-pons; GBCA = gadolinium-based contrast agent; MNI = Montreal Neurological Institute; SUIT = Spatially Unbiased Atlas Template of the Cerebellum and Brain Stem

Gadolinium-based contrast agents (GBCAs) have been used extensively in the pediatric population for the evaluation of various central nervous system and non-CNS pathologies. The American College of Radiology Appropriateness Criteria, a set of evidence-based guidelines developed by the American College of

Radiology to assist physician decision-making, considers post-contrast MR imaging appropriate in several pediatric clinical scenarios.<sup>1</sup> The contrast agents available for use in children in the United States have FDA approval only for CNS indications, and several agents are not approved for pediatric use. At present only 1 GBCA (gadoteridol) is approved for children younger than 2

Received May 2, 2016; accepted after revision June 13.

From the Departments of Radiology and Radiological Sciences (D.R.R., A.R.C., M.Y., B.M., T.B., H.C., G.B.), Neurosciences and Neuroscience Research (D.R.R.), Radiation Oncology (J.M.J.), Biostatistics (P.J.N.), and Public Health Sciences (P.J.N.), Medical University of South Carolina, Charleston, South Carolina; and Department of Psychology (X.Z.), Normal College, Shihezi University, Xinjiang, China.

This work was funded, in part, by the National Institutes of Health, National Center for Advancing Translational Science (grant No. UL1TR001450).

Paper previously presented at: Annual Meeting of the American Society of Neuroradiology and the Foundation of the ASNR Symposium, May 23–26, 2016; Washington, DC.

Please address correspondence to Donna R. Roberts, MD, Department of Radiology and Radiological Sciences, 96 Jonathan Lucas St, MSC 323, Medical University of South Carolina, Charleston, SC 29425-3230; e-mail: robertdr@muscc.edu

 Indicates open access to non-subscribers at [www.ajnr.org](http://www.ajnr.org)

<http://dx.doi.org/10.3174/ajnr.A4891>

years of age. Therefore, in many clinical situations, the use of GBCAs in children is considered off-label but is well-supported as a standard-of-care in clinical practice.

GBCAs have been used safely in the pediatric population since their introduction into clinical practice in the late 1980s.<sup>2-7</sup> Indeed, pediatric GBCA administration has been associated with lower incidences of acute adverse reactions than GBCA administration in adults, with a 0.04% frequency in children compared with 0.07% in adults.<sup>8</sup> Furthermore, there are only a few case reports of children developing nephrogenic systemic fibrosis, a rare complication of GBCA administration associated with acute or severe chronic renal disease resulting in a scleroderma-like reaction of the skin along with systemic involvement of the internal organs.<sup>9</sup> To our knowledge, there are no reported cases of nephrogenic systemic fibrosis in patients younger than 2 years of age despite the clinical use of GBCAs in this age group and the known renal immaturity of neonates. In these very young patients, the estimated glomerular filtration rate (milliliters/minute/1.73 m<sup>2</sup>) values do not typically reach 60 mL/min/1.73 m<sup>2</sup> until the patient is older than 3 months of age or later in preterm infants.<sup>10</sup>

Recently, however, there have been reports of gadolinium deposition in the brain and other tissues of adult patients with normal renal function. This was first recognized by Kanda et al<sup>11</sup> as a progressive increase in intrinsic T1 signal in the dentate nucleus and globus pallidus on unenhanced T1-weighted imaging that correlated with the number of previously administered doses of GBCA. This initial report by Kanda et al was quickly followed by other collaborating studies in adult patients<sup>12-16</sup> and by pathologic confirmation that the increasing T1-weighted signal within the dentate nucleus corresponded to areas of gadolinium deposition.<sup>17,18</sup> It is unknown, however, whether the pediatric brain is also susceptible to gadolinium deposition, given differences in physiology and the smaller GBCA doses pediatric patients are typically administered based on weighted-adjusted dosing. Despite case reports of 2 pediatric patients,<sup>19,20</sup> retrospective series have not been described in children. Here, we present a series of pediatric patients exposed to multiple doses of GBCAs who developed T1-weighted hyperintensity in the dentate nucleus, which correlated with the number of administered GBCA doses. We also introduce an automated method for ROI delineation to eliminate reader bias.

## MATERIALS AND METHODS

The study was approved by the Medical University of South Carolina institutional review board and was compliant with the Health Insurance Portability and Accountability Act. Informed consent was waived due to the retrospective nature of the study.

### Patients

To determine our total institutional pediatric GBCA exposure, we included all pediatric patients who had been administered any GBCA at our institution during an approximately 20-year period (January 1, 1995, to June 30, 2014). All patients who received at least 1 dose of a GBCA at our institution and who were 18 years of age or younger at the time of administration were included. Many of these patients had also received additional doses of GBCAs at outside institutions, which could not be verified; therefore, these

gadolinium doses were not included in the calculated total number of documented GBCA administrations.

During the period investigated, the most widely used MR imaging contrast agent for pediatric MR imaging at our institution was gadopentetate dimeglumine (Magnevist; Bayer HealthCare Pharmaceuticals, Wayne, New Jersey), though gadodiamide (Omniscan; GE Healthcare, Piscataway, New Jersey), gadoteridol (ProHance; Bracco Diagnostics, Princeton, New Jersey), and gadobenate dimeglumine (MultiHance; Bracco Diagnostics) were also available at various times during the 20-year period. To limit assessment to 1 agent, we included those patients who had received at least 5 consecutive doses of only Magnevist, as recorded by the MR imaging technologist at the time of the scan. We cannot, however, completely exclude the possibility that the patients received other agents such as an unknown GBCA at an outside institution.

Of the total pediatric population who had contrast-enhanced MR imaging examinations at our institution from January 1, 1995, to June 30, 2014, we identified 58 pediatric patients who had undergone at least 5 consecutive MR imaging scans following a documented intravenous injection of gadopentetate dimeglumine. Thirty-six patients were excluded from analysis with any form of posterior fossa pathology involving the cerebellum, including cerebellar tumors, infection, or congenital malformations. Finally, 6 additional patients who had undergone posterior fossa radiation therapy were excluded. Radiation therapy was defined as whole-brain radiation or any radiation treatment that included the posterior fossa in the radiation field. Therefore, 16 patients meeting the inclusion criteria were analyzed. We screened these patients for any degree of renal failure as defined by an estimated glomerular filtration rate value of <60 mL/min/1.73 m<sup>2</sup>, liver failure, parenteral nutrition, or the presence of additional underlying disorders such as congenital metabolic diseases. Clinical information, imaging data, and the administered GBCA were obtained from the electronic medical records of our hospital, PACS, and the radiology information management system. See Table 1 for patient clinical information.

### MR Imaging Protocol

All patients underwent MR imaging on either a 1.5T or 3T system. Various MR imaging systems were available for patient imaging during the 20-year period, including both Philips Healthcare (Best, the Netherlands) and Siemens (Erlangen, Germany). In all patients, the MR imaging protocol included a sagittal, unenhanced, T1-weighted spin-echo sequence (section thickness, 3–5 mm; gap, 1–2.5 mm; TR, 300–691 ms; TE, 8–20 ms). The in-plane resolution ranged from 0.69 to 1.1 mm, with most being 0.86 mm (matrix, 256 × 256). Most commonly, the sagittal T1-weighted sequence was of the whole brain; however, occasionally, patients underwent imaging per a dedicated protocol (pituitary, face, or neck) that did not include whole-brain coverage. These scans were also evaluated if the reviewer deemed the sequence adequate for visualization of the dentate nucleus and cerebellar white matter. Gadopentetate dimeglumine was administered as an intravenous bolus by using body weighted-adjusted dosing at 0.1 mmol/kg per departmental protocol.

**Table 1: Clinical description and number of doses of GBCA for patients who underwent ROI analysis<sup>a</sup>**

Patient No.	Diagnosis	Chemotherapy	Total Parenteral Nutrition	No. of Gadopentetate Dimeglumine Doses Prior to MRI Study Evaluated by Blinded Reader	No. of MRI Studies with GBCA Administration Evaluated by Automated Analysis
1	Temporal astrocytoma/glioblastoma	Yes	No	12	14
2	Optic glioma/neurofibromatosis type 1	No	No	7	NA
3	Temporal desmoplastic infantile ganglioma	No	No	7	6
4	Temporoparietal pleomorphic xanthoastrocytoma	Yes	No	7	10
5	Craniopharyngioma	No	No	7	4
6	Parieto-occipital desmoplastic infantile ganglioma	No	No	4	11
7	Marfan syndrome with CSF leaks	No	No	7	8
8	Parotid hemangiomas	No	No	4	4
9	Multiple sclerosis	No	No	5	5
10	Thalamic astrocytoma	No	No	12	14
11	Parapharyngeal rhabdomyosarcoma	Yes	No	7	NA
12	Maxillary sinus vascular malformation	No	No	16	15
13	Brain stem encephalitis	No	No	6	6
14	Thoracic spinal cord pilocystic astrocytoma	Yes	Yes	7	NA
15	Parietal low-grade astrocytoma	Yes	No	6	27
16	Frontal pleomorphic xanthoastrocytoma	Yes	No	6	5

**Note:**—NA indicates not applicable.

<sup>a</sup>None of the patients had documented renal failure. A few patients occasionally had mildly elevated liver function test levels, but none were diagnosed with liver failure.

### Image Analysis: User-Defined ROIs

We used methods similar to those reported in the literature.<sup>11,21</sup> For each patient, the last contrasted MR imaging scan with documented gadopentetate dimeglumine administration was evaluated. By visual inspection, a board-certified neuroradiologist, blinded to the patient's clinical history and the number of prior contrast administrations, placed ROIs within the dentate nucleus and the cerebellar white matter on unenhanced sagittal T1-weighted images. ROIs were placed in the right dentate nucleus and in the adjacent cerebellar white matter on the same sagittal section. If the right dentate nucleus or cerebellar white matter was obscured by overlying artifacts, then ROIs were placed on the corresponding structures on the left. The mean signal intensity of each ROI was obtained and used to calculate dentate-to-cerebellar white matter (DN/C) ratios for each subject.

### Automated Image Analysis

To eliminate reader bias, we also performed automated ROI placement. Of the 16 patients evaluated by the blinded reader, 3 patients had not undergone whole-brain imaging to fully cover the entire posterior fossa (MRIs performed per pituitary or neck protocols) and, therefore, were not included in automated analysis because complete coverage of the posterior fossa was required to perform image registration. Therefore, the sagittal, unenhanced T1-weighted sequences from 13 patients were subjected to automated analysis. Unlike the analysis by the blinded reader, all scans for each patient performed at our institution, available on the PACS and adequate for computer analysis, were included. In other words, the automated analysis was not limited to documented serial administrations of gadopentetate dimeglumine in order to increase our number of data points but was restricted to only those scans with whole-brain coverage. Therefore, the number of GBCA doses before the last MR imaging study examined by the blinded reader and the number of contrasted MR studies evaluated by automated analysis do not correspond (Table 1).

Image processing was performed by using the Spatially Un-

biased Atlas Template of the Cerebellum and Brain Stem (SUIT; [http://www.diedrichsenlab.org/imaging/suit\\_download.htm](http://www.diedrichsenlab.org/imaging/suit_download.htm)) toolbox,<sup>22,23</sup> implemented in the statistical parametric mapping software package (SPM8; <http://www.fil.ion.ucl.ac.uk/spm/>). This toolbox uses a probabilistic atlas of the human cerebellum defined by the Montreal Neurological Institute (MNI) 152 template (<http://neuro.debian.net/pkgs/fsl-mni152-templates.html>) optimized for delineation of the deep cerebellar nuclei.<sup>23</sup> Our procedure involved the following steps: 1) cropping and isolating the cerebellum and brain stem from the T1-weighted anatomic images, 2) normalizing each cropped image into SUIT space, 3) placing ROIs based on MNI 152 template coordinates, 4) reflecting the ROIs into individual subject space by using the deformation parameters from the normalization, 5) manually inspecting the results, and 6) calculating the median intensity value in each ROI.

The atlas provided by the SUIT toolbox is a probability atlas, so the dentate nucleus ROI was defined as voxels with >75% probability of being within the dentate nucleus. Using this threshold, we found the mean volume of the dentate nucleus ROI to be 0.66 mL, similar to the volume of the dentate nucleus as reported for high-resolution 3T images.<sup>24</sup>

ROIs placed in the pons, cerebellar white matter, CSF, and cerebellar gray matter were investigated for potential use as normalization factors (Fig 1). Cerebellar gray matter (MNI coordinates: ±20, -68, -50), cerebellar white matter of the middle cerebellar peduncles (MNI coordinates: ±18, -40, -36), CSF within the fourth ventricle (MNI coordinates: 0, -44, -30), and the central pons (MNI coordinates: 0, -24, -32) ROIs were defined in SUIT space as spheres of 7-mm radii. The radius of the CSF ROI was 4 mm due to the size limitation of the fourth ventricle.

For each ROI, the median signal intensity was obtained. Scatterplots were constructed showing all dentate ROIs across all subjects and all scans versus those of the pons, cerebellar white mat-

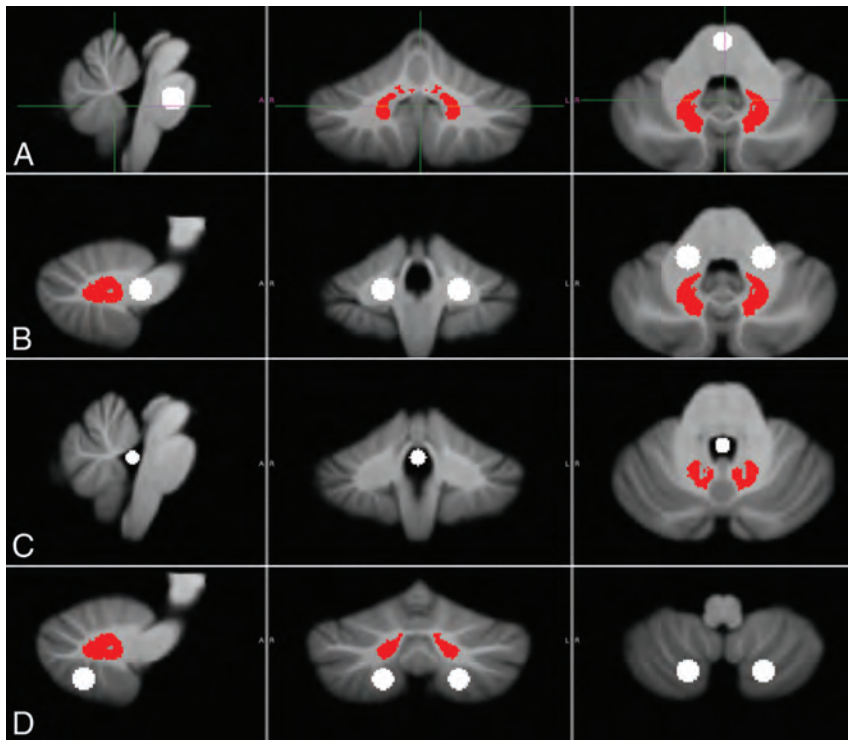


**FIG 1.** ROIs were defined by the SUIT template within the dentate nucleus (in red) and within the pons (A), cerebellar white matter (B), CSF (C), and cerebellar gray matter (D) (ROIs in white) to serve as potential references for normalization.

**Table 2: Total number of pediatric patients who underwent at least 1 contrast-enhanced MRI at our institution from January 1, 1995, to June 30, 2014**

No. of Doses GBCAs Administered	No. of Pediatric Patients
1	9306
2	1488
3	452
4	183
5	101
6	48
7	40
8	19
9	20
10	10
11	13
12	8
13	3
14	2
15	3
16	5
17	3
18	1
19	1
20	1
21	1
38	1
Total No. of pediatric patients	11,709

ter, CSF within the fourth ventricle, and cerebellar gray matter. CSF was found to be the worst reference point for normalizing the dentate signal intensities because it was more susceptible to noise due to the low intensity of CSF on T1-weighted images. Cerebellar white matter and the pons appeared to be the best choices for a ratio-based reference because they exhibited the least noise in the

dataset. The dentate-to-pons (DN/P) ratios and DN/C ratios were then calculated for each subject for each MR imaging scan with an adequate sagittal T1-weighted sequence available on our institutional PACS system.

### Statistical Analysis

For the blinded reader's scores, the Spearman rank order correlation was used to identify associations among non-normally distributed variables, and 2-tailed *P* values are reported. Sixteen subjects were included in the analyses, and the correlations between the number of doses and the DN/C ratios at the time of the last MR imaging scan were examined.

For statistical analysis of the automated scores, general linear mixed models were used.<sup>25</sup> For each dependent variable (DN/P and DN/C ratios), a general linear mixed model was constructed by using the number of prior doses as the primary independent variable. To account for repeat measurements being obtained on the study subjects, we cre-

ated several general linear mixed models for each dependent variable; the models involved different types of random effects (intercepts, slopes) and different types of residual correlation structures (eg, unstructured, compound symmetry, spatial power). A final model was selected for each dependent variable by comparing the Akaike information criteria and overall model parsimony. Analysis was performed by using SAS, Version 9.4 (SAS Institute, Cary, North Carolina).

### RESULTS

Between January 1995 and June 2014 at our institution, 11,709 pediatric patients received at least 1 dose of a GBCA (Table 2). The maximum number of doses was 38 in 1 patient, though 16 patients received at least 15 doses and 280 patients received at least 5 doses of contrast. These data do not include additional GBCA doses received by some patients at outside institutions.

Sixteen patients met the inclusion/exclusion criteria for analysis. The patient ages ranged from 2 months to 14 years at the time of the first contrast dose (mean age,  $7.4 \pm 4.8$  years). None of the patients had documented renal failure or abnormal renal function, with all measured estimated glomerular filtration rate values  $>60$  mL/min/1.73 m<sup>2</sup>. A few patients occasionally had mildly elevated liver function test results, but none were diagnosed with liver failure. One patient had undergone total parenteral nutrition for approximately 5 weeks during the imaging period. For 2 patients, unenhanced sagittal T1-weighted images were unavailable on our institutional PACS following the fifth dose of gadopentetate dimeglumine. For these 2 cases, we used ROI values obtained on the preceding MR imaging (following only 4 doses of gadopentetate dimeglumine). Therefore, the number of contrast

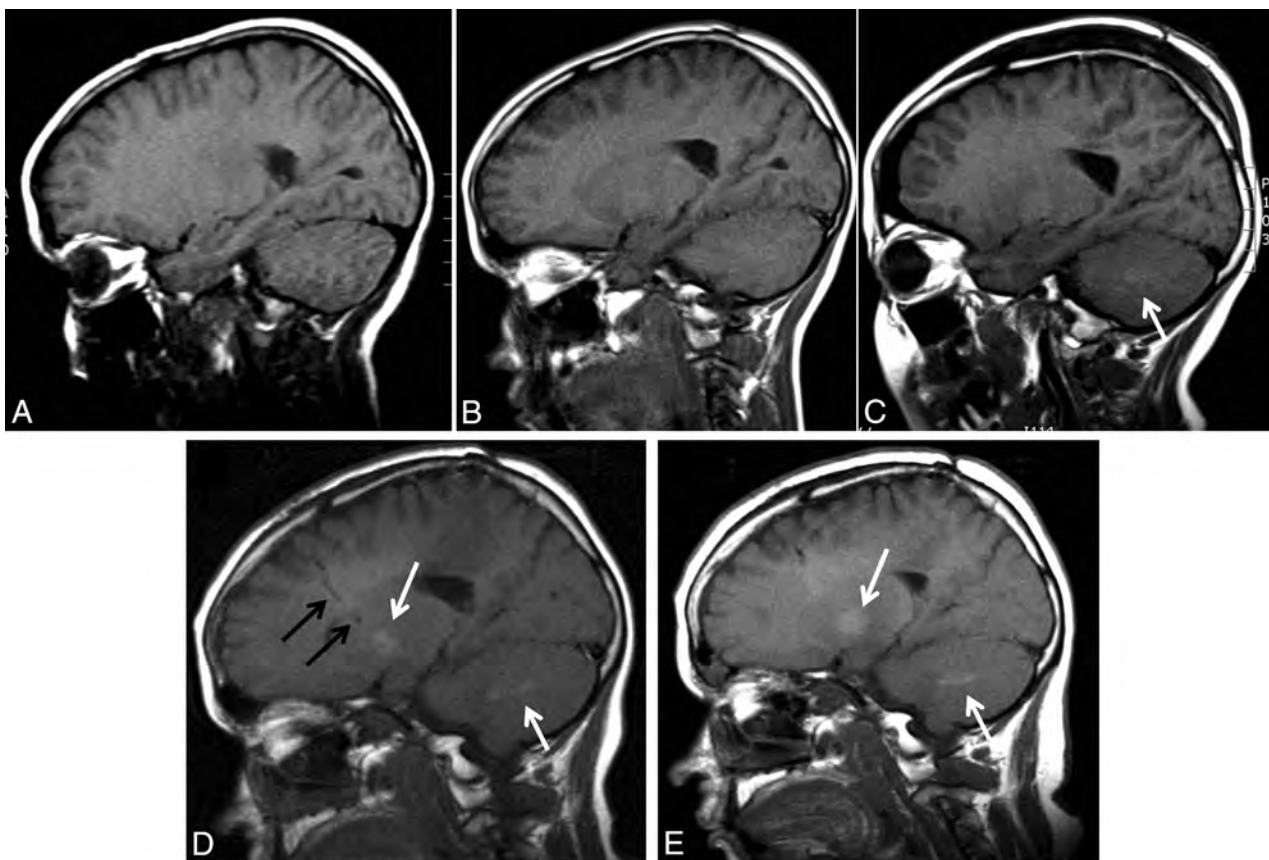


**FIG 2.** A, Sagittal unenhanced T1-weighted image from the initial MR imaging of a patient who presented with a parietal lobe low-grade astrocytoma at 10 years of age. B, Sagittal unenhanced T1-weighted image from an MR imaging at 13 years of age after 6 doses of GBCAs. C, Sagittal unenhanced T1-weighted image from an MR imaging following lesion biopsy at 13 years of age after 12 doses of GBCAs. There is faint hyperintensity within the dentate nucleus (*white arrow*). D, Sagittal unenhanced T1-weighted image from an MR imaging at 15 years of age after 17 doses of GBCAs. *Black arrows* indicate the tract of a ventricular catheter. There is distinct hyperintensity within the dentate nucleus and the globus pallidus (*white arrows*). E, Sagittal unenhanced T1-weighted image from an MR imaging scan at 17 years of age after 27 doses of GBCAs. Hyperintensity within the dentate nucleus and the globus pallidus is again seen (*white arrows*).

doses before the last brain MR imaging with gadopentetate dimeglumine examined by the blinded reader ranged from 4 to 16.

Hyperintensity was visible within the dentate nucleus on unenhanced images in the patients in our series who had received at least 7 prior doses of GBCA (Fig 2). For blinded reader analysis, the prior number of doses of GBCA before the last scan was significantly associated with the DN/C ratio ( $r_s = 0.77, P = .001$ ). As the number of doses increased, so did the DN/C ratio.

All computer-placed ROIs were confirmed by manual inspection (Fig 3). Figure 4 shows all DN/P and DN/C ratios plotted against the number of prior contrast doses for all time points for all 13 subjects who underwent automated analysis. Analysis of the computer-placed ROIs by using general linear mixed modeling demonstrated a significant correlation between the number of prior doses and both the DN/P ratio ( $t = 4.98, P < .0001$ ) and the DN/C ratio ( $t = 2.73, P < .02$ ). Figure 5 shows the predicted mean values along with their 95% confidence bands. Note that only 16 prior contrast doses were plotted because only 1 subject contributed to measurements for  $>16$  doses. Overall, as the number of doses increased with each scan, so did both the DN/P and DN/C ratios as detected by automated ROI analysis.

## DISCUSSION

Several reports have now described the deposition of gadolinium in the brain of adult patients with normal renal function.<sup>11-18</sup> Here we present a pediatric case series demonstrating a significant correlation between the DN/C and the DN/P ratios and the prior number of doses of GBCA administered. These data strongly support an association in children between increasing cumulative GBCA dose and hyperintensity within the dentate nucleus on unenhanced T1-weighted imaging, a finding shown by pathologic confirmation in adults to correspond to areas of gadolinium deposition.<sup>17,18</sup>

Improved imaging, along with advances in neurosurgery, radiation oncology, and chemotherapy, has contributed to improvement in the cure rates of childhood cancers during the past 2 decades, and ongoing advances in genomics technologies are expected to dramatically transform pediatric neuro-oncology.<sup>26</sup> The improved cure rates of childhood cancers and longer term survival have led to increasing numbers of children exposed to greater cumulative doses of GBCAs. In our study, the maximum number of doses was 38 in 1 patient, though 280 pediatric patients received at least 5 doses of contrast.

Pathologic evaluation of the brain in patients with normal

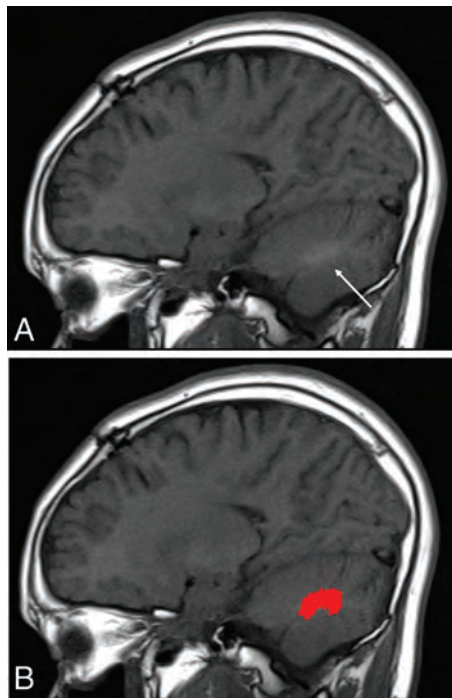


**FIG 3.** A, Sagittal unenhanced T1-weighted image from an MR imaging of a patient at 13 years of age after the 12th dose of GBCA. An arrow marks the location of the dentate nucleus. B, A computer-assigned dentate ROI reflected back into the individual patient's space.

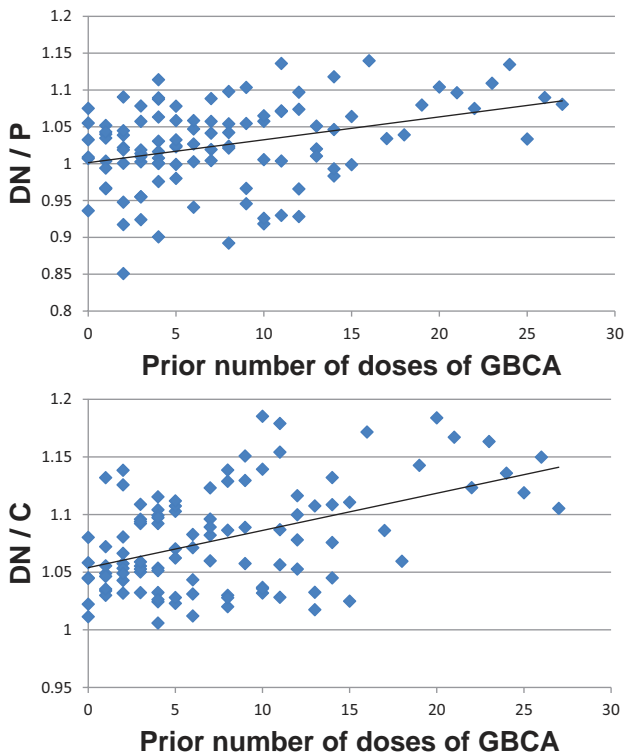


**FIG 4.** Computer-selected DN/P and DN/C ratios plotted against the number of prior contrast doses for all time points for all 13 subjects who underwent automated analysis.

renal function who were administered GBCAs has shown that gadolinium is deposited not only in the dentate nucleus but throughout the brain, including the frontal lobe white matter and

frontal cortex.<sup>17,18,27</sup> While the clinical significance of the long-term retention of gadolinium in the brain is unknown, it is particularly concerning for pediatric patients, who are undergoing neurodevelopment. Brain development begins during fetal life and continues throughout adolescence with prefrontal, posterior parietal, and other high-order association areas being the last areas to undergo myelination.<sup>28</sup> There is a dramatic proliferation of synapses in the prefrontal cortex during early and mid-childhood, reaching numbers that exceed adult levels by 2- or 3-fold during puberty, followed by a plateau phase during adolescence with subsequent elimination and reorganization of prefrontal synaptic connections.<sup>28</sup> During this critical period of development, the brain is particularly vulnerable to toxin exposure,<sup>29</sup> and it is unknown whether the processes of active myelination, growth, and neuronal pruning could be affected by exposure to gadolinium deposition. Further research is needed to address the clinical significance, if any, of gadolinium deposition in the body of pediatric patients.

In a study measuring total gadolinium deposition by using inductive coupled plasma mass spectroscopy, Murata et al<sup>27</sup> demonstrated the presence of gadolinium within the brain, skin, and bones of adult patients following the administration of 1–11 doses of GBCA. In their study, the gadolinium levels within the bones were 23 times higher than those in the brain,<sup>27</sup> suggesting that gadolinium deposition in the brain may represent a marker for even higher levels of gadolinium stored in the bones. This finding is particularly concerning for pediatric patients exposed to high cumulative doses of GBCAs during skeletal ossification and periods of rapid bone growth. It has been hypothesized that high levels of gadolinium storage in the bones could represent an internal source of gadolinium exposure throughout a patient's lifetime, with the mobilization of gadolinium later in life during conditions favoring calcium mobilization from bones (renal failure, osteoporosis, long-term bed rest, hyperparathyroidism, and pregnancy).<sup>30</sup>

Currently, there are 9 GBCAs approved for use in the United States. Each commercially available GBCA is composed of gadolinium along with a ligand molecule whose structure varies among the agents. There are 2 distinct categories of GBCAs based on the structure of the ligand: the “macrocytic” molecules, in which the gadolinium ion is “caged” into a preorganized cavity of the ligand, and the “open-chain linear” chelates, in which the metal ion is attached to the end of the ligand molecule. Gadolinium chelates can also be either nonionic or ionic. These structural differences result in differing thermodynamic and kinetic stabilities, with the highest thermodynamic and kinetic stability achieved by an ionic, macrocytic structure.<sup>31</sup> Recent reports suggest that the stability of the GBCA may play a role in the deposition of gadolinium in the brain because administration of linear agents is associated with hyperintensity in the dentate nucleus, while administration of macrocytic agents has not shown this association.<sup>14,21</sup> Higher stability, macrocytic agents have been shown to be associated with lower levels of gadolinium deposition in the body in both human and animal studies.<sup>32,33</sup> Given the current uncertainties concerning the clinical significance of gadolinium deposition within the body, in pediatric imaging, we would recommend taking a cautious stance and considering the

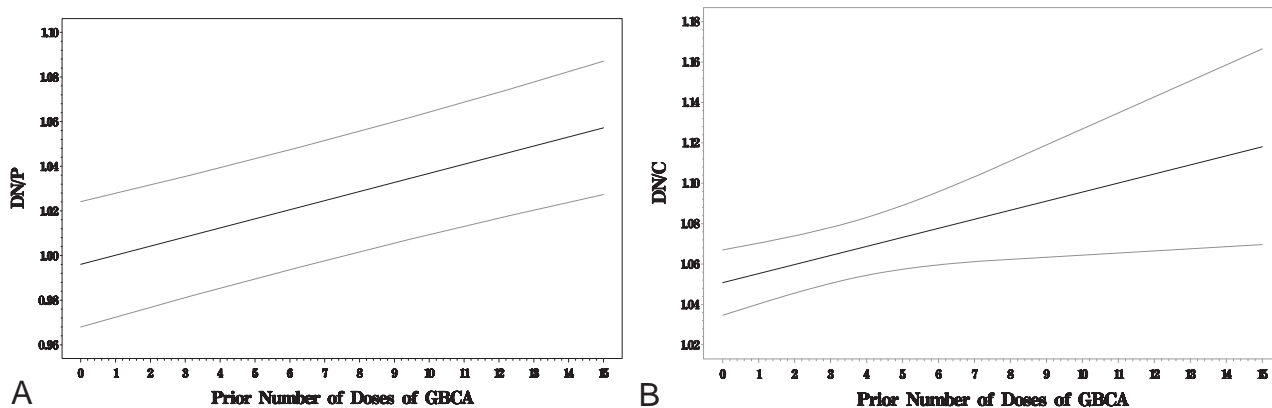


**FIG 5.** A, Association between DN/P ratio and the number of prior doses of GBCA. The *dark solid line* reflects the predicted average response among subjects' median DN/P ratio values at the given number of prior doses of GBCA, and the *light solid lines* represent the associated 95% confidence band. B, Association between the DN/C ratio and the number of prior doses of GBCA. The *dark solid line* reflects the predicted average response among subjects' median DN/C ratio values at the given number of prior doses of GBCA, and the *light solid lines* represent the associated 95% confidence band.

use of only higher stability, macrocyclic agents in pediatric patients, given their unique vulnerability, while awaiting the results of long-term research studies to address any potential clinical significance of gadolinium deposition in the body.

Our study had several potential sources of error. The MR imaging scans were acquired using various MR imaging systems and scanning parameters. A single GBCA was not used consistently for all patients, and outside GBCA doses could not be verified. Age-matched controls were not included. For the subjectively placed ROIs, sources of error include image noise resulting in large variations in ROI values and reader bias. Despite our reader being blinded, the clearly visible hyperintense appearance of the dentate nucleus in patients with larger cumulative GBCA doses could have influenced ROI placement. Sources of error in the automated ROI analysis include areas of artifacts overlying the dentate nucleus, cerebellar white matter, or pons, such as flow artifacts from the transverse sinuses and metallic artifacts from implanted hardware. Our reader excluded these areas visually during ROI placement; however, these areas marred by artifacts could not be omitted by the image-processing software. Errors in the registration process cannot be excluded though all computer-placed ROIs were confirmed by manual inspection. Differences in white matter myelination could be a confounding variable in the automated ROI analysis in the youngest age groups; however, only 2 of the 16 patients were younger than 1 year of age at the time of the first scan and both were older than 2 years of age at the time of their last scan. Despite the limitations of using an automated method for delineation of the dentate nucleus, pons, and cerebellar white matter, we believe the advantage of eliminating reader bias is important due to the large variation in ROI values obtained with only slight adjustment of ROI placement.

## CONCLUSIONS

As in the adult population, pediatric patients also demonstrate progressive T1-weighted hyperintensity in the dentate nucleus correlating with the number of administered doses of GBCA, suggesting a causal relationship between gadolinium administration and the signal changes seen on MR imaging. Confirmation of gadolinium deposition within the pediatric brain requires biopsy

confirmation as was demonstrated in the adult population. The clinical significance of long-term retention of gadolinium in the developing brain is currently unknown. Therefore, pediatric imagers should continue to use prudence in selecting patients to undergo contrasted MR imaging and in selecting the appropriate contrast agents to use in this population, particularly in patients requiring multiple contrast exposures. A risk-benefits analysis, incorporating the potential for long-term gadolinium deposition in brain tissue should be considered in the decision-making process for all pediatric patients. When a decision is made to proceed with contrast administration in a pediatric patient, the specific agent administered, the dose, and the cumulative dose should always be recorded for each examination. Most important, a patient should not be deprived of a well-indicated contrasted MR examination.

## ACKNOWLEDGMENTS

The authors acknowledge the contributions of Nancy J. Monogan, Alden Finlayson, R.T. (R) (MR), and Sarah L. Brewer in preparing the data for this article.

Disclosures: Donna R. Roberts—*RELATED: Grant:* National Institutes of Health\*; *UNRELATED: Board Membership:* Guerbet, *Comments:* I serve as an advisory board member and consultant for Guerbet; *Consultancy:* Guerbet, *Comments:* I serve as an advisory board member and consultant for Guerbet; *Other:* Guerbet.\* *Comments:* I am a site principal investigator for a current clinical trial sponsored by Guerbet and have been a site principal investigator for previous Guerbet-sponsored clinical trials; *OTHER:* I am a member of the FDA Medical Imaging Drugs Advisory Committee and serve on the FDA advisory panel recommending approval for the gadobutrol contrast agent. Genevieve Bolles—*RELATED: Grant:* National Institutes of Health.\* Paul J. Nietert—*RELATED: Grant:* National Institutes of Health (grant UL1TR001450).\* \*Money paid to the institution.

## REFERENCES

1. American College of Radiology. ACR Appropriateness Criteria. <http://www.acr.org/Quality-Safety/Appropriateness-Criteria>. Accessed March 14, 2016
2. Balassy C, Roberts D, Miller SF. **Safety and efficacy of gadoteric acid in pediatric magnetic resonance imaging: overview of clinical trials and post-marketing studies.** *Pediatr Radiol* 2015;45:1831–41 CrossRef Medline
3. Ball WS Jr, Nadel SN, Zimmerman RA, et al. **Phase III multicenter**

- clinical investigation to determine the safety and efficacy of gadoteridol in children suspected of having neurologic disease. *Radiology* 1993;186:769–74 CrossRef Medline
4. Elster AD. Cranial MR imaging with Gd-DTPA in neonates and young infants: preliminary experience. *Radiology* 1990;176:225–30 CrossRef Medline
  5. Hahn G, Sorge I, Gruhn B, et al. Pharmacokinetics and safety of gadobutrol-enhanced magnetic resonance imaging in pediatric patients. *Invest Radiol* 2009;44:776–83 CrossRef Medline
  6. Lundby B, Gordon P, Hugo F. MRI in children given gadodiamide injection: safety and efficacy in CNS and body indications. *Eur J Radiol* 1996;23:190–96 CrossRef Medline
  7. Schneider G, Schürholz H, Kirchin MA, et al. Safety and adverse effects during 24 hours after contrast-enhanced MRI with gadobenate dimeglumine (MultiHance) in children. *Pediatr Radiol* 2013;43:202–11 CrossRef Medline
  8. Dillman JR, Ellis JH, Cohan RH, et al. Frequency and severity of acute allergic-like reactions to gadolinium-containing i.v. contrast media in children and adults. *AJR Am J Roentgenol* 2007;189:1533–38 CrossRef Medline
  9. Girardi M, Kay J, Elston DM, et al. Nephrogenic systemic fibrosis: clinicopathological definition and workup recommendations. *J Am Acad Dermatol* 2011;65:1095–1106.e7 CrossRef Medline
  10. Cooper S. Nephrology. In: Tschudy MM, Arcara KM, eds. *The Harriet Land Handbook*. 19th ed. Philadelphia: Elsevier Mosby; 2012:476–503
  11. Kanda T, Ishii K, Kawaguchi H, et al. High signal intensity in the dentate nucleus and globus pallidus on unenhanced T1-weighted MR images: relationship with increasing cumulative dose of a gadolinium-based contrast material. *Radiology* 2014;270:834–41 CrossRef Medline
  12. Errante Y, Cirimele V, Mallio CA, et al. Progressive increase of T1 signal intensity of the dentate nucleus on unenhanced magnetic resonance images is associated with cumulative doses of intravenously administered gadodiamide in patients with normal renal function, suggesting dechelation. *Invest Radiol* 2014;49:685–90 CrossRef Medline
  13. Quattrocchi CC, Mallio CA, Errante Y, et al. Gadodiamide and dentate nucleus T1 hyperintensity in patients with meningioma evaluated by multiple follow-up contrast-enhanced magnetic resonance examinations with no systemic interval therapy. *Invest Radiol* 2015;50:470–72 CrossRef Medline
  14. Radbruch A, Weberling LD, Kieslich PJ, et al. Gadolinium retention in the dentate nucleus and globus pallidus is dependent on the class of contrast agent. *Radiology* 2015;275:783–91 CrossRef Medline
  15. Radbruch A, Weberling LD, Kieslich PJ, et al. High-signal intensity in the dentate nucleus and globus pallidus on unenhanced T1-weighted images: evaluation of the macrocyclic gadolinium-based contrast agent gadobutrol. *Invest Radiol* 2015;50:805–10 CrossRef Medline
  16. Weberling LD, Kieslich PJ, Kickingreder P, et al. Increased signal intensity in the dentate nucleus on unenhanced T1-weighted images after gadobenate dimeglumine administration. *Invest Radiol* 2015;50:743–48 CrossRef Medline
  17. Kanda T, Fukusato T, Matsuda M, et al. Gadolinium-based contrast agent accumulates in the brain even in subjects without severe renal dysfunction: evaluation of autopsy brain specimens with inductively coupled plasma mass spectroscopy. *Radiology* 2015;276:228–32 CrossRef Medline
  18. McDonald RJ, McDonald JS, Kallmes DF, et al. Intracranial gadolinium deposition after contrast-enhanced MR imaging. *Radiology* 2015;275:772–82 CrossRef Medline
  19. Roberts DR, Holden KR. Progressive increase of T1 signal intensity in the dentate nucleus and globus pallidus on unenhanced T1-weighted MR images in the pediatric brain exposed to multiple doses of gadolinium contrast. *Brain Dev* 2016;38:331–36 CrossRef Medline
  20. Miller JH, Hu HH, Pokorney A, et al. MRI brain signal intensity changes of a child during the course of 35 gadolinium contrast examinations. *Pediatrics* 2015;136:e1637–40 CrossRef Medline
  21. Kanda T, Osawa M, Oba H, et al. High signal intensity in dentate nucleus on unenhanced T1-weighted MR images: association with linear versus macrocyclic gadolinium chelate administration. *Radiology* 2015;275:803–09 CrossRef Medline
  22. Diedrichsen J, Balsters JH, Flavell J, et al. A probabilistic MR atlas of the human cerebellum. *Neuroimage* 2009;46:39–46 CrossRef Medline
  23. Diedrichsen J, Maderwald S, Küper M, et al. Imaging the deep cerebellar nuclei: a probabilistic atlas and normalization procedure. *Neuroimage* 2011;54:1786–94 CrossRef Medline
  24. Deoni SC, Catani M. Visualization of the deep cerebellar nuclei using quantitative T1 and rho magnetic resonance imaging at 3 Tesla. *Neuroimage* 2007;37:1260–66 CrossRef Medline
  25. Fitzmaurice GM, Laird NM, Ware JH. *Applied Longitudinal Analysis*. Hoboken: Wiley-Interscience; 2004
  26. Gajjar A, Bowers DC, Karajannis MA, et al. Pediatric brain tumors: innovative genomic information is transforming the diagnostic and clinical landscape. *J Clin Oncol* 2015;33:2986–98 CrossRef Medline
  27. Murata N, Gonzalez-Cuyar LF, Murata K, et al. Macrocyclic and other non-group 1 gadolinium contrast agents deposit low levels of gadolinium in brain and bone tissue: preliminary results from 9 patients with normal renal function. *Invest Radiol* 2016;51:447–53 CrossRef Medline
  28. Blakemore SJ. Imaging brain development: the adolescent brain. *Neuroimage* 2012;61:397–406 CrossRef Medline
  29. Stein J, Schettler T, Wallinga D, et al. In harm's way: toxic threats to child development. *J Dev Behav Pediatr* 2002;23:S13–22 CrossRef Medline
  30. Abraham JL, Thakral C. Tissue distribution and kinetics of gadolinium and nephrogenic systemic fibrosis. *Eur J Radiol* 2008;66:200–07 CrossRef Medline
  31. Port M, Idée JM, Medina C, et al. Efficiency, thermodynamic and kinetic stability of marketed gadolinium chelates and their possible clinical consequences: a critical review. *Biomaterials* 2008;21:469–90 CrossRef Medline
  32. Robert P, Violas X, Grand S, et al. Linear gadolinium-based contrast agents are associated with brain gadolinium retention in healthy rats. *Invest Radiol* 2016;51:73–82 CrossRef Medline
  33. White GW, Gibby WA, Tweedle MF. Comparison of Gd(DTPA-BMA) (Omniscan) versus Gd(HP-DO3A) (ProHance) relative to gadolinium retention in human bone tissue by inductively coupled plasma mass spectroscopy. *Invest Radiol* 2006;41:272–78 CrossRef Medline

# Automated MRI Volumetric Analysis in Patients with Rasmussen Syndrome

Z.I. Wang, B. Krishnan, D.W. Shattuck, R.M. Leahy, A.N.V. Moosa, E. Wyllie, R.C. Burgess, N.B. Al-Sharif, A.A. Joshi, A.V. Alexopoulos, J.C. Mosher, U. Udayasankar, the Pediatric Imaging, Neurocognition and Genetics Study, and S.E. Jones



## ABSTRACT

**BACKGROUND AND PURPOSE:** Rasmussen syndrome, also known as Rasmussen encephalitis, is typically associated with volume loss of the affected hemisphere of the brain. Our aim was to apply automated quantitative volumetric MR imaging analyses to patients diagnosed with Rasmussen encephalitis, to determine the predictive value of lobar volumetric measures and to assess regional atrophy differences as well as monitor disease progression by using these measures.

**MATERIALS AND METHODS:** Nineteen patients (42 scans) with diagnosed Rasmussen encephalitis were studied. We used 2 control groups: one with 42 age- and sex-matched healthy subjects and the other with 42 epileptic patients without Rasmussen encephalitis with the same disease duration as patients with Rasmussen encephalitis. Volumetric analysis was performed on T1-weighted images by using BrainSuite. Ratios of volumes from the affected hemisphere divided by those from the unaffected hemisphere were used as input to a logistic regression classifier, which was trained to discriminate patients from controls. Using the classifier, we compared the predictive accuracy of all the volumetric measures. These ratios were used to further assess regional atrophy differences and correlate with epilepsy duration.

**RESULTS:** Interhemispheric and frontal lobe ratios had the best prediction accuracy for separating patients with Rasmussen encephalitis from healthy controls and patient controls without Rasmussen encephalitis. The insula showed significantly more atrophy compared with all the other cortical regions. Patients with longitudinal scans showed progressive volume loss in the affected hemisphere. Atrophy of the frontal lobe and insula correlated significantly with epilepsy duration.

**CONCLUSIONS:** Automated quantitative volumetric analysis provides accurate separation of patients with Rasmussen encephalitis from healthy controls and epileptic patients without Rasmussen encephalitis, and thus may assist the diagnosis of Rasmussen encephalitis. Volumetric analysis could also be included as part of follow-up for patients with Rasmussen encephalitis to assess disease progression.

**ABBREVIATIONS:** HRvol = interhemispheric ratio (affected side/unaffected side); IVIG = intravenous immunoglobulin; RE = Rasmussen encephalitis; SVReg = surface and volume registration

Rasmussen syndrome, also known as Rasmussen encephalitis (RE), is a chronic inflammatory disease of the brain, which typically affects only 1 hemisphere. It is usually associated with a

progressive course of focal seizures, characterized by epilepsy partialis continua and neurologic deficits (most frequently hemiparesis). It is generally believed that RE is driven by a T-cell-

Received May 2, 2016; accepted after revision July 4.

From the Epilepsy Center (Z.I.W., B.K., A.N.V.M., E.W., R.C.B., A.V.A., J.C.M.) and Imaging Institute (S.E.J.), Cleveland Clinic, Cleveland, Ohio; Ahmanson-Lovelace Brain Mapping Center (D.W.S., N.B.A.-S.), Department of Neurology, David Geffen School of Medicine, University of California, Los Angeles, Los Angeles, California; Signal and Image Processing Institute (A.A.J., R.M.L.), University of Southern California, Los Angeles, California; and Department of Radiology (U.U.), University of Arizona College of Medicine, Tucson, Arizona.

Part of the data used in the preparation of this article were obtained from the Pediatric Imaging, Neurocognition and Genetics Study (PING) database (<http://ping.chd.ucsd.edu>). As such, the investigators within PING contributed to the study by providing data but did not participate in the analysis or writing of this study.

Research reported in this publication was supported by the National Institute of Neurological Disorders and Stroke of the National Institutes of Health under award No. R01 NS074980 (Z.I.W., S.E.J., D.W.S., R.M.L., J.C.M.) and R01 NS089212 (R.M.L.). Healthy control data collection and sharing for this project were funded

by the Pediatric Imaging, Neurocognition and Genetics Study via the National Institutes of Health grant RC2DA029475 and the National Institute on Drug Abuse and the Eunice Kennedy Shriver National Institute of Child Health and Human Development.

The content is solely the responsibility of the authors and does not necessarily represent the official views of the National Institutes of Health.

Paper previously presented in part at: Annual Meeting of the American Society of Neuroradiology and the Foundation of the ASNR Symposium, April 25–30, 2015; Chicago, Illinois.

Please address correspondence to Irene Wang, PhD, Desk 551, Epilepsy Center, Cleveland Clinic, Cleveland, OH 44195; e-mail: [wangi2@ccf.org](mailto:wangi2@ccf.org)

Indicates open access to non-subscribers at [www.ajnr.org](http://www.ajnr.org)

Indicates article with supplemental on-line appendix.

Indicates article with supplemental on-line photo.

<http://dx.doi.org/10.3174/ajnr.A4914>

mediated inflammation that leads to neuronal and astrocytic cell death in 1 hemisphere.<sup>1,2</sup> The disease is characterized by 3 stages: 1) the prodromal stage of mild hemiparesis and infrequent seizures; 2) an acute stage with frequent seizures from 1 hemisphere characterized by epilepsy partialis continua, with deterioration of neurologic functions (histopathology in this stage shows the highest inflammatory intensity); and 3) a residual stage with severe, fixed neurologic deficits and drug-resistant seizures (histopathology in this stage shows a decrease in inflammation).<sup>1</sup>

MR imaging characteristics of RE include early cortical swelling followed by cortical and subcortical hyperintensity on fluid-attenuated inversion recovery and T2-weighted images, with progressive atrophy of the affected hemisphere.<sup>1</sup> The peri-Sylvian region has been observed to be the predominant site for signal abnormality and atrophy.<sup>3</sup> Volume loss of the ipsilateral caudate head is also frequently observed.<sup>3</sup>

During the past decade, MR imaging has become an increasingly important tool in the diagnosis of RE as well as in assessing disease progression and therapeutic effectiveness. The degree of hemispheric atrophy in RE can be obtained from MR imaging on the basis of manual planimetry<sup>1</sup> and manual volumetry,<sup>4</sup> both of which can be labor-intensive, time-consuming, and rater-dependent. Fully automated volumetric methods have been proposed that showed a high concordance with planimetric methods and clinical parameters.<sup>5</sup>

To date, no studies have examined how volumetric measures can help predict RE—that is, when a new patient presents with suspected RE, can the extent of atrophy on MR imaging be quantified to predict the probability that the patient truly has RE? In the early stage of the disease, atrophy can be too subtle for visual inspection to detect; therefore, diagnosis is often uncertain and delayed. Can fully automated volumetric methods be used to complement visual analysis? Furthermore, progression of RE can be slow, especially at the residual stage. Can fully automated volumetric methods be used to reveal slow changes across the years? In an attempt to answer these questions, in this study, we examined 15 volumetric measures in a cohort of patients with RE and 2 control groups: One group consisted of 42 age- and sex-matched healthy controls; the other group consisted of 42 patients with non-RE epilepsy and matched disease duration. Once the volumetric measures were obtained, we used them to form a statistical model to classify patients and controls, and determined the measure with the highest predictive accuracy. The same volumetric measures were then used to examine regional atrophy differences and were correlated with disease progression.

## MATERIALS AND METHODS

### Patients

This retrospective study was approved by the Cleveland Clinic institutional review board. Patients evaluated at the Cleveland Clinic Epilepsy Center were included by using the following criteria: 1) clinical diagnosis of RE following general guidelines specified in the literature,<sup>3</sup> and 2) MR imaging available with T1-weighted MPRAGE sequence.

### Controls

Forty-two healthy controls (34 provided by the Pediatric Imaging, Neurocognition and Genetics Study [<http://ping.chd.ucsd.edu>] and 8 from the Cleveland Clinic) were chosen to be age- and sex-matched to the scans of 42 patients with RE. The control subjects were free of any neurologic diseases.

An additional group of 42 controls with non-RE epilepsy (all from the Cleveland Clinic) were chosen with matching epilepsy duration with the 42 scans from patients with RE. All the controls with non-RE epilepsy had negative (nonlesional) findings on MR imaging and had clearly lateralizing epilepsy as documented by their video-electroencephalography monitoring.

### MR Imaging Protocol

Of the 42 scans from patients with RE, 18 MRIs were performed with a 1.5T Avanto scanner (Siemens, Erlangen, Germany), 22 were performed with a 3T Skyra scanner (Siemens), and 2 were performed with a 3T Trio scanner (Siemens) at the Cleveland Clinic. The 3D volumetric T1-weighted MPRAGE sequence was used for the volumetric processing. Sequence parameters at 1.5T were the following: TR = 11 ms, TE = 4.6 ms, no inversion, flip angle = 20°, bandwidth = 130 kHz, section thickness = 1.25 mm, no gap, in-plane resolution = 0.9 mm. Sequence parameters at 3T (Trio/Skyra) were the following: TR = 1860/1800 ms, TE = 3.4/2.56 ms, TI = 1100/900 ms, flip angle = 10°, bandwidth = 130/220 kHz, section thickness = 0.94/1 mm, no gap, in-plane resolution = 0.94/0.41 mm.

Of the 42 healthy control scans, 24 were obtained with a 3T Signa scanner (GE Healthcare, Milwaukee, Wisconsin) by using the echo-spoiled gradient-echo sequence. Sequence parameters were the following: TR = 8.132 ms, TE = 3.452 ms, TI = 640 ms, flip angle = 8°, bandwidth = 244 kHz, section thickness = 1.2 mm, no gap, in-plane resolution of 0.94 mm. Eighteen patients were scanned with a 3T Trio scanner with the MPRAGE sequence (with the same parameters as reported in the previous section). Of the 42 non-RE epilepsy control scans, 15 MRIs were performed by using a 1.5T Avanto scanner, 25 MRIs were performed by using a 3T Skyra scanner, and 2 MRIs were performed by using a 3T Trio scanner, with the same parameters as reported in the previous section.

### Volumetric Analysis

All MR imaging processing was performed by using standard procedures of the freely available BrainSuite software (Version 15b; <http://brainsuite.org/>). BrainSuite provides an automatic sequence to extract surface models of the cerebral cortex. The procedure uses anatomic information from both the surface models and volume of the brain images for accurate coregistration between the subject and an atlas.<sup>6-8</sup> The final parcellation computes volumes of 140 brain regions (70 from each hemisphere). WM, GM, and CSF volumes are generated separately by surface and volume registration (SVReg) for each of the brain regions. Details can be found in the On-line Appendix.

The following volumes on each side of the brain are calculated in milliliters by using built-in statistical tools of BrainSuite:

1) Hemispheric Volume = GM + WM without brain stem and cerebellum

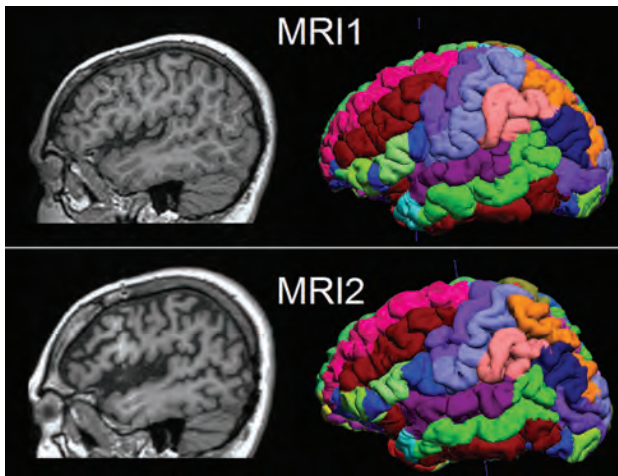


**FIG 1.** Illustration of 2 serial MRIs from the same patient (P6) and the SVReg output of BrainSuite. First row: MR imaging at 10 years of age. Second row: MR imaging at 17 years of age. Shown in the left column are the sagittal T1-weighted MPRAGE images. The right column is the cortical rendering of the SVReg labels, with different colors denoting different anatomic areas of the brain. Pronounced atrophy can be observed at the left peri-Sylvian area, and HRvol shows a decrease from 0.79 to 0.70.

2) Lobar volume = GM + WM of a particular lobe

3) Mesial and subcortical structure volume = volume of amygdala + hippocampus, putamen, caudate nucleus, thalamus, globus pallidus, brain stem, and cerebellum.

Ratios of the volumes were calculated in the following manner:

1) Interhemispheric ratio (HRvol) = volume of the affected hemisphere (AH)/volume of the unaffected hemisphere (UH)

2) Lobar/GM/WM/mesial/subcortical structure ratios: volume of Lobar/GM/WM/mesial/subcortical structure from the AH/volume of Lobar/GM/WM/mesial/subcortical structure from the UH

3) In total, we generated 15 volumetric ratio measures: HRvol, insular, frontal, temporal, parietal, occipital, GM, WM, amygdala and hippocampus (combined), putamen, caudate nucleus, thalamus, globus pallidus, brain stem, and cerebellum.

Visualization of the parcellated brain regions (the final output of BrainSuite processing) in 1 patient is shown in Fig 1 as an example. This patient underwent 2 MRIs, separated by 7 years, with the second scan showing progressive atrophy around the left peri-Sylvian area.

Scans from controls were processed with the same methodology as patients. In healthy controls (who did not have an affected hemisphere), all the ratios were calculated by randomly dividing the 2 sides. In controls with non-RE epilepsy, all ratios were determined by dividing the epileptic side by the nonepileptic side.

### Statistics

Statistical analyses were performed by using the Statistics Toolbox in Matlab 2013b (MathWorks, Natick, Massachusetts). The Mann-Whitney *U* test was performed to compare the degree of atrophy between different brain regions (multiple comparison corrected by the false discovery rate<sup>9</sup>). The 2-tailed Pearson correlation coefficient test was used to assess the correlation between the lobar ratios and epilepsy duration. The significance level was

set at  $P < .05$ . The methodology of classification is described below.

### Overall Workflow

As shown in On-line Fig 1, the 15 volumetric ratio measures from both patients and controls were first normalized by subtracting the pooled mean and dividing by the pooled SD. The logistic regression classifier was trained to discriminate the patients and controls by using each of the volumetric ratio measures. The binary logistic regression classifier can be described as follows:

$$1) \quad \pi[f_i(n)] = \frac{1}{1 + e^{-[\beta_0 + \beta_1 f_i(n)]}},$$

where  $f_i(n)$  is the  $n^{\text{th}}$  observation from the  $i^{\text{th}}$  feature,  $\beta_0$ ,  $\beta_1$  are the regression parameters, and  $\pi[f_i(n)]$  is the probability that the feature  $f_i(n)$  belongs to the patient class. For example, a value of  $\pi[f_i(n)] = 0.8$  denotes an 80% probability that the feature  $f_i(n)$  belongs to the patient class. The decision boundary for the classifier was set at 0.5 (ie, a value of  $\pi[f_i(n)] > 0.5$  denotes a patient class).

### Cross-Validation

The performance of the classifier was assessed via 5-fold cross-validation. For the cross-validation, the original features were randomly partitioned into 5 equal-sized subgroups ( $G_1, G_2, \dots, G_5$ ) containing equal numbers of patients and controls. From the 5 subgroups, a single subgroup was used as a validation dataset for testing the model and the remaining 4 subgroups were used as training data. The process was repeated 5 times so that each of the subgroups was used once as the testing dataset. The performance of the classifier was then quantified by estimating the accuracy (*Acc*) of the predictor on the validation dataset (or test data) as follows:

$$2) \quad Acc = \frac{TP + TN}{TP + FP + FN + TN},$$

where *TP*, *TN*, *FP*, and *FN* denote the number of true-positives, true-negatives, false-positives, and false-negatives, respectively. The mean values of accuracy across the 5 trials were used to quantify the performance of the classifier.

### Classifier Design

Based on the results of the cross-validation analysis described in the previous section, the feature with the highest accuracy was selected for constructing the optimal classifier. A leave-one-out cross-validation strategy was used—ie, the classifier was constructed by using  $N-1$  samples and was tested on the left-out sample. The process was repeated  $N$  times so that each of the samples was used once as the testing data. The sensitivity and specificity of the classifier were estimated, and the receiver operating characteristic curve was constructed. The performance of the classifier was evaluated by estimating the area under the curve.

### Probability Curve

Equation 1 was used to generate a probability curve to describe how the chosen feature predicts the probability of the patient belonging to the RE group. The probability curve was generated from the 42 RE scans and 42 non-RE epilepsy scans from this

**Table 1: Detailed demographics and clinical data of the 19 patients with RE and 2 control groups**

Demographics	
Patients with RE (N = 19)	
Mean age and SD at epilepsy onset (median) (range) (yr)	7.3 ± 5.3; 8; 1.5–22
Mean disease duration and SD at first MRI (median) (range) (yr)	4.0 ± 4.8; 2.9; 0.1–20
Sex (No.)	
Female	11
Male	8
Handedness (No.)	
Right	13
Left	5
Ambidextrous	1
Surgery location (No.)	
Hemispherectomy	12 (10 SF)
Frontal	1 (1 SF)
Insular/opercular	1
Temporal	1
No surgery	4
No. of MRI scans	
Single scan	10
Multiple scans	9 (range, 2–7)
Mean age and SD at MRI (N = 42 scans) (median) (range) (yr)	
RE scans	14.2 ± 8.0; 14.8; 3–43
Healthy controls	14.3 ± 8.0; 14.0; 3.6–43
Controls with non-RE epilepsy	16.9 ± 7.6; 15.5; 5–31
Mean disease duration and SD at MRI (N = 42 scans) (median) (range) (yr)	
RE scans	7.0 ± 5.6; 6.3; 0.8–21.4
Controls with non-RE epilepsy	7.6 ± 5.1; 6.5; 1–22

**Note:**—SF indicates seizure-free with >12 months postoperative follow-up.

study (assuming a pretest probability of 50%); another probability curve was additionally generated to correct for the difference in incidence of RE and non-RE epilepsy (1 in 1,000,000 versus 1 in 100) with the methods established by Whittemore.<sup>10</sup>

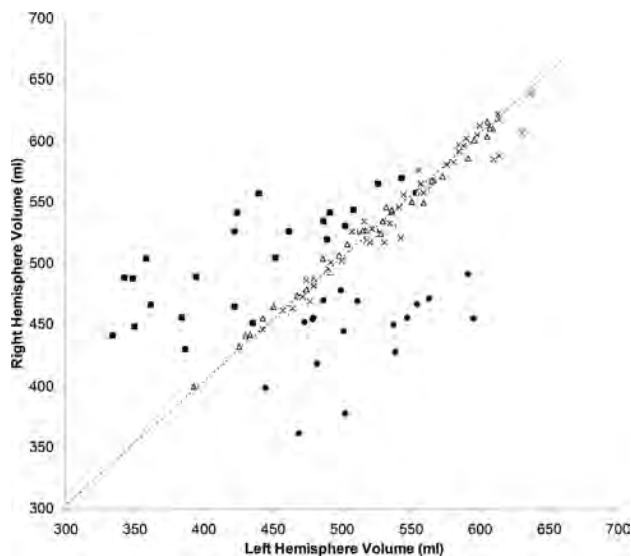
## RESULTS

### Patient and Control Demographics

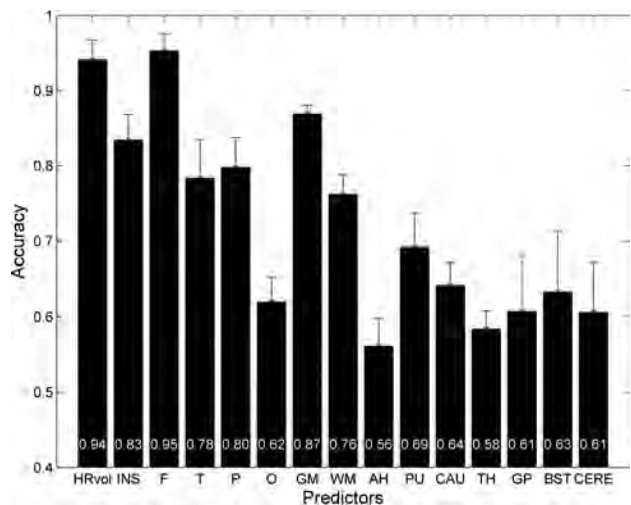
Table 1 describes the 19 patients with RE included in this study. All patients met the diagnostic criteria as previously published.<sup>3</sup> In 15 patients, the diagnosis was confirmed by biopsy and/or surgical pathology. In the remaining 4 patients, the RE diagnosis was based on the presence of the following features: 1) focal seizures and unilateral cortical deficits, 2) electroencephalography with unihemispheric slowing with or without epileptiform activity and unilateral seizure onset, and 3) MR imaging with unihemispheric atrophy and T2/FLAIR hyperintense signal in the GM/WM or caudate. Forty-two MRIs from these 19 patients with RE were included in this study.

### Predictive Values

As shown in Fig 2, hemispheric asymmetry of total brain volume produced a clearly defined separation of patients with RE from controls (both healthy and those with non-RE epilepsy). Both control groups clustered tightly along the diagonal line that represents hemispheres with equal volumes, whereas the patients (regardless of left- or right-sided) showed markedly more dispersion in the hemispheric volumes. In all patients with RE, HRvol was <1.0, indicating a smaller volume of the affected hemisphere.



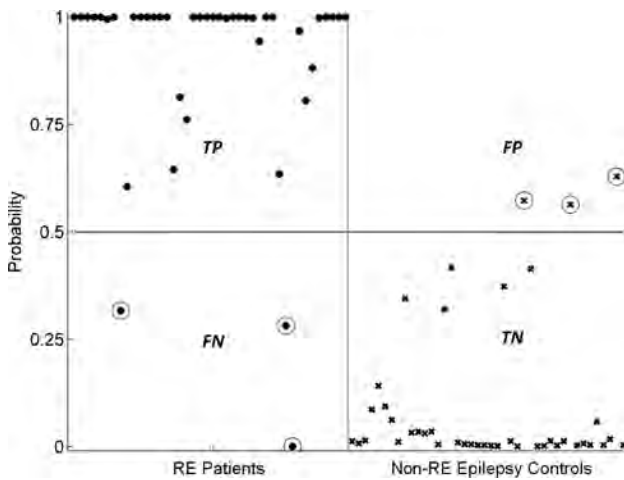
**FIG 2.** Absolute volume of the right hemisphere versus volume of the left hemisphere in patients with RE and 2 control groups. *Triangles* indicate healthy controls; *crosses*, controls with non-RE epilepsy; *squares*, patients with left RE; and *circles*, patients with right RE. The *dashed line* is the diagonal line representing hemispheres with equal volumes.



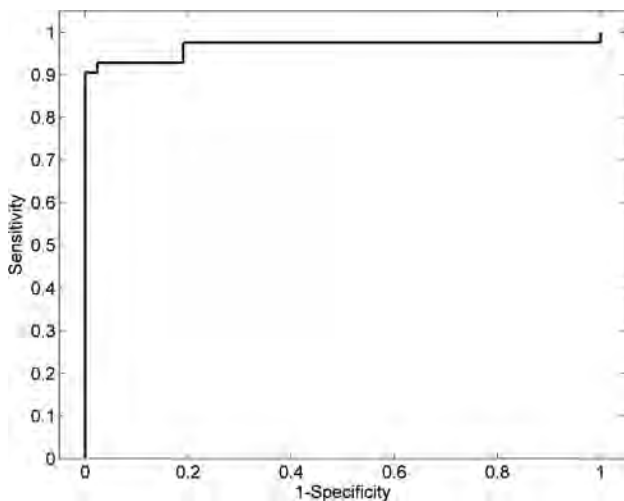
**FIG 3.** Mean accuracy across the 5 cross-validation runs of the logistic regression classifier for 15 volumetric ratio measures. Patients with RE were compared with controls with non-RE epilepsy with matching disease durations. Error bars denote the SD. The mean accuracy values for each measure were plotted at the bottom of the bars. INS indicates insula; F, frontal; T, temporal; P, parietal; O, occipital; AH, amygdala and hippocampus; PU, putamen; CAU, caudate nucleus; TH, thalamus; GP, globus pallidus; BST, brain stem; and CERE, cerebellum.

Figure 3 shows the mean accuracy of the logistic regression classifier for all volumetric measure ratios, using controls with non-RE epilepsy. The highest prediction accuracy was for HRvol and frontal lobe ratio (0.94 and 0.95), which were not significantly different.

We used HRvol as the feature for the classifier and evaluated its performance. With this classifier, most of the patients and controls were correctly classified. As shown in Fig 4, of 42 scans of patients with RE, only 3 were misclassified; of 42 controls with non-RE epilepsy, only 3 were misclassified. The classifier attained



**FIG 4.** Performance of the classifier using HRvol. Patients with RE are denoted with dots, and controls with non-RE epilepsy were denoted with crosses. True-positives (TP) are defined as patients correctly identified as patients by the classifier. True-negatives (TN) are defined as controls correctly identified as controls. False-positives (FP) are defined as controls incorrectly identified as patients. False-negatives (FN) are defined as patients incorrectly identified as controls. *Circled dots/crosses* denote the subjects who were misclassified (3 FPs and 3 FNs).



**FIG 5.** Receiver operating characteristic analyses showing a highly discriminative classifier using HRvol.

a sensitivity of 0.93 and a specificity of 0.93. The receiver operating characteristic curve of the detector is shown in Fig 5. The area under the curve was 0.97, which denotes a highly discriminative classifier. Figure 6 shows the probability curves that depict the relationship between HRvol and the probability of the patient belonging to the RE group. The classifier using the frontal lobe ratio had a similar performance (sensitivity = 0.95, specificity = 0.97, area under the curve = 0.97).

#### Degree of Atrophy

As shown in Table 2, among all the lobar regions, the insula exhibited the most atrophy at the most recent MRI ( $P < .05$ ). Among all the basal ganglia and mesial temporal structures, the regional atrophy differences were not statistically significant. Nine patients showed ipsilateral brain stem atrophy, and 3 pa-

tients showed contralateral cerebellar atrophy, with a ratio of  $<0.95$  at the most recent MRI.

#### Longitudinal Analyses

Figure 7A shows the disease progression in the 9 patients with multiple scans. The median change of HRvol per year was  $-1.4\%$ . All patients had decreasing HRvols, indicating disease progression, with the exception of 1 patient (P5) who showed an increase of HRvol with time. Seven of these 9 patients had intravenous immunoglobulin (IVIG) treatment with varying responses. P9 responded well with a reduction of seizures; P1 and P6 had only transient responses in terms of seizure control after each IVIG cycle; and patients 2, 4, 5, and 16 had no clear benefit. In P2, a marked drop of HRvol was observed at the sixth MRI, at which time the patient was admitted for status epilepticus. The seventh MRI in the same patient was performed after seizures were controlled (IVIG + steroids + tacrolimus), and a slight increase of HRvol was observed at that time, though not back to the baseline level of the previous 5 MRIs.

Additional information can be obtained by analyzing absolute volumes of the hemispheres as shown in Fig 7B. The volumes of most patients moved downward (toward origin) with time, as indicated by the arrows. P2 (who had a marked drop of HRvol at the sixth MRI due to status epilepticus) had abrupt changes in the absolute volumes, and review of the MR imaging showed bilateral swelling, more on the unaffected side. P1 and P9 did not show a clear downward trend.

#### Correlation of Volume Loss with Disease Duration

The ratios of frontal lobe and insular volumes were significantly negatively correlated with disease duration ( $P = .018$ ,  $P < .01$ , respectively, 2-tailed Pearson correlation test). The correlation was not significant for the ratio of the other lobes, mesial or deep brain structures, or interhemispheric ratio.

#### DISCUSSION

We present here automated volumetric analyses of a large series of patients diagnosed with Rasmussen syndrome. Independently using a different platform of processing routines, our results confirmed the volumetric findings reported in a previous study by Wagner et al.<sup>5</sup> We further expanded the previous study by evaluating the predictive values of volumetric findings, with the addition of healthy and epilepsy controls. Our study provides further evidence that automatic volumetric analysis can be useful in the diagnosis of patients with RE on an individual basis.

The most important finding from our study is that volumetric measures, particularly interhemispheric and frontal lobe ratios, had a high degree of accuracy in separating patients from those with non-RE epilepsy with the same disease duration. Used in the relevant clinical settings, such as initial and follow-up investigations in patients with epilepsy with suspected RE, the probability curve that was estimated by using HRvol can potentially provide an objective measure to solidify the confidence of the diagnosis. Additionally, with the methodology established in this article, such patients can be studied prospectively with volumetric findings compared with surgical pathology/biopsy.

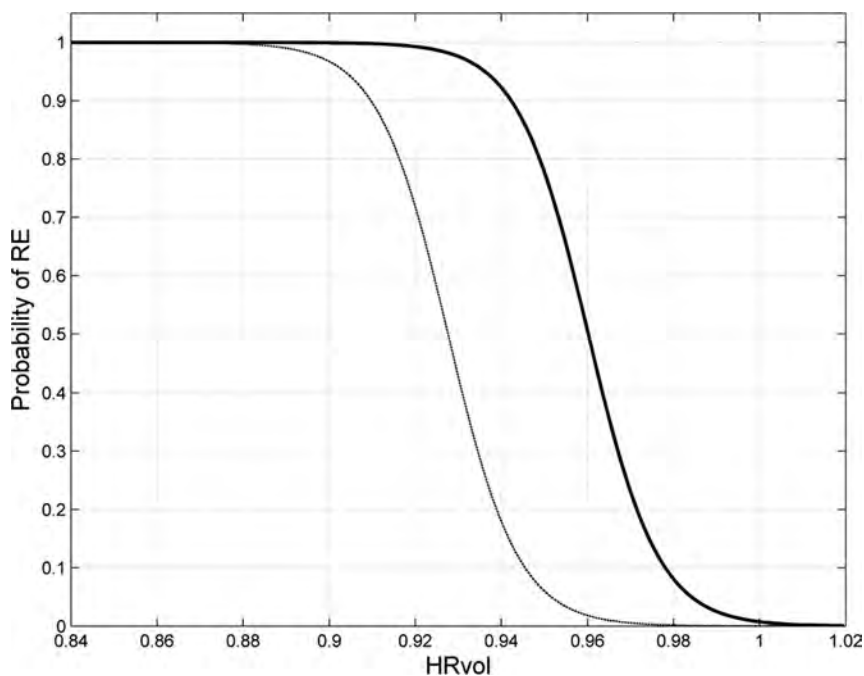


**FIG 6.** Probability curves depicting the relationship between HRvol and the probability of RE. The *solid curve* was estimated on the basis of comparison of 42 scans from patients with RE and 42 scans from controls with non-RE epilepsy with the same disease duration. The *thin dashed curve* was additionally generated to correct for the difference in incidence of RE and non-RE epilepsy (1 in 1,000,000 versus 1 in 100).

**Table 2: Regional atrophy difference in all the lobar, basal ganglia and mesial temporal structure regions**

Region	Ratio of Atrophy ( $\pm$ SD)
Lobar	
Insula	0.77 $\pm$ 0.04
Frontal	0.84 $\pm$ 0.03
Temporal	0.88 $\pm$ 0.03
Parietal	0.87 $\pm$ 0.03
Occipital	0.90 $\pm$ 0.05
GM	0.85 $\pm$ 0.02
WM	0.88 $\pm$ 0.02
Basal ganglia and mesial temporal structures	
AH	0.90 $\pm$ 0.02
PU	0.88 $\pm$ 0.03
CAU	0.89 $\pm$ 0.06
TH	0.95 $\pm$ 0.04
GP	0.94 $\pm$ 0.02

**Note:**—AH indicates amygdala and hippocampus combined; PU, putamen; CAU, caudate nucleus; TH, thalamus; GP, globus pallidus.

In terms of lobar atrophy, we found the insula to be significantly more atrophic than all the other lobes. In terms of predictive value, the frontal lobe ratio was found to be the most predictive measure for RE among all lobes—that is, the frontal lobe ratio separated patients from controls with the highest accuracy. One should not confuse prediction accuracy with the size of an effect (atrophy) because having a large effect does not necessarily imply higher accuracy. This was seen in our data, in which the frontal lobe ratio had the best accuracy but the insula had the most atrophy. Segmentation of the insula cortex can be difficult, and thickness can be overestimated; these issues cause more noise in the measured data, which can explain the lower accuracy. Both frontal and insular ratios, however, correlated significantly with dis-

ease duration. These findings support the frontal lobe and insula being preferentially involved in the atrophic process, compared with the temporal, parietal, and occipital lobes. This finding is consistent with those from previous studies.<sup>1,5,11-13</sup>

Our results show that the predictive accuracy of GM is greater than that of WM; these findings may suggest that GM is preferentially affected in RE compared with WM. In terms of the severity of atrophy, both GM and WM were affected and lost volume across the years. Although GM had a lower mean ratio than WM, the difference was not statistically significant. Overall, this finding is consistent with findings in the previous study by Wagner et al,<sup>5</sup> in which the authors found a preferential effect of RE on GM, and other studies that documented additional WM involvement (especially at the advanced stages of RE) by pathology and imaging methods.<sup>14,15</sup>

Three patients (P8, P9, P16) were misclassified as healthy by the HRvol

classifier and the frontal lobe ratio classifier. All 3 patients had pathologic confirmation of RE based on biopsy and/or surgical pathology. In P9 and P16, the MRIs that were misclassified were at 3 years and 1 year of epilepsy onset, respectively; later MRIs (at 3.5 and 2 years, respectively) were correctly classified as RE. These data indicate a need for improving the sensitivity of our methodology, especially for detecting subtle changes at an early stage of the disease; alternatively, these data could suggest that volume loss in select patients at the initial stage of RE may not be sufficient to be differentiated from normal variations. On the other hand, the 3 patients in our cohort who had the shortest disease duration at the first MRI (0.1, 0.83, 0.91 years, respectively) were all correctly classified; this result demonstrates the effectiveness of our methodology in these patients.

Our findings also demonstrated the feasibility that progression of RE can be measured by volumetric analysis. Most patients with serial MRIs showed a decrease in HRvol, indicating disease progression despite IVIG and antiepileptic drug treatments. Additionally, by analyzing the absolute hemispheric volumes, we found that patients with RE also had atrophy in the unaffected hemisphere and had bilateral brain volume loss—that is, the volume of most patients moved downward (toward origin) across time as shown on the absolute hemisphere volume plot. The patients who showed unusual time courses of longitudinal hemispheric volumes and ratios could be explained in several ways: 1) natural progression of the disease (acute and chronic); for example, P2 had abrupt changes in the absolute volumes due to status epilepticus, and review of the MRI showed bilateral swelling which might have contributed to the volume change; 2) transient response to treatment; for example, P1 had had transient response

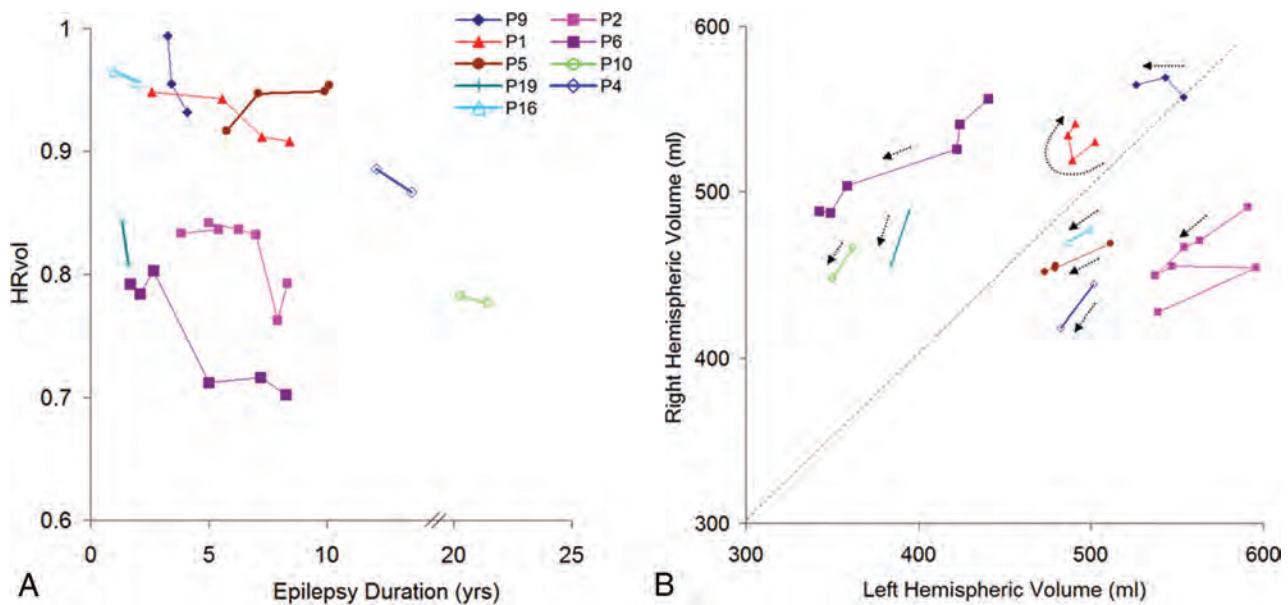


**FIG 7.** A, HRvol plotted over epilepsy duration in the 9 patients with serial MR imaging. All except P5 show a decrease in HRvol for the observed time. The axis is broken from 14 to 20 years because there are no data points for these durations. B, Absolute hemispheric volume (right-sided versus left-sided plots) of the same 9 patients. The direction of each dotted arrow shows the progression of disease over time in each patient. A and B share the same symbol for each patient for direct comparison.

to IVIG, which may have caused corresponding volume changes; 3) natural brain development; for example, P1 and P9, who did not show a clear downward trend of the arrows, were 8 and 3 years of age, respectively. It is conceivable that between the scans, the brains were still developing and growing; therefore, absolute volume may not be a good measure of disease progression. In fact, HRvol of both patients showed a clear downward trend with time. 4) The last reason is the possibility of bilateral RE; for example, P5 was the only patient whose HRvol increased with time, indicating a higher volume of atrophy in the unaffected hemisphere than in the affected hemisphere. This finding raises the possibility of bilateral RE, despite the seizures being found in the affected hemisphere only by electroencephalography. However, the presence of bilateral RE is debated and likely very rare; only 2 cases of the reported 200–300 cases in the literature showed histopathologic proof for bilateral RE.<sup>16,17</sup> No biopsy was obtained from the unaffected hemisphere to confirm or disprove the possibility of bilateral RE in P5.

The performance of the classifier constructed in our study was similar when comparing patients with RE to either the healthy controls or the controls with non-RE epilepsy. If one takes into account the epilepsy controls having the same disease duration as the patients with RE, our data provide quantitative evidence that brain volume decrease (likely caused by extensive neuronal loss<sup>1-3</sup>) is a characteristic of RE, which, as we show in this study, can be used to accurately separate patients with RE from those with non-RE epilepsy.

Several limitations should be considered when interpreting the results of our study:

1) Three patients in this study had an adolescent or adult-onset age (13, 13, and 22 years of age, respectively). These patients are considered to have a less common presentation of RE<sup>18</sup> and could bring heterogeneity to the study cohort. Additionally, 4

patients did not have pathology/biopsy to confirm RE. Although we followed the commonly accepted diagnostic criteria,<sup>3</sup> the lack of pathologic confirmation could still potentially contribute to an inaccurate diagnosis of RE.

2) Due to the retrospective design of the study, there was a relatively long interval between disease onset and the earliest MR imaging available for volumetric analysis in our cohort. Only in a small subset of patients with RE (3 of 19) did we have access MRI data within 1 year of their initial disease onset. For the other patients, the initial MRI was either performed outside the Cleveland Clinic or not performed with volumetric T1 sequences and could not be used for analysis. Therefore, on the basis of the current data, it was not possible to determine the effectiveness of our methodology for early diagnosis. Additionally, many of the patients with RE were referred to our center for surgery; in these patients, only 1 presurgical MRI was available for analysis and there were no data for the later stages of the disease. Overall, further prospective studies are warranted to confirm the validity of the findings from our current study.

3) The 42 MRIs from the 19 patients with RE were treated as 42 different cases and were matched to 42 different control subjects, introducing potential bias in the comparison.

4) This study was not set up to evaluate the effectiveness of immune therapy. We could not assess whether IVIG was an effective treatment to alleviate the disease impact because there was no proper control group (patients without IVIG). A more rigorous study design is needed to make any definite conclusions on treatment effectiveness.

As future work, it is conceivable to use the established methodology to prospectively analyze patients with suspected RE and compare with biopsy and surgical pathology. Our methodology can also be used to monitor disease progression in patients with confirmed RE by calculating volumetric changes in hemispheric

and lobar regions on their repeat MRIs. In terms of methodologic improvement, in addition to volumetric measures, we will also extract other important features of the T1 dataset (such as signal change) to be used as the input to the classifier, to improve classification of patients at the early stage of the disease.

## CONCLUSIONS

Our study highlights the usefulness of volumetric analysis to assist the diagnosis of patients with Rasmussen syndrome. We demonstrate that interhemispheric and frontal lobe ratios can accurately classify individual patients with RE from healthy controls and patients with non-RE epilepsy with the same disease duration. The probability curves generated in our study can be used in appropriate clinical settings to solidify the confidence of the diagnosis of RE. We also demonstrate that progression of hemispheric atrophy can be measured reliably by volumetric analysis. Such analysis, when used in conjunction with other clinical data, can provide insight into disease progression and treatment effectiveness, and could be considered as part of the follow-up process for patients with suspected RE.

## ACKNOWLEDGMENTS

We thank James Bena, Lead Biostatistician, Cleveland Clinic Quantitative Health Sciences, for his assistance on the statistical analyses.

Disclosures: Z. Irene Wang—RELATED: Grant: National Institute of Neurological Disorders and Stroke R01 NS074980.\* David W. Shattuck—RELATED: Grant: National Institute of Neurological Disorders and Stroke R01 NS074980.\* Richard M. Leahy—RELATED: Grant: National Institute of Neurological Disorders and Stroke R01 NS074980, R01 NS089212.\* Elaine Wyllie—UNRELATED: Royalties: Wolters Kluwer Publishing, Lippincott, Comments: royalties for being the editor-in-chief of *Wyllie's Treatment of Epilepsy*, 6th ed. John C. Mosher—RELATED: Grant: National Institutes of Health National Institute of Neurological Disorders and Stroke R01 NS074980.\* Stephen E. Jones—RELATED: Grant: National Institutes of Health National Institute of Neurological Disorders and Stroke R01 NS074980\*; UNRELATED: Congressionally Directed Medical Research Programs\*; Payment for Lectures (including service on Speakers Bureaus); Siemens, Monteris Medical, Comments: for speaking about 7T and about advanced imaging; Royalties: Academic Press (for *MRI Atlas of Pituitary Pathology*); Payment for Development of Educational Presentations: Webinar on MS imaging (Cleveland Clinic). \*Money paid to the institution.

## REFERENCES

1. Bien CG, Widman G, Urbach H, et al. **The natural history of Rasmussen's encephalitis.** *Brain* 2002;125:1751–59 CrossRef Medline
2. Bauer J, Elger CE, Hans VH, et al. **Astrocytes are a specific immuno-**

- logical target in Rasmussen's encephalitis. *Ann Neurol* 2007;62:67–80 CrossRef Medline
3. Varadkar S, Bien CG, Kruse CA, et al. **Rasmussen's encephalitis: clinical features, pathobiology, and treatment advances.** *Lancet Neurol* 2014;13:195–205 CrossRef Medline
4. Larionov S, König R, Urbach H, et al. **MRI brain volumetry in Rasmussen encephalitis: the fate of affected and "unaffected" hemispheres.** *Neurology* 2005;64:885–87 CrossRef Medline
5. Wagner J, Schoene-Bake JC, Bien CG, et al. **Automated 3D MRI volumetry reveals regional atrophy differences in Rasmussen encephalitis.** *Epilepsia* 2012;53:613–21 CrossRef Medline
6. Joshi AA, Shattuck DW, Leahy RM. **A method for automated cortical surface registration and labeling.** *Biomed Image Regist Proc* 2012;7359:180–89 CrossRef Medline
7. Shattuck DW, Leahy RM. **BrainSuite: an automated cortical surface identification tool.** *Med Image Anal* 2002;6:129–42 CrossRef Medline
8. Pantazis D, Joshi A, Jiang J, et al. **Comparison of landmark-based and automatic methods for cortical surface registration.** *Neuroimage* 2010;49:2479–93 CrossRef Medline
9. Benjamini Y, Hochberg Y. **Controlling the false discovery rate: a practical and powerful approach to multiple testing.** *J R Stat Soc Series B Methodol* 1995;57:289–300
10. Whittemore AS. **Logistic regression of family data from case-control studies.** *Biometrika* 1995;82:57–67 CrossRef
11. Bhatjwale MG, Polkey C, Cox TC, et al. **Rasmussen's encephalitis: neuroimaging findings in 21 patients with a closer look at the basal ganglia.** *Pediatr Neurosurg* 1998;29:142–48 CrossRef Medline
12. Chiapparini L, Granata T, Farina L, et al. **Diagnostic imaging in 13 cases of Rasmussen's encephalitis: can early MRI suggest the diagnosis?** *Neuroradiology* 2003;45:171–83 Medline
13. Rajesh B, Kesavadas C, Ashalatha R, et al. **Putaminal involvement in Rasmussen encephalitis.** *Pediatr Radiol* 2006;36:816–22 CrossRef Medline
14. Cauley KA, Burbank HN, Filippi CG. **Diffusion tensor imaging and tractography of Rasmussen encephalitis.** *Pediatr Radiol* 2009;39:727–30 CrossRef Medline
15. Pardo CA, Vining EP, Guo L, et al. **The pathology of Rasmussen syndrome: stages of cortical involvement and neuropathological studies in 45 hemispherectomies.** *Epilepsia* 2004;45:516–26 CrossRef Medline
16. Chinchilla D, Dulac O, Robain O, et al. **Reappraisal of Rasmussen's syndrome with special emphasis on treatment with high doses of steroids.** *J Neurol Neurosurg Psychiatry* 1994;57:1325–33 CrossRef Medline
17. Tobias SM, Robitaille Y, Hickey WF, et al. **Bilateral Rasmussen encephalitis: postmortem documentation in a five-year-old.** *Epilepsia* 2003;44:127–30 CrossRef Medline
18. Oguni H, Andermann F, Rasmussen TB. **The syndrome of chronic encephalitis and epilepsy: a study based on the MNI series of 48 cases.** *Adv Neurol* 1992;57:419–33 Medline

# Quantitative Evaluation of Medial Temporal Lobe Morphology in Children with Febrile Status Epilepticus: Results of the FEBSTAT Study

A.C. McClelland, W.A. Gomes, S. Shinnar, D.C. Hesdorffer, E. Bagiella, D.V. Lewis, J.A. Bello, S. Chan, J. MacFall, M. Chen, J.M. Pellock, D.R. Nordli Jr, L.M. Frank, S.L. Moshé, R.C. Shinnar, and S. Sun, for the FEBSTAT Study Team



## ABSTRACT

**BACKGROUND AND PURPOSE:** The pathogenesis of febrile status epilepticus is poorly understood, but prior studies have suggested an association with temporal lobe abnormalities, including hippocampal malrotation. We used a quantitative morphometric method to assess the association between temporal lobe morphology and febrile status epilepticus.

**MATERIALS AND METHODS:** Brain MR imaging was performed in children presenting with febrile status epilepticus and control subjects as part of the Consequences of Prolonged Febrile Seizures in Childhood study. Medial temporal lobe morphologic parameters were measured manually, including the distance of the hippocampus from the midline, hippocampal height:width ratio, hippocampal angle, collateral sulcus angle, and width of the temporal horn.

**RESULTS:** Temporal lobe morphologic parameters were correlated with the presence of visual hippocampal malrotation; the strongest association was with left temporal horn width ( $P < .001$ ; adjusted OR, 10.59). Multiple morphologic parameters correlated with febrile status epilepticus, encompassing both the right and left sides. This association was statistically strongest in the right temporal lobe, whereas hippocampal malrotation was almost exclusively left-sided in this cohort. The association between temporal lobe measurements and febrile status epilepticus persisted when the analysis was restricted to cases with visually normal imaging findings without hippocampal malrotation or other visually apparent abnormalities.

**CONCLUSIONS:** Several component morphologic features of hippocampal malrotation are independently associated with febrile status epilepticus, even when complete hippocampal malrotation is absent. Unexpectedly, this association predominantly involves the right temporal lobe. These findings suggest that a spectrum of bilateral temporal lobe anomalies are associated with febrile status epilepticus in children. Hippocampal malrotation may represent a visually apparent subset of this spectrum.

**ABBREVIATIONS:** EEG = electroencephalography; FEBSTAT = Consequences of Prolonged Febrile Seizures in Childhood; FSE = febrile status epilepticus; HIMAL = hippocampal malrotation; SFS = simple febrile seizure

Prolonged febrile seizures are associated with subsequent development of epilepsy, whereas brief febrile seizures are not.<sup>1</sup> The factors that predispose to prolonged febrile seizures are there-

fore of profound interest but are not well-understood. The Consequences of Prolonged Febrile Seizures in Childhood (FEBSTAT) study is a prospective multicenter trial studying children who presented with febrile status epilepticus (FSE), defined as febrile seizures lasting longer than 30 minutes, in comparison with a control group consisting of children presenting with brief, simple febrile seizures.<sup>2</sup> The initial evaluation of subjects in the FEBSTAT study identified several risk factors for FSE, including the morphologic anomaly hippocampal malrotation (HIMAL).<sup>3,4</sup> While these findings suggest a relationship between a medial tem-

Received May 19, 2016; accepted after revision July 4.

From Departments of Radiology (A.C.M., W.A.G., J.A.B.), Neurology (S. Shinnar, S.L.M., R.C.S.), Pediatrics (S. Shinnar, S.L.M.), Epidemiology and Population Health (S. Shinnar), and Neuroscience (S.L.M.), Montefiore Medical Center, Albert Einstein College of Medicine, Bronx, New York; Departments of Epidemiology (D.C.H., M.C.) and Radiology (S.C.), Gertrude H. Sergievsky Center, Columbia University, New York, New York; Department of Health Evidence and Policy (E.B.), Mount Sinai School of Medicine, New York, New York; Departments of Pediatrics (Neurology) (D.V.L.) and Radiology (J.M.), Duke University Medical Center, Durham, North Carolina; Departments of Neurology (J.M.P.) and Biostatistics (S. Sun), Medical College of Virginia, Virginia Commonwealth University, Richmond, Virginia; Department of Neurology (D.R.N.), Ann & Robert H. Lurie Children's Hospital of Chicago, Chicago, Illinois; and Department of Neurology (L.M.F.), Children's Hospital of The King's Daughters and Eastern Virginia Medical School, Norfolk, Virginia.

This work was supported by the National Institute of Neurological Disorders and Stroke grant 2R37 NS43209 (Principal Investigator: S. Shinnar, MD, PhD) and the National Institute of Child Health and Human Development grant 36867 (Principal Investigator: D.C. Hesdorffer, PhD).

Paper previously presented in abstract form at: Annual Meeting of the American Society of Neuroradiology and the Foundation of the ASNR Symposium, April 25–30, 2015; Chicago, Illinois.

Please address correspondence to William A. Gomes, MD, PhD, Division of Neuroradiology, Department of Radiology, Montefiore Medical Center, 111 East 210th St, Bronx, NY 10467; e-mail: wgomes@montefiore.org

Indicates open access to non-subscribers at [www.ajnr.org](http://www.ajnr.org)

<http://dx.doi.org/10.3174/ajnr.A4919>

poral lobe anatomic variation and FSE, the precise nature and extent of this relationship are not clear.

Medial temporal lobe structural anatomy is the result of a complex developmental process in which the medial temporal lobe cortex infolds and rotates around the hippocampal gyrus.<sup>5,6</sup> Qualitative descriptions of abnormal hippocampal morphology have been reported in a number of pathologic conditions, including temporal lobe epilepsy, both as an isolated finding<sup>7</sup> and in association with other developmental abnormalities.<sup>8</sup> HIMAL is a specific anomaly of hippocampal development, which has also been described by other terms, including “incomplete hippocampal inversion.”<sup>7</sup> Published criteria for HIMAL vary slightly among reports but include an abnormally rounded, “globular” configuration of the hippocampus on coronal images, blurring of internal hippocampal architecture, an abnormally medial location of the hippocampus, vertical orientation of the collateral sulcus, and enlargement of the temporal horn of the lateral ventricle (apparently reflecting medial displacement of the hippocampus).

Visual interpretation of scans obtained in FEBSTAT revealed an increased incidence of HIMAL in subjects presenting with FSE relative to control subjects, establishing HIMAL as a risk factor for FSE.<sup>9</sup> However, the specific morphologic features of HIMAL that are most associated with prolonged febrile seizures remain undefined. In addition, a substantial majority of scans in children with febrile seizures from the FEBSTAT study demonstrated no abnormality on visual interpretation. It is unclear what role the variation in medial temporal lobe morphology may play in these visually healthy subjects.

The goal of this study was to elucidate the relationship between medial temporal lobe morphology and prolonged febrile seizures by performing a quantitative analysis of medial temporal lobe morphology in subjects from the FEBSTAT study. We address 3 primary questions: 1) Does the visual interpretation of HIMAL by experienced interpreters reflect quantitative variation in underlying temporal lobe morphology? 2) Of the individual morphologic features of HIMAL, which are most strongly associated with FSE? 3) In subjects without HIMAL or other overt abnormal findings, does subtle variation in temporal lobe morphology predict FSE?

## **MATERIALS AND METHODS**

### ***Subject Groups and Imaging***

Cohort selection, patient recruitment, and imaging procedures for the FEBSTAT study have been described in detail previously.<sup>2,9,10</sup> All procedures were approved by the Institutional Review Board for the Protection of Human Subjects at all participating institutions. Written informed consent was obtained from the parents of all subjects. FSE was defined as a provoked seizure in which the sole acute provocation was fever (temperature of  $>38.4^{\circ}\text{C}$ ,  $101.0^{\circ}\text{F}$ ) without a prior history of afebrile seizures and without evidence of an acute CNS infection or insult.<sup>11</sup> The 226 subjects with FSE in this study were enrolled from 3 prospective studies as described previously<sup>12</sup>: 191 from the FEBSTAT cohort,<sup>9</sup> 23 from the Duke FEBSTAT pilot study,<sup>13</sup> and 12 from the Columbia first febrile seizure study.<sup>14</sup> A control group of 96 children who presented with a simple febrile seizure (SFS) and who underwent baseline MR imaging similar to those with FSE was also obtained from the Columbia study.<sup>14</sup> SFSs are febrile seizures lasting

$<10$  minutes without focal features and without recurrence during the febrile illness.<sup>15</sup>

In patients with FSE, 67% of scans were obtained within 3 days of presentation and 88% were obtained within 7 days.<sup>9</sup> Seizure classification was performed by review of source documents by a central phenomenology core blinded to electroencephalography (EEG) and MR imaging findings.<sup>2</sup> MR imaging sequences have been described in detail previously<sup>9,10</sup> and included coronal oblique T2-weighted fast spin-echo sequences. All scans were performed at 1.5T. Visual analysis of MRIs was performed by 2 experienced American Board of Radiology–certified radiologists (J.A.B. and S.C.) with Certificates of Advanced Qualification in neuroradiology. MR imaging readers were informed of the subject’s age at the time of the examination but were blinded to all other clinical parameters. HIMAL was scored as negative for HIMAL, left HIMAL, bilateral HIMAL, or equivocal. Hippocampal T2 signal was scored from 0 to 4 with 0 = normal, 1 = equivocal, 2 = mildly abnormal T2 signal on  $\geq 1$  section, 3 = moderately abnormal, and 4 = markedly abnormal findings throughout the hippocampus. All studies were read independently, but discordant reads were discussed for consensus. For this study, visually normal cases were those in which HIMAL was scored as negative for HIMAL and T2 signal was scored as zero. The results of the initial qualitative analysis from the baseline MR imaging scans have been reported previously.<sup>9</sup>

### ***Quantitative Image Analysis***

Quantitative evaluation of bilateral medial temporal lobe morphology was performed by manual measurement of predetermined structures of interest on a T2-weighted coronal oblique image at the level of the cerebral aqueduct. All measurements were performed blinded to all clinical data except patient age. The measurement strategy is illustrated in Fig 1. The subject’s midline was defined as a line through the cerebral aqueduct. Unless otherwise specified, measurements were performed parallel to the horizontal axis of the patient, defined as a line orthogonal to the subject’s midsagittal plane. Hippocampal shape was evaluated by calculating the ratio of hippocampal height to width. The medial aspect of the hippocampus was defined as the point at the most medial extent of the hippocampal body as distinct from the subiculum. The width of the hippocampus was defined by extending the longest line possible from the medial aspect of the hippocampus laterally to the border of the hippocampus and the temporal horn CSF. The hippocampal height was defined as the greatest extent of the hippocampal body orthogonal to the line defining the hippocampal width.

The medial/lateral location of the hippocampus was evaluated at both the medial aspect of the hippocampus by the distance of the hippocampus from midline and at the lateral aspect of the hippocampus by the width of the temporal horn of the lateral ventricle. The distance of the hippocampus from midline was determined by measuring the distance from the subject’s midline to the medial aspect of the hippocampus. To account for differences in brain size, we normalized this distance of the hippocampus from the midline to the distance of the uncus from midline, defined on the same image as the distance from the midline to the most medial aspect of the temporal lobe. The width of the temporal horn of the lateral ventricle was defined as the distance from

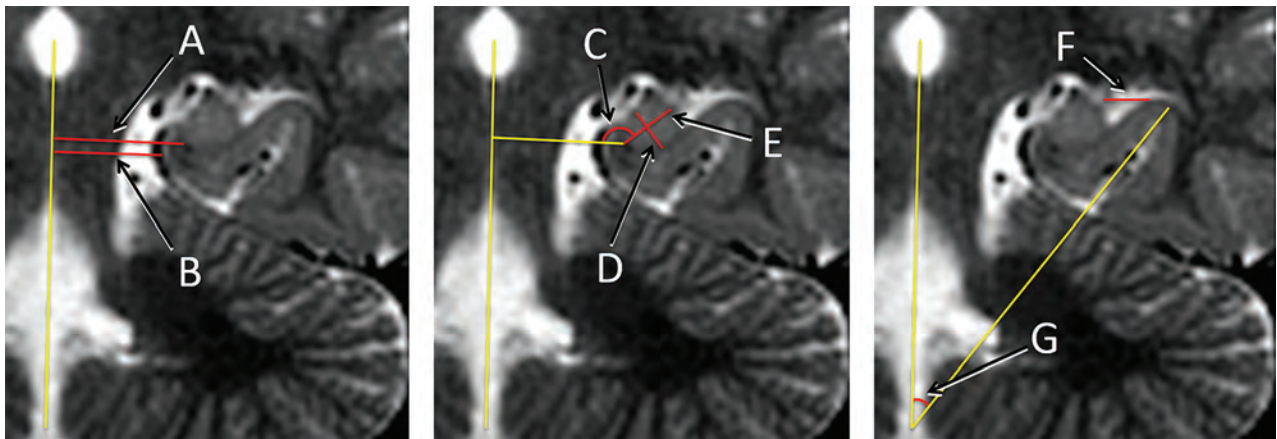


**FIG 1.** Medial temporal lobe morphologic measurements. Linear and angular measurements, shown in red, were obtained in relation to reference lines, shown in yellow. Measurements were obtained bilaterally; right-sided measurements are omitted here for clarity. Note the presence of HIMAL in this subject. *A* and *B*, Distances of the hippocampal formation and uncus from the midline. *C*, Angle of the hippocampal formation. *D* and *E*, Height and width of the hippocampal formation. *F*, Width of the temporal horn. *G*, Angle of the collateral sulcus.

the most lateral aspect of the hippocampus to the most lateral aspect of the lateral CSF space. If a thin curvilinear CSF space extended from the lateral aspect of the temporal horn around the collateral eminence (Fig 1), this region was not included in the temporal horn width.

Hippocampal rotation was evaluated by determining the angles of the hippocampus and the collateral sulcus. The angle of the hippocampus was defined as the angle of the line defining the hippocampal width as described above relative to the subject's horizontal axis. The collateral sulcus angle was determined with a single line drawn through the middle of the collateral sulcus relative to the subject's midline.

HIMAL is reportedly associated with blurring of the internal hippocampal architecture. However, the internal hippocampal architecture is not reliably demonstrated in young children at 1.5T, the magnet strength used in most of the FEBSTAT cohort at initial presentation. This component of HIMAL therefore could not be assessed in this study.

Scans in which accurate and comparable measurements could not be made due to imaging factors such as artifacts, patient rotation, or section selection were not included in this analysis. Of the 226 subjects with FSE and 96 subjects with SFS described above, 33 subjects with FSE and 4 subjects with SFS were excluded due to imaging features, for a final analysis of 193 subjects with FSE and 92 subjects with SFS. In most cases, all measurements were made from a single image. In several cases, one or both of the collateral sulci could not be identified on the chosen image. If the collateral sulcus could be identified on an adjacent section, this measurement was included. If not, a collateral sulcus measurement was not included for that subject. The left collateral sulcus measurement was not obtained for 17 subjects, and the right collateral sulcus measurement was not obtained for 8 subjects. In addition, right-sided measurements were not included for a single case in which a choroidal fissure cyst distorted the right medial temporal lobe anatomy.

### Statistical Analysis

All analyses were performed in SAS 9.4 (SAS Institute, Cary, North Carolina), and *P* values  $\leq .05$  were considered statistically

**Table 1: Descriptive summary of the MRI measurements**

Measurement	No.	Mean	SD
Left side			
Collateral sulcus angle (°)	268	61.9534	12.3098
Lateral ventricle width (cm)	285	0.3604	0.2053
Hipp angle (°)	285	174.4526	12.5996
Hipp height:width	285	0.7129	0.1106
Hipp distance from midline	285	1.5141	0.217
Right side			
Collateral sulcus angle (°)	277	68.9564	9.6766
Lateral ventricle width (cm)	284	0.257	0.158
Hipp angle (°)	284	184.1936	9.0709
Hipp height:width	284	0.6862	0.0919
Hipp distance from midline	284	1.5267	0.2166

**Note:**—Hipp indicates hippocampal.

significant. Descriptive statistics for all MR imaging measurements were generated (Table 1). Univariate statistical comparisons were performed between the MR imaging measures and both HIMAL (present versus absent) and seizure duration (SFS versus FSE). Multivariate statistical analyses of the MR imaging data were then performed. Cutoff measurements were determined by conducting univariate logistic regression for each of the MR imaging measurements separately, with a binary outcome variable. This analysis was performed separately by using as the outcome variable either the consensus determination of HIMAL (present versus absent) or the subject's seizure duration (FSE versus SFS). The optimal cutoff point was obtained for each of the measurements by selecting the one resulting in the maximum sum of sensitivity and specificity (the Youden index)<sup>16</sup> for the outcome variable. From this, a dummy variable was created for each of the MR imaging measurements on the basis of the corresponding cutoffs. Values at or below the cutoff were the reference for each measurement. Univariate logistic analysis was repeated with the newly created dummy variables. Multivariate logistic regression analyses were then fit with all 5 MR imaging dummy variables. This step was performed separately for each side (left and right) for the seizure-duration outcome variable. A similar analysis was conducted with seizure duration (FSE versus SFS) as the outcome variable.

**Table 2: Association between left hippocampal quantitative morphology and HIMAL**

Measurement	Cutoff	Sensitivity	Specificity	Unadjusted OR (95% CI)	P Value	Adjusted OR (95% CI)	P Value
Collateral sulcus angle (°)	56.26	0.5789	0.7355	0.26 (0.10–0.68)	.0059		
Lateral ventricle width (cm)	0.53	0.8421	0.861	33.04 (9.16–119.11)	<.0001	10.59 (2.65–42.34)	.0009
Hipp angle (°)	178.37	0.8421	0.4595	0.22 (0.06–0.78)	.0184		
Hipp height:width	0.75	0.6842	0.7181	5.52 (2.02–15.07)	.0009	3.69 (1.11–12.24)	.0332
Hipp distance from midline	1.42	0.8947	0.6988	0.05 (0.01–0.23)	<.0001	0.12 (0.02–0.59)	.0094

**Table 3: Association between quantitative temporal lobe morphology and FSE**

Measurement	Cutoff	Sensitivity	Specificity	Unadjusted OR (95% CI)	P Value	Adjusted OR (95% CI)	P Value
Left side							
Collateral sulcus angle (°)	70.68	0.3017	0.7977	1.70 (0.93–3.13)	.0858	1.73 (0.91–3.32)	.0971
Lateral ventricle width (cm)	0.17	0.8756	0.2609	2.49 (1.32–4.68)	.0048	2.79 (1.39–5.59)	.0038
Hipp angle (°)	183.66	0.8394	0.2391	0.61 (0.33–1.13)	.1133	0.62 (0.31–1.23)	.168
Hipp height:width	0.61	0.1658	0.913	0.48 (0.21–1.09)	.0781	0.46 (0.20–1.08)	.0756
Hipp distance from midline	1.51	0.4922	0.6196	1.58 (0.95–2.62)	.0774	1.69 (0.96–2.99)	.0714
Right side							
Collateral sulcus angle (°)	71.35	0.4785	0.6593	1.78 (1.06–2.99)	.0305	1.87 (1.05–3.34)	.0351
Lateral ventricle width (cm)	0.20	0.6198	0.6087	2.54 (1.52–4.22)	.0003	4.56 (2.48–8.41)	<.0001
Hipp angle (°)	185.50	0.5052	0.6739	2.11 (1.26–3.55)	.0049	2.26 (1.26–4.05)	.0065
Hipp height:width	0.66	0.651	0.4891	1.79 (1.08–2.96)	.0244	2.06 (1.17–3.61)	.0119
Hipp distance from midline	1.52	0.4948	0.663	1.93 (1.15–3.23)	.0128	2.29 (1.23–4.25)	.0091

**Table 4: Association between quantitative temporal lobe morphology and FSE in visually normal subjects**

Measurement	Cutoff	Sensitivity	Specificity	Unadjusted OR (95% CI)	P Value	Adjusted OR (95% CI)	P Value
Left side							
Collateral sulcus angle (°)	70.65	0.3247	0.7931	1.84 (0.99–3.42)	.0529	1.83 (0.95–3.55)	.0715
Lateral ventricle width (cm)	0.17	0.8631	0.2667	2.29 (1.21–4.34)	.0113	2.61 (1.29–5.31)	.0078
Hipp angle (°)	183.66	0.8394	0.2391	0.66 (0.35–1.24)	.195	0.62 (0.30–1.28)	.1947
Hipp height:width	0.61	0.1667	0.9111	0.49 (0.21–1.12)	.0907	0.44 (0.18–1.04)	.0604
Hipp distance from midline	1.51	0.5298	0.6111	1.77 (1.05–2.98)	.0317	1.90 (1.06–3.42)	.0315
Right side							
Collateral sulcus angle (°)	71.35	0.4731	0.6556	1.71 (1.01–2.904)	.0478	1.746 (0.97–3.15)	.0636
Lateral ventricle width (cm)	0.20	0.593	0.6158	2.33 (1.39–3.923)	.001	4.07 (2.18–7.58)	<.0001
Hipp angle (°)	185.49	0.5233	0.6813	2.35 (1.38–4.00)	.0049	2.43 (1.33–4.42)	.0038
Hipp height:width	0.70	0.4419	0.7033	1.88 (1.09–3.22)	.0227	1.81 (1.002–3.28)	.0494
Hipp distance from midline	1.52	0.4942	0.6593	1.89 (1.18–3.20)	.0177	2.062 (1.10–3.87)	.0245

## RESULTS

### Relationship of Medial Temporal Lobe Morphology to Visual HIMAL

Descriptive statistics for the 5 bilateral measurements are detailed in Table 1. To determine whether our quantitative evaluation of medial temporal lobe morphology captured the subjective differences in cases identified as HIMAL, we first evaluated the relationship between medial temporal lobe morphology and visual HIMAL. Because HIMAL was almost exclusively identified on the left side, we analyzed the relationship between left-sided measurements and cases read as either left-sided HIMAL or bilateral HIMAL. The cutoff values for left-sided measurements that maximize the Youden index for distinguishing cases with and without left-sided HIMAL are detailed in Table 2. Univariate logistic regression analysis using these cutoff values revealed significant associations between each of the 5 left-sided measurements and the presence of left-sided HIMAL (Table 2). In the final multivariate model, HIMAL was associated with an increased left lateral ventricle width ( $>0.5283$  cm,  $P = .0009$ ), and a “rounder” hippocampus (hippocampal height:width ratio of  $>0.7502$  cm,  $P =$

.0332). A negative relationship was seen between HIMAL and the distance of the hippocampus from the midline, with a value of this distance normalized to the distance of the uncus from the midline of  $>1.4236$  ( $P = .0094$ ). Although HIMAL was associated with a more vertical angle of the left hippocampus ( $178.4^\circ$ ,  $P = .0184$ ) and a more vertical orientation of the collateral sulcus ( $56.26^\circ$ ,  $P = .0059$ ) in the univariate logistic regression analysis, these relationships were not significant in the multivariate logistic regression analysis.

### Relationship of Medial Temporal Lobe Morphology to Seizure Duration

We next evaluated the relationship between medial temporal lobe morphology and seizure duration, by using a multivariate model approach similar to that used for comparison of MR imaging measurements with the HIMAL. The cutoffs for temporal lobe measurements to maximize the Youden index for distinguishing FSE and SFS are detailed in Table 3. In both univariate and multivariate logistic regression analysis, we found a significant relationship between increased width of the left lateral ventricle and

FSE (Table 3). In the multivariate analysis, a left lateral ventricle width of  $>0.169$  cm was associated with FSE ( $P = .0038$ ). We also observed a relationship between multiple right-sided measurements and FSE (Table 3). In the multivariate logistic regression model, FSE was associated with the width of the right lateral ventricle of  $>0.202$  cm ( $P < .0001$ ), normalized distance of the right hippocampus from the midline of  $1.523$  ( $P = .0091$ ), ratio of right hippocampal height:width of  $0.660$  ( $P = .0119$ ), right collateral sulcus angle of  $71.35^\circ$  ( $P = .0351$ ), and right hippocampal angle of  $185.5^\circ$  ( $P = .0065$ ). Univariate  $t$  tests were also performed to compare group means for the temporal lobe measurements. No significant difference was observed in this analysis;  $P$  values approaching significance were observed for the normalized distance of the right hippocampus from the midline ( $P = .0681$ ) and the width of the right lateral ventricle ( $P = .0524$ ).

Visual analysis of MR images in FEBSTAT has previously demonstrated that HIMAL is present in an increased percentage of patients with FSE compared with SFS, but overall HIMAL was seen in only a small proportion of both groups.<sup>9</sup> To determine whether the associations between medial temporal lobe morphology and seizure duration were due to the small subset of cases that were visually identified as having abnormal findings, we evaluated the relationship between temporal lobe morphology and seizure duration limited to cases that were visually identified as having normal findings, excluding those with HIMAL or increased T2 signal. Optimal cutoffs for distinguishing FSE versus SFS in these scans with visually normal findings are presented in Table 4. We observed a relationship of multiple bilateral temporal lobe morphologic measurements to FSE in these subjects with visually normal findings (Table 4). In the multivariate model, FSE was associated with a lateral ventricle width of  $>0.169$  cm ( $P = .0078$ ) and a normalized distance of the left hippocampus from the midline of  $>1.51$  ( $P = .0315$ ). FSE was associated with a right lateral ventricle width of  $>0.202$  cm ( $P < .0001$ ), a normalized distance of the right hippocampus from the midline of  $>1.52$  ( $P = .0245$ ), right hippocampal height:width of  $>0.6999$  ( $P = .0494$ ), and a right hippocampal angle of  $>185.5^\circ$  ( $P < .0038$ ).

## DISCUSSION

Hippocampal anomalies similar to HIMAL were initially described in association with agenesis of the corpus callosum and lissencephaly.<sup>6,17</sup> HIMAL was subsequently identified as an isolated anomaly, and an association with epilepsy was suggested,<sup>7</sup> though this association has been questioned.<sup>18</sup> We previously described an increased incidence of HIMAL in children presenting with FSE, suggesting that developmental abnormalities of the temporal lobe are an important risk factor for prolonged febrile seizures.<sup>4,9</sup> However, most subjects in the FEBSTAT study presenting with FSE and most patients with epilepsy more generally do not have HIMAL. The contribution of morphologic variation in the temporal lobe to FSE was therefore unclear in most subjects.

HIMAL consists of a constellation of individual morphologic components, any of which may be present to varying degrees and in varying combinations in an individual patient. We wished to determine whether the component features of HIMAL are indi-

vidually associated with FSE and whether this association extends to subjects without the complete HIMAL constellation. We therefore performed quantitative measurements of temporal lobe morphologic features in the FEBSTAT cohort, focusing on features associated with HIMAL.

We found that multiple morphologic components of HIMAL independently predicted the clinical categorization of febrile seizures (SFS versus FSE) in the FEBSTAT cohort. We considered the possibility that inclusion of patients with HIMAL might confound these findings; therefore, we repeated the analysis after exclusion of patients with HIMAL or any other visible temporal lobe abnormality. The results of this subgroup analysis were essentially identical to those of the full cohort, indicating that the observed associations were not attributable to HIMAL or other visually apparent abnormalities. These findings suggest a model in which subtle bilateral temporal lobe morphologic abnormalities may predispose to FSE, and HIMAL represents a particular subset in which the abnormalities are visually evident. These findings are consistent with those in our prior reports that as a group, hippocampal volumes are slightly smaller in children with FSE and visually normal MRIs than in those with SFS.<sup>10</sup> The current FEBSTAT data therefore suggest that there are subtle underlying abnormalities predisposing to FSE and that FSE is an insult that may result in hippocampal injury.<sup>10</sup>

HIMAL was almost exclusively left-sided in the FEBSTAT cohort, and we therefore expected that correlations between our morphologic measurements and prolonged seizures might be found predominantly on the left. In fact, we found the opposite of the expected lateralization: All 5 right-sided morphologic parameters were significant predictors of FSE in our multivariate model, whereas only 1 left-sided parameter (left temporal horn width) was a significant predictor. Unexpectedly, we have also observed a predominance of right-sided EEG abnormalities and acute hippocampal MR imaging findings in FEBSTAT.<sup>10,19</sup> The subtle hippocampal volume abnormalities seen at baseline and at 1 year in the visually normal MRIs of children with FSE<sup>10</sup> were also much more pronounced on the right. Data from animal models of FSE also suggest a predominance of right-sided abnormalities.<sup>20</sup> These findings may indicate preferential involvement of the right temporal lobe in FSE based on an asymmetric incidence of predisposing anatomic features.

The significance of HIMAL as a risk factor for epilepsy is unclear and somewhat controversial. In part, this uncertainty reflects divergent conclusions of prior investigators regarding the frequency of HIMAL in the general population and patients with epilepsy, possibly reflecting divergent application of the subjective criteria that identify HIMAL.<sup>21,22</sup> We found that the subjective identification of HIMAL by experienced readers can be predicted with high accuracy through quantitative measurement of the individual component features of HIMAL. The predictive value of individual features varies substantially, however. Increased width of the temporal horn of the lateral ventricle is shown to be the strongest predictor of HIMAL (a width of  $>0.53$  cm predicts HIMAL with a sensitivity of 84.2% and a specificity of 86.1%; adjusted odds ratio, 10.6). A decreased distance of the hippocampus from the midline and an increased hippocampal height:width ratio (ie, a rounder hippocampus) are also strong

predictors. These features of temporal lobe anatomy are easily measured on coronal MR images and may provide a basis for improved consistency in the visual identification of HIMAL among interpreters. Angles of the hippocampus and collateral sulcus, in contrast, are not significant predictors of HIMAL in our multivariate model. While these features may be associated with HIMAL, the lack of a predictive value in our model suggests that variance of these features in the healthy population may be sufficiently high to render them less helpful in the identification of HIMAL.

The findings of this study suggest that subtle anatomic differences in temporal lobe morphology, not appreciable on visual inspection, are associated with and may predispose to prolonged febrile seizures. This suggestion is in keeping with a large body of prior evidence correlating subtle anatomic abnormalities found on automated, quantitative brain MR imaging analysis to various types of epilepsy.<sup>23</sup> Application of automated analysis techniques to young children, including the FEBSTAT cohort, is complicated by rapid brain growth and progressive myelination during this period. Nevertheless, we anticipate that application of similar automated or semiautomated techniques may further define the nature and extent of anatomic abnormalities associated with prolonged febrile seizures.

The anatomic differences described in this article could, in theory, reflect either anomalous development of the temporal lobes or secondary degeneration resulting from pathologic processes. We consider an anomaly of primary development the more likely explanation because subjects in the FEBSTAT cohort were previously healthy children who were scanned shortly after their first febrile seizure. Most of the measurements included in this study (eg, distance of the hippocampus from the midline) are unlikely to change significantly in the acute postictal setting. The ratio of hippocampal height to width is an exception because it could, in theory, be affected by hippocampal edema. This is unlikely to be a significant confounding factor, however, because the relationship of an increased hippocampal height:width ratio to FSE was unchanged after exclusion of patients with overt evidence of hippocampal edema (increased T2-weighted signal).

Two limitations of the current study must be recognized. First, our results demonstrate an association between morphologic variation in the medial temporal lobes and the duration of febrile seizures, in particular with FSE. While patients presenting with FSE are at increased risk of later epilepsy, further observation of the FEBSTAT cohort will be required to determine which subjects develop epilepsy and, accordingly, whether the medial temporal lobe anatomic anomalies considered here are risk factors for epilepsy.

A second limitation of the current work is the use of only a single coronal image for our temporal lobe measurements. This was necessary given the time-intensive nature of manual measurements and the large size of the FEBSTAT cohort. Nevertheless, evaluation of the temporal lobe at a single anteroposterior location may result in underestimation of the incidence of anatomic anomalies of limited spatial extent. This limitation could be addressed with automated whole-brain analysis techniques as discussed above.

## CONCLUSIONS

We found that the morphologic component features of HIMAL are independent predictors of FSE, even in the absence of HIMAL or other overt temporal lobe abnormalities. We conclude that a broader spectrum of subtly anomalous temporal lobe development exists that may confer increased risk for prolonged febrile seizures and resulting hippocampal injury. Those cases with HIMAL may represent a subset of this spectrum that is particularly amenable to visual identification. Further studies on other aspects of brain development in these children are planned.

## APPENDIX

### FEBSTAT Study Team

Montefiore and Jacobi Medical Centers, Bronx, New York: Shlomo Shinnar, MD, PhD (Principal Investigator); Jacqueline Bello, MD; William Gomes, MD, PhD; James Hannigan, RT; Sharyn Katz, R-EEGT, FASET; David Masur, PhD; Solomon L. Moshé, MD; Ruth Shinnar, RN, MSN; Erica Weiss, PhD.

Ann & Robert Lurie Children's Hospital, Chicago, Illinois: Douglas Nordli, MD (site Principal Investigator); John Curran, MD; Leon G. Epstein, MD; Andrew Kim, MD; Diana Miazga; Julie Rinaldi, PhD.

Columbia University, New York, New York: Dale Hesdorffer, PhD (site Principal Investigator); Stephen Chan, MD; Binyi Liu, MS; Yokasta Tineo, BA.

Duke University Medical Center, Durham, North Carolina: Darrell Lewis, MD (site Principal Investigator); Melanie Bonner, PhD; Karen Cornett, BS, MT; William Gallentine, DO; James MacFall, PhD; James Provenzale, MD; Allen Song, PhD; James Voyvodic, PhD; Yuan Xu, BS.

Eastern Virginia Medical School, Norfolk, Virginia: L. Matthew Frank, MD (site Principal Investigator); Joanne Andy, RT; Terrie Conklin, RN; Susan Grasso, MD; Connie S. Powers, R-EEGT; David Kushner, MD; Susan Landers, RT; Virginia Van de Water, PhD.

International Epilepsy Consortium/Department of Biostatistics, Virginia Commonwealth University, Richmond, Virginia: Shumei Sun, PhD (site Principal Investigator); John M. Pellock, MD; Brian J. Bush, MSMIT; Lori L Davis, BA; Xiaoyan Deng, MS; Christiane Rogers; Cynthia Shier Sabo, MS.

Mount Sinai Medical Center, New York, New York: Emilia Bagiella, PhD.

Virginia Commonwealth University, Richmond, Virginia: John M. Pellock, MD (site Principal Investigator); Tanya Brazemore, R-EEGT; James Culbert, PhD; Kathryn O'Hara, RN; Syndi Seinfeld, DO; Jean Snow, RT-R.

Additional collaborators: Joan Conry, MD; Children's National Medical Center, Safety Monitor; Tracy Glauser, MD; Cincinnati Children's Medical Center, Genomics; Jeffrey L. Noebels, MD, PhD; Baylor College of Medicine, Genetics.

Disclosures: William A. Gomes—*RELATED: Grant:* National Institute of Neurological Disorders and Stroke (NS43209)\*; *UNRELATED: Grants/Grants Pending:* Gerber Foundation.\* Shlomo Shinnar—*RELATED: Grant:* National Institutes of Health,\* *Comments:* funded by grants NS 43209 from National Institute of Neurological Disorders and Stroke (Principal Investigator: S. Shinnar) and HD 36867 from the National Institute of Child Health and Human Development (Principal Investigator: D.C. Hesdorffer); *UNRELATED: Consultancy:* Acorda Therapeutics, Neurelis, Upsher-Smith Laboratories, Xeris Pharmaceuticals, *Comments:* consulting fees on preclinical

development of drugs for treatment of acute repetitive seizures; not directly related to this work but included as related to treatment of seizures; *Royalties*: royalties on the book *Febrile Seizures* edited by Baram and Shinnar, Academic Press 2002 (<\$100 per annum for the past 5 years). Dale C. Hesdorffer—*RELATED: Grant*: There has been funding from National Institute of Neurological Disorders and Stroke, though I was not part of that grant. The funding no longer exists, even during the time that the data submitted were analyzed; *UNRELATED: Board Membership*: Acorda Therapeutics, Upsher-Smith Laboratories, *Comments*: Both are advisory boards; *Consultancy*: Cyberonics, Mount Sinai Medical Center Rehabilitation; *Grants/Grants Pending*: Centers for Disease Control and Prevention, National Institute of Neurological Disorders and Stroke, The Patient-Centered Outcomes Research Institute, Finding a Cure for Epilepsy and Seizures, Citizens United for Research in Epilepsy, Epilepsy Study Consortium; *Travel/Accommodations/Meeting Expenses Unrelated to Activities Listed*: travel reimbursed from the International League Against Epilepsy, where I serve on several task forces in the Epidemiology Commission and in other areas; *Other: Epilepsia*, Associate Editor. Emilia Bagiella—*RELATED: Grant*: National Institute of Neurological Disorders and Stroke.\* *Comments*: subcontract to Dr Shinnar's grant. Darrell V. Lewis—*RELATED: Grant*: National Institute of Neurological Disorders and Stroke.\* *Comments*: grant support for the FEBSTAT study. Stephen Chan—*RELATED: Grant*: National Institute of Neurological Disorders and Stroke, *Comments*: supported by grant R01 NS-043209 (to S. Shinnar) from the National Institutes of Health. Ruth C. Shinnar—*RELATED: Grant*: National Institute of Neurological Disorders and Stroke (NS43209).\* James MacFall—*RELATED: Grant*: National Institute of Neurological Disorders and Stroke.\*; *Support for Travel to Meetings for the Study or Other Purposes*: National Institute of Neurological Disorders and Stroke.\*; *UNRELATED: Grants/Grants Pending*: National Institute of Neurological Disorders and Stroke.\* John M. Pellock—*RELATED: Grant*: National Institute of Neurological Disorders and Stroke.\*; *UNRELATED: Board Membership*: Acorda Therapeutics, Upsher-Smith Laboratories; *Consultancy*: Acorda Therapeutics, Upsher-Smith Laboratories. Douglas R. Nordli Jr—*RELATED: Grant*: National Institutes of Health.\* *Comments*: I participated as an investigator in this National Institutes of Health-sponsored project for FEBSTAT. Ludwig Frank—*RELATED: Grant*: National Institutes of Health-sponsored grant, "FEBSTAT"; *Support for Travel to Meetings for the Study or Other Purposes*: National Institute of Neurological Disorders and Stroke, *Comments*: study meeting reimbursement. Solomon L. Moshé—*RELATED: Grant*: National Institute of Neurological Disorders and Stroke.\*; *UNRELATED: Grants/Grants Pending*: National Institute of Neurological Disorders and Stroke.\* Citizens United for Research in Epilepsy,\* Department of Defense,\* Rett Syndrome Research Trust,\* *Comments*: funded to carry out various projects in epilepsy; *Payment for Lectures (including service on Speakers Bureaus)*: Eisai, UCB; *Patents (planned, pending or issued)*: animal model of infantile spasms; *Royalties*: Elsevier. Shumei Sun—*RELATED: Grant*: National Institute of Neurological Disorders and Stroke.\*; *UNRELATED: Grants/Grants Pending*: National Institutes of Health.\* \*Money paid to the institution.

## REFERENCES

1. Shinnar S. Febrile seizures and mesial temporal sclerosis. *Epilepsy Curr* 2003;3:115–18 CrossRef Medline
2. Hesdorffer DC, Shinnar S, Lewis DV, et al; FEBSTAT Study Team. Design and phenomenology of the FEBSTAT study. *Epilepsia* 2012; 53:1471–80 CrossRef Medline
3. Hesdorffer DC, Shinnar S, Lewis DV, et al; Consequences of Prolonged Febrile Seizures in Childhood (FEBSTAT) Study Team. Risk factors for febrile status epilepticus: a case-control study. *J Pediatr* 2013;163:1147–51.e1 CrossRef Medline
4. Chan S, Bello JA, Shinnar S, et al; FEBSTAT Study Team. Hippocampal malrotation is associated with prolonged febrile seizures: results of the FEBSTAT study. *AJR Am J Roentgenol* 2015;205:1068–74 CrossRef Medline

5. Humphrey T. The development of the human hippocampal fissure. *J Anat* 1967;101:655–76 Medline
6. Kier EL, Kim JH, Fulbright RK, et al. Embryology of the human fetal hippocampus: MR imaging, anatomy, and histology. *AJNR Am J Neuroradiol* 1997;18:525–32 Medline
7. Barsi P, Kenéz J, Solymosi D, et al. Hippocampal malrotation with normal corpus callosum: a new entity? *Neuroradiology* 2000;42: 339–45 CrossRef Medline
8. Lehericy S, Dormont D, Sémah F, et al. Developmental abnormalities of the medial temporal lobe in patients with temporal lobe epilepsy. *AJNR Am J Neuroradiol* 1995;16:617–26 Medline
9. Shinnar S, Bello JA, Chan S, et al; FEBSTAT Study Team. MRI abnormalities following febrile status epilepticus in children: the FEBSTAT study. *Neurology* 2012;79:871–77 CrossRef Medline
10. Lewis DV, Shinnar S, Hesdorffer DC, et al; FEBSTAT Study Team. Hippocampal sclerosis after febrile status epilepticus: the FEBSTAT study. *Ann Neurol* 2014;75:178–85 CrossRef Medline
11. Maytal J, Shinnar S. Febrile status epilepticus. *Pediatrics* 1990;86: 611–16 Medline
12. Lewis DV, Barboriak DP, MacFall JR, et al. Do prolonged febrile seizures produce medial temporal sclerosis? Hypotheses, MRI evidence and unanswered questions. *Prog Brain Res* 2002;135:263–78 CrossRef Medline
13. VanLandingham KE, Heinz ER, Cavazos JE, et al. Magnetic resonance imaging evidence of hippocampal injury after prolonged focal febrile convulsions. *Ann Neurol* 1998;43:413–26 CrossRef Medline
14. Hesdorffer DC, Chan S, Tian H, et al. Are MRI-detected brain abnormalities associated with febrile seizure type? *Epilepsia* 2008;49: 765–71 CrossRef Medline
15. National Institutes of Health. *Febrile Seizures: Consensus Development Conference Summary*. Vol 3. Bethesda: National Institutes of Health; 1980:1–11
16. Youden WJ. Index for rating diagnostic tests. *Cancer* 1950;3:32–35 Medline
17. Baker LL, Barkovich AJ. The large temporal horn: MR analysis in developmental brain anomalies versus hydrocephalus. *AJNR Am J Neuroradiol* 1992;13:115–22 Medline
18. Raininko R, Bajic D. "Hippocampal malrotation": no real malrotation and not rare. *AJNR Am J Neuroradiol* 2010;31:E39; author reply E40 CrossRef Medline
19. Nordli DR Jr, Moshé SL, Shinnar S, et al; FEBSTAT Study Team. Acute EEG findings in children with febrile status epilepticus: results of the FEBSTAT study. *Neurology* 2012;79:2180–86 CrossRef Medline
20. Dubé CM, Zhou JL, Hamamura M, et al. Cognitive dysfunction after experimental febrile seizures. *Exp Neurol* 2009;215:167–77 CrossRef Medline
21. Gamss RP, Slasky SE, Bello JA, et al. Prevalence of hippocampal malrotation in a population without seizures. *AJNR Am J Neuroradiol* 2009;30:1571–73 CrossRef Medline
22. Bajic D, Canto Moreira N, Wikström J, et al. Asymmetric development of the hippocampal region is common: a fetal MR imaging study. *AJNR Am J Neuroradiol* 2012;33:513–18 CrossRef Medline
23. Memarian N, Thompson PM, Engel J Jr, et al. Quantitative analysis of structural neuroimaging of mesial temporal lobe epilepsy. *Imaging Med* 2013;5 CrossRef Medline

# Early Antiretroviral Therapy in HIV-Infected Children Is Associated with Diffuse White Matter Structural Abnormality and Corpus Callosum Sparing

C. Ackermann, S. Andronikou, M.G. Saleh, B. Loughton, A.A. Alhamud, A. van der Kouwe, M. Kidd, M.F. Cotton, and E.M. Meintjes



## ABSTRACT

**BACKGROUND AND PURPOSE:** Fractional anisotropy in the frontal white matter, corpus callosum, and internal capsule is abnormal in human immunodeficiency virus–positive (HIV+) adults. We describe the distribution and nature of white matter abnormalities in a cohort of children who started antiretroviral therapy within the first year of life and the benefit of early treatment by using DTI measures (fractional anisotropy and mean, axial, and radial diffusion).

**MATERIALS AND METHODS:** DTI was performed on children in a neurodevelopmental substudy from the Children with HIV Early Antiretroviral trial. Voxel-based group comparisons were obtained to determine regions where fractional anisotropy and mean diffusion differed between HIV+ and uninfected children. Associations of DTI parameters with the timing of antiretroviral therapy initiation were examined.

**RESULTS:** Thirty-nine HIV+ children (15 boys; mean age, 5.4 years) and 13 controls (5 boys; mean age, 5.7 years) were scanned. Two clusters with lower fractional anisotropy and 7 clusters with increased mean diffusion were identified in the HIV+ group, with symmetric distribution predominantly due to increased radial diffusion, suggestive of decreased myelination. Corticospinal tracts rather than the corpus callosum were predominantly involved. Children on early-interrupted antiretroviral therapy had lower fractional anisotropy compared with those receiving continuous treatment.

**CONCLUSIONS:** HIV+ children at 5 years of age have white matter abnormalities measured by fractional anisotropy, despite early antiretroviral therapy, suggesting that early antiretroviral therapy does not fully protect the white matter from either peripartum or in utero infection. In contrast to adults, the corticospinal tracts are predominantly involved rather than the corpus callosum, possibly due to early antiretroviral therapy. Continuous early antiretroviral therapy can limit white matter damage.

**ABBREVIATIONS:** AD = axial diffusivity; ART = antiretroviral therapy; CC = corpus callosum; CHER = Children with HIV Early Antiretroviral trial; CST = corticospinal tract; FA = fractional anisotropy; HIV = human immunodeficiency virus; HIV+ = human immunodeficiency virus–positive; MD = mean diffusivity; RD = radial diffusivity

White matter structural abnormalities can be assessed by using quantitative parameters determined from DTI.<sup>1</sup> Fractional anisotropy (FA) provides information about the microstructural integrity of highly oriented microstructures but is not specific to

the type of injury. Mean diffusivity (MD) is a measure of average molecular motion independent of any tissue directionality.

Loss of axonal integrity decreases FA and increases MD; however, increased FA may also indicate loss of complexity in the underlying axonal matrix due to loss of crossing and other non-parallel fibers. Increased radial diffusivity (RD), a marker of excessive axonal packing attenuation and/or poor myelination,<sup>2</sup> and

Received April 5, 2016; accepted after revision July 4.

From the Departments of Radiodiagnosis (C.A.) and Paediatrics and Child Health (B.L., M.F.C.), Faculty of Medicine and Health Sciences, and Centre for Statistical Consultation (M.K.), Stellenbosch University, Tygerberg, South Africa; Clinical Research and Imaging Centre, Bristol (S.A.), University of Bristol, Bristol, UK; Department of Paediatric Radiology (S.A.), Bristol Royal Hospital for Children, Bristol, UK; Department of Human Biology (M.G.S., A.A.A., E.M.M.), Medical Research Council/University of Cape Town Medical Imaging Research Unit, University of Cape Town, Cape Town, South Africa; and Athinoula A. Martinos Center for Biomedical Imaging (A.v.d.K.), Massachusetts General Hospital, Charlestown, Massachusetts.

This work was supported by grants from the Harry Crossley Foundation, the South African Medical Research Council, the National Research Foundation grant CPR20110614000019421, the South African National Research Foundation/Department of Science and Technology South African Research Chairs Initiative, the National Institute of Allergy and Infectious Diseases through the Comprehensive

International Program of Research on AIDS network, grant U19 AI53217, and the National Institutes of Health R01 HD071664 and R21MH096559.

The content is solely the responsibility of the authors and does not necessarily represent the official views of the National Institutes of Health.

Paper previously presented as a digital poster and preliminary findings at: European Society of Pediatric Radiology Annual Congress, June 2–6, 2014; Amsterdam, the Netherlands.

Please address correspondence to Christelle Ackermann, MD, Kanonnier Crescent 27, Kanonberg, Bellville, 7530, Cape Town, South Africa; e-mail: ca@sun.ac.za

Indicates open access to non-subscribers at [www.ajnr.org](http://www.ajnr.org)

<http://dx.doi.org/10.3174/ajnr.A4921>

decreased axial diffusivity (AD), an index of axonal damage, occur in human immunodeficiency virus (HIV)-associated WM injury.<sup>3-5</sup> FA in the frontal subcortical WM, corpus callosum (CC), and internal capsule is abnormal in HIV-positive (HIV+) adults.<sup>6-8</sup> Those with the most advanced HIV disease have the highest diffusion constant elevations and the largest anisotropy reductions, specifically in the CC and frontal WM.<sup>6</sup> Most early studies used a priori ROI analyses. Subsequently, more widespread WM damage has been shown by using voxelwise and whole-brain analyses.<sup>1,3,7,9,10</sup> Animal neuro-AIDS models also show WM damage: Macaques show reduced FA in the CC genu,<sup>11</sup> and mice have reduced FA (mainly due to increased RD) and increased MD in the CC.<sup>12</sup>

Few studies have used DTI to examine HIV-associated alterations in WM in children. Lower FA and higher MD and RD in the CC and higher MD in the superior longitudinal fasciculus have been demonstrated in antiretroviral therapy (ART)-naïve children (8–12 years of age) compared with age-matched controls,<sup>13</sup> while ART failure was associated with decreased FA in the left superior and right posterior corona radiata and decreased AD in the left inferior cerebellar peduncle in 50 children on first-line ART (6–15 years of age).<sup>14</sup> Regional and whole-brain decreases in FA and increased MD and RD, compared with controls, have been reported in HIV+ children and adolescents (6–20 years of age),<sup>15,16</sup> irrespective of treatment status.<sup>15</sup> Regional alterations were related to past disease severity, measured by nadir CD4%, and peak viral loads.<sup>16</sup> ART-naïve children (6–11 years of age) showed reduced myelin compared with children on ART (6–16 years of age) but were also younger.<sup>15</sup> These studies did not document ART history.

Adolescents stable on ART ( $n = 15$ , 13–17 years of age; mean age at ART initiation, 9.5 years) had lower FA in the CC, superior and posterior corona radiata, frontal and parietal WM, pre- and postcentral gyrus, and superior longitudinal fasciculus (mainly due to increased RD) than controls ( $n = 26$ ).<sup>17</sup>

Despite consistent evidence of HIV-related WM alterations, studies have included wide age ranges over developmental phases when both WM volume and FA demonstrates notable increase.<sup>18-20</sup> Few studies have controlled adequately for age or ART regimens. To date, no DTI studies have been performed in younger children, and none, in children receiving standardized early ART (within the first year of life), to our knowledge.

The aim of the present study was to determine the spatial distribution and nature of WM abnormalities at 5 years of age in a cohort of HIV+ children beginning ART well within the first year of life. An additional aim was to explore the association of the timing of ART initiation and DTI-derived parameters (FA, AD, RD), to interrogate the potential protection of early ART on WM microstructures.

We hypothesized poorer WM integrity when starting ART after 12 weeks of age.

## MATERIALS AND METHODS

### Subjects

We present data for 52 of 62 children enrolled in a neurodevelopmental substudy of the Children with HIV Early Antiretroviral (CHER) trial<sup>21,22</sup> in Cape Town, South Africa. The group com-

prised HIV+ children on ART and age-matched controls from a parallel vaccine study, with informed consent from parents or caregivers.<sup>23</sup>

Exclusions were the following: 6 HIV+ subjects with mixed ancestry (the genetic determinants of ethnicity could influence brain growth and maturity and we felt that having a more homogeneous study population and control group would remove bias), 1 HIV+ child whose structural image was motion-corrupted, 1 control child with incidental periventricular leukoencephalopathy, and 2 HIV+ children with data intersection instabilities.

The CHER trial was a 2-center study in which HIV+ infants between 6 and 12 weeks of age and CD4  $\geq 25\%$  were randomized to 1 of 3 treatment strategies: ART-deferred until indicated, early-limited ART for 40 weeks, and early-limited ART for 96 weeks. Infants with a CD4%  $< 25\%$  were enrolled into a separate group (Part B), initially to be randomized into ART for 40 weeks and ART for 96 weeks but then retained on early-continuous ART. The entire cohort comprised 451 HIV-infected infants younger than 12 weeks of age. Four hundred eleven infants had baseline CD4  $\geq 25\%$ , of whom 377 were reported in the main trial.<sup>22</sup>

Continuous ART was initiated in the ART-Deferred arm when the CD4 declined below 25% in the first year of life and 20% thereafter or for the Centers for Disease Control severe stage B or C disease. These criteria also applied to restarting ART in the ART for 40 weeks and ART for 96 weeks arms. Because some children in ART-Deferred began ART early, we stratified children into those starting ART after (late ART) or before 12 weeks (early ART), irrespective of the treatment arm. In addition, because some in the ART for 40 weeks and ART for 96 weeks arms met the end points during primary therapy, the early ART group was subdivided into those with or without treatment interruption.

First-line ART was lopinavir-ritonavir, lamivudine, and zidovudine. Most mothers had participated in the prevention of mother-to-child transmission program, which included zidovudine antenatally from 32 weeks and single-dose nevirapine at delivery. Mothers with a CD4 count below 250 cells per cubic millimeter received ART antenatally. Neonates received a single dose of nevirapine at birth and zidovudine for 7 days.

Children were in regular follow-up with 3 monthly clinical assessments.

Baseline laboratory and clinical data at enrollment and within 6 months of MR imaging scan, including CD4, CD8 parameters, and viral load, were obtained from participant medical records and the CHER data base. A viral load of  $>750,000$  copies/mL was assigned as 750,001, and that with  $<400$  copies/mL, as 399 (viral suppression).

Ethics approval for the study was obtained from ethics boards of all institutions involved.

### MR Imaging Data Acquisition

The children were imaged on a 3T MR imaging scanner by using structural T1 imaging followed by 2 DTI acquisitions with opposite phase-encoding directions by using a twice-refocused spin-echo sequence.<sup>24</sup> The 3D EPI-navigated<sup>25</sup> multiecho MPRAGE<sup>26</sup> sequence was acquired in a sagittal orientation with the following parameters: FOV = 224  $\times$  224 mm, 144 sections, TR = 2530 ms, TE = 1.53/3.19/4.86/6.53 ms, TI = 1160 ms, flip

**Table 1: Sample characteristics of HIV-infected children<sup>a</sup>**

	Late ART (>12 wk)	Early ART (<12 wk) Interrupted	Early ART (<12 wk) Not Interrupted	P Value
No.	13	16	10	
Sex	4 M/9 F	5 M/11 F	6 M/4 F	.30
Age at scan (yr)	5.3 (0.30)	5.4 (0.24)	5.6 (0.43)	.20
Age ART started (wk)	36 (17)	8 (2)	8 (2)	<.01 <sup>b</sup>
Time on ART (wk)	241 (22)	203 (59)	285 (22)	<.01 <sup>b</sup>
Time interrupted (wk) <sup>c</sup>	NA	85 (90)	NA	
Clinical measures at baseline				
CD4 count	2064 (711)	1969 (1118)	1720 (978)	.57
CD4%	37 (7)	35 (10)	30 (13)	.21
CD8 count	1751 (1109)	1460 (675)	1978 (945)	.34
VL > 750,000 (%) (No.)	69 (9)	56 (9)	40 (4)	.37
400 < VL < 750,000 (%) (No.)	31 (4)	44 (7)	60 (6)	
Clinical measures within 6 mo of scan				
CD4 count	1027 (392)	1110 (460)	1289 (592)	.58
CD4%	37 (8)	34 (7)	36 (10)	.49
CD8 count	902 (450)	1083 (544)	1087 (625)	.57
VL > 750,000 (%) (No.)	8 (1)	0	0	.14
400 < VL < 750,000 (%) (No.)	23 (3)	6 (1)	0	
Suppressed VL (%) (No.)	69 (9)	94 (15)	100 (10)	

**Note:**—NA indicates not applicable; VL, viral load.

<sup>a</sup> Values are mean (SD).

<sup>b</sup> Significant.

<sup>c</sup> Calculated up to the time of scanning in 3 children who had not restarted ART.

angle = 7°, voxel size = 1.3 × 1.0 × 1.0 mm<sup>3</sup>. DWI was performed in 30 directions with  $b=1000$  s/mm<sup>2</sup>, voxel size = 2 × 2 × 2 mm<sup>3</sup>, TR/TE = 9500/86 ms, and 4 volumes with  $b = 0$  s/mm<sup>2</sup>.

## Data Analysis

**Preprocessing.** Diffusion-weighted volumes with signal dropout or motion-corrupted sections were removed,<sup>27</sup> and the diffusion-encoding scheme was adjusted, with a constraint that the same volumes be removed in both DTI acquisitions. Coregistration and susceptibility correction were performed.<sup>28,29</sup> Briefly, coregistration of individual volumes to the first unweighted image was performed by using linear affine (12 *df*) transformation (FMRIB Linear Image Registration Tool, FLIRT; <http://www.fmrib.ox.ac.uk/>) in FSL (<http://www.fmrib.ox.ac.uk/fsl>). Subsequently, these images were imported to Matlab (MathWorks, Natick, Massachusetts) for susceptibility correction and outlier rejection.<sup>29</sup> Outliers of each acquisition were examined by first calculating *z* scores on the basis of 25 and 75 percentile limits; data points above 3 SDs beyond the mean were discarded. The 2 acquisitions were combined into a single corrected image; FA, MD, and eigenvalue ( $e_1$ ,  $e_2$ , and  $e_3$ ) images were generated. The first eigenvalue ( $e_1$ ) was AD; the remaining 2 were used to compute RD ( $e_{23} = [e_2 + e_3] / 2$ ).

**Coregistration.** The FA images were first coregistered to corresponding structural images to achieve intrasubject alignment. Structural images of all subjects were then coregistered to a “most representative” control image; then they were subsequently coregistered to the National Institutes of Health pediatric MRI Data Repository T1-template image for children 4.5–8.5 years of age, with an isotropic resolution of 1.0 × 1.0 × 1.0 mm<sup>3</sup> by using linear (FLIRT) and nonlinear (FMRIB Nonlinear Registration Tool, FNIRT; <http://fsl.fmrib.ox.ac.uk/fsl/fslwiki/FNIRT>) coregistration algorithms in FSL.<sup>30</sup> FA images were warped by using the

same transforms for intersubject alignment. The same transforms were applied to MD, AD, and RD images. A WM binary mask was generated for each subject by applying an FA threshold of 0.2. Individual masks were multiplied to generate a final binary image representing WM regions with FA ≥ 0.2 in all subjects. The binary image was multiplied by the coregistered FA and MD images of each subject to localize statistical analyses, explained below, to the same WM regions.

**Statistical Analysis.** Voxel-based group comparisons were performed in FSL to determine regions where FA and MD differed significantly between HIV+ and control children and between HIV+ children starting ART late or early and those with and without interruption. To account for multiple comparisons when determining significant clusters, we used the AlphaSim command

([http://afni.nimh.nih.gov/pub/dist/doc/program\\_help/AlphaSim.html](http://afni.nimh.nih.gov/pub/dist/doc/program_help/AlphaSim.html)) in Analysis of Functional Neuro Images (AFNI; <http://afni.nimh.nih.gov/afni>) with an overall significance level of  $\alpha = .05$  and an individual voxelwise significance level of  $P = .01$ . Full width at half maximum values ranged between 3.8 and 5.2 mm across the masked thresholded WM masks, and we performed 5000 Monte Carlo simulations.<sup>31</sup> Clusters of at least 258 mm<sup>3</sup> were significant at these levels.

Locations of clusters showing group differences were identified by using the Harvard-Oxford cortical and subcortical and Johns Hopkins University WM tractography atlases provided in FSL and an MR imaging atlas of human WM anatomy.<sup>32,33</sup> For each cluster, average FA and MD and corresponding AD and RD values were extracted.

Categoric variables were summarized by using frequency and percentage of frequency distributions overall and by group. Continuous measurements were summarized by using means and SDs. Variables were compared between the groups by using ANOVA and  $\chi^2$  tests.

## RESULTS

After exclusions, we present data for 13 healthy controls (mean age, 5.7 ± 0.5 years; 5 boys) and 39 HIV+ children (mean age, 5.4 ± 0.3 years; 15 boys). Demographic and clinical data of HIV+ children are presented in Table 1.

Ten children receiving early ART fulfilled the criteria for continuous ART. ART in 16 children was interrupted after primary therapy, and 3 had not restarted ART by the time of MR imaging. Parents of 1 child randomized to ART at 96 weeks initially withheld ART without knowledge of the investigators. This child was included in the late-treatment group.

Four children started ART under Part B; treatments of 2 were interrupted, and 2 were on continuous ART.

**Table 2: Clusters in which FA was lower in HIV+ children compared with controls<sup>a</sup>**

Cluster Location/CST	Size (mm <sup>3</sup> )	Coordinates	AD			RD		
			HIV+	Control	P Value	HIV+	Control	P Value
Right internal capsule	365	27, -23, -1	1.18 (0.03)	1.20 (0.03)	.10	0.60 (0.10)	0.56 (0.02)	<.001
Right parietal lobe	294	19, -24, 42	1.18 (0.06)	1.22 (0.07)	.08	0.60 (0.04)	0.56 (0.03)	<.001

<sup>a</sup> Values are mean (SD).

**Table 3: Clusters in which HIV+ children had significantly greater MD compared with controls<sup>a</sup>**

Cluster Location	Size (mm <sup>3</sup> )	Coordinates	AD			RD		
			Control	HIV+	P Value	Control	HIV+	P Value
ILF/SLF								
Right temporal	7503	32, 0, -24	1.19 (0.03)	1.23 (0.03)	.001	0.62 (0.02)	0.65 (0.03)	<.001
Left putamen	6916	-29, -26, -2	1.20 (0.03)	1.25 (0.03)	.001	0.59 (0.02)	0.62 (0.03)	<.001
CST								
Right brain stem	916	21, -15, -9	1.25 (0.04)	1.29 (0.03)	.01	0.58 (0.02)	0.63 (0.02)	<.001
IFOF								
Left temporal	555	-37, -10, -17	1.19 (0.05)	1.25 (0.04)	.003	0.66 (0.02)	0.70 (0.04)	<.001
Forceps minor								
Left frontal	336	-19, 43, 14	1.20 (0.06)	1.24 (0.06)	.04	0.63 (0.03)	0.67 (0.05)	.0030
Left frontal	266	-17, 42, -1	1.22 (0.06)	1.26 (0.06)	.05	0.62 (0.03)	0.65 (0.05)	.0040
UF								
Right frontal	330	15, 38, -12	1.19 (0.05)	1.25 (0.06)	.003	0.64 (0.03)	0.67 (0.04)	.0046

**Note:**—ILF/SLF indicates inferior/superior longitudinal fasciculus; IFOF, inferior fronto-occipital fasciculus; UF, uncinate fasciculus.

<sup>a</sup> Values are mean (SD).

The cumulative period on ART was longest for those receiving early-continuous ART.

Eighty-seven percent ( $n = 34$ ) had viral load suppression (<400 copies/mL). Of the 13% ( $n = 5$ ) unsuppressed at MR imaging, 4 were in the late-ART group (with viral load of 3590, 5980, 8870, and >750,000 HIV RNA copies/mL) and 1 was in the early ART-interrupted group (204,000 HIV RNA copies/mL).

### Imaging

On the T1-weighted MR images, structural abnormalities were identified in 3 HIV+ children (mild cerebellar atrophy, mild generalized atrophy, pineal multilobed cyst), and none in controls.

Two clusters were identified in the right corticospinal tract (CST), where FA was lower in HIV+ children than in controls (mean FA,  $0.42 \pm 0.03$  versus  $0.46 \pm 0.03$ ; and  $0.43 \pm 0.04$  versus  $0.49 \pm 0.04$ ). Differences in FA were attributable to increased RD ( $P < .001$ , Table 2). Left-sided similar clusters were seen, however, not surviving cluster-size correction. The FA and RD values in these clusters for the child with viral load > 750,000 HIV RNA copies/mL at scan were below the group average (excluding this child) but not the lowest overall. FA values did not differ significantly between the other 4 unsuppressed children and the remaining group.

Seven clusters showed higher MD at  $P < .01$  in infected children than in controls, the largest being 7503 mm<sup>3</sup>, which included several tracts. Both AD and RD contributed to the increased MD (Table 3).

### Comparison of FA between Children Starting ART before and after 12 Weeks of Age

Against our hypothesis, children starting ART later did not demonstrate poorer white matter integrity as measured by FA. Rather, 1 cluster was identified in the brain stem in the left CST, where FA was lower in early compared with late ART initiation. When comparing early-continuous and early-interrupted ART individually

against late ART, we found lower FA only in the early-interrupted ART group, suggesting that interruption is harmful to WM. No regions showed FA differences between early-continuous and late ART. The reduced FA in the children on early-interrupted ART was attributable to increased RD and AD.

### DISCUSSION

We demonstrated WM areas with significantly reduced FA in HIV+ children initiating ART at a median age of 4 months compared with uninfected controls.

### No Frontal or Parietal White Matter Predilection for Abnormal Findings

Our findings confirm the presence of FA abnormalities found in HIV+ adults and adolescents but differ in volume and distribution. Young children on early ART had very few regions with abnormal FA. The predilection for frontal lobe involvement described in adults<sup>34-38</sup> was not seen possibly due to the small sample size, specifically the control group ( $n = 13$ ). We previously reported multifocal WM signal abnormalities on standard T2-weighted MR imaging sequences in frontal (91%) and parietal WM (82%) of HIV+ children at a mean age 31.9 months.<sup>39</sup> Twenty of these children are also included in the present study. Ten had WM signal abnormality on FLAIR.<sup>39</sup> Unfortunately, a limitation in the present study was the absence of FLAIR, thus an inability to assess interval WM signal change. However, the absence of frontal and parietal involvement in FA does suggest interval improvement on ART.

Although clusters showing left-sided FA differences did not survive cluster-size correction, FA reductions were bilateral in the CST. The MD differences were more widely distributed and included the inferior longitudinal fasciculus (bilateral), CST, inferior fronto-occipital fasciculus, forceps minor, and uncinate fasciculus.

Because frontal WM myelination continues into adulthood, children demonstrate inherently lower frontal FA values than adults.<sup>40</sup> To exclude frontal predominance of WM abnormality being maturational,<sup>41</sup> we determined areas of significant FA difference between HIV+ children and age-matched controls by using voxelwise group comparisons. The predominant contribution to decreased FA was RD, while the increased MD was due to both RD and AD, indicating both reduced myelin and loss of axonal integrity.<sup>42</sup>

The age difference between the HIV+ and control groups was only a few months, not considered clinically significant. Our study has a much narrower age range than previous studies, facilitating improved comparison with controls representing the age-related normally developing brain.

### **Children's Ages and ART Relevance**

The higher FA values in those beginning ART after 12 weeks was surprising because we expected this finding in those beginning ART before 12 weeks. However, the difference was attributable to ART interruption, possibly negating the benefits of early ART, rather than neurotoxicity due to longer ART exposure.<sup>43–45</sup>

The timing of the interruption may be important with reference to WM maturation. Three phases of maturation are observed by FA: rapid change in the first 3–6 months, slower change until 24 months, and relative stability thereafter. Most WM tracts are formed at birth; then they increase in size together with FA during 24 months.<sup>46</sup> Deep WM structures such as the CC and internal capsule have high FA at birth, which rapidly rises. In contrast, frontal WM has low FA, increasing to intermediate values around 24 months. In neonates, the CST is present within the brain stem, but the size and intensity are much lower than in the older brain.<sup>47</sup> Postmortem studies, however, have shown that the CST and the superior cerebellar peduncles mature early.<sup>48,49</sup> ART was interrupted at 40 weeks (around 10 months of age); this interruption may have coincided with a critical stage of CST maturation.

Notably, we found no CC involvement in HIV+ children. HIV-associated FA abnormalities in the CC have been reported in adults and in children.<sup>6,7,8,13</sup> In contrast, our children started ART early compared with those in other studies. Most interesting, CC volume and thickness were similar to those in controls in a study by Andronikou et al,<sup>50</sup> which included the 20 HIV+ children previously reported. The CC genu demonstrates a variable growth spurt at 2 months of age, followed by similar growth in the splenium by 4–6 months, with myelination being visible on T1-weighted MR imaging from 4–6 months.<sup>51</sup> Our data support early ART being neuroprotective for the CC.

That no FA differences were noted between the late and early-continuous groups may have been a “survivor effect.” Eight children in the ART-Deferred arm died in the first year of life and were not studied. In addition, those on early-continuous rather than early-limited ART were more severely affected by HIV, having already reached a trial end point during primary ART, thus being ineligible for interruption. All participants on continuous therapy had suppressed viral loads at the time of scanning. Notably, those from Part B had a baseline CD4 below 25% and therefore had more advanced HIV. Nevertheless, the early-interrupted

children had the most WM damage, suggesting that WM is more vulnerable at the time that ART interruption occurred.

Our data strongly suggest that WM damage, though not prevented by early ART, can be ameliorated or reversed, possibly through reduced neuroinflammation.<sup>52</sup> The children in this study are enrolled in a longitudinal neuroimaging study that includes DTI at age 7 and 9 years, which will provide vital information on the continuous effect of ART and/or HIV as well as answer questions relating to the influence of white matter maturation.

### **CONCLUSIONS**

HIV+ children at 5 years of age have WM fiber abnormalities measured by FA despite early ART, suggesting that early ART does not fully protect the WM from either peripartum or in utero infection. In contrast to adults, the CSTs of children are predominantly involved rather than the CC, possibly due to early ART. Continuous ART can limit WM damage.

### **ACKNOWLEDGMENTS**

We thank GlaxoSmithKline/ViiVplc Healthcare and the Departments of Health of the Western Cape and Gauteng for supporting the CHER trial.

Disclosures: Barbara Laughton—RELATED: Grant: National Institutes Of Health,\* Comments: R01 HD071664–01: Longitudinal Neuroimaging and Cognitive Study of HIV-Infected Children. I am a co-Principal Investigator on this study. The grant was awarded to Massachusetts General Hospital, and Stellenbosch University has a sub-contract. Andre van der Kouwe—RELATED: Grant: National Institutes of Health,\* Comments: National Institutes of Health National Institute of Child Health and Human Development R01 HD071664; this grant supports the published work in part; Support for Travel to Meetings for the Study or Other Purposes: National Institutes of Health,\* Comments: National Institutes of Health National Institute of Child Health and Human Development R01 HD071664; this grant supports travel to achieve the aims of the grant, which, in part, supports the published work; UNRELATED: Grants/Grants Pending: National Institutes of Health,\* Bertarelli Foundation,\* Travel/Accommodations/Meeting Expenses Unrelated to Activities Listed: National Institutes of Health,\* Bertarelli Foundation.\* Mark F. Cotton—RELATED: Grant: National Institutes of Health,\* Comments: grant U19 AI53217 for the CHER trial; Provision of Materials: ViiVplc Healthcare, Comments: supply of zidovudine and lamivudine. Ernesta M. Meintjes—RELATED: Grant: National Institutes of Health,\* National Research Foundation of South Africa.\* \*Money paid to the institution.

### **REFERENCES**

1. Stebbins GT, Smith CA, Bartt RE, et al. **HIV-associated alterations in normal-appearing white matter: a voxel-wise diffusion tensor imaging study.** *J Acquir Immune Defic Syndr* 2007;46:564–73 CrossRef Medline
2. Beaulieu C. **The basis of anisotropic water diffusion in the nervous system: a technical review.** *NMR Biomed* 2002;15:435–55 CrossRef Medline
3. Leite SC, Corrêa DG, Doring TM, et al. **Diffusion tensor MRI evaluation of the corona radiata, cingulate gyri, and corpus callosum in HIV patients.** *J Magn Reson Imaging* 2013;38:1488–93 CrossRef Medline
4. Hoare J, Ransford GL, Phillips N, et al. **Systematic review of neuroimaging studies in vertically transmitted HIV positive children and adolescents.** *Metab Brain Dis* 2014;29:221–29 CrossRef Medline
5. Alexander AL, Lee JE, Lazar M, et al. **Diffusion tensor imaging of the brain.** *Neurotherapeutics* 2007;4:316–29 CrossRef Medline
6. Filippi CG, Ulug AM, Ryan E, et al. **Diffusion tensor imaging of patients with HIV and normal-appearing white matter on MR images of the brain.** *AJNR Am J Neuroradiol* 2001;22:277–83 Medline
7. Gongvatana A, Schweinsburg BC, Taylor MJ, et al. **White matter tract injury and cognitive impairment in human immunodeficiency**

- ciency virus-infected individuals. *J Neurovirol* 2009;15:187–95 CrossRef Medline
8. Pomara N, Crandall DT, Choi SJ, et al. **White matter abnormalities in HIV-1 infection: a diffusion tensor imaging study.** *Psychiatry Res* 2001;106:15–24 CrossRef Medline
  9. Stubbe-Drger B, Deppe M, Mohammadi S, et al; German Competence Network HIV/AIDS. **Early microstructural white matter changes in patients with HIV: a diffusion tensor imaging study.** *BMC Neurol* 2012;12:23 CrossRef Medline
  10. Gongvatana A, Cohen RA, Correia S, et al. **Clinical contributors to cerebral white matter integrity in HIV-infected individuals.** *J Neurovirol* 2011;17:477–86 CrossRef Medline
  11. Li C, Zhang X, Komery A, et al. **Longitudinal diffusion tensor imaging and perfusion MRI investigation in a macaque model of neuro-AIDS: a preliminary study.** *Neuroimage* 2011;58:286–92 CrossRef Medline
  12. Lentz MR, Peterson KL, Ibrahim WG, et al. **Diffusion tensor and volumetric magnetic resonance measures as biomarkers of brain damage in a small animal model of HIV.** *PLoS One* 2014;9:e105752 CrossRef Medline
  13. Hoare J, Fouché JP, Spottiswoode B, et al. **A diffusion tensor imaging and neurocognitive study of HIV-positive children who are HAART-naïve “slow progressors.”** *J Neurovirol* 2012;18:205–12 CrossRef Medline
  14. Hoare J, Fouché JP, Phillips N, et al. **Clinical associations of white matter damage in cART-treated HIV-positive children in South Africa.** *J Neurovirol* 2015;21:120–28 CrossRef Medline
  15. Hoare J, Fouché JP, Phillips N, et al. **White matter micro-structural changes in ART-naïve and ART-treated children and adolescents infected with HIV in South Africa.** *AIDS* 2015;29:1793–801 CrossRef Medline
  16. Uban KA, Herting MM, Williams PL, et al; Pediatric HIV/AIDS Cohort and the Pediatric Imaging, Neurocognition, and Genetics Studies. **White matter microstructure among youth with perinatally acquired HIV is associated with disease severity.** *AIDS* 2015;29:1035–44 CrossRef Medline
  17. Li J, Wu Z, Wen Z, et al. **White matter development is potentially influenced in adolescents with vertically transmitted HIV infections: a tract-based spatial statistics study.** *AJNR Am J Neuroradiol* 2015;36:2163–69 CrossRef Medline
  18. Barnea-Goraly N, Menon V, Eckert M, et al. **White matter development during childhood and adolescence: a cross-sectional diffusion tensor imaging study.** *Cereb Cortex* 2005;15:1848–54 CrossRef Medline
  19. Giedd JN, Blumenthal J, Jeffries NO, et al. **Brain development during childhood and adolescence: a longitudinal MRI study.** *Nat Neurosci* 1999;2:861–63 CrossRef Medline
  20. Brouwer RM, Mandl RCW, Schnack HG, et al. **White matter development in early puberty: a longitudinal volumetric and diffusion tensor imaging twin study.** *PLoS One* 2012;7:e32316 CrossRef Medline
  21. Violarì A, Cotton MF, Gibb DM, et al; CHER Study Team. **Early antiretroviral therapy and mortality among HIV-infected infants.** *N Engl J Med* 2008;359:2233–44 CrossRef Medline
  22. Cotton MF, Violarì A, Otway K, et al; CHER Study Team. **Early time-limited antiretroviral therapy versus deferred therapy in South African infants infected with HIV: results from the children with HIV early antiretroviral (CHER) randomised trial.** *Lancet* 2013;382:1555–63 CrossRef Medline
  23. Madhi S, Adrian P, Cotton M, et al; Comprehensive International Program of Research on AIDS 4 Study Team. **Effect of HIV infection status and anti-retroviral treatment on quantitative and qualitative antibody responses to pneumococcal conjugate vaccine in infants.** *J Infect Dis* 2010;202:355–61 CrossRef Medline
  24. Reese TG, Heid O, Weisskoff RM, et al. **Reduction of eddy-current-induced distortion in diffusion MRI using a twice-refocused spin echo.** *Magn Reson Med* 2003;49:177–82 CrossRef Medline
  25. Tisdall MD, Hess AT, Reuter M, et al. **Volumetric navigators for prospective motion correction and selective reacquisition in neuroanatomical MRI.** *Magn Reson Med* 2012;68:389–99 CrossRef Medline
  26. van der Kouwe AJ, Benner T, Salat DH, et al. **Brain morphometry with multiecho MPRAGE.** *Neuroimage* 2008;40:559–69 CrossRef Medline
  27. Tournier JD, Mori S, Leemans A. **Diffusion tensor imaging and beyond.** *Magn Reson Med* 2011;65:1532–56 CrossRef Medline
  28. Jenkinson M, Bannister P, Brady M, et al. **Improved optimization for the robust and accurate linear registration and motion correction of brain images.** *Neuroimage* 2002;17:825–41 CrossRef Medline
  29. Andersson JL, Skare S, Ashburner J. **How to correct susceptibility distortions in spin-echo echo-planar images: application to diffusion tensor imaging.** *Neuroimage* 2003;20:870–88 CrossRef Medline
  30. Fonov V, Evans AC, Botteron K, et al; Brain Development Cooperative Group. **Unbiased average age-appropriate atlases for pediatric studies.** *Neuroimage* 2011;54:313–27 CrossRef Medline
  31. Forman SD, Cohen JD, Fitzgerald M, et al. **Improved assessment of significant activation in functional magnetic resonance imaging (fMRI): use of a cluster-size threshold.** *Magn Reson Med* 1995;33:636–47 CrossRef Medline
  32. Mori S, Wakana S, Van Zijl PC, et al. *MRI Atlas of Human White Matter.* Amsterdam: Elsevier; 2005
  33. Peters B, Szeszko P, Radua J, et al. **White matter development in adolescence: diffusion tensor imaging and meta-analytic results.** *Schizophr Bul* .2012;38:1308–17 CrossRef Medline
  34. Ragin AB, Wu Y, Storey P, et al. **Diffusion tensor imaging of subcortical brain injury in patients infected with human immunodeficiency virus.** *J Neurovirol* 2005;11:292–98 CrossRef Medline
  35. Thurnher MM, Castillo M, Stadler A, et al. **Diffusion-tensor MR imaging of the brain in human immunodeficiency virus-positive patients.** *AJNR Am J Neuroradiol* 2005;26:2275–81 Medline
  36. Wu Y, Storey P, Cohen BA, et al. **Diffusion alterations in corpus callosum of patients with HIV.** *AJNR Am J Neuroradiol* 2006;27:656–60 Medline
  37. Pfefferbaum A, Rosenbloom MJ, Rohlfing T, et al. **Frontostriatal fiber bundle compromise in HIV infection without dementia.** *AIDS* 2009;23:1977–85 CrossRef Medline
  38. Chen Y, An H, Zhu H, et al. **White matter abnormalities revealed by diffusion tensor imaging in non-demented and demented HIV+ patients.** *Neuroimage* 2009;47:1154–62 CrossRef Medline
  39. Ackermann C, Andronikou S, Laughton B, et al. **White matter signal abnormalities in children with suspected HIV-related neurologic disease on early combination antiretroviral therapy.** *Pediatr Infect Dis J* 2014;33:e207–12 CrossRef Medline
  40. Klingberg T, Vaidya CJ, Gabrieli JD, et al. **Myelination and organization of the frontal white matter in children: a diffusion tensor MRI study.** *Neuroreport* 1999;10:2817–21 CrossRef Medline
  41. Snook L, Paulson LA, Roy D, et al. **Diffusion tensor imaging of neurodevelopment in children and young adults.** *Neuroimage.* 2005;26:1164–73 CrossRef Medline
  42. Song S, Sun S, Ramsbottom M, et al. **Dysmyelination revealed through MRI as increased radial (but unchanged axial) diffusion of water.** *Neuroimage* 2002;17:1429–36 CrossRef Medline
  43. Cicarelli N, Fabbiani M, Di Giambenedetto S, et al. **Efavirenz associated with cognitive disorders in otherwise asymptomatic HIV-infected patients.** *Neurology* 2011;76:1403–09 CrossRef Medline
  44. Abers MS, Shandera WX, Kass JS. **Neurological and psychiatric adverse effects of antiretroviral drugs.** *CNS Drugs* 2014;28:131–45 CrossRef Medline
  45. Tardieu M, Brunelle F, Raybaud, et al. **Cerebral MR imaging in uninfected children born to HIV-seropositive mothers and perinatally exposed to zidovudine.** *AJNR Am J Neuroradiol* 2005;26:695–701 Medline
  46. Huang H, Zhang J, Wakana S, et al. **White and gray matter development in human fetal, newborn and pediatric brains.** *Neuroimage* 2006;33:27–38 CrossRef Medline
  47. Hermoye L, Saint-Martin C, Cosnard G, et al. **Pediatric diffusion**

- tensor imaging: normal database and observation of the white matter maturation in early childhood.** *Neuroimage* 2006;29:493–504 CrossRef Medline
48. Brody BA, Kinney HC, Kloman AS, et al. **Sequence of central nervous system myelination in human infancy, I: an autopsy study of myelination.** *J Neuropathol Exp Neurol* 1987;46:283–301 CrossRef Medline
49. Kinney HC, Brody BA, Kloman AS, et al. **Sequence of central nervous system myelination in human infancy, II: patterns of myelination in autopsied infants.** *J Neuropathol Exp Neurol* 1988;47:217–34 CrossRef Medline
50. Andronikou S, Ackermann C, Laughton B, et al. **Corpus callosum thickness on mid-sagittal MRI as a marker of brain volume: a pilot study in children with HIV-related brain disease and controls.** *Pediatr Radiol* 2015;45:1016–25 CrossRef Medline
51. Barkovich AJ, Kjos BO. **Normal postnatal development of the corpus callosum as demonstrated by MR imaging.** *AJNR Am J Neuroradiol* 1988;9:487–91 Medline
52. Wright PW, Heaps JM, Shimony JS, et al. **The effects of HIV and combination antiretroviral therapy on white matter integrity.** *AIDS* 2012;26:1501–08 CrossRef Medline

# Relative ADC and Location Differ between Posterior Fossa Pilocytic Astrocytomas with and without Gangliocytic Differentiation

J.H. Harreld, S.N. Hwang, I. Qaddoumi, R.G. Tatevossian, X. Li, J. Dalton, K. Hauptfear, Y. Li, and D.W. Ellison



## ABSTRACT

**BACKGROUND AND PURPOSE:** Pilocytic astrocytomas, the most common posterior fossa tumors in children, are characterized by *KIAA1549-BRAF* fusions and shows excellent 5-year survival rates. Pilocytic astrocytoma with gangliocytic differentiation, a recently defined pilocytic astrocytoma variant that includes glial and neuronal elements similar to a ganglioglioma, may be distinguished from a classic ganglioglioma by molecular, radiologic, and histopathologic features. This study investigated whether imaging could distinguish posterior fossa pilocytic astrocytoma with and without gangliocytic differentiation.

**MATERIALS AND METHODS:** Preoperative MRIs ( $\pm$  CTs) of 41 children (age range, 7 months to 15 years; mean age,  $7.3 \pm 3.7$  years; 58.5% male) with pilocytic astrocytoma with gangliocytic differentiation ( $n = 7$ ) or pilocytic astrocytoma ( $n = 34$ ) were evaluated; differences in tumor location, morphology, and minimum relative ADC between tumor types were compared (Wilcoxon rank sum test, Fisher exact test). Histopathology and *BRAF* fusion/mutation status were reviewed. Associations of progression-free survival with diagnosis, imaging features, and *BRAF* status were examined by Cox proportional hazards models.

**RESULTS:** Pilocytic astrocytoma with gangliocytic differentiation appeared similar to pilocytic astrocytoma but had lower minimum relative ADC (mean,  $1.01 \pm 0.17$  compared with  $2.01 \pm 0.38$  for pilocytic astrocytoma;  $P = .0005$ ) and was more commonly located within midline structures ( $P = .0034$ ). *BRAF* status was similar for both groups. Non-total resection (hazard ratio, 52.64;  $P = .0002$ ), pilocytic astrocytoma with gangliocytic differentiation diagnosis (hazard ratio, 4.66;  $P = .0104$ ), and midline involvement (hazard ratio, 3.32;  $P = .0433$ ) were associated with shorter progression-free survival.

**CONCLUSIONS:** Minimum relative ADC and tumor location may be useful adjuncts to histopathology in differentiating pilocytic astrocytoma with gangliocytic differentiation from pilocytic astrocytoma. Shorter progression-free survival in pilocytic astrocytoma with gangliocytic differentiation is likely due to a propensity for involvement of midline structures and poor resectability.

**ABBREVIATIONS:** GG = ganglioglioma; GTR = gross total resection; MAPK = mitogen-activated protein kinase; NTR = non-total resection; PA = pilocytic astrocytoma; PA-GD = pilocytic astrocytoma with gangliocytic differentiation; PFS = progression-free survival; rADC = relative ADC

Genetic alterations resulting in constitutive activation of *BRAF*, a key tyrosine kinase in the mitogen-activated protein kinase (MAPK) pathway, are the defining abnormality in most

pediatric low-grade gliomas.<sup>1-3</sup> The most common activating mutations are tandem duplications at chromosomal band 7q34, which generate *KIAA1549-BRAF* fusions,<sup>4-6</sup> and *BRAF*:p.V600E point mutations.<sup>4-6</sup> Pilocytic astrocytoma (PA) is the most common posterior fossa tumor in children, accounting for ~25% of infratentorial pediatric brain tumors.<sup>7</sup> PAs are World Health Organization grade I tumors with biphasic architecture, elongated bipolar (piloid) cells, microvascular proliferation or hyalinization, and degenerative changes such as Rosenthal fibers. Almost all posterior fossa PAs contain a *KIAA1549-BRAF* fusion, and this alteration differentiates PAs from other low-grade gliomas with high specificity.<sup>6</sup> Their imaging characteristics are variable, with 2/3 demonstrating a typical “cyst with enhancing mural nodule” appearance and the remainder appearing solid or partially necrotic.<sup>8</sup> Overall survival rates are excellent, around 96% at 5 years.<sup>9,10</sup>

Received April 18, 2016; accepted after revision June 13.

From the Departments of Diagnostic Imaging (J.H.H., S.N.H.), Neuro-Oncology (I.Q.), Pathology (R.G.T., J.D., K.H., D.W.E.), and Biostatistics (X.L., Y.L.), St. Jude Children's Research Hospital, Memphis, Tennessee.

This work was supported, in part, by grant No. CA21765 from the National Cancer Institute and by the American Lebanese Syrian Associated Charities.

Paper previously presented, in part, at: Annual Meeting of the Radiological Society of North America, November 29 to December 4, 2015; Chicago, Illinois.

Please address correspondence to Julie H. Harreld, MD, St. Jude Children's Research Hospital, Department of Diagnostic Imaging, 262 Danny Thomas Place, MS-220, Memphis, TN 38105; e-mail: julie.harreld@stjude.org

Indicates open access to non-subscribers at www.ajnr.org

Indicates article with supplemental on-line table.

<http://dx.doi.org/10.3174/ajnr.A4892>

Pediatric gangliogliomas (GGs) are uncommon World Health Organization grade I glioneuronal tumors. They are rarely found in the posterior fossa, where GGs comprise ~1% of all tumors,<sup>11–13</sup> and frequently contain BRAF:p.V600E mutations (35%–58%).<sup>14,15</sup> Overall 5-year survival rates of ~95% are similar to those seen for PAs, but lower rates (~78%–81%) have been reported for infratentorial GGs, which frequently involve the brain stem.<sup>12,16,17</sup> Similar to PAs, the imaging characteristics of posterior fossa GGs are variable; they may be solid, partially necrotic, or have a “cyst with mural nodule” appearance, reminiscent of PAs.<sup>17–20</sup>

A recent study found that posterior fossa GGs could be divided into 2 distinct categories, by using histopathologic, molecular, and radiologic features.<sup>21</sup> One category comprises classic gangliogliomas (70%), which may contain BRAF:p.V600E mutations and are more frequently solid and enhancing. The other consists largely of PAs with foci of gangliocytic differentiation (PA-GDs, 30%), which more frequently appear cystic/necrotic. These frequently contain *KIAA1549-BRAF* fusions, but not a BRAF:p.V600E mutation, and are better characterized as PAs with gangliocytic differentiation.

In this study, we investigated whether imaging features could distinguish PAs with and without gangliocytic differentiation and whether clinicopathologic, imaging, and/or molecular features influenced progression-free survival (PFS).

## MATERIALS AND METHODS

### Study Population

We performed a retrospective review of our institutional pathology data base, with institutional review board approval and a waiver of consent. Seven patients with posterior fossa PA-GDs and 43 patients with posterior fossa pilocytic astrocytomas were identified, which were diagnosed between February 2006 and February 2014. Tumors involving the cervical spinal cord and patients with neurofibromatosis type 1 were excluded. Five subjects with PA were excluded for insufficient preoperative imaging. Four had insufficient tissue for diagnosis, yielding a final cohort of 34 PAs. We recorded the following clinical data: dates of diagnosis, surgery, and progression; treatment with chemotherapy and/or radiation therapy; whether there was gross total resection (GTR) of tumor, leptomeningeal metastasis, or history of epilepsy; and time and site of progression, if applicable.

### Imaging

Preoperative and postoperative MR imaging studies were available for all subjects. Preoperative noncontrast CTs were available for 10 subjects with PA, and none with PA-GD. Most preoperative and immediate postoperative imaging was performed at other institutions (because our institution is a referral-based children’s cancer treatment hospital) with equipment by multiple vendors (GE Healthcare, *n* = 30; Siemens, *n* = 6; and Philips Healthcare, *n* = 5) and variable field strengths (1T, *n* = 1; 1.5T, *n* = 30; and 3T, *n* = 10). Imaging sequences acquired for each group are listed in the Table. Section thicknesses for diffusion imaging ranged from 2.5 to 5 mm, with interslice gaps of 0–1 mm except for 1 PA examination with a gap of 2 mm. Other sequences were acquired with variable section thickness ranging from 1 to 6 mm.

All imaging examinations were reviewed by 2 board-certified

### MRI sequences by group

Sequence	PA (n = 34)	PA-GD (n = 7)
T1	34	7
T2	34	6
FLAIR	34	5
T1+C	34	7
DWI	31	6
ADC	28	5
Exp ADC	19	1
SWI	2	1
T2*/GRE	5	4

**Note:**—T1+C indicates T1WI with contrast; Exp, exponential ADC map; GRE, gradient recalled-echo.

radiologists (J.H.H. and S.N.H.) with Certificates of Added Qualification in neuroradiology; both were blinded to the diagnosis. Each scored tumors according to the following criteria: dominant site (cerebellar hemisphere, vermis, middle cerebellar peduncle, brain stem); side (left, right, midline); circumscription (yes, no, mixed); hemorrhage (yes, no); cyst+ nodule morphology (yes, no); percentage enhancement, percentage cystic/necrotic (0% = 0, <25% = 1, 25%–49% = 2, 50%–75% = 3, >75% = 4); and edema (none = 0, minimal = 1, mild = 2, moderate = 3, severe = 4). Differences were resolved in consensus. For relative ADC (rADC) analysis, ROI ellipses were drawn within the region of lowest ADC within the solid component of each tumor, avoiding areas of hemorrhage or mineralization, and in the contralateral thalamus. rADC was calculated as  $ADC_{\text{tumor}}/ADC_{\text{thalamus}}$ .<sup>22</sup>

### Pathology

The histopathologic diagnosis was reviewed in each case (D.W.E.). Hematoxylin-eosin stained 4- $\mu$ m formalin-fixed paraffin-embedded sections were supplemented with immunohistochemical analysis with antibodies to glial fibrillary acidic protein (1:400, M076101; Dako, Carpinteria, California), Ki67 (1:200, M7240; Dako), microtubule-associated protein 2 (1:10,000, M4403; Sigma-Aldrich, St Louis, Missouri), Neu-N (1:5000, MAB377; EMD Millipore, Billerica, Massachusetts), neurofilament protein (1:100, M076229; Dako), and synaptophysin (1:400, NCL-L-SYNAP-299; Leica Biosystems, Buffalo Grove, Illinois).

### Molecular Analysis and Interphase Fluorescence in Situ Hybridization

Tumors were screened for the presence or absence of a *KIAA1549-BRAF* fusion by using 2 complementary methods: dual-color interphase fluorescence in situ hybridization for *BRAF* duplication at 7q34 as a surrogate marker for the presence of fusions, and real-time quantitative reverse-transcription polymerase chain reaction to detect specific *KIAA1549-BRAF* fusion transcripts. Interphase fluorescence in situ hybridization was performed on 4- $\mu$ m formalin-fixed paraffin-embedded sections by using bacterial artificial chromosome clones as described previously.<sup>21,23</sup> Genomic DNA and total RNA were extracted from 10- $\mu$ m formalin-fixed paraffin-embedded scrolls, as previously described.<sup>21</sup> The BRAF:p.V600 mutation hotspot was sequenced in genomic DNA, and quantitative reverse-transcription polymerase chain reaction was performed by using first-strand complementary DNA synthesized from total RNA, both as previously described.<sup>21</sup>

### Statistical Analysis

The Wilcoxon rank sum test was used to assess differences in continuous variables (rADC, age) between PA and PA-GD groups. The Fisher exact test was used to assess differences in categorical variables (sex, dominant site, hemorrhage, cyst + nodule morphology, circumscription, percentage enhancement, percentage cystic/necrotic, and degree of edema) between the PA and PA-GD groups. Because of the small number of subjects with PA-GD, the dominant site was divided into “midline” (brain stem, vermis) versus “off-midline” (cerebellar hemisphere, middle cerebellar peduncle) structures for comparison.

Progression-free survival was calculated as the following: Date of First Progression (or last imaging follow-up date if no progression) – Diagnosis Date + 1. The Cox proportional hazards model was used to explore the relationship of PFS to diagnosis (PA versus PA-GD), dominant site, and extent of resection (GTR versus non-total resection [NTR]). The association between the dominant site and the extent of resection was assessed by a  $\chi^2$  test. Associations of *BRAF* fusion status with the dominant site and the extent of resection were assessed by the Fisher exact test. All statistical tests were performed with SAS, Version 9.3 (SAS Institute, Cary, North Carolina).

### RESULTS

Demographic, imaging, and molecular features are summarized in the On-line Table. Children with PA-GD (age range, 4.7–13.3 years; mean age,  $10.3 \pm 3$  years) were older at diagnosis than those with PA (age range, 7.2 months to 15.0 years; mean age,  $6.7 \pm 3.6$  years) ( $P = .0232$ ). A slight preponderance of males in the PA-GD group (5 of 7 or 71.4%) was not statistically significant compared with the PA group (19 of 34 or 55.9%) ( $P = .6786$ ).

### Treatment

Twenty-three of 34 subjects with PA achieved GTR at the initial operation; none developed metastasis. None of the 23 subjects in whom GTR was achieved underwent chemotherapy or radiation therapy; one had tumor progression, underwent successful repeat GTR, and received no further therapy. Eleven subjects with PA had NTR at presentation; 9/11 had local progression, and 2 received focal radiation therapy alone and had no tumor progression. GTR was achieved at a subsequent operation in 3/6 subjects who underwent repeat resection, which occurred at an average of  $489 \pm 361$  days (range, 25–962 days) after the first operation. In general, unsuccessful repeat operations were performed earlier (mean,  $251 \pm 197$  days after the initial operation) than those that ultimately resulted in GTR (mean,  $726 \pm 344$  days after the initial operation).

GTR was not achieved at the initial operation for any of the 7 subjects with PA-GD. One subject had no progression before or after successful GTR 140 days after the initial operation and had no other therapy; this outcome was classified as GTR for survival and progression analyses. One subject was lost to follow-up after initial postoperative imaging, and a third received chemotherapy and survived to the time of this study, though progression status was not known. The remaining 4 subjects had local progression between 17 and 554 days (mean,  $242 \pm 238$  days) postoperatively. Of these, 1 had repeat NTR 197 days postdiagnosis, with no further therapy, 1 had leptomeningeal metastasis at diagnosis and

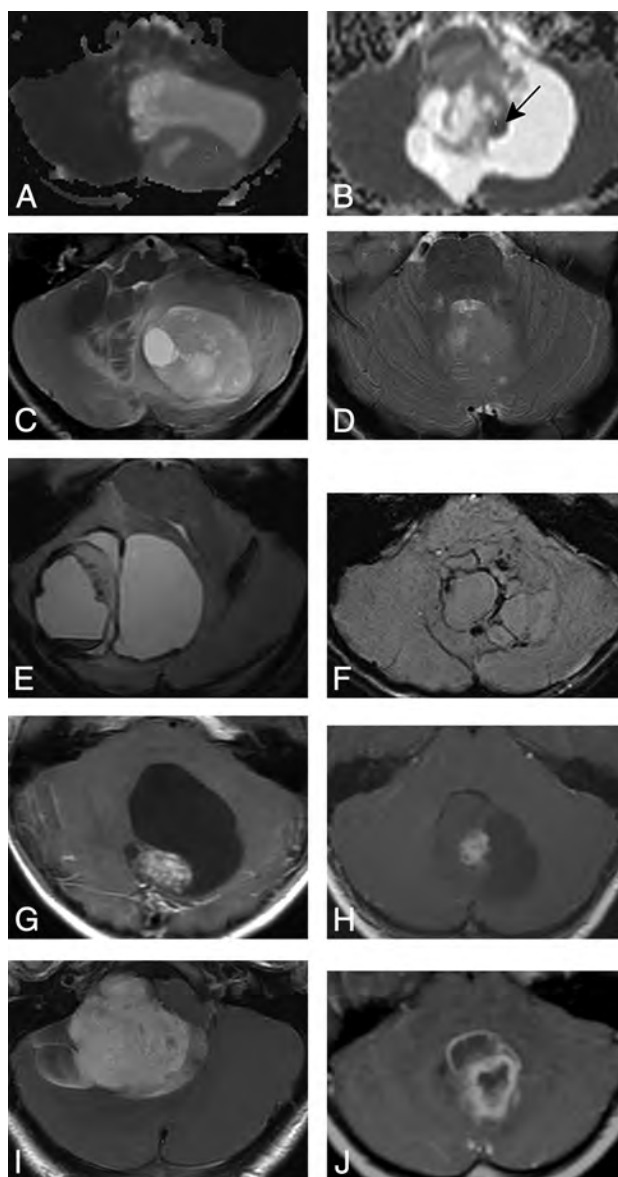


**FIG 1.** Imaging features of 10 different tumors, 5 PAs and 5 PA-GDs. On axial ADC maps, the solid portions of PAs (A) tend to be homogeneous with relatively elevated ADC; PA-GDs (B) appear more heterogeneous and have foci of lower ADC (arrow). PA-GDs primarily involve midline structures; the PA in C displaces the vermis, while a PA-GD (D) infiltrates the vermis. PA and PA-GD have a similar frequency of hemorrhage, seen in the PA on T2\* (E) and in the PA-GD on SWI (F). Both tumors tend to appear circumscribed and may appear solid or necrotic or have cyst-and-nodule morphology as seen on axial contrast-enhanced T1WI of a PA (G) and a PA-GD (H). The percentage of solid tumor components showing enhancement was similar between PA (I) and PA-GD (J).

received craniospinal irradiation, and the remaining 2 subjects received chemotherapy.

### Imaging

Imaging features of PAs and PA-GDs are compared in Fig 1. Most PAs and PA-GDs were well-circumscribed with minimal edema (On-line Table). The percentages of enhancing tumor and cystic/necrotic components did not differ significantly between tumor types, nor did the propensity for hemorrhage. Twenty-one percent of PAs and 43% of PA-GDs showed signs of hemorrhage, a

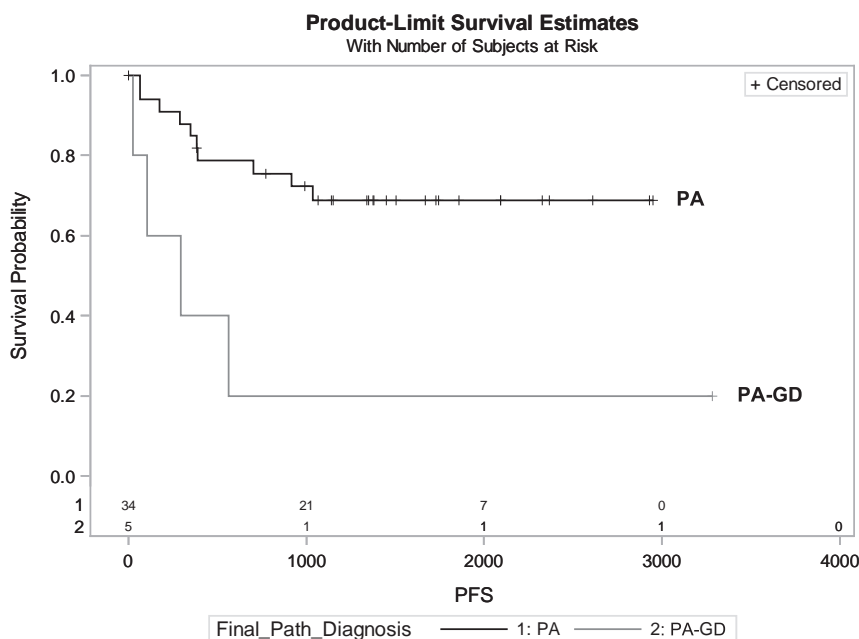


**FIG 2.** Progression-free survival was significantly lower for PA-GD compared with PA ( $P = .0104$ ; hazard ratio, 4.66).

difference that was not significant ( $P = .3324$ ). Although only 1 of 7 (14%) PA-GDs had a classic cyst+nodule morphology compared with 10/34 (29%) PAs, this was not a distinguishing feature ( $P = .6514$ ). PA-GDs were more likely to occur in midline structures ( $P = .0034$ ); all 7 PA-GDs predominantly involved either the vermis ( $n = 5$ ) or brain stem ( $n = 2$ ), while PAs were more commonly off-midline. Nineteen PAs involved the cerebellar hemisphere, and 2, the middle cerebellar peduncle.

Diffusion imaging was available for 6/7 PA-GDs and 31/34 PAs. Trace-weighted DWI was provided without ADC maps for 1 subject with PA-GD and 3 subjects with PAs. These subjects were excluded from rADC analysis. An ADC map was provided without trace-weighted DWI for 1 subject with PA. For the 28 PAs and 5 PA-GDs with ADC maps, the minimum tumor rADC was significantly lower for PA-GD (range, 0.81–1.20; mean,  $1.01 \pm 0.17$ ) than for PA (range, 1.24–2.89; mean,  $2.01 \pm 0.38$ ), with no overlap in values ( $P = .0005$ ). For a threshold rADC of 1.22, set midway between the lowest PA rADC of 1.24 and the largest PA-GD rADC of 1.20, the sensitivity and specificity of minimum rADC for differentiation of PA and PA-GD were both 100%.

### Pathology/Molecular Analysis

Five of 7 PA-GDs (71%) and 31 of 33 PAs (94%) had a *KIAA1549-BRAF* gene fusion. Fusion screening was not performed for 1 subject with PA due to insufficient material. There was no significant difference in *BRAF* fusion status by diagnosis. Four tumors (2 PAs and 2 PA-GDs) did not have a *BRAF* duplication; all were located in the midline (vermis or brain stem,  $P = .0424$ ) and were less likely to have undergone GTR ( $P = .026$ ). No *BRAF*:p.V600E mutations were identified in 34/41 tumors tested (7 PA-GDs, 27 PAs). Insufficient material was available to complete mutation analysis for 7 tumors (all PAs).

### Progression-Free Survival

Two subjects with PA-GD were lost to imaging follow-up after postoperative MR imaging; progression status and survival data were unavailable for one of these. All 40 remaining children were alive at the most recent follow-up, which ranged from 1.0 to 8.1 years (mean,  $4.4 \pm 2.0$  years) after diagnosis for patients with PA and 1.4–9.0 years (mean,  $4.4 \pm 2.7$  years) for children with PA-GDs. Local tumor progression was seen in 3/5 subjects with PA-GDs and 11/34 subjects with PAs; only 1 of these (PA) had undergone GTR. Subjects with *KIAA1549-BRAF* fusion were more likely to have GTR than those without ( $P = .0199$ ), but fusion status alone did not predict improved progression-free survival in the entire cohort ( $P = .1165$ ) or in patients whose tumors were incompletely resected ( $P = .59$ ).

Progression-free survival was significantly lower for PA-GD than PA ( $P = .0104$ ; hazard ratio, 4.66) (Fig 2). Midline

tumors of either type were more likely to progress compared with off-midline tumors ( $P = .0433$ ; hazard ratio, 3.319). The strongest predictor of tumor progression was non-total resection, with a hazard ratio of 52.644 compared with GTR ( $P = .0002$ ). NTR was most strongly associated with a PA-GD diagnosis ( $P = .0141$ ) and midline location ( $P = .0187$ ), but when only midline tumors were considered, there was no difference in the likelihood of GTR ( $P = .1577$ ) or in progression-free survival ( $P = .0833$ ) between PA and PA-GD, and PFS did not differ between patients with NTR of PA versus PA-GD ( $P = .1800$ ).

### DISCUSSION

PA-GD is a recently defined rare variant of PA, from which it may be histopathologically differentiated only by the presence of foci of gangliocytic differentiation. In this study, we found that conventional imaging features such as circumscription, enhancement, and cysts/necrosis cannot reliably differentiate PA and PA-GD, both of which may have the cyst+nodule imaging appearance considered characteristic for PA. However, PA-GDs were more likely to involve midline structures than PAs ( $P = .0034$ ), and a minimum rADC  $< 1.22$  reliably differentiated posterior fossa PA-GD from PA ( $P = .0005$ ). This simple and rapid approach to differential diagnosis requires no specialized software and may serve as a valuable adjunct to histopathologic diagnosis.

A growing body of literature suggests that activating mutations of *BRAF* may be tumor- and site-specific in the CNS and have morphologic, prognostic, and therapeutic implications.<sup>5,17,21,24-30</sup> Most cerebellar PAs carry *BRAF* duplications in conjunction with a *KIAA1549-BRAF* fusion, which is highly specific for PA (98.5%)<sup>26,31</sup> and is associated with a well-defined tumor margin and a good prognosis.<sup>26,32</sup> The *BRAF*:p.V600E point mutation is a recurring alteration in gangliogliomas (up to 58%) but is rare in pilocytic astrocytoma.<sup>1,5,14,15,24,31,33</sup> Fusions

were observed in 94% (31/33) of evaluated PAs and in 71.4% of PA-GDs in this series, further supporting classification of PA-GD as a PA variant, and most tumors were well-circumscribed; however, neither feature influenced progression-free survival. No BRAF:p.V600E mutation was found in this study.

PA-GDs had significantly worse PFS than PAs in this study. This finding aligns with prior studies describing a poorer prognosis for posterior fossa gangliogliomas compared with PAs.<sup>34-36</sup> The presence of residual tumor (NTR) was the strongest predictor of tumor progression ( $P = .0002$ ) and was associated with absence of fusion ( $P = .0199$ ), midline involvement ( $P = .0187$ ), and PA-GD diagnosis ( $P = .0141$ ). All 4 tumors negative for fusion in this series (2 PAs and 2 PA-GDs) were located in either the vermis or brain stem and were incompletely resected ( $P = .0424$  and  $0.026$ , respectively). PAs and PA-GDs involving midline structures had similarly poor resectability ( $P = .1577$ ) and PFS ( $P = .0833$ ), and in patients with residual tumor, neither BRAF fusion status ( $P = .59$ ) nor tumor type ( $P = .1800$ ) influenced PFS. PA-GDs were more likely than PAs to involve midline structures (vermis or brain stem) (On-line Table). Thus, shorter progression-free survival in PA-GD is more likely due to its proclivity for midline structures, rather than underlying histology or BRAF fusion status.

PA-GD of the posterior fossa is rare, and the small sample size for PA-GD ( $n = 7$ ) is the major limitation of this study. This may have limited our ability to detect the impact of BRAF status on progression-free survival and to determine whether additional imaging features could distinguish PA from PA-GD. Because we are a referral-only pediatric cancer specialty hospital with a busy consult service, uncommon tumors are disproportionately referred to us for consultation or care; thus, the relative frequencies of PA-GD and PA in this study are not representative of those in the general population. Imaging techniques were also not consistent for this study; not all patients had ADC maps, limiting the sample size for ADC analysis, and vendors and techniques were not uniform. However, although absolute ADC varies between vendors and field strengths,<sup>37,38</sup> rADC is robust across MR imaging vendors and platforms and may therefore be considered reliable.<sup>22</sup> The ROI-based ADC measures used in this study are readily performed in the typical fast-paced clinical setting but may be subjective. Histogram-based whole-tumor ADC analysis continues to mature and may one day become widely available for clinical use, promising to decrease the subjectivity of ADC measures in future assessments.<sup>39,40</sup> Finally, because rADC was not used to guide biopsy in this retrospective study, it was not possible to evaluate whether regions of lower ADC in PA-GD correlated with hypercellularity or dysplastic neuronal elements, the histologic feature distinguishing PA-GD from PA.<sup>21</sup>

With the advent of targeted cancer therapy, imaging-based identification of classic PA-like features in a ganglioglioma may be therapeutically relevant. BRAF inhibitors such as vemurafenib are effective for tumors positive for BRAF:p.V600E mutation but cause paradoxical activation of the MAPK pathway and progression in tumors with KIAA1549-BRAF fusion or wild-type BRAF.<sup>17,28,29</sup> PAs and PA-GDs would not respond favorably to this class of BRAF inhibitor; this scenario highlights the need to separate PA-GDs from classic GGs in the posterior fossa.

## CONCLUSIONS

A minimum rADC of  $>1.22$  reliably differentiates PA from PA-GD, which is more likely than PA to involve midline structures. This simple approach may be used by any radiologist to suggest PA-GD in the differential diagnosis of a posterior fossa mass that otherwise resembles PA, augmenting histologic and molecular diagnosis. Poorer progression-free survival in PA-GD compared with PA is likely due to its proclivity for midline structures and related poor resectability. As more molecular features of pediatric low-grade gliomas emerge, careful correlation with imaging phenotype may permit imaging-based prediction of molecular features, with therapeutic and prognostic implications.

Disclosures: Julie H. Harreld—RELATED: Grant: National Cancer Institute (grant No. CA21765)\*; Other: American Lebanese Syrian Associated Charities,\* Comments: American Lebanese Syrian Associated Charities is the fundraising entity that supports research and clinical care at St. Jude; UNRELATED: Travel/Accommodations/Meeting Expenses Unrelated to Activities Listed: World Federation of Neuroradiological Societies; Society of Pediatric Radiology, Comments: World Federation of Neuroradiological Societies: travel expenses for invited talk, 2014; Society for Pediatric Radiology: travel expenses and honorarium for invited talk, 2013. David W. Ellison—UNRELATED: Grants/Grants Pending: National Institutes of Health\*, Comments: 5 P01 CA096832-II, coinvestigator; 1 U10CA180886-01, coinvestigator. \*Money paid to the institution.

## REFERENCES

1. Brandner S, von Deimling A. **Diagnostic, prognostic and predictive relevance of molecular markers in gliomas.** *Neuropathol Appl Neurobiol* 2015;41:694–720 CrossRef Medline
2. Dougherty MJ, Santi M, Brose MS, et al. **Activating mutations in BRAF characterize a spectrum of pediatric low-grade gliomas.** *Neuro Oncol* 2010;12:621–30 CrossRef Medline
3. Tatevossian RG, Lawson AR, Forshew T, et al. **MAPK pathway activation and the origins of pediatric low-grade astrocytomas.** *J Cell Physiol* 2010;222:509–14 CrossRef Medline
4. Dhillon AS, Hagan S, Rath O, et al. **MAP kinase signalling pathways in cancer.** *Oncogene* 2007;26:3279–90 CrossRef Medline
5. Schindler G, Capper D, Meyer J, et al. **Analysis of BRAF V600E mutation in 1,320 nervous system tumors reveals high mutation frequencies in pleomorphic xanthoastrocytoma, ganglioglioma and extra-cerebellar pilocytic astrocytoma.** *Acta Neuropathol* 2011;121:397–405 CrossRef Medline
6. Korshunov A, Meyer J, Capper D, et al. **Combined molecular analysis of BRAF and IDH1 distinguishes pilocytic astrocytoma from diffuse astrocytoma.** *Acta Neuropathol* 2009;118:401–05 CrossRef Medline
7. Poretti A, Meoded A, Huisman TA. **Neuroimaging of pediatric posterior fossa tumors including review of the literature.** *J Magn Reson Imaging* 2012;35:32–47 CrossRef Medline
8. Koeller KK, Rushing EJ. **From the archives of the AFIP: pilocytic astrocytoma—radiologic-pathologic correlation.** *Radiographics* 2004;24:1693–708 CrossRef Medline
9. Fisher PG, Tihan T, Goldthwaite PT, et al. **Outcome analysis of childhood low-grade astrocytomas.** *Pediatr Blood Cancer* 2008;51:245–50 CrossRef Medline
10. Stokland T, Liu JF, Ironside JW, et al. **A multivariate analysis of factors determining tumor progression in childhood low-grade glioma: a population-based cohort study (CCLG CNS9702).** *Neuro Oncol* 2010;12:1257–68 CrossRef Medline
11. Chang T, Teng MM, Lirng JF. **Posterior cranial fossa tumours in childhood.** *Neuroradiology* 1993;35:274–78 CrossRef Medline
12. Dudley RW, Torok MR, Gallegos DR, et al. **Pediatric low-grade ganglioglioma: epidemiology, treatments, and outcome analysis on 348 children from the surveillance, epidemiology, and end results database.** *Neurosurgery* 2015;76:313–19; discussion 319; quiz 319–20 CrossRef Medline

13. Rickert CH, Paulus W. **Epidemiology of central nervous system tumors in childhood and adolescence based on the new WHO classification.** *Childs Nerv Syst* 2001;17:503–11 CrossRef Medline
14. Koelsche C, Wöhrer A, Jeibmann A, et al. **Mutant BRAF V600E protein in ganglioglioma is predominantly expressed by neuronal tumor cells.** *Acta Neuropathol* 2013;125:891–900 CrossRef Medline
15. Qaddoumi I, Orisme W, Wen J, et al. **Genetic alterations in uncommon low-grade neuroepithelial tumors: BRAF, FGFR1, and MYB mutations occur at high frequency and align with morphology.** *Acta Neuropathol* 2016;131:833–45 CrossRef Medline
16. Compton JJ, Laack NN, Eckel LJ, et al. **Long-term outcomes for low-grade intracranial ganglioglioma: 30-year experience from the Mayo Clinic.** *J Neurosurg* 2012;117:825–30 CrossRef Medline
17. Lindsay AJ, Rush SZ, Fenton LZ. **Pediatric posterior fossa ganglioglioma: unique MRI features and correlation with BRAF V600E mutation status.** *J Neurooncol* 2014;118:395–404 CrossRef Medline
18. Castillo M, Davis PC, Takei Y, et al. **Intracranial ganglioglioma: MR, CT, and clinical findings in 18 patients.** *AJR Am J Roentgenol* 1990;154:607–12 CrossRef Medline
19. Safavi-Abbasi S, Di Rocco F, Chantra K, et al. **Posterior cranial fossa gangliogliomas.** *Skull Base* 2007;17:253–64 CrossRef Medline
20. Zhang D, Henning TD, Zou LG, et al. **Intracranial ganglioglioma: clinicopathological and MRI findings in 16 patients.** *Clin Radiol* 2008;63:80–91 CrossRef Medline
21. Gupta K, Orisme W, Harreld JH, et al. **Posterior fossa and spinal gangliogliomas form two distinct clinicopathologic and molecular subgroups.** *Acta Neuropathol Commun* 2014;2:18 CrossRef Medline
22. Koral K, Alford R, Choudhury N, et al. **Applicability of apparent diffusion coefficient ratios in preoperative diagnosis of common pediatric cerebellar tumors across two institutions.** *Neuroradiology* 2014;56:781–88 CrossRef Medline
23. Forshew T, Tatevossian RG, Lawson AR, et al. **Activation of the ERK/MAPK pathway: a signature genetic defect in posterior fossa pilocytic astrocytomas.** *J Pathol* 2009;218:172–81 CrossRef Medline
24. Bannykh SI, Mirocha J, Nuno M, et al. **V600E BRAF mutation in pilocytic astrocytoma is associated with a more diffuse growth pattern but does not confer a more aggressive clinical behavior.** *Clin Neuropathol* 2014;33:388–98 CrossRef Medline
25. Hawkins C, Walker E, Mohamed N, et al. **BRAF-KIAA1549 fusion predicts better clinical outcome in pediatric low-grade astrocytoma.** *Clin Cancer Res* 2011;17:4790–98 CrossRef Medline
26. Horbinski C, Hamilton RL, Nikiforov Y, et al. **Association of molecular alterations, including BRAF, with biology and outcome in pilocytic astrocytomas.** *Acta Neuropathol* 2010;119:641–49 CrossRef Medline
27. Koelsche C, Sahn F, Wöhrer A, et al. **BRAF-mutated pleomorphic xanthoastrocytoma is associated with temporal location, reticulin fiber deposition and CD34 expression.** *Brain Pathol* 2014;24:221–29 CrossRef Medline
28. Sievert AJ, Lang SS, Boucher KL, et al. **Paradoxical activation and RAF inhibitor resistance of BRAF protein kinase fusions characterizing pediatric astrocytomas.** *Proc Natl Acad Sci U S A* 2013;110:5957–62 CrossRef Medline
29. Hatzivassiliou G, Song K, Yen I, et al. **RAF inhibitors prime wild-type RAF to activate the MAPK pathway and enhance growth.** *Nature* 2010;464:431–35 CrossRef Medline
30. Rodriguez FJ, Ligon AH, Horkayne-Szakaly I, et al. **BRAF duplications and MAPK pathway activation are frequent in gliomas of the optic nerve proper.** *J Neuropathol Exp Neurol* 2012;71:789–94 CrossRef Medline
31. Jones DT, Kocialkowski S, Liu L, et al. **Tandem duplication producing a novel oncogenic BRAF fusion gene defines the majority of pilocytic astrocytomas.** *Cancer Res* 2008;68:8673–77 CrossRef Medline
32. Pollack IF, Jakacki RI. **Childhood brain tumors: epidemiology, current management and future directions.** *Nat Rev Neurol* 2011;7:495–506 CrossRef Medline
33. Dahiya S, Haydon DH, Alvarado D, et al. **BRAF(V600E) mutation is a negative prognosticator in pediatric ganglioglioma.** *Acta Neuropathol* 2013;125:901–10 CrossRef Medline
34. Burkhard C, Di Patre PL, Schüler D, et al. **A population-based study of the incidence and survival rates in patients with pilocytic astrocytoma.** *J Neurosurg* 2003;98:1170–74 CrossRef Medline
35. Lang FF, Epstein FJ, Ransohoff J, et al. **Central nervous system gangliogliomas: part 2, clinical outcome.** *J Neurosurg* 1993;79:867–73 CrossRef Medline
36. Miller DC, Lang FF, Epstein FJ. **Central nervous system gangliogliomas: part 1, pathology.** *J Neurosurg* 1993;79:859–66 CrossRef Medline
37. Malyarenko DI, Newitt D, Wilmes LJ, et al. **Demonstration of non-linearity bias in the measurement of the apparent diffusion coefficient in multicenter trials.** *Magn Reson Med* 2016;75:1312–23 CrossRef Medline
38. Sasaki M, Yamada K, Watanabe Y, et al; Acute Stroke Imaging Standardization Group-Japan (ASIST-Japan) Investigators. **Variability in absolute apparent diffusion coefficient values across different platforms may be substantial: a multivendor, multi-institutional comparison study.** *Radiology* 2008;249:624–30 CrossRef Medline
39. Jenkinson MD, Smith TS, Brodbelt AR, et al. **Apparent diffusion coefficients in oligodendroglial tumors characterized by genotype.** *J Magn Reson Imaging* 2007;26:1405–12 CrossRef Medline
40. Rodriguez Gutierrez D, Awwad A, Meijer L, et al. **Metrics and textural features of MRI diffusion to improve classification of pediatric posterior fossa tumors.** *AJNR Am J Neuroradiol* 2014;35:1009–15 CrossRef Medline

# Effectiveness of 3D T2-Weighted FLAIR FSE Sequences with Fat Suppression for Detection of Brain MR Imaging Signal Changes in Children

M. Mascalchi, A. Bianchi, M. Basile, P. Gulino, M.R. Trifan, D. Difeo, E. Bartolini, C. Defilippi, and S. Diciotti

## ABSTRACT

**BACKGROUND AND PURPOSE:** T2-weighted FLAIR can be combined with 3D-FSE sequences with isotropic voxels, yielding higher signal-to-noise ratio than 2D-FLAIR. Our aim was to explore whether a T2-weighted FLAIR–volume isotropic turbo spin-echo acquisition sequence (FLAIR-VISTA) with fat suppression shows areas of abnormal brain T2 hyperintensities with better conspicuity in children than a single 2D-FLAIR sequence.

**MATERIALS AND METHODS:** One week after a joint training session with 20 3T MR imaging examinations (8 under sedation), 3 radiologists independently evaluated the presence and conspicuity of abnormal areas of T2 hyperintensities of the brain in FLAIR-VISTA with fat suppression (sagittal source and axial and coronal reformatted images) and in axial 2D-FLAIR without fat suppression in a test set of 100 3T MR imaging examinations (34 under sedation) of patients 2–18 years of age performed for several clinical indications. Their agreement was measured with weighted  $\kappa$  statistics.

**RESULTS:** Agreement was “substantial” (mean, 0.61 for 3 observers; range, 0.49–0.69 for observer pairs) for the presence of abnormal T2 hyperintensities and “fair” (mean, 0.29; range, 0.23–0.38) for the comparative evaluation of lesion conspicuity. In 21 of 23 examinations in which the 3 radiologists agreed on the presence of abnormal T2 hyperintensities, FLAIR-VISTA with fat suppression images were judged to show hyperintensities with better conspicuity than 2D-FLAIR. In 2 cases, conspicuity was equal, and in no case was conspicuity better in 2D-FLAIR.

**CONCLUSIONS:** FLAIR-VISTA with fat suppression can replace the 2D-FLAIR sequence in brain MR imaging protocols for children.

**ABBREVIATION:** VISTA = volume isotropic turbo spin-echo acquisition

3D (volume) gradient-echo T1-weighted sequences are a well-established part of brain MR imaging protocols due to the intrinsically higher SNR compared with 2D sequences and the ability to obtain optimal MPR.<sup>1</sup> However, abnormalities of the brain are usually detected as nonspecific areas of variably increased signal in T2WI. FLAIR images are preferable to FSE images for detecting such T2 abnormalities because suppression of the

CSF high signal results in an improved gray-scale dynamic range.<sup>2</sup>

T2-weighted FLAIR can be combined with 3D-FSE sequences with isotropic voxels that are variably named by different vendors, including volume isotropic turbo spin-echo acquisition (VISTA; Philips Healthcare, Best, the Netherlands), SPACE (sampling perfection with application-optimized contrasts by using different flip angle evolution; Siemens, Erlangen, Germany), Cube (GE Healthcare, Milwaukee, Wisconsin), isoFSE (<http://www.hitachimed.com/products/mri/oasis/Neurological/isoFSE>), and 3D mVox (Toshiba, Tokyo, Japan). Such T2-weighted FLAIR 3D-FSE sequences have a higher SNR than 2D-FLAIR, enable MPR, and are less affected by CSF flow artifacts,<sup>3–6</sup> which are more prominent in sedated children at a higher field strength 3T magnet.<sup>7–9</sup>

Theoretically, suppression of fat signal with spectral presaturation could improve the sensitivity of FLAIR-VISTA by further narrowing the gray-scale dynamic range.<sup>2</sup>

The purpose of the present study was to evaluate whether a

Received February 12, 2016; accepted after revision July 4.

From the “Mario Serio” Department of Experimental and Clinical Biomedical Sciences (M.M., A.B.), University of Florence, Florence, Italy; Structural and Functional Neuroradiology Research Unit (M.M.), Diagnostic Radiology (M.B., P.G., M.R.T., D.D., C.D.), and Neurology Unit and Laboratories (E.B.), Meyer Children’s Hospital, Florence, Italy; and Department of Electrical, Electronic, and Information Engineering “Guglielmo Marconi” (S.D.), University of Bologna, Cesena, Italy.

Please address correspondence to Mario Mascalchi, MD, University of Florence, “Mario Serio” Department of Clinical and Experimental Biomedical Sciences, Viale Morgagni 50, Firenze 50134, Italy; e-mail: m.mascalchi@dfc.unifi.it

<http://dx.doi.org/10.3174/ajnr.A4915>

**Table 1: Patient demographic characteristics, number of MRI examinations under sedation, and clinical indications in the training and test sets**

	Training Set	Test Set
No.	20	100
Age (mean) (range) (yr)	9 ± 6.5, 2–17	9 ± 7, 2–18
Sex	Female, <i>n</i> = 10; male, <i>n</i> = 10	Female, <i>n</i> = 45; male, <i>n</i> = 55
No. of sedations	8	34
Clinical indications		
Epilepsy	9	40
Postsurgery for tumor or epilepsy	3	13
Headache	–	12
Malformation	–	5
Perinatal damage	1	2
Others	7	28

FLAIR-VISTA sequence with fat suppression shows abnormal brain T2 signal hyperintensities with better conspicuity than a 2D-FLAIR sequence on a single axial plane in children.

### MATERIALS AND METHODS

This prospective study was approved by the Meyer Children's Hospital of Florence institutional review board. Parental informed consent was obtained before inclusion of each subject in the study.

#### Selection of the Case Material

One hundred twenty brain MR imaging examinations not affected by motion artifacts performed over a 6-month period at a children's hospital (Meyer Children's Hospital of Florence) constituted the basis for the present study. They were performed in subjects 2–18 years of age for a variety of clinical indications (Table 1). Children younger than 2 years of age were excluded because of incomplete WM myelination, which implies a relative hyperintensity of the normal WM and hinders the visual perception of abnormally increased T2 signal.<sup>10,11</sup>

From the 120 MR imaging examinations, a neuroradiologist with 30 years of experience in brain MR imaging (M.M.) randomly selected 20 cases for a training set and 100 further cases for a test set. Overall, 42 MR imaging examinations included in the training (*n* = 8) or test (*n* = 34) sets were performed with the patients under sedation obtained by breathing vaporized sevoflurane through a mask.

#### MR Imaging Examination

All the MR imaging examinations were performed on a 3T system (Achieva, Release 2.6.3.7; Philips Healthcare, Best, the Netherlands) equipped with an 8-channel phased array head coil according to the following protocol: after localizers, volume T1-weighted gradient-echo 1-mm-thick images on a sagittal plane (TR = 8.2 ms, TE = 3.8 ms, flip angle = 8°, FOV = 256 × 256 mm, matrix = 252 × 220, 155–175 sections, NEX = 1, duration = 7 minutes); FLAIR-VISTA with fat suppression 1-mm-thick images on the sagittal plane (TR = 8000 ms, TE = 355 ms, TI = 2400 ms, variable [10°–180°] flip angle, echo-train length = 110, FOV = 256 × 256 mm, matrix = 232 × 232, 155–175 sections, NEX = 1, sensitivity encoding factor = 3.0, fat suppression with spectral selection attenuated inversion recovery, duration =

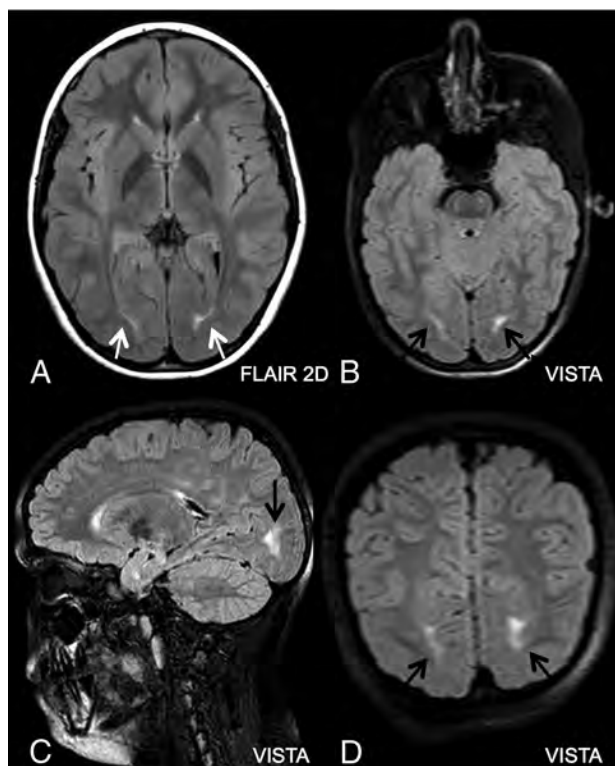


**FIG 1.** T2 hyperintensity of the WM adjacent to the occipital horns of the lateral ventricles (arrows) in a 9-year-old girl referred for MR imaging for episodes of hypersomnia. This is often observed as an isolated finding in children with otherwise normal MR imaging examination and was indicated in the training session to represent a borderline or normal finding to the 3 observers and not to be marked as abnormal T2 hyperintensity.

**Table 2: Expert neuroradiologist's evaluation of the training set**

MRI Diagnosis	Presence of Abnormal T2 Hyperintensity	
	No.	
None	4	–
WM UBOs	4	4
Leukoencephalopathy	2	2
Focal cortical dysplasia	1	1
Neuronal migration disorders	1	–
UBOs, neurofibromatosis type 1	1	1
Tuber in tuberous sclerosis	1	1
Multiple sclerosis plaques	1	1
Brain infarct	–	–
Intra-axial tumor	–	–
Postsurgical tumor evaluation	3	3
Myelination delay	1	1
Brain malformations	–	–
Others	1	1

**Note:**—UBOs indicates unidentified bright objects.

5 minutes 28 seconds); 2D-FLAIR 4-mm-thick images on the axial plane parallel to the bicommissural line (TR = 11,000 ms, TE = 122 ms, TI = 2800 ms, flip angle = 90°, echo-train length = 31, FOV = 256 × 256 mm, matrix = 292 × 198, 36 sections, NEX = 2, sensitivity encoding factor = 2.2, duration = 4 minutes 30 seconds); T2-weighted FSE 3-mm-thick images on the coronal plane parallel to the main axis of the cerebral aqueduct (TR = 3000 ms, TE = 80 ms, echo-train length = 15, FOV = 250 × 190 mm, matrix = 312 × 231, 40 sections, NEX = 3, duration = 4 minutes); T2\*-weighted gradient-echo 4-mm-thick images on

the axial plane parallel to the bicommissural line (TR = 1068 ms, TE = 16 ms, flip angle = 18°, FOV = 250 × 202 mm, matrix = 244 × 194, 24 sections, NEX = 1, duration = 3 minutes). In 28 (7 training set; 21 test set) MR imaging examinations, the volume T1-weighted gradient-echo sequence was repeated after intravenous administration of gadolinium chelates.

### Image Analyses

The expert neuroradiologist preliminarily evaluated the presence of CSF flow artifacts in the middle and posterior cranial fossa in a

**Table 3: Expert neuroradiologist's evaluation of the test set**

MRI Diagnosis	No.	Presence of Abnormal T2 Hyperintensity
None	28	–
WM UBOs	22	22
Leukoencephalopathy	9	9
Focal cortical dysplasia	4	4
Neuronal migration disorders	1	–
UBOs, neurofibromatosis type 1	2	2
Tuber in tuberous sclerosis	1	1
Multiple sclerosis plaques	–	–
Brain infarct	3	3
Intra-axial tumor	2	2
Postsurgical tumor evaluation	11	11
Myelination delay	2	2
Brain malformations	5	–
Others	10	10

**Note:**—UBOs indicates unidentified bright objects.

binary way (yes/no) on 2D-FLAIR and FLAIR-VISTA images. Three radiologists with at least 5 years of clinical experience in brain MR imaging in children (M.B., P.G., M.R.T.) were involved in image analyses. They had not previously evaluated the MR imaging examinations selected for the study. They participated in a joint session with the expert neuroradiologist on the 20 cases of the training set in which he illustrated the type of contrast in FLAIR-VISTA images with fat suppression on MR imaging examinations with normal and abnormal findings. In particular, he made them aware of the usually greater conspicuity in FLAIR-VISTA images with fat suppression of T2 hyperintense caps observed in the cerebral posterior periventricular WM corresponding to terminal zones of myelination (Fig 1).

Then the 3 observers separately assessed the 100 cases of the test set by using the hospital PACS. The shortest interval between the joint session and beginning of individual sessions was 1 week. Overall, the observers took a maximum of 1 month to complete individual readings of the 100 cases of the test set. They were blinded to the clinical indications for the MR imaging examinations and to the expert neuroradiologist's reports. In addition, most important, the observers were not informed of the study hypothesis, namely that FLAIR-VISTA could demonstrate brain lesions with more conspicuity compared with 2D-FLAIR. They had access to all source images obtained for each examination and to the 3-mm-thick images reconstructed on the axial (parallel to the bicommissural plane) and coronal planes (parallel to the brain stem) from both the source 1-mm-thick sagittal T1WI and FLAIR-VISTA with fat suppression images. No indication was given to the observers concerning the order or method of evaluation of the provided MR images. They were able to look at all images simultaneously on multiple panel monitors of a diagnostic workstation and were allowed to manipulate the image visualization by changing the gray-scale window width and level.

The observers were requested to perform 2 assessments: first, to judge in a binary way (yes/no) whether the FLAIR-VISTA or 2D-FLAIR demonstrated abnormal focal or diffuse T2 hyperintensities of the brain. If the observer identified such abnormalities in only 1 sequence, his or her judgment was considered negative for abnormal T2 hyperintensities. Second, in case they identified abnormal T2 hyperintensities on both sequences, they were to evaluate in which sequence the areas of signal changes were shown with better conspicuity or whether the conspicuity was equal.

### Statistical Analyses

Possible differences between the training and test sets were assessed with the Student *t* test for parametric variables

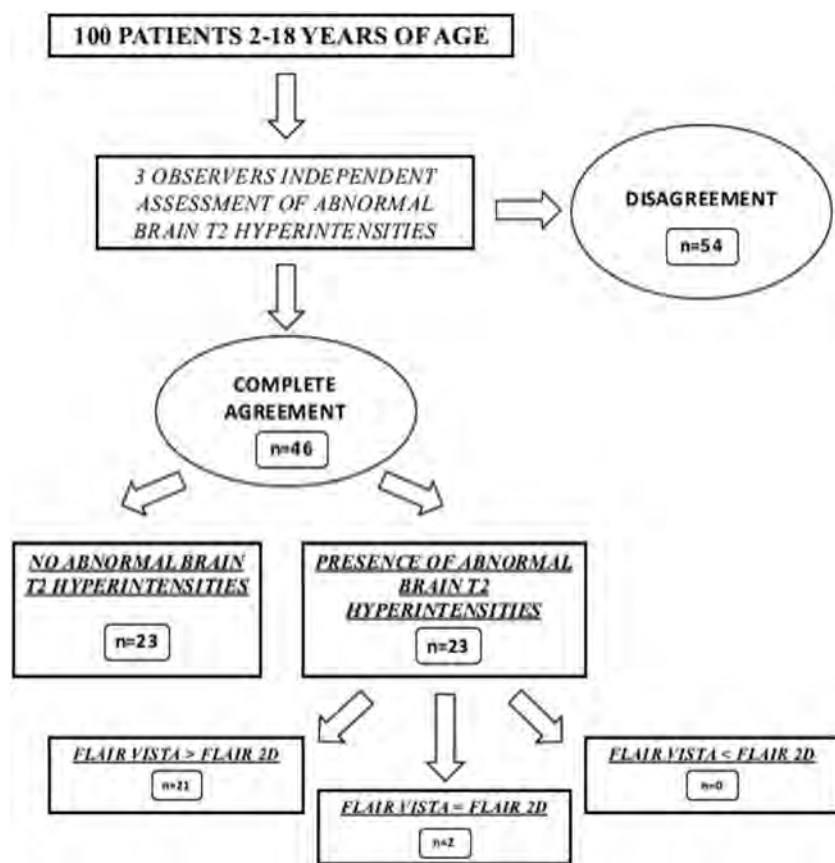


**FIG 2.** Results of the visual assessment by the 3 observers of T2 hyperintensities in 100 MR imaging examinations.

**Table 4: Weighted  $\kappa$  statistic assessment of the agreement of the 3 observers**

	Observers 1 and 2	Observers 1 and 3	Observers 2 and 3	Mean Value
Presence of abnormal T2 hyperintensities of the brain ( $n = 100$ )	0.69	0.49	0.64	0.61
Conspicuity of abnormal T2 hyperintensities in FLAIR-VISTA vs 2D-FLAIR ( $n = 23$ )	0.27	0.38	0.23	0.29

and with the  $\chi^2$  test for categorical variables. Statistical significance was set at  $P < .05$ . The interobserver agreement concerning the presence and conspicuity of abnormal T2 hyperintensities in the test set was evaluated by the linear-weighted Cohen  $\kappa$  statistic, which measures agreement beyond chance.<sup>12</sup> Cohen  $\kappa$  coefficient values are categorized into 5 levels of agreement: slight (0–0.2), fair (0.21–0.4), moderate (0.41–0.6), substantial (0.61–0.8), and almost perfect (0.81–1.0). We considered agreement of pairs of observers (A versus B, A versus C, and B versus C) and the overall mean of the results of the 3 pairs.

In particular, we first measured the agreement of the 3 observers in the entire 100 MR imaging examinations of the test set in judging the presence or lack of abnormal T2 hyperintensities. Then we measured the agreement in judging relative conspicuity of the abnormal T2 hyperintensities in the sample of MR imaging examinations in which all 3 observers recognized the presence of the abnormal T2 hyperintensities.

## RESULTS

The training set and test set were not significantly different for the patient demographic data, clinical indications, and number of MR imaging examinations of patients under sedation (Table 1). The expert neuroradiologist judged CSF flow artifacts to be present in 2D-FLAIR in 96 of 100 cases of the test set, but in FLAIR-VISTA, they were seen in only 2 cases. His assessment of 120 MR imaging examinations is summarized in Tables 2 and 3. In particular, he reported the presence of abnormal T2 hyperintensities in 66 of 100 examinations of the test set. In 5 patients of the test set who underwent an operation, pathologic diagnoses included type IB focal cortical dysplasia, type IIB focal cortical dysplasia, a cortical tuber in tuberous sclerosis, a primary neuroectodermal tumor, and recurrence of a dysembryoplastic neuroepithelial tumor.

Abnormal T2 hyperintensities of the brain were judged present in 61/100 FLAIR-VISTA images and 59/100 2D-FLAIR images by observer 1, in 71/100 FLAIR-VISTA images and 69/100 2D-FLAIR images by observer 2, and in 60/100 FLAIR-VISTA images and 62/100 2D-FLAIR images by observer 3.

Figure 2 shows the results of the visual assessment of the 100 MR imaging examinations of the test set by the 3 observers. Agreement about the presence or lack of abnormal T2 hyperintensities was achieved in 46 of 100 patients, whereas some disagreement occurred in 54 patients. In 23 patients, the radiologists all identified some abnormal brain T2 hyperintensities, and in 23, they all identified none. In 26 patients, 2 operators identified abnormal T2 hyperintensities, and one did not, and in 28, 1 operator only identified abnormal T2 hyperintensities.

Table 4 shows the results of the weighted  $\kappa$  statistics in the test set concerning agreement of the 3 observer pairs for the presence of abnormal T2 hyperintensities and for comparative evaluation

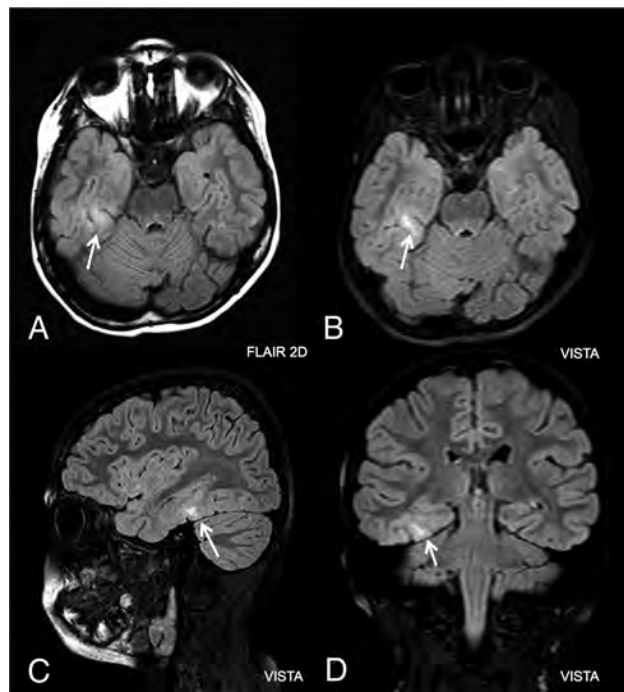


**FIG 3.** Abnormal focal T2 hyperintensity (arrows) consistent with focal cortical dysplasia type II in the right fusiform gyrus of a 10-year-old boy with partial epilepsy. All 3 observers judged that the abnormal T2 hyperintensity was more conspicuous in FLAIR-VISTA (B–D) than in axial 2D-FLAIR (A).

of the conspicuity of these signal changes in FLAIR-VISTA with fat suppression and in 2D-FLAIR.

The weighted  $\kappa$  statistics indicated that agreement for the presence of abnormal focal or diffuse T2 signal hyperintensities was “substantial” (mean, 0.61 for the 3 observers; range, 0.49–0.69 for the 3 observer pairs).

All 3 observers judged FLAIR-VISTA with fat suppression images as showing the abnormal T2 signal hyperintensities with better conspicuity than 2D-FLAIR in 21 of the 23 cases in which they identified abnormal T2 hyperintensities (Fig 3). The conspicuity was similar in 2 of 23 (Fig 4), and in no case was conspicuity better on 2D-FLAIR. The weighted  $\kappa$  statistics indicated that the 3 observers showed a “fair” (mean, 0.29; range, 0.23–0.38) agreement for the comparative evaluation of relative conspicuity of the abnormal T2 hyperintensities in the 23 cases.

Notably, in 21 of the 26 cases in which 2 observers identified abnormal focal T2 hyperintensities whereas the third operator did not, the abnormality was detected on VISTA-FLAIR but not on 2D-FLAIR (Fig 5).

## DISCUSSION

Since its introduction in the early 1990s, the 2D-FLAIR sequence has been added to or replaced 2D T2-weighted spin-echo se-

quences for the detection of abnormal T2 hyperintensities of the brain tissue.<sup>2</sup> Technologic developments, including multislab acquisition and variable flip angle radiofrequency excitation,<sup>13,14</sup> have made 3D-FLAIR sequences compatible with clinical use. Accordingly, 3D-FLAIR has found wide application for MR imaging evaluation of the adult brain in healthy subjects and in patients with a variety of diseases or tumors.<sup>14-17</sup> The lesser conspicuity of CSF flow artifacts in our study is in line with findings in previous reports.<sup>3-6</sup> So far, few studies have compared the capability of 3D-FLAIR (4 without<sup>6,18-20</sup> and 2 with fat suppression<sup>21,22</sup>) and

2D-FLAIR in identifying areas of abnormal T2 hyperintensities of the brain.<sup>6,18-22</sup>

Three of these studies compared the 2 sequences in revealing focal areas of abnormal T2 hyperintensities in the WM of adult patients with MS, and all concluded that 3D-FLAIR might replace 2D-FLAIR in clinical protocols for brain MR imaging of MS.<sup>19-21</sup> Instead, Kakeda et al<sup>6</sup> compared the 2 sequences in adult patients with a variety of diseases and conditions. Also supported by the analysis of the contrast ratio between the signal intensity of the lesion and normal GM or WM, they confirmed the general superiority of 3D-FLAIR. However they reported that leptomeningeal metastases and hippocampal sclerosis were more conspicuous in 2D-FLAIR and that the “ivy sign” in Moyamoya disease (diffuse leptomeningeal T2 hyperintensity, presumably reflecting slowed flow in superficial vessels involved in collateral circulation phenomena) was frequently obscured in 3D-FLAIR. Finally, 2 studies addressed the relative contribution of 3D-FLAIR without<sup>18</sup> or with<sup>22</sup> fat suppression versus 2D-FLAIR in evaluating adults and children with specialized protocols for focal cortical dysplasia. The studies reported conflicting results because 3D-FLAIR was judged superior to 2D-FLAIR in one study<sup>18</sup> and equal in the other study,<sup>22</sup> at least on visual qualitative analysis.

Our study partially differs from the above studies in 3 main aspects. First, we focused exclusively on a population of pediatric patients referred to a children’s hospital with heterogeneous clinical indications and MR imaging findings. Second, like Tschampa et al,<sup>22</sup> we implemented a FLAIR-VISTA sequence with fat suppression. Third, we used FLAIR-VISTA as a supplement to a general protocol and not to a specialized one for epilepsy. The substantial agreement of our 3 observers for the presence of areas of abnormal T2 hyperintensities in FLAIR-VISTA and 2D-FLAIR appears reasonable when one considers the above heterogeneities and that the observers were blinded to the clinical indications of the MR imaging examination. The latter choice was made to decrease the variable influence that such knowledge might have on the observers’ assessments.

Most areas of abnormal T2 hyperintensity in FLAIR sequences in our study were the focal nonspecific ones, commonly referred to as unidentified bright objects, which can have a number of underlying pathologic changes (microinfarct, gliosis, demyelination, and so forth).

In our opinion, the “fair” agreement of the 3 observers about the relative conspicuity of the abnormal T2 hyperintensities might reflect their having had no prior clinical experience with FLAIR-VISTA, whereas 2D-FLAIR has been part of the MR imaging brain protocol since the installation of the MR imaging system 7 years earlier.

Remarkably, in no case did the observers agree in judging the abnormal T2 hyperintensities more conspicuous on 2D-FLAIR than on FLAIR-VISTA. The possible partial discrepancy between our findings and those of Kakeda et al<sup>6</sup> can be explained by our having no case of

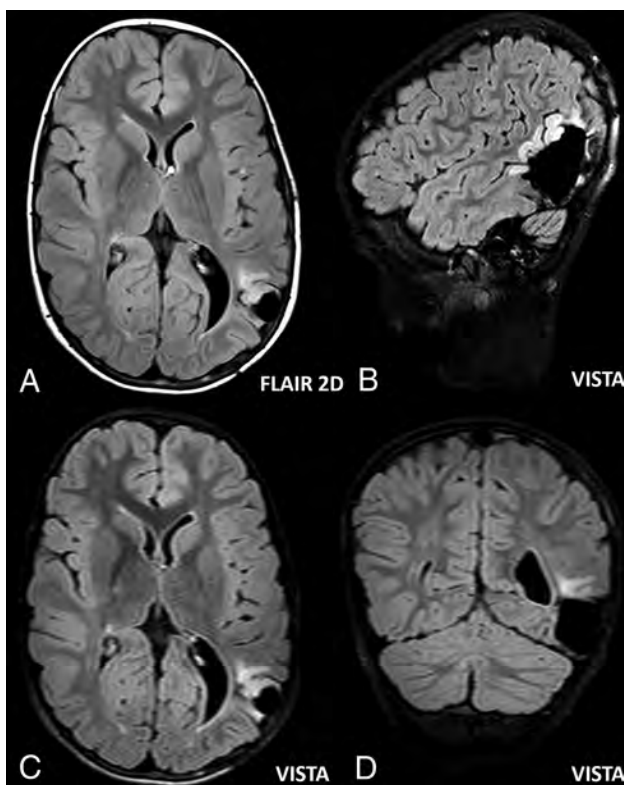


**FIG 4.** Abnormal focal T2 hyperintensity corresponding to pathologically verified recurrence of dysembryoplastic neuroepithelial tumor in the left parietal-occipital region of a 10-year-old boy. Two observers judged that the abnormal T2 hyperintensity was more conspicuous in FLAIR-VISTA (B–D) than in axial 2D-FLAIR (A), whereas 1 observer judged that the conspicuity was similar.

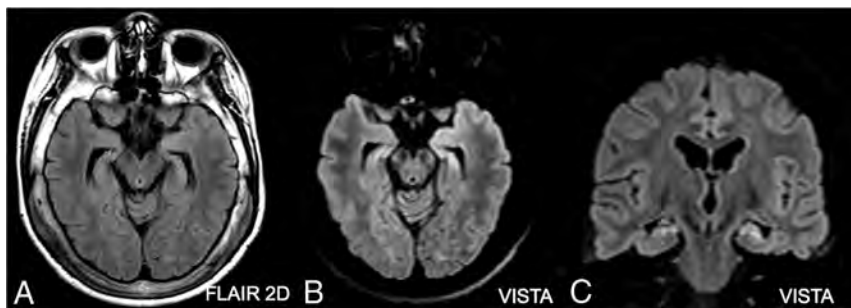


**FIG 5.** Abnormal focal T2 hyperintensity consistent with mesial temporal sclerosis in both hippocampi of a 13-year-old boy with partial epilepsy, which followed an acute encephalopathy of undefined etiology. The abnormal focal hyperintensity was judged to be present (and more conspicuous on FLAIR-VISTA) by 2 observers, whereas 1 observer did not report it. Note the marked diffuse T2 hyperintensity of the thickened skull in 2D-FLAIR (A), which is not present on axial (B) and coronal (C) reformatted images of FLAIR-VISTA with fat suppression.

leptomeningeal metastases or Moyamoya disease. However in the single case of hippocampal sclerosis in our series, 2 of 3 observers judged abnormal T2 hyperintensity of the mesial temporal lobe to be present on FLAIR-VISTA but not on 2D-FLAIR. In our opinion, the fat suppression adopted in our study but not in that of Kakeda et al<sup>6</sup> might have improved detection of this abnormality in our patients.

Notably, we compared a 3D-FLAIR sequence with sagittal source and axial and coronal reformatted images with a 2D-FLAIR sequence on a single axial plane. Although 2D-FLAIR images were obtained on the axial and coronal planes in a study comparing 3D-FLAIR and 2D-FLAIR in patients with focal cortical dysplasia,<sup>22</sup> this procedure entails a proportional increase of the acquisition time of the 2D sequence that definitely overcomes the small (18%) increase in the acquisition time of FLAIR-VISTA compared with a single 2D-FLAIR in our study.

We recognize the following limitations of our study: First, we compared FLAIR-VISTA with fat suppression with 2D-FLAIR without fat suppression. Although spectral presaturation of fat is also possible with 2D (spin-warp) acquisition schemes, these are more demanding for the magnet hardware compared with 3D acquisition schemes and imply an increase of sequence duration and generally entail a worse result in terms of homogeneity of fat suppression. Second, we compared visual assessment of FLAIR-VISTA and 2D-FLAIR, which is affected by the observer's experience and other variables, including room light and the observer's fatigue, which can compromise the interobserver reproducibility. Moreover, aiming to reproduce the conditions of current clinical work, observers had simultaneous access to the 2 types of images they were requested to evaluate for the presence and relative conspicuity of areas of abnormal T2 hyperintensities. Admittedly, after training, they could easily recognize the FLAIR-VISTA and the 2D-FLAIR images they were observing. These factors may have introduced biases that a different, more experimental, study setup could have overcome. Third, we focused on detection and comparative evaluation of FLAIR-VISTA with fat suppression and 2D-FLAIR for areas of abnormally increased T2 signal of the brain, whereas we skipped the evaluation of areas of abnormally decreased T2 signal of the brain and of leptomeningeal (extra-axial) lesions.

## CONCLUSIONS

FLAIR-VISTA with fat suppression shows abnormal T2 signal hyperintensities of brain gray and white matter with better conspicuity than the 2D-FLAIR sequence without fat suppression on a single axial plane in subjects 2–18 years of age examined for a variety of indications.

## REFERENCES

1. Barkhof F, Pouwels P, Watterjes M. **The holy grail in diagnostic neuroradiology: 3T or 3D?** *Eur Radiol* 2011;21:449–56 CrossRef Medline
2. De Coene B, Hanjal JV, Gatehouse P, et al. **MR of the brain using fluid-attenuated inversion recovery (FLAIR) pulse sequences.** *AJNR Am J Neuroradiol* 1992;13:1555–64 Medline
3. Kallmes D, Hui FK, Mugler JP 3rd. **Suppression of cerebrospinal fluid and blood flow artifacts in FLAIR MR imaging with a single-slab three-dimensional pulse sequence: initial experience.** *Radiology* 2001;221:251–55 CrossRef Medline
4. Naganawa S, Kawai H, Fakatsu H, et al. **High speed imaging at 3 Tesla: a technical and clinical review with an emphasis on whole-brain 3D imaging.** *Magn Reson Med Sci* 2004;3:177–87 CrossRef Medline
5. Lummel N, Schoepf V, Burke M, et al. **3D Fluid-attenuated inversion recovery imaging: reduced CSF artifacts and enhanced sensitivity and specificity for subarachnoid hemorrhage.** *AJNR Am J Neuroradiol* 2011;32:2054–60 CrossRef Medline
6. Kakeda S, Korogi Y, Hiai Y, et al. **Pitfalls of 3D brain imaging: a prospective comparison with 2D FLAIR.** *Acad Radiol* 2012;19:1225–32 CrossRef Medline
7. Frigon C, Shaw DW, Heckbert SR, et al. **Supplemental oxygen causes increased signal intensity in subarachnoid cerebrospinal fluid on brain FLAIR MR images obtained in children during general anesthesia.** *Radiology* 2004;233:51–55 CrossRef Medline
8. Ozcan U, Isik U, Ozpinar A, et al. **Assessment of sedated pediatric brain with 3D-FLAIR sequence at 3T MRI.** *Brain Dev* 2015;37:495–500 CrossRef Medline
9. Lavdas E, Tsougos I, Kogia S, et al. **T2 FLAIR artifacts at 3-T brain magnetic resonance imaging.** *Clin Imaging* 2014;38:85–90 CrossRef Medline
10. Murakami J, Weinberger E, Shaw DW. **Normal myelination of the pediatric brain imaged with fluid-attenuated inversion-recovery (FLAIR) MR imaging.** *AJNR Am J Neuroradiol* 1999;20:1406–11 Medline
11. Dubois J, Dehaene-Lambertz G, Kulikova S, et al. **The early development of brain white matter: a review of imaging studies in fetuses, newborns and infants.** *Neuroscience* 2014;276:48–71 CrossRef Medline
12. Cohen J. **Weighted kappa: nominal scale agreement with provision for scale disagreement or partial credit.** *Psychol Bull* 1968;70:213–20 CrossRef Medline
13. Mugler J. **Optimized three-dimensional fast-spin-echo MRI.** *J Magn Reson Imaging* 2014;39:745–67 CrossRef Medline
14. Naganawa S. **The technical and clinical features of 3D-FLAIR in neuroimaging.** *Magn Reson Med Sci* 2015;14:93–106 CrossRef Medline
15. Bink A, Schmitt M, Gaa J, et al. **Detection of lesion in multiple sclerosis by 2D FLAIR and single-slab 3D FLAIR sequences at 3.0 T: initial results.** *Eur Radiol* 2006;16:1104–10 CrossRef Medline
16. Kitajima M, Hirai T, Shigematsu Y, et al. **Comparison of 3D FLAIR, 2D FLAIR, and 2D T2-weighted MR imaging of brain stem anatomy.** *AJNR Am J Neuroradiol* 2012;33:922–27 CrossRef Medline
17. Yoshida A, Tha KK, Fujima N, et al. **Detection of brain metastases by 3-dimensional magnetic resonance imaging at 3 T: comparison between T1-weighted volume isotropic turbo spin echo acquisition and 3-dimensional T1-weighted fluid-attenuated inversion recovery imaging.** *J Comput Assist Tomogr* 2013;37:84–90 CrossRef Medline
18. Saini J, Singh A, Kesavadas C, et al. **Role of three-dimensional fluid attenuated inversion-recovery (3D FLAIR) and proton density magnetic resonance imaging for the detection and evaluation of lesion extent of focal cortical dysplasia in patients with refractory epilepsy.** *Acad Radiol* 2010;51:218–25 CrossRef Medline
19. Paniagua-Bravo A, Sánchez Hernández JJ, Ibáñez Sanz L, et al. **A comparative MRI study for white matter hyperintensities detection: 2D-FLAIR, FSE PD 2D, 3D FLAIR and FLAIR MIP.** *Br J Radiol* 2014;87:20130360 CrossRef Medline
20. Patzig M, Burke M, Brückmann H, et al. **Comparison of 3D cube FLAIR with 2D FLAIR for multiple sclerosis imaging at 3 Tesla.** *Rof* 2014;186:484–88 CrossRef Medline
21. Tan IL, Powels PJ, van Schijndel RA, et al. **Isotropic 3D fast FLAIR imaging of the brain in multiple sclerosis patients: initial experience.** *Eur Radiol* 2002;12:559–67 CrossRef Medline
22. Tschampa HJ, Urbach H, Malter M, et al. **Magnetic resonance imaging of focal cortical dysplasia: comparison of 3D and 2D fluid attenuated inversion recovery sequences at 3T.** *Epilepsy Res* 2015;16:8–14 CrossRef

# Prenatal Evaluation, Imaging Features, and Neurodevelopmental Outcome of Prenatally Diagnosed Periventricular Pseudocysts

S. Cooper, O. Bar-Yosef, M. Berkenstadt, C. Hoffmann, R. Achiron, and E. Katorza



## ABSTRACT

**BACKGROUND AND PURPOSE:** Periventricular pseudocysts are cystic cavities that lack the ependymal cell lining found in true cysts. The aim of this study was to characterize periventricular pseudocysts and related findings and their neurodevelopmental outcome.

**MATERIALS AND METHODS:** This was a retrospective study of periventricular pseudocysts detected prenatally on fetal MR imaging in 26 fetuses. The fetuses were divided into group A ( $n = 8$ ), which included cases with isolated periventricular pseudocysts, and group B ( $n = 18$ ), which included cases of periventricular pseudocysts with additional findings. Cases were further subdivided into connatal cysts and subependymal pseudocysts. Data collected included prenatal history, MR imaging features, sonographic follow-up, and neurodevelopmental outcome.

**RESULTS:** All cases in group A ( $n = 8$ ) had a normal outcome. In group B ( $n = 18$ ), 6 pregnancies were terminated and 2 had an abnormal outcome. Both cases with an abnormal outcome involved patients with subependymal pseudocysts. No significant association was found between the morphologic features on MR imaging and the neurodevelopmental outcome.

**CONCLUSIONS:** Neurodevelopmental outcome in cases of isolated periventricular pseudocysts detected prenatally appears to be normal. A detailed evaluation should be performed to rule out additional brain findings, chromosomal aberration, and fetal malformation. This evaluation should include the following: maternal TORCH status, detailed fetal sonographic anatomic evaluation, fetal echocardiogram, fetal brain MR imaging, amniocentesis and karyotyping/comparative genomic hybridization, and genetic counseling. Additional findings on MR imaging, including mild-to-moderate dilated ventricles, asymmetric ventricles, or T2 hyperintense signal in the white matter without other findings or major fetal abnormality, appear to be benign. Connatal cysts appear to be benign.

**ABBREVIATIONS:** CMV = cytomegalovirus; IUGR = intrauterine growth restriction; PVPC = periventricular pseudocysts; SEPC = subependymal pseudocysts; TOP = termination of pregnancy; US = ultrasound; TORCH = toxoplasmosis, rubella, cytomegalovirus, and herpes virus

Periventricular pseudocysts (PVPC) are cystic cavities that lack the ependymal cell lining found in true cysts.<sup>1</sup> They are found in 0.5%–5% of healthy term neonates by using transfontanellar sonography in the first days of life.<sup>2,3</sup> For a long time, periventricular leukomalacia and PVPC have been confused. Maligner et al<sup>4</sup> and Rademaker et al<sup>5</sup> differentiated PVPC, which are found below the external angle of the lateral ventri-

cles, from periventricular leukomalacia, which is located above it and has a different prognosis (Fig 1A).<sup>4</sup> PVPC occur in the germinal matrix during the time of its exponential development in the beginning of the second trimester and during its rapid lysis toward its end. Therefore, Rademaker et al<sup>5</sup> suggested that they should be referred to as “germinolytic cysts.” Epelman et al<sup>6</sup> further divided PVPC into connatal cysts, also known as frontal horn cysts, and subependymal pseudocysts (SEPC). Connatal cysts are located at the external angle, anterior to the foramina of Monro. SEPC are located posterior to the foramina of Monro (Fig 1B).<sup>6</sup>

There are 2 types of pathogenesis in the formation of PVPC: germinal matrix hemorrhage and germinolysis, which are associated with congenital infections,<sup>7–9</sup> metabolic disorders,<sup>10</sup> and chromosomal aberration.<sup>11</sup> Nevertheless, PVPC have been reported as isolated findings.<sup>4,11–13</sup>

There are scarce data regarding the neurodevelopmental outcome of infants with PVPC. The studies conducted are of

Received March 9, 2016; accepted after revision July 4.

From the Antenatal Diagnostic Unit (S.C., R.A., E.K.), Department of Obstetrics and Gynecology; Department of Pediatric Neurology (O.B.-Y.); The Danek Gertner Institute of Human Genetics (M.B.); and Department of Diagnostic Radiology (C.H.), Sheba Medical Center, Tel HaShomer, Ramat Gan, Israel; Affiliated with Sackler School of Medicine, Tel Aviv University, Tel Aviv, Israel.

Shiri Cooper and Omer Bar-Yosef contributed equally to this study.

Please address correspondence to Shiri Cooper, MD, Department of Obstetrics and Gynecology, Sheba Medical Center, Tel HaShomer, Ramat Gan 52621; e-mail: shirabe61@gmail.com

Indicates article with supplemental on-line tables.

<http://dx.doi.org/10.3174/ajnr.A4916>

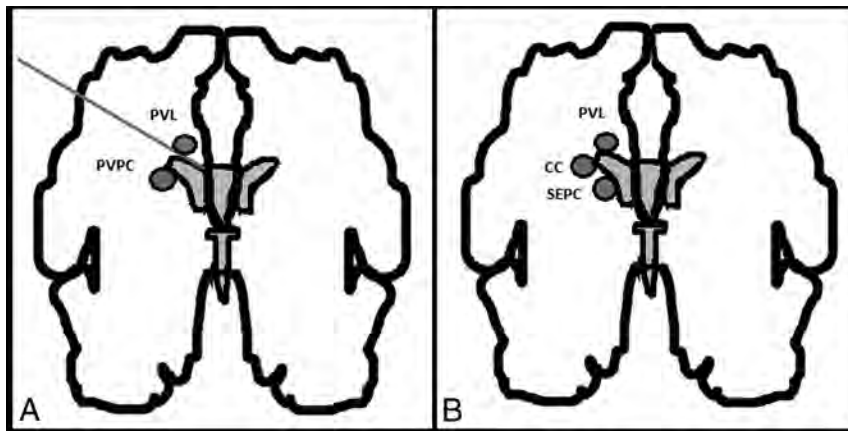


**FIG 1.** A, Schematic representation of the differential diagnosis between periventricular pseudocysts and periventricular leukomalacia. Originally published by Maligner et al.<sup>4</sup> B, Differential diagnosis between the cystic lesions seen in periventricular leukomalacia (PVL), connatal cysts (CC), and subependymal cysts (SC). Maligner et al.<sup>4</sup> original publication modified by Epelman et al.<sup>6</sup>

small cohorts and describe mostly neonates and premature infants. They have suggested that isolated PVPC have a good prognosis.<sup>4,12-16</sup>

The growing use of prenatal imaging such as fetal ultrasound (US) and MR imaging led to an increase in prenatal detection of PVPC. However, the significance of these findings is not well-established. Maligner et al<sup>4</sup> were the first to describe the characteristics and outcome of prenatally detected PVPC in 2002. Since then, only a few case reports have been added.<sup>17,18</sup> Recently, Esteban et al<sup>13</sup> described an association between SEPC morphologic features and clinical outcome. To our knowledge, the characteristics of connatal cysts and outcome were only described in neonates, and they are considered benign.<sup>5,12,19-25</sup>

The objectives of the present study were to determine whether findings in addition to PVPC affect the neurodevelopmental outcome, characterize PVPC-related factors, and describe the differences between connatal cysts and SEPC. The strength of this work is in the wide range of parameters recorded, including PVPC-related clinical prenatal and perinatal factors; morphologic characteristics of fetal MRI; and the long-term follow-up of the cases.

## MATERIALS AND METHODS

### Population and Setting

This was an observational retrospective study that included all pregnant women who underwent fetal brain MR imaging in which PVPC were detected at Sheba Medical Center, Israel, between 2011 and 2014.

Data obtained from the records include the following: maternal history (age, medical history, previous pregnancy outcome, and the presence of known risk factors associated with PVPC), abnormal pregnancy events, prenatal history (sex, prenatal testing, fetal echocardiogram, and TORCH [toxoplasmosis, rubella, cytomegalovirus, and herpes virus] serology), US and MR imaging features of PVPC, associated findings, perinatal history (gestational age, birth weight, Apgar score, and mode of delivery), sonographic follow-up, and clinical follow-up. Fetal cy-

tomegalovirus (CMV) infection was confirmed by amniocentesis.

Following genetic and parental counseling, termination of pregnancy (TOP) was performed in several cases. Postmortem examination and MR imaging were performed on the fetuses of patients who went through TOP in our institution.

To establish whether isolated PVPC have a better prognosis as suggested by several studies,<sup>4,12-16</sup> cases were divided into 2 groups (Fig 2):

- Group A (isolated PVPC): cases with PVPC as a single finding on MR imaging and with no additional fetal abnormalities such as intrauterine growth restriction (IUGR), fetal infection, abnormal fetal echocardiogram findings, or chromosomal aberration.
- Group B (nonisolated PVPC): cases with additional pathologic findings on fetal MR imaging, additional fetal abnormalities, or both.

Each group was further subdivided, according to the location of the PVPC, into connatal cysts and SEPC.

### Sonography

Patients were referred to our institution when diagnosed by an US structural survey performed by specialized gynecologists or as part of the routine pregnancy follow-up. Additional focused US examinations were performed in most patients by a dedicated fetal sonographer by using a multiplanar approach (4 coronal and 3 sagittal planes) to evaluate the brain selectively and precisely according to the International Society of Ultrasound in Obstetrics and Gynecology guidelines.<sup>26</sup>

### MR Imaging

All patients were referred for fetal brain MR imaging due to a specific suspected anomaly demonstrated by US or evidence of maternal CMV or toxoplasma infection. The preferred timing for fetal brain MR imaging at our institution is in the 32nd week of gestation due to the ability to assess brain maturation (sulcation and gyration) and parenchyma, in addition to a comprehensive brain structure scan.<sup>27,28</sup> MR imaging was performed for the following reasons: suspected PVPC on US ( $n = 13$ ), dilated or asymmetric lateral ventricles on US ( $n = 3$ ), suspected PVPC and dilated or asymmetric lateral ventricles on US ( $n = 3$ ), asymmetric lateral ventricles with multiple extracerebral malformations ( $n = 1$ ), maternal infection ( $n = 4$ ), follow-up after fetoscopic laser coagulation in twin-to-twin transfusion syndrome ( $n = 1$ ), and IUGR with a previous child with white matter disease ( $n = 1$ ).

Fetal MR imaging was performed and evaluated by an obstetrician who specializes in fetal US and MR imaging (E.K.), an expert MR imaging neuroradiologist (C.H.), and an experienced pediatric neurologist (O.B.-Y.) in a group analysis. A 1.5T MR imaging system (Optima 1.5T; GE Healthcare, Milwaukee, Wisconsin) was used. Single-shot fast spin-echo T2-weighted se-

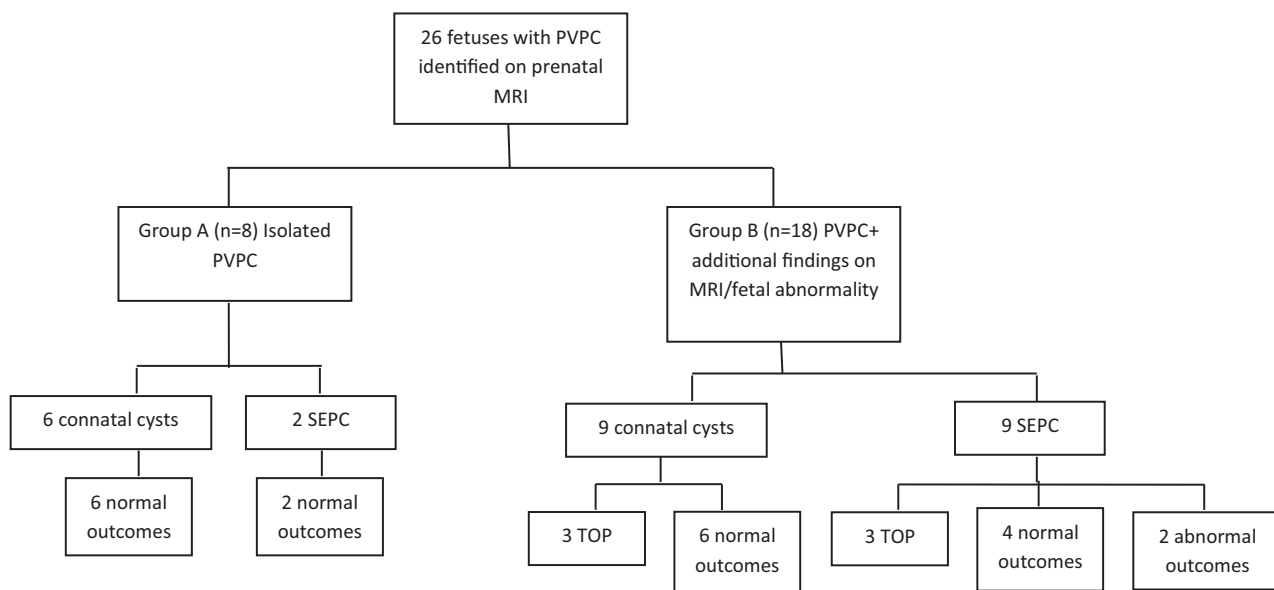


**FIG 2.** Flowchart illustrating the study design and outcome. Cases are divided to 2 groups: fetuses in group A had only PVPC on MR imaging, while fetuses on group B had additional findings on MR imaging or fetal abnormality. Fetal abnormality is defined as the presence of fetal infection, chromosomal abnormality, IUGR, abnormal echocardiogram findings, or other fetal malformation. The groups were further subdivided into connatal cysts or subependymal pseudocysts.

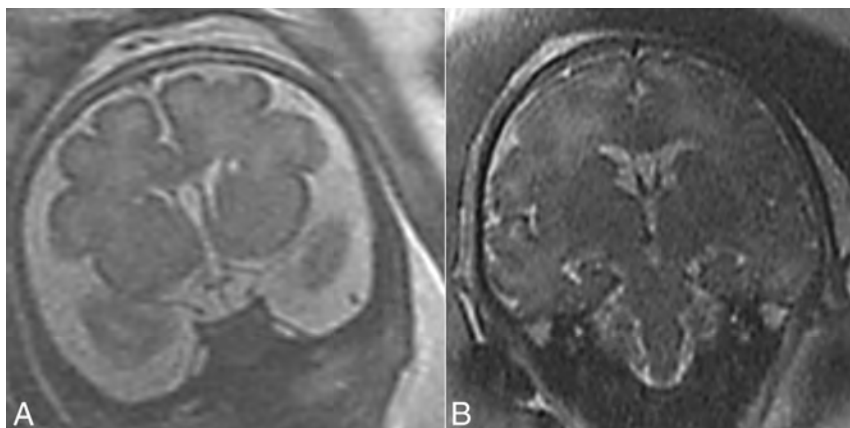


**FIG 3.** T2 MR imaging coronal view. A, Case 5, bilateral connatal cysts located at the external angle, anterior to the foramina of Monro. B, Case 17, bilateral subependymal pseudocysts located posterior to the foramina of Monro.

quences in 3 orthogonal planes were used with section thicknesses of 3–4 mm, no gap, and a flexible coil (8-channel cardiac coil). The FOV was determined by the size of the fetal head, 24 cm for smaller fetuses and up to 30 cm for larger ones. Other parameters were a matrix of 320/224, TE of 90 ms, and TR of 1298 ms. The fast spoiled gradient-echo T1 sequence was performed only in the axial plane with a larger FOV of 40 cm, 4-mm section thickness, 0.5-mm gap, a TR of 160 ms, and a TE of 2.3 ms.

Mildly dilated ventricles were defined as an atrial measurement of 10–12 mm, and moderately dilated ventricles, as 13–15 mm.<sup>29</sup>

#### **PVPC Imaging Features**

PVPC were defined according to Malinger et al<sup>4</sup> (Fig 1A) and were subdivided into 2 groups: connatal cysts and SEPC according to Epelman et al (Figs 1A and 3).<sup>6</sup>

Features and morphology of PVPC were described according to Esteban et al<sup>13</sup> and included the following: uni-/bilaterality,

uni-/multilocularity, and size and anatomic location in relation to the frontal, temporal, and occipital horns and the caudothalamic notch. Morphology features included the anteroposterior diameter and height of the pseudocysts that were evaluated on parasagittal sections and the shape and margins of the PVPC. PVPC were considered atypical when they showed ill-defined margins, were square (as opposed to oval), or had a height greater than the anteroposterior diameter.

#### **Neurodevelopmental Outcome**

Children were evaluated by using Vineland II Adaptive Behavior Scale,<sup>30</sup> which examines 4 areas of development:

communication, daily living skills, socialization, and motor skills. The score derived from this instrument has a mean of  $100 \pm 15$ . The published Israeli version of the Vineland II Adaptive Behavior Scale was administered, but no Israeli norms are available for the full age range. Because there was no reason to believe that Israeli and US children would develop mental and motor skills differently, we used US norms. Scores of children were considered abnormal if the standard score was  $<70$ . The mean age of children evaluated by using the Vineland II Adaptive Behavior Scale was  $2.07 \pm 0.86$  years.

In addition, records of neurologic clinical follow-up were collected retrospectively.

#### **Statistical Analysis**

The Fisher exact test was used for categorical variables, and a *t* test, for continuous variables. The data were analyzed by using

GraphPad QuickCalcs software (GraphPad Software, San Diego, California).

### Ethics Approval

The research was approved by the hospital research ethics board.

## RESULTS

### Population

Between 2011 and 2014, 1849 patients underwent a fetal brain MR imaging examination due to brain anomalies detected on fetal US and maternal TORCH infection. In 26 cases (1.41%), fetal PVPC were detected. TORCH serology was documented for 23/26 patients. Amniocentesis and karyotyping were performed in 14/26 patients. None of the patients were known to have a drug addiction or were documented as HIV-positive. The pregnancy and neonatal characteristics are described in Table 1. Abnormal preg-

nancy events included twin-to-twin transfusion syndrome with laser coagulation treatment and fetal reduction (case 5) and TIA during the pregnancy (case 15). There was no apparent difference in the incidence between male and female fetuses. Seven fetuses (26.9%) had additional fetal abnormalities: Three had IUGR, 2 had fetal CMV infection, 1 had chromosomal aberration, and 1 had IUGR in addition to chromosomal aberration and a ventricular septal defect detected on echocardiography. The chromosomal aberrations found included a 1P36 microdeletion and a translocation in chromosomes 11 and 22 (Emanuel syndrome; Online Mendelian Inheritance in Man No. 609029; <http://omim.org/>). The median birth gestational age was 38 weeks (range, 35–41 weeks), and the median birth weight was 3210 g (range, 2445–4060 g).

Termination of pregnancy was performed in 6 cases: Two had fetal CMV infection, 2 had porencephalic cysts, and 2 had PVPC with additional abnormal MR imaging findings. Four patients went through TOP in our institution; 3 of them had a postmortem examination and postmortem MR imaging. One patient underwent a fetal reduction in a twin pregnancy; as a result, no postmortem examination was performed. Characteristics of pregnancy and MR imaging data of patients who underwent TOP are described in On-line Table 1.

### Imaging Findings

Five (19.2%) cases of PVPC were not identified on US examination and were diagnosed only on MR imaging. The mean gestational age at MR imaging diagnosis was  $33.4 \pm 2.6$  weeks.

### Morphologic Features of PVPC on MR Imaging

Fifteen cases had connatal cysts and 11 cases had SEPC.

PVPC were bilateral in 24 cases (92.3%), all of which were multilocular. Mean PVPC height was  $5.36 \pm 0.89$  mm, and mean anteroposterior diameter was  $8.71 \pm 2.46$  mm. In 25 cases (96.1%), PVPC were located along the frontal horns, while in only 1 case were they located along the frontal and occipital horns. In 4 cases (15.4%), PVPC were extended posterior to the caudothalamic notch. One case (3.84%) had an atypical morphology. MR imaging morphologic features subdivided into connatal cysts and SEPC are described in Table 2.

Sixteen cases from group B had additional MR imaging findings, including asymmetric lateral ventricles with or without dilation ( $n = 5$ ), T2 hyperintense signal in the white matter ( $n = 2$ ), a combination of asymmetric or dilated lateral ventricles and T2 hyperintense signal in the white matter ( $n = 4$ ), mildly dilated lateral ventricles with evidence of GM bleeding ( $n = 1$ ), porencephalic cyst ( $n = 2$ ), a small cerebellum and an abnormal structure of the fourth ventricle ( $n = 1$ ), and asymmetric lateral ventricles in addition to T2 hyperintense signal in the white matter and an abnormal structure of the fourth ventricle ( $n = 1$ ).

Two cases in group B did not have additional findings on MR imaging. However, they had fetal abnormalities, including fetal CMV infection and IUGR.

**Table 1: Main population, neonatal, and delivery characteristics (n = 26)<sup>a</sup>**

Characteristics	
Pregnancy and maternal	
Maternal age (yr)	32.5 (21–42)
In vitro fertilization	3/26 (11.5%)
Multiple pregnancies	2/26 (7.7%)
Maternal infection	5/26 (19.2%)
CMV	4/26 (15.3%)
Toxoplasma	1/26 (3.8%)
Maternal medical treatment	5/26 (19.2%)
Maternal hypercoagulable disorder	4/26 (15.3%)
TOP	6/26 (23.1%)
Fetal and neonatal	
Male/female ratio (15:11)	1.4:1
Fetal abnormalities	
IUGR	4/26 (15.4%)
CMV infection	2/26 (7.7%)
Chromosomal aberration	2/26 (7.7%)
Abnormal fetal echocardiogram findings	1/26 (3.8%)
GA at MRI diagnosis (wk)	33 (29–38)
Birth GA (wk)	38 (35–41)
BW (g)	3210 (2445–4060)
Apgar score	
At 1 min	9 (8–9)
At 5 min	10 (8–10)
Mode of delivery (n = 20)	
Vaginal delivery	11/20 (55%)
Cesarean delivery	7/20 (35%)
Assisted vaginal delivery	2/20 (10%)

**Note:**—GA indicates gestational age, BW, birth weight.

<sup>a</sup> Data are expressed as median (range) or number (percentage).

**Table 2: MRI morphologic features and neurodevelopmental outcome of connatal cysts and subependymal pseudocysts**

MRI Morphologic Feature	Connatal Cysts	SEPC	P Value
Bilateral (No.)	15/15 (100%)	9/11 (82%)	.17
Multilocular (No.)	14/15 (93.3%)	10/11 (91%)	1.00
Mean height	$5.17 \pm 1.03$	$5.61 \pm 0.63$	.22
Mean AP diameter	$8.53 \pm 2.76$	$8.97 \pm 2.10$	.65
Near the occipital horns (No.)	0	1/11 (9%)	.42
Posterior to the caudothalamic notch (No.)	0	4/11 (36%)	.02
Atypical morphology (No.)	1/15 (6.6%)	0	.42
Abnormal neurodevelopmental outcome (No.)	0	2/11 (18%)	.15
TOP (No.)	3/15 (20%)	3/11 (27%)	—

**Note:**—AP indicates anteroposterior.

### Postnatal Sonographic Follow-Up

Postnatal sonographic follow-up was performed in 13/20 neonates (65%). The mean follow-up was  $3.32 \pm 2.51$  months. In 4/13 (30.7%) neonates, PVPC did not appear on an US performed during the first 3 days of life. In 8/13 (61.5%) neonates, the PVPC resolved at up to 8 months of age. In 1 neonate, PVPC were demonstrated on the first day of life with no other sonographic follow-up.

### Neurodevelopmental Outcome

Group A included 8 cases (On-line Table 2), all of which had a normal outcome. Group B included 18 cases (On-line Tables 3 and 4): 6 pregnancies were terminated (On-line Table 1), 10 had a normal outcome, and 2 had an abnormal outcome (Fig 2):

- Case 19 was 2 years 2 months of age at the time of the study and was evaluated by using the Vineland II Adaptive Behavior Scale. His score was 58, and he had a low adaptive level. He had a low standard score in all 4 areas of development. He also had vision problems and seizures.
- Case 20 was 1 year 9 months of age at the time of the study and was evaluated by using the Vineland II Adaptive Behavior Scale. His score was 63, and he had a low adaptive level. He had a low standard score in all 4 areas of development and was diagnosed postnatally with Emanuel syndrome (Online Mendelian Inheritance in Man, No. 609029).

The Vineland II adaptive behavior composite standard scores are presented in On-line Table 5.

### Morphologic Features of PVPC on MR Imaging and Neurodevelopmental Outcome

Laterality and locularity of PVPC were not significantly associated with an abnormal outcome ( $P = 1$ ,  $P = 1$ , respectively; Fisher exact test). Mean height and mean anteroposterior diameter of PVPC were not significantly different between cases with normal and abnormal findings ( $P = .71$ ,  $P = .31$ , respectively;  $t$  test) or between groups A and B ( $P = .32$ ,  $P = .34$ , respectively;  $t$  test). The association between occipital horn location and an abnormal outcome was not significant ( $P = .1$ , Fisher exact test). No significant association was found between the relation to the caudothalamic notch and an abnormal outcome ( $P = .36$ , Fisher exact test).

Eighty percent of the cases in the connatal cyst (12/15) subgroup had a normal outcome; the remaining 20% (3/15) underwent TOP. In the SEPC subgroup, only 55% of the cases (6/11) had a normal outcome, 18% (2/11) had an abnormal outcome, and 27% (3/11) underwent TOP. The association between PVPC subtype (connatal versus SEPC) and an abnormal outcome showed a trend but was not statistically significant ( $P = .15$ , Fisher exact test).

## DISCUSSION

The aim of this study was to describe characteristics of prenatally diagnosed PVPC and additional findings and to determine their association with neurodevelopmental outcome. In the literature, PVPC have been associated with a variable outcome. Most of the studies reported a good neurodevelopmental outcome in the

presence of isolated PVPC.<sup>4,11-16</sup> Makhoul et al,<sup>11</sup> in a meta-analysis of the literature on infants, concluded that in the absence of additional factors, including IUGR, fetal infections, malformations, and chromosomal aberrations or persistence of PVPC, a favorable outcome is expected. Cevey-Macherel et al<sup>16</sup> described the biggest cohort, which included 74 neonates. They concluded that isolated PVPC are associated with normal neurodevelopment and suggested that a neurologic examination at birth is a good outcome predictor. There are scarce data of prenatally diagnosed PVPC. Malinger et al<sup>4</sup> described 9 cases of prenatally detected PVPC, of which 5 were isolated findings. One of those underwent TOP, and the other 4 were reported to have normal neurodevelopmental outcome. Esteban et al<sup>13</sup> found that prenatal cases with isolated PVPC had a normal outcome. In accordance with the literature, all of the cases with isolated PVPC in our study, regardless of their subtype (connatal versus SEPC), had a normal neurodevelopment.

Two cases in the group of nonisolated PVPC had an abnormal outcome with developmental delay. In both cases, the PVPC subtype was SEPC, and both had additional findings on MR imaging and chromosomal aberrations.

Evaluation of the nonisolated PVPC with a normal outcome group ( $n = 10$ ) revealed 5 cases with asymmetric lateral ventricles with or without mild-to-moderate ventriculomegaly; 3 cases with T2 hyperintense signal in the white matter; and 2 cases with both characteristics, one of them with an additional abnormal structure of the fourth ventricle. These findings might suggest that the combination of PVPC with mildly or moderately dilated or asymmetric lateral ventricles or with T2 hyperintense signal in the white matter is benign. The outcome of asymmetric lateral ventricles detected prenatally seems to be benign, but it is not well-established because there are very limited data.<sup>31-33</sup> Mild isolated lateral ventriculomegaly is associated with a good outcome.<sup>34</sup> To our knowledge, the significance of an isolated T2 hyperintense signal in the white matter detected prenatally is yet to be determined. Further investigation with a larger series is needed to establish the significance of these findings.

In the literature, several studies suggested an association between the morphologic features of PVPC and the etiology. Bilateral and multilobular PVPC were associated with an etiology that involves >1 part of the brain, such as viral infection or genetic anomalies rather than a focal cerebrovascular insult.<sup>14,20,35,36</sup> However, in accordance with our findings, Cevey-Macherel et al<sup>16</sup> and Esteban et al<sup>13</sup> found no association between laterality and those etiologies.

Esteban et al<sup>13</sup> suggested that further investigations should be performed when the great axis of the cyst is  $\geq 9$  mm, when PVPC face the temporal horns, when PVPC are located posterior to the caudothalamic notch, and in the presence of PVPC with atypical morphology. In our study, no association was found between the size of PVPC and their location in relation to the caudothalamic notch and adverse outcome. We hypothesized that the different timing of the occurrence of PVPC explains the differences between our study and that of Esteban et al.<sup>13</sup> The occurrence of PVPC in the germinal matrix before the initiation of its lysis (26 weeks) or after could have an effect on morphology and outcome. This hypothesis was not supported by our data

because the characteristics of PVPC and neurodevelopmental outcome were equally distributed over the gestational age at diagnosis.

PVPC in the occipital horns were associated with CMV infection in the literature.<sup>37</sup> The 1 case with PVPC in the occipital horns in our study had CMV infection. The only case with atypical PVPC morphology underwent TOP.

Studies regarding connatal cysts, also known as frontal horn cysts, suggest that they are benign,<sup>5,12,15,19-24</sup> but the number of cases described is very limited. Unger et al,<sup>25</sup> in their review of the literature, found 87 cases of connatal cysts reported so far. From those cases, 49 (56%) had a normal outcome, 21 had an abnormal outcome, and 17 were lost to follow-up. In our study, all cases with connatal cysts had a normal outcome.

In this study, 6 cases underwent TOP. At present, there are no established indications for TOP when PVPC are diagnosed. The traditional approach to CMV in pregnancy is to consider termination of pregnancy in cases of viral transfer to the fetus. However, recent studies suggest that normal fetal imaging findings rule out almost entirely the presence of any major neurologic damage other than varying degrees of hearing impairment and minor neurologic sequelae.<sup>38,39</sup> Isolated findings such as PVPC were suggested to have a better prognosis,<sup>37,40</sup> but this statement is not well-established. In our study, 2 cases with CMV infection underwent TOP at another institution. The remaining 2 cases had normal outcome. This should raise the question of whether TOP is justified in those cases with CMV or PVPC as an isolated finding. Further studies are needed to resolve this question. Within the limits of this study, we suggest that TOP should be considered only when PVPC are part of a major brain anomaly or when significant fetal malformation or genetic abnormalities exist. When PVPC are detected on US, the following evaluations should be made: maternal TORCH status, detailed fetal sonographic anatomic evaluation, fetal echocardiogram, fetal brain MR imaging, amniocentesis, and karyotyping/comparative genomic hybridization, and genetic counseling.

The strength of our study is by adding to the limited data of prenatally detected PVPC and by its relatively large number of cases ( $n = 26$ ) and high follow-up rate ( $n = 20$ ). Moreover, the patients in this study were extensively evaluated for additional findings in the prenatal period. Twenty-three patients (88.5%) had TORCH serologies, 17 patients (65.4%) had a fetal echocardiogram, 15 patients (57.7%) had amniocentesis with karyotyping, and 7 patients (26.9%) had comparative genomic hybridization testing.

## CONCLUSIONS

Neurodevelopmental outcome in cases of isolated PVPC detected prenatally was normal. Additional findings on MR imaging, including mild-to-moderate dilated ventricles, asymmetric ventricles, or T2 hyperintense signal in the white matter without other findings or major fetal abnormality, appear to be benign. Associated fetal abnormalities may have a poor outcome. Connatal cysts appear to have a better prognosis than SEPC. Further large prospective research is needed to confirm our findings.

## REFERENCES

1. Larroche JC. **Sub-ependymal pseudo-cysts in the newborn.** *Biol Neonate* 1972;21:170–83 CrossRef Medline
2. Shen EY, Huang FY. **Subependymal cysts in normal neonates.** *Arch Dis Child* 1985;60:1072–74 CrossRef Medline
3. Heibel M, Heber R, Bechinger D, et al. **Early diagnosis of perinatal cerebral lesions in apparently normal full-term newborns by ultrasound of the brain.** *Neuroradiology* 1993;35:85–91 CrossRef Medline
4. Malinger G, Lev D, Ben Sira L, et al. **Congenital periventricular pseudocysts: prenatal sonographic appearance and clinical implications.** *Ultrasound Obstet Gynecol* 2002;20:447–51 CrossRef Medline
5. Rademaker KJ, De Vries LS, Barth PG. **Subependymal pseudocysts: ultrasound diagnosis and findings at follow-up.** *Acta Paediatr* 1993; 82:394–99 CrossRef Medline
6. Epelman M, Daneman A, Blaser SI, et al. **Differential diagnosis of intracranial cystic lesions at head US: correlation with CT and MR imaging.** *Radiographics* 2006;26:173–96 CrossRef Medline
7. Stadlan EM, Sung JG. **Congenital rubella encephalopathy.** *J Neuropathol Exp Neurol* 1967;26:115 CrossRef
8. Gilles F. **Congenital rubella encephalopathy.** *J Neuropathol Exp Neurol* 1967;26:116
9. Bale JF Jr, Sato Y, Eisert D. **Progressive postnatal subependymal necrosis in an infant with congenital cytomegalovirus infection.** *Paediatr Neurol* 1986;2:367–70 CrossRef
10. Russel IM, van Sonderen L, van Straaten HL, et al. **Subependymal germinolytic cysts in Zellweger syndrome.** *Pediatr Radiol* 1995;25: 254–55 CrossRef Medline
11. Makhoul IR, Zmora O, Tamir A, et al. **Congenital subependymal pseudocysts: own data and meta-analysis of the literature.** *Isr Med Assoc J* 2001;3:178–83 Medline
12. Zorzi C, Angonese I. **Subependymal pseudocysts in the neonate.** *Eur J Pediatr* 1989;148:462–64 CrossRef Medline
13. Esteban H, Blondiaux E, Audureau E, et al. **Prenatal features of isolated subependymal pseudocysts associated with adverse pregnancy outcome.** *Ultrasound Obstet Gynecol* 2015;46:678–87 CrossRef Medline
14. Larcos G, Gruenewald SM, Lui K. **Neonatal subependymal cysts detected by sonography: prevalence, sonographic findings, and clinical significance.** *Am J Roentgenol* 1994;162:953–56 CrossRef Medline
15. Ramenghi LA, Domizio S, Quartulli L, et al. **Prenatal pseudocysts of the germinal matrix in preterm infants.** *J Clin Ultrasound* 1997;25: 169–73 Medline
16. Cevey-Macherel M, Forcada Guex M, Bickle Graz M, et al. **Neurodevelopment outcome of newborns with cerebral subependymal pseudocysts at 18 and 46 months: a prospective study.** *Arch Dis Child* 2013;98:497–502 CrossRef Medline
17. Bats AS, Molho M, Senat MV, et al. **Subependymal pseudocysts in the fetal brain: prenatal diagnosis of two cases and review of the literature.** *Ultrasound Obstet Gynecol* 2002;20:502–05 CrossRef Medline
18. Zoppi MA, Luculano A, Peltz MT, et al. **Prenatal detection of periventricular pseudocysts by ultrasound: diagnosis and outcome.** *Case Reports in Perinatal Medicine* 2012;1:75–78 CrossRef
19. Chang CL, Chiu NC, Ho CS, et al. **Frontal horn cysts in normal neonates.** *Brain Dev* 2006;28:426–30 CrossRef Medline
20. Lu JH, Emons D, Kowalewski S. **Connatal periventricular pseudocysts in the neonate.** *Pediatr Radiol* 1992;22:55–58 CrossRef Medline
21. Pal BR, Preston PR, Morgan ME, et al. **Frontal horn thin walled cysts in preterm neonates are benign.** *Arch Dis Child Fetal Neonatal Ed* 2001;85:F187–93 CrossRef Medline
22. Sudakoff GS, Mitchell DG, Stanley C, et al. **Frontal periventricular cysts on the first day of life: a one-year clinical follow up and its significance.** *J Ultrasound Med* 1991;10:25–30 Medline
23. Thun-Hohenstein L, Forster I, Künzle C, et al. **Transient bifrontal solitary periventricular cysts in term neonates.** *Neuroradiology* 1994;36:241–44 CrossRef Medline
24. Wong F, Fraser S, Kelly E, et al. **Clinical significance of isolated para-**

- ventricular cysts on cranial ultrasonography. *J Paediatr Child Health* 2004;40:552–55 CrossRef Medline
25. Unger S, Salem S, Wylie L, et al. **Newborn frontal horn cysts: cause for concern?** *J Perinatol* 2011;31:98–103 CrossRef Medline
  26. International Society of Ultrasound in Obstetrics & Gynecology Education Committee. **Sonographic examination of the fetal central nervous system: guidelines for performing the 'basic examination' and the 'fetal neurosonogram.'** *Ultrasound Obstet Gynecol* 2007;29:109–16 CrossRef Medline
  27. Salomon LJ, Garel C. **Magnetic resonance imaging examination of the fetal brain.** *Ultrasound Obstet Gynecol* 2007;30:1019–32 CrossRef Medline
  28. Vazquez E, Mayolas N, Delgado I, et al. **Fetal neuroimaging: US and MRI.** *Pediatr Radiol* 2009;39(suppl 3):422–35 CrossRef Medline
  29. Signorelli M, Tiberti A, Valseriati D, et al. **Width of the fetal lateral ventricular atrium between 10 and 12 mm: a simple variation of the norm?** *Ultrasound Obstet Gynecol* 2004;23:14–18 CrossRef Medline
  30. Sparrow SS, Cicchetti VD, Balla AD. *Vineland Adaptive Behavior Scales*. 2nd ed. Circle Pines: American Guidance Service; 2005
  31. Sadan S, Malinger G, Schweiger A, et al. **Neuropsychological outcome of children with asymmetric ventricles or unilateral mild ventriculomegaly identified in utero.** *BJOG* 2007;114:596–602 CrossRef Medline
  32. Achiron R, Yagel S, Rotstein Z, et al. **Cerebral lateral ventricular asymmetry: is this a normal ultrasonographic finding in the fetal brain?** *Obstet Gynecol* 1997;89:233–37 CrossRef Medline
  33. Atad-Rapoport M, Schweiger A, Lev D, et al. **Neuropsychological follow-up at school age of children with asymmetric ventricles or unilateral ventriculomegaly identified in utero.** *BJOG* 2015;122:932–38 CrossRef Medline
  34. Pagani G, Thilaganathan B, Prefumo F. **Neurodevelopmental outcome in isolated mild fetal ventriculomegaly: systematic review and meta-analysis.** *Ultrasound Obstet Gynecol* 2014;44:254–60 CrossRef Medline
  35. Beltinger C, Saule H. **Sonography of subependymal cysts in congenital rubella syndrome.** *Eur J Pediatr* 1988;148:206–07 CrossRef Medline
  36. Alvarez JF, Amess PN, Gandhi RS, et al. **Diagnostic value of subependymal pseudocysts and choroid plexus cysts on neonatal cerebral ultrasound: a meta-analysis.** *Arch Dis Child Fetal Neonatal Ed* 2009;94:F443–46 CrossRef Medline
  37. Malinger G, Lev D, Lerman-Sagie T. **Imaging of fetal cytomegalovirus infection.** *Fetal Diagn Ther* 2011;29:117–26 CrossRef Medline
  38. Lipitz S, Yinon Y, Malinger G, et al. **Risk of cytomegalovirus-associated sequelae in relation to time of infection and findings on prenatal imaging.** *Ultrasound Obstet Gynecol* 2013;41:508–14 CrossRef Medline
  39. Amir J, Atias J, Linder N, et al. **Follow-up of infants with congenital cytomegalovirus and normal fetal imaging.** *Arch Dis Child Fetal Neonatal Ed* 2016 Jan 18. [Epub ahead of print] CrossRef Medline
  40. Capretti MG, Lanari M, Tani G, et al. **Role of cerebral ultrasound and magnetic resonance imaging in newborns with congenital cytomegalovirus infection.** *Brain Dev* 2014;36:203–11 CrossRef Medline

# Superficial Siderosis after Germinal Matrix Hemorrhage

U. Yilmaz, S. Meyer, L. Gortner, H. Körner, M. Türkyilmaz, A. Simgen, W. Reith, and R. Mühl-Benninghaus

## ABSTRACT

**BACKGROUND AND PURPOSE:** Germinal matrix hemorrhage is a frequent complication of prematurity and can be associated with adverse neurodevelopmental outcome, depending on its severity. In addition to parenchymal damage, intraventricular residues of hemorrhage and hydrocephalus MR imaging findings include superficial siderosis. The purpose of this study was to investigate the prevalence and location of superficial siderosis in patients with a history of germinal matrix hemorrhage.

**MATERIALS AND METHODS:** We retrospectively identified patients with a history of germinal matrix hemorrhage who underwent MR imaging in our institution between 2008 and 2016. Imaging was evaluated for the presence and location of superficial siderosis. The presence of subependymal siderosis and evidence of hydrocephalus were assessed.

**RESULTS:** Thirty-seven patients with a history of germinal matrix hemorrhage were included; 86.5% had preterm births. The mean age at the first MR imaging was 386 days (range 2–5140 days). The prevalence of superficial siderosis was 67.6%. Superficial siderosis was detected significantly more often when MR imaging was performed within the first year of life (82.8% versus 12.5%,  $P < .000$ ). When present, superficial siderosis was located infratentorially in all cases, while additional supratentorial superficial siderosis was detectable in 27%.

**CONCLUSIONS:** Here we report that superficial siderosis is a common MR imaging finding in the first year of life of patients with a history of germinal matrix hemorrhage, but it dissolves and has a low prevalence thereafter. A prospective analysis of its initial severity and speed of dissolution during this first year might add to our understanding of the pathophysiology of neurodevelopmental impairment after germinal matrix hemorrhages.

The germinal matrix is a highly cellular and vascularized layer between the thalamus and caudate nucleus. It is the origin of neurons and glial cells during fetal development and begins to involute at 28 weeks' gestational age. Due to the friability of its capillaries, it is vulnerable to bleeding when autoregulation of cerebral blood flow is not yet established as in preterm infants.<sup>1</sup> Germinal matrix hemorrhage is a frequent complication of prematurity associated with developmental delay, cerebral palsy, neurosensory impairment, and deafness.<sup>2</sup> The risk of neurodevelopmental impairment increases with the severity of the hemorrhage,<sup>3</sup> which is graded according to the Papile classification.<sup>1,4</sup> Grade I hemorrhages (restricted to germinal matrix without extension into ventricles) are not associated with developmental delay.

In addition to parenchymal damage, intraventricular residues of hemorrhage and hydrocephalus superficial siderosis is a finding that has been described in cases of germinal matrix hemorrhage.<sup>5,6</sup> In adult neurology, superficial siderosis has been associated with gait ataxia, cerebellar dysarthria, and sensorineural hearing impairment.<sup>7</sup> After germinal matrix hemorrhage however, it is assumed to be an incidental finding without neurodevelopmental implications.<sup>6</sup> The purpose of this study was to investigate the prevalence and location of superficial siderosis in patients with a history of germinal matrix hemorrhage.

## MATERIALS AND METHODS

We retrospectively included all patients with a known history of germinal matrix hemorrhage who underwent MR imaging in our institution between 2008 and 2016. Patients were identified by a search in our electronic in-hospital data base (SAP, Walldorf, Germany) of clinical records for the key words “germinal matrix hemorrhage.”

Inclusion criteria were as follows:

1) A history of germinal matrix hemorrhage diagnosed by sonography or MR imaging.

Received May 24, 2016; accepted after revision July 20.

From the Departments of Neuroradiology (U.Y., H.K., M.T., A.S., W.R., R.M.-B.) and Pediatrics (S.M., L.G.), Saarland University Hospital, Homburg/Saar, Germany.

Please address correspondence to Umut Yilmaz, MD, Saarland University Hospital, Department of Neuroradiology, Kirrberger Str, D-66424 Homburg/Saar, Germany; e-mail: umut.yilmaz@uks.eu

<http://dx.doi.org/10.3174/ajnr.A4935>

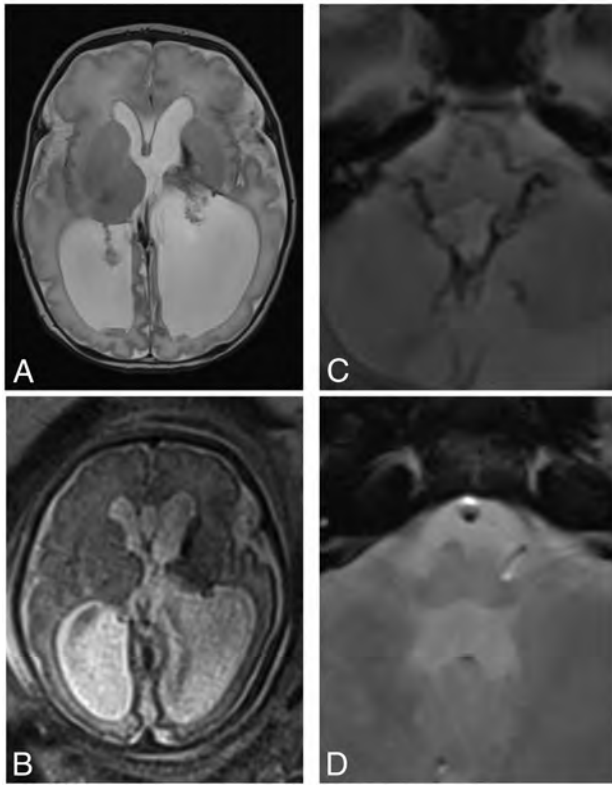


**FIG 1.** Superficial siderosis after germinal matrix hemorrhage. T2-weighted (A) image of a male neonate at 2 days of age shows residues of a left germinal matrix hemorrhage and secondary hydrocephalus. Gestational age at birth was 34 weeks. At the gestational age of 32 weeks, a fetal MR imaging had been performed (B) after hemorrhage had been suspected on a prenatal sonography examination. Postnatal T2\*-weighted image (C) shows infratentorially located superficial siderosis, which had dissolved on the T2\*-weighted image at 26 months of age (D).

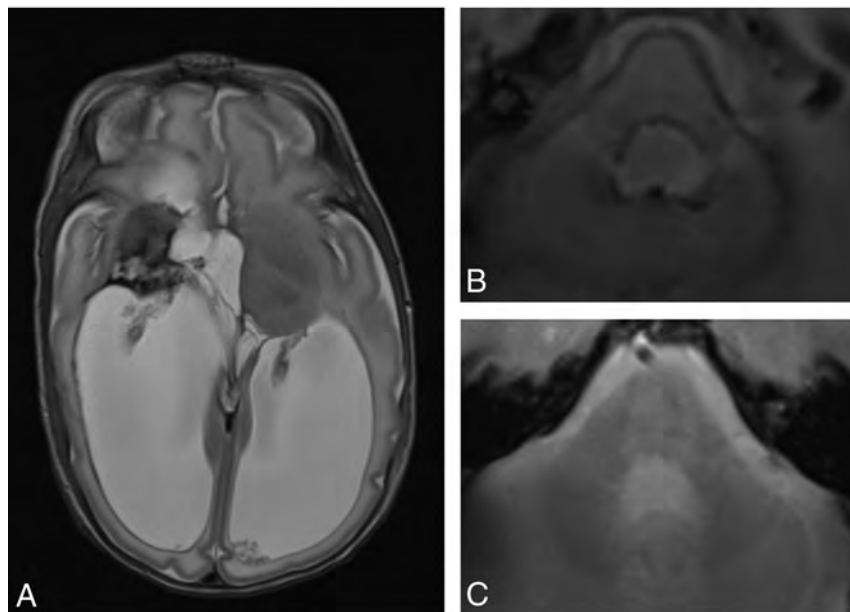


**FIG 2.** Superficial siderosis after germinal matrix hemorrhage. T2-weighted (A) image of a female infant at the age of 2 months shows residues of a right germinal matrix hemorrhage with parenchymal defects and secondary hydrocephalus. T2\*-weighted image (B) shows infratentorially located superficial siderosis, which had dissolved on the T2\*-weighted image at 3 years of age (C).

2) MR imaging including a T2\*-weighted sequence or SWI.

The exclusion criterion was imaging quality insufficient to recognize the presence of superficial siderosis.

Imaging was performed on a 1.5T scanner (Sonata; Siemens, Erlangen, Germany) between 2008 and 2011 and on either a 1.5T scanner (Symphony; Siemens) or a 3T scanner (Skyra; Siemens) between 2011 and 2016.

At our institution, MR imaging in children is routinely performed with the patient under deep sedation or general anesthesia. MR imaging was typically performed to confirm the finding of a germinal matrix hemorrhage in a sonography examination and to plan surgery in case of hydrocephalus.

Image interpretation was performed by 2 neuroradiologists in consensus. T2\*-weighted images or SWI were evaluated for the presence and location of superficial siderosis. The presence of subependymal siderosis and evidence of hydrocephalus were also assessed. Gestational age at birth and age at MR imaging were noted. Statistical analysis was performed by using SPSS 20.0 (IBM, Armonk, New York). The  $\chi^2$  test was applied to determine differences in frequencies.

$P < .05$  was considered statistically significant.

## RESULTS

Thirty-seven patients with a history of germinal matrix hemorrhage were included. Thirty-two (86.5%) had preterm births. The mean gestational age at birth was 30 weeks (range, 25–39 weeks). Data on the severity of the hemorrhage were available for 31 patients. Two patients had grade I hemorrhages according to the Papile classification and the initial sonography examinations. However, grades were corrected to grade II because MR imaging showed subependymal siderosis exceeding the germinal matrix in both cases. Frequencies according to the Papile classification were the following: grade I, 0%; grade II, 45.2% (12/31); grade III, 41.9% (13/31); and grade IV, 12.9% (4/31). The mean age at the first MR imaging investigation was 386 days (range, 2–5140 days). Subependymal siderosis was detectable in every case (37/37). Thirty-two patients (86.5%) had evidence of hydrocephalus. The prevalence of superficial siderosis was 67.6% (25/37). Superficial siderosis was located infratentorially in all of those cases, while additional supratentorial superficial siderosis was detectable in 27% (10/37).

Superficial siderosis was detected significantly more often when the first MR imaging was performed within the first year of life (82.8% [24/29] versus 12.5% [1/8],  $P < .000$ ). The first MR imaging was performed within the first 6 months in 20 neonates. In this group, superficial siderosis was found in 90% (18/20). Follow-up MR imaging after their first year of life was available in 10 of those patients who had superficial siderosis on MR imaging in their first year of life. The mean age at the fol-

low-up MR imaging investigation was 1013 days (range, 424–2371 days). Superficial siderosis was detected in 1 case on follow-up MR imaging (9.1%), whereas subependymal siderosis was present in all cases (11/11) (exemplary cases are shown in Figs 1 and 2). Two of the 5 patients without hydrocephalus had the first MR imaging within their first year of life (at 55 days and 56 days). Superficial siderosis was detected in both cases. Neither patient underwent follow-up MR imaging. The other 3 patients without hydrocephalus underwent MR imaging at 1 and 2 years of age. None of these MRIs showed superficial siderosis. Data on the severity of the hemorrhage were available for 4 patients without hydrocephalus. Two of them had grade II hemorrhages, and 2, grade III hemorrhages.

## DISCUSSION

In this study, we investigated superficial siderosis in patients with a history of germinal matrix hemorrhage. Gomori et al<sup>5</sup> first described 2 cases of large germinal matrix hemorrhages with signs of superficial siderosis on MR imaging in 1987. Glasier et al<sup>6</sup> later reported superficial siderosis in 7 infants with a history of intraventricular/periventricular hemorrhage. In addition, they retrospectively analyzed the neurodevelopmental outcomes of their patients with particular attention to cerebellar and auditory dysfunction and concluded that superficial siderosis is an incidental finding without neurodevelopmental implications. However very recently, a cohort study of extremely preterm infants<sup>2</sup> reported higher rates of neurosensory impairment and hearing loss in infants with intraventricular hemorrhages compared with preterm controls at 2–3 years' corrected age. Increasing grades of hemorrhages were associated with higher rates of neurosensory impairment (12.1% in controls, 21.1% for grade I, 24% for grade II, 41% for grade III, and 46% for grade IV).<sup>2</sup> The mechanism of brain injury is thought to result from parenchymal damage and impaired cortical development.<sup>2</sup> In addition, Silva et al<sup>8</sup> recently reported that peri-/intraventricular hemorrhages influence alterations in auditory brain stem responses in preterm infants.

In our study, superficial siderosis was commonly seen in patients with a history of germinal matrix hemorrhage when MR imaging was performed in the first year of life, with dissolution in >90% thereafter. To our knowledge, this is the first report of the age-dependent dissolution of superficial siderosis after germinal matrix hemorrhage. Because superficial siderosis has been associated with gait ataxia, cerebellar dysarthria, and sensorineural hearing impairment in adults,<sup>7</sup> it may also have an impact on the neurodevelopmental outcome in infants with germinal matrix hemorrhages. In this context, it would be interesting to prospectively investigate the extent of the superficial siderosis, the gesta-

tional age at which it occurs, and the speed of its dissolution as potential modifying factors with regard to neurologic outcome.

## Limitations

Our study has some limitations. Because the disappearance of superficial siderosis is probably a gradual process, it would be interesting to quantify its extent with time. However, because imaging quality was very divergent in our analysis due to different scanners with different field strengths and different section thicknesses, we decided not to attempt to quantify the siderosis but to restrict our analysis to its presence or absence. In this context, it would also be interesting to analyze factors that might influence the extent of superficial siderosis, such as the size of the initial hematoma. Because our study was retrospective in character, such information was not sufficiently available.

## CONCLUSIONS

Superficial siderosis is a common MR imaging finding in the first year of life in neonates with a history of germinal matrix hemorrhage, but it dissolves and has a low prevalence thereafter. A prospective analysis of its initial severity and speed of dissolution during this first year may add to our understanding of the pathophysiology of neurodevelopmental impairment after germinal matrix hemorrhages.

## REFERENCES

1. Volpe JJ. *Neurology of the Newborn*. 4th ed. Philadelphia: W.B. Saunders; 2001
2. Bolisetty S, Dhawan A, Abdel-Latif M, et al; New South Wales and Australian Capital Territory Neonatal Intensive Care Units' Data Collection. **Intraventricular hemorrhage and neurodevelopmental outcomes in extreme preterm infants.** *Pediatrics* 2014;133:55–62 CrossRef Medline
3. Mukerji A, Shah V, Shah PS. **Periventricular/intraventricular hemorrhage and neurodevelopmental outcomes: a meta-analysis.** *Pediatrics* 2015;136:1132–43 CrossRef Medline
4. Papile LA, Burstein J, Burstein R, et al. **Incidence and evolution of subependymal and intraventricular hemorrhage: a study of infants with birth weights less than 1,500 gm.** *J Pediatr* 1978;92:529–34 CrossRef Medline
5. Gomori JM, Grossman RI, Goldberg HI, et al. **High-field spin-echo MR imaging of superficial and subependymal siderosis secondary to neonatal intraventricular hemorrhage.** *Neuroradiology* 1987;29:339–42 CrossRef Medline
6. Glasier CM, Garcia-Thomas GI, Allison JW. **Superficial CNS siderosis in the newborn: MR diagnosis.** *Pediatr Radiol* 1999;29:76–77 CrossRef Medline
7. Kumar N. **Neuroimaging in superficial siderosis: an in-depth look.** *AJNR Am J Neuroradiol* 2010;31:5–14 CrossRef Medline
8. Silva Dd, Lopez P, Mantovani JC. **Auditory brainstem response in term and preterm infants with neonatal complications: the importance of the sequential evaluation.** *Int Arch Otorhinolaryngol* 2015;19:161–65 CrossRef Medline

# Contralateral Hypoplastic Venous Draining Sinuses Are Associated with Elevated Intracranial Pressure in Unilateral Cerebral Sinovenous Thrombosis

R. Farias-Moeller, R. Avery, Y. Diab, J. Carpenter, and J. Murnick



## ABSTRACT

**SUMMARY:** Variations in cerebral venous development can influence the ability to regulate drainage. In cerebral sinovenous thrombosis, these variations can be associated with elevated intracranial pressure. We present a series of pediatric patients with unilateral cerebral sinovenous thrombosis and investigate whether the contralateral venous sinus size increases the risk of developing elevated intracranial pressure. Patients diagnosed with a unilateral cerebral sinovenous thrombosis were identified by querying our institutional radiology data base. The difference in the occurrence of elevated intracranial pressure in patients with cerebral sinovenous thrombosis with and without hypoplastic venous sinuses was studied. Twelve cases of unilateral cerebral sinovenous thrombosis met the inclusion criteria and had sufficient images. Six patients had hypoplastic contralateral venous sinuses. The presence of hypoplastic contralateral venous sinus in the setting of thrombosis of a dominant sinus was associated with elevation of intracranial pressure (83% versus 0%,  $P = .015$ ). Patients with cerebral sinovenous thrombosis and contralateral hypoplastic venous sinuses are at higher risk of developing elevated ICP and may benefit from screening with an ophthalmologic examination.

**ABBREVIATIONS:** CSVT = cerebral sinovenous thrombosis; ICP = intracranial pressure

Cerebral sinovenous thrombosis (CSVT) affects 0.34–0.67 per 100,000 children annually.<sup>1</sup> Mortality rates are 3%–12%,<sup>1</sup> and neurologic sequelae can be seen in 22%–50% of survivors.<sup>2</sup> The etiology is multifactorial and frequently includes acute provoking illnesses such as head and neck infections, dehydration, central venous lines, chronic medical conditions, prothrombotic states, and head trauma.<sup>1</sup> The clinical presentation of pediatric CSVT is highly variable and includes headache, papilledema, seizures, and focal neurologic deficits.<sup>3</sup> Diagnostic evaluation of pediatric CSVT almost invariably includes brain imaging with CT, possibly along with CTV or MR imaging with MRV.

Anatomic variations in cerebral venous development exist, which may influence the ability to appropriately regulate venous drainage from the head and subsequently increase the risk of developing elevated intracranial pressure (ICP), especially in patients with CSVT. Recognizing these anatomic variations may be important when determining treatment and monitoring proto-

cols for children with CSVT.<sup>3</sup> We present a series of pediatric patients with unilateral CSVT involving the transverse/sigmoid sinuses and jugular vein and the influence of an anatomic variation (ie, the structure of the unaffected contralateral venous sinus) on the elevation of intracranial pressure and clinical outcome.

## MATERIALS AND METHODS

Our institutional radiology data base was queried from 2010 to 2015 by using the search terms “venous sinus thrombus,” “venous thrombosis,” and “venous thrombus.” All reports of cranial imaging positive for one of these terms were reviewed. Reports with a unilateral transverse and/or sigmoid sinus thrombus were included. One hundred one patients were identified. Infants younger than 28 days, patients with a Glasgow Coma Scale score of <10, and fetuses were excluded. Additionally, patients with other potential causes of increased ICP such as intracranial mass lesions or hemorrhage with mass effect were excluded. Twelve patients were identified for this study. Clinical and radiologic data were extracted from the electronic health record to investigate basic demographic data, location of the CSVT, and size of the affected side in proportion to the unaffected side as well as the presence of elevated ICP. Outcomes were determined from clinic notes and imaging performed 3–6 months after hospitalization.

For each patient, the cross-sectional area of both transverse sinuses was measured on sagittal images in a plane 1.5 cm lateral

Received March 28, 2016; accepted after revision June 13.

From the Divisions of Child Neurology (R.F.-M., R.A., J.C.), Ophthalmology (R.A.), Pediatric Hematology (Y.D.), and Diagnostic Imaging and Radiology (J.M.), Children's National Health System, Washington, DC.

Please address correspondence to Jonathan Murnick, MD, Children's National Health System, Division of Diagnostic Imaging and Radiology, 111 Michigan Ave NW, Washington, DC 20010; e-mail: jmurnick@cnmc.org

Indicates article with supplemental on-line table.

<http://dx.doi.org/10.3174/ajnr.A4899>

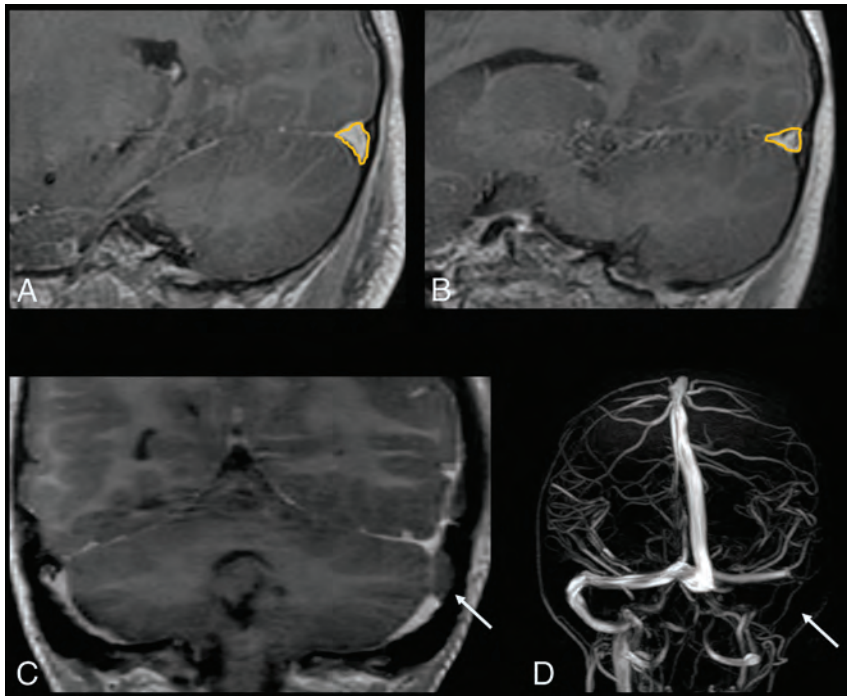


**FIG 1.** Method for measuring sinus cross-sectional area. Patient 8 is shown. *A*, Sagittal post-contrast echo-spoiled gradient-echo image of the left transverse sinus. An orange outline encloses an area of 51.3 mm<sup>2</sup>. *B*, The right transverse sinus cross-sectional area is 30.8 mm<sup>2</sup>. *C*, Coronal reformat of a post-contrast spoiled gradient-echo image. Arrow demonstrates a filling defect in the proximal left sigmoid sinus, consistent with thrombus. *D*, MIP image of a sagittal Inflow MRV (GE Healthcare, Milwaukee, Wisconsin). Arrow shows lack of flow in the left sigmoid sinus. The ratio of the nonthrombosed-to-thrombosed-side cross-sectional area is 0.60.

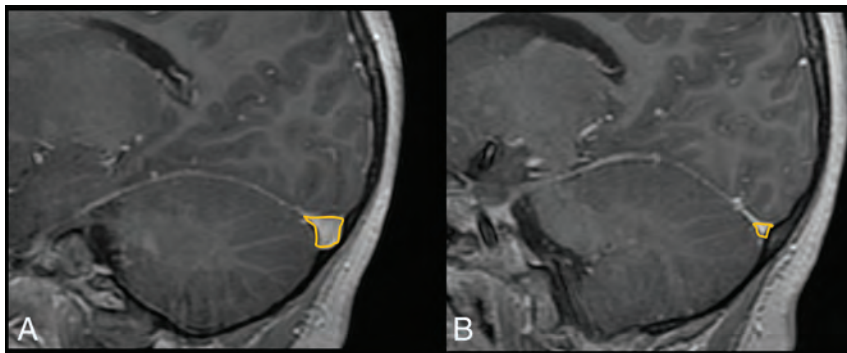


**FIG 2.** Measurements in a patient with hypoplastic right transverse sinus (patient 2). *A*, The left cross-sectional area is 61.1 mm<sup>2</sup>. *B*, The right sinus area is 6.2 mm<sup>2</sup>. The ratio is 0.10.

to the confluence of the sinuses. This distance was chosen because the transverse sinus is most nearly perpendicular to the sagittal plane in this location. An ROI was drawn around each sinus on sagittal post-contrast echo-spoiled gradient-echo images when available. When no contrast-enhanced MR imaging was available, measurements were performed on unenhanced echo-spoiled gradient-echo images or CTV images if no MR imaging was performed (Figs 1 and 2).

We defined hypoplasia of the transverse sinus when the cross-sectional area of one sinus was <50% of the area of the contralateral side. Elevated ICP was defined as the presence of symptoms such as headache, vomiting, or diplopia associated with clinical signs of elevation of ICP such as sixth cranial nerve palsy or encephalopathy. Papilledema confirmed on

ophthalmologic assessment was used as our noninvasive criterion standard to diagnose elevation of ICP. Several patients had headache. While headache can be a symptom of ICP, other confounding causes of headache such as trauma and mastoiditis were present in much of our patient cohort. Therefore, headache in isolation was not considered sufficient to diagnose elevated ICP.

The difference in the occurrence of elevated ICP in patients with and without hypoplastic draining sinuses was obtained by using the Fisher exact test. Statistical analysis was performed by using STATA/IC 13.1 (Stata Corp, College Station, Texas).

## RESULTS

The initial search identified 101 patients. Twelve patients with unilateral CSVT met our inclusion criteria, of whom 6 had a hypoplastic contralateral venous draining sinus and 6 did not. Basic demographic data and clinical characteristics, imaging findings, and location of the CSVT as well as the presence of elevated ICP with associated symptoms can be found in the On-line Table.

The 12 consecutive pediatric patients with unilateral CSVT were analyzed. This cohort included patients 2 months to 16 years of age who presented at our institution between 2011 and 2014. The causes of CSVT were otogenic in 50%, traumatic in 42%, and associated with hypercoagulability in 8%. All except 2 patients were additionally followed as outpatients to assess their response to therapy and outcome.

Of the 6 patients with hypoplastic contralateral draining sinuses, all had signs and symptoms of elevated ICP (vomiting, encephalopathy, diplopia, or sixth cranial nerve palsy). All 6 were formally assessed for the presence of papilledema by the ophthalmology department. Five of 6 patients had elevated ICP confirmed by papilledema. The sixth patient did not have papilledema and was not considered to have elevated ICP in our analysis.

Of the 6 patients with normal contralateral venous sinuses, several had headaches on presentation but none had any other signs or symptoms of elevated ICP. One had undergone a formal ophthalmologic evaluation in which papilledema was ruled out. The presence of a hypoplastic contralateral venous sinus in the setting of thrombosis of a dominant sinus was highly associated with elevation of ICP (83% versus 0%,  $P = .015$ ).

## DISCUSSION

The aim of this study was to report 6 pediatric patients with unilateral CSVT with contralateral hypoplastic venous sinuses whose course was complicated by increased ICP and development of papilledema. We compared this cohort with 6 patients with unilateral CSVT and normal contralateral venous sinuses who did not have elevated ICP. There is sparse literature on the implications of venous drainage variants in CSVT. According to the International Pediatric Stroke Study<sup>1</sup> 41% of children with CSVT had an acute illness or acute head/neck disorder identified; these findings made these conditions the primary cause of CSVT in otherwise healthy children. The diagnosis of CSVT in a child can be elusive: Most children either present with vague signs and symptoms or the CSVT is found incidentally as part of a diagnostic evaluation for an associated condition (eg, mastoiditis). Treatment usually includes parenteral antibiotics for infectious causes and anticoagulation<sup>4</sup>; however, there is no established consensus regarding systemic thrombolysis<sup>5</sup> or surgical options such as mastoidectomy, endovascular thrombectomy, or internal jugular vein ligation,<sup>6</sup> especially with a hypoplastic contralateral venous draining sinus.

Time-of-flight MRV is often used to evaluate the intracranial dural sinuses and confirm or exclude CSVT.<sup>7</sup> Variations in the normal anatomy of venous sinuses not only make the diagnosis of CSVT more difficult but also imply a different prognosis and could justify a more aggressive treatment approach. Alper et al<sup>7</sup> reported that in healthy adults, symmetric sinuses were seen in only 31%, while aplasia of the left sinus was seen in 20%; hypoplasia of the left sinus, in 39%; hypoplasia of the right sinus, in 6%; and aplasia of the right sinus, in 4%. Widjaja and Griffiths<sup>8</sup> reported that in healthy children, variations are also common and include 1 transverse sinus being absent or hypoplastic in 52% of cases in their cohort, with or without the presence of an occipital sinus as an alternative drainage system. Leach et al<sup>9</sup> reported asymmetric transverse sinuses in up to 49% of cases. Consistent with these reports, in our cohort, the right transverse sinus was the dominant sinus in 5 of 6 cases. It is plausible that if the dominant venous sinus is occluded due to a thrombus, the contralateral side will not drain sufficiently and there will be an increased predisposition to the development of increased ICP.

Csákányi et al<sup>6</sup> reported a case series of 8 patients with otogenic CSVT in whom various treatment approaches were used, including internal jugular vein ligation, anticoagulation, and thrombectomy. Of this cohort, 3 patients had hypoplasia of the left venous draining sinus by CT and MR imaging. Two of these 3 had complications secondary to long-standing ICP, including permanent visual impairment and prolonged sixth cranial nerve palsy. Of the remaining 5 patients with symmetric venous draining sinus, all did well, though 2 underwent steroid therapy due to progression of papilledema and 1 had mild headaches. Of the 8 patients in this series, 6 underwent anticoagulation for a variable number of months. Of the 2 patients who did not undergo anticoagulation, 1 had hypoplasia of the left venous sinus, and this patient underwent an internal jugular vein ligation and thrombectomy and mastoidectomy.

In our cohort of 12 patients, 9 were initially started on anticoagulation. All 6 patients with contralateral hypoplasia of venous draining sinus were started on anticoagulation, and 4/6 (66%) had a good outcome with no remaining symptoms and minimal complications (On-line Table). One developed persistently elevated ICP and required optic nerve fenestration for deteriorating vision. One patient was lost to follow-up.

Four of the 6 patients without contralateral hypoplasia had no persistent symptoms attributable to their CSVT, and the other 2 were lost to follow-up. Three of these patients underwent anticoagulation, and no associated complications were reported.

The onset of signs and symptoms of CSVT are often insidious, and though vomiting, lethargy, and headache are commonly seen in children with severe otogenic infections, focal neurologic deficits such as diplopia due to a sixth cranial nerve palsy or papilledema warrant brain imaging. Of the 12 patients with unilateral CSVT, 6 underwent dilated ophthalmologic evaluation during their hospitalization, which confirmed the presence of papilledema in 5, all of whom had contralateral hypoplasia of the venous draining sinus. In all patients with CSVT, especially in those with a hypoplastic contralateral venous sinus, an ophthalmologic evaluation as an indirect measure of elevated ICP is essential. In CSVT and venous backpressure, parenchymal injury can occur secondary to vasogenic and cytotoxic edema and possible hemorrhagic venous infarction, which can cause substantial morbidity and mortality. The post-thrombotic complications, such as the development of pseudotumor cerebri and papilledema, can cause long-term morbidity as well.<sup>3</sup>

The authors recognize that a limiting factor of this study is the small sample size, including a solely pediatric cohort. We support the call for larger studies including adult and pediatric populations with unilateral CSVT and contralateral venous draining sinus hypoplasia. The inclusion of both adult and pediatric patients might elucidate differences in the incidence of elevated ICP, treatment tendencies, and complications.

## CONCLUSIONS

There are significant variations in venous sinus anatomy in about 50% of healthy children, with one side being hypoplastic to various degrees. We report 5 patients with unilateral CSVT associated with a hypoplastic contralateral venous draining sinus that developed raised ICP and papilledema and compare them with 6 patients with normal contralateral venous sinuses without elevation of ICP. Although unilateral hypoplastic venous draining sinus is a common incidental and benign variant, in CSVT of the dominant draining side, it can pose a considerable problem, leading to increased ICP and substantial morbidity. Children with unilateral CSVT and contralateral venous hypoplasia should be evaluated and followed closely for development of elevated ICP. Early aggressive medical and surgical therapy to eradicate the underlying infection in cases of otogenic CSVT, in combination with systemic anticoagulation to prevent thrombus extension and promote recanalization, can lead to favorable outcomes with minimal adverse events.

Disclosures: Robert Avery—UNRELATED: Grants/Grants Pending: National Institutes of Health K23 award (Topic: Optical Imaging in Children with Tumors of the Visual Pathway).

## REFERENCES

1. Ichord RN, Benedict SL, Chan AK et al; International Paediatric Stroke Study Group. **Paediatric cerebral sinovenous thrombosis: findings of the International Paediatric Stroke Study.** *Arch Dis Child* 2015;100:174–79 CrossRef Medline
2. Mortimer AM, Bradley MD, O’Leary S, et al. **Endovascular treatment of children with cerebral venous sinus thrombosis: a case series.** *Pediatr Neurol* 2013;49:305–12 CrossRef Medline
3. Hedlund GL. **Cerebral sinovenous thrombosis in pediatric practice.** *Pediatr Radiol* 2013;43:173–88 CrossRef Medline
4. Bektaş Ö, Teber S, Akar N, et al. **Cerebral sinovenous thrombosis in children and neonates: clinical experience, laboratory, treatment, and outcome.** *Clin Appl Thromb Hemost* 2015;21:777–82 CrossRef Medline
5. Viegas LD, Stolz E, Canhão P, et al. **Systemic thrombolysis for cerebral venous and dural sinus thrombosis: a systematic review.** *Cerebrovasc Dis* 2014;37:43–50 CrossRef Medline
6. Csákányi Z, Rosdy B, Kollár K, et al. **Timely recanalization of lateral sinus thrombosis in children: should we consider hypoplasia of contralateral sinuses in treatment planning?** *Eur Arch Otorhinolaryngol* 2013;270:1991–98 CrossRef Medline
7. Alper F, Kantarci M, Dane S, et al. **Importance of anatomical asymmetries of transverse sinuses: an MR venographic study.** *Cerebrovasc Dis* 2004;18:236–39 CrossRef Medline
8. Widjaja E, Griffiths PD. **Intracranial MR venography in children: normal anatomy and variations.** *AJNR Am J Neuroradiol* 2004;25:1557–62 Medline
9. Leach JL, Fortuna RB, Jones BV, et al. **Imaging of cerebral venous thrombosis: current techniques, spectrum of findings, and diagnostic pitfalls.** *Radiographics* 2006;26(suppl 1):S19–41; discussion S42–43 CrossRef Medline

# Spine Cryoablation: A Multimodality Image-Guided Approach for Tumors Adjacent to Major Neural Elements

J.P. Guenette, K. Tuncali, N. Himes, S. Tatli, and T.C. Lee

## ABSTRACT

**SUMMARY:** We report percutaneous cryoablation of spine tumors in 7 consecutive patients (5 men, 2 women [mean age, 47 years; range, 17–68 years]) by using intraprocedural image monitoring of ice ball margins to protect adjacent neural elements. Complete tumor ablation was achieved in all patients without neurologic complication. Pain relief was achieved in 4 of 5 (80%) patients; the patient with persistent pain was later found to have enlarging metastases at other sites.

Risk of sensory and motor damage is a concern when thermally ablating tumors adjacent to major neural elements.<sup>1</sup> Cryoablation is a promising technique for the treatment of such tumors given that ice ball margins can be visualized intraprocedurally with CT or MR imaging, allowing for better prevention of injury to adjacent structures compared with other forms of thermal ablation.<sup>2</sup> A recent case series has demonstrated safety and efficacy of CT-guided cryoablation in spine tumors with the use of nerve monitoring and thermal protection techniques,<sup>3</sup> and another successful case has been reported using a similar technique followed by cement augmentation and radiation therapy.<sup>4</sup> We expand upon that literature by describing a feasible and potentially safe cryoablation method using near-real-time intraprocedural ice ball visualization, preferably with MR imaging, allowing for dynamic adjustment of cryogen gas flow to shape the ice ball to the spine tumor while preserving immediately adjacent neural structures.

## MATERIALS AND METHODS

We retrospectively reviewed the medical records and diagnostic imaging of 7 patients (5 men, 2 women) with a mean age of 47 years (range, 17–68 years) who underwent 9 consecutive percutaneous image-guided cryoablation procedures on spine tumors adjacent to major neural elements at our institution between January 2014 and September 2015. Patient demographics and

tumor information are presented in Table 1. Because of concern for surgical morbidity, surgery was either determined to be not indicated or was refused by the patient. The study was approved by our institutional review board and performed in compliance with the Health Insurance Portability and Accountability Act.

All procedures were performed in a multimodality image-guided procedure suite, the capabilities of which have been previously described.<sup>5</sup> Intraoperative CT fluoroscopy (Biograph mCT 64 or Somatom Sensation 64; Siemens, Erlangen, Germany) or DynaCT (Artis zee; Siemens) was performed in the axial plane. Sagittal, coronal, and oblique reconstructions were generated from the axial dataset at the scanner whenever necessary. Intraoperative MR imaging (3T Magnetom Verio; Siemens) monitoring was typically performed with intermittent axial T2 TSE (TR, 3000; TE, 87; section thickness, 3 mm) and sagittal T2 TSE (TR, 3000; TE, 106; section thickness, 3 mm) or axial and sagittal T2 BLADE (Siemens) (TR, 2000; TE, 113; section thickness, 4 mm) sequences during active cryoablation.

When necessary, bone access was obtained with an Arrow On-Control Power Driver drill (Teleflex, Limerick, Pennsylvania). Cryoablation was performed using IceSphere, IceSeed, or IceRod cryoprobes with the SeedNet cryoablation system (Galil Medical, Arden Hills, Minnesota). An anesthesiologist performed general endotracheal anesthesia for all cases. Antibiotics were not administered in any case.

In general, CT or PET/CT was used to guide drilling and cryoprobe placement because they offer superior visualization of bone architecture, whereas MR imaging was favored for monitoring because it offers superior visualization of ice ball formation (Fig 1). MR imaging guidance and monitoring in patient 1 was previously reported in a review paper.<sup>6</sup> The procedure on patient 4 was performed entirely with CT because of

Received April 13, 2016; accepted after revision July 8.

From the Department of Radiology, Brigham & Women's Hospital, Boston, Massachusetts.

Please address correspondence to Jeffrey P. Guenette, MD, Department of Radiology, Brigham & Women's Hospital, 75 Francis St, Boston, MA 02135; e-mail: jpguenette@bwh.harvard.edu; @gunetty

<http://dx.doi.org/10.3174/ajnr.A4923>

**Table 1: Demographics of spine ablations in chronological order**

Patient #	Age (yr)	Sex	Location	Size (mm)	Pathology
1	68	M	L4 lamina and inferior facet	12	Presumed DLBCL; mixed chronic inflammation on pathology
2	17	M	C7 pedicle	11	Osteoid osteoma
3	22	M	L1 pedicle	15	Osteoblastoma
4	66	F	T4 vertebral body/paraspinal	28	Leiomyosarcoma metastasis
5	50	M	C2–C3 neural foramen	16	Adenoid cystic carcinoma metastasis
2	17	M	C7 pedicle (repeat)	11	Osteoid osteoma
6	51	F	T10 vertebral body	31	Lung adenocarcinoma metastasis
7	54	M	T12 vertebral body	15	Atypical spindle cell tumor
3	23	M	L1 pedicle (repeat)	15	Osteoblastoma

**Note:**—DLBCL indicates diffuse large B-cell lymphoma.

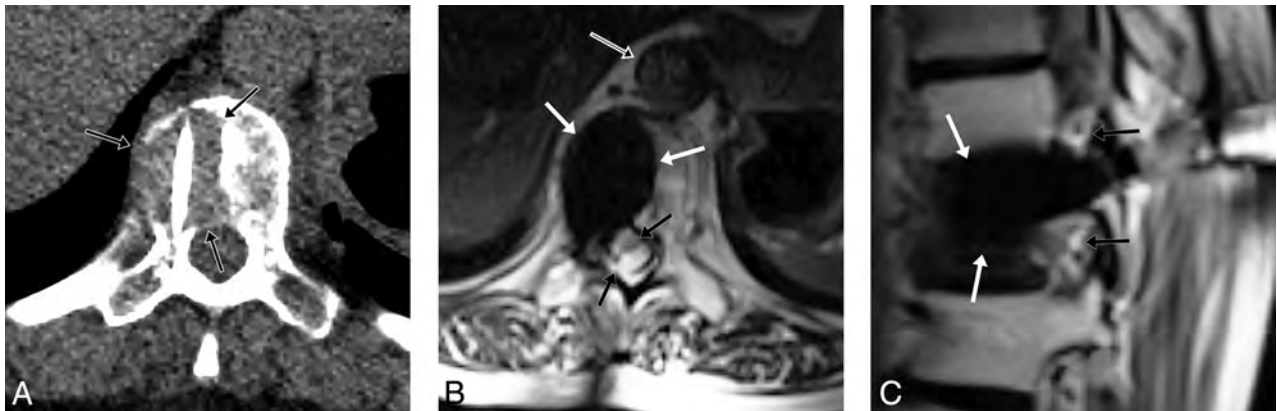


**FIG 1.** 51-year-old woman with lytic T10 lung adenocarcinoma metastasis. *A*, Intraoperative axial prone CT image rotated for visual convenience demonstrates destructive lesion (*black arrows*) extending to the thecal sac with a cryoprobe within the mass. *B*, Intraoperative TSE T2-weighted image in the axial plane demonstrates ice ball (*white arrows*) covering the lesion with preservation of the thecal sac (*black arrows*) and aorta (*black arrow with white border*), and *C*, sagittal plane demonstrates the ice ball (*white arrows*) with preservation of the neural foramina (*black arrows*).

a large paraspinous component simultaneously ablated by our abdominal interventionalists. The entire procedure on patient 5 was performed with PET/CT (Fig 2) because of simultaneous ablation of a head tumor. Image-guidance and monitoring modalities and technical goals, either pain relief or complete tumor ablation for local disease control, are presented in Table 2.

## RESULTS

A total of 9 procedures were performed in 7 patients. Outcomes are presented in Table 2. There were no temporary or permanent neurologic or functional deficits.

Two patients required 2 procedures to achieve complete ablation and pain relief. Conservative approaches were initially taken with a 17-year-old man with cervical osteoid osteoma and a 22-year-old man with lumbar osteoblastoma. Both patients had slight residual pain after ablation of the tumor nidus, and both patients opted to pursue ablation of small residual components immediately adjacent to the thecal sac and nerve root. To minimize the risk of complication when ablating the deep regions of residual tumor, preprocedure planning with advanced visualization techniques and simulation with a 3D model were performed.<sup>7</sup> Complete cryoablation resulted in complete pain relief in both patients. Complete ablation was achieved in the other 5 patients after a single cryoablation procedure.

Four of 5 patients with preablation pain experienced complete and sustained pain relief after ablation. Patient 6, who experi-

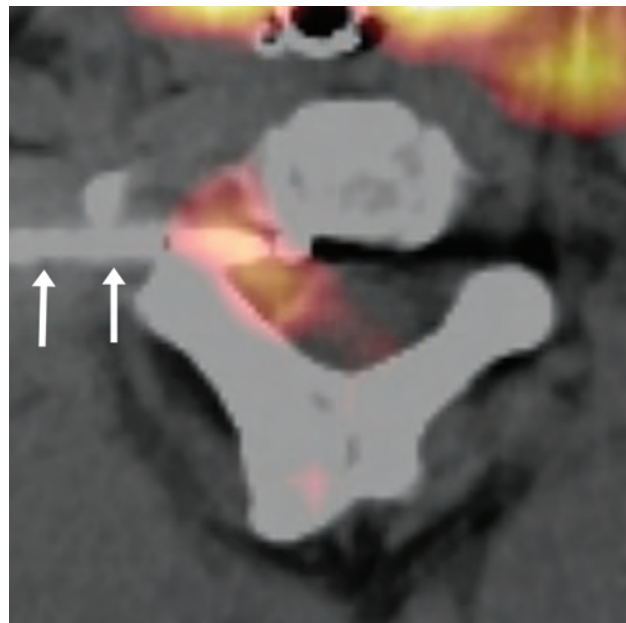


**FIG 2.** 50-year-old man with PET-avid C2–C3 neural foramen adenoid cystic carcinoma metastasis largely occult on CT. Intraoperative axial fused PET/CT image demonstrates cryoprobe (*white arrows*) coursing immediately posterior to the styloid process within FDG-avid lesion at the end of the second freeze; the ice ball was not well visualized. The carotid artery was immediately anterolateral to the styloid process.

enced persistent pain after cryoablation, was found on 1-month postprocedure MR imaging to have complete ablation of the targeted T10 tumor, but also new tumor in T9 and T12.

**Table 2: Methods and results of spine ablations in chronological order**

Patient #	Guidance Modality	Monitoring Modality	Procedure Goal	Outcomes
1	MRI	MRI	Complete ablation	No increase in size or posterior element destruction on CT 22 months postprocedure
2	CT	MRI	Pain relief	Second procedure for less severe but residual pain
3	CT	MRI	Pain relief	Second procedure for less severe but residual pain
4	CT	CT	Complete ablation	Sustained resolution of pain 5 months postprocedure; no increase in lesion size on CT 5 months postprocedure
5	PET/CT	PET/CT	Complete ablation	Lost to follow-up
2	CT	MRI	Complete ablation	Sustained resolution of pain 7 months postprocedure without imaging at the time of writing
6	PET/CT	MRI	Complete ablation	Continued pain postprocedure, with MRI 1 month postprocedure demonstrating likely tumor at the inferior endplate of T9 but complete ablation of the targeted T10 lesion; subsequent systemic chemotherapy and surgery
7	PET/CT	MRI	Complete ablation	Sustained resolution of pain and no increase in lesion size 6 months postprocedure
3	CT	MRI	Complete ablation	Sustained resolution of pain 4 months postprocedure without imaging at the time of writing

Patient 5 had a left neck lymph node metastasis ablated simultaneously to the right C2–C3 neural foramen metastasis.

Follow-up imaging ranging from 1 month to 22 months postprocedure was available for 5 of the 7 patients and demonstrated no new or enlarging residual tumor at the ablation site in any patient.

## DISCUSSION

This report describes the methods and early outcomes of percutaneous image-guided cryoablation of spine tumors in 7 consecutive patients by using intraprocedural MR imaging to visualize and protect adjacent neural elements. Near-real-time monitoring of the cryogenic ice ball, particularly with MR imaging, allows for adjustment of cryogen gas flow to shape the ice ball to the tumor while preserving immediately adjacent neural structures. Such monitoring should reduce the risk of the neural damage that has been described after CT-guided radiofrequency ablation<sup>1</sup> because the ice ball margin is not as distinct on CT. The major drawback to our approach is that an MR imaging–safe power drill bit for percutaneous procedures is not currently commercially available, and, therefore, CT guidance is necessary for cryoprobe placement. When MR imaging is not available as a monitoring technique, use of thermoprotective techniques as previously described<sup>3,8–11</sup> should be considered if the ice ball is not easily visualized with CT, particularly with ice ball formation in bone.

Complete tumor ablation was achieved in all 7 of our patients, and complete pain relief was achieved in 4 of 5 (80%) patients with preprocedure pain. There were no temporary or permanent neurologic complications or functional deficits. First ablation of the central nidus of an osteoid osteoma and central nidus of an osteoblastoma resulted in partial pain relief, and complete pain relief was achieved in both patients after second ablation of small residual tumor components, consistent with prior evidence that ablation of the tumor–bone interface correlates with successful pain relief.<sup>12</sup>

The primary limitations of this study are the small number of treated patients and short-term follow-up. Larger studies and increased radiologist experience, hopefully achievable through 2 ac-

tive prospective trials,<sup>13,14</sup> will help establish the safety profile and long-term outcomes of this technique.

In summary, percutaneous cryoablation of spine tumors by using intraprocedural MR imaging monitoring is a feasible treatment option, even when tumors are adjacent to major neural elements and surgery is not a good option. Continued research is encouraged to establish this treatment as an effective and safe option for patients with nonsurgical or surgically morbid disease.

Disclosures: Kemal Tuncali—UNRELATED: Grants/Grants Pending: Canon USA\*; Patents (planned, pending or issued): Canon USA.\* \*Money paid to the institution.

## REFERENCES

- Nakatsuka A, Yamakado K, Takaki H, et al. **Percutaneous radiofrequency ablation of painful spinal tumors adjacent to the spinal cord with real-time monitoring of spinal canal temperature: a prospective study.** *Cardiovasc Intervent Radiol* 2009;32:70–75 CrossRef Medline
- Tatli S, Acar M, Silverman S. **Percutaneous cryoablation techniques and clinical applications.** *Diagn Interv Radiol* 2010;16:90–95 CrossRef Medline
- Tomasian A, Wallace A, Northrup B, et al. **Spine cryoablation: pain palliation and local tumor control for vertebral metastases.** *AJNR Am J Neuroradiol* 2016;37:189–95 CrossRef Medline
- Greenwood TJ, Wallace A, Friedman MV, et al. **Combined ablation and radiation therapy of spinal metastases: a novel multimodality treatment approach.** *Pain Physician* 2015;18:573–81 Medline
- Tempany CM, Jayender J, Kapur T, et al. **Multimodal imaging for improved diagnosis and treatment of cancers.** *Cancer* 2015;121: 817–27 CrossRef Medline
- Himes NC, Chansakul T, Lee TC. **Magnetic resonance imaging–guided spine interventions.** *Magn Reson Imaging Clin* 2015;23: 523–32 CrossRef Medline
- Guenette JP, Himes N, Giannopoulos AA, et al. **Computer-based vertebral tumor cryoablation planning and procedure simulation involving two cases using MRI-visible 3D printing and advanced visualization.** *AJR Am J Roentgenol* 2016 Aug 9. [Epub ahead of print] CrossRef Medline
- Costa de Freitas RM, de Menezes MR, Cerri GG, et al. **Sclerotic vertebral metastases: pain palliation using percutaneous image-guided cryoablation.** *Cardiovasc Intervent Radiol* 2011;34 Suppl 2:S294–99 CrossRef
- Rybak LD, Gangi A, Buy X, et al. **Thermal ablation of spinal osteoid**

- osteomas close to neural elements: technical considerations. *Am J Roentgenol* 2010;195:W293–98 CrossRef
10. Anchala PR, Irving WD, Hillen TJ, et al. **Treatment of metastatic spinal lesions with a navigational bipolar radiofrequency ablation device: a multicenter retrospective study.** *Pain Physician* 2014;17:317–27 Medline
  11. Kurup AN, Morris JM, Boon AJ, et al. **Motor evoked potential monitoring during cryoablation of musculoskeletal tumors.** *J Vasc Interv Radiol* 2014;25:1657–64 CrossRef Medline
  12. Guenette JP, Lopez MJ, Kim E, et al. **Solitary painful osseous metastases: correlation of imaging features with pain palliation after radiofrequency ablation—a multicenter American College of Radiology Imaging Network study.** *Radiology* 2013;268:907–15 CrossRef Medline
  13. Image-guided cryoablation of head, neck and spine tumors. <https://clinicaltrials.gov/ct2/show/NCT02085941>. Accessed June 28, 2016
  14. MRI-guided cryoablation to alleviate pain in head, neck and spine. <https://clinicaltrials.gov/ct2/show/NCT01788410>. Accessed June 28, 2016

# Effect of Systemic Therapies on Outcomes following Vertebroplasty among Patients with Multiple Myeloma

R.J. McDonald, J.S. McDonald, D.F. Kallmes, V.T. Lehman, F.E. Diehn, J.T. Wald, K.R. Thielen, A. Dispenzieri, and P.H. Luetmer

## ABSTRACT

**BACKGROUND AND PURPOSE:** The role of vertebroplasty in patients with myeloma remains relatively undefined. Accordingly, we sought to better define the efficacy of vertebroplasty for myeloma-associated fractures and determine the effect of procedure timing relative to the initiation of systemic therapy on outcomes and complication rates.

**MATERIALS AND METHODS:** Clinical, laboratory, and medication data were retrieved for 172 patients with multiple myeloma treated with vertebroplasty since October 2000. Quantitative outcome data (Roland-Morris Disability Questionnaire [scale, 0–24] and the Numeric Rating Scale [0–10] for pain at rest and with activity) were collected immediately pre- and postoperatively and at 1 week, 1 month, 6 months, and 1 year following vertebroplasty. Patients with  $\geq 50\%$  improvement on the Numeric Rating Scale and  $\geq 40\%$  improvement on the Roland-Morris Disability Questionnaire were classified as “responders.” Peri- and postoperative complications were also collected.

**RESULTS:** Significant median improvement in the Roland-Morris Disability and rest and activity Numeric Rating Scale scores (15, 2, and 6 points, respectively;  $P < .0001$ ) persisted at 1 year without significant change from the immediate postoperative scores ( $P > .36$ ). Patients on systemic therapy at the time of vertebroplasty were more likely to achieve “responder status,” compared with patients not on systemic therapy, for the Numeric Rating Scale pain at rest score ( $P < .01$ ) and the Roland-Morris Disability Questionnaire score ( $P < .003$ ), with no difference in complication rates ( $\chi^2 = 0.17$ ,  $P = .68$ ).

**CONCLUSIONS:** Vertebroplasty is an effective therapy for patients with myeloma with symptomatic compression fractures. Favorable outcomes are more likely to be achieved when spinal augmentation is performed after systemic therapy is initiated. Complication rates were not affected by the timing of systemic therapy.

**ABBREVIATIONS:** IQR = interquartile range; NRS = Numeric Rating Scale; RDQ = Roland-Morris Disability Questionnaire

For the past 20 years, vertebroplasty has been shown to be an effective treatment for symptomatic vertebral compression fractures refractory to medical therapy.<sup>1,2</sup> Although recent evidence suggests that the pain reduction derived from this procedure may not be attributable to the injection of the cement itself, the data are clear that vertebroplasty recipients experience durable improvement in mobility and reduced narcotic use that persist for months to years following therapy.<sup>3</sup> Although patients with osteoporosis comprise most vertebroplasty recipients in the United States, traumatic and pathologic fractures have also

been treated with percutaneous spinal augmentation.<sup>4–6</sup> Among pathologic fracture etiologies, multiple myeloma is one of the more common indications for intervention. Patients with myeloma are particularly prone to pathologic vertebral compression fractures due to systemic osteoporosis from cytokine-mediated imbalance of osteoclast and osteoblast function and systemic corticosteroid therapy.<sup>6</sup>

Although a large body of evidence exists demonstrating the efficacy of vertebroplasty among patients with benign osteoporotic vertebral compression fractures, the data in support of its use in the treatment of pathologic fractures among patients with multiple myeloma remain limited. In part, data from patients with myeloma are limited due to their reduced survival time, clinical uncertainty with respect to improvement in pain in the setting of diffuse disease, uncertainty as to when to treat, and a higher threshold of treatment criteria for patients with diffuse disease. In contradistinction to patients with benign compression fractures, patients with myeloma are often on multidrug systemic therapy

Received April 27, 2016; accepted after revision July 8.

From the Departments of Radiology (R.J.M., J.S.M., D.F.K., V.T.L., F.E.D., J.T.W., K.R.T., P.H.L.), Neurosurgery (D.F.K.), and Hematology (A.D.), College of Medicine, Mayo Clinic, Rochester, Minnesota.

Please address correspondence to Robert J. McDonald, MD, PhD, Department of Radiology, Mayo Clinic, 200 1st St SW, Rochester, MN 55905; e-mail: mcdonald.robert@mayo.edu

<http://dx.doi.org/10.3174/ajnr.A4925>

and may have hematologic derangements related to their disease and/or treatment. These factors may confound outcomes and potentially render patients with myeloma more predisposed to adverse events.

The purpose of this study was to better define the efficacy of vertebroplasty for myeloma-associated fractures and determine the effect of procedure timing relative to the initiation of systemic chemotherapy and the extent of disease on outcomes and complication rates.

## **MATERIALS AND METHODS**

### **Study Design and Population**

Design and execution of this single-center retrospective study were approved by our institutional review board and complied with Health Insurance Portability and Accountability Act privacy guidelines. Patients were included in this study if they met the following 3 criteria: 1) They had an established diagnosis of multiple myeloma or myeloma-related disease (plasmacytoma or plasma cell proliferative disease) within 30 days of spine augmentation, 2) demonstrated MR imaging evidence of a vertebral compression fracture, and 3) were evaluated and subsequently underwent percutaneous vertebroplasty at our medical center. Patients who underwent ablation during their augmentation, lacked radiographic evidence of compression fracture, experienced improvement in clinical pain syndrome with conservative management, had technical contraindications to vertebroplasty, or had noncorrelating pain were excluded from enrollment in our longitudinal vertebroplasty patient data base. Although rarely treated in our practice, large symptomatic lytic lesions without radiographic evidence of vertebral body fracture were not included in this study cohort. Among patients who underwent multiple vertebroplasty procedures across time, data were limited to the first vertebroplasty procedure to mitigate potential confounding effects of recurrent fractures on treatment outcomes. Approximately 40% of patients in this study were included in a previous publication that did not specifically examine the effects of systemic therapy timing on outcomes.<sup>6</sup>

### **Clinical Evaluation**

Multiple myeloma or myeloma-related disease was diagnosed by using standard clinical, laboratory, and imaging criteria.<sup>7</sup> In patients with multiple fractures, clinical assessment of painful spinal levels included collection of clinical history, physical examination, and imaging. Clinical findings of pain on palpation or imaging evidence of intervertebral marrow edema with MR imaging or both were used to guide treatment-level selection.

### **Radiologic Evaluation**

Radiographic evaluation of myeloma-related fractures consisted primarily of MR imaging supplemented with CT and/or bone radiographs. MR imaging examinations of patients meeting all inclusion and exclusion criteria were re-evaluated by 5 neuroradiologists (V.T.L., F.E.D., J.T.W., K.R.T., P.H.L.) with 3, 6, 19, 19, and 24 years of respective experience who were blinded to clinical data and patient outcomes. MR imaging studies included appropriate spin-echo enhancement and inversion recovery suppres-

sion techniques to increase the conspicuity of malignant fractures and ascertain the extent of spinal disease.

### **MR Imaging Classification of Spinal Lesions and Involvement**

In an effort to characterize vertebroplasty-treated compression fractures in the myeloma population, preoperative MR images of treated fractures were grouped into 3 categories, as previously described<sup>6</sup>: Type 1 compression fractures had no MR imaging evidence of myeloma involvement and were classified by using the following morphologies: normal-appearing fatty marrow in some portion of the vertebral body with no evidence of pedicle involvement or epidural or paraspinal disease; and/or absence of focal or diffusely abnormal marrow signal intensity within the treated vertebral body. Type 2 compression fractures were considered indeterminate for underlying myelomatous disease and were classified by diffusely low T1 marrow signal intensity of the treated vertebral body and absence of paraspinal disease. Type 3 compression fractures had definitive MR imaging evidence of myelomatous disease within the vertebral body with additional involvement of the pedicles, paraspinal tissue, and/or epidural tissue. The appearance of adjacent marrow remote from the treated vertebrae had no impact on fracture characterization.

The extent of myelomatous disease in the untreated thoracic and lumbar vertebral bodies was characterized independently from the treated vertebra as previously described<sup>6</sup>: grade I, normal appearance of the remainder of the visualized spine; grade II, 1 or several focal vertebral lesions consistent with myeloma (<10 lesions involving the thoracic and lumbar spine or <6 lesions involving either the thoracic or lumbar spine); or grade III, diffuse vertebral bone marrow involvement ( $\geq 10$  lesions involving the thoracic and lumbar spine or  $\geq 6$  lesions involving either thoracic or lumbar spine).

### **Vertebroplasty Procedure**

Vertebroplasties were performed by 9 experienced staff radiologists as previously described.<sup>1,7,8</sup> Periprocedural pain management included a combination of intravenous conscious sedation and local anesthesia of the soft tissues superficial to the targeted spinous pedicles. Biplanar fluoroscopy was used to monitor needle position, trajectory, and intraosseous injection of polymethylmethacrylate. After needle position was confirmed, polymethylmethacrylate was freshly prepared by mixing barium sulfate-doped solid copolymer (methylmethacrylate) with a small amount of liquid initiator (N,N-dimethyl para-toluidine) and subsequently injected into the compressed vertebral body. Cement injection was terminated when there was adequate filling of the vertebral body (typically 1–4 mL of polymethylmethacrylate) or fluoroscopic evidence of epidural, venous, or transdiscal extravasation or extrusion of cement into the posterior quarter of the vertebral body. Following vertebroplasty, patients were discharged after 2 hours of strict bed rest and a postprocedural visit from the performing radiologist.

### **Data Sources**

Vertebroplasty data (dates of diagnosis, treatment, approximate onset of symptoms, procedural data and notes, and radiologic

studies), laboratory data, and pharmacy data were obtained from archived institutional electronic medical records. Vertebroplasty outcome data were retrieved from our institutional electronic data base used to monitor safety and efficacy; this data base contains data from approximately 2350 patients treated with vertebroplasty at our medical center since 1999.

### Outcome Measures

Patient outcome scores were collected by trained nursing staff in person immediately before and after vertebroplasty and via telephone 1 week, 1 month, 6 months, and 1 year following vertebroplasty. Quantitative patient outcomes included the Numeric Rating Scale (NRS) of pain at rest and pain with activity scored on a 0–10 scale and the Deyo-modified Roland-Morris Disability Questionnaire (RDQ) scored on a 0- to 24-point scale.<sup>9</sup> Outcomes were calculated as median values with interquartile ranges and percentage changes for each time point and patient group. Percentage changes from the preoperative baseline were calculated for the NRS and RDQ scores for each patient at each time point; patients who attained  $\geq 50\%$  improvement in NRS and  $\geq 40\%$  improvement in RDQ scores were classified as “responders,” patients with  $< 50\%$  improvement in NRS and  $< 40\%$  improvement in RDQ scores were classified as “suboptimal responders,” and patients with no change or worsening of scores were classified as “nonresponders” based on standard definitions.<sup>10</sup> After 3 failed attempts, patients who could not be reached by phone were designated as “nonreporter status” for that specific time point; nonreporter status did not preclude telephone contact at a later time unless the patient formally withdrew from further study participation.

### Statistical Analysis

All statistical analyses were performed by using R statistical and computing software (<http://www.r-project.org/>) and JMP, Version 10 (SAS Institute, Cary, North Carolina). Continuous data were displayed as median scores with interquartile ranges due to non-normal distributions and were compared by using the Wilcoxon signed rank test. Categorical data were displayed as relative frequencies (percentages) and were compared by using  $\chi^2$  tests of significance. Comparisons of means of continuous datasets between  $\geq 2$  categorical groups were performed by using analysis of variance. Nonparametric pair-wise correlations between continuous data were performed by using the Wilcoxon rank sum test. Significance was assigned to differences of  $P \leq .05$ .

## RESULTS

### Patient Population

Among 2350 patients treated with vertebroplasty between October 2000 and December 2014, 181 (8%) had a diagnosis of myeloma or myeloma-related disease. One hundred seventy-two of the 181 patients had undergone preprocedural MR imaging (cervical spine MR imaging examinations,  $n = 21$ ; thoracic spine MR imaging examinations,  $n = 108$ ; lumbar spine MR imaging examinations,  $n = 82$ ) and were included for further study. Sixty-seven (39%) of these patients with myeloma were included in a previous publication detailing our initial vertebroplasty experience in this patient subpopulation that did not address the timing of systemic

### Comparison of demographics of patients with myeloma on systemic therapy at the time of vertebroplasty (treated group) with patients not on systemic therapy (untreated group)<sup>a</sup>

Variable	Treated Group ( $n = 134$ )	Untreated Group ( $n = 38$ )
Male sex (No.) (%)	74 (55%)	23 (61%)
Deceased at 1 yr	19 (14%)	4 (11%)
Duration of pain (mo)	3 (1–7)	2 (1–3)
Delay in diagnosis (mo)	9.5 (2.5–45)	NA
No. of affected levels	5 (3–10)	5 (2–12)
No. of treated levels	2 (1–3)	2 (1–3)

Note:—NA indicates not applicable.

<sup>a</sup>Data are median (IQR) unless otherwise indicated.

therapy on clinical outcomes or adverse events.<sup>6</sup> Among the treated patients with myeloma, 134 (76%) were on systemic drug therapy at the time of vertebroplasty, while the remaining 38 (24%) either were recently diagnosed or initially presented with vertebral compression fracture as the first symptomatic manifestation of multiple myeloma. The clinical and demographic characteristics of these groups are shown in the Table.

### Treated and Affected Levels

Vertebroplasty was performed on 287 vertebral levels in the 172 patients in our study group. The distribution of spinal levels treated and affected by multiple myeloma is shown in Fig 1A, -B, respectively. In our study population, the prevalence of fractures followed a bimodal distribution, being most common at T7/T8 and T12/L1. More diffuse cases of spine involvement were noted in 18 patients, representing 10% of all patients included in this study. Ten patients included in this study had concomitant cervical spinal fractures; vertebroplasty was never performed on these cervical fractures due to technical reasons and the presence of concomitant symptomatic fractures at lower load-bearing vertebral levels. Within this study cohort, the median number of fractured vertebrae (4; interquartile range [IQR], 2–5) was significantly greater than the median number of treated vertebrae (2; IQR, 1–3) per patient ( $P = .001$ ). The median number of untreated, presumably asymptomatic, vertebral compression fractures was 2.5 (IQR, 1–4) per patient. No significant differences in the number of affected or treated levels per patient were identified between male and female patients (affected level:  $\chi^2 = 0.48$ ,  $P = .49$ ; treated level:  $\chi^2 = 0.17$ ,  $P = .68$ ).

Among the patients in the study population, 64 (37%) had diffuse (grade III) disease at the time of vertebroplasty, while the remaining 108 patients (63%) had more localized (grade I or II) disease limited to  $< 10$  thoracic and lumbar vertebral bodies. Of the 287 treated vertebral fractures, 138 (48%) had no MR imaging evidence of myelomatous involvement (type 1), 71 (25%) had indeterminate myelomatous involvement (type 2), and 78 (27%) had definite MR imaging evidence of pathologic vertebral compression fracture (type 3). Representative examples of each compression fracture type are shown in Fig 2.

### Time to Treatment

Among the 172 patients with myeloma, 38 (22%) presented with a painful compression fracture as the first evidence of multiple myeloma, while the remaining 134 (78%) had a diagnosis of myeloma before the discovery of a fracture. Within the subset of patients who initially presented with vertebral fracture, systemic

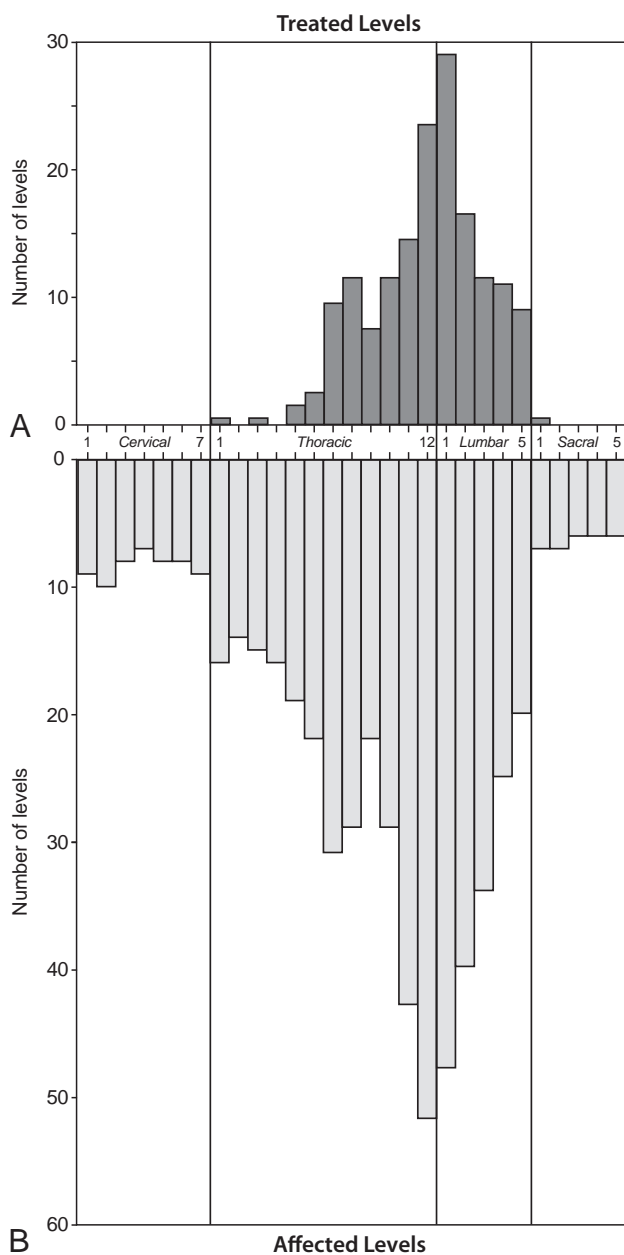


**FIG 1.** Treated and affected levels. Vertebral level frequency histograms of 287 treated vertebral levels (A) and 493 affected vertebral levels (B) in the 172 patients comprising the study population of patients with myeloma.

drug therapy was initiated in 2 (5%) patients before vertebroplasty, and these systemic therapies began within several days of vertebroplasty. Among the remaining 134 patients with a diagnosis of myeloma at the time of vertebroplasty, 111 (82%) were on systemic therapy before vertebroplasty, while the remaining 23 (18%) were treated for myeloma after vertebroplasty. The median time between the diagnosis of myeloma and the initiation of systemic drug therapy was 10 months, with a range of 1–279 months (IQR = 3–45 months) (Fig 3A). Seventy-one (53%) of these patients underwent vertebroplasty within 12 months of the initial diagnosis. The median time between the onset of symptoms (back pain with subsequent radiologic evidence of compression fracture) to systemic treatment was 3 months, with a range of 0–84 months (IQR = 1–7 months) (Fig 3B).

### Clinical Outcomes

Quantitative pain and disability data were collected postoperatively on all 172 patients. To date, 148 (86%) patients had quantitative (NRS pain at rest/activity and RDQ) outcome data collected at the 1-month end point; 135 (78%), at the 6-month end point; and 111 (65%), at the 1-year end point. Of the 61 patients missing follow-up data at the 1-year end point following vertebroplasty, 26 (43%) had an intervening vertebroplasty procedure (<1 year ago), 12 (20%) were lost to follow-up for unspecified reasons, and 23 (38%) died. The relatively high mortality rate in our cohort can be attributed to the more enriched pool of patients with advanced and refractory disease that seek care at our quaternary care center; on review of the medical records, none of these deaths were directly attributable to vertebroplasty therapy.

### Clinical Outcome Analysis

For the entire study population, median preoperative quantitative outcome scores (NRS pain at rest, NRS pain with activity, RDQ score) were 4 (IQR = 2–6), 9 (IQR = 7–10), and 20 (IQR = 17–22), respectively (Fig 4A). All 3 quantitative outcome measures of pain and disability demonstrated significant decreases in the postprocedural setting ( $P < .0001$ ). NRS data for pain at rest significantly improved in the postprocedural period following vertebroplasty ( $P < .0001$ ), with a median improvement of 2 points at 1 week, with no significant intervening change in scores at 1 month, 6 months, and 1 year ( $P = .36$ –.99). The NRS data for pain with activity significantly improved in the postprocedural period following vertebroplasty ( $P < .0001$ ), with a median improvement of 6 points at 1 week with no significant intervening change in scores at 1 month, 6 months, and 1 year ( $P = .41$ –.99). RDQ scores demonstrated a significant median improvement of 15 points 1 week after vertebroplasty, with additional non-significant improvement at 6 months and 1 year following spinal augmentation ( $P = .61$ –.99). There was no significant difference in the magnitude of response among the cohort of patients with loss to follow-up due to subsequent vertebroplasty and those patients who were followed for the entire study duration (NRS pain at rest,  $P = .57$ ; NRS pain with activity,  $P = .32$ ; RDQ score,  $P = .49$ ).

For NRS pain outcomes, at least 47% and 44% of patients met the criteria for responder status ( $\geq 50\%$  improvement in pain) for pain at rest and pain with activity in the immediate postoperative setting, respectively (Fig 4B). In general, the total fraction of patients meeting responder and/or suboptimal responder status increased with time (NRS pain with rest, 67%–81%; NRS pain with activity, 78%–100%). Likewise, for RDQ outcomes, at least 40% of patients met the criteria for responder status ( $\geq 40\%$  improvement in the RDQ score), with a large fraction of total favorable cases meeting suboptimal responder status (0%–67%). The relative fraction of responders also increased with time. Furthermore, there was no significant difference in outcomes between patients who had more acute back pain ( $\leq 6$  months of pain) and those with more chronic back pain ( $> 6$  months of pain) for pain at rest ( $P = .28$ –.74), pain with activity ( $P = .06$ –.90), and the RDQ score ( $P = .22$ –.93) at any postoperative time point.

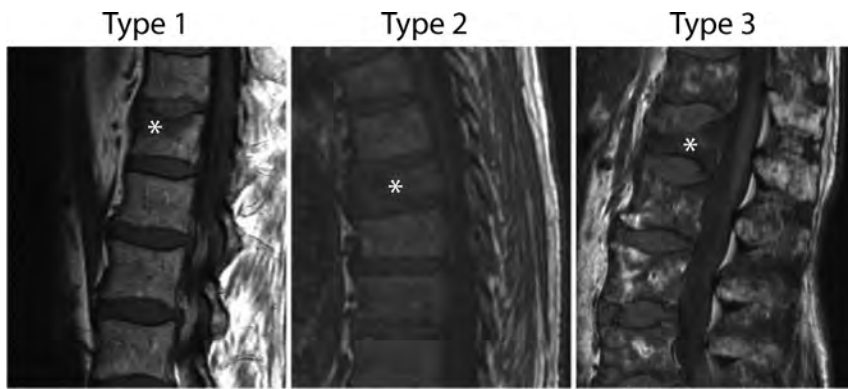


**FIG 2.** Sagittal T1 MR images demonstrating fracture types. Stars indicate treated fractures. A, Type 1 fracture, considered likely osteoporotic. Areas of preserved, high T1 signal within the fractured vertebral body, without a focal intravertebral lesion and no evidence of pedicle involvement or epidural or paraspinal disease (not shown). B, Type 2 fracture, indeterminate for underlying lesions. Diffusely low-signal marrow throughout the spine. No focal lesion or epidural or paraspinal lesion within the treated vertebral body. C, Type 3 fracture, with clear evidence of a myelomatous lesion within the treated vertebral body.

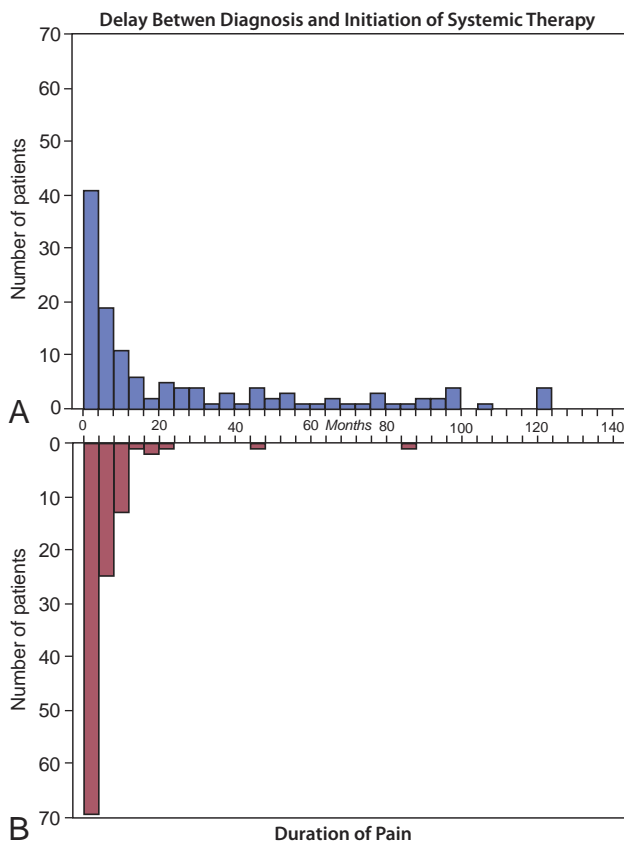


**FIG 3.** Diagnostic interval and duration of pain. The time interval between the diagnosis and initiation of systemic therapy (A) and the duration of pain (B) are shown as frequency histograms with each bin representing a 4-month interval.

### Effects of Systemic Treatment on Outcomes

In an effort to determine whether systemic drug therapy affected clinical outcomes, we compared clinical outcomes and complication rates between untreated and treated patient groups. Compared with the group not treated with systemic drug therapy at the time of vertebroplasty, a significant favorable treatment effect was observed for the treated group having pain with activity ( $F = 8.97$ ,

$P = .030$ ) but not with RDQ ( $F = 0.02$ ,  $P = .89$ ) or pain at rest ( $F = 1.01$ ,  $P = .22$ ) scores. Furthermore, there were significant differences in the response across time between the untreated and treated groups having pain with activity ( $F = 10.14$ ,  $P = .025$ ) and RDQ ( $F = 6.16$ ,  $P = .029$ ) scores, but again not with pain at rest ( $F = 1.92$ ,  $P = .78$ ).

Among categoric outcomes, there was no significant difference between the treated and untreated groups at any time point for NRS pain at rest ( $P = .22-.96$ ) (Fig 4B). Among the NRS pain-with-activity categoric outcomes, a significantly higher fraction of favorable responders were present in the systemic treatment group at 1 and 6 months following vertebroplasty ( $P < .01$ ); a border-

line significant finding was also observed for NRS pain-with-activity scores in the immediate postoperative setting ( $P = .059$ ). For RDQ outcomes, the systemic treatment group also had significantly higher numbers of favorable outcomes at 1 week, 1 month, and 1 year following vertebroplasty compared with the untreated group ( $P < .003$ ).

### Complications

Forty-one (24%) patients experienced some form of clinically asymptomatic periprocedural complication; these complications included 15 cases of inadvertent disc-space extravasation, 14 cases of inadvertent paravertebral-space extravasation, and 12 cases of cement extravasation into the epidural space without clinical sequelae. No symptomatic complications were observed in this patient cohort, and the complications did not confound further assessment of clinical status. The median white blood cell count was  $4.3 \times 10^9$  cells/L (IQR =  $3.4-5.6 \times 10^9$  cells/L), while the platelet count was  $154 \times 10^9$ /L (IQR =  $76-215 \times 10^9$ /L). The lowest white blood cell count and platelet count at the time of vertebroplasty were  $1.5 \times 10^9$  cells/L and  $41 \times 10^9$ /L, respectively. Complications were not significantly affected by the presence of ongoing systemic therapy ( $\chi^2 = 0.17$ ,  $P = .68$ ) or derangement in laboratory values at the time of vertebroplasty ( $P > .79$ ).

### DISCUSSION

The findings from this single-center, retrospective study provide robust evidence that vertebroplasty confers significant and durable improvement in pain and disability among patients with myeloma with symptomatic vertebral compression fractures. Our findings suggest that vertebroplasty may be more efficacious among patients with multiple myeloma already on systemic therapy compared with those who undergo vertebroplasty before or at the initiation of therapy. Improvement in pain and disability was similar between patients with more acute and chronic durations of fracture-related pain. Furthermore, complications, when present, were clinically asymptomatic, with no known long-term sequelae and were not correlated with the timing of systemic therapy or derangement in blood chemistries; this result suggests that

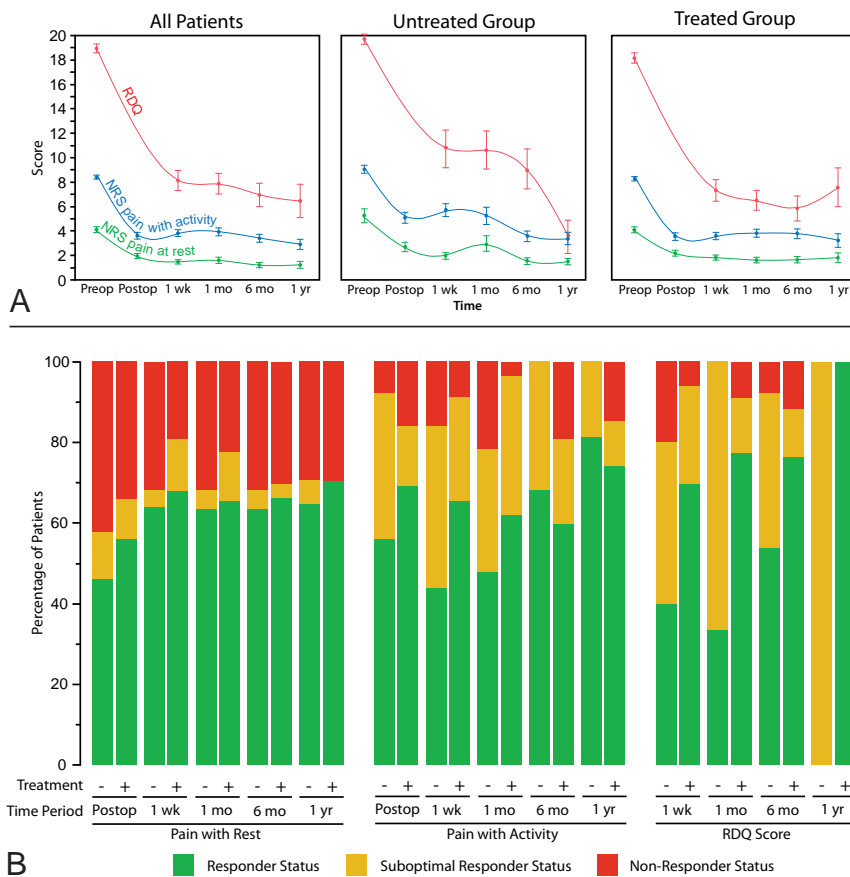


**FIG 4.** Clinical outcomes. Change in median (A) and categoric (B) clinical outcome scores of pain at rest, pain with activity, and RDQ scores. Median scores are shown at preoperative baseline (preop); postoperatively (postop); and 1 week, 1 month, 6 months, and 1 year following vertebroplasty for the entire study cohort (all patients), patients not on systemic therapy at the time of vertebroplasty (untreated group) and patients on systemic therapy at the time of vertebroplasty (treated group). Median RDQ scores are shown in red; NRS pain with activity, in blue; and NRS pain at rest, in green. Categoric clinical outcomes are represented as changes in pain with rest; pain with activity; RDQ scores relative to the preoperative baseline in the immediate postoperative setting (postop); and 1 week, 1 month, 6 months, and 1 year following vertebroplasty. The fraction of patients meeting criteria for responder status are shown in green; suboptimal responder status, in yellow; and nonresponder, status in red.

the safety of vertebroplasty in the patient population with myeloma mirrors that observed in patients with osteoporotic vertebral compression fractures.

These findings complement a 2008 investigation of vertebroplasty in the population with the myeloma by demonstrating the beneficial effects on a much larger patient population and expand these findings by demonstrating that vertebroplasty may confer more favorable outcomes on patients who have already initiated systemic therapy.<sup>6</sup> Such findings can provide guidance to clinicians and radiologists with respect to the timing of their vertebroplasty therapy and provide additional evidence of the efficacy of spinal augmentation in the palliation of pain and disability as demonstrated in multiple recent studies.<sup>11,12</sup> The observation that patients on systemic drug therapy have better postoperative pain and disability scores compared with patients not on systemic therapy was unexpected and may suggest that vertebroplasty can be delayed in patients with early disease to optimize the therapeutic response. Indeed, ongoing systemic drug therapy (corticosteroids, chemotherapy, targeted therapy, or biologic therapy) may be advantageous to vertebroplasty by reducing the amount of

bone turnover and mitigating the amount of bone pain from aberrant osteoblast and osteoclast function. However, it is also possible that the differences in outcomes may be unrelated to systemic therapy and could be a manifestation of an unmeasured confounder or differences in reporting pain among patients with more long-standing bone pain from myeloma. For example, the excess pain reported in the untreated group could reflect additional occult pathologic fractures that are not as common following the initiation of systemic therapy. Furthermore, it is difficult, if not impossible, to extricate myeloma bone pain from mechanical pain in patients not on systemic therapy at the time of vertebroplasty. The origins of this finding merit additional investigation because patients on systemic therapy do experience better outcomes.

The lack of a significant association between the duration of pain and the clinical response to intervention has been previously reported in the vertebroplasty literature but differs somewhat from reports on other spinal procedures (eg, epidural steroid injections) in which patients with longer duration pain have more attenuated benefits to intervention.<sup>13-15</sup> The discrepancies in these findings may be due to several factors. First, the origin of pain from vertebral compression fractures differs from that of radicular-type pain associated with degenerative disease. Second, patients with radicular-type pain are more

likely to have long-standing pain that has failed conservative management, while fracture-related pain is more likely rapidly treated after diagnosis. As such, it is more likely that patients with long-term radicular pain have undergone the physiologic changes associated with chronic pain, with central sensitization and psychological adaptation.<sup>16</sup> Because the phenomenon of central sensitization has been shown to be related to inflammatory changes in the dorsal root ganglion, such causative mechanisms are not expected to be present in most vertebral compression fracture deformities.

This study has several limitations. First, retrospective studies of chronic pain are subject to reporting bias because patients' long-term tolerance to chronic pain can overestimate the significance of a treatment effect, even among newer methods of quantifying chronic pain. While such concerns are valid among long-term pain scores, the observed immediate and short-term improvements in pain and disability are unlikely to be affected by such bias and strongly argue for a favorable treatment effect. Second, our study had substantial loss to follow-up, eliminating 35% of respondents at the 1-year time point. Such loss to follow-up is

common among longitudinal studies and can confound results if this loss is a result of unfavorable clinical outcomes following treatment. However, in the case of this study, loss to follow-up was largely due to repeat vertebroplasty treatment or mortality from multiple myeloma. This outcome would argue against the possibility that the lost cohort represented clinical nonresponders. Third, while we observed better outcomes in the patient group already undergoing systemic therapy, the retrospective nature of this study makes it impossible to identify the origins of this observation or ascribe causality. Furthermore, while the observed significant differences between those on systemic therapy and the untreated group suggest that this study is sufficiently powered for these outcomes, sample size limitations prohibit analysis of outcomes for specific systemic therapies. Fourth, selection bias is also likely a confounder in this study because patients who were not referred and/or offered vertebroplasty were not included in this study. It is unknown whether inclusion of these patients, had they undergone vertebroplasty, would have resulted in a similar degree of pain relief.

## CONCLUSIONS

Vertebroplasty provides a safe and effective means of achieving durable pain relief among patients with myeloma with vertebral compression fractures. Outcomes appear to be more favorable among patients who have previously been initiated on systemic drug therapy, yet the reasons for these differences in outcomes remain unclear and should continue to be investigated.

Disclosures: Jennifer S. McDonald—UNRELATED: Grants/Grants Pending: GE Healthcare,\* Comments: investigator-initiated research grants for contrast-induced nephropathy studies. David F. Kallmes—UNRELATED: Patents (planned, pending or issued): Mayo Foundation,\* Comments: spine augmentation; Royalties: University of Virginia Patent Foundation, Comments: Spine Fusion. Kent R. Thielens—UNRELATED: Royalties: Nevro Corp; Stock/Stock Options: Nevro Corp. Angela Dispenzieri—UNRELATED: Grants/Grants Pending: Celgene,\* Takeda Pharmaceutical Company,\* Janssen Biotech,\* Pfizer,\* Alnylam Pharmaceuticals,\* Comments: research dollars to conduct clinical trials. \*Money paid to the institution.

## REFERENCES

1. Kallmes DF, Jensen ME. Percutaneous vertebroplasty. *Radiology* 2003;229:27–36 CrossRef Medline
2. Klazen CA, Lohle PN, de Vries J, et al. Vertebroplasty versus conservative treatment in acute osteoporotic vertebral compression frac-

3. tures (Vertos II): an open-label randomised trial. *Lancet* 2010;376:1085–92 CrossRef Medline
3. Kallmes DF, Comstock BA, Heagerty PJ, et al. A randomized trial of vertebroplasty for osteoporotic spinal fractures. *N Engl J Med* 2009;361:569–79 CrossRef Medline
4. Cortet B, Cotten A, Boutry N, et al. Percutaneous vertebroplasty in patients with osteolytic metastases or multiple myeloma. *Rev Rhum Engl Ed* 1997;64:177–83 Medline
5. Layton KF, Thielen KR, Cloft HJ, et al. Acute vertebral compression fractures in patients with multiple myeloma: evaluation of vertebral body edema patterns on MR imaging and the implications for vertebroplasty. *AJNR Am J Neuroradiol* 2006;27:1732–34 Medline
6. McDonald RJ, Trout AT, Gray LA, et al. Vertebroplasty in multiple myeloma: outcomes in a large patient series. *AJNR Am J Neuroradiol* 2008;29:642–48 CrossRef Medline
7. Kyle RA, Gertz MA, Witzig TE, et al. Review of 1027 patients with newly diagnosed multiple myeloma. *Mayo Clin Proc* 2003;78:21–33 CrossRef Medline
8. Deramond H, Depriester C, Galibert P, et al. Percutaneous vertebroplasty with polymethylmethacrylate: technique, indications, and results. *Radiol Clin North Am* 1998;36:533–46 CrossRef Medline
9. Patrick DL, Deyo RA, Atlas SJ, et al. Assessing health-related quality of life in patients with sciatica. *Spine (Phila Pa 1976)* 1995;20:1899–908; discussion 909 CrossRef Medline
10. Lauridsen HH, Hartvigsen J, Manniche C, et al. Responsiveness and minimal clinically important difference for pain and disability instruments in low back pain patients. *BMC Musculoskelet Disord* 2006;7:82 CrossRef Medline
11. Wardlaw D, Cummings SR, Van Meirhaeghe J, et al. Efficacy and safety of balloon kyphoplasty compared with non-surgical care for vertebral compression fracture (FREE): a randomised controlled trial. *Lancet* 2009;373:1016–24 CrossRef Medline
12. Jha RM, Hirsch AE, Yoo AJ, et al. Palliation of compression fractures in cancer patients by vertebral augmentation: a retrospective analysis. *J Neurointerv Surg* 2010;2:221–28 CrossRef Medline
13. Alvarez L, Pérez-Higueras A, Granizo JJ, et al. Predictors of outcomes of percutaneous vertebroplasty for osteoporotic vertebral fractures. *Spine (Phila Pa 1976)* 2005;30:87–92 CrossRef Medline
14. Kaufmann TJ, Geske JR, Murthy NS, et al. Clinical effectiveness of single lumbar transforaminal epidural steroid injections. *Pain Med* 2013;14:1126–33 CrossRef Medline
15. Rad AE, Kallmes DF. Pain relief following vertebroplasty in patients with and without localizing tenderness on palpation. *AJNR Am J Neuroradiol* 2008;29:1622–26 CrossRef Medline
16. Latremoliere A, Woolf CJ. Central sensitization: a generator of pain hypersensitivity by central neural plasticity. *J Pain* 2009;10:895–926 CrossRef Medline

# In Vivo Monitoring of Rat Spinal Cord Metabolism Using Hyperpolarized Carbon-13 MR Spectroscopic Imaging

I. Park, S.J. Nelson, and J.F. Talbott



## ABSTRACT

**SUMMARY:** This study demonstrated the feasibility of using hyperpolarized  $^{13}\text{C}$ -MR spectroscopic imaging with  $[1-^{13}\text{C}]$ -pyruvate to evaluate in vivo spinal cord metabolism. High pyruvate and relatively small lactate signal were observed in the cervical spinal cords of naive rats. Lactate and pyruvate measures were similar for spinal cord and supratentorial brain. The results from this study establish baseline measures for spinal cord hyperpolarized MRS imaging with  $^{13}\text{C}$  pyruvate. This technique holds promise as a valuable molecular imaging tool for monitoring biochemical processes in the normal and diseased spinal cord.

**ABBREVIATION:** MRSI = MR spectroscopic imaging

Traumatic spinal cord injury is a devastating neurologic disorder affecting approximately 12,000 people in the United States each year.<sup>1</sup> Secondary injury, which occurs hours to months after initial primary traumatic insult, contributes to metabolic stress and progressive tissue damage and serves as a prime target for therapeutic intervention.<sup>2</sup> Current noninvasive methods to monitor these processes are significantly limited.  $^1\text{H}$ -MRS of spine suffers from low SNR, physiologic motion, and magnetic field inhomogeneity related to the bony spine.<sup>3</sup>

Dissolution dynamic nuclear polarization enables the acquisition of  $^{13}\text{C}$  MR data with a dramatic gain in sensitivity over conventional  $^{13}\text{C}$  MR methods.<sup>4</sup> Recent studies using the hyperpolarized substrate  $[1-^{13}\text{C}]$ -pyruvate have demonstrated the promise of this technique for examining in vivo metabolism in brain.<sup>5,6</sup> A first-in-human study using hyperpolarized  $^{13}\text{C}$ -MR spectro-

scopic imaging (MRSI) showed the safety and feasibility of this technology for evaluating real-time metabolism in humans.<sup>7</sup>

The purpose of this study was to explore the feasibility of using hyperpolarized  $^{13}\text{C}$ -MRSI with  $[1-^{13}\text{C}]$ -pyruvate for evaluating in vivo metabolism of the spinal cord in rodents and establish baseline spectroscopic measures in the spinal cord relative to brain.

## MATERIALS AND METHODS

A total of 6 healthy male Sprague-Dawley rats (median weight, 320 g) were included in this study. Animal studies were approved by the Institutional Animal Care and Use Committee.

Animals were scanned on a 3T clinical MR imaging system (Discovery MR750; GE Healthcare, Milwaukee, Wisconsin) with 40 mT/m, 150 mT/m/ms gradients, a multinuclear spectroscopy hardware package, and a custom-designed, dual-tuned volume radiofrequency coil with a quadrature  $^{13}\text{C}$  channel and linear  $^1\text{H}$  channel with a length of 9 cm. During each imaging session, rats were placed prone on a heated pad positioned inside the radiofrequency coil and scanner. Cervical lordosis was straightened with padding under the ventral neck to minimize partial volume effects with nonspinal tissue when imaging in the axial plane (Fig 1A). The spine at C4–C5 was placed at the center of the radiofrequency coil so that both the spine at C4–C5 position and the supratentorial brain were located within the 7-cm effective region of the coil. Anesthesia was maintained with a constant delivery of isoflurane (approximately 1.5%). Before each  $^{13}\text{C}$  imaging session, high-resolution T2WI was obtained in the axial plane by using an FSE sequence (TE, 60 ms; TR, 4000 ms; FOV, 8 cm; matrix size, 256 × 256; 2-mm section thickness; and NEX, 8). For each  $^{13}\text{C}$  experiment, a mixture of 35  $\mu\text{L}$  of  $[1-^{13}\text{C}]$ -pyruvate, 15 mmol/L OX063 trityl radical (GE Healthcare), and 1.5 mmol/L Gd-DOTA was

Received June 3, 2016; accepted after revision July 6.

From the Department of Radiology and Biomedical Imaging (I.P., S.J.N., J.F.T.), Department of Bioengineering and Therapeutic Sciences (S.J.N.), and Brain and Spinal Injury Center (BASIC), San Francisco General Hospital (J.F.T.), University of California, San Francisco, San Francisco, California.

Dr. Ilwoo Park was supported by a National Cancer Institute training grant in translational brain tumor research (T32 CA151022). Support for the research studies came from National Institutes of Health grants R01EB013427, P41EB013598, and R21CA170148.

Paper previously presented in part at: Annual Meeting of the International Society of Magnetic Resonance in Medicine (ISMRM), May 30–31, 2015; Toronto, Ontario, Canada.

Please address correspondence to Ilwoo Park, PhD, Department of Radiology & Biomedical Imaging, 1700 4th St, Box 2532, BH-303, University of California, San Francisco, San Francisco, CA 94158; e-mail: ilwoo.park@ucsf.edu

Indicates open access to non-subscribers at www.ajnr.org

<http://dx.doi.org/10.3174/ajnr.A4920>

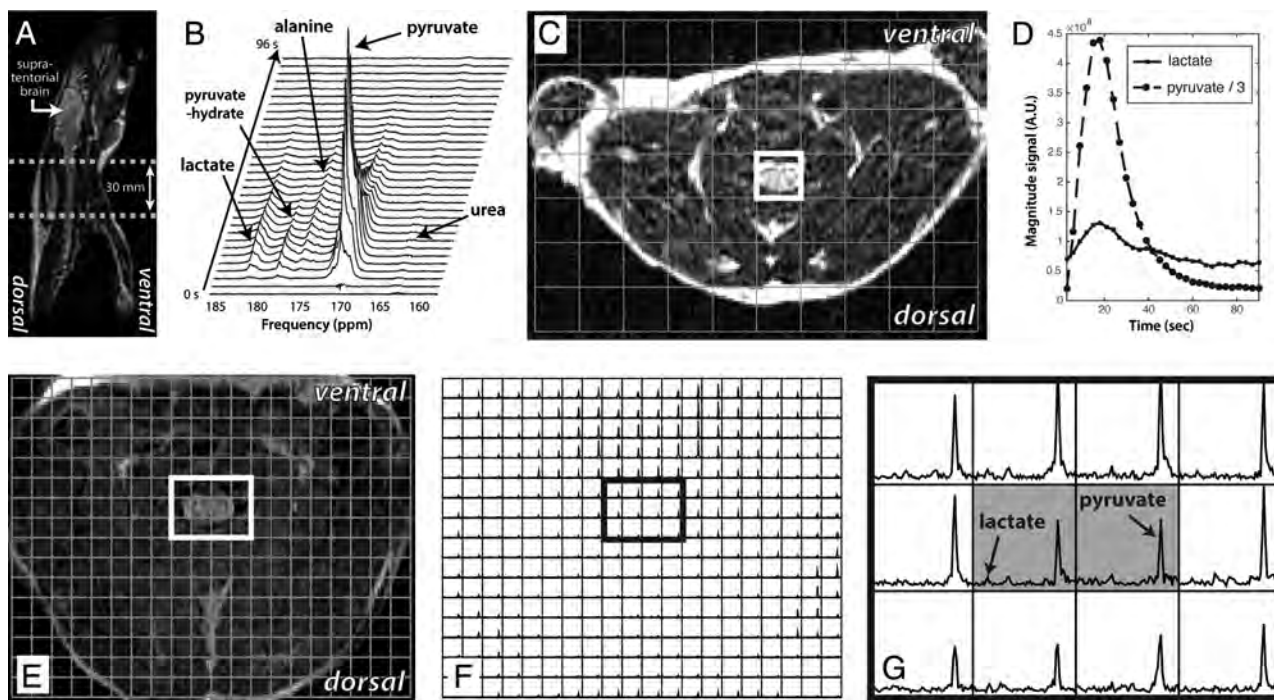


**FIG 1.** An example of hyperpolarized  $^{13}\text{C}$  data from a naive rat. *A*, Horizontal dashed lines encompassing the neck delimit a 30-mm axial slab used for acquiring dynamic data in *B*. *B*, A stack plot of dynamic  $^{13}\text{C}$  data from a 30-mm slab. *C*, Axial T2WI of the neck centered at C4 with  $^{13}\text{C}$  spectral grid overlay for 2D-localized  $^{13}\text{C}$  dynamic data. *D*, Dynamic pyruvate and lactate signal change over time as measured from a  $4.8 \times 4.8 \times 15$  mm voxel primarily limited to the cervical spinal cord (white box, *C*). *E*, Axial T2WI with  $^{13}\text{C}$  spectral grid overlay for 3D  $^{13}\text{C}$ -MRS imaging. *F*, The corresponding  $^{13}\text{C}$  spectra with high spatial resolution ( $2 \times 2$  mm in-plane voxel size) from a 5.4-mm axial section centered at the C4 vertebral level. *G*, Zoomed-in  $^{13}\text{C}$  spectra targeting the spinal cord show high pyruvate and relatively small lactate signal in the spinal cord (highlighted voxels).

polarized by using a HyperSense polarizer (Oxford Instruments, Oxfordshire, United Kingdom) at 3.35T and 1.4K by irradiation with 94.1 GHz microwaves by using methods described previously.<sup>4</sup> After 60 minutes of microwave irradiation, the mixture was rapidly dissolved in a saline solution with 5.96 g/L Tris (40 mmol/L), 4.00 g/L NaOH (100 mmol/L), and 0.1 mg/L Na<sup>2</sup> ethylenediaminetetraacetic acid. The final solution had a concentration of 100 mmol/L pyruvate and pH  $\sim 7.5$ . A sample from the dissolved pyruvate solution with volume of 2.8 mL was injected into the tail vein of the rat over a 10-second duration.

To determine an optimal temporal imaging window for acquiring 3D MRSI data, initial dynamic  $^{13}\text{C}$  spectroscopic data were acquired from 2 rats. In 1 animal, section-localized data from a 30-mm axial slab encompassing the entire neck were acquired (Fig 1A, -B; TE, 35 ms; TR, 3000 ms; flip angle, 10°; 3-second temporal resolution; and 32 total time points). To more specifically gauge temporal evolution of signal within spinal tissue of the neck, 2D-localized multivoxel data from a 15-mm axial section centered at the C4 vertebral level were acquired in a single animal (TE, 6.1 ms; TR, 130 ms; flip angle, 5°; 3-second temporal resolution; 30 total time points; 10 phase encodes in the right-left direction; and a symmetric echo-planar readout in the anteroposterior direction providing  $4.8 \times 4.8$  mm in-plane resolution).<sup>8</sup> Section-localized and multivoxel 2D-localized data were acquired from each animal simultaneously with the injection of pyruvate solution.

Compressed-sensing  $^{13}\text{C}$  3D-MRSI data then were separately acquired from a total of 6 rats (including 2 rats described above)

by using a double spin-echo sequence (TE, 140 ms; TR, 215 ms) with centric *k*-space encoding, a variable flip angle scheme, and flyback echo-planar readout on the z-axis<sup>5</sup> at 18 seconds from the start of the injection. Eighty-six phase encodes were collected from a  $20 \times 16$  matrix in 18 seconds, resulting in  $2 \times 2$  mm in-plane resolution with 16 5.4-mm sections.

The methods for processing  $^{13}\text{C}$  data have been described previously.<sup>5-8</sup> The SNR of lactate, pyruvate, and ratio of lactate over pyruvate were calculated from the  $^{13}\text{C}$  3D-MRSI data by using the magnitude spectra. To estimate the SNR, the peak height for lactate and pyruvate were scaled by the standard deviation of the noise estimated from the spectrum that contained no metabolite resonances. The SNR of lactate, pyruvate, and ratio of lactate over pyruvate were estimated from voxels in the spine and compared with the corresponding values from voxels in supratentorial brain by using a 2-tailed paired *t* test.

## RESULTS

Representative spectroscopic data are provided in Fig 1.  $^{13}\text{C}$  spectra from the 30-mm axial section-localized acquisition encompassing the entire neck revealed  $[1-^{13}\text{C}]$ -pyruvate signal (171 ppm) reaching its maximum amplitude at approximately 15 seconds after the start of hyperpolarized pyruvate injection, followed by the maximum  $[1-^{13}\text{C}]$ -lactate signal (183 ppm) at approximately 18 seconds (Fig 1B). After reaching its maximum, the pyruvate signal decreased rapidly, and the lactate signal decreased at a slower rate than pyruvate. Small  $[1-^{13}\text{C}]$ -alanine, pyruvate-

### Summary of $^{13}\text{C}$ metabolite quantification<sup>a</sup>

Location	Pyruvate SNR	Lactate SNR	Lac/Pyr
Normal spine ( $n = 6$ )	$32.1 \pm 7.5$	$6.1 \pm 1.0$	$0.23 \pm 0.05$
Supratentorial normal brain ( $n = 6$ )	$29.2 \pm 5.2$	$6.0 \pm 0.8$	$0.23 \pm 0.04$

**Note:**—Lac/Pyr indicates the ratio of lactate to pyruvate.

<sup>a</sup> All values are mean  $\pm$  standard error.

hydrate, and urea peaks from an external reference also were observed.

Dynamic acquisition of pyruvate and lactate signal from a  $4.8 \times 4.8 \times 15$  mm voxel primarily encompassing the spinal cord (white box in Fig 1C) were plotted over time (Fig 1D). Both pyruvate and lactate signal reached maximum amplitude approximately 18 seconds after pyruvate injection, very similar to the temporal profile for  $^{13}\text{C}$  spectra sampling the entire neck. This  $^{13}\text{C}$  temporal profile closely matches results observed in the normal rat brain.<sup>5</sup> The period of 18–35 seconds after injection was therefore used as an imaging window for subsequent  $^{13}\text{C}$  3D-MRSI studies.

$^{13}\text{C}$  3D-MRSI reveals prominent pyruvate signal symmetrically within the ventrolateral soft tissues of the neck corresponding to the anatomic location of major neck vessels, consistent with blood pool signal (Fig 1F). The  $^{13}\text{C}$  spectra corresponding to the spinal cord exhibited pyruvate peaks with excellent SNR and relatively small lactate peaks in the normal cord (highlighted voxels in Fig 1G). The SNR of pyruvate and lactate as well as ratio of lactate over pyruvate were compared between the spine and supratentorial brain in the Table. Ratio of lactate over pyruvate in the spine was  $0.23 \pm 0.05$  (mean  $\pm$  standard error), which is similar to the respective value from supratentorial normal brain tissue ( $P > .8$ ).

### DISCUSSION

We have demonstrated the feasibility of using hyperpolarized  $^{13}\text{C}$  metabolic imaging for assessing in vivo metabolism in the cervical spine of rats. The use of hyperpolarized [ $1\text{-}^{13}\text{C}$ ]-pyruvate provided sufficient signal to detect its transfer of the  $^{13}\text{C}$  label to lactate in the spinal cord. High spatial resolution of  $^{13}\text{C}$  spectra ( $2 \times 2$  mm in-plane voxel size) enabled the voxel segmentation of the cord into hemicords, which will enable the comparison of hemicord lesion with a contralateral hemicord.<sup>9</sup>

We believe that the molecular imaging technique presented in this paper will be most valuable in the setting of moderate spinal cord injuries, where prognosis is unclear based on clinical and conventional MR imaging sequences.<sup>10</sup> In case of severe spinal

cord trauma with the presence of significant hemorrhage, the susceptibility artifact due to blood products might pose a challenge in analyzing data acquired using hyperpolarized  $^{13}\text{C}$  metabolic imaging.

The results from this study establish baseline pyruvate and lactate measures in the normal spinal cord and suggest that hyperpolarized  $^{13}\text{C}$  pyruvate MRSI is a promising noninvasive tool for monitoring biochemical processes in the spinal cord.

**Disclosures:** Ilwoo Park—RELATED: Grant: National Institutes of Health,\* Comments: National Institutes of Health grants R01EB013427, P41EB013598, and R21CA170148. National Cancer Institute,\* Comments: National Cancer Institute training grant in translational brain tumor research (T32 CA151022). Sarah J. Nelson—UNRELATED: Grants/Grants Pending: GE Healthcare,\* Comments: academic-industry partnership related to imaging technology development. Jason Talbott—UNRELATED: Consultancy: StemCells, Inc, Comments: data monitoring committee for clinical trial; now dissolved.\*Money paid to the institution.

### REFERENCES

1. Looby S, Flanders A. **Spine trauma.** *Radiol Clin North Am* 2011;49:129–63 CrossRef Medline
2. Oyinbo CA. **Secondary injury mechanisms in traumatic spinal cord injury: a nugget of this multiply cascade.** *Acta Neurobiol Exp (Wars)* 2011;71:281–99 Medline
3. Stroman PW, Wheeler-Kingshott C, Bacon M, et al. **The current state-of-the-art of spinal cord imaging: methods.** *Neuroimage* 2014;84:1070–81 CrossRef Medline
4. Ardenkjaer-Larsen JH, Fridlund B, Gram A, et al. **Increase in signal-to-noise ratio of  $> 10,000$  times in liquid-state NMR.** *Proc Natl Acad Sci U S A* 2003;100:10158–63 CrossRef Medline
5. Park I, Hu S, Bok R, et al. **Evaluation of heterogeneous metabolic profile in an orthotopic human glioblastoma xenograft model using compressed sensing hyperpolarized 3D  $^{13}\text{C}$  magnetic resonance spectroscopic imaging.** *Magn Reson Med* 2013;70:33–39 CrossRef Medline
6. Park I, Mukherjee J, Ito M, et al. **Changes in pyruvate metabolism detected by magnetic resonance imaging are linked to DNA damage and serve as a sensor of temozolomide response in glioblastoma cells.** *Cancer Res* 2014;74:7115–24 Medline
7. Nelson SJ, Kurhanewicz J, Vigneron DB, et al. **Metabolic imaging of patients with prostate cancer using hyperpolarized [ $1\text{-}^{13}\text{C}$ ]pyruvate.** *Sci Transl Med* 2013;5:198ra108 CrossRef Medline
8. Park I, Larson PE, Tropp JL, et al. **Dynamic hyperpolarized carbon-13 MR metabolic imaging of nonhuman primate brain.** *Magn Reson Med* 2014;71:19–25 CrossRef Medline
9. Gensel JC, Tovar CA, Hamers FP, et al. **Behavioral and histological characterization of unilateral cervical spinal cord contusion injury in rats.** *J Neurotrauma* 2006;23:36–54 CrossRef Medline
10. Bozzo A, Marcoux J, Radhakrishna M, et al. **The role of magnetic resonance imaging in the management of acute spinal cord injury.** *J Neurotrauma* 2011;28:1401–11 CrossRef Medline

## Regarding “Computer-Assisted Detection of Cerebral Aneurysms in MR Angiography in a Routine Image-Reading Environment: Effects on Diagnosis by Radiologists”

**W**e thank Miki et al<sup>1</sup> for presenting their results on using computer-assisted detection (CAD) with MR angiography to identify cerebral aneurysms. Their article raises some pertinent questions and concerns.

With the final consensus by 2 radiologists as the reference standard, the sensitivity for MRA detection of aneurysms was 64% and 69%, respectively, and went up to 69% with CAD. Such poor sensitivity raises the question of the utility of MRA as a screening test, despite all these studies having been performed on a 3T scanner. Should <70% sensitivity be considered adequate for a screening test of the whole population?

To assess the utility of CAD, one has to look at the aneurysms supposedly missed by radiologists and picked up by CAD. In 124/203 cases, the radiologist did not see the aneurysm even after CAD pointed it out. In 90 of these cases, the radiologists did not change their diagnoses, even after CAD, but changed their minds when consensus was reached with another person.

CAD failed to detect 37/203 aneurysms as the top 3 lesion candidates, including 2 aneurysms measuring  $\geq 5$  mm.

Most of the aneurysms missed by CAD were  $\leq 4$  mm. As expected, these are also the ones missed frequently by the radiologists. As per the study, CAD detected 24 additional aneurysms, only 1 of which was  $>4$  mm.

The authors report that the median time required for reviewing the CAD results and giving feedback was 16 seconds. However, in a routine clinical setting, it is difficult to imagine that incorporating CAD would have such little impact on workflow and reading time, especially when the finding considered suspi-

cious by CAD is frequently not considered positive by the radiologist subsequently.

Using consensus as the reference standard also raises an important question based on the frequency at which opinions were changed after consulting with another radiologist, creating subjectivity on the results.

It would be interesting to see whether the authors could share the outcomes/differences in patient management on the basis of these results. Very small aneurysms have a very low reported rupture rate.<sup>2</sup> The prevalence of a 7% incidental detection rate, with most being small aneurysms, begs the question of how to manage these small incidental lesions and the utility of such a screening program.

The authors' conclusions that CAD is feasible and can add value is open to interpretation, given the data in this study. A screening program with such inadequate sensitivity, high subjectivity, and unclear outcome needs further clarification and consideration.

### REFERENCES

1. Miki S, Hayashi N, Masutani Y, et al. **Computer-assisted detection of cerebral aneurysms in MR angiography in a routine image-reading environment: effects on diagnosis by radiologists.** *AJNR Am J Neuroradiol* 2016;37:1038–43 CrossRef Medline
2. Murayama Y, Takao H, Ishibashi T, et al. **Risk analysis of unruptured intracranial aneurysms: prospective 10-year cohort study.** *Stroke* 2016;47:365–71 CrossRef Medline

 X. Wu

 V.B. Kalra

 D. Durand

 R.C. Liu

 A. Malhotra

Department of Radiology and Biomedical Imaging  
Yale School of Medicine  
New Haven, Connecticut

<http://dx.doi.org/10.3174/ajnr.A4926>

**REPLY:**

We appreciate the insightful comments by Wu et al on our recent article “Computer-Assisted Detection of Cerebral Aneurysms in MR Angiography in a Routine Image-Reading Environment: Effects on Diagnosis by Radiologists.”<sup>1</sup> We would like to address their comments and concerns.

**Apparently Low Sensitivity of Both Human and Computer-Assisted Detection**

First, as we described in the “Limitations” section, these “sensitivity” figures should be seen as rough estimates because the reference standard diagnoses were not determined independently by the 2 assigned radiologists. These figures largely reflect the relatively high interobserver disagreement between the 2 radiologists. Second, having a low sensitivity does not necessarily mean that we do not need screening or computer-assisted detection (CAD). Breast cancer screening by mammography, which is commonly performed with the aid of CAD, also has an unsatisfactory sensitivity, but this per se is not a limiting factor for the use of CAD. We consider that more important points are the following: 1) how often the radiologist changes his or her mind after reviewing CAD, and 2) whether that change is beneficial or detrimental. On our radiologist-oriented analysis, we found that roughly 10% more aneurysms were reported by radiologists by using CAD, which is not negligible. In addition, if we consider these additional aneurysms (ie, “missed true-positive” cases), findings for all except 1 were positive in the final diagnosis—that is, although CAD tended not to change radiologists’ initial diagnoses very often, when it did, the aneurysms were obvious ones that were purely overlooked. Therefore, we believe CAD can help radiologists interpret at least in a consistent manner, reducing the inter- and intraobserver disagreement.

<http://dx.doi.org/10.3174/ajnr.A4941>

**Management of Small Aneurysms**

We agree that small aneurysms have a low rupture rate, and invasive interventions are generally no longer justified. In The University of Tokyo Hospital, all aneurysms are reported regardless of their size, but most cases with small aneurysms are simply followed up. The number of cases with large aneurysms in our study was not large enough, and we admit this small number was one of the limitations of our study.

**Time to Check CAD Results**

The seemingly short reviewing time (median, 16 seconds) was because the Web-based CAD server has the basic built-in paging functionality, which enables the radiologist to dismiss obvious false-positive results within a few seconds. If CAD is to be used in routine clinical practice, the effectiveness of the reviewing process is a vital requirement. When there is a suspicious lesion, the reviewing process will naturally take much longer, and there were actually many cases in which it took minutes to review the CAD results. However, because this study was conducted in a routine environment, these included some cases for which the interpretation was interrupted by a sudden phone call, for example. Therefore, we only presented the median time as the meaningful value.

**REFERENCE**

1. Miki S, Hayashi N, Masutani Y, et al. **Computer-assisted detection of cerebral aneurysms in MR angiography in a routine image-reading environment: effects on diagnosis by radiologists.** *AJNR Am J Neuroradiol* 2016;37:1038–43 CrossRef Medline

**S. Miki  
N. Hayashi  
Y. Nomura**

Department of Computational Diagnostic Radiology and Preventive Medicine  
The University of Tokyo Hospital  
Tokyo, Japan

**Y. Masutani**

Faculty of Information Sciences and Graduate School of Information Sciences  
Hiroshima City University  
Hiroshima, Japan

## Addressing Concerns Regarding the Use of Gadolinium in a Standardized MRI Protocol for the Diagnosis and Follow-Up of Multiple Sclerosis

The “Consortium of MS Centers Task Force for a Standardized MRI Protocol and Clinical Guidelines for the Diagnosis and Follow-Up of Multiple Sclerosis”<sup>1</sup> recommended the use of brain MR imaging with gadolinium for the diagnosis and routine follow-up of patients with multiple sclerosis. Soon after the publication of these recommendations, we became aware of the concerns regarding gadolinium deposition in the brain.<sup>2</sup> Because the adverse health effects of gadolinium deposits in the brains of patients are unknown, we believe gadolinium-based contrast agents (GBCA) should be used judiciously as part of a standardized MR imaging protocol. This is an important change compared with our recommendations published earlier this year.<sup>1</sup>

The US Food and Drug Administration announcement noted that accumulation of GBCA may occur after  $\geq 4$  MR imaging scans, even long after administration.<sup>2</sup> Low-stability agents are the GBCA most often associated with gadolinium deposits in the brain.<sup>3</sup> To date, although there have been no reports of signs or symptoms of central nervous system toxicity related to GBCA, to reduce the potential for gadolinium accumulation, the FDA has recommended that “health care professionals should consider limiting GBCA use to clinical circumstances in which the additional information provided by the contrast is necessary. Health care professionals are also urged to reassess the necessity of repetitive GBCA MRIs in established treatment protocols.”<sup>2</sup>

Using a standardized protocol to follow patients with MS is of the utmost importance. Annual MRIs that detect new clinically silent disease activity enable health care providers to treat patients earlier in the course of the disease and modify and change therapy. Thus, routine monitoring of individuals with MS is recommended. The use of GBCA is helpful but not essential for detecting subclinical disease activity because new T2 MS lesions can be identified on well-performed standardized MR imaging.

GBCA continue to play an invaluable role in specific circumstances related to the diagnosis and assessment of individuals with MS.<sup>1</sup> It is important to use GBCA in patients presenting with their first clinical attack (or so called “clinically isolated syndrome”) in the initial diagnosis of MS; the use of GBCA allows an earlier diagnosis by demonstrating lesion dissemination in space and

time, the hallmarks for a diagnosis of MS, with the first MR imaging scan. Early diagnosis is a special circumstance in which gadolinium is indispensable because an early diagnosis leads to early treatment, which helps in preventing disease progression and may improve the patient’s long-term prognosis.

There are a number of other clinical circumstances in which use of GBCA is essential, including following a patient with highly active disease, when a patient’s condition is rapidly declining and unexplained, and when there is a high concern regarding an alternate diagnosis other than MS. However, pending a revision of the recommendations published earlier this year, gadolinium could be considered optional for the routine monitoring of an otherwise stable patient with MS.

Use of a standardized protocol for patients with active disease is especially important. The new phenotypes as defined by Lublin et al<sup>4</sup> include the objective criteria of disease activity provided by imaging findings in addition to disease progression. Use of MR imaging is important in providing accurate clinical course descriptions,<sup>4</sup> but again, this may be accomplished without the use of GBCA for every scan by the detection of new T2 lesions on standardized T2/FLAIR sequences, which can be compared across studies.

Physicians and health care professionals caring for patients with MS are strongly encouraged to adopt the “Recommendations of the Consortium of MS Centers Task Force for a Standardized MRI Protocol and Clinical Guidelines for the Diagnosis and Follow-Up of Multiple Sclerosis.”<sup>1</sup> As indicated, we would recommend judicious use of GBCA in certain circumstances, including early diagnosis of MS. We anticipate revisions to the guidelines based on evolving knowledge surrounding gadolinium safety and the new McDonald criteria.

### REFERENCES

1. Traboulsee A, Simon JH, Stone L, et al. **Revised Recommendations of the Consortium of MS Centers Task Force for a Standardized MRI Protocol and Clinical Guidelines for the Diagnosis and Follow-Up of Multiple Sclerosis.** *AJNR Am J Neuroradiol* 2016;37:394–401 CrossRef Medline
2. U.S. Food and Drug Administration. FDA Drug Safety Communication: FDA evaluating the risk of brain deposits with repeated use of gadolinium-based contrast agents for magnetic resonance im-

- aging (MRI). Safety Announcement. July 27, 2015. <http://www.fda.gov/Drugs/DrugSafety/ucm455386.htm>. Accessed June 29, 2016
3. Ramalho J, Semelka RC, Ramalho M, et al. **Gadolinium-based contrast agent accumulation and toxicity: an update.** *AJNR Am J Neuroradiol* 2016;37:1192–98 CrossRef Medline
  4. Lublin FD, Reingold SC, Cohen JA, et al. **Defining the clinical course of multiple sclerosis: the 2013 revisions.** *Neurology* 2014;83:278–86 CrossRef Medline

 **A. Trabousee**

Department of Medicine (Neurology)

 **D. Li**

Department of Radiology  
University of British Columbia  
Vancouver, Canada